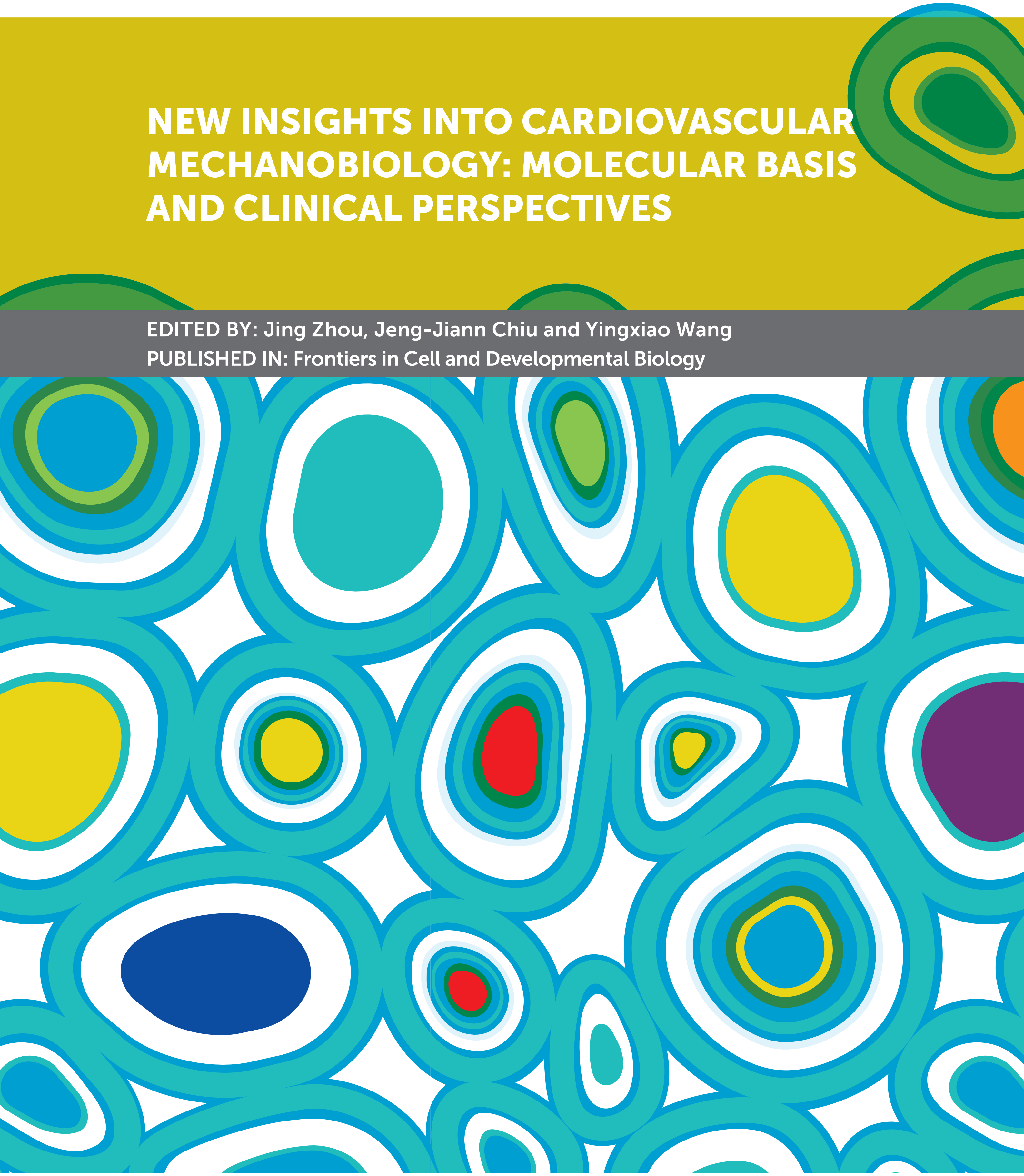

NEW INSIGHTS INTO CARDIOVASCULAR MECHANOBIOLOGY: MOLECULAR BASIS AND CLINICAL PERSPECTIVES

EDITED BY: Jing Zhou, Jeng-Jiann Chiu and Yingxiao Wang
PUBLISHED IN: Frontiers in Cell and Developmental Biology

frontiers Research Topics

ISSN 1664-8714
ISBN 978-2-88971-738-5
DOI 10.3389/978-2-88971-738-5

About Frontiers

Frontiers is more than just an open-access publisher of scholarly articles: it is a pioneering approach to the world of academia, radically improving the way scholarly research is managed. The grand vision of Frontiers is a world where all people have an equal opportunity to seek, share and generate knowledge. Frontiers provides immediate and permanent online open access to all its publications, but this alone is not enough to realize our grand goals.

Frontiers Journal Series

The Frontiers Journal Series is a multi-tier and interdisciplinary set of open-access, online journals, promising a paradigm shift from the current review, selection and dissemination processes in academic publishing. All Frontiers journals are driven by researchers for researchers; therefore, they constitute a service to the scholarly community. At the same time, the Frontiers Journal Series operates on a revolutionary invention, the tiered publishing system, initially addressing specific communities of scholars, and gradually climbing up to broader public understanding, thus serving the interests of the lay society, too.

Dedication to Quality

Each Frontiers article is a landmark of the highest quality, thanks to genuinely collaborative interactions between authors and review editors, who include some of the world's best academicians. Research must be certified by peers before entering a stream of knowledge that may eventually reach the public - and shape society; therefore, Frontiers only applies the most rigorous and unbiased reviews.
Frontiers revolutionizes research publishing by freely delivering the most outstanding research, evaluated with no bias from both the academic and social point of view.
By applying the most advanced information technologies, Frontiers is catapulting scholarly publishing into a new generation.

What are Frontiers Research Topics?

Frontiers Research Topics are very popular trademarks of the Frontiers Journals Series: they are collections of at least ten articles, all centered on a particular subject. With their unique mix of varied contributions from Original Research to Review Articles, Frontiers Research Topics unify the most influential researchers, the latest key findings and historical advances in a hot research area! Find out more on how to host your own Frontiers Research Topic or contribute to one as an author by contacting the Frontiers Editorial Office: frontiersin.org/about/contact

NEW INSIGHTS INTO CARDIOVASCULAR MECHANOBIOLOGY: MOLECULAR BASIS AND CLINICAL PERSPECTIVES

Topic Editors:
Jing Zhou, Peking University, China
Jeng-Jiann Chiu, National Health Research Institutes (Taiwan), Taiwan
Yingxiao Wang, University of California, San Diego, United States

Citation: Zhou, J., Chiu, J.-J., Wang, Y., eds. (2021). New Insights into Cardiovascular Mechanobiology: Molecular Basis and Clinical Perspectives. Lausanne: Frontiers Media SA. doi: 10.3389/978-2-88971-738-5

Table of Contents

frontiers
in Cell and Developmental Biology

ORIGINAL RESEARCH
published: 23 October 2020
doi: 10.3389/fcell.2020.583700

Inflammatory Cytokines Alter Mesenchymal Stem Cell Mechanosensing and Adhesion on Stiffened Infarct Heart Tissue After Myocardial Infarction

Dan Zhu[1†], Peng Wu[1,2†], Changchen Xiao[1], Wei Hu[3], Tongtong Zhang[3], Xinyang Hu[1], Wei Chen[1,3]* and Jian'an Wang[1]*

[1] Department of Cardiology of the Second Affiliated Hospital, Zhejiang University School of Medicine, Hangzhou, China, [2] Department of Pharmacology, Zhejiang University School of Medicine, Hangzhou, China, [3] Key Laboratory for Biomedical Engineering of the Ministry of Education, College of Biomedical Engineering and Instrument Science, Zhejiang University, Hangzhou, China

Mesenchymal stem cell (MSC) transplantation has demonstrated its potential in repairing infarct heart tissue and recovering heart function after myocardial infarction (MI). However, its therapeutic effect is still limited due to poor MSC engraftment at the injury site whose tissue stiffness and local inflammation both dynamically and rapidly change after MI. Whether and how inflammatory cytokines could couple with stiffness change to affect MSC engraftment in the infarct zone still remain unclear. In this study, we characterized dynamic stiffness changes of and inflammatory cytokine expression in the infarct region of rat heart within a month after MI. We found that the tissue stiffness of the heart tissue gradually increased and peaked 21 days after MI along with the rapid upregulation of tumor necrosis factor-α (TNF-α), interleukin-6 (IL-6), and interleukin-1β (IL-1β) in the first 3 days, followed by a sharp decline. We further demonstrated *in vitro* that immobilized inflammatory cytokine IL-6 performed better than the soluble form in enhancing MSC adhesion to stiffened substrate through IL-6/src homology 2 (SH2) domain-containing tyrosine phosphatase-2 (SHP2)/integrin signaling axis. We also confirmed such mechano-immune coupling of tissue stiffness and inflammatory cytokines in modulating MSC engraftment in the rat heart after MI *in vivo*. Our study provides new mechanistic insights of mechanical–inflammation coupling to improve MSC mechanosensing and adhesion, potentially benefiting MSC engraftment and its clinical therapy for MI.

Keywords: cytokine, mechanosensing, adhesion, mesenchymal stem cell, myocardial infarction

Edited by:
Jing Zhou,
Peking University, China

Reviewed by:
Xiaohai Zhou,
University of California, San Diego,
United States
Chia-Ching Wu,
National Cheng Kung University,
Taiwan

***Correspondence:**
Wei Chen
jackweichen@zju.edu.cn
Jian'an Wang
wangjianan111@zju.edu.cn

[†] *These authors share first authorship*

Specialty section:
This article was submitted to Cell Adhesion and Migration, a section of the journal Frontiers in Cell and Developmental Biology

Received: *15 July 2020*
Accepted: *01 October 2020*
Published: *23 October 2020*

Citation:
Zhu D, Wu P, Xiao C, Hu W, Zhang T, Hu X, Chen W and Wang J (2020) Inflammatory Cytokines Alter Mesenchymal Stem Cell Mechanosensing and Adhesion on Stiffened Infarct Heart Tissue After Myocardial Infarction. Front. Cell Dev. Biol. 8:583700. doi: 10.3389/fcell.2020.583700

INTRODUCTION

Acute myocardial infarction (AMI) is a leading cause of human mortality worldwide. It triggers an acute inflammatory response and tissue fibrosis that significantly stiffen the infarct tissue of the heart, impairing the contraction ability of the myocardium and heart function (Liehn et al., 2011; Frangogiannis, 2014). Most clinically approved treatments for MI only modulate hemodynamics to reduce early mortality but are unable to repair infarcted myocardium or recover heart function to reduce the following incidence of heart failure (Ranganath et al., 2012; Miao et al., 2017).

In recent decades, mesenchymal stem cell (MSC) transplantation has demonstrated its potential for repairing infarcted myocardium and restoring heart function through its anti-inflammation and anti-fibrosis functions (Miao et al., 2017). However, its therapeutic efficacy observed in randomized controlled clinical trials has been limited. A meta-analysis reported that an increase of the left ventricular ejection fractions (LVEFs) with MSC therapy by only 2.92% and reducing the incidence of heart failure in response to the therapy is not significantly better compared to revascularization procedure [percutaneous coronary intervention (PCI) or thrombolysis or coronary artery bypass surgery] (Afzal et al., 2015). It was reported that only a small percentage of MSCs are retained at the injury site after transplantation (Lee et al., 2009). This low MSC engraftment rate could be one of the major obstacles in enhancing the efficacy of MSC-based therapy (Sanganalmath and Bolli, 2013). In fact, several approaches have been developed to enhance MSC engraftment. For example, preconditioning MSCs with hypoxia has been shown to maintain cell viability and improve MSC engraftment through the leptin signaling pathway (Hu et al., 2014). Although pro-survival strategies have been proven to be effective, they still have not solved the problem of poor adhesion of MSCs to the extracellular matrix (ECM), which is the prerequisite for a successful engraftment of MSC therapy.

Cell adhesion to the ECM is modulated by mechanical properties of ECM, which change dynamically after the onset of AMI due to the pathological process of inflammation and tissue fibrosis (Discher et al., 2005; Trichet et al., 2012; Elosegui-Artola et al., 2016). Cells probe substrate stiffness through mechanosensing machinery that involves integrins, focal adhesion (FA) proteins, and the actomyosin cytoskeleton (Roca-Cusachs et al., 2012; Elosegui-Artola et al., 2016), among which integrin's binding with ECM provides the main mechanical linkage. In response to matrix stiffness increase, cells generate larger force, which not only strengthens the integrin/ECM binding through "catch bond" but also induces clustering of integrin to promote adhesion development (Kong et al., 2009; Roca-Cusachs et al., 2009; Changede et al., 2015). Stiffness of the infarct region along with the progression of heart remodeling after MI was reported to range from several kPa to tens of MPa (Berry, 2006; Zhang et al., 2011; Arunachalam et al., 2018; Rusu et al., 2019), which may differentially promote MSC adhesion and engraftment.

Other than remodeling of mechanical properties of the infarct region, inflammatory cytokines also dynamically change after MI. The three main inflammatory cytokines, including tumor necrosis factor-α (TNF-α), interleukin-1β (IL-1β), and interleukin-6 (IL-6), have been reported to be upregulated after MI (Frangogiannis, 2014; Hu et al., 2016). In addition to its soluble form, TNF-α can also bind to the N-terminal of fibronectin (FN) to be an immobilized form, which augments integrin β_1-mediated adhesion of $CD4^+$ T lymphocytes to FN (Alon et al., 1994). *In vivo*, pretreating MSCs with TNF-α enhances MSC engraftment into the infarcted heart (Kim et al., 2009). Phosphatase SHP2, which is activated upon IL-6 stimulation (Sun et al., 2017), has been reported to promote FA growth in response to matrix stiffness (Lee et al., 2013). However, whether and how these inflammatory cytokines integrate with tissue stiffness to cooperatively regulate MSC adhesion to the infarct heart still remain unclear.

In the present study, we integrated *in vitro* biomechanical assays along with *in vivo* characterization and revealed that MSC adhesion could be enhanced by stiffened substrate and that immobilized inflammatory cytokine IL-6 can further strengthen MSC adhesion through IL-6/SHP-2/integrin signaling axis. We also demonstrated that enhancement of MSC engraftment *in vivo* after MI temporally coincides with cytokine upregulation and tissue stiffness increase, respectively, confirming the role of mechanical–chemical coupling in the modulation of MSC engraftment.

MATERIALS AND METHODS

Animals

All animal experiments were conducted in accordance with the Guide for the Care and Use of Laboratory Animals published by the United States National Institutes of Health (National Institutes of Health publication no. 85-23, revised 1996) and were approved by the Institutional Animal Care and Use Committee of Zhejiang University. Male Sprague-Dawley rats were purchased from Shanghai Slac Laboratory Animal Technology Corporation. The animals were fed a standard laboratory diet and maintained under a 12-h light/dark cycle.

Acute Myocardial Infarction Induction

Male Sprague-Dawley rats (weighing 250–300 g) were anesthetized with chloral hydrate (35 mg/kg) by intraperitoneal injection, mechanically ventilated, and left thoracotomy performed to expose the left anterior descending (LAD) coronary artery. MI was induced by permanent ligation of the LAD coronary artery using a 6-0 silk suture, and regional myocardial ischemia was observed by a rapid discoloration over the at-risk area. After induction of MI, the rats' thoraces were closed and the rats recovered.

Atomic Force Microscopy Characterization

Hearts of rats were obtained at 1, 3, 7, 14, and 21 days after MI to perform atomic force microscopy (AFM) measurements of elasticity in the infarct region. Tissue from the infarct region was cut into small blocks, each of which was about 10 mm (length) × 5 mm (width) × 1 mm (thickness) and was then attached to poly-L-lysine-coated coverslips in Dulbecco's modified Eagle's medium (DMEM) and mounted on the AFM (Asylum Research, Santa Barbara, CA, United States) sample stage for probing. The tissue blocks were indented with a blunted pyramid-tipped cantilever (TR400PSA, Olympus, Tokyo, Japan)

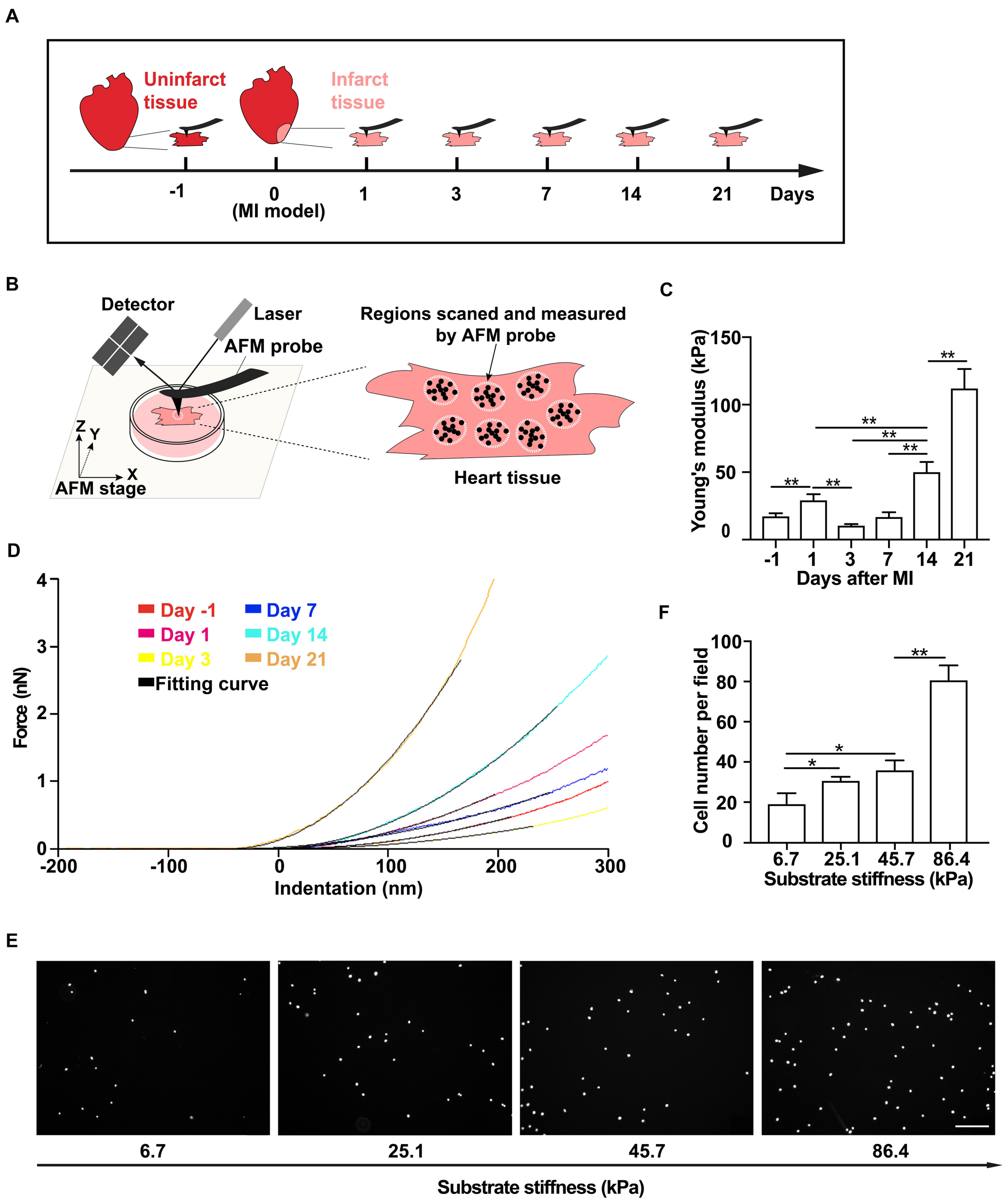

FIGURE 1 | Tissue stiffness of the infarct region of the rat heart increases after myocardial infarction (MI) and promotes mesenchymal stem cell (MSC) adhesion. **(A–D)** Schematics of the measurement time course of rat heart tissue stiffness by atomic force microscopy (AFM) **(A)** and the illustration of AFM micro-indentation to measure rat heart tissue stiffness by AFM **(B)** after MI, of which are the representative force-indentation curves **(D)** and means of tissue stiffness **(C)**. Tissue from the infarct region was cut into small blocks for AFM probing. At least 10 varied positions over the tissue block surface were measured, and 10–15 indentations were made on each position. White dotted circles and black dots in panel **(B)** indicate randomly selected positions and different indentations, respectively. Dashed lines in panel **(D)** are the best fit to corresponding stiffness measurements by AFM with the Hertz Cone model. **(E,F)** Representative images **(E)** and average numbers **(F)** of the attached MSCs after wash assay on PAA gel substrates with different stiffnesses that mimic infarct regions after MI. Scale bar in panel **(E)** refers to 200 μm. ** and * in panels **(C,F)** refer to $p < 0.01$ and $p < 0.05$, respectively. Error bars in panels **(C,F)** represent SEM of three repeats.

at rates <2 μm/s to avoid detection of viscoelastic properties of cells and the ECM. The spring constant (60–80 pN/nm) and deflection sensitivity of the cantilever were calibrated before each round of micro-indentation experiments. To obtain data over the entire sample surface, at least 10 different positions of the tissue blocks were measured, and 10–15 indentations were made on each position (**Figure 1B**). Each force-indentation curve was fitted to a Hertz cone model to determine an elastic modulus, and the elastic moduli were averaged for each rat.

Mesenchymal Stem Cell Culture

Mouse MSCs were obtained from Cyagen Biosciences (Guangzhou, China) and cultured in DMEM (Corning, Manassas, VA, United States) supplemented with 10% fetal bovine serum (FBS) (Invitrogen, Carlsbad, CA, United States) at 37°C in a 5% CO_2 incubator. The characteristic surface marker expressions of MSCs were confirmed with flow cytometry before the experiments (**Supplementary Figures 1B–E**).

Cell Preparation and Transplantation

Before transplantation, MSCs were engineered to express ZsGreen *via* lentiviral transfection as described previously (Zhu et al., 2018). Briefly, lentivirus particles were purchased from GeneChem, Shanghai, and the transduction efficiency was evaluated by fluorescence microscopy. One, 3, 7, 14, and 21 days after MI, the thoraces of the rats (six animals in each group) were reopened to perform intramyocardial cell transplantation. Each rat was injected with 1×10^7 MSCs in 1 ml DMEM from five sites (2×10^6 cells/site) in the infarct region *via* a Hamilton syringe. Twenty-four hours later, hearts were collected, and cell engraftment was analyzed with quantitative polymerase chain reaction (qPCR) and fluorescence microscopy.

Quantitative Analysis of Cell Engraftment

The number of engrafted cells in the heart was determined *via* qPCR assessments of ZsGreen DNA levels as described previously (Hu et al., 2014). Genomic DNA was prepared from cells and tissues according to the manufacturer's instructions of TAKARA MiNiBEST Universal Genomic DNA Extraction Kit (#9765, Takara Biotechnology Co., Dalian, China). The purified DNA was amplified with ZsGreen forward (5′ GCGAGAAGATCATCCCCGTG 3′) and reverse (5′ ACTTCTGGTTCTTGGCGTCG3′) primers by using SYBR Premix Ex Taq (#RR420, Takara Biotechnology Co., Dalian, China). Absolute standard curves were generated from serial dilution of the genomic DNA of a known number of MSCs (diluting the genomic DNA of ZsGreen-positive MSCs in normal heart tissue genomic DNA at a ratio from 1:1 to 1:1,000) and served as the reference for calculating the number of engrafted cells. The engraftment rate was determined from the ratio between engrafted cell number and injected cell number.

Immunohistochemical Analysis

The whole hearts were dehydrated in 30% sucrose solution, embedded in Tissue-Tek OCT compound (Sakura Finetek USA, Inc., Torrance, CA, United States), and snap frozen in liquid nitrogen. Heart tissue from the infarct region (site of cell injection) was sliced to obtain frozen sections of 6.0 μm thick. The slides were fixed in 4% paraformaldehyde, permeabilized in 0.2% Triton X-100, blocked with 5% bovine serum albumin (BSA), and incubated with different primary antibodies, including anti-α-actinin antibody (#ab9465, Abcam, Cambridge, MA, United States), anti-CD68 antibody (#ab31630, Abcam, Cambridge, MA, United States), anti-IL-1β antibody (#ab9722, Abcam, Cambridge, MA, United States), anti-IL-6 antibody (#LS-C746886, Biocompare, San Francisco, CA, United States), and anti-TNFα antibody (#ab6671, Abcam, Cambridge, MA, United States) overnight at 4°C. Then, the slides were incubated with the cognate secondary antibodies for 1 h at room temperature (RT). Sections incubated with only secondary antibody were used as negative control for non-specific staining. Nuclei were stained with Hoechst 33258 (Invitrogen, Carlsbad, CA, United States). After the staining, the sections were mounted on a fluorescent microscope for examination. Images were taken at a magnification of 600×, and the number of $CD68^+$ or $CD68^+cytokine^+$ cells from each high-power field (HPF) image was calculated and averaged for each rat.

Preparation of Polyacrylamide Gels

Glass-bottom dishes were activated with 2% 3-aminopropyltrimethoxysilane (Sigma-Aldrich, St Louis, MO, United States) in acetone, washed three times with ddH_2O, and air-dried for 10 min. Stock solutions were prepared from a mixture of 40% acrylamide and 2% bis-acrylamide and optimized for preparation of polyacrylamide (PAA) gels of different stiffness (see **Supplementary Table**). Working solutions containing the final desired concentrations of acrylamide/bis-acrylamide were obtained from stock solutions (see **Supplementary Table**). Ammonium persulfate (APS) and tetramethylethylenediamine (TEMED) were added to initiate gel polymerization. Then, 8–10 μl of the acrylamide solution were added to the center of glass-bottom dishes and covered with 12-mm-diameter glass coverslips. After gel polymerization, top coverslips were removed. Then, 200 μl of Sulfo-SANPAH (Thermo Scientific, Waltham, MA, United States) were applied to the gel surface and exposed to UV light. After UV activation, Sulfo-SANPAH changed its color from orange to brown. The gel surface was then washed and incubated with 20 μg/ml of FN (Sigma-Aldrich, St. Louis, MO, United States) overnight at 4°C. PAA gels were washed three times with sterile phosphate-buffered saline (PBS) and sterilized under a germicidal lamp for 2 h.

Wash Assay

Mesenchymal stem cells were trypsinized and resuspended at 2×10^5 cells/ml in DMEM with 10% FBS. Then, 1 ml of cell suspension was added to each dish from different groups. The dishes were incubated at 37°C for 30 min to allow the cells to adhere to the surface and washed three times with PBS to remove any non-adherent cells. After washing, DMEM with 10% FBS were added to each dish, and the cells were incubated at 37°C for 4 h for recovery. After cell recovery, the cells were fixed in 4% paraformaldehyde, permeabilized in 0.2% Triton X-100, and stained with Hoechst 33258 (Invitrogen, Carlsbad, CA, United States). Fluorescent images were acquired at a magnification of 400×, and cell number from each image was counted and averaged for each dish of the different groups.

Cell Adhesion Under Flow

Fibronectin and octadecyl rhodamine B chloride (R18) were obtained from Sigma-Aldrich (St. Louis, MO, United States) and

Invitrogen (Carlsbad, CA, United States), respectively. IL-1β, IL-6, and TNF-α were obtained from Sino Biological (Beijing, China). Adhesive substrates were prepared from perfusion of microfluidic channels in the BioFlux plate with different concentration of FN at 5 dyn/cm^2 for 15 min, followed by incubation at RT for 1 h, and blocked with 0.5% BSA at 5 dyn/cm^2 for 15 min. All cytokine-containing adhesive substrates were prepared from perfusion of cytokines together with FN. MSCs were trypsinized, stained with 300 nM R18, resuspended at 1×10^6 cells/ml in PBS, and perfused from the inlet wells for 10 min at 10 dyn/cm^2. In experiments that assess the effect of soluble cytokines, cells were incubated with different cytokines for 30 min at RT before perfusion. Images of attached cells after the perfusion were captured at a magnification of 100× using a Nikon TS100 microscope (Nikon Instruments, Inc., Melville, NY, United States) equipped with a CCD camera (QICAM, QImaging, Surrey, British Columbia) and the BioFlux 200 software. Cell number from each image was counted and averaged for each group.

Flow Cytometry and Western Blotting

For cell surface marker characterization, MSCs were stained with anti-CD45 FITC (#553080, BD Biosciences, San Jose, CA, United States), anti-Stem-cell antigen 1 FITC (SCA-1; #11-5981-85, eBioscience, San Diego, CA, United States), anti-CD44 PE (#12-0441-81, eBioscience, San Diego, CA, United States), and anti-CD31 PE (#553373, BD Biosciences, San Jose, CA, United States) for 15 min at RT and analyzed by flow cytometry after washing with PBS. For integrin β1 and β3 expression determination, MSCs (1×10^5 cells/group) untreated or stimulated with FN, IL-6, and FN + IL-6 were digested with trypsin and stained with anti-integrin β1 PE (#102215, BioLegend, San Diego, CA, United States) or β3 antibody (#104305, BioLegend, San Diego, CA, United States) and further analyzed with flow cytometry. For Western blotting, MSCs (1×10^6 cells/group) untreated or stimulated with FN, IL-6, and FN + IL-6 were digested and lysed with 80 μl lysis buffer containing 2% NP-40 and 1× protease inhibitor cocktail (#B14001, BioTool, Switzerland). The samples were heated for 5 min at 95°C after adding 20 μl 5× loading buffer. Equal volumes of samples were separated *via* electrophoresis on 10% sodium dodecyl sulfate (SDS)-polyacrylamide gel electrophoresis (PAGE) gels, transferred onto polyvinylidene fluoride (PVDF) membranes (Millipore, Billerica, MA, United States), and blocked with 5% (w/v) non-fat dry milk (BD Biosciences, Franklin Lakes, NJ, United States) in Tris-buffered saline with 0.1% Tween20 for 1 h at RT. The membranes were incubated with primary antibodies against β-actin (#KC-5A08, Aksomics, Chengdu, China) and SHP2 (#sc-7384, Santa Cruz, CA, United States) overnight at 4°C. The blots were then incubated with the appropriate horseradish peroxidase-conjugated secondary antibodies and visualized with an enhanced chemiluminescence (ECL) system (Millipore, Boston, MA, United States).

Statistical Analysis

Data are presented as mean ± SEM. Two-tailed Student's t-test was used when two groups were compared, and analysis of variance (ANOVA) tests were applied when more groups were analyzed. All statistical analyses were performed with the SPSS software, version 17.0. Differences were considered statistically significant at $p < 0.05$.

RESULTS

Tissue Stiffness of the Infarct Region of the Rat Heart Increases Gradually Within 21 Days After Myocardial Infarction

To determine the tissue stiffness of the infarct region of the rat heart, we collected the heart tissues on day 1 from normal groups and on days 1, 3, 7, 14, and 21 from MI groups (**Figure 1A** and **Supplementary Figure 1A**). We then used AFM indentation assay to quantitatively measure the stiffness of non-infarcted rat heart tissue and the infarct region of the rat heart on different days after MI (**Figure 1B**). We found that the stiffness of non-infarcted tissue is 17.4 ± 2.2 kPa before MI (**Figures 1C,D**), similar to previous reported values (Berry, 2006). After MI, the stiffness of the infarcted tissue increased to 29.2 ± 4.5 kPa on day 1 and slightly decreased to 10.5 ± 1.1 kPa on day 3, followed by rapid and progressive increase to 112.0 ± 14.5 kPa from day 7 to day 21 (**Figures 1C,D**). These data demonstrate that the stiffness of the infarct region of rat heart after MI dynamically changes, that is, gradually becoming stiffer along with MI progression in 21 days.

Increased Substrate Stiffness Promotes Mesenchymal Stem Cell Adhesion *in vitro*

As MSC adhesion is the critical step toward a successful transplantation, we next tested whether the stiffened tissue substrate would affect MSC adhesion. Using mouse MSC cell line (**Supplementary Figures 1B–E**), we performed wash assay to wash away pre-adhered MSCs on FN-coated substrates. These substrates were made of PAA gels to mimic various stiffnesses of the infarct region of the rat heart after MI. We found that the number of pre-adhered cells remained attached after washing increased with substrate stiffness increase (**Figures 1E,F**), demonstrating that the stiff substrate promotes MSC adhesion *in vitro*.

Rapid Upregulation of Inflammatory Cytokines in the Infarct Region of the Rat Heart in the First 3 Days After Myocardial Infarction

We next characterized the infiltration of macrophages and the expression of inflammatory cytokines in the infarct region on different days after MI. We performed the co-staining of α-actinin with IL-1β, IL-6, or TNF-α and found that inflammatory cytokines were not co-localized with cardiac tissues (**Supplementary Figure 2**). The result showed a rapid upregulation of IL-1β, IL-6, and TNF-α and infiltration of macrophage in the first 3 days after MI in the peri-infarct/infarct zone, followed by a sharp decline of the expression level of these three cytokines and the number of infiltrated macrophages (**Figures 2A,D,G**). These cytokines and macrophages declined to a low level on day 21 after MI (**Figures 2B,E,H** and **Supplementary Figures 2**, **3**). In addition, we observed a very similar alteration of the number of macrophages producing these three inflammatory cytokines on different days after MI (**Figures 2C,F,I**), demonstrating that different from a progressive rise of the tissue stiffness of the infarct region, inflammatory cytokines and infiltrated macrophages are mainly upregulated early after MI.

Immobilized IL-6 Promotes Mesenchymal Stem Cell Adhesion Under Shear Flow

Whether the elevation of inflammatory cytokines early after MI affects MSC adhesion is unclear. To answer this question, we used flow chamber assay to determine the adhesion strength of MSC binding to FN-coated microfluidic channels under shear stress to examine the mechano-regulated MSC adhesion (**Figure 3A**). We at first verified and confirmed that the MSC adhesion was mainly mediated through specific binding of cells to substrate-coated FN as the number of attached MSCs increased with an increasing concentration of FN (**Figures 3B,C**). We then determined the effect of IL-1β, IL-6, and TNF-α on MSC adhesion under shear flow. We found that the pretreatment of MSC with soluble IL-6 or TNF-α had no effect on MSC adhesion to FN under shear flow, but pretreatment with soluble IL-1β inhibited MSC adhesion to FN under shear stress (**Supplementary Figure 4**).

Previous study reported that endothelium-presented but not soluble chemokines trigger instantaneous lymphocyte adhesiveness to endothelial cells (Shamri et al., 2005). So, we further determined whether immobilized (substrate-coated) cytokines would enhance MSC adhesion. Indeed, we found that the number of MSCs attached to FN increased with increasing concentration of immobilized IL-6 (**Figures 3D,E**). In contrast, immobilized IL-1β or TNF-α failed to do so (**Supplementary Figure 5**). Collectively, these results demonstrate that immobilized IL-6 promotes MSC adhesion under shear force, suggesting that mechanical force coupling with cytokine IL-6 signaling activates integrin to enhance MSC adhesion.

The IL-6-Dependent Adhesion Enhancement on Mesenchymal Stem Cells Under Shear Force Is Mediated Through SHP2–Integrin$\alpha_5\beta_1$ Signaling Axis

It has been demonstrated that integrins $\alpha_5\beta_1$ and $\alpha_v\beta_3$, the FN-binding receptors, play different roles in the process of substrate mechanosensing (Roca-Cusachs et al., 2009; Schiller et al., 2013) and during MSC adhesion and migration (Docheva et al., 2007; Veevers-Lowe et al., 2011; Nitzsche et al., 2017). Integrin $\alpha_5\beta_1$ probes the extracellular mechanical environment at the leading edge to search for appropriate adhesion sites (Galbraith et al., 2007) and determines the adhesion strength of cells to the ECM (Roca-Cusachs et al., 2009), while integrin $\alpha_v\beta_3$ enables mechanotransduction that results in the directional orientation of the actin cytoskeleton and remodeling of FAs (Roca-Cusachs et al., 2009; Schiller et al., 2013). To further reveal the underlying mechanism of immobilized IL-6 in promoting MSC adhesion under shear force, we next tested whether IL-6 signaling activates integrins $\alpha_5\beta_1$ and $\alpha_v\beta_3$ binding to FN under force. As expected, blocking integrin $\alpha_5\beta_1$ with its inhibitory antibody reduces the number of MSCs attached to FN-coated substrates under shear force in both the absence and presence of immobilized IL-6 (**Figures 4A,B,E**). In contrast, when cells were incubated with 0.5 mM of the cyclic GPenRGDSPCA (GPen) peptide to block $\alpha_v\beta_3$, we did not observe any inhibitory effect on MSC adhesion in either the presence or the absence of immobilized IL-6 (**Figures 4A,C,F**). Collectively, these data demonstrate that immobilized IL-6 enhances integrin $\alpha_5\beta_1$/FN binding-mediated MSC adhesion under shear force.

We next examined the underlying mechanism by which IL-6 signaling enhances integrin $\alpha_5\beta_1$-mediated MSC adhesion from inside out. SHP2 has been reported as a key molecule in IL-6 signaling (Sun et al., 2017), and its deficiency impairs the maturation of cell–ECM adhesion (Lee et al., 2013; Sun et al., 2017). To determine whether SHP2 cross-linked IL-6 signaling to integrin $\alpha_5\beta_1$, we thus inhibited SHP2 activity with an SHP2 allosteric inhibitor shp099 (Chen et al., 2016) and examined whether MSC adhesion to FN-coated substrates was affected by the presence or absence of immobilized IL-6. Interestingly, shp099 only reduced the number of MSCs adhering to FN-coated substrates in the presence of immobilized IL-6, but not in the absence of immobilized IL-6 (**Figures 4F,G**), suggesting that immobilized IL-6 signaling activates integrin $\alpha_5\beta_1$ through SHP2 more efficiently than soluble IL-6 to enhance MSC adhesion. In conclusion, our results demonstrate that immobilized IL-6 promotes MSC adhesion through SHP2-integrin$\alpha_5\beta_1$ signaling axis.

To further test whether the effect of immobilized IL-6 is mediated through upregulation of SHP2 and integrin, we performed flow cytometry and Western blot analysis of the expression levels of integrins β_1 and β_3 and SHP2, respectively, in the presence or absence of immobilized IL-6. Our results showed that immobilized IL-6 alone did not upregulate the expression of these molecules (**Supplementary Figure 6**). Collectively, along with the results that shp099 treatment abolished the enhancement effect of immobilized IL-6 (**Figures 4A,D,G**) on MSC adhesion, we speculate that conformational activation of SHP2 may serve as the downstream regulator of immobilized IL-6 to promote β_1 integrin-dependent MSC adhesion.

The Enhancement of Mesenchymal Stem Cell Engraftment *in vivo* After Myocardial Infarction Temporally Coincides With Cytokine Upregulation and Tissue Stiffness Increase

The dynamic changes of infarct tissue stiffness and inflammatory cytokine level after MI suggest that finding an optimal timing for MSC transplantation is essential for successful MSC engraftment.

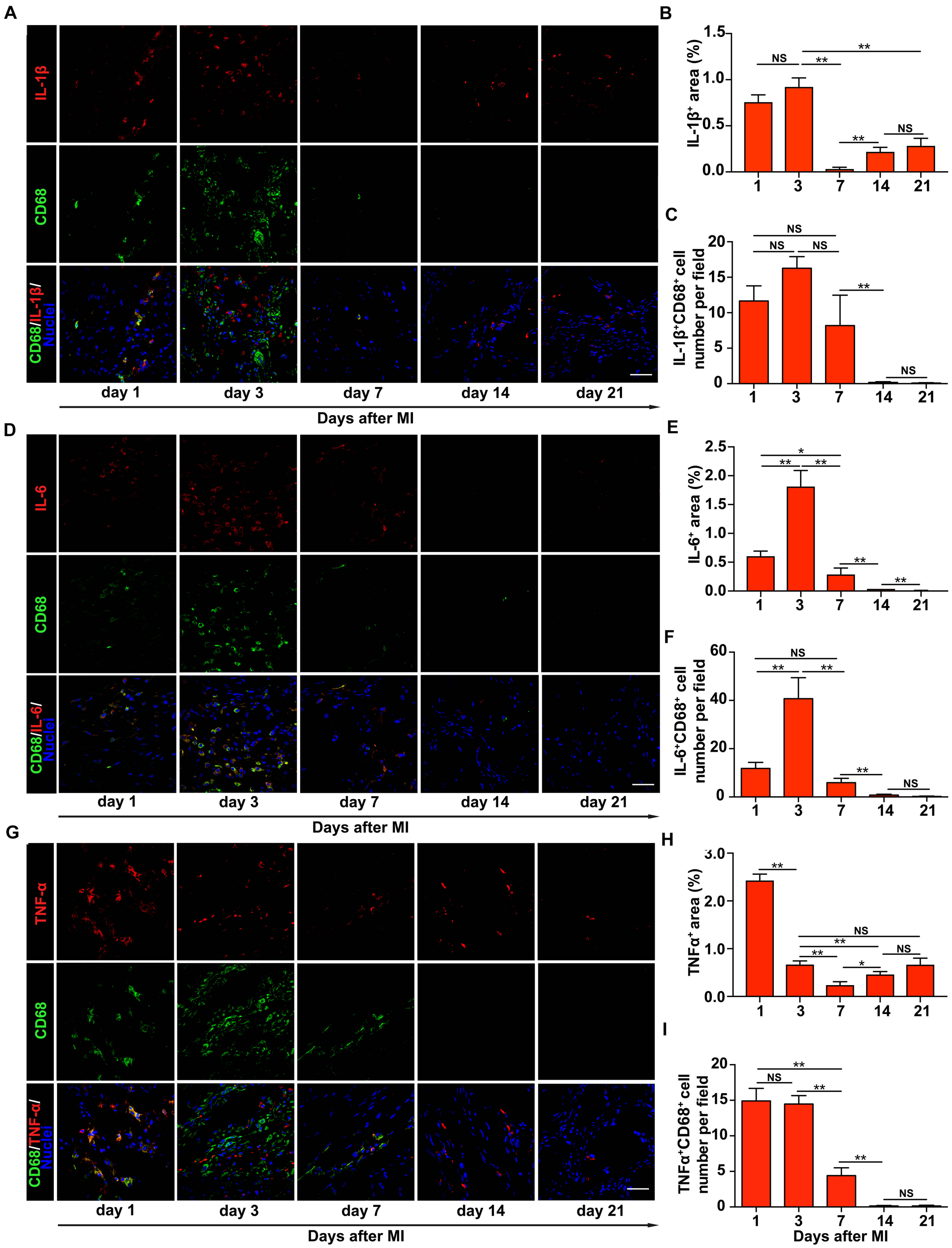

FIGURE 2 | Upregulation of inflammatory cytokines in the infarct region of the rat heart early after myocardial infarction (MI). Representative images of immunohistochemical staining of interleukin-1β (IL-1β) **(A)**, interleukin-6 (IL-6) **(D)**, and tumor necrosis factor-α (TNF-α) **(G)** in the infarct region of the rat heart at different times after MI. Comparisons of the numbers of IL-1β^+CD68$^+$ **(B)**, IL-6$^+$CD68$^+$ **(E)**, and TNF-α^+CD68$^+$ **(H)** cells per field, respectively, and the percentage of the surface area within the infarct region that was stained positively for IL-1β **(C)**, IL-6 **(F)**, and TNF-α **(I)**, respectively. In panels **(A,D,G)**, scale bars refer to 40 μm. **, *, and NS refer to $p < 0.01$, $p < 0.05$, and no significance, respectively. $N = 3$ rats for each time point. Error bars in panels **(B,C,E,F,H,I)** represent SEM of three repeats.

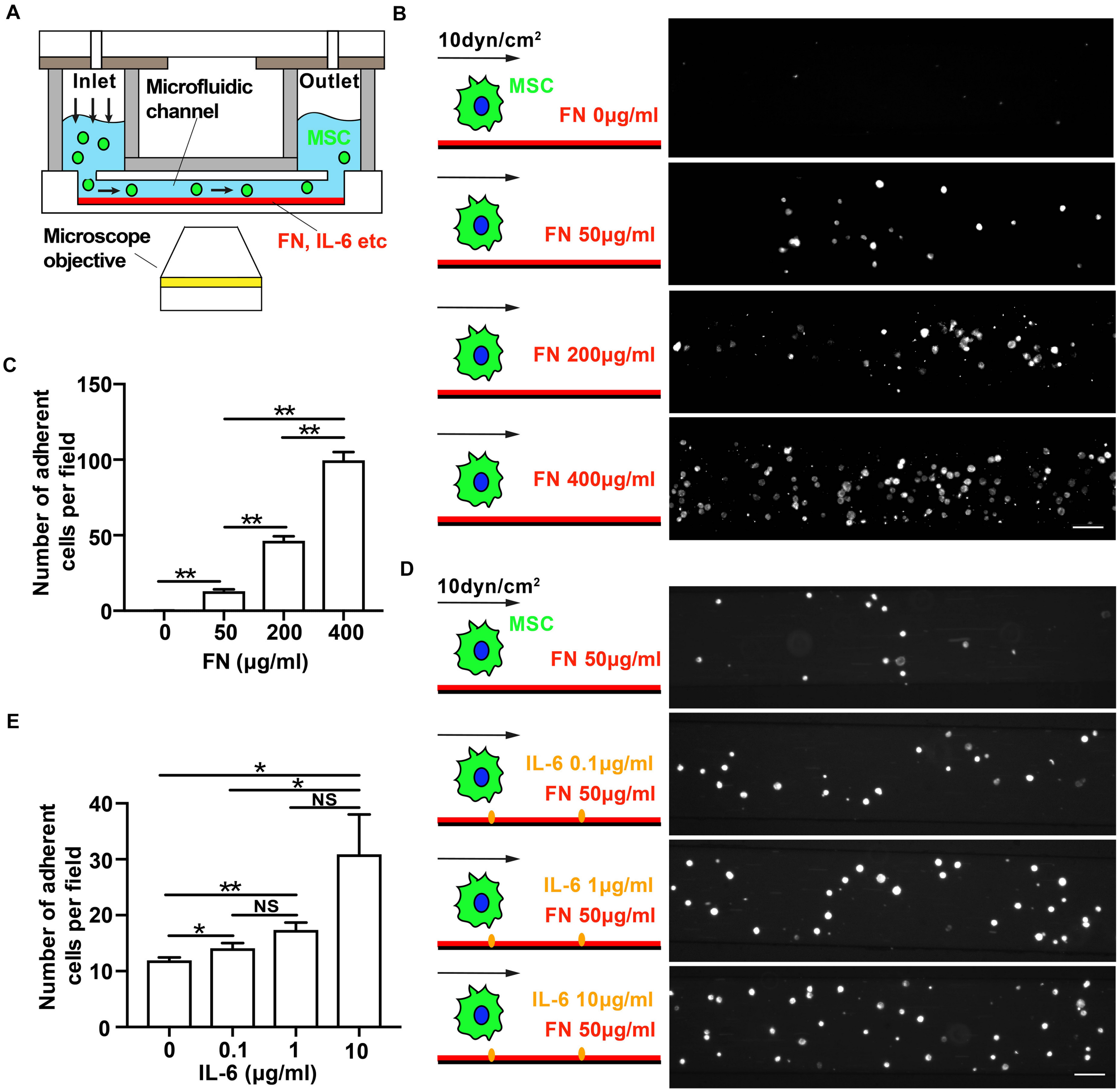

FIGURE 3 | Immobilized interleukin-6 (IL-6) promotes mesenchymal stem cell (MSC) adhesion under shear flow. **(A)** Schematics of flow chamber assay to qualitatively measure shear force-dependent adhesion strength of MSCs to microfluidic channel's substrate coated with fibronectin (FN) in the absence or presence of immobilized IL-6. **(B–E)** Representative images of attached MSCs after perfusion over microfluidic channels coated with increasing concentrations of FN **(B)** or IL-6 **(D)** at shear stress of 10 dyn/cm^2. Quantitative results of average numbers of adherent MSCs per field are shown in panels **(C,E)**, respectively. Scale bars in panels **(B,D)** refer to 200 µm. **, *, and NS in panels **(D,E)** refer to $p < 0.01$, $p < 0.05$, and no significance, respectively. Error bars in panels **(D,E)** represent SEM of three repeats.

To determine how the injection timing of MSCs affects MSC function *in vivo,* especially MSC engraftment to the infarct region of the rat heart, we injected MSCs expressing ZsGreen into the infarct region of rat hearts on different days after MI (**Figure 5A**), collected the hearts 24 h after each injection, and characterized their engraftment efficiency. We found that only a few MSCs were retained in the infarct heart 1 day after MI (**Figures 5B,C**). However, the number of engrafted MSCs increased dramatically 3 days after MI, and 7 days after MI, it rapidly dropped to the level approximate to that on day 1. Since then, the number of engrafted MSCs gradually increased from day 7 to day 21 (**Figures 5B,C**). To confirm these results obtained from fluorescence microscopy examination, we further performed qPCR and found a very similar efficiency of MSC engraftment at different times after MI (**Figure 5D**). A detailed analysis of the results further reveals the temporal coincidence of highest MSC engraftment efficiency with highest IL-6 expression and tissue stiffness on day 3 and day 21, respectively (**Figures 5E–G**), indicating that both heart

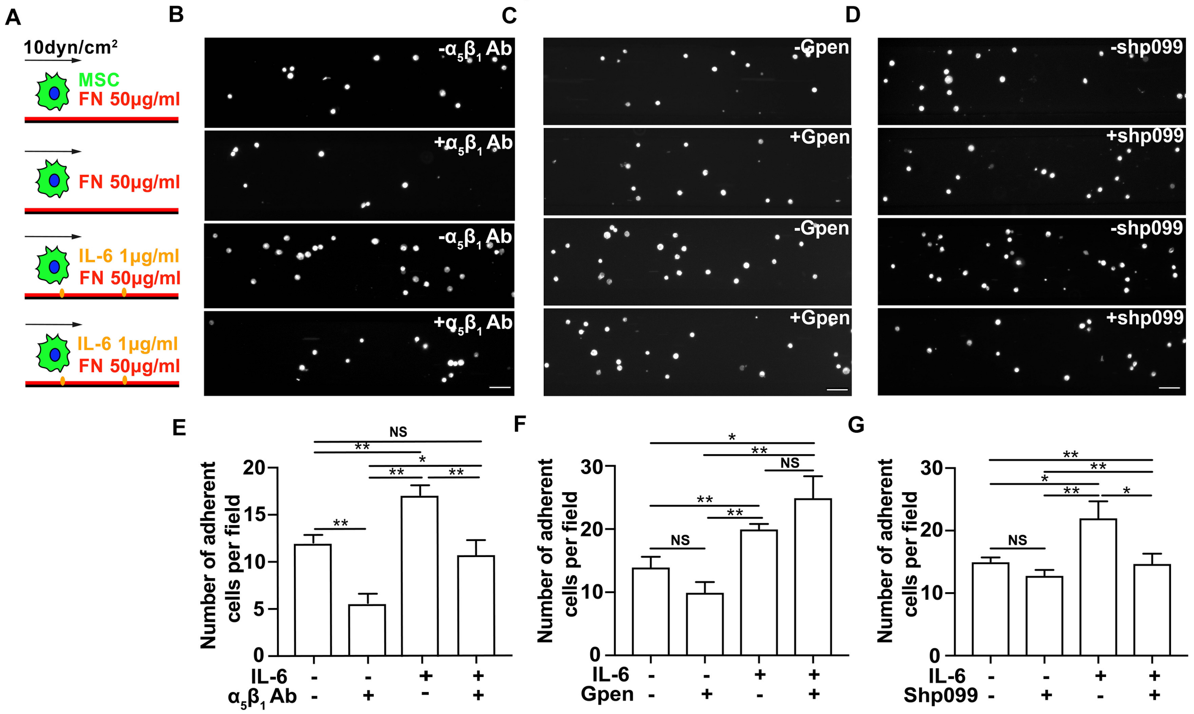

FIGURE 4 | The interleukin-6 (IL-6)-dependent adhesion enhancement on mesenchymal stem cell (MSC) adhesion under shear is mediated through SHP2–integrinα5β1 signaling axis. Schematics **(A)** of MSC perfusion over microfluidic channels coated with 50 μg/ml of fibronectin (FN) in the absence (first and second rows in **B–D**) or in the presence of 1 μg/ml IL-6 (third and fourth rows in **B–D**), of which are their representative images of attached MSCs pretreated with $\alpha_5\beta_1$ blocking mAb **(B)**, Gpen **(C)**, or shp099 **(D)** for 30 min before perfusion and are corresponding average numbers of adherent MSCs per field **(E–G)**, respectively. Scale bars in panels **(B–D)** refer to 200 μm. **, *, and NS in panels **(E–G)** refer to $p < 0.01$, $p < 0.05$, and no significance, respectively. Error bars in panels **(E–G)** represent SEM of three repeats.

stiffness and inflammatory cytokines and their dynamic coupling are essential regulators for MSC adhesion and engraftment on the infarct region of rat hearts. Collectively, these results demonstrate that both day 3 and day 21 after MI should be the best timing to inject MSCs for achieving the highest MSC engraftment efficiency.

DISCUSSION

We demonstrated the immunomodulation of MSC mechanosensing to regulate MSC engraftment in the heart infarct zone after MI, providing evidences of mechano-immune coupling-dependent cell adhesion on different stiffness substrates.

Immobilized IL-6 strengthens MSC adhesion on rigid substrate through integrin $\alpha_5\beta_1$ signaling axis rather than $\alpha_v\beta_3$'s. Integrin $\alpha_5\beta_1$ activates myosin-II-dependent force generation and substrate mechanosensing to induce nascent adhesion assembly (Galbraith et al., 2007; Schiller et al., 2013), while integrin $\alpha_v\beta_3$ enables mechanotransduction that results in remodeling of FAs and the directional orientation of the actin cytoskeleton (Roca-Cusachs et al., 2009; Schiller et al., 2013). The selective activation of integrin $\alpha_5\beta_1$ indicated by immobilized IL-6 suggests its essential role in regulating the early stage of MSC mechanosensing, specifically in regulating MSC adhesion on a rigid substrate by promoting nascent adhesion formation. Thus, our data further imply that the decline of inflammatory cytokine level in the later phase after MI may impair MSC mechanosensing and engraftment on the rigid infarct zone.

We demonstrated that the immobilized IL-6-induced enhancement of MSC adhesion was dependent on phosphatase SHP2. SHP2 has been reported to regulate both integrin $\alpha_5\beta_1$'s affinity and avidity to FN. On one hand, SHP2 dephosphorylates and activates Rho-associated protein kinase II (ROCKII) (Lee et al., 2013), the main effector enabling myosin-II-mediated force generation (Sun et al., 2019), to further inside out strengthen the force-dependent binding between integrin $\alpha_5\beta_1$ and FN through catch bond (Kong et al., 2009, 2013). On the other hand, SHP2 promotes integrin β_1 clustering (avidity) in a lipid raft-dependent manner and accelerates cell spreading (Lacalle et al., 2002). Targeting SHP-2 to lipid raft domains induces integrin β_1 clustering (Lacalle et al., 2002), which enhances bond lifetimes with FN and clustering sizes with increasing substrate stiffness to further promote focal adhesion kinase (FAK) Y397 phosphorylation and mechanosensing (Cheng et al., 2020). Furthermore, SHP2 has been implicated in signaling pathways initiated by inflammatory mediators other than IL-6, suggesting its more general role of immune-mechano coupling in regulating cell

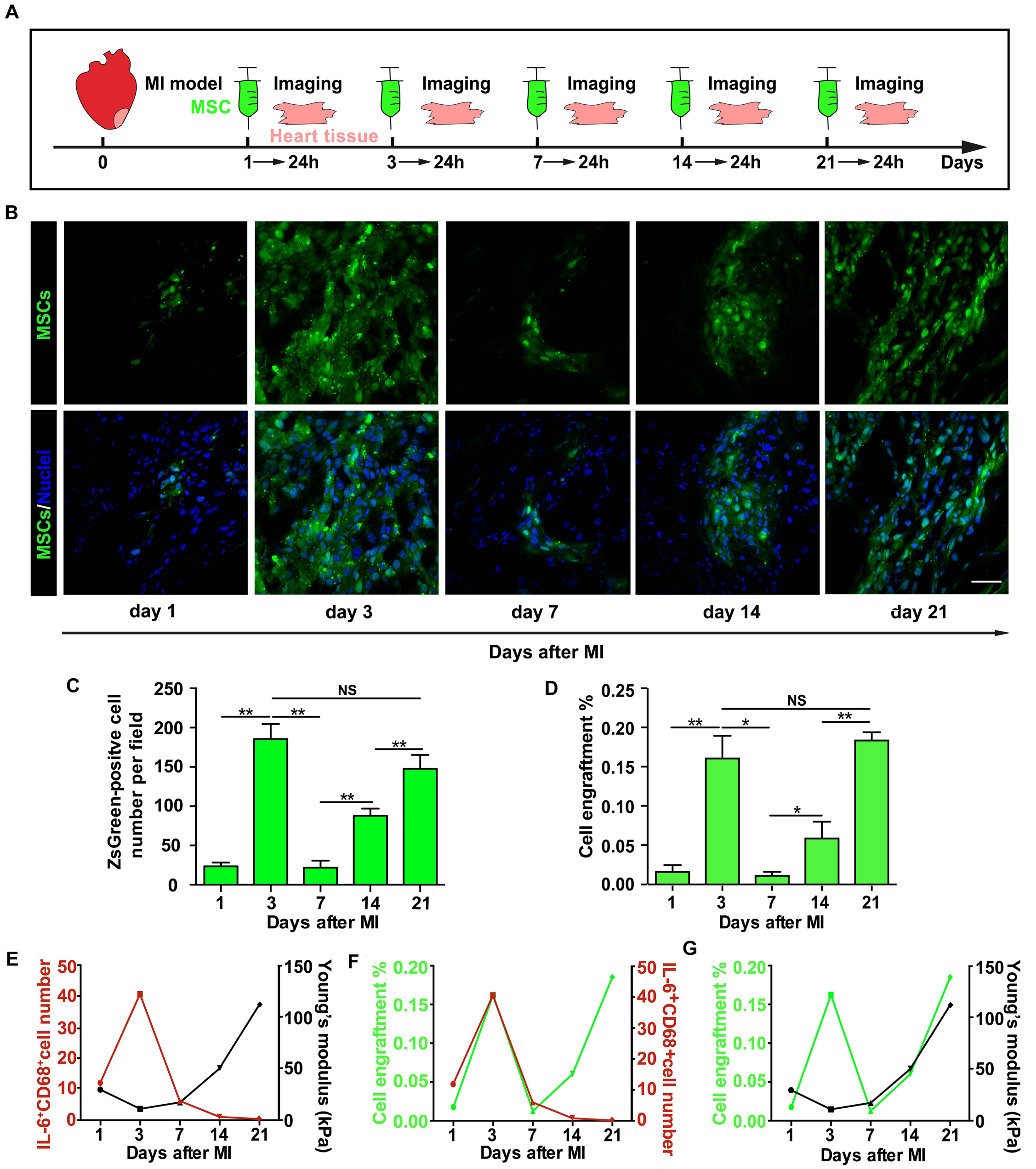

FIGURE 5 | The enhancement of mesenchymal stem cell (MSC) engraftment *in vivo* after myocardial infarction (MI) temporally coincides with cytokine upregulation and tissue stiffness increase. **(A–C)** The illustration of experimental procedure of MSC transplantation, tissue harvest, and imaging of MSC engraftment **(A)**, of which are the representative fluorescence images of engrafted ZsGreen-labeled MSCs in the infarct region **(B)** and average numbers of engrafted MSCs per field **(C)**. qPCR measurements of ZsGreen gene level were used to confirm fluorescence microscopy examination, and the percentage of MSC engraftment **(D)** is calculated by dividing the number of adherent MSCs with total cell number administered in tissue samples from heart apex. **(E–G)** Correlation analyses of the number of IL-6^+CD68^+ cells with tissue stiffness of infarct region after MI **(E)** or of the number of IL-6^+CD68^+ cells with MSC engraftment **(F)** or of MSC engraftment with tissue stiffness of infarct region after MI **(G)**. Scale bars in panel **(B)** refer to 40 μm. **, *, and NS in panels **(C,D)** refer to $p < 0.01$, $p < 0.05$, and no significance, respectively. $N = 3$ rats for each time point. Error bars in panels **(C,D)** represent SEM of three repeats.

adhesion. Together, these results demonstrate that SHP2 can be activated by immobilized IL-6 and then transduce inside-out signaling to regulate the affinity and avidity of integrin $\alpha_5\beta_1$ for enhancing MSC mechanosensing, adhesion, and engraftment in the infarct zone.

Inflammatory cytokines are released in a soluble form and can also be in immobilized form by binding to the N-terminal of FN in the infarct region (Alon et al., 1994; Frangogiannis, 2014). Our result showed that only immobilized IL-6 promoted MSC adhesion under shear flow. We speculate that immobilized

IL-6 enhances MSC adhesion from three aspects. Firstly, immobilized IL-6 may provide additional anchorage site other than FN/integrin linkages for MSC adhesion, helping stabilize MSC and substrate adhesion and facilitate mechanical force to induce integrin's conformational change and outside-in activation of integrin (Chen et al., 2012). Secondly, the immobilized form may enable force transduction from IL-6 receptor to its downstream signaling molecules (e.g., SHP2), activating potential mechano-regulation-dependent IL-6/SHP2 signaling pathway. Supporting this speculation, SHP2 has been reported to be mainly recruited and activated in membrane ruffles (Sun et al., 2013), the peripheral cellular constructions bearing large force and under which nascent adhesions assemble (Giannone et al., 2007). The force-bearing membrane ruffles localization and activation implies potential force regulation of SHP2 activity. Thirdly, immobilized IL-6/SHP2 signaling may be triggered in immediate proximity to FN occupancy that can temporally and physically couple inside-out and outside-in bidirectional activation of integrin $\alpha_5\beta_1$ to accelerate MSC adhesion on rigid substrate. In contrast, a global signal induced by soluble IL-6 fails to induce the full bidirectional activation of integrin.

In addition to IL-6, we also observed the effect of IL-1β and TNF-α on enhancing MSC adhesion. While both IL-1β and TNF-α have been reported to promote cell adhesion through upregulating expressions of FA proteins, we did not observe their effect on MSC adhesion under flow (Xia et al., 1998; Rajshankar et al., 2012). One possible explanation for this discrepancy is that our investigation of MSC adhesion under shear flow is restricted to a short contact duration mainly involving interaction between integrin and FN rather than FA remodeling and connection to the actin cytoskeleton.

In vivo, the temporal coincidence of enhancement of MSC engraftment with inflammatory cytokine upregulation and tissue stiffness increase indicates that simultaneous modulation of the inflammatory and mechanical environment may further promote MSC engraftment into the infarct heart after MI. Despite a relatively favorable inflammatory environment early after MI, the mechanical property of the infarcted myocardium is unsuited for MSC adhesion. Mimicking infarcted heart stiffness *in vitro*, we showed that MSC adhesion strengthens with increasing substrate stiffness, implying that the relatively softer tissue stiffness at the earlier phase after MI hinders MSC adhesion and engraftment. Encapsulating MSCs in hydrogel with tunable mechanical properties has been shown to improve MSC engraftment into the heart (Burdick et al., 2016), whose effect may be partially attributed to overcoming the mechanical limitation of soft tissue stiffness on MSC adhesion at the early stage. However, hydrogel may isolate MSCs from its surrounding inflammatory environment and block the biochemical signal stimulation. This defect could be overcome by modification of hydrogel with IL-6 coating to promote MSC adhesion. In addition, small molecule intervention that targets signaling molecules such as SHP2 may have the same effect.

What is more interesting, our *in vivo* immunohistochemical staining results showed a very similar alteration of the number of infiltrated macrophages on different days after MI as the upregulation of inflammatory cytokines, suggesting potential regulation of macrophage adhesion to the infarcted heart tissue by inflammatory cytokines. In fact, our *in vitro* flow chamber assay showed that immobilized IL-6 promoted the adhesion of the macrophage cell line RAW264.7 cells to FN-coated substrate, and this adhesion enhancement effect was blocked by both $\alpha_5\beta_1$ blocking mAb and shp099 (**Supplementary Figure 7**), demonstrating a more general role of immobilized IL-6/SHP2/$\alpha_5\beta_1$ signaling axis on cell adhesion in addition to MSCs. As inflammatory cytokines are mainly produced by immune cells including macrophages, this immobilized IL-6-mediated adhesion enhancement may provide a positive feedback mechanism to promote immune cell infiltration into the infarct region and augmentation of immune response after MI. Combined with our result that only immobilized IL-6 but not its soluble counterpart promotes cell adhesion on stiffened substrate, these data further indicate a potential mechano-regulation of immune response mechanism that have been reported on other immune receptors (Chen and Zhu, 2013; Wu et al., 2019; Zhu et al., 2019).

Taken together, we revealed inflammatory cytokine couples with substrate stiffness can cooperatively modulate MSC mechanosensing, adhesion *in vitro*, and engraftment *in vivo* after MI. If MSC transplantation strategies can cooperatively modulate the mechanical and inflammatory environment for better MSC adhesion, the efficiency of MSC engraftment to benefit clinical MI treatment might be improved.

DATA AVAILABILITY STATEMENT

All datasets presented in this study are included in the article/**Supplementary Material**.

ETHICS STATEMENT

The animal study was reviewed and approved by the Institutional Animal Care and Use Committee of Zhejiang University.

AUTHOR CONTRIBUTIONS

WC, JW, and XH conceived and designed the project. DZ performed AFM, MI induction, and MSC transplantation experiments. PW performed PCR and immunohistochemical experiments. CX performed flow chamber assay. DZ, PW, WH, and TZ performed data analysis. WC, DZ, and PW wrote the manuscript. All authors contributing to its revision.

FUNDING

This work was supported by the National Key R&D Program of China (2019YFA0110400, 2016YFC1301204 for JW, 2017YFA0103700 to XH), grants from the National Natural Science Foundation of China (Nos. 81870292 to JW, 81622006, 81670261 to XH, and 31971237 to WC), and the Key R&D Projects of Zhejiang Province (Nos. 2015C03028 to JW and 2018C03014 to XH).

ACKNOWLEDGMENTS

We thank Dr. Hongguang Xia for kindly providing us shp099, Drs. Hu Hu and Xiaoyan Chen for kind support on BioFlux 200, and Drs. Jin Qian and Fengbo Zhu for kind technical support on AFM.

SUPPLEMENTARY MATERIAL

The Supplementary Material for this article can be found online at: https://www.frontiersin.org/articles/10.3389/fcell.2020.583700/full#supplementary-material

REFERENCES

Afzal, M. R., Samanta, A., Shah, Z. I., Jeevanantham, V., Abdel-Latif, A., Zuba-Surma, E. K., et al. (2015). Adult bone marrow cell therapy for ischemic heart disease: evidence and insights from randomized controlled trials. *Circ. Res.* 117, 558–575. doi: 10.1161/CIRCRESAHA.114.304792

Alon, R., Cahalon, L., Hershkoviz, R., Elbaz, D., Reizis, B., Wallach, D., et al. (1994). TNF-alpha binds to the N-terminal domain of fibronectin and augments the beta 1-integrin-mediated adhesion of CD4+ T lymphocytes to the glycoprotein. *J. Immunol.* 152, 1304–1313.

Arunachalam, S. P., Arani, A., Baffour, F., Rysavy, J. A., Rossman, P. J., Glaser, K. J., et al. (2018). Regional assessment of in vivo myocardial stiffness using 3D magnetic resonance elastography in a porcine model of myocardial infarction. *Magn. Reson. Med.* 79, 361–369. doi: 10.1002/mrm.26695

Berry, M. F. (2006). Mesenchymal stem cell injection after myocardial infarction improves myocardial compliance. *Am. J. Physiol. Heart Circ. Physiol.* 290, H2196–H2203. doi: 10.1152/ajpheart.01017.2005

Burdick, J. A., Mauck, R. L., and Gerecht, S. (2016). To serve and protect: hydrogels to improve stem cell-based therapies. *Cell Stem Cell* 18, 13–15. doi: 10.1016/j.stem.2015.12.004

Changede, R., Xu, X., Margadant, F., and Sheetz, M. P. (2015). Nascent integrin adhesions form on all matrix rigidities after integrin activation. *Dev. Cell* 35, 614–621. doi: 10.1016/j.devcel.2015.11.001

Chen, W., Lou, J., Evans, E. A., and Zhu, C. (2012). Observing force-regulated conformational changes and ligand dissociation from a single integrin on cells. *J. Cell Biol.* 199, 497–512. doi: 10.1083/jcb.201201091

Chen, W., and Zhu, C. (2013). Mechanical regulation of T-cell functions. *Immunol. Rev.* 256, 160–176. doi: 10.1111/imr.12122

Chen, Y.-N. P., LaMarche, M. J., Chan, H. M., Fekkes, P., Garcia-Fortanet, J., Acker, M. G., et al. (2016). Allosteric inhibition of SHP2 phosphatase inhibits cancers driven by receptor tyrosine kinases. *Nature* 535, 148–152. doi: 10.1038/nature18621

Cheng, B., Wan, W., Huang, G., Li, Y., Genin, G. M., Mofrad, M. R. K., et al. (2020). Nanoscale integrin cluster dynamics controls cellular mechanosensing via FAKY397 phosphorylation. *Sci. Adv.* 6:eaax1909. doi: 10.1126/sciadv.aax1909

Discher, D. E., Janmey, P., and Wang, Y.-L. (2005). Tissue cells feel and respond to the stiffness of their substrate. *Science* 310, 1139–1143. doi: 10.1126/science.1116995

Docheva, D., Popov, C., Mutschler, W., and Schieker, M. (2007). Human mesenchymal stem cells in contact with their environment: surface characteristics and the integrin system. *J. Cell. Mol. Med.* 11, 21–38. doi: 10.1111/j.1582-4934.2007.00001.x

Elosegui-Artola, A., Oria, R., Chen, Y., Kosmalska, A., Pérez-González, C., Castro, N., et al. (2016). Mechanical regulation of a molecular clutch defines force transmission and transduction in response to matrix rigidity. *Nat. Cell Biol.* 18, 540–548. doi: 10.1038/ncb3336

Frangogiannis, N. G. (2014). The inflammatory response in myocardial injury, repair, and remodelling. *Nat. Rev. Cardiol.* 11, 255–265. doi: 10.1038/nrcardio.2014.28

Galbraith, C. G., Yamada, K. M., and Galbraith, J. A. (2007). Polymerizing actin fibers position integrins primed to probe for adhesion sites. *Science* 315, 992–995. doi: 10.1126/science.1137904

Giannone, G., Dubin-Thaler, B. J., Rossier, O., Cai, Y., Chaga, O., Jiang, G., et al. (2007). Lamellipodial actin mechanically links myosin activity with adhesion-site formation. *Cell* 128, 561–575. doi: 10.1016/j.cell.2006.12.039

Hu, X., Wu, R., Jiang, Z., Wang, L., Chen, P., Zhang, L., et al. (2014). Leptin signaling is required for augmented therapeutic properties of mesenchymal stem cells conferred by hypoxia preconditioning. *Stem Cells* 32, 2702–2713. doi: 10.1002/stem.1784

Hu, X., Xu, Y., Zhong, Z., Wu, Y., Zhao, J., Wang, Y., et al. (2016). A large-scale investigation of hypoxia-preconditioned allogeneic mesenchymal stem cells for myocardial repair in non-human primates: paracrine activity without remuscularization. *Circ. Res.* 118, 970–983. doi: 10.1161/CIRCRESAHA.115.307516

Kim, Y. S., Park, H. J., Hong, M. H., Kang, P. M., Morgan, J. P., Jeong, M. H., et al. (2009). TNF-alpha enhances engraftment of mesenchymal stem cells into infarcted myocardium. *Front. Biosci.* 14:2845–2856. doi: 10.2741/3417

Kong, F., Garcia, A. J., Mould, A. P., Humphries, M. J., and Zhu, C. (2009). Demonstration of catch bonds between an integrin and its ligand. *J. Cell Biol.* 185, 1275–1284. doi: 10.1083/jcb.200810002

Kong, F., Li, Z., Parks, W. M., Dumbauld, D. W., García, A. J., Mould, A. P., et al. (2013). Cyclic mechanical reinforcement of integrin-ligand interactions. *Mol. Cell* 49, 1060–1068. doi: 10.1016/j.molcel.2013.01.015

Lacalle, R. A., Mira, E., Gómez-Moutón, C., Jiménez-Baranda, S., Martínez-A, C., and Mañes, S. (2002). Specific SHP-2 partitioning in raft domains triggers integrin-mediated signaling via Rho activation. *J. Cell Biol.* 157, 277–289. doi: 10.1083/jcb.200109031

Lee, H.-H., Lee, H.-C., Chou, C.-C., Hur, S. S., Osterday, K., del Álamo, J. C., et al. (2013). Shp2 plays a crucial role in cell structural orientation and force polarity in response to matrix rigidity. *Proc. Natl. Acad. Sci. U.S.A.* 110, 2840–2845. doi: 10.1073/pnas.1222164110

Lee, R. H., Pulin, A. A., Seo, M. J., Kota, D. J., Ylostalo, J., Larson, B. L., et al. (2009). Intravenous hMSCs improve myocardial infarction in mice because cells embolized in lung are activated to secrete the anti-inflammatory protein TSG-6. *Stem Cell* 5, 54–63. doi: 10.1016/j.stem.2009.05.003

Liehn, E. A., Postea, O., Curaj, A., and Marx, N. (2011). Repair after myocardial infarction. Between fantasy and reality. *JAC* 58, 2357–2362. doi: 10.1016/j.jacc.2011.08.034

Miao, C., Lei, M., Hu, W., Han, S., and Wang, Q. (2017). A brief review: the therapeutic potential of bone marrow mesenchymal stem cells in myocardial infarction. *Stem Cell Res. Ther.* 8:242. doi: 10.1186/s13287-017-0697-9

Nitzsche, F., Müller, C., Lukomska, B., Jolkkonen, J., Deten, A., and Boltze, J. (2017). Concise review: MSC adhesion cascade-insights into homing and transendothelial migration. *Stem Cells* 35, 1446–1460. doi: 10.1002/stem.2614

Rajshankar, D., Downey, G. P., and McCulloch, C. A. (2012). IL-1β enhances cell adhesion to degraded fibronectin. *FASEB J.* 26, 4429–4444. doi: 10.1096/fj.12-207381

Ranganath, S. H., Levy, O., Inamdar, M. S., and Karp, J. M. (2012). Harnessing the mesenchymal stem cell secretome for the treatment of cardiovascular disease. *Stem Cell* 10, 244–258. doi: 10.1016/j.stem.2012.02.005

Roca-Cusachs, P., Gauthier, N. C., Del Rio, A., and Sheetz, M. P. (2009). Clustering of alpha(5)beta(1) integrins determines adhesion strength whereas alpha(v)beta(3) and talin enable mechanotransduction. *Proc. Natl. Acad. Sci. U.S.A.* 106, 16245–16250. doi: 10.1073/pnas.0902818106

Roca-Cusachs, P., Iskratsch, T., and Sheetz, M. P. (2012). Finding the weakest link: exploring integrin-mediated mechanical molecular pathways. *J. Cell Sci.* 125, 3025–3038. doi: 10.1242/jcs.095794

Rusu, M., Hilse, K., Schuh, A., Martin, L., Slabu, I., Stoppe, C., et al. (2019). Biomechanical assessment of remote and postinfarction scar remodeling following myocardial infarction. *Sci. Rep.* 9:16744. doi: 10.1038/s41598-019-53351-7

Sanganalmath, S. K., and Bolli, R. (2013). Cell therapy for heart failure: a comprehensive overview of experimental and clinical studies, current challenges, and future directions. *Circ. Res.* 113, 810–834. doi: 10.1161/CIRCRESAHA.113.300219

Schiller, H. B., Hermann, M.-R., Polleux, J., Vignaud, T., Zanivan, S., Friedel, C. C., et al. (2013). β1- and αv-class integrins cooperate to regulate myosin II during rigidity sensing of fibronectin-based microenvironments. *Nat. Cell Biol.* 15, 625–636. doi: 10.1038/ncb2747

Shamri, R., Grabovsky, V., Gauguet, J.-M., Feigelson, S., Manevich, E., Kolanus, W., et al. (2005). Lymphocyte arrest requires instantaneous induction of an extended LFA-1 conformation mediated by endothelium-bound chemokines. *Nat. Immunol.* 6, 497–506. doi: 10.1038/ni1194

Sun, J., Lu, S., Ouyang, M., Lin, L.-J., Zhuo, Y., Liu, B., et al. (2013). Antagonism between binding site affinity and conformational dynamics tunes alternative cis-interactions within Shp2. *Nat. Commun.* 4:2037. doi: 10.1038/ncomms3037

Sun, X., Zhang, J., Wang, Z., Ji, W., Tian, R., Zhang, F., et al. (2017). Shp2 Plays a critical role in IL-6-Induced EMT in breast cancer cells. *IJMS* 18:395. doi: 10.3390/ijms18020395

Sun, Z., Costell, M., and Fässler, R. (2019). Integrin activation by talin, kindlin and mechanical forces. *Nat. Cell Biol.* 21, 25–31. doi: 10.1038/s41556-018-0234-9

Trichet, L., Le Digabel, J., Hawkins, R. J., Vedula, S. R. K., Gupta, M., Ribrault, C., et al. (2012). Evidence of a large-scale mechanosensing mechanism for cellular adaptation to substrate stiffness. *Proc. Natl. Acad. Sci. U.S.A.* 109, 6933–6938. doi: 10.1073/pnas.1117810109

Veevers-Lowe, J., Ball, S. G., Shuttleworth, A., and Kielty, C. M. (2011). Mesenchymal stem cell migration is regulated by fibronectin through 5 1-integrin-mediated activation of PDGFR- and potentiation of growth factor signals. *J. Cell Sci.* 124, 1288–1300. doi: 10.1242/jcs.076935

Wu, P., Zhang, T., Liu, B., Fei, P., Cui, L., Qin, R., et al. (2019). Mechano-regulation of Peptide-MHC Class I conformations determines TCR antigen recognition. *Mol. Cell* 73, 1015.e7–1027.e7. doi: 10.1016/j.molcel.2018.12.018

Xia, P., Gamble, J. R., Rye, K. A., Wang, L., Hii, C. S., Cockerill, P., et al. (1998). Tumor necrosis factor-alpha induces adhesion molecule expression through the sphingosine kinase pathway. *Proc. Natl. Acad. Sci. U.S.A.* 95, 14196–14201. doi: 10.1073/pnas.95.24.14196

Zhang, S., Sun, A., Ma, H., Yao, K., Zhou, N., Shen, L., et al. (2011). Infarcted myocardium-like stiffness contributes to endothelial progenitor lineage commitment of bone marrow mononuclear cells. *J. Cell. Mol. Med.* 15, 2245–2261. doi: 10.1111/j.1582-4934.2010.01217.x

Zhu, C., Chen, W., Lou, J., Rittase, W., and Li, K. (2019). Mechanosensing through immunoreceptors. *Nat. Immunol.* 20, 1269–1278. doi: 10.1038/s41590-019-0491-1

Zhu, K., Wu, Q., Ni, C., Zhang, P., Zhong, Z., Wu, Y., et al. (2018). Lack of remuscularization following transplantation of human embryonic stem cell-derived cardiovascular progenitor cells in infarcted nonhuman primates. *Circ. Res.* 122, 958–969. doi: 10.1161/CIRCRESAHA.117.311578

Conflict of Interest: The authors declare that the research was conducted in the absence of any commercial or financial relationships that could be construed as a potential conflict of interest.

frontiers
in Cell and Developmental Biology

ORIGINAL RESEARCH
published: 05 November 2020
doi: 10.3389/fcell.2020.576826

VAMP3 and SNAP23 as Potential Targets for Preventing the Disturbed Flow-Accelerated Thrombus Formation

Juan-Juan Zhu[1,2,3,4†], **Zhi-Tong Jiang**[1,2,3†], **Chen Liu**[5], **Yi-Feng Xi**[6], **Jin Wang**[1,2,3], **Fang-Fang Yang**[1,2,3], **Wei-Juan Yao**[1], **Wei Pang**[1], **Li-Li Han**[1], **Yong-He Zhang**[4], **An-Qiang Sun**[6*] and **Jing Zhou**[1,2,3*]

[1] Department of Physiology and Pathophysiology, School of Basic Medical Sciences, Peking University, Beijing, China, [2] Key Laboratory of Molecular Cardiovascular Sciences, Ministry of Education, Beijing, China, [3] National Health Commission of the People's Republic of China Key Laboratory of Cardiovascular Molecular Biology and Regulatory Peptides, Peking University, Beijing, China, [4] Department of Pharmacology, School of Basic Medical Science, Peking University, Beijing, China, [5] Department of Clinical Laboratory, Peking University People's Hospital, Beijing, China, [6] School of Biological Science and Medical Engineering, Beijing Advanced Innovation Center for Biomedical Engineering, Beihang University, Beijing, China

Edited by:
Claudia Tanja Mierke,
Leipzig University, Germany

Reviewed by:
Nagaraj Balasubramanian,
Indian Institute of Science Education and Research, Pune, India
Yi Zhu,
Tianjin Medical University, China

***Correspondence:**
Jing Zhou
jzhou@bjmu.edu.cn
An-Qiang Sun
saq@buaa.edu.cn

†These authors have contributed equally to this work

Specialty section:
This article was submitted to Cell Adhesion and Migration, a section of the journal Frontiers in Cell and Developmental Biology

Received: 27 June 2020
Accepted: 05 October 2020
Published: 05 November 2020

Citation:
Zhu J-J, Jiang Z-T, Liu C, Xi Y-F, Wang J, Yang F-F, Yao W-J, Pang W, Han L-L, Zhang Y-H, Sun A-Q and Zhou J (2020) VAMP3 and SNAP23 as Potential Targets for Preventing the Disturbed Flow-Accelerated Thrombus Formation. Front. Cell Dev. Biol. 8:576826. doi: 10.3389/fcell.2020.576826

Disturbed blood flow has been recognized to promote platelet aggregation and thrombosis via increasing accumulation of von Willebrand factor (VWF) at the arterial post-stenotic sites. The mechanism underlying the disturbed-flow regulated endothelial VWF production remains elusive. Here we described a mouse model, in which the left external carotid artery (LECA) is ligated to generate disturbed flow in the common carotid artery. Ligation of LECA increased VWF accumulation in the plasma. Carotid arterial thrombosis was induced by ferric chloride ($FeCl_3$) application and the time to occlusion in the ligated vessels was reduced in comparison with the unligated vessels. *In vitro*, endothelial cells were subjected to oscillatory shear (OS, 0.5 ± 4 dynes/cm^2) or pulsatile shear (PS, 12 ± 4 dynes/cm^2). OS promoted VWF secretion as well as the cell conditioned media-induced platelet aggregation by regulating the intracellular localization of vesicle-associated membrane protein 3 (VAMP3) and synaptosomal-associated protein 23 (SNAP23). Disruption of vimentin intermediate filaments abolished the OS-induced translocation of SNAP23 to the cell membrane. Knockdown of VAMP3 and SNAP23 reduced the endothelial secretion of VWF. Systemic inhibition of VAMP3 and SNAP23 by treatment of mice with rapamycin significantly ameliorated the $FeCl_3$-induced thrombogenesis, whereas intraluminal overexpression of VAMP3 and SNAP23 aggravated it. Our findings demonstrate VAMP3 and SNAP23 as potential targets for preventing the disturbed flow-accelerated thrombus formation.

Keywords: thrombosis, VAMP3, endothelial cells, disturbed flow, SNAP23, VWF

INTRODUCTION

Arterial thrombosis is thought to initiate with events such as rupture or erosion of atherosclerotic plaques, vessel damage, and dysfunction of vascular endothelium. In advanced atherosclerosis, plaques become stenotic and can cause progressive obstruction of the arterial lumen, and correspondingly, the local arterial geometries change to result in alteration of the hemodynamic microenvironment (Hyun et al., 2000). Computational simulation of stenotic flow has indicated that the wall shear rate peak sharply just upstream of the apex of the stenosis, with sustained high shear conditions within the stenosis (Hathcock, 2006). The flow pattern upstream of and within the stenosis is typically characterized as laminar or pulsatile. Fluid layers may separate from each other as it decelerates downstream of the stenosis to form stagnation zones (with near-zero wall shear stress) and areas of recirculation, resulting in a transition of laminar to disturbed flow (Hyun et al., 2000; Hathcock, 2006). Disturbed flow with unorganized, chaotic flow regime has been recognized to influence vascular endothelial behavior and therefore favors platelet aggregation by increasing accumulation of von Willebrand factor (VWF) at post-stenotic sites (Westein et al., 2013). Although flow disturbance has a well-defined role in impairing endothelial function, the mechanisms by which disturbed blood flow affects thrombotic process in particular the endothelial secretion of VWF remain poorly understood. Moreover, appropriate animal models to study the flow-regulated thrombosis formation are ill-defined.

Thrombogenic component VWF is a multimeric glycoprotein, stored in secretory vesicles called Weibel-Palade bodies (WPBs) in endothelial cells, α-granules in megakaryocytes and platelets (Wagner et al., 1982; Sporn et al., 1985). Plasma VWF is produced mainly by endothelial cells, with a minor contribution from megakaryocytes or platelets (Valentijn and Eikenboom, 2013). VWF secretion can occur from both apical and basolateral sides of endothelial cells via constitutive, basal, and regulated secretory pathways, the latter two are dependent on WPB exocytosis (Lopes da Silva and Cutler, 2016). Thrombogenic stimuli such as fluid turbulence may trigger a regulated rapid exocytosis of endothelial WPBs and a release of VWF, which interact with platelet glycoprotein Ib-IX-V receptor, integrin $\alpha_{IIb}\beta_3$ and other components of the exposed sub-endothelium to initiate the primary thrombus formation (Mustard et al., 1962, 1966). WPB exocytosis is a multistep process that includes tethering, docking, priming, and membrane fusion (Burgoyne and Morgan, 2003). Regulation of WPB exocytosis involves multiple layers of cellular machineries with the cooperation of vesicle secretion-related proteins such as Rab proteins (Rab27a, Rab27b, Rab3A, Rab15b) (Zografou et al., 2012), Rab effector proteins (MyRIP, granuphilin/Slp4a, Slp2a, Slp3, Munc13-4, Munc18c, Noc2) (Bierings et al., 2012; Zografou et al., 2012; Nightingale and Cutler, 2013), vesicle transport-associated proteins SNAREs (soluble N-ethylmaleimide-sensitive factor attachment protein receptors) (Valentijn et al., 2011), and the small GTPase RalA (de Leeuw et al., 2001). SNARE complexes are the core components of the exocytosis machinery for WPB. Studies have shown that the SNARE complexes that consist of the WPB exocytosis machinery contain vesicle-associated membrane protein (VAMP) 3, VAMP8, syntaxin4 and synaptosomal-associated protein 23 (SNAP23) (Predescu et al., 2005; Pulido et al., 2011; Zhu et al., 2015). SNAP23 is the only SNAP homolog that localizes on the endothelial cell membrane and regulates endothelial cell exocytosis, deficiency of SNAP23 can impair endothelial exocytosis. SNAP23 has been reported to associate with vimentin intermediate filaments in fibroblasts, where vimentin filaments serve as a reservoir for SNAP23 (Faigle et al., 2000). VAMP3 are present on WPB, forming stable complexes with SNAP23, the plasma membrane-associated SNAREs in endothelial cells to allow fusion of WPB with the plasma membrane (Pulido et al., 2011). In previous study we found that disturbed blood flow upregulates the expressions of VAMP3 and SNAP23 and enhances their interaction in vascular endothelia. How important the hemodynamically drove regulation on VAMP3 and SNAP23 is in promoting thrombus formation remains unclear.

In the present study, we developed an animal model to investigate the disturbed flow-accelerated thrombosis in the murine carotid artery *in vivo*. In addition, we studied the influences of shear stress with distinct flow patterns on VWF secretion as well as the underlying regulatory mechanism in cultured endothelial cells by using parallel-plate flow apparatus. Our data show that, both *in vivo* and *in vitro*, the disturbed fluid shear stress aggravates VWF secretion and local platelet aggregation in a VAMP3/SNAP23 dependent manner. We report for the first time that vimentin associates with SNAP23 to modulate the oscillatory shear stress-induced translocation of SNAP23 to the cell membrane. This work highlights a critical role for the mechano-sensitive SNAREs in converting the hemodynamic microenvironment into prothrombotic responses and suggests VAMP3 and SNAP23 as potential targets for preventing the disturbed flow-accelerated thrombus formation.

MATERIALS AND METHODS

Cell Culture

Human umbilical vein endothelial cells (HUVECs) were cultured in medium 199 (M-199) supplemented with 10% fetal bovine serum (FBS), 4 μg/mL of β-Endothelial Cell Growth Factor (Sigma, Burlington, MA, USA), 1% penicillin/streptomycin (Harvey-bio, Beijing, China), at 37°C with 5% CO_2. Cells at passages 5–7 were used for all *in vitro* experiments. Human umbilical vein endothelial cells (HUVECs) were obtained from umbilical cords from healthy patients after full-term deliveries. Umbilical cords were obtained with the agreement of the patients and approved by the Peking University People's Hospital Medical Ethics Committee (2015PHB024).

Parallel-Plate Flow Apparatus

The monocultured HUVECs seeded on glass slides pre-coated with collagen I (50 μg/mL) were subjected to shear stress in a parallel-plate flow chamber. Channel in the chamber was created by a silicon gasket with dimensions of 2.496 cm in width (w), 5.725 cm in length, and 0.025 cm in height (h). The system was kept in a constant-temperature controlled enclosure, with pH maintained at 7.4 by continuous gassing with a humidified mixture of 5% CO_2, 20% O_2, and 75% N_2. The shear stress (τ) generated on the cells seeded on the membrane was estimated as $6QA\mu/wh^2$, where QA is flow rate and μ is perfusate viscosity. The flow with pulsatile shear (PS, 12 ± 4 dynes/cm^2) or oscillatory shear (OS, 0.5 ± 4 dynes/cm^2) is composed of a low level of mean flow with shear stress at 12 or 0.5 dynes/cm^2 supplied by a hydrostatic flow system to provide the basal nutrient and oxygen delivery, and the superimposition of a sinusoidal oscillation using a piston pump with a frequency of 1 Hz and a peak-to-peak amplitude of ± 4 dynes/cm^2. Cells were exposed to either PS or OS for the indicated time periods. In some experiments, the conditioned media collected from sheared cells were used to study VWF accumulation and its influences on platelet aggregation.

Antibodies, Reagents, and Adenovirus

Rabbit polyclonal antibody (pAb) against VAMP3, rabbit pAb against E-selectin, rabbit pAb against ICAM-1 were purchased from Proteintech (Chicago, Illinois, USA). Rabbit pAb against SNAP23 was from Abcam (Cambridge, United Kingdom). Mouse pAb against CD31 and mouse mAb against VCAM1 were from Santa Cruz Biotechnology (Dallas, TX, USA). Rabbit pAb against VWF was from Dako (Agilent, Beijing, China). Rabbit pAb against GAPDH was from Easybio (Beijing, China). Mouse monoclonal antibody against Vimentin was from Bioss (Beijing, China). Rapamycin was from Alexis. Recombinant adenovirus expressing GFP-fused full-length human SNAP23 (Ad-SNAP23) or VAMP3 (Ad-VAMP3) and the control adenovirus expressing GFP (Ad-GFP) only were obtained from Vigene Biosciences (Jinan, Sandong, China). SiRNAs for knocking down VAMP3 or SNAP23 and the control siRNAs were from GenePharma (soochow, Jiangshu, China).

Infection and Transient Transfection

For loss-of-function study of VAMP3 and SNAP23, cells at 80% confluence were transfected with siRNAs specific for VAMP3 (#1, 5′-CACUGUAAUCACCUAAAUAAATT-3′, #2, 5′-CCCAAAUAUGAAGAUAAACUATT-3′, GenePharma), SNAP23 (5′-CUUUGAGUCUGGCAAGGCUTT-3′, GenePharma), or the scrambled siRNA control using lipofectamine 2000 transfection agent (Thermo Fisher Scientific, Waltham, MA, USA) according to the manufacturer's instructions. The efficiency of siRNA-mediated knockdown on SNAP23 and VAMP3 was tested (Zhu et al., 2017). For gain-of-function study of VAMP3 and SNAP23, cells were infected with Ad-VAMP3, Ad-SNAP23 or Ad-GFP.

Western Blot Assay and Sodium Dodecyl Sulfate (SDS)-Polyacrylamide Gel Electrophoresis

Cells were lysed in RIPA lysis buffer: 50 mM Tris (pH 7.4), 1% NP-40, 0.5% deoxycholate, 0.1% SDS, 150 mM NaCl, 5 mM EDTA, 50 mM NaF, protease inhibitor cocktail tablets (Roche, Basel, Switzerland). Equal amounts of proteins were separated on SDS-polyacrylamide gel electrophoresis, transferred to nitrocellulose membranes. Non-specific binding was blocked in 5% skimmed milk in Tris-buffered saline (TBS) containing 0.1% Tween 20, and then the membranes were incubated with specific primary antibodies overnight at 4°C, followed by their detection using donkey anti-rabbit/-mouse/-goat IgG (H&L) antibody IRDye 800/700 Conjugated (Rockland, Philadelphia, Pennsylvania, USA). Visualization was performed with an Odyssey infrared imaging system (LI-COR Biosciences).

Western Blot Assay and SDS-Agarose Gel Electrophoresis

Plasma and the conditioned media collected from sheared cells were diluted in sample buffer [10 mM Tris, 1 mM Na_2EDTA, 2% (w/v) SDS, 8 M Urea, 2 mg/mL bromophenol blue]. The ratio of plasma or conditioned media to sample buffer is 1:10 and 1:5, respectively. The dilutions were incubated at 60°C for 30 min. Stack gel [0.8% agarose (w/v), 70 mM Tris, 4 mM EDTA, 0.4% SDS (W/V), pH 6.8] and separating gel [2% agarose (w/v), 0.1 M Tris, 0.1 M glycine, 0.4% (w/v) SDS, pH 8.8] were prepared. Equal amounts of diluted samples were loaded into the wells. The gel was subsequently soaked in running buffer [50 mM Tris, 384 mM glycine, 0.1% SDS (W/V) pH 8.3] and was subjected to electrophoretic migration process at a constant current density of 10 mA. After electrophoresis, the gel was soaked in transfer buffer (48 mM Tris, 39 mM glycine, 20% methanol, 0.037% SDS, pH 9.2) coated with 1 mM 2-mercaptoethanol (2-ME), and was then equilibrated for 30 min at room temperature. Following washing with transfer buffer (without 2-ME) for 15 min, the proteins in the gel were transferred at 4°C under a constant voltage of 30 V for 16 h to a 0.2-μm pore nitrocellulose membrane. The membrane was then incubated with polyclonal rabbit anti-VWF primary antibody at 4°C overnight. After washing with TBST buffer (60.57 g/L Tris Base, 87.75 g/L NaCl, 5 mL/L Tween 20, pH 7.4), the membrane was incubated with donkey anti-rabbit IgG antibody IRDye 800/700 Conjugated protected from light for 1 h at room temperature. Visualization was performed with an Odyssey infrared imaging system.

Immunofluorescence

Tissues were fixed in 4% paraformaldehyde (PFA) and were embedded in 30% sucrose solution before being frozen in TissueTek cutting medium (Sakura Finetek). Six micrometer sections were processed for immunofluorescent analyses. For *en face* preparation of mouse tissues, the common carotid arteries were harvested and post-fixed in this 4% PFA for no more than 1 day. Tissues were first washed with phosphate-buffered saline (PBS) buffer and adventitia was removed carefully. Aortas were then longitudinally dissected with microdissecting scissors and pinned flatly on a black wax dissection pan. The luminal surfaces of the common carotid artery were immediately blocked with 3% bovine serum albumin (BSA) (w/v) for 1 h. For immunostaining of attached cells, the cells were fixed in 4% PFA for 15 min and were permeabilized with 0.25% Triton X-100 in PBS for 10 min. Nonspecific binding was blocked by 3% BSA in PBS. The sections/tissues/cells were probed with primary antibodies (CD31, VCAM1, ICAM1, VWF, SNAP23, VAMP3, VE-cadherin, Vimentin), washed and then probed with secondary antibodies including Alexa Fluor 488-conjugated donkey/goat anti-rabbit/-mouse IgG (1:500, Thermo Fisher Scientific) or Alexa Fluor 555-conjugated donkey anti-rabbit/-goat IgG (1:500, Thermo Fisher Scientific). Nuclei were counterstained with Hoechst 33342. After mounting, the slips were visualized by fluorescence microscopy (Leica DMI6000B; Leica TCS SP8, Wetzlar, Germany). To quantify co-localization, Pearson's correlation coefficient was calculated by ImageJ Coloc 2 Fiji's plugin for colocalization analysis.

Proximity Ligation Assay (PLA)

Duolink *in situ* PLA was performed according to the protocol from the manufacturer (Sigma-Aldrich). In brief, HUVECs were sheared by PS or OS for 1 h, and then fixed with 4% PFA for 10 min at room temperature, washed with clod PBS three times and permeabilized with 0.5% Saponin for 10 min at room temperature. Unspecific binding sites for antibodies were blocked with blocking solution, the sample were incubated in a heated chamber for 1 h at 37°C. Next, the samples were incubated with primary antibodies solution of SNAP23 (1:100) and Vimentin (1:100) overnight at 4°C. Wash the samples in wash buffer A (0.01 mol/L Tris, 0.15 mol/L NaCl, and 0.05% Tween 20) at room temperature. Secondary antibodies conjugated with oligonucleotides (PLA probe MINUS and PLA probe PLUS) were added into the reaction and the mixtures were incubated in a pre-heated humidity chamber for 1 h at 37°C. Tap off the PLA probe solution from the samples. Samples were washed with wash buffer A and incubated with ligation solution for 30 min at 37°C. The Ligation solution consists of two oligonucleotides (illustrated as red bands) and ligase. Samples were then washed with buffer A and were incubated with amplification solution for 100 min at 37°C. The Amplification solution consists of nucleotides, fluorescently labeled oligonucleotides, and polymerase. The oligonucleotide arm of one of the PLA probes acts as a primer for a rolling-circle amplification (RCA) reaction using the ligated circle as a template, generating a concatemeric (repeated sequence) product. Tap off the amplification solution from the samples. Wash the samples in wash buffer B (0.2 mol/L Tris and 0.1 mol/L NaCl) at room temperature. Nuclei were counterstained with Hoechst 33342. After mounting, the samples were visualized by fluorescence microscopy (Leica TCS SP8). The ratio of fluorescence signal to cell number in each visual field was counted.

VWF Level Was Quantitatively Detected by Enzyme Linked Immunosorbent Assay (ELISA)

HUVECs subjected to PS or OS for indicated hours were rinsed and incubated in serum-free M199 medium supplemented with 1% BSA for 1 h at 37°C. The conditioned media were then collected and the remaining cells were lysed with RIPA lysis buffer. Cell lysates were collected to determine total VWF levels. Relative amounts of VWF were determined by ELISA. Ninety-six-well plates were coated with the anti-VWF antibody (1:000) and were then blocked before adding the conditioned media. Serially diluted human plasma served as standards. The plates were washed, and the horseradish peroxidase (HRP)-conjugated anti-VWF antibody (1:2,000) was added. After further rounds of washing, the plates were developed with o-phenylenediamine dihydrochloride and hydrogen peroxide in citrate phosphate buffer. Absorbance was analyzed at 490 nm. Basal and the stimulated release are presented as a percentage of the total VWF present in the cells.

Co-immunoprecipitation (Co-IP)

HUVECs were trypsinized and lysed with lysis buffer containing pH 7.4, 50 mM Tris-HCl, 100 mM NaCl, 1% NP-40, 1 mM EDTA, 1 mM PMSF, 1 mM NaVO4 and a protease inhibitor cocktail (Roche). Protein concentration of the lysate was adjusted to be 2–3 μg/μl. Five-hundred microliter of cell lysates were precleared with 1 μg of control IgG and 30 μl of protein A/G plus-agarose beads for 2 h rotation at 4°C. Five micro grams of SNAP23 antibody or corresponding IgG were added into the precleared cell lysates. After incubation and rotation at 4°C overnight, the immune complexes were pulled down with 30 μl of protein A/G plus-agarose beads and were washed with the lysis buffer. Sixty microliter of 2 × SDS buffer was added into each sample, which was then subjected to Western blot analysis.

Platelet Aggregation Assay

Blood samples were obtained with the agreement and approved by the Peking University People's Hospital Medical Ethics Committee (2018PHB210-01) from healthy volunteers without hematological history, platelet or coagulation dysfunction, or taking drugs that may influence hematological function. Platelet-rich plasma (PRP) were obtained from anticoagulated whole blood by centrifugation at 800 rpm for 10 min at room temperature. PRP on the top were transferred to a clean Eppendorf tube. Platelet-poor plasma (PPP) were obtained from re-centrifuging the remaining blood samples at 3,000 rpm for 10 min at room temperature. PRP with the same volume were mixed with the conditioned media derived from sheared HUVECs or saline solution. PPP were mixed with saline solution. Platelet aggregation was triggered by the addition of adenosine diphosphate (ADP, 0.2 μM) (Ya et al., 2019; Chaudhary et al., 2020) and were monitored and recorded using an aggregometer (Chrono-Log, Model Number 700, U.S.A).

Ligation of the LECA

All animal studies were performed in accordance with the approved protocol of the Animal Care and Use Committee of Peking University and approved by the Ethics Committee of Peking University Health Science Center (LA2018160). Anesthetization and euthanasia were performed by intraperitoneal injection of sodium pentobarbital (50 and 150 mg/kg, respectively). C57BL/6 wild-type mice (8–12 weeks old, 18–25 g) were anesthetized and were subjected to ligation of the left external carotid artery (LECA) with 6-0 silk suture, while other branches remained intact. After surgery, some mice were injected intraperitoneally every other day with rapamycin (1 mg/kg body weight) or with control reagent DMSO. Some mice received a locally intraluminal incubation of 50 μl per mouse of Ad-SNAP23 and Ad-VAMP3 viruses [a titer of 1 ×

10^9 plaque-forming units (pfu)/mL] or control virus for 30 min. Briefly, the left common carotid artery was exposed and the heart proximal end of the artery was clamped temporarily. The indicated adenoviruses were injected into the common carotid artery through the external carotid with an insulin needle, and then the LECA was immediately ligated. Clamp was removed after 30 min of incubation. Mice were kept in specific pathogen-free cages, 12 h light-dark cycle, controlled temperature and humidity, and had water and food *ad libitum*. One day or 1 week after ligation, the mice were sacrificed and fixed for 5 min by perfusion through left cardiac ventricle with 4% PFA in PBS buffer under physiological pressure. Carotid arteries were harvested and subjected to histology and immunostaining analyses of the vessels.

High-Resolution Ultrasound Measurements

C57BL/6 mice were placed on a heat mat and were anesthetized. Hairs on the neck were removed using depilatory cream. Mice were subjected to ligation of the LECA or sham operation. After an indicated duration post-surgery, the mice were examined by using a Vevo 770 high-resolution ultrasound imaging system (FUJIFILM VisualSonics, Toronto, ON, Canada). The system was equipped with RMV-707B microimaging ultrasound system with a 30-MHz mouse probe (Visualsonics). Heart rate, temperature, and respirations were continuously monitored. Pulse wave doppler mode was used at the inlet, midpoint, and outlet of the common carotid arteries for measuring flow velocity.

$FeCl_3$-Induced Mouse Thrombosis Model

C57BL/6 mice were anesthetized and the left common carotid arteries (LCA) were isolated. A doppler flow probe (model 0.5 VB, Transonic Systems Inc, Ithaca, NY) was applied around the common carotid artery. The probe was connected to a flowmeter (transonic perivascular flow module, TS420). Blood flow in the vessel was monitored continuously. A section of a least 5 mm of the artery was isolated and 3 × 6 mm^2 parafilm was placed below the artery. Two or three drops of saline were applied to the vessel to avoid drying up. A piece of filter paper saturated with 20% (w/v) $FeCl_3$ solution was placed on the artery and incubated for 3 min (Liang et al., 2015b; Li et al., 2017). After incubation the artery was rinsed with saline. Thrombus formation was assessed by monitoring blood flow immediately after $FeCl_3$ application and for up to 40 min, if the blood flow did not stop after 40 min, the time of thrombus formation was recorded as 40 min (Allende et al., 2017). The time to occlusion was calculated as the time required for blood flow through the carotid artery was monitored until vessel occlusion reached 95% (Liang et al., 2015a).

Real-Time Observation of Carotid Artery Thrombosis

C57BL/6 mice were anesthetized and were subjected to ligation of the LECA. The right jugular vein was exposed, and 150 μL of 0.5 mg/mL rhodamine 6G solution (labeling platelets) were injected through the vein using an insulin syringe with 30 G needle (2–3 mm tip of the needle was bent to a 90° angle with a needle holder) (Li et al., 2016). The injection site was clamped using a hemostat and was then ligated with 6-0 silk suture. The left common carotid artery was isolated and was then subjected to 20% $FeCl_3$-induced thrombosis. Thrombus formation was immediately observed and recorded using a fluorescence microscope in real-time.

Magnetic Resonance Image (MRI) Scan, Three-Dimensional Reconstruction (3D) and Blood Flow Simulation

To obtain the *in vivo* geometries of carotid arteries, one mouse was selected for MRI scanning (192 × 192 image resolution, 1 mm slice thickness, 7.0 T Bruker BioSpec 70/20 USR) before and 1 week after ligation in the National Center for Nanoscience and Technology of China. MRI scan images were segmented, 3D reconstructed and smoothed using Mimics (Materialize Interactive Medical Image Control System v15.0, Materialize, Ann Arbor, MI, USA) and Geomagic (Geomagic Studio, v12, Geomagic, USA). Pulsatile velocity selected from the ultrasound measurements of the two groups (before and 1 week after ligation) were used as the inlet boundary condition and outflow was used as the outlets condition with split ratio of 0.683:0.317 (IC:EC). Mesh generation and flow simulation were conducted using commercial software ANSYS ICEM CFD (ANSYS Inc., Canonsburg, PA). In the simulation process, the vessel wall was assumed as rigid. Blood was assumed as Newtonian, homogeneous and incompressible fluid (Sakalihasan et al., 2005; Li and Kleinstreuer, 2006). Numerical simulations were based on the Navier-Stokes equation and the continuity equation:

$$\rho\left[\frac{\partial \vec{u}}{\partial t}+\left(\vec{u}\cdot\nabla\right)\vec{u}\right]+\nabla p-\nabla\cdot\tau=0 \tag{1}$$

$$\nabla\cdot\vec{u}=0 \tag{2}$$

Where μ is the velocity vector, $\rho = 1{,}060\ \mathrm{Kg/m^3}$ is blood density, $\mu = 0.0035$ Pas is the dynamics viscosity (Feintuch et al., 2007; Nemeth et al., 2009), p is the pressure and τ is the stress tensor.

The time average wall shear stress (TAWSS) is the average of the wall shear stress in one cardiac cycle:

$$TAWSS=\frac{1}{T}\int_0^T\left|WSS\left(s,t\right)\right|\ .\ dt \tag{3}$$

Where T is the cardiac cycle time.

The Oscillation Shear Index (OSI) is a measure of the change in the direction of shear stress (He and Ku, 1996), which is often used to describe how even in time does the WSS positively and negatively change. The high OSI usually accompanies with low and oscillated flow condition:

$$OSI=0.5[1-\left(\frac{\left|\frac{1}{T}\int_0^T WSS\left(s,t\right)\ .\ dt\right|}{\frac{1}{T}\int_0^T WSS\left(s,t\right)\ .\ dt}\right)] \tag{4}$$

Where T is the cardiac cycle, and WSS is wall shear stress vector.

Relative residence time (RRT) is a parameter to evaluate the resident time of the blood flow and indicate regions suffering from either low WSS or high OSI. It is inversely proportional to the magnitude of the TAWSS vector and has obvious connections to the biological mechanisms of atherosclerosis (Lee et al., 2009):

$$RRT = \frac{1}{(1 - 2 \cdot OSI) \cdot TAWSS} \tag{5}$$

Statistical Analysis

Data are expressed as mean ± standard error of the mean (SEM) from at least three independent experiments. Statistical analysis was performed by unpaired *t*-test for two groups of data and by one-way ANOVA for multiple comparisons. Statistical significance among multiple groups was determined by *post hoc* analysis (Tukey honestly significant difference test). Values of $P < 0.05$ were considered to be statistically significant.

RESULTS

Ligation of LECA Causes Low and Disturbed Blood Flow in the Common Carotid Artery

To determine whether flow disturbance accelerates arterial thrombosis, we initially utilized a well-defined disturbed-flow model, partial ligation of mouse carotid artery (Nam et al., 2009), in which the external carotid, internal carotid, and occipital arteries of LCA were ligated (**Supplementary Figure 1**). Flow velocity and directions in LCA and the right common carotid arteries (RCA) were determined by flowmeter and high-resolution ultrasonography. As expected, these were a reduction in flow velocity and an appearance of flow reversal (indicated by arrows) in LCA at 1 day and 1 week post-ligation (**Supplementary Figure 1C**). The peak flow velocity in LCA dropped from 63.06 ± 12.51 cm/s (pre-ligation) to 9.17 ± 0.08 cm/s (1 day post-ligation) (**Supplementary Figure 1C**). Unfortunately, the very low flow velocity (**Supplementary Figure 1B**) forbade this model being used in combination with the $FeCl_3$-induced arterial injury to study thrombus formation. We therefore modified the ligation model as followed: Only the LECA was ligated while the other branches of the LCA were preserved (**Figure 1A**). To determine whether ligation of the LECA causes changes in the magnitudes and directions of the wall shear stress in LCA, we performed computational fluid dynamics (CFD) modeling. MRI of mouse neck was performed before and after ligation and three-dimensional images were reconstructed to obtain the precise *in vivo* anatomy of the LCA (**Figures 1B,C**). The values of flow velocity, direction, and vessel dimensions of LCA and RCA were measured by high resolution ultrasonography (**Figure 1D**). The results showed a 50 and 62% reduction, respectively, in flow velocity during systole in LCA at 1 and 7 days after ligation (**Figures 1D,E**), indicating that the flow velocity was much higher than that in the original partial ligation model (**Supplementary Figure 1C**). There was no flow reverse in the RCA in the cardiac cycle, while in the LCA there was a significant reverse flow at the very end of systole (**Figures 1D,F**). Based on the flow curve measured by ultrasonography, blood flow fields and hemodynamic parameters such as flow velocity (**Figures 1F,G**), time-averaged wall shear stress (TAWSS) (**Figure 1H**), relative residence time (RRT) (**Figure 1I**) and oscillatory shear index (OSI) (**Figure 1J**) in the common carotid arteries were calculated by the CFD analysis (**Figures 1F–J**). In the reverse flow phase of the ligated LCA, oscillatory recirculation zones and lower flow velocity were observed in comparison with that in the unligated vessels (**Figures 1F,G**). Since the low and reverse flow, the lower TAWSS, higher RRT and higher OSI that have been previously suggested as athero-prone parameters appeared in the LCA (Lee et al., 2009), these results indicated that ligation of LECA causes blood flow disturbance in the common carotid artery.

Ligation of LECA Induces Endothelial Inflammation

To further validate our modified disturbed-flow model, we tested whether ligation of the LECA results in functional consequences in the common carotid artery. Disturbed flow has been indicated by numerous studies to promote the expressions of pro-inflammatory adhesion molecules in vascular endothelium (Chiu and Chien, 2011). We performed immunofluorescence staining on sections of RCA and LCA from mice after 1 week of ligation to detect the expression of endothelial marker gene, cluster of differentiation 31 (CD31), and the pro-inflammatory genes E-selectin, vascular cell adhesion molecule 1 (VCAM-1) and intercellular cell adhesion molecule 1 (ICAM-1). Ligation of LECA did not lead to endothelial denudation (**Figure 2A**), however, it caused increases in expressions of E-selectin, VCAM-l, and ICAM-1 in the endothelia of the common carotid arteries, in comparison with the expression from the unligated RCA (**Figures 2B–D**). These findings indicated that ligation of the LECA does result in endothelial dysfunction, which is very likely attributable to the effects of disturbed blood flow.

Ligation of LECA Induces the Endothelial Secretion of VWF

The hemostatic protein VWF plays a crucial role in thrombus formation. We measured the VWF levels on the intimal surface of LCA and RCA from mice at 1 day after ligation by immunofluorescent staining. The images showed that the VWF-positive staining on the surface of vascular endothelium in LCA was much greater than that in RCA (**Figure 2E**), implying that the secretion of VWF from endothelia is enhanced by disturbed flow. Studies have shown that traumatic vascular injury results in ultra-large VWF formation and increased plasma VWF levels (Dyer et al., 2020; Plautz et al., 2020). Therefore, we detected the levels of VWF in circulating blood plasma from mice with ligation of the LECA or those with a sham surgery by Western blot assay followed with SDS-agarose gel electrophoresis or SDS-polyacrylamide gel electrophoresis (**Figure 2F**, left panel and **Figure 2G**). In plasma, VWF appeared as a series of multimers of regularly decreasing molecular mass from several thousand to hundreds kDa that could be separated and distinguished by

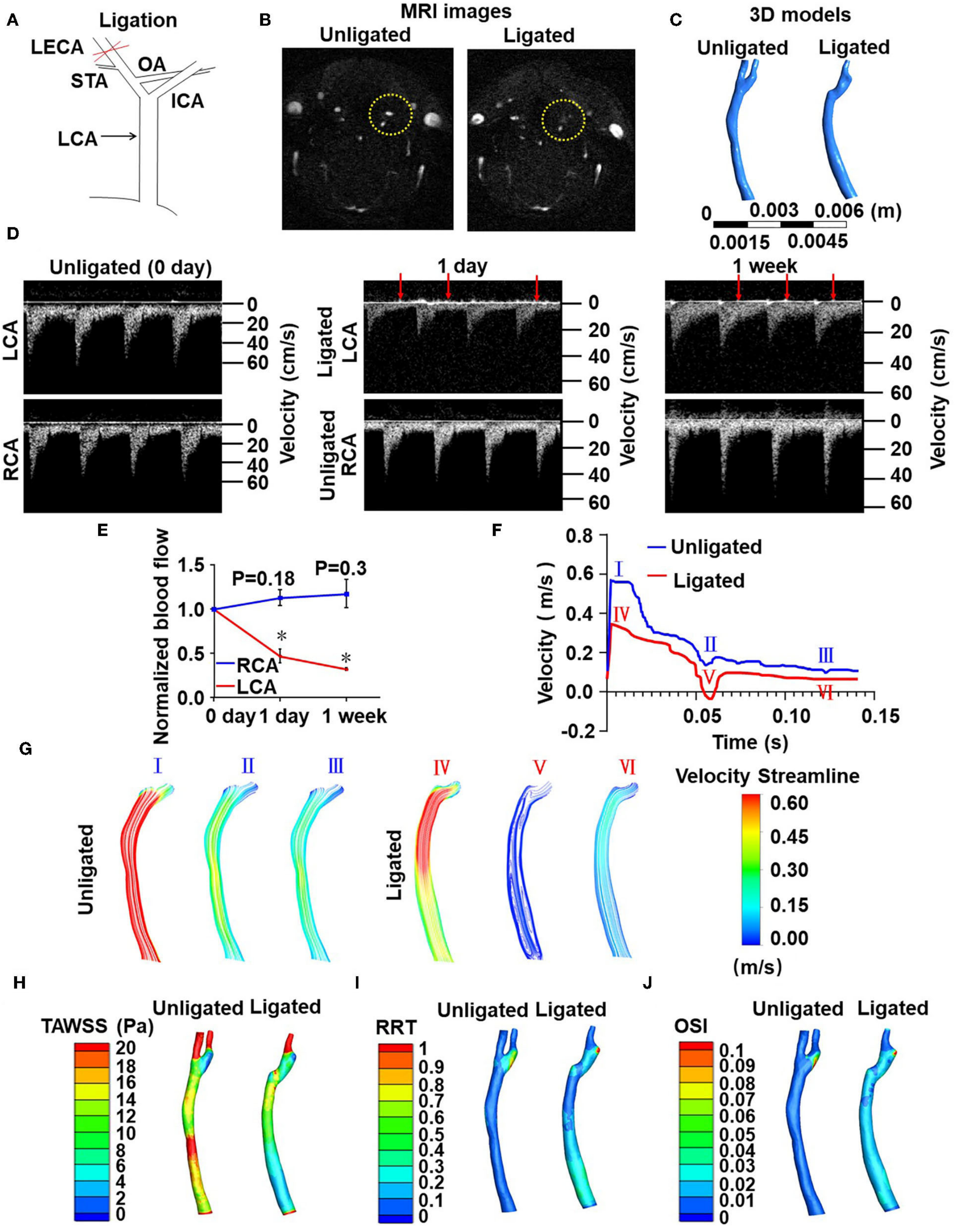

FIGURE 1 | Ligation of LECA causes blood flow disturbance in the common carotid artery. **(A)** Ligation of LECA. LCA, left common carotid artery; ICA, internal carotid artery; STA, superior thyroid artery; OA, occipital artery. **(B)** Representative magnetic resonance imaging (MRI) of the neck of mice before (unligated) and after (ligated) ligation of LECA. Yellow circles indicate the LCA from unligated and ligated mouse. **(C)** 3D reconstruction of blood vessels in the neck from MRI images.

(Continued)

FIGURE 1 | (D) Blood flow velocity and directions of LCA and RCA were measured by high-resolution ultrasound doppler before ligation and 1 day or 1 week after ligation. Red arrows indicate reversals of blood flow. **(E)** Ligation of LECA reduces the blood flow of LCA, without significantly increasing RCA blood flow. **(F)** The velocity over a cardiac cycle in unligated and ligated mice. Peak systole (I and IV), end systole (II and V), distole (III and VI) in the pre- and post-ligation flow curves are indicated. **(G)** Images were color streamline of velocity magnitude in three time points of the pre- and post-ligation models. **(H–J)** Pseudocolor images of time-averaged wall shear stress (TAWSS) **(H)**, Relative residence time (RRT) **(I)**, and oscillation shear index (OSI) **(J)** in the common carotid arteries before and 1 week after ligation. The results represent the ratio of blood flow velocity after ligation to that before ligation. Data are mean ± SEM, $n = 5$, $^*P < 0.05$.

SDS-agarose gel electrophoresis but not SDS-polyacrylamide gel electrophoresis. Densitometric analysis of VWF multimers was performed with Image J software according to VWF multimers electrophoretic gel images. Optical density values representing the concentrations of VWF multimers of different molecular weights were processed as grayscale data (Studt et al., 2001). The analysis confirmed the presence of high- and middle-molecular-weight VWF multimers (**Figure 2F**, right panel). The largest VWF multimers contain multiple sites for interaction with platelets and vessel wall components and are therefore thought to have a greater thrombogenic potential (Ruggeri, 2001). The results from the two gel electrophoreses indicated that ligation of LECA promotes VWF secretion.

Ligation of LECA Accelerates Thrombosis After the $FeCl_3$-Induced Arterial Injury

To study the influence of disturbed flow on arterial thrombus formation *in vivo*, we combined the ligation of LECA with $FeCl_3$-induced arterial injury, the latter is a well-established technique to induce the formation of thrombi rapidly and accurately in an exposed artery (Kurz et al., 1990; Farrehi et al., 1998). $FeCl_3$-induced thrombus formation was performed in mouse RCA and the ligated LCA or carotid arteries which had been previously subjected to ligation (ligated) or sham surgery (unligated). When the comparison was conducted between the RCA and LCA in one mouse, the average time to occlusion in RCA was 28.75 ± 7.63 min, while in LCA it was reduced to 11.23 ± 2.73 min which was significantly shorter than that in the unligated vessels (**Supplementary Figure 2**). When the sham or ligated operated mice were compared, the average times to occlusion were 16.67 ± 5.16 and 10.87 ± 2.69 min, respectively (**Figures 3A–C**). To further validate the role of flow disturbance in pro-thrombosis, real-time observation of carotid artery thrombi formation was performed. In this assay, rhodamine 6G solution was injected into the right jugular vein to label the circulating platelets, as previously described (Li et al., 2016). *In vivo* fluorescence microscopy of the common carotid artery showed that the platelets labeled with rhodamine 6G accumulated along the vessel wall immediately upon 20% $FeCl_3$ treatment, and thrombi formation was observed in all mice 1 min upon injury (**Figure 3D**). The initially formed thrombi were unstable and parts of them were usually washed away by the blood flow, so the formed thrombi did not enlarge in the unligated vessels (**Figures 3D,E**). By contrast, there was a significantly accelerated thrombi formation and stabilization duration in the ligated vessels, in which thrombi started to enlarge from 3 to 4 min after removing the filter paper with $FeCl_3$ and usually filled the vessel segment within 5 min (**Figures 3D,E**). These results provide *in vivo* evidence demonstrating that disturbed flow promotes thrombosis.

Oscillatory Shear Enhances Endothelial VWF Secretion and Provokes Platelet Aggregation

Next, we examined the influences of shear stress with distinct flow patterns on endothelial cell VWF secretion and platelet aggregation at the cellular level. OS at 0.5 ± 4 dynes/cm^2 was used to mimic the fluid shear stress at regions downstream of the stenotic wall and near the reattachment point, where low (near-zero) and oscillatory wall shear stress occurs (Hyun et al., 2000). PS at 12 ± 4 dynes/cm^2 derives from a typical laminar flow at straight part of the main arteries (Hathcock, 2006). Application of OS to endothelial cells for 6 h markedly increased the level of VWF in the conditioned media, as compared with the application of PS (**Figures 4A**,**B**, left and **Figure 4C**). The conditioned media were collected from the endothelial cell culture (an incubation for 30 min) with pre-exposure to PS or OS for 6 h. OS appeared to reduce the intracellular VWF levels compared with PS (**Figures 4A,B**, right panel), which might be due to the increase in VWF secretion. VWF multimers in the conditioned media were analyzed by SDS-agarose gel electrophoresis, followed by densitometric analysis. The results indicated that OS promoted the secretion of high-molecular-weight VWF multimers, as compared with PS (**Figure 4D**). To examine the role of fluid shear stress applied to endothelial cells in hemostasis, we evaluated the influences of endothelial cell conditioned media on platelet aggregation induced by ADP in PRP. Conditioned media from the indicated treatments were mixed with PRP from human whole blood and platelet aggregator was used to detect platelet aggregation. The aggregation rate in conditioned media from cells with OS was significantly higher than that with PS (**Figures 4E,F**). These results suggest that oscillatory shear stress enhances endothelial VWF secretion and provokes platelet aggregation.

Oscillatory Shear Stress Enhances Endothelial VWF Secretion via Promoting Activation of VAMP3 and SNAP23

Our previous research has demonstrated the disturbed flow- or oscillatory shear stress-activated VAMP3 and SNAP23 expressions and association in vascular endothelial cells (Zhu et al., 2017). Here we sought to investigate the role of VAMP3 and SNAP23 in OS-evoked VWF secretion. Cells were subjected to PS or OS for 1 h and the subcellular localizations of VAMP3, SNAP23, and VWF were detected. In contrast to previous study in which prolonged shear stress load (6 or 24 h) was utilized, in

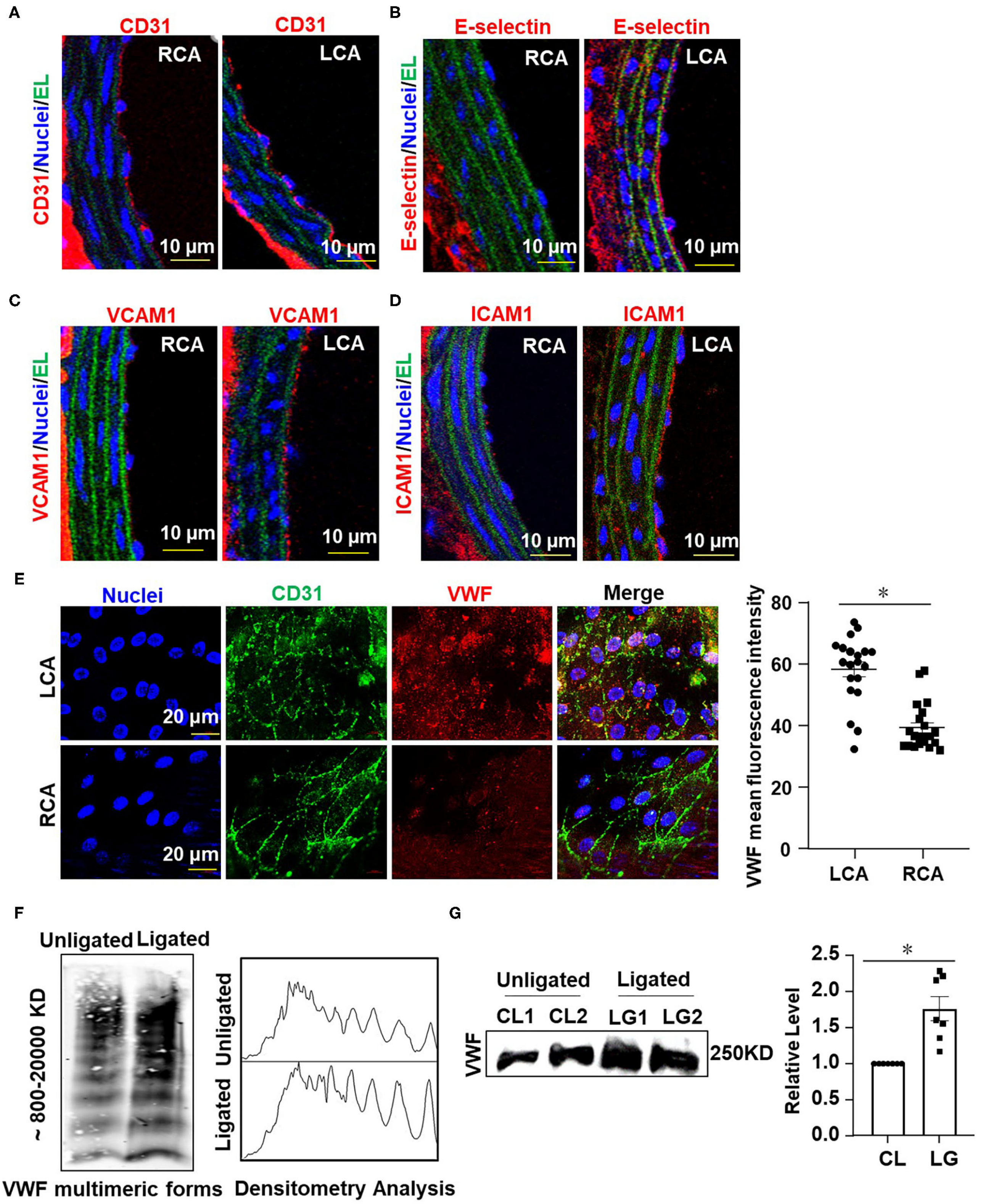

FIGURE 2 | Ligation of LECA induces endothelial inflammation and VWF secretion. **(A–D)** Representative images for immunofluorescent staining of E-selectin (red), VCAM-1 (red), ICAM-1 (red), and endothelial marker CD31 (red) in the unligated RCA or the ligated LCA 1 week-post ligation. EL, elastic lamina (green), the number of tissue samples in **(A–D)** was 7 ($n = 7$). **(E)** VWF levels on the endothelial surfaces of the ligated LCA and the unligated RCA were assessed by *en face*

(Continued)

FIGURE 2 | immunofluorescence 1 day after external carotid artery ligation, and VWF mean fluorescence intensity in LCA and RCA were quantified. $n = 20$ (ligated LCA), $n = 21$ (unligated RCA). **(F,G)** The plasma level of VWF was determined at 1 day after ligation. VWF multimeric patterns and the total VWF level in plasma from the unligated or ligated mice were detected by Western blot assay followed with SDS-agarose gel electrophoresis **(F)** or SDS-polyacrylamide gel electrophoresis **(G)**. CL represented plasma was obtained from unligated mouse; LG represented plasma was derived from the ligated mice. Densitometric analysis of VWF multimers was performed (**F**, right panel) and the average gray values of VWF were analyzed quantitatively (**G**, right panel). Data are mean ± SEM, $n = 7$, $^*P < 0.05$.

the current mechanistic study we were focusing on short-term regulation to avoid the effects of shear stress on expressions of VAMP3 and SNAP23 (**Supplementary Figure 3**). The subcellular localizations of VAMP3 and SNAP23 were distinct in cells subjected to PS or OS. The most predominant phenotype for VAMP3 in cells under PS was perinuclear localization with a condensed appearance, whereas in cells under OS it exhibited a dispersed appearance (**Supplementary Figure 4**). SNAP23 was located mainly in the plasma membrane and also in scattered cytoplasmic structures in cells exposed to PS; in comparison, it was intensively localized to the plasma membrane following OS exposure (**Supplementary Figure 4**). This phenomenon is in line with our previous findings (Zhu et al., 2017). Quantification of the degree of colocalization between fluorophores using Pearson's correlation coefficient indicated an increased co-localization between VAMP3 and SNAP23 in OS vs. PS (**Supplementary Figure 4**), suggesting an enhancement of SNARE-mediated WPB fusion with the plasma membrane. The colocalization of VAMP3 with VWF was actually a bit lower in OS than PS (**Figure 5A**). Since VAMP3 is mainly located at WPB membrane, the colocalization of VAMP3 with VWF might decrease once the release of VWF is activated by OS. The colocalization of SNAP23 with VWF was found higher in OS than PS (**Figure 5B**). The results suggest that more WPBs fuse with cell membrane in OS.

To determine whether VAMP3 and SNAP23 mediate the OS-induced VWF secretion, cells transfected with siRNAs targeting VAMP3 or/and SNAP23 or the control siRNA (**Supplementary Figure 5**) were subjected to PS or OS for 6 h and VWF secretion was then examined. Western blot assay demonstrated a compromised constitutive or OS-induced secretion of VWF in the VAMP3 and SNAP23 inhibited cells (**Figures 5C–E** and **Supplementary Figure 5**). Taken together, these results validated the role of VAMP3 and SNAP23 in mediating the OS-evoked VWF secretion.

Vimentin Associates With SNAP23 to Modulate the Oscillatory Shear Stress-Induced Translocation of SNAP23 to the Cell Membrane

To explore that how OS activates SNAP23, cells were exposed to PS or OS for 1 h and the translocation of SNAP23 to the cell membrane induced by OS was confirmed by immunofluorescence-based colocalization analysis of SNAP23 and vascular endothelial cadherin (VE-cadherin), which is localized at adherent junctions (**Figure 6A**). It has been reported that SNAP23 is targeted to vimentin filaments in fibroblasts and that transfer of SNAP23 from the vimentin-associated reservoir to functional plasma membrane pool may modulate the availability of SNAP23 to form SNARE complexes (Faigle et al., 2000). This prompted us to hypothesize that vimentin associates with SNAP23 in endothelial cells to modulate the OS-induced translocation of SNAP23 to the plasma membrane. To test this hypothesis, we first verified the colocalization of vimentin with SNAP23 in endothelial cells without shearing by immunofluorescent staining, which suggests a potential constitutive association between vimentin and SNAP23 (**Figure 6B**). To validate a physical interaction between vimentin and SNAP23, co-IP assay was performed (**Figures 6C,D**). The results revealed that compared with the control IgG, the SNAP23 antibody-precipitated immunocomplexes were vimentin enriched, suggesting a constitutive physical interaction between vimentin and SNAP23 (**Figure 6C**). Their association could be enhanced by OS exposure vs. PS (**Figure 6D**). The OS-promoted interaction between vimentin and SNAP23 was further confirmed by immunofluorescent staining (**Figure 6E** and **Supplementary Figure 6**) and proximity ligation assay determination of these two proteins (**Supplementary Figure 7**). It should be noted that shear stress altered the cellular localization of vimentin, as vimentin filaments redistributed to the adjacent areas of the cortex during exposure to OS (**Figure 6E**). To disrupt vimentin, cells were treated with monomeric acrylamide at a final concentration of 4 mM (Haudenschild et al., 2011) or control reagent and were then subjected to PS or OS. Treatment with acrylamide resulted in a condensed and perinuclear distribution of vimentin, indicating that the normal organization and function of vimentin networks may have been impaired (**Supplementary Figure 8A**). In the control treatments, OS promoted the plasma membrane-localization of vimentin and SNAP23, in comparison with PS (**Figure 6F**, left panels). Treatment with acrylamide not only prevented the redistribution of vimentin but also prohibited the translocation of SNAP23 to the cell membrane in cells with OS (**Figure 6F**, right panels and **Supplementary Figure 8B**). Altogether, these findings suggest that OS induces movement of vimentin intermediate filaments to mediate the translocation of SNAP23.

Targeting VAMP3 and SNAP23 Could Influence the Disturbed Flow-Induced Thrombosis

To clarify the role of VAMP3 and SNAP23 in mediating the disturbed flow-accelerated thrombosis *in vivo*, we performed loss- and gain-of-function studies of VAMP3/SNAP23 in mice with ligation of the LECA followed by $FeCl_3$-induced arterial injury. Our previous studies have shown that systemic delivery of mTOR complex 1 (mTORC1) inhibitor, rapamycin, can reduce the expressions of VAMP3 and SNAP23 in arterial endothelium

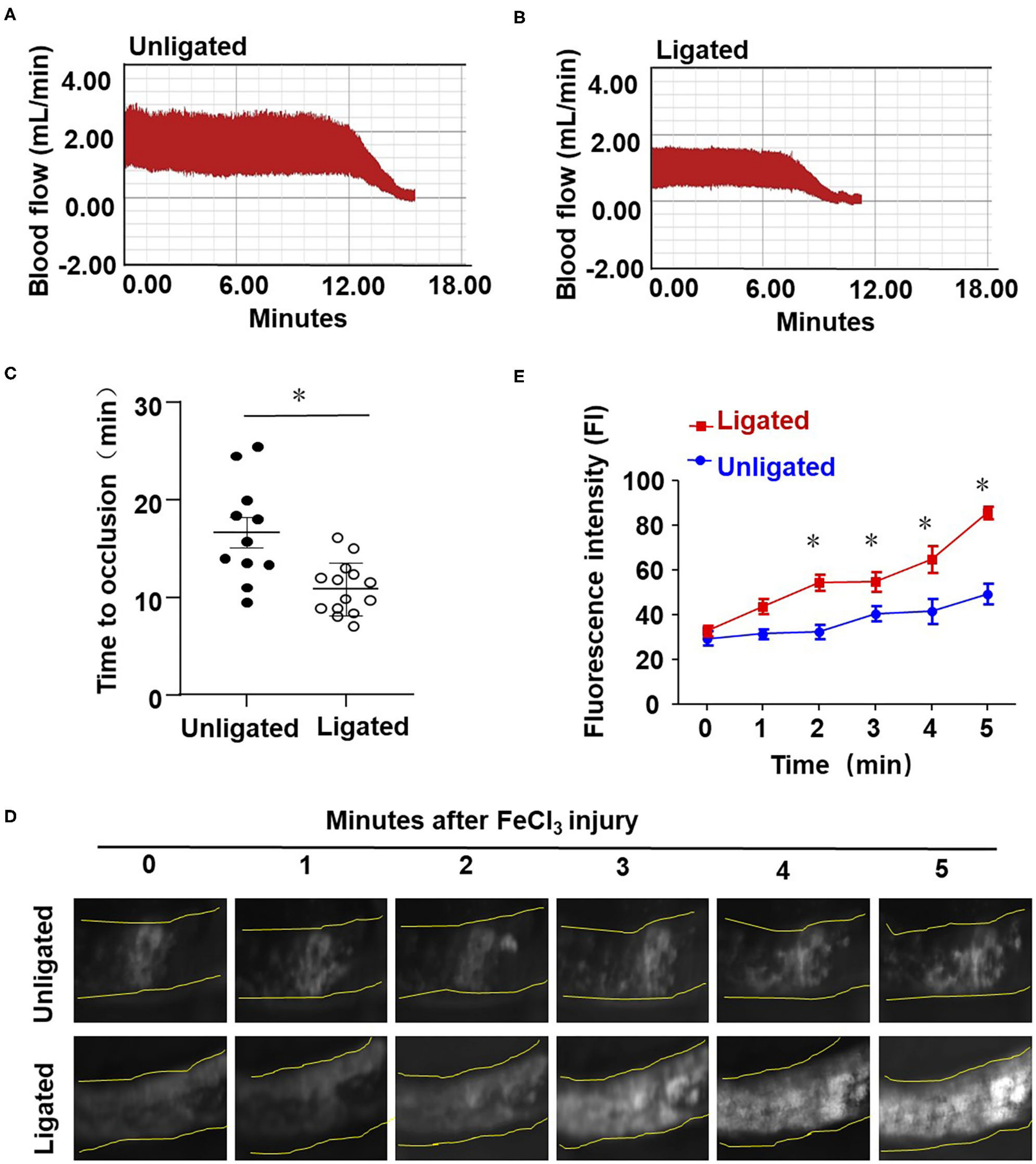

FIGURE 3 | Ligation of LECA accelerates thrombosis upon FeCl$_3$-induced arterial injury. **(A,B)** The LECA of C57BL/6 mice were ligated or unligated (sham operation), and blood flow in the LCA following 20% FeCl$_3$ induced injury was monitored by a doppler echocardiogram. The FeCl$_3$ injury-induced thrombosis assay was performed at 1 day after ligation. Representative image is the timeline starting immediately from placement of the 20% FeCl$_3$ filter paper to the time to occlusion of the unligated **(A)** or ligated mice **(B)**. **(C)** The time of thrombus formation in unligated and ligated mice was analyzed quantitatively, $n = 11$ (unligated mice), $n = 14$ (ligated mice). **(D)** Rhodamine 6G was injected into the right jugular vein of unligated and ligated mice to label platelets, and platelet adhesion to LCA was monitored immediately upon application of 20% FeCl$_3$ (1 day after ligation). Images showed platelet adhesion and thrombus formation in carotid arteries within the indicated durations (3 min) after the application of 20% FeCl$_3$. **(E)** Comparison of the fluorescence intensity in FeCl$_3$-treated arteries from unligated and ligated mice, $n = 5$ (unligated mice), $n = 5$ (ligated mice). Data are mean ± SEM, $^*P < 0.05$.

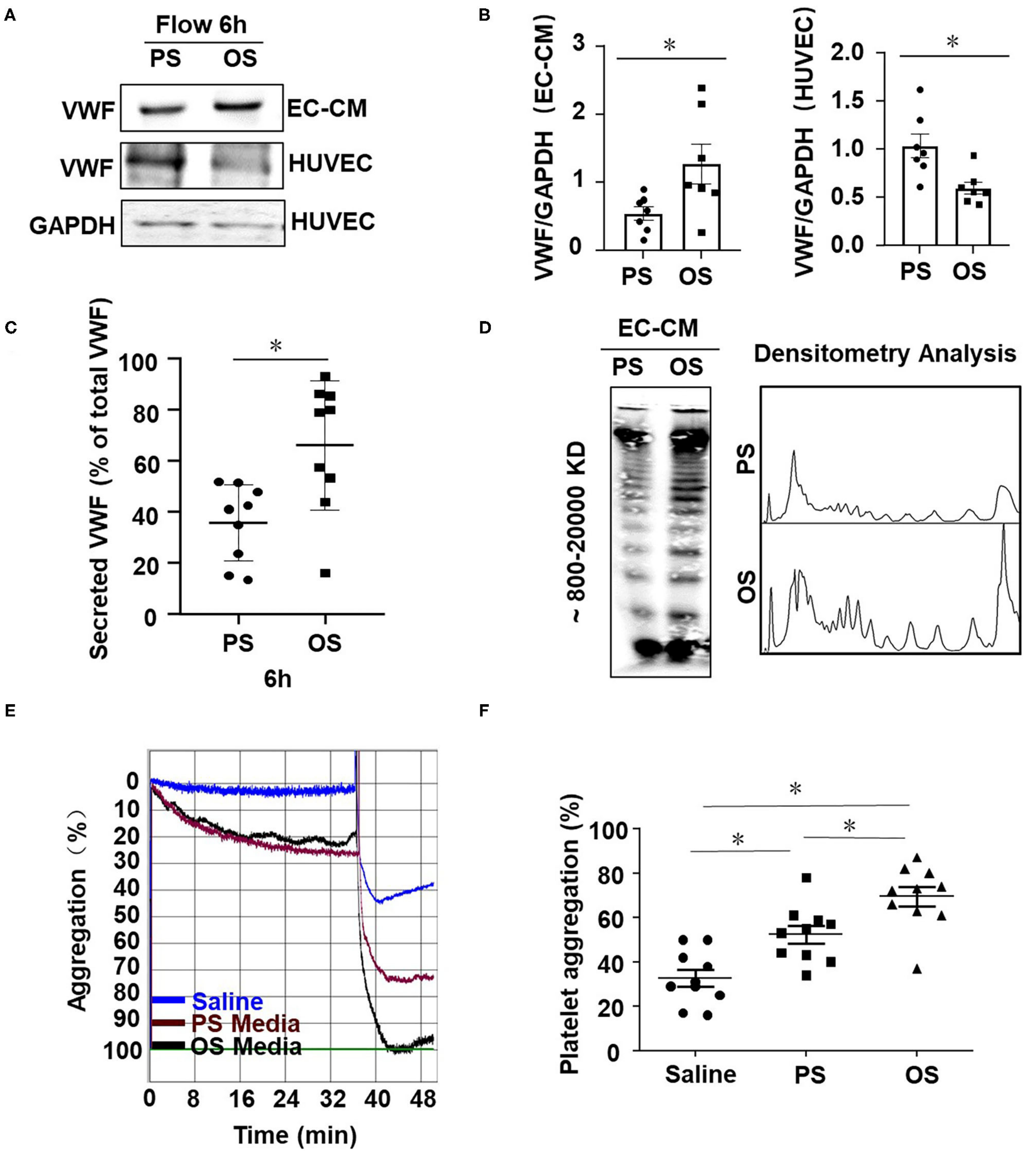

FIGURE 4 | Oscillatory shear enhances endothelial VWF secretion and provokes platelet aggregation. **(A)** Cells were exposed to PS (12 ± 4 dynes/cm^2) or OS (0.5 ± 4 dynes/cm^2) for 6 h and the expressions of VWF in the conditioned media and cells were analyzed by Western blot assay followed with SDS-polyacrylamide gel electrophoresis. **(B)** The average gray values of VWF in **(A)** were analyzed quantitatively. **(C)** The secreted VWF in conditioned media were detected by ELISA, $n = 9$ (PS), $n = 9$ (OS). **(D)** VWF multimers were analyzed by Western blot assay followed with SDS-agarose gel electrophoresis and densitometric analysis. **(E)** Representative curves of human platelet aggregation assay. The platelet-rich plasma (PRP) were mixed with saline solution or the conditioned media from the sheared endothelial cells and platelet aggregation was induced by adding ADP into the mixture. **(F)** Platelet aggregation is expressed as the percentage of light transmittance (y-axis) over time (x-axis). Platelet aggregation in each group were recorded and quantitatively analyzed using one-way ANOVA. $n = 10$ (Saline), $n = 10$ (PS), $n = 10$ (OS). Data are mean ± SEM, $^*P < 0.05$.

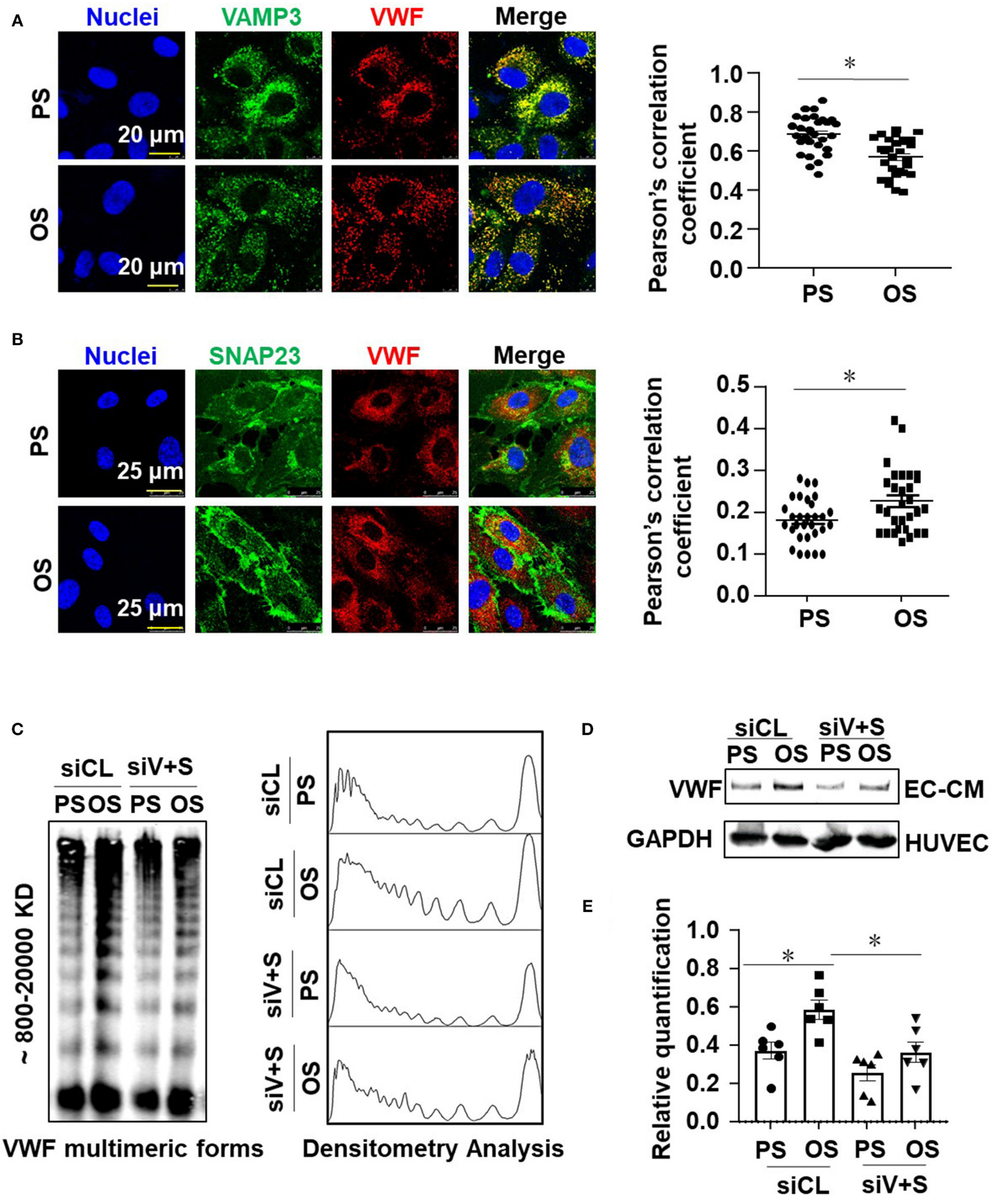

FIGURE 5 | Oscillatory shear stress enhances endothelial VWF secretion via promoting the activation of VAMP3 and SNAP23. **(A,B)** Cells were exposed to PS (12 ± 4 dynes/cm^2) or OS (0.5 ± 4 dynes/cm^2) for 1 h, and then the subcellular localizations of VAMP3, SNAP23, and VWF were assessed. The colocalization of VAMP3 and VWF **(A)**, SNAP23 and VWF **(B)** were quantified. **(C,D)** Cells were transfected with siRNAs targeting VAMP3 (siV) and SNAP23 (siS) or the control siRNAs at a concentration of 40 nmol/L, and were then exposed to PS or OS for 6 h. **(C)** The VWF multimers, and **(D)** the total levels of VWF in conditioned media were assessed. **(E)** The bands from SDS-polyacrylamide gel electrophoresis were quantified. Results in **(E)** are mean ± SEM from **(D)**, $n = 6$, $^*P < 0.05$.

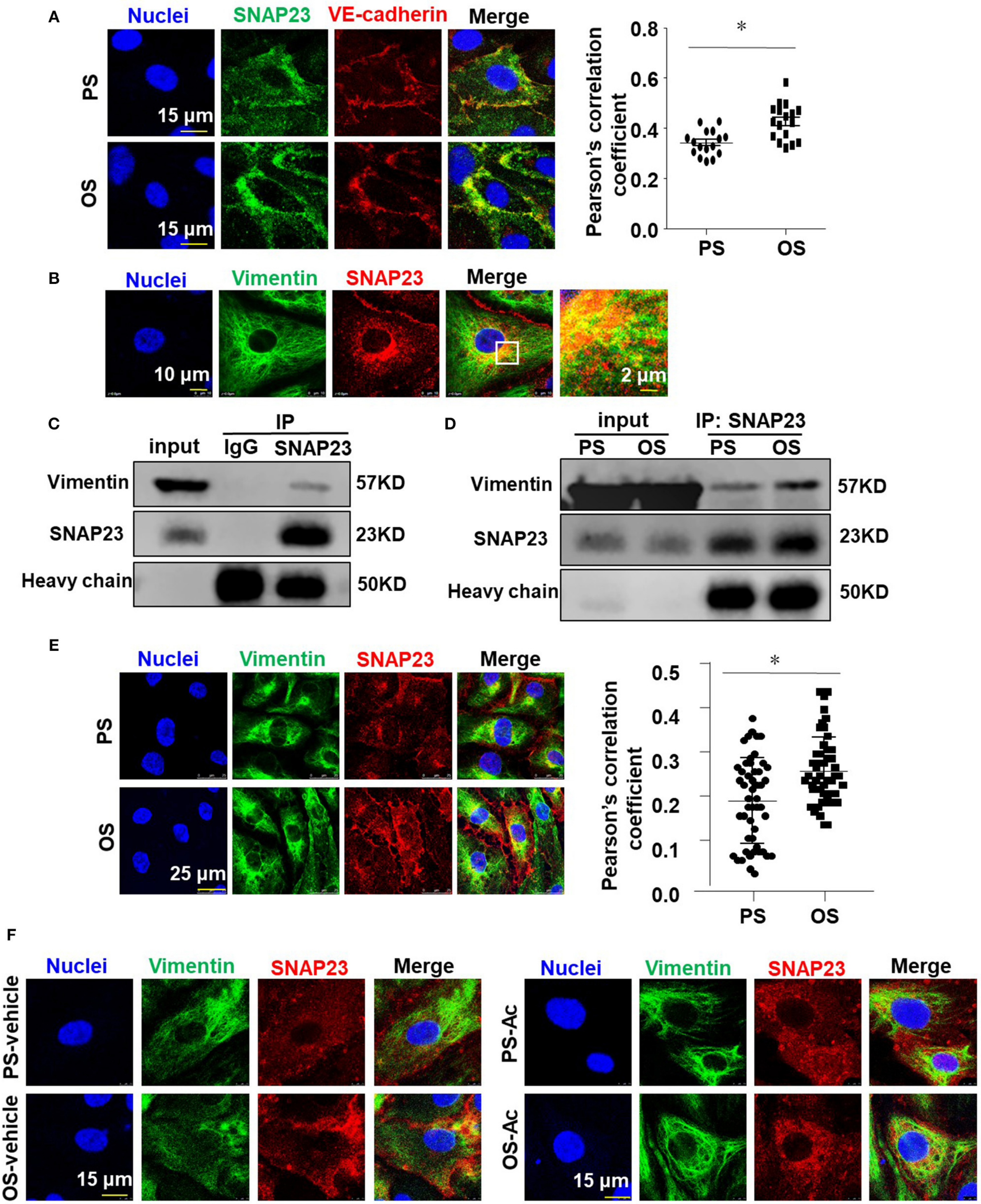

FIGURE 6 | Vimentin associates with SNAP23 to modulate the oscillatory shear stress-induced translocation of SNAP23 to the cell membrane. **(A,B,E)** Cells were exposed to PS (12 ± 4 dynes/cm^2) or OS (0.5 ± 4 dynes/cm^2) for 1 h **(A,E)** or kept in static condition **(B)**, and then the subcellular localizations of SNAP23, VE-cadherin and vimentin were assessed by immunofluorescence. Pearson's correlation coefficient was calculated to quantify their colocalizations. **(C,D)** Cells were

(Continued)

FIGURE 6 | exposed to PS or OS for 1 h **(D)** or kept in static condition **(C)**, and the association of SNAP23 with vimentin was assessed by co-IP (IP: SNAP23, IB: Vimentin). **(F)** Cells were pretreated with acrylamide (Ac, 4 mM) or with the control vehicle (H_2O) for 16 h, exposed to PS or OS for 1 h, and the subcellular localizations of vimentin and SNAP23 were assessed. Numbers of quantified cells or fields in each experiment are as followed: in **(A)**, $n = 17$ (PS), $n = 17$ (OS); in **(E)**, $n = 50$ (PS), $n = 50$ (OS). Results in **(A,E)** are mean ± SEM, $^{*}P < 0.05$.

(Zhu et al., 2017). Thus, to inhibit VAMP3 and SNAP23, mice were either received intraperitoneal injection of rapamycin or its control solvent in current experiments. For the gain-of-function of VAMP3/SNAP23, the LCAs of mice were subjected to a local intraluminal incubation of adenovirus expressing SNAP23/VAMP3 (Ad-SNAP23 and Ad-VAMP3) or its control virus before ligation. As expected, ligation of LECA resulted in increased expressions of VAMP3 and SNAP23 in the endothelial of the common carotid arteries at 1 week post-surgery. The increase could be suppressed by systemic delivery of rapamycin or be further enhanced by intraluminal application of Ad-VAMP3 and Ad-SNAP23 viruses (**Figures 7A–D**). Treatment with rapamycin significantly reduced VWF level on the intimal surface. In contrast, intraluminal application of Ad-SNAP23 and Ad-VAMP3 viruses significantly increased VWF level on the intimal surface (**Figures 7E,F**). Treatment with rapamycin significantly ameliorated the $FeCl_3$-induced thrombogenesis in the carotid arteries of mice with average time to occlusion extended from 9.12 ± 2.2 min to 13.17 ± 6.07 min (**Figure 7G**). On the contrary, intraluminal application of Ad-SNAP23 and Ad-VAMP3 viruses significantly exaggerated $FeCl_3$-induced thrombogenesis in the treated arteries in compared with those in the controls (**Figure 7H**). The average time to occlusion was reduced from 25.88 ± 11.68 min to 11.84 ± 2.88 min (**Figure 7H**). Our results suggest VAMP3 and SNAP23 as potential targets for preventing the disturbed flow-accelerated thrombus formation.

DISCUSSION

Atherosclerotic geometries-resulted fluid mechanical conditions have been suggested to promote platelet aggregation and thrombus formation (Nesbitt et al., 2009). To study the phenomenon and the underlying mechanisms, sophisticated and dedicated research models have been developed and applied. In Nesbitt et al. (2009) study, the vessel geometry as well as local blood flow were altered by mechanically compressing the vessel with a blunted microinjection needle to progressively stenose the vessel lumen. CFD modeling of the stenotic vessel geometry revealed generation of disturbed blood flow downstream of the stenotic site. Similarly in Westein et al. (2013) study, stenosis was induced by localized vessel compression with a 27-gauge needle. Synergetic effects of atherosclerotic geometries and vessel injury on platelet aggregation and thrombosis were investigated on the basis of the disturbed flow model mentioned above in combination with photoactivation with an excitation wavelength at 550 nm or microinjection of 6% $FeCl_3$ into the tissue adjacent to the arteriole of interest (Nesbitt et al., 2009). Although these studies indicate that flow disturbance is associated with thrombus formation, they do not provide evidence showing how disturbed flow affects the endothelium-dependent regulation on thrombosis and hemostasis. Another limitation of the mechanical compression model is that the areas exposed to disturbed flow are very small which makes it difficult to analyze endothelial gene expression and function in those areas.

Partial ligation of carotid artery was initially described as a model of flow reduction to study vascular remodeling (Sullivan and Hoying, 2002). In this model, all branches originating from LCA, except for the left thyroid artery, were ligated, resulting in a substantial flow reduction in LCA. By using CFD modeling incorporated the geometry of mouse arteries as determined by high-resolution ultrasound measurements, Nam et al. described partial carotid ligation as a model of disturbed flow with characteristics of low and oscillatory wall shear stress (Nam et al., 2009). In response to partial ligation, blood flow significantly decreased (−90%) in LCA. The substantial local application of $FeCl_3$ might induce thrombus formation in the operated LCA as well as decrease and stagnation of blood flow as the flowmeter would detected. Since the assessment of thrombosis is based on the time to cessation of blood flow, it becomes very difficult to determine a further decrease if the flow rate is compared with an extreme low baseline. We therefore modified the partial ligation model. In our adapted model only the LECA is ligated, resulting in a generation of low and oscillatory shear stress in the LCA. CFD simulation on the basis of vessel geometry and flow velocity provided by MRI and high-resolution ultrasound measurements revealed decreases in blood flow velocity and TAWSS, and increases in OSI and RRT in LCA in comparison with pre-ligation (**Figures 1E–J**), suggesting a successful generation of disturbed flow. To note that the flow velocity in the ligated LCA is appropriate 20–30 cm/s, which is much higher than that in the partially ligated LCA in previous model. To validate the functional consequences of disturbed flow applying to the vessel wall, expressions of pro-inflammatory factor E-selectin, VCAM-1 and ICAM-1 in the common carotid artery endothelial cells were measured and verified an induction of endothelial inflammation (**Figures 2B–D**). These results agree with previous reports showing the partial ligation-induced endothelial dysfunction (Nam et al., 2009).

Regulations of fluid shear stress on expression and secretion of VWF have been studied previously by the utilization of various *in vitro* models. Using a parallel plate flow apparatus, Hough et al. found that exposure of endothelial cells to laminar shear stress at 15 dynes/cm^2 for 6 or 24 h enhanced VWF promoter activity to increase the mRNA level of VWF (Hough et al., 2008). By the utilization of the same flow apparatus,

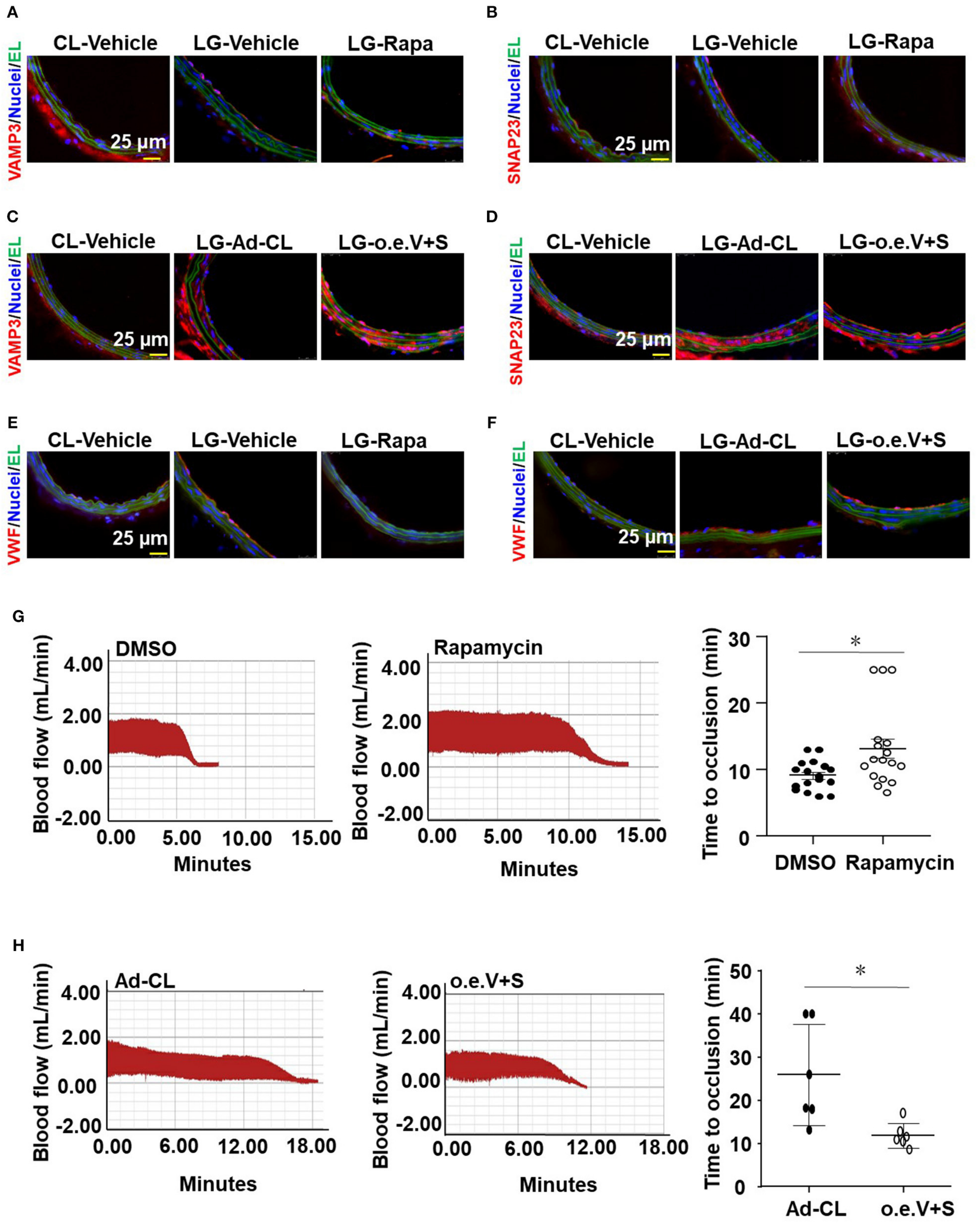

FIGURE 7 | VAMP3 and SNAP23 play important roles in disturbed flow-induced thrombosis. C57BL/6 mice were subjected to ligation of LECA. Some mice were then subjected to intraperitoneal injection with rapamycin (Rapa, 1 mg/kg body weight) or the control vehicle (DMSO) every other day for 7 days **(A,B)**, others were subjected to a locally intraluminal incubation with adenovirus expressing VAMP3(Ad-VAMP3) and SNAP23(Ad-SNAP23) or the control virus (Ad-CL)

(Continued)

FIGURE 7 | (C,D). **(A–F)** Representative images of immunofluorescent staining of VAMP3, SNAP23 and VWF in unligated RCA or ligated LCA of mice. CL, the unligated RCA; LG, the ligated LCA; EL, Elastic lamina; o.e.V+S, Ad-VAMP3 and Ad-SNAP23. **(G,H)** LCA of the ligated mice were then subjected to $FeCl_3$-induced arterial injury. Blood flows in the LCA were monitored by a doppler echocardiogram. Representative images are the timeline starting immediately from placement of the $FeCl_3$ filter paper to time to occlusion of the carotid artery occlusion. **(G,H)** Quantification and statistical analysis of the time to occlusion. Data are mean ± SEM, $n = 17$ per group **(G)**, $n = 6$ per group **(H)**, $^* P < 0.05$.

Gomes et al. reported that exposure of endothelial cells to laminar shear stress at 13 dynes/cm^2 for 2 h promoted the secretion of VWF (Gomes et al., 2005) with no mechanistic explanations were mentioned. Similar results reported by Galbusera et al. using a cone-and-plate flow device showed that exposure of endothelial cells to laminar shear stress of varying magnitude (from 2 to 12 dynes/cm^2) for 6 h increased the VWF secretion in a magnitude dependent manner (Galbusera et al., 1997). It should be noted that in the above studies the controls were set to be static condition, which may not be physiologically relevant in the study of shear-modulated endothelial function. To the best of our knowledge, this present work is the first study to compare the regulation of OS vs. PS on VWF secretion.

Vesicular-transport protein VAMP3 was originally found to be enriched in the membrane of GluT4 secretory granules and undergoes translocation form the cytoplasmic subcompartment to the plasma membrane in response to insulin to mediate glucose transport in adipocyte (Cain et al., 1992). In endothelial cells, VAMP3 was found localized on the surface of WPBs, cooperated with SNAP23 that are localized predominantly to the plasma membrane to direct the fusion of WPBs with the plasm membrane, and thus mediating the exocytosis of VWF (Pulido et al., 2011). Enhancement in the on-WPBs-surface-localization of VAMP3 and on-plasma-membrane-localization of SNAP23 would increase the chances of an encounter with each other, allowing aggravated WPB exocytosis and the consequently promoted VWF secretion happen. In previous study we have shown that disturbed flow increased the endothelial secretion of athero-prone microRNAs via the activation of VAMP3 and SNAP23 at both transcriptional and translocational levels; pharmacological intervention of mTORC1 inhibited the transcription of both VAMP3 and SNAP23. In the current study we extended our research and explored the mechanisms by which disturbed flow or oscillatory shear stress damage the endothelium to initiate platelet capture and thrombus formation. Our study has fully proved that flow disturbance accelerates the $FeCl_3$-induced thrombosis and the effects are dependent on the VAMP3 and SNAP23-mediated VWF secretion (**Figures 3–5**, **7**). Our study showed that knockdown of VAMP3 and SNAP23 could compromise the flow disturbance-evoked endothelial VWF secretion (**Figures 5C–E**), providing direct evidence demonstrating the contribution of endothelial VAMP3/SNAP23 to thrombosis. Notably the *in vivo* intervention of VAMP3/SNAP23 by systemic delivery of rapamycin ameliorates thrombi formation (**Figure 7G**), echoing the value of mTOR inhibition in preventing the development of atherosclerosis (Kurdi et al., 2016; Zhu et al., 2017). Furthermore, we provided mechanistic evidence showing that how disturbed flow activates the translocation of SNAP23 (**Figure 6**). Vimentin is the major and important intermediate filament protein that makes up cytoskeletons (Dave and Bayless, 2014). It is widely expressed in endothelial cells, mesenchymal cells, leukocytes, neurons cell and some epithelial cell to regulate cell adhesion, migration, secretion, and other fundamental cellular behaviors (Ikawa et al., 2014; Antfolk et al., 2017; Costigliola et al., 2017). Rapid displacement and re-organization of vimentin intermediate filaments have been observed in living endothelial cells exposed to laminar shear stress at 12 dynes/cm^2 (Helmke et al., 2000). However, how the organization/distribution of vimentin networks response to OS vs. PS had not been characterized before. Our results revealed that OS promoted a distribution of vimentin near the cell cortex (**Figures 6E,F**). The subcellular localization of vimentin under OS that we observed is consistent with previous study showing that vimentin presents in endothelial cell apical cortex to provide mechanical supply to the cell (Pesen and Hoh, 2005). Vimentin filaments also interact with actin at the cell cortex to coordinate cell growth and division (Duarte et al., 2019). They may also coordinate the endothelial secretion of VWF, as our data have shown that vimentin physically interacts with SNAP23 to mediate the OS-induced translocation of SNAP23 to the cell membrane (**Figure 6** and **Supplementary Figure 7**), and probably the consequent SNAP23-dependent fusion of WPBs with the plasma membranes. Our findings together with reports by others lead to a conclusion that vimentin is essentially involved in the mechanical force-elicited stress responses. Future studies are warranted to determine the mechanisms by which disturbed flow activatesVAMP3.

DATA AVAILABILITY STATEMENT

The original contributions presented in the study are included in the article/**Supplementary Materials**, further inquiries can be directed to the corresponding author/s.

ETHICS STATEMENT

The animal study was reviewed and approved by Biomedical Ethics Committee of Peking University.

AUTHOR CONTRIBUTIONS

JZ, J-JZ, and Z-TJ designed study. J-JZ and Z-TJ performed research. J-JZ, Z-TJ, CL, Y-FX, JW, F-FY, W-JY, WP, L-LH, and Y-HZ discussed the data. J-JZ, A-QS, JZ, and Z-TJ analyzed data.

JZ, A-QS, J-JZ wrote the paper. All authors contributed to the article and approved the submitted version.

FUNDING

This work was funded by the National Natural Science Foundation of China (Project 91939302, 81974052, 91949112, and 81921001 to JZ, 11872096 to A-QS, 31800785 to J-JZ) and China Postdoctoral Science Foundation (Project 2017M620008 to J-JZ).

SUPPLEMENTARY MATERIAL

The Supplementary Material for this article can be found online at: https://www.frontiersin.org/articles/10.3389/fcell.2020.576826/full#supplementary-material

REFERENCES

Allende, M., Molina, E., Lecumberri, R., Sanchez-Arias, J. A., Ugarte, A., Guruceaga, E., et al. (2017). Inducing heat shock protein 70 expression provides a robust antithrombotic effect with minimal bleeding risk. *Thromb. Haemost.* 117, 1722–1729. doi: 10.1160/TH17-02-0108

Antfolk, D., Sjoqvist, M., Cheng, F., Isoniemi, K., Duran, C. L., Rivero-Muller, A., et al. (2017). Selective regulation of Notch ligands during angiogenesis is mediated by vimentin. *Proc. Natl. Acad. Sci. U. S. A.* 114, E4574–E4581. doi: 10.1073/pnas.1703057114

Bierings, R., Hellen, N., Kiskin, N., Knipe, L., Fonseca, A. V., Patel, B., et al. (2012). The interplay between the Rab27A effectors Slp4-a and MyRIP controls hormone-evoked Weibel-Palade body exocytosis. *Blood* 120, 2757–2767. doi: 10.1182/blood-2012-05-429936

Burgoyne, R. D., and Morgan, A. (2003). Secretory granule exocytosis. *Physiol. Rev.* 83, 581–632. doi: 10.1152/physrev.00031.2002

Cain, C. C., Trimble, W. S., and Lienhard, G. E. (1992). Members of the VAMP family of synaptic vesicle proteins are components of glucose transporter-containing vesicles from rat adipocytes. *J. Biol. Chem.* 267, 11681–11684.

Chaudhary, P. K., Kim, S., Jee, Y., Lee, S. H., Park, K. M., and Kim, S. (2020). Role of GRK6 in the Regulation of platelet activation through selective G protein-coupled receptor (GPCR) desensitization. *Int. J. Mol. Sci.* 21:3932. doi: 10.3390/ijms21113932

Chiu, J. J., and Chien, S. (2011). Effects of disturbed flow on vascular endothelium: pathophysiological basis and clinical perspectives. *Physiol. Rev.* 91, 327–387. doi: 10.1152/physrev.00047.2009

Costigliola, N., Ding, L., Burckhardt, C. J., Han, S. J., Gutierrez, E., Mota, A., et al. (2017). Vimentin fibers orient traction stress. *Proc. Natl. Acad. Sci. U. S. A.* 114, 5195–5200. doi: 10.1073/pnas.1614610114

Dave, J. M., and Bayless, K. J. (2014). Vimentin as an integral regulator of cell adhesion and endothelial sprouting. *Microcirculation* 21, 333–344. doi: 10.1111/micc.12111

de Leeuw, H. P., Fernandez-Borja, M., Reits, E. A., Romani de Wit, T., Wijers-Koster, P. M., Hordijk, P. L., et al. (2001). Small GTP-binding protein Ral modulates regulated exocytosis of von Willebrand factor by endothelial cells. *Arterioscler. Thromb. Vasc. Biol.* 21, 899–904. doi: 10.1161/01.ATV.21.6.899

Duarte, S., Viedma-Poyatos, A., Navarro-Carrasco, E., Martinez, A. E., Pajares, M. A., and Perez-Sala, D. (2019). Vimentin filaments interact with the actin cortex in mitosis allowing normal cell division. *Nat. Commun.* 10:4200. doi: 10.1038/s41467-019-12029-4

Dyer, M. R., Plautz, W. E., Ragni, M. V., Alexander, W., Haldeman, S., Sperry, J. L., et al. (2020). Traumatic injury results in prolonged circulation of ultralarge von Willebrand factor and a reduction in ADAMTS13 activity. *Transfusion* 60, 130–1318. doi: 10.1111/trf.15856

Faigle, W., Colucci-Guyon, E., Louvard, D., Amigorena, S., and Galli, T. (2000). Vimentin filaments in fibroblasts are a reservoir for SNAP23, a component of the membrane fusion machinery. *Mol. Biol. Cell.* 11, 3485–3494. doi: 10.1091/mbc.11.10.3485

Farrehi, P. M., Ozaki, C. K., Carmeliet, P., and Fay, W. P. (1998). Regulation of arterial thrombolysis by plasminogen activator inhibitor-1 in mice. *Circulation* 97, 1002–1008. doi: 10.1161/01.CIR.97.10.1002

Feintuch, A., Ruengsakulrach, P., Lin, A., Zhang, J., Zhou, Y. Q., Bishop, J., et al. (2007). Hemodynamics in the mouse aortic arch as assessed by MRI, ultrasound, and numerical modeling. *Am. J. Physiol. Heart Circ. Physiol.* 292, H884–892. doi: 10.1152/ajpheart.00796.2006

Galbusera, M., Zoja, C., Donadelli, R., Paris, S., Morigi, M., Benigni, A., et al. (1997). Fluid shear stress modulates von Willebrand factor release from human vascular endothelium. *Blood* 90, 1558–1564. doi: 10.1182/blood.V90.4.1558.1558_1558_1564

Gomes, N., Legrand, C., and Fauvel-Lafeve, F. (2005). Shear stress induced release of von Willebrand factor and thrombospondin-1 in HUVEC extracellular matrix enhances breast tumour cell adhesion. *Clin. Exp. Metastasis* 22, 215–223. doi: 10.1007/s10585-005-7359-5

Hathcock, J. J. (2006). Flow effects on coagulation and thrombosis. *Arterioscler. Thromb. Vasc. Biol.* 26, 1729–1737. doi: 10.1161/01.ATV.0000229658.76797.30

Haudenschild, D. R., Chen, J., Pang, N., Steklov, N., Grogan, S. P., Lotz, M. K., et al. (2011). Vimentin contributes to changes in chondrocyte stiffness in osteoarthritis. *J. Orthop. Res.* 29, 20–25. doi: 10.1002/jor.21198

He, X., and Ku, D. N. (1996). Pulsatile flow in the human left coronary artery bifurcation: average conditions. *J. Biomech. Eng.* 118, 74–82. doi: 10.1115/1.2795948

Helmke, B. P., Goldman, R. D., and Davies, P. F. (2000). Rapid displacement of vimentin intermediate filaments in living endothelial cells exposed to flow. *Circ. Res.* 86, 745–752. doi: 10.1161/01.RES.86.7.745

Hough, C., Cameron, C. L., Notley, C. R., Brown, C., O'Brien, L., Keightley, A. M., et al. (2008). Influence of a GT repeat element on shear stress responsiveness of the VWF gene promoter. *J. Thromb. Haemost.* 6, 1183–1190. doi: 10.1111/j.1538-7836.2008.03011.x

Hyun, S., Kleinstreuer, C., and Archie, J. P. Jr. (2000). Hemodynamics analyses of arterial expansions with implications to thrombosis and restenosis. *Med. Eng. Phys.* 22, 13–27. doi: 10.1016/S1350-4533(00)00006-0

Ikawa, K., Satou, A., Fukuhara, M., Matsumura, S., Sugiyama, N., Goto, H., et al. (2014). Inhibition of endocytic vesicle fusion by Plk1-mediated phosphorylation of vimentin during mitosis. *Cell Cycle* 13, 126–137. doi: 10.4161/cc.26866

Kurdi, A., De Meyer, G. R., and Martinet, W. (2016). Potential therapeutic effects of mTOR inhibition in atherosclerosis. *Br. J. Clin. Pharmacol.* 82, 1267–1279. doi: 10.1111/bcp.12820

Kurz, K. D., Main, B. W., and Sandusky, G. E. (1990). Rat model of arterial thrombosis induced by ferric chloride. *Thromb. Res.* 60, 269–280. doi: 10.1016/0049-3848(90)90106-M

Lee, S. W., Antiga, L., and Steinman, D. A. (2009). Correlations among indicators of disturbed flow at the normal carotid bifurcation. *J. Biomech. Eng.* 131:061013. doi: 10.1115/1.3127252

Li, B., Fu, C., Ma, G., Fan, Q., and Yao, Y. (2017). Photoacoustic imaging: a novel tool for detecting carotid artery thrombosis in mice. *J. Vasc. Res.* 54, 217–225. doi: 10.1159/000477631

Li, W., Nieman, M., and Sen Gupta, A. (2016). Ferric chloride-induced murine thrombosis models. *J. Vis. Exp*. 54479. doi: 10.3791/54479

Li, Z., and Kleinstreuer, C. (2006). Analysis of biomechanical factors affecting stent-graft migration in an abdominal aortic aneurysm model. *J. Biomech.* 39, 2264–2273. doi: 10.1016/j.jbiomech.2005.07.010

Liang, M. L., Da, X. W., He, A. D., Yao, G. Q., Xie, W., Liu, G., et al. (2015a). Pentamethylquercetin (PMQ) reduces thrombus formation by inhibiting platelet function. *Sci. Rep.* 5:11142. doi: 10.1038/srep11142

Liang, Y., Fu, Y., Qi, R., Wang, M., Yang, N., He, L., et al. (2015b). Cartilage oligomeric matrix protein is a natural inhibitor of thrombin. *Blood* 126, 905–914. doi: 10.1182/blood-2015-01-621292

Lopes da Silva, M., and Cutler, D. F. (2016). von Willebrand factor multimerization and the polarity of secretory pathways in endothelial cells. *Blood* 128, 277–285. doi: 10.1182/blood-2015-10-677054

Mustard, J. F., Jorgensen, L., Hovig, T., Glynn, M. F., and Rowsell, H.C. (1966). Role of platelets in thrombosis. *Thromb. Diath. Haemorrh. Suppl.* 21, 131–158.

Mustard, J. F., Murphy, E. A., Rowsell, H. C., and Downie, H. G. (1962). Factors influencing thrombus formation *in vivo*. *Am. J. Med.* 33, 621–647. doi: 10.1016/0002-9343(62)90243-7

Nam, D., Ni, C. W., Rezvan, A., Suo, J., Budzyn, K., Llanos, A., et al. (2009). Partial carotid ligation is a model of acutely induced disturbed flow, leading to rapid endothelial dysfunction and atherosclerosis. *Am. J. Physiol. Heart Circ. Physiol.* 297, H1535–1543. doi: 10.1152/ajpheart.00510.2009

Nemeth, N., Alexy, T., Furka, A., Baskurt, O. K., Meiselman, H. J., Furka, I., et al. (2009). Inter-species differences in hematocrit to blood viscosity ratio. *Biorheology* 46, 155–165. doi: 10.3233/BIR-2009-0533

Nesbitt, W. S., Westein, E., Tovar-Lopez, F. J., Tolouei, E., Mitchell, A., Fu, J., et al. (2009). A shear gradient-dependent platelet aggregation mechanism drives thrombus formation. *Nat. Med.* 15, 665–673. doi: 10.1038/nm.1955

Nightingale, T., and Cutler, D. (2013). The secretion of von Willebrand factor from endothelial cells; an increasingly complicated story. *J Thromb. Haemost.* 11 (Suppl. 1), 192–201. doi: 10.1111/jth.12225

Pesen, D., and Hoh, J. H. (2005). Micromechanical architecture of the endothelial cell cortex. *Biophys. J.* 88, 670–679. doi: 10.1529/biophysj.104.049965

Plautz, W. E., Matthay, Z. A., Rollins-Raval, M. A., Raval, J. S., Kornblith, L. Z., and Neal, M. D. (2020). Von Willebrand factor as a thrombotic and inflammatory mediator in critical illness. *Transfusion* 60, S158–S166. doi: 10.1111/trf.15667

Predescu, S. A., Predescu, D. N., Shimizu, K., Klein, I. K., and Malik, A. B. (2005). Cholesterol-dependent syntaxin-4 and SNAP-23 clustering regulates caveolar fusion with the endothelial plasma membrane. *J. Biol. Chem.* 280, 37130–37138. doi: 10.1074/jbc.M505659200

Pulido, I. R., Jahn, R., and Gerke, V. (2011). VAMP3 is associated with endothelial weibel-palade bodies and participates in their Ca(2+)-dependent exocytosis. *Biochim. Biophys. Acta* 1813, 1038–1044. doi: 10.1016/j.bbamcr.2010.11.007

Ruggeri, Z. M. (2001). Structure of von Willebrand factor and its function in platelet adhesion and thrombus formation. *Best Pract. Res. Clin. Haematol.* 14, 257–279. doi: 10.1053/beha.2001.0133

Sakalihasan, N., Limet, R., and Defawe, O. D. (2005). Abdominal aortic aneurysm. *Lancet* 365, 1577–1589. doi: 10.1016/S0140-6736(05)66459-8

Sporn, L. A., Chavin, S. I., Marder, V. J., and Wagner, D. D. (1985). Biosynthesis of von Willebrand protein by human megakaryocytes. *J. Clin. Invest.* 76, 1102–1106. doi: 10.1172/JCI112064

Studt, J. D., Budde, U., Schneppenheim, R., Eisert, R., von Depka Prondzinski, M., Ganser, A., et al. (2001). Quantification and facilitated comparison of von Willebrand factor multimer patterns by densitometry. *Am. J. Clin. Pathol.* 116, 567–574. doi: 10.1309/75CQ-V7UX-4QX8-WXE7

Sullivan, C. J., and Hoying, J. B. (2002). Flow-dependent remodeling in the carotid artery of fibroblast growth factor-2 knockout mice. *Arterioscler. Thromb. Vasc. Biol.* 22, 1100–1105. doi: 10.1161/01.ATV.0000023230.17493.E3

Valentijn, K. M., and Eikenboom, J. (2013). Weibel-Palade bodies: a window to von Willebrand disease. *J. Thromb. Haemost.* 11, 581–592. doi: 10.1111/jth.12160

Valentijn, K. M., Sadler, J. E., Valentijn, J. A., Voorberg, J., and Eikenboom, J. (2011). Functional architecture of Weibel-Palade bodies. *Blood* 117, 5033–5043. doi: 10.1182/blood-2010-09-267492

Wagner, D. D., Olmsted, J. B., and Marder, V. J. (1982). Immunolocalization of von Willebrand protein in Weibel-Palade bodies of human endothelial cells. *J. Cell Biol.* 95, 355–360. doi: 10.1083/jcb.95.1.355

Westein, E., van der Meer, A. D., Kuijpers, M. J., Frimat, J. P., van den Berg, A., and Heemskerk, J. W. (2013). Atherosclerotic geometries exacerbate pathological thrombus formation poststenosis in a von Willebrand factor-dependent manner. *Proc. Natl. Acad. Sci. U. S. A.* 110, 1357–1362. doi: 10.1073/pnas.1209905110

Ya, F., Xu, X. R., Shi, Y., Gallant, R. C., Song, F., Zuo, X., et al. (2019). Coenzyme Q10 Upregulates platelet cAMP/PKA pathway and attenuates integrin alphaIIbbeta3 signaling and thrombus growth. *Mol. Nutr. Food Res.* 63:e1900662. doi: 10.1002/mnfr.201900662

Zhu, J. J., Liu, Y. F., Zhang, Y. P., Zhao, C. R., Yao, W. J., Li, Y. S., et al. (2017). VAMP3 and SNAP23 mediate the disturbed flow-induced endothelial microRNA secretion and smooth muscle hyperplasia. *Proc. Natl. Acad. Sci. U. S. A.* 114, 8271–8276. doi: 10.1073/pnas.1700561114

Zhu, Q., Yamakuchi, M., and Lowenstein, C. J. (2015). SNAP23 regulates endothelial exocytosis of von Willebrand Factor. *PLoS ONE* 10:e0118737. doi: 10.1371/journal.pone.0118737

Zografou, S., Basagiannis, D., Papafotika, A., Shirakawa, R., Horiuchi, H., Auerbach, D., et al. (2012). A complete Rab screening reveals novel insights in Weibel-Palade body exocytosis. *J. Cell Sci.* 125 (Pt 20), 4780–4790. doi: 10.1242/jcs.104174

Conflict of Interest: The authors declare that the research was conducted in the absence of any commercial or financial relationships that could be construed as a potential conflict of interest.

frontiers
in Cell and Developmental Biology

ORIGINAL RESEARCH
published: 09 December 2020
doi: 10.3389/fcell.2020.606989

Cyclic Stretch Induces Vascular Smooth Muscle Cells to Secrete Connective Tissue Growth Factor and Promote Endothelial Progenitor Cell Differentiation and Angiogenesis

*Jing Yan†, Wen-Bin Wang†, Yang-Jing Fan†, Han Bao, Na Li, Qing-Ping Yao, Yun-Long Huo, Zong-Lai Jiang, Ying-Xin Qi and Yue Han**

School of Life Sciences and Biotechnology, Institute of Mechanobiology and Medical Engineering, Shanghai Jiao Tong University, Shanghai, China

Endothelial progenitor cells (EPCs) play a vital role in endothelial repair following vascular injury by maintaining the integrity of endothelium. As EPCs home to endothelial injury sites, they may communicate with exposed vascular smooth muscle cells (VSMCs), which are subjected to cyclic stretch generated by blood flow. In this study, the synergistic effect of cyclic stretch and communication with neighboring VSMCs on EPC function during vascular repair was investigated. *In vivo* study revealed that EPCs adhered to the injury site and were contacted to VSMCs in the Sprague–Dawley (SD) rat carotid artery injury model. *In vitro*, EPCs were cocultured with VSMCs, which were exposed to cyclic stretch at a magnitude of 5% (which mimics physiological stretch) and a constant frequency of 1.25 Hz for 12 h. The results indicated that stretched VSMCs modulated EPC differentiation into mature endothelial cells (ECs) and promoted angiogenesis. Meanwhile, cyclic stretch upregulated the mRNA expression and secretion level of connective tissue growth factor (CTGF) in VSMCs. Recombinant CTGF (r-CTGF) treatment promoted endothelial differentiation of EPCs and angiogenesis, and increased their protein levels of FZD8 and β-catenin. CTGF knockdown in VSMCs inhibited cyclic stretch-induced EPC differentiation into ECs and attenuated EPC tube formation via modulation of the FZD8/β-catenin signaling pathway. FZD8 knockdown repressed endothelial differentiation of EPCs and their angiogenic activity. Wnt signaling inhibitor decreased the endothelial differentiation and angiogenetic ability of EPCs cocultured with stretched VSMCs. Consistently, an *in vivo* Matrigel plug assay demonstrated that r-CTGF-treated EPCs exhibited enhanced angiogenesis; similarly, stretched VSMCs also induced cocultured EPC differentiation toward ECs. In a rat vascular injury model, r-CTGF improved EPC reendothelialization capacity. The present results indicate that cyclic stretch induces VSMC-derived CTGF secretion, which, in turn, activates FZD8 and β-catenin to promote both differentiation of cocultured EPCs into the EC lineage and angiogenesis, suggesting that CTGF acts as a key intercellular mediator and a potential therapeutic target for vascular repair.

Keywords: cyclic stretch, endothelial progenitor cells, differentiation, angiogenesis, vascular smooth muscle cells, connective tissue growth factor

Edited by:
Jing Zhou,
Peking University, China

Reviewed by:
Xiaohong Wang,
Tianjin Medical University, China
Suzanne Scarlata,
Worcester Polytechnic Institute, United States

***Correspondence:**
Yue Han
hanyue625@sjtu.edu.cn

†These authors have contributed equally to this work

Specialty section:
This article was submitted to Cell Adhesion and Migration, a section of the journal Frontiers in Cell and Developmental Biology

Received: *16 September 2020*
Accepted: *10 November 2020*
Published: *09 December 2020*

Citation:
Yan J, Wang W-B, Fan Y-J, Bao H, Li N, Yao Q-P, Huo Y-L, Jiang Z-L, Qi Y-X and Han Y (2020) Cyclic Stretch Induces Vascular Smooth Muscle Cells to Secrete Connective Tissue Growth Factor and Promote Endothelial Progenitor Cell Differentiation and Angiogenesis. Front. Cell Dev. Biol. 8:606989. doi: 10.3389/fcell.2020.606989

INTRODUCTION

Vascular injury leads to the initiation and progression of atherosclerotic vascular disease and may result in neointimal hyperplasia, in-stent restenosis, and acute stent thrombosis (Deanfield et al., 2007). Therefore, regeneration of the vascular endothelium is very important. Due to a low proliferative ability, the capacity of mature endothelial cells (ECs) to replace damaged endothelium is limited during vascular repair (Hristov et al., 2003; Deanfield et al., 2007). Accumulating studies indicate that bone marrow-derived endothelial progenitor cells (EPCs) play a crucial role in maintaining endothelial integrity. When damage occurs, EPCs are mobilized and home to the injury sites and then differentiate into ECs, which participate in angiogenesis, neovascularization, and tissue repair (Asahara et al., 1997; Deanfield et al., 2007; Zhang et al., 2014; Li et al., 2019). In this process, EPCs communicate with the exposed vascular smooth muscle cells (VSMCs), which compose the medial layer of the vessel wall. However, the impact of VSMCs on EPC function or the underlying signal mechanisms is little known.

Many studies have shown that EC and VSMC interaction in hemodynamic environments participates in the regulation of vascular stabilization, remodeling, and function, which suggests a role for mechanical forces generated by the pulsatile nature of blood pressure and flow in these processes (Chien, 2007; Qi et al., 2011; Chen et al., 2013; Deng et al., 2015). For example, VSMCs secrete exosomes enriched with miR-143-3p that are transported to ECs, and endothelial proliferation is subsequently induced under pathologically elevated cyclic stretch (Deng et al., 2015). Mesenchymal stem cells promote the differentiation of EPCs into ECs via secreting VEGF and increasing expression of CD31 and vWF (Ge et al., 2018). These studies indicated that the cellular microenvironment and the resident cells might participate in determining EPC differentiation fate. Under physiological conditions, VSMCs are constantly subjected to mechanical stretching *in vivo*; therefore, we aimed to investigate whether mechanical forces and neighboring VSMCs modulate the endothelial differentiation of EPCs during endothelium repair.

Several studies have revealed that EPCs differentiate into either myocardial cells or endothelial cells, related to the cellular microenvironment of cytokines and coexisting cells (Murasawa et al., 2005; Ge et al., 2018). Resident cells contribute to the vascular repair process mostly via paracrine processes, secreting a mixture of growth factors and cytokines to recruit numerous cells to the injured sites and modulate the cell functions (Armulik et al., 2005; Ostriker et al., 2014). Connective tissue growth factor (CTGF), also known as CCN2, is a secreted protein of the CCN family, which includes Cyr61, CTGF, NOV, WISP1, WISP2, and WISP3 (Kubota and Takigawa, 2007; Yu et al., 2010; Jun and Lau, 2011; Liu et al., 2014). It has been reported that CTGF is implicated in vascular diseases, including atherosclerosis, hypertension, restenosis, and thrombosis. CTGF promotes neointimal hyperplasia after vascular injury and in rupture-prone atherosclerotic plaques; especially in areas of neovascularization and in the neointima in restenosis after balloon injuries, high CTGF expression levels are detected (Cicha et al., 2005; Kundi et al., 2009). It was also found that CTGF was strongly expressed in vascular cells, such as VSMCs, ECs, and fibroblasts (Jun and Lau, 2011). In our previous study, we found that CTGF is upregulated both *in vivo* and *in vitro* during hypertension, and 15% cyclic stretch significantly increased CTGF expression in VSMCs via microRNA-19b-3p, which indicated that CTGF is a key mechanical-sensitive molecule (Wang et al., 2019). Moreover, CTGF also plays a significant role in cell growth and differentiation. CTGF and VEGF induced pluripotent stem cells to differentiate into mature ECs (Kelly et al., 2020), and adipose-derived stem cells can differentiate and proliferate with CTGF stimulation to enhance tendon repair (Li et al., 2019). However, the relationship between CTGF and EPCs has not been widely concerned and studied. Therefore, we hypothesized that VSMC-derived CTGF contributes to the endothelial differentiation of EPCs in the process of vascular repair.

In this study, a rat vascular injury model and *in vivo* Matrigel plug assay were established to explore the effect of CTGF on EPC differentiation during vascular repair. An *in vitro* EPC//VSMC coculture system that included cyclic stretch was developed to detect the intercellular relationship between them. Here, we aimed to investigate whether CTGF is a key cell-to-cell interaction regulator for EPC differentiation in vascular repair.

MATERIALS AND METHODS

Rat Carotid Artery Intimal Injury Model and Reendothelialization Assay

Sprague–Dawley (SD) rats were anesthetized with isoflurane, and then the carotid arteries were exposed under the anatomical microscope. After the bifurcation above the common carotid artery was found, the occipital artery, the internal carotid artery, the thyroid artery, and the external carotid artery were ligated with a surgical suture in turn, and the thoracic segment of the common carotid artery was clamped with a hemostatic forceps. A balloon inserted (0.67 mm; Edwards Lifesciences, CA, USA) was applied to damage the intima through a small opening from the proximal end of the thyroid artery. EPCs (1×10^6) were pretreated with CM-Dil (1 μM, YEASEN, Shanghai, China) for 5 min at 37°C for labeling cells in red. Then, the cells were resuspended in 200 μl of PBS and the suspension was instilled into and incubated with the freshly injured arterial bed for 25–30 min (Griese et al., 2003; Yan et al., 2020). Postoperative rats continue to be housed with the experimental animal center. Recombinant CTGF (2 μg/kg/day) was firstly injected from the tail vein 3 h after injury and continued for 7 days. To observe the adhesion of EPCs, the left common carotid arteries were collected from the carotid bifurcation, incised longitudinally, and flattened between coverslips. The samples were fixed with 4% paraformaldehyde for 24 h and permeabilized with 0.3% Triton

---

Abbreviations: CTGF, connective tissue growth factor; DMEM, Dulbecco's modified Eagle medium; EPCs, endothelial progenitor cells; ECs, endothelial cells; EGM-2, endothelial growth medium-2; ELISA, enzyme-linked immunosorbent assay; FBS, fetal bovine serum; IPA, ingenuity pathway analysis; PET, polyethylene terephthalate; SD rats, Sprague–Dawley rats; siRNA, small interfering RNA; VSMCs, vascular smooth muscle cells.

X-100 for 30 min. Nucleus was marked with DAPI (1:1,000) for 15 min at room temperature, and confocal microscopy (LV1000; Olympus, Tokyo, Japan) was used to take and analyze fluorescent images. Evans blue (2%, 40 mg/kg) was injected into the tail vein 30 min before sacrifice for the detection of reendothelialization assay on the seventh day after intimal injury. Photographs were taken with a digital camera. We quantified the reendothelialized parts that defined as areas not stained in blue with ImageJ software (Yan et al., 2020).

Cell Culture and Identification

VSMCs were harvested from the thoracic aorta of male SD rats by an explant technique (Qi et al., 2008, 2010). VSMCs were cultured in Dulbecco's modified Eagle medium (DMEM, Gibco) containing 10% fetal bovine serum (FBS, Gibco) and incubated at 37°C with 5% CO_2. These cells were characterized by immunofluorescent staining, which was performed with an antibody recognizing smooth muscle specific α-actin (Sigma). VSMCs from passages 4 to 8 were used in the following study.

EPCs derived from the bone marrow of SD rats were isolated and cultured as reported (Kuliszewski et al., 2009; Li et al., 2012). Briefly, total mononuclear cells were isolated from the tibias and femurs of male SD rats by density-gradient centrifugation with Histopaque-1083 (Sigma); the cells were then cultured in six-well plates with endothelial growth medium-2 (EGM-2) (Lonza) supplemented with fetal bovine serum (FBS), vascular endothelial growth factor (VEGF), fibroblast growth factor-B, epidermal growth factor, hydrocortisone, R3 insulin-like growth factor-1 (R3 IGF-1), ascorbic acid, and GA-1000 at 37°C in a 5% CO_2 incubator. The medium was changed after 4 days, and subsequent media changes were made every 3 days.

EPCs were identified by classical method (Asahara et al., 1997; Wei et al., 2015). The cells were incubated with FITC-UEA-1 (Sigma) and Dil-Ac-LDL (Molecular Probes) as described previously. Double-positive staining for Dil-Ac-LDL and FITC-UEA-I was considered an indication of EPCs. Surface markers for flow cytometry analysis include the stem cell markers CD133 and CD34, as well as the endothelial marker CD31. EPCs were stained with a panel of monoclonal antibodies including anti-CD133 (1:100, Proteintech), anti-CD34-PE (1:100, eBioscience), anti-CD31-PE-Cy7 (1:100, eBioscience), and anti-CD45-PE (1:100, eBioscience). EPCs stained with anti-CD133 were incubated with an FITC-conjugated anti-mouse antibody. Unstained cells were incubated in parallel with antibody immunoglobulin (IgG) controls. Cells that were positive for CD133, CD34, and CD31 and negative for CD45 were considered to be EPCs. All samples were analyzed by flow cytometry (Becton Dickinson). EPCs from passages 2 and 3 were used (Li et al., 2018).

EPC//VSMC Coculture Model and Cyclic Stretch Application

EPCs (1×10^5 cells per well) were seeded on the inner side of a cell culture insert (Becton Dickinson), which has a 10-μm-thick polyethylene terephthalate (PET) membrane containing 0.4-μm pores. Flexible silicone bottom plates (Flexcell International) were either kept unseeded (EPC//O static group) or seeded with VSMCs (2×10^5 cells per well, EPC//VSMC static group). The insert with EPCs was incorporated into the flexible silicone bottom plates, which were loaded with an FX-5000T strain unit system (Flexcell International) for the application of cyclic stretch at 5% stretch magnitude and 1.25 Hz frequency (Qi et al., 2016) for 6 or 12 h (EPC//VSMC stretch group) to mimic arterial mechanical conditions, as illustrated in **Figure 2A**.

Western Blotting

Western blotting was performed as described previously (Qi et al., 2008). Proteins were separated by 10% SDS-PAGE and transferred to PVDF membranes (Millipore, 0.22 μm). The membranes were incubated overnight with primary antibodies, respectively, against CTGF (1:800, Proteintech), FZD8 (1:1,000, Abcam), β-catenin (1:1,000, Cell Signaling Technology), Lamin A (1:1,000, Abcam), and GAPDH (1:1,000, Proteintech) at 4°C, which was followed by immunoblotting with anti-rabbit or anti-mouse IgG (1:2,000, Cell Signaling Technology) conjugated to HRP. Protein bands were detected by a standard enhanced chemiluminescence (ECL; Tanon) method and quantified by Quantity One software (Bio-Rad). Nuclear extracts were prepared by the Nuclear Extraction kit (Beyotime) according to the manufacturer's instructions.

Quantitative Real-Time Polymerase Chain Reaction (QPCR)

Total RNA was extracted from EPCs using Trizol reagent (Invitrogen) and was followed by cDNA synthesis using a RevertAid First Strand cDNA kit (Thermo Fisher Scientific). The resulting cDNA was used as a template in quantitative real-time polymerase chain reactions with SYBR Green Supermix on an ABI Prism 7500 sequence detection PCR system (Applied Biosystems) according to the manufacturer's protocol. The specific primer sequences are listed in **Table 1**. PCR conditions were as follows: 95°C for 30 s followed by 40 cycles at 95°C for 5 s, 60°C for 45 s, and 72°C for 30 s. The results were normalized to the GAPDH expression level, and relative quantification of the ratios was performed using the $2^{-\Delta\Delta Ct}$ method.

TABLE 1 | The sequences of primers.

Gene	Primer sequences (5′-3′)	
CD31	Fwd: GACAGCCAAGGCAGATGCAC	Rev: ATTGGATGGCTTGGCCTGAA
vWF	Fwd: GCGTGGCAGTGGTAGAGTA	Rev: GGAGATAGCGGGTGAAATA
KDR	Fwd: GGCACCACTCAAACGCTGAC	Rev: CCTCTCTCCTCTCCCGACTT
CTGF	Fwd: GGAAATGCTGTGAGGAGTGGGTGT	Rev: TGTCTTCCAGTCGGTAGGCAGCTA
GAPDH	Fwd: GGCACAGTCAAGGCTGAGAAT	Rev: ATGGTGGTGAAGACGCCAGTA

Fwd, forward; Rev, reverse.

Transfection of Small Interfering RNA

The mRNA sequences of rat CTGF (NM_022266) were acquired from NCBI GenBank. Small interfering RNA (siRNA) against rat CTGF was designed and synthesized by GenePharma Biological Company (Shanghai, China). The sequences of the CTGF siRNAs were 5′-GGU CAA GCU GCC CGG GAA ATT-3′ and 5′-UUU CCC GGG CAG CUU GAC CTT-3′. The sequences of the FZD8 siRNAs were 5′-GGA AGU GAC CUC GCU ACU ATT−3′ and 5′-UAG UAG CGA GGU CAC UUC CTT -3′.

For the RNA interfering experiment, VSMCs were transfected with 100 nM specific siRNA or scrambled siRNA with 5 μl of Lipofectamine^{TM} 2000 (Invitrogen) in Opti-MEM (Gibco) for 48 h following the manufacturer's instructions.

Matrigel Tube Formation Assay

An *in vitro* tube formation assay was performed as previously described (Malinda, 2009). In brief, Matrigel (Corning) was added to 24-well plates at 300 μl per well and to polymerize at 37°C for 30 min. Then, 2×10^4 EPCs were seeded onto the coated wells and cultured with 500 μl EBM-2 at 37°C with 5% CO_2 for 6 h. EPC tube formation was assessed by microscopy, and photographs were randomly taken of five fields. The total tube length was calculated using imaging analysis software (Image-Pro Plus 6.0).

In vivo Matrigel Plug Angiogenesis Assay

An *in vivo* angiogenesis assay was performed as previously described (Han et al., 2016). EPCs were treated with or without recombinant CTGF (r-CTGF; 20 ng/ml) for 24 h. Growth factor-reduced Matrigel (400 μl/plug) was thawed and mixed with EPCs (1×10^6/plug), and Matrigel supplemented only with r-CTGF in the absence of EPCs was used as a blank control. In addition, to investigate how VSMCs and stretch affect EPC differentiation, EPCs were cultured by themselves under static conditions or cocultured with VSMCs, which had cyclic stretch applied at 5% stretch magnitude and 1.25 Hz frequency. After 12 h, EPCs under different conditions were harvested by treatment with 0.25% trypsin and were mixed with Matrigel. Each plug was subcutaneously injected into the flank of 6-week-old male nude mice ($n = 4$ in each group). Mice were euthanized 7 days after surgery. Matrigel plugs were harvested, fixed in 10% formalin, and embedded in paraffin; multiple 5-μm-thick slices were prepared. Immunofluorescent staining was performed using an anti-CD31 antibody (Abcam) and anti-CD34 antibody (Santa Cruz).

Enzyme-linked Immunosorbent Assay (ELISA)

The concentration of CTGF in cell culture medium from VSMCs was determined by enzyme-linked immunosorbent assay by using a rat CTGF ELISA kit (Cloud-Clone Corp). The assay was performed according to the manufacturer's instructions.

Ingenuity Pathway Analysis

Ingenuity Pathway Analysis (IPA) software (Qiagen) was used to search for the genes that possibly interact with CTGF. The software predicted the downstream genes of specific target through Grow Tool. After prediction, the possible canonical pathways and functional classifications of the target genes of CTGF were obtained with IPA. The significance values for analyses of network and pathway generation were calculated using the right-tailed Fisher's Exact Test by comparing the number of proteins that participate in a given function or pathway relative to the total number of occurrences of these proteins in all functional/pathway annotations stored in the Ingenuity Pathway Knowledge Base (IPKB). IPA was used to understand the complex biological and chemical systems at the core of life science research based on lectures or predicated analysis (Dai et al., 2009).

Statistical Analysis

Data are expressed as the mean ± *SD* from at least three independent experiments. Statistical analysis was performed with Student's *t*-tests for two groups of data and with one-way ANOVA for multiple comparisons, followed by Bonferroni's *post-hoc* test. Non-parametric data were analyzed with the Mann–Whitney *t*-test in GraphPad Prism software. Values of P that were <0.05 were considered statistically significant.

RESULTS

The Adhesion of EPCs at Intimal Injury Site *in vivo*

We established a carotid artery intimal injury model that is shown in **Figure 1A** to explore the potential interaction between EPCs and VSMCs. The left and right common carotid artery of each rat were used as the experimental group and autologous control, respectively. After 4 weeks, hematoxylin–eosin (HE) staining results indicated that vessel wall was significantly thickened, which revealed the intimal hyperplasia (**Figure 1B**). To confirm that the intimal injury model was successfully established, we harvested the injury and control vessels right after the surgery. Immunofluorescence staining results showed that the von Willebrand factor (vWF), a marker of the ECs marked in red, was not detected on the inner wall of vessels right after the injury surgery, indicating that the model was successfully established (**Figure 1C**). In the initial stage of intimal injury, EPCs are mobilized to the injury site; hence, we then examined the adhesion of EPCs 1 h after intimal injury, which were identified by vWF (EC marker) and CD34 (stem cell marker) expression. Due to the balloon injury, the endothelial layer was damaged and did not express vWF, hence, the co-expression of CD34 (red) and vWF (green) indicated the adhesion of EPCs at the injury site (**Figure 1D**). *In vivo* experiment results suggested that carotid intimal injury caused EPCs homing and adhering to the injury site, which were connected to the exposed VSMCs, which are subjected to physiological stretch at the damaged intima. Hence, we hypothesized that the intercellular communication between EPCs and VSMCs might have an effect on EPC function.

Stretched VSMCs Promoted the Endothelial Differentiation of Cocultured EPCs

To examine the effect of VSMCs and physiological cyclic stretch on EPC function, an EPC//VSMC coculture with a cyclic stretch

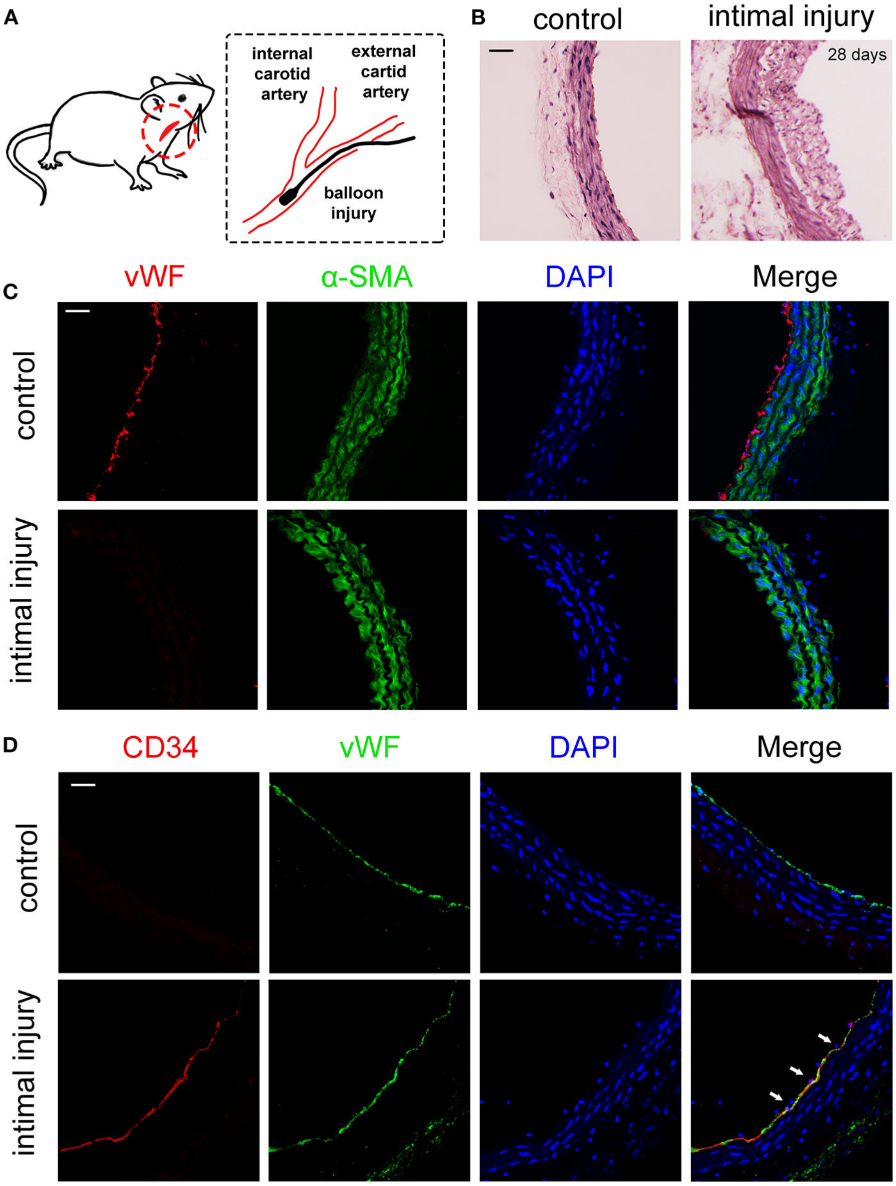

FIGURE 1 | EPCs adhered to the injury site 1 h after balloon damaged the intimal. **(A)** Schematic diagrams of the establishment of rat intimal balloon damage model. **(B)** HE staining indicated the significant intimal hyperplasia and the thickening blood vessel wall after 28 days compared with control group ($n = 4$). **(C)** We harvested the vessels for the immunofluorescence staining right after the surgery. The immunofluorescence staining results showed that vWF (red) was not expressed after the balloon injury, indicating that the intima fell off and the model was successfully constructed. The α-SMA (green) and DAPI (blue) were used to identify VSMCs and nuclei, respectively ($n = 4$). Scale bar = 50 µm. **(D)** The adhesion of EPCs *in situ* 1 h after intimal injury was identified by CD34 (stem cell marker, red) and vWF (EC marker, green) by immunofluorescence staining. The results showed that CD34 and vWF were co-expressed at same place, indicating that EPCs adhered to the damaged endothelial layer. The results showed that CD34 and vWF were colocalized, indicating that EPCs adhered to the inner wall of blood vessels. The staining of vWF in the control group was due to the presence of ECs. Nuclei are stained in blue by DAPI. The white arrows indicate the adhered EPCs at the injury site ($n = 4$). Scale bar = 50 µm.

application system was used (**Figure 2A**). EPCs were isolated from SD rat bone marrow by density gradient centrifugation and identified by fluorescence microscopy and flow cytometry. EPCs were characterized as adherent cells that were double positive for Dil-acLDL uptake and FITC-UEA-lectin binding (**Figure 2B**). Moreover, these cells were found to be positive for CD31, CD34, and CD133 but negative for CD45 by flow cytometric analysis (**Figure 2B**). VSMCs were identified by immunofluorescent staining with α-smooth muscle actin (SMA), which is shown in green (**Supplementary Figure 1**).

In the static system, the mRNA levels of the EC markers CD31, vWF, and KDR in EPCs cocultured with VSMCs showed no significant change at 6 h (**Figure 2C**) or 12 h (**Figure 2D**), compared to the levels observed in monocultured EPCs.

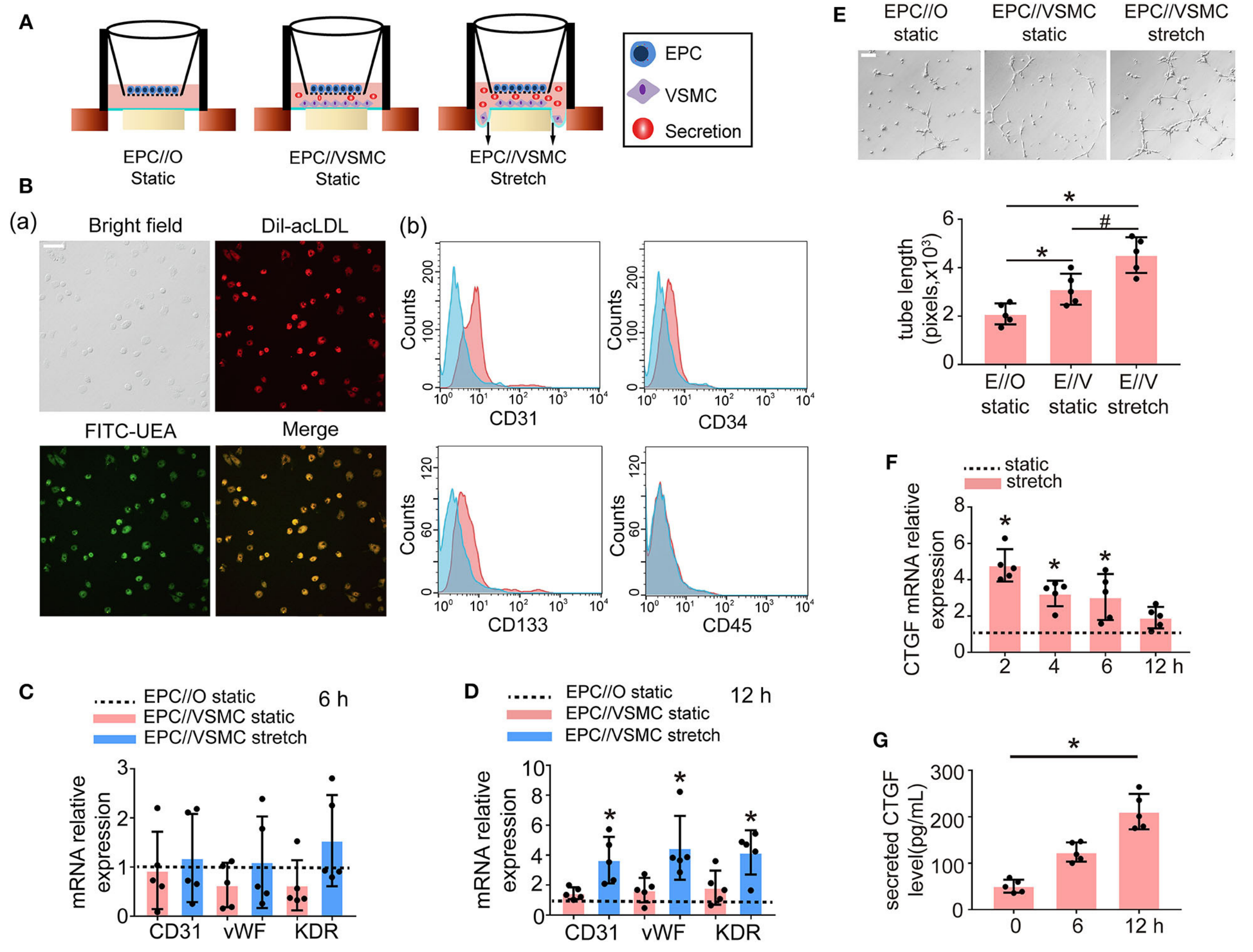

FIGURE 2 | Five percent cyclic stretch induces VSMC-derived CTGF secretion and promotes the differentiation of cocultured EPCs into ECs. **(A)** Schematic diagrams show EPC//VSMC coculture and the cyclic stretch system. **(B)** EPCs showed a spindle-shaped morphology after 8 days. Staining of FITC-UEA-lectin (green) and Dil-acLDL (red) revealed double-positive cells that were identified as EPCs (a). FACS analysis showed that EPCs were positive for the endothelial cell marker CD31 and hematopoietic stem cell markers CD34 and CD133, and they were negative for the leukocyte marker CD45. Controls (blue area) were overlaid on the histogram of each surface antigen (red areas) tested (b). **(C)** The mRNA levels of the EC markers CD31, vWF, and KDR showed no differences in EPCs among different cocultured conditions after 6 h ($n = 5$). Monocultured EPCs under static were used as control groups, shown as the dotted line. **(D)** The mRNA levels of the EC markers CD31, vWF, and KDR were induced in EPCs cocultured with stretched VSMCs after 12 h ($n = 5$). **(E)** EPCs cocultured with stretched VSMCs had an increased tube formation ability after 12 h ($n = 5$). **(F)** QPCR results revealed that CTGF mRNA levels were increased at different time points in stretched VSMCs ($n = 5$). **(G)** The level of CTGF secretion from stretched VSMCs was significantly elevated at 12 h ($n = 5$). For quantitative analysis, five fields per plate were photographed, and tube lengths were measured using Image-Pro Plus software. Scale bar = 100 μm. Values are expressed as the mean ± *SD*. $^{*,\#}P < 0.05$ compared with the respective control. Statistical analysis was performed with Student's *t*-test and one-way ANOVA for **(C–G)**.

However, once the VSMCs were subjected to 5% cyclic stretch for 12 h, the expression of EC markers in cocultured EPCs was significantly increased as compared with monocultured EPCs (**Figure 2D**). To determine the role of stretched VSMCs in the angiogenic capability of EPCs, Matrigel tube formation assays were performed. As shown in **Figure 2E**, the total length of tube-like structures was significantly greater in EPCs cocultured with VSMCs under 5% cyclic stretch than in the static cocultured (E//V, static) or monocultured EPCs (E//O, static) at 12 h. These results indicated that the differentiation of EPCs is regulated by paracrine factors secreted from stretched VSMCs.

In addition, to explore the effect of cyclic stretch on CTGF expression in VSMCs, we detected CTGF expression levels at different time points. The results revealed that both the mRNA and secretion levels of CTGF were elevated in VSMCs exposed to 5% cyclic stretch *in vitro* (**Figures 2F,G**). The results suggested that CTGF may participate in stretched VSMC-induced EPC differentiation.

CTGF Induced EPC Differentiation Toward ECs *in vitro*

To investigate whether CTGF modulates EPC differentiation and angiogenesis, EPCs were treated with r-CTGF. We stimulated EPCs with different doses of r-CTGF protein (0, 5, 10, 15, 20, and 30 ng/ml) for 24 h under static conditions (**Figure 3A**). Exogenous CTGF at a concentration of 20 ng/ml promoted the

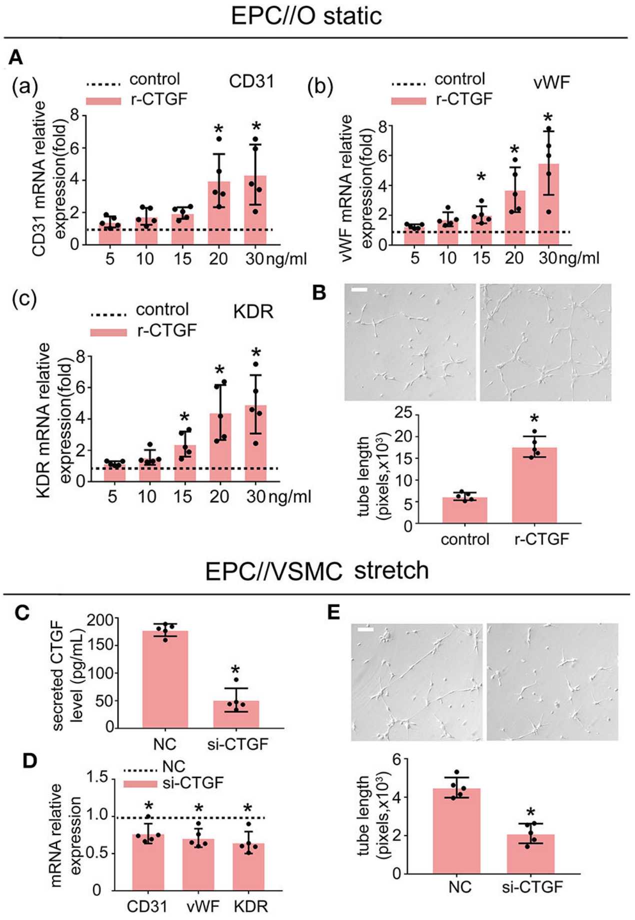

FIGURE 3 | r-CTGF induced EPC differentiation into ECs under static conditions; stretched VSMCs modulate the differentiation of EPCs via CTGF *in vitro*. **(A)** EPCs were treated with different doses of r-CTGF (5, 10, 15, 20, and 30 ng/ml) for 24 h, and the mRNA expression of EC markers CD31, vWF, and KDR were significantly increased at a concentration of 20 ng/ml and 30 ng/ml ($n = 5$). EPCs treated without r-CTGF were used as control groups. **(B)** EPCs treated with r-CTGF (20 ng/ml) for 24 h significantly exhibited increased tube formation ($n = 5$). **(C)** CTGF siRNA was transfected under 5% cyclic stretch conditions, and the CTGF secretion level was significantly decreased in VSMCs. **(D,E)** Transfection with CTGF siRNA under 5% cyclic stretch conditions with cocultured EPCs resulted in the inhibition of EPC differentiation toward ECs and decreased their tube formation ($n = 5$). Scale bar = 100 µm. For quantitative analysis, five fields per plate were photographed, and tube lengths were measured using Image-Pro Plus software. Values are expressed as the mean ± *SD*. $^*P < 0.05$ compared with the respective control. Statistical analysis was performed with Student's *t*-test for **(A–E)**.

expression of the EC markers CD31, vWF, and KDR remarkably in EPCs. Meanwhile, r-CTGF at the concentration of 20 ng/ml promoted EPC tube formation (**Figure 3B**). To further determine the role of CTGF, its expression was knocked down in VSMCs by CTGF-specific siRNA. After transfected with CTGF siRNA for 48 h, VSMCs were then subjected to cyclic stretch. The effect of CTGF siRNA on the secretion level of CTGF was significantly decreased in VSMCs (**Figure 3C**). CTGF knockdown in stretched VSMCs could reverse EPC differentiation and angiogenesis capabilities (**Figures 3D,E**) in comparison with the control group. Overall, the results indicated that CTGF plays a key role in stretched VSMC-induced EPC differentiation *in vitro*.

The Potential Downstream Targets of CTGF Were Predicted by Ingenuity Pathway Analysis

CTGF is essential for the differentiation of EPCs; however, the underlying mechanism involved remains unclear and needs to be further studied. By using ingenuity pathway analysis (IPA) with high prediction criteria, the top 20 molecules that are potentially downstream of CTGF were selected (**Figure 4A**). Then, IPA analysis allowed further insights into the cellular functions (**Figure 4B**) and canonical pathways (**Figure 4C**) of the top 20 genes. The top molecular and cellular function was cellular development, and the top canonical pathway that was identified was the Wnt/β-catenin signaling pathway, which plays an essential role in developmental decisions and regulating progenitor cell fate during embryonic development. According to reports, FZD8, a member of Frizzled receptors located on the cell membrane, functions as a key component of the Wnt signaling pathway (Chakravarthi et al., 2018; Murillo-Garzon et al., 2018). When Wnt proteins bind to transmembrane FZD8 receptors and coreceptors, β-catenin-dependent signals can be activated (Murillo-Garzon et al., 2018). Thus, we hypothesized that FZD8 and β-catenin, which are key regulators of the Wnt/β-catenin signaling pathway, might participate in the process of CTGF-induced EPC differentiation.

CTGF Regulated FZD8/β-catenin Expression in EPCs

To further determine the effect of CTGF on FZD8 and β-catenin expression, EPCs were treated with r-CTGF *in vitro*. Western blot results revealed that r-CTGF induced the expression of FZD8 (**Figure 5A**). Moreover, the protein level of β-catenin was increased in both nuclear and cytosolic lysates from EPCs (**Figure 5B**). As shown in **Figure 5C**, r-CTGF treatment leads to significant increases of β-catenin in both the cytoplasm and the nucleus of EPCs. To further determine the role of CTGF under cyclic stretch conditions, its expression was knocked down in VSMCs by CTGF-specific siRNA. VSMCs were treated with CTGF siRNA for 48 h and then subjected to cyclic stretch. In contrast to the effect of r-CTGF, knockdown of CTGF in VSMCs not only suppressed FZD8 (**Figure 5D**) and β-catenin (**Figure 5E**) protein expression but also decreased the expression of β-catenin in both the cytoplasm and the nucleus of EPCs (**Figure 5F**). Taken together, these findings suggest that CTGF may modulate EPC differentiation and angiogenesis via the FZD8 and β-catenin pathways.

To better understand the role of FZD8 and Wnt signaling in regulating EPC differentiation, EPCs were treated with an FZD8-specific siRNA and with XAV-939 (specific inhibitor of Wnt signaling), respectively. The effect of the siRNA treatments on FZD8 mRNA levels was assessed (**Supplementary Figure 2**). The results indicated that FZD8 knockdown in EPCs could decrease angiogenic ability (**Figure 6A**) and could decrease EPC differentiation into the EC lineage (**Figure 6B**). To confirm the

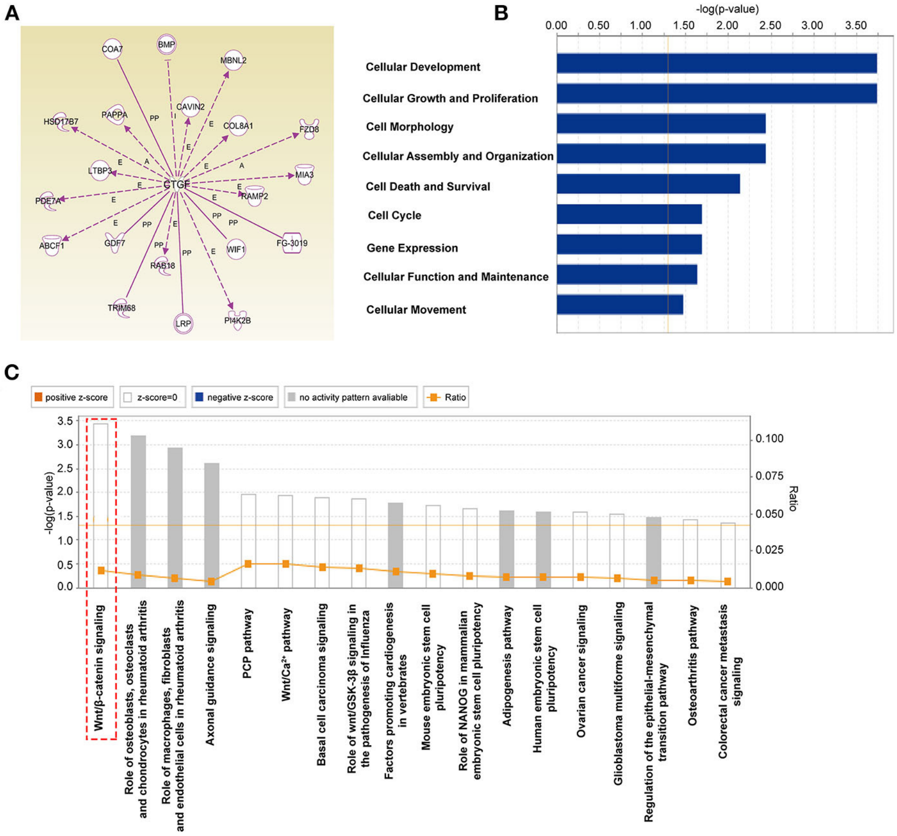

FIGURE 4 | The potential downstream targets of CTGF that were predicted by IPA are shown. **(A)** Molecules predicted to interact with CTGF were determined using IPA software. IPA analysis showed that downstream targets are involved in molecular and cellular functions **(B)** and canonical pathways **(C)**.

role of Wnt signaling in cyclic stretch-induced actions of CTGF on EPCs, the inhibitor of Wnt signaling, XAV-939, was used to treat cocultured EPCs at the concentration of 5 μM. XAV-939 treatment remarkably inhibited EPC tube formation (**Figure 6C**). Meanwhile, XAV-939 treatment decreased the expression of the EC markers CD31, vWF, and KDR in EPCs (**Figure 6D**).

CTGF Promoted the Differentiation of EPCs *in vivo*

To examine the role of CTGF in EPC differentiation *in vivo*, the Matrigel plug assay was performed. In this assay, EPCs with or without r-CTGF treatment were mixed with Matrigel and subcutaneously injected into the flank of nude mice, and Matrigel supplemented only with r-CTGF in the absence of EPCs was used as a blank control. On day 7, mice were sacrificed, and Matrigel plugs were harvested (**Figure 7A**). Abundant vessel formation was shown in the plugs of EPCs treated with r-CTGF compared with what was observed in the controls. In addition, few cells invaded the plug in the Matrigel that was injected r-CTGF in the absence of EPCs. The Matrigel plugs were embedded in paraffin to enable histological analysis and the level of EPC differentiation was detected using an antibody against the EC marker CD31. We observed a significant increase in CD31 staining in the group of r-CTGF-treated EPCs, and there was no CD31 staining in the sections of plugs mixed with r-CTGF and no EPCs (**Figure 7B**). To further demonstrate that r-CTGF promoted endothelial differentiation of EPCs *in vivo*, we also performed the stem cell marker CD34 immunofluorescence staining. CD34 staining results showed that protein expression levels in EPCs treated with r-CTGF were significantly reduced compared to the control group (**Figure 7B**). The results indicated that CTGF enhanced the differentiation of EPCs into ECs *in vivo*.

Furthermore, to investigate how VSMCs and stretch affect EPC differentiation, another Matrigel plug assay was also performed. EPCs were monocultured under static conditions or cocultured with VSMCs that were subjected to cyclic stretch at 5% stretch magnitude and 1.25 Hz frequency. After 12 h, EPCs under different conditions were harvested and mixed with growth factor-reduced Matrigel. Matrigel was injected subcutaneously into the flank of nude mice. On day 7, the Matrigel plugs were harvested after mice were sacrificed. The results show that there is a significant increase in CD31 staining and decrease in CD34 in the plugs mixed with cocultured EPCs under cyclic stretch conditions in comparison to the group with monocultured EPCs under static conditions; these results indicate that VSMCs and stretching prompt the differentiation of EPCs into the endothelial lineage (**Figure 7C**).

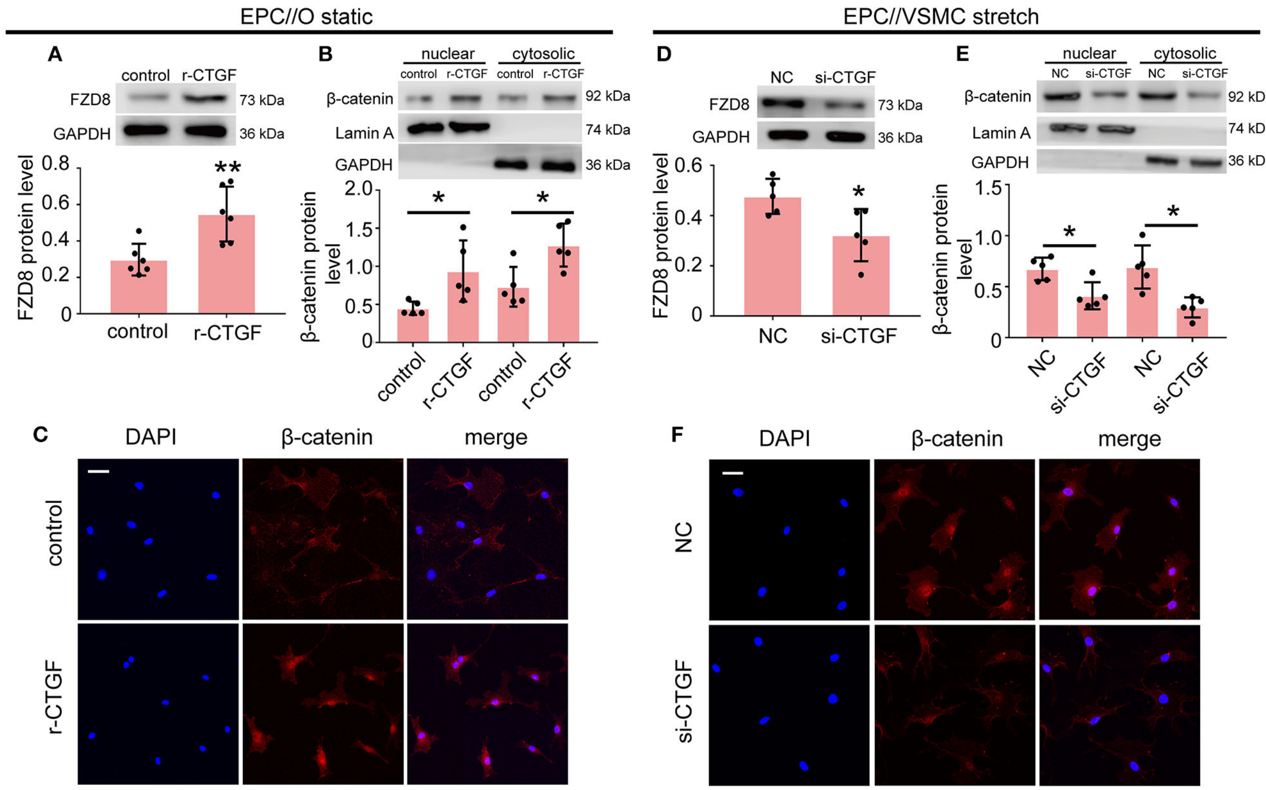

FIGURE 5 | CTGF regulates FZD8/β-catenin expression in EPCs. **(A)** The FZD8 protein level was markedly induced in EPCs treated with r-CTGF (20 ng/ml) for 24 h in comparison with the control ($n = 5$). **(B,C)** Both Western blotting and immunofluorescent staining showed upregulated β-catenin protein levels in the nuclei and cytosol of EPCs stimulated with r-CTGF. **(D)** Transfection with CTGF siRNA in VSMCs under 5% cyclic stretch conditions repressed the FZD8 protein level in cocultured EPCs ($n = 5$), and **(E,F)** nuclear and cytosolic β-catenin protein expression was also suppressed in cocultured EPCs. Scale bar = 50 μm. Values are expressed as the mean ± *SD*. $^*P < 0.05$ compared with the control. Statistical analysis was performed with Student's *t*-test for **(A,B,D,E)**.

CTGF Promoted Reendothelialization Capacity of EPCs After Intimal Injury *in vivo*

To further verify the effect of CTGF on EPC differentiation after intimal injury, the rat carotid intimal injury model was established. After carotid intimal injury, CM-Dil-labeled EPCs were incubated at the fresh injury site. The adherent EPCs directly contacted with VSMCs, and meanwhile, both cells were under cyclic stretch. The degree of reendothelialization after vascular injury is widely recognized and used in the detection of differentiation of EPCs and the repair of intimal injury by Evans blue dye. The flow diagram of the experimental protocol was shown in **Figure 8A**. Immunofluorescence staining results indicated that CM-Dil-labeled EPCs adhered to the vascular lesion *in situ* (**Figure 8B**). The rat left carotid artery without surgery was imaged in **Figure 8C**. Evans blue staining was used to detect reendothelialization after intimal injury. Compared with the sham operation group, the experimental group treated with PBS injection only had the largest blue area. The blue area decreased slightly after systemic injection of r-CTGF, indicating an increase of vascular reendothelialization. Furthermore, after intimal injury, local incubation with EPCs significantly increased intimal repair, and tail vein injection of r-CTGF for 7 days significantly promoted reendothelialization capacity of EPCs and upregulated reendothelialization area (**Figure 8D**).

DISCUSSION

In this study, we characterized the so far unknown synergistic effect of physiological cyclic stretch and communication with neighboring VSMCs on endothelial differentiation of EPCs and their angiogenic activity. Our results highlight and help to better understand the role of mechanical stretch and regulation of intracellular communication in vascular repair, which indicate that cyclic stretch induces VSMC-derived CTGF secretion, which in turn activates FZD8 and β-catenin to promote both the endothelial differentiation of cocultured EPCs and angiogenesis.

Increasing reports have shown that EPCs, which quiescently reside in physiological bone marrow and can be recruited to sites of injury, are important for maintaining endothelial integrity and take part in the process of re-endothelization, neovascularization, and wound healing by differentiating into mature ECs and secreting angiogenic factors when endothelial injury occurs (Hristov et al., 2003; Hur et al., 2004; Zhang et al., 2014). Previous studies have revealed that the differentiation fate of EPCs is affected by many factors, such as mechanical

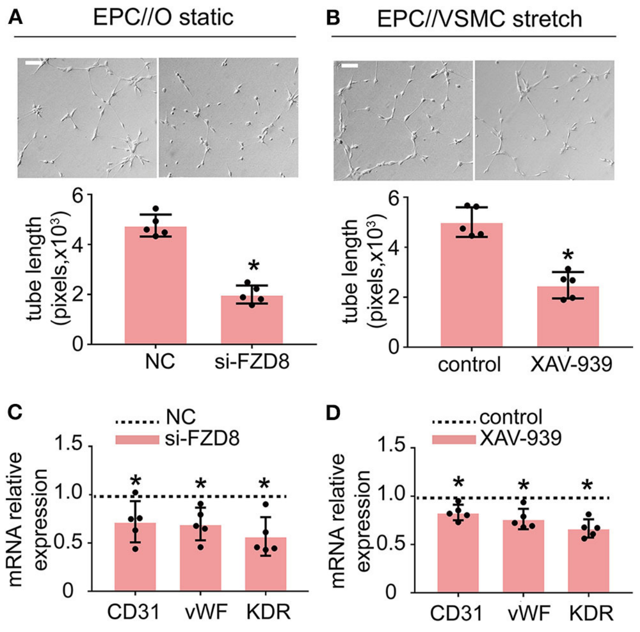

FIGURE 6 | Treatment with FZD8 siRNA and XAV-939 decreased EPC differentiation and tube formation. **(A,B)** EPCs transfected with FZD8 siRNA for 24 h exhibited significantly decreased tube formation and decreased expression of EC markers (CD31, vWF, and KDR) ($n = 5$). **(C,D)** Treatment with XAV-939 (5 μM) decreased tube formation and inhibited EPC differentiation toward ECs ($n = 5$). Scale bar = 100 μm. For quantitative analysis, five fields per plate were photographed, and tube lengths were measured using Image-Pro Plus software. Values are expressed as the mean ± *SD*. $^*P < 0.05$ compared with the control. Statistical analysis was performed with Student's *t*-test for **(A–D)**.

forces (including shear stress and cyclic stretch) and angiogenic factors (such as VEGF and CCN61) (Yu et al., 2010; Cheng et al., 2014; Li et al., 2017, 2018). Mesenchymal stem cells promote the endothelial differentiation of EPCs with the upregulation of CD31 and vWF (Ge et al., 2018). It has been reported that smooth muscle progenitor cells were reported to promote the neovascularization of EPCs and enhance the efficiency of EPC therapy during the wound-healing process (Joo et al., 2014; Foubert et al., 2015). Shudo et al. showed that the normal interactions between VSMCs and EPCs increased functional microvasculature and enhanced myocardial function in a rodent ischemic cardiomyopathy model (Shudo et al., 2013). However, the influences of neighboring VSMCs and physiological stretch on EPC functions are unknown. In this study, we developed a coculture system that assured intimate cellular communication between EPCs and VSMCs and included the application of physiological mechanical stretching. The present findings show that VSMCs facilitate EPC differentiation into ECs that have elevated expression of EC markers (CD31, vWF, and KDR) and increased angiogenic ability in the presence of mechanical stretch, indicating the importance of the synergistic effect of VSMCs and mechanical forces on EPC function.

In the present study, the Flexcell FX-5000T Strain Unit was applied to generate mechanical stretch *in vitro*. The 5% cyclic stretch (mimicking the physiological cyclic stretch) magnitude is based on previous clinical ultrasound data, which indicated that the large artery dilates by as much as 5% during cyclic stretch in normotension (Asanuma et al., 2003; Maul et al., 2011). Furthermore, the frequency used in the present study simulates the adult heart rate (70–80 beats) (Wachowiak et al., 2016), and some studies on rat VSMC cultures use an even lower frequency. The magnitude and frequency used here have also been used in our previous publications (Qi et al., 2016; Yao et al., 2017).

It has been shown that mechanical stretching increased the amount of CTGF secretion in anterior cruciate ligament-derived cells (Miyake et al., 2011), indicating that CTGF is a mechano-sensitive molecule. Blomme et al. reported that valvular interstitial cells showed the significant upregulation of CTGF at 1.15 Hz (heart frequency) and 14% elongation mechanical stretch, which was promoted through RhoC and MEK/Erk signaling pathways (Blomme et al., 2019). Additionally, in our previous study, we found that pathological cyclic stretch induces vascular remodeling by promoting VSMC proliferation via the miR-19b-3p/CTGF pathway (Wang et al., 2019).

Accumulating evidence indicates that CTGF, as a potent angiogenic inducer, supports cell metastasis, invasion, and angiogenesis in several tumor cells, and it induces tube formation in ECs (Kubota and Takigawa, 2007). It suggests that there is probably an interaction between angiogenesis of EPCs and CTGF. Our previous results indicated that 5% cyclic stretch induced the expression of CTGF in VSMCs; hence, in the current study, we aimed to investigate whether stretch-induced CTGF plays a role in EPC function. The results showed that r-CTGF significantly enhanced the expression of endothelial markers at the mRNA level and enhanced tube formation, whereas VSMCs transfected with a CTGF-specific siRNA suppressed this expression. Meanwhile, by using IPA bioinformatics analysis, FZD8 was found to be a putative downstream target regulated by CTGF.

FZD8 and β-catenin are key regulators in the Wnt/β-catenin signaling pathway that have essential roles in the regulation of progenitor cell fate, adult tissue homeostasis, proliferation during embryonic development, and developmental decisions (Majidinia et al., 2018). For example, ATP activates Wnt/β-catenin signaling in mesenchymal stem cells (MSCs), which contributes to neuronal differentiation by inducing the expressing of neuronal markers, Tuj1 and NeuN (Tu et al., 2014). Attenuation of Wnt/β-catenin signaling by exposure to the epidermal growth factor receptor is required for hair follicle development (Tripurani et al., 2018). In addition, during retinal neovascularization in oxygen-induced retinopathy, the Wnt/β-catenin signaling pathway had an important role in EPC recruitment (Liu et al., 2013). In our study, the positive effect of CTGF on FZD and β-catenin expression was detected. Therefore, CTGF may modulate the differentiation fate and angiogenic ability of EPCs by activating the FZD8/β-catenin pathway. Moreover, to better understand the regulation mechanism, we further detected the FZD8 mRNA level of EPCs after the r-CTGF stimulation. Results showed that the mRNA level was significantly increased by r-CTGF, which suggested that

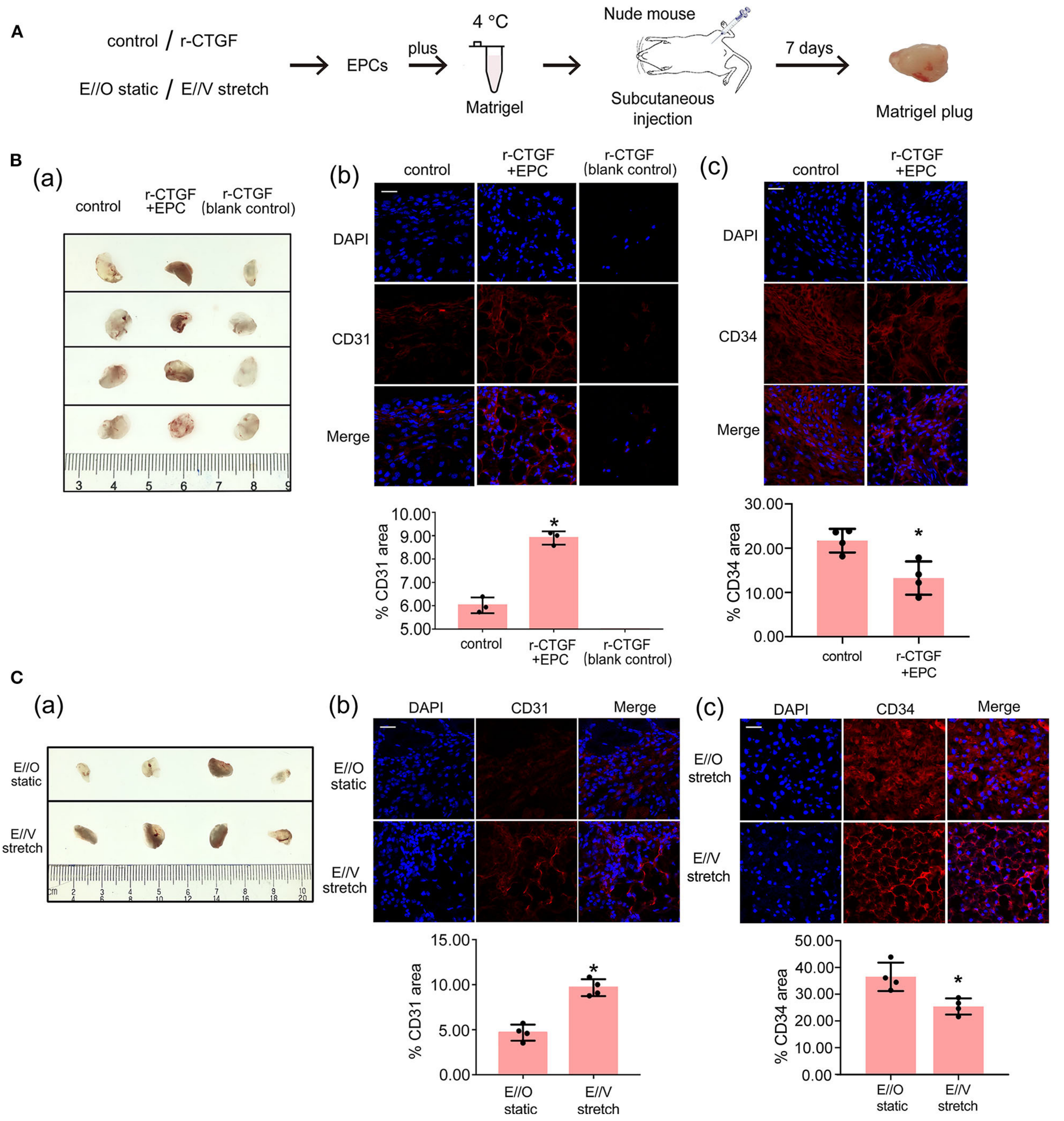

FIGURE 7 | The Matrigel plug assay results shows that r-CTGF or stretched VSMCs promote the differentiation of EPCs *in vivo*. **(A)** Transplantation scheme is shown for the *in vivo* Matrigel plug assay. **(B)** r-CTGF promoted angiogenesis of EPCs in *vivo*. Immunofluorescent staining for CD31 revealed increased arterial endothelium formation in the Matrigel with r-CTGF-treated EPCs. In addition, few cells invaded the plug in the Matrigel that was injected r-CTGF in the absence of EPCs. The stem cell marker CD34 staining results showed that protein expression levels in EPCs treated with r-CTGF were significantly reduced compared to the control group. **(C)** Stretched VSMCs promoted the ability of EPCs to form tubes *in vivo*. Immunofluorescent staining for CD31 revealed that CD31 expression in EPCs cocultured with stretched VSMCs was significantly increased. EPCs that were cocultured with VSMCs that were exposed to cyclic stretch in Matrigel plug expressed lower level of CD34 compared with monocultured under static conditions ($n = 4$). Scale bar = 50 μm. Values are expressed as the mean ± *SD*. $^*P < 0.05$ compared with the control. Statistical analysis was performed with Mann–Whitney *t*-test for **(B,C)**.

FZD8 was regulated by CTGF via transcriptional regulation (**Supplementary Figure 3**). We also further examined the effect of FZD8 loss of function or Wnt signaling in EPCs to confirm whether they are important for EPC differentiation. Our results indicated that FZD8/β-catenin is vital for EPC differentiation and angiogenic activities.

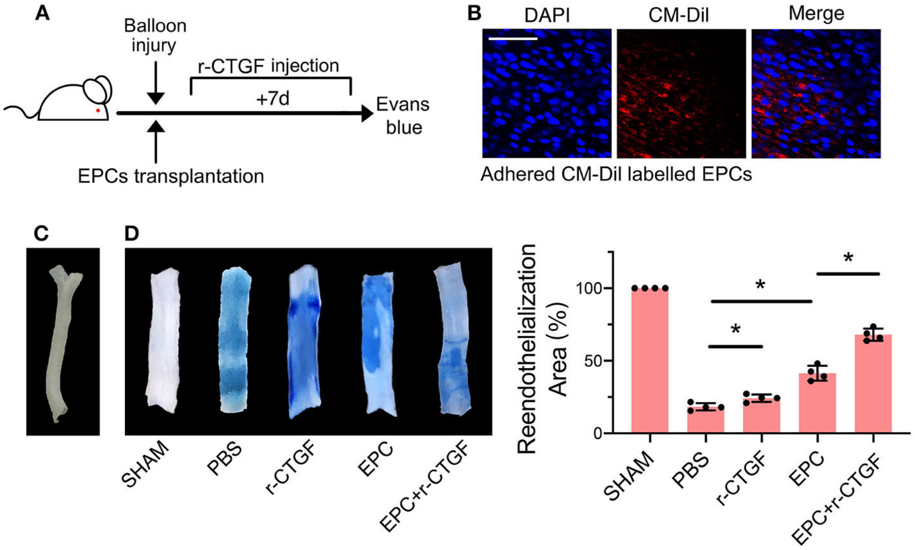

FIGURE 8 | EPC and r-CTGF promoted vascular intimal injury repair. **(A)** Schematic diagrams of the animal experimental protocol. **(B)** CM-Dil-labeled EPCs (red) adhered to the vascular lesion in situ. **(C)** The image of rat left carotid artery. **(D)** Intimal injury site was incubated with or without EPCs for 25–30 min, and injection of r-CTGF (2 μg/kg/day) promoted vascular repair. Reendothelialization area was observed by Evans blue staining after 7 days of the surgery. The percentage of the white area indicated the degree of reendothelialization. Scale bar = 50 μm. Values are expressed as the mean ± *SD*. $^*P < 0.05$ compared with the control. Statistical analysis was performed with Mann-Whitney *t*-test for D.

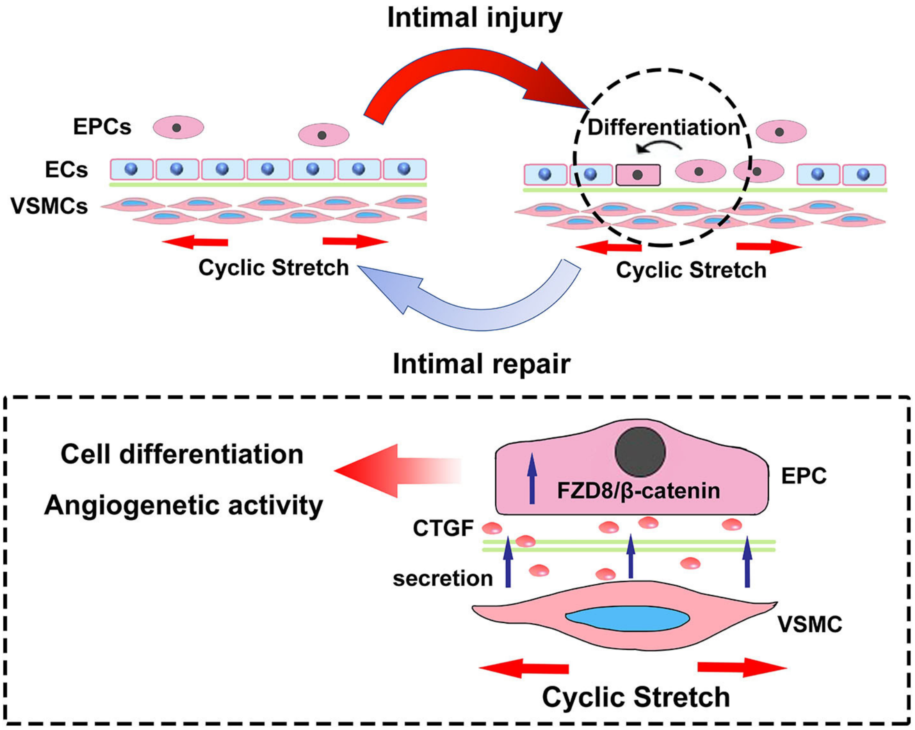

FIGURE 9 | The scheme here depicts the microenvironmental roles of VSMCs under cyclic stretch in EPC differentiation and angiogenesis during vascular repair. Cyclic stretch promotes the secretion of CTGF from VSMCs, which subsequently activates the FZD8/β-catenin signaling pathway in EPCs, and increased β-catenin nuclear translocation eventually induces the differentiation and angiogenic abilities of EPCs.

In conclusion, the present results revealed critical microenvironmental roles for VSMCs in the differentiation and angiogenesis process of EPCs during vascular injury. As is shown in **Figure 9**, physiological cyclic stretch (5%) increased the secretion of CTGF from VSMCs. Secreted CTGF activated FZD8 in EPCs, which subsequently promoted β-catenin nuclear translocation from the cytoplasm and finally encouraged EPC differentiation fate toward ECs with enhanced angiogenic ability and reendothelialization capacity. *In vivo* study also indicated that stretched VSMCs induced cocultured EPC differentiation toward ECs; furthermore, r-CTGF enhanced angiogenesis and improved EPC reendothelialization capacity. The CTGF/FZD8/β-catenin signaling axis may become a promising therapeutic target for vascular repair.

DATA AVAILABILITY STATEMENT

The original contributions presented in the study are included in the article/**Supplementary Materials**, further inquiries can be directed to the corresponding author.

ETHICS STATEMENT

The animal study was reviewed and approved by the Animal Research Committee of Shanghai Jiao Tong University.

AUTHOR CONTRIBUTIONS

JY: planned, performed, and analyzed animal studies and some of the cell and microscopy studies, prepared figures, and wrote part of the manuscript. W-BW: planned, performed, and analyzed the cell and microscopy studies, prepared figures, and wrote part of the manuscript. Y-JF: contributed to the immunofluorescence staining studies and the supplementary experiments in this project. HB: contributed to some of the animal studies. NL: contributed to the initial studies in this project. Q-PY, Y-LH, Z-LJ, Y-XQ, and YH: contributed to experimental facilities and reagents in this project. YH: planned and supervised the study and contributed to the writing of the final manuscript. The first draft of the manuscript was written by W-BW, JY, and YH. All authors contributed to the study conception and design, read, and approved the final manuscript.

FUNDING

This study was supported by grants from the National Natural Science Foundation of China (Nos. 11572198 and 11625209).

ACKNOWLEDGMENTS

A part of the abstract previously appeared as a conference abstract in the International Society for Heart Research (ISHR) world congress 2019.

SUPPLEMENTARY MATERIAL

The Supplementary Material for this article can be found online at: https://www.frontiersin.org/articles/10.3389/fcell.2020.606989/full#supplementary-material

Supplementary Figure 1 | VSMC identities are confirmed. Staining with α-SMA (green) revealed that the positively stained cells were VSMCs. Scale bar = 100 μm.

Supplementary Figure 2 | Transfection with an FZD8 siRNA significantly decreased the FZD8 mRNA level ($n = 3$). Values are expressed as the mean ± *SD*. $^*P < 0.05$ compared with the control.

Supplementary Figure 3 | The mRNA expression level of FZD8 in EPCs was stimulated by r-CTGF ($n = 4$). Values are expressed as the mean ± *SD*. $^*P < 0.05$ compared with the control.

REFERENCES

Armulik, A., Abramsson, A., and Betsholtz, C. (2005). Endothelial/pericyte interactions. *Circ. Res.* 97, 512–523. doi: 10.1161/01.RES.0000182903.16652.d7

Asahara, T., Murohara, T., Sullivan, A., Silver, M., Zee, R. V. D., Li, T., et al. (1997). Isolation of putative progenitor endothelial cells for angiogenesis. *Science* 275, 964–966. doi: 10.1126/science.275.5302.964

Asanuma, K., Magid, R., Johnson, C., Nerem, R. M., and Galis, Z. S. (2003). Uniaxial strain upregulates matrix-degrading enzymes produced by human vascular smooth muscle cells. *Am. J. Physiol. Heart Circ. Physiol.* 284, H1778–H1784. doi: 10.1152/ajpheart.00494.2002

Blomme, B., Deroanne, C., Hulin, A., Lambert, C., Defraigne, J. O., Nusgens, B., et al. (2019). Mechanical strain induces a pro-fibrotic phenotype in human mitral valvular interstitial cells through RhoC/ROCK/MRTF-A and Erk1/2 signaling pathways. *J. Mol. Cell Cardiol.* 135, 149–159. doi: 10.1016/j.yjmcc.2019.08.008

Chakravarthi, B., Chandrashekar, D. S., and Hodigere, B. S. A. (2018). Wnt receptor Frizzled 8 is a target of ERG in prostate cancer. *Prostate* 78, 1311–1320. doi: 10.1002/pros.23704

Chen, L. J., Wei, S. Y., and Chiu, J. J. (2013). Mechanical regulation of epigenetics in vascular biology and pathobiology. *J. Cell. Mol. Med.* 17, 437–448. doi: 10.1111/jcmm.12031

Cheng, B. B., Qu, M. J., Wu, L. L., Shen, Y., Yan, Z. Q., Zhang, P., et al. (2014). MicroRNA-34a targets Forkhead box j2 to modulate differentiation of endothelial progenitor cells in response to shear stress. *J. Mol. Cell. Cardiol.* 74, 4–12. doi: 10.1016/j.yjmcc.2014.04.016

Chien, S. (2007). Mechanotransduction and endothelial cell homeostasis: the wisdom of the cell. *Am. J. Physiol. Heart Circ. Physiol.* 292, H1209–H1224. doi: 10.1152/ajpheart.01047.2006

Cicha, I., Yilmaz, A., Klein, M., Raithel, D., Brigstock, D. R., Daniel, W. G., et al. (2005). Connective tissue growth factor is overexpressed in complicated atherosclerotic plaques and induces mononuclear cell chemotaxis *in vitro. Arterioscler Thromb. Vasc. Biol.* 25, 1008–1013. doi: 10.1161/01.ATV.0000162173.27682.7b

Dai, L., Li, C., Shedden, K. A., Misek, D. E., and Lubman, D. M. (2009). Comparative proteomic study of two closely related ovarian endometrioid adenocarcinoma cell lines using cIEF fractionation and pathway analysis. *Electrophoresis* 30, 1119–1131. doi: 10.1002/elps.200800505

Deanfield, J. E., Halcox, J. P., and Rabelink, T. J. (2007). Endothelial function and dysfunction: testing and clinicalrelevance. *Circulation* 115, 1285–1295. doi: 10.1161/CIRCULATIONAHA.106.652859

Deng, L., Blanco, F. J., Stevens, H., Lu, R., Caudrillier, A., McBride, M., et al. (2015). MicroRNA-143 activation regulates smooth muscle and endothelial cell crosstalk in pulmonary arterial hypertension. *Circ. Res.* 117, 870–883. doi: 10.1161/CIRCRESAHA.115.306806

Foubert, P., Squiban, C., Holler, V., Buard, V., Dean, C., Levy, B., et al. (2015). Strategies to enhance the efficiency of endothelial progenitor cell therapy by ephrin B2 pretreatment and coadministration with smooth muscle progenitor cells on vascular function during the wound-healing process in irradiated or nonirradiated condition. *Cell Transplant*. 24, 1343–1361. doi: 10.3727/096368913X672064

Ge, Q., Zhang, H., Hou, J., Wan, L., Cheng, W., Wang, X., et al. (2018). VEGF secreted by mesenchymal stem cells mediates the differentiation of endothelial progenitor cells into endothelial cells via paracrine mechanisms. *Mol. Med. Rep*. 17, 1667–1675. doi: 10.3892/mmr.2017.8059

Griese, D. P., Achatz, S., Batzlsperger, C. A., Strauch, U. G., Grumbeck, B., Weil, J., et al. (2003). Vascular gene delivery of anticoagulants by transplantation of retrovirally-transduced endothelial progenitor cells. *Cardiovasc. Res*. 58, 469–477. doi: 10.1016/S0008-6363(03)00266-9

Han, J. K., Kim, B. K., Won, J. Y., Shin, Y., Choi, S. B., Hwang, I., et al. (2016). Interaction between platelets and endothelial progenitor cells via LPA-Edg-2 axis is augmented by PPAR-δ activation. *J. Mol. Cell Cardiol*. 97, 266–277. doi: 10.1016/j.yjmcc.2016.06.002

Hristov, M., Erl, W., and Weber, P. C. (2003). Endothelial progenitor cells: mobilization, differentiation, and homing. *Arterioscler Thromb. Vasc. Biol*. 23, 1185–1189. doi: 10.1161/01.ATV.0000073832.49290.B5

Hur, J., Yoon, C. H., Kim, H. S., Choi, J. H., Kang, H. J., Hwang, K. K., et al. (2004). Characterization of two types of endothelial progenitor cells and their different contributions to neovasculogenesis. *Arterioscler Thromb. Vasc. Biol.* 24, 288–293. doi: 10.1161/01.ATV.0000114236.77009.06

Joo, H. J., Seo, H. R., Jeong, H. E., Choi, S. C., Park, J. H., Yu, C. W., et al. (2014). Smooth muscle progenitor cells from peripheral blood promote the neovascularization of endothelial colony-forming cells. *Biochem. Bioph. Res. Co*. 449, 405–411. doi: 10.1016/j.bbrc.2014.05.061

Jun, J. I., and Lau, L. F. (2011). Taking aim at the extracellular matrix: CCN proteins as emerging therapeutic. targets. *Nat. Rev. Drug Discov*. 10, 945–963. doi: 10.1038/nrd3599

Kelly, M., Joseph, C. G., Andrew, P. V., Megan, J. R., Dalyz, O., Ian, C. H., et al. (2020). Stepwise differentiation and functional characterization of human induced pluripotent stem cell-derived choroidal endothelial cells. *Stem Cell. Res. Ther.* 11, 409. doi: 10.1186/s13287-020-01903-4

Kubota, S., and Takigawa, M. (2007). CCN family proteins and angiogenesis: from embryo to adulthood. *Angiogenesis* 10, 1–11. doi: 10.1007/s10456-006-9058-5

Kuliszewski, M. A., Fujii, H., Liao, C., Smith, A. H., Xie, A., Lindner, J. R., et al. (2009). Molecular imaging of endothelial progenitor cell engraftment using contrast-enhanced ultrasound and targeted microbubbles. *Cardiovasc. Res*. 83, 653–662. doi: 10.1093/cvr/cvp218

Kundi, R., Hollenbeck, S. T., Yamanouchi, D., Herman, B. C., Edlin, R., Ryer, E. J., et al. (2009). Arterial gene transfer of the TGF-beta signalling protein Smad3 induces adaptive remodelling following angioplasty: a role for CTGF. *Cardiovasc. Res*. 84, 326–335. doi: 10.1093/cvr/cvp220

Li, H., Zhang, X. Y., Guan, X. M., Cui, X. D., Wang, Y. L., Chu, H. R., et al. (2012). Advanced glycation end products impair the migration, adhesion and secretion potentials of late endothelial progenitor cells. *Cardiovasc. Diabetol.* 11:46. doi: 10.1186/1475-2840-11-46

Li, L., Liu, H., Xu, C., Deng, M., Song, M., Yu, X., et al. (2017). VEGF promotes. endothelial progenitor cell differentiation and vascular repair through connexin 43. *Stem Cell Res. Ther*. 8:237. doi: 10.1186/s13287-017-0684-1

Li, N., Wang, W. B., Bao, H., Shi, Q., Jiang, Z. L., Qi, Y. X., et al. (2018). MicroRNA-129-1-3p. regulates cyclic stretch-induced endothelial progenitor cell differentiation by targeting Runx2. *J. Cell. Biochem*. 120, 5256–5267. doi: 10.1002/jcb.27800

Li, X., Pongkitwitoon, S., Lu, H., Lee, C., Gelberman, R., and Thomopoulos, S. (2019). CTGF induces tenogenic differentiation and proliferation of adipose-derived stromal cells. *J. Orthop. Res*. 37, 574–582. doi: 10.1002/jor.24248

Liu, S. C., Chuang, S. M., Hsu, C. J., Tsai, C. H., Wang, S. W., and Tang, C. H. (2014). CTGF increases. vascular endothelial growth factor-dependent angiogenesis in human synovial fibroblasts by increasing miR-210 expression. *Cell Death Dis*. 5:e1485. doi: 10.1038/cddis.2014.453

Liu, X., McBride, J., Zhou, Y., Liu, Z., and Ma, J. X. (2013). Regulation of endothelial progenitor cell. release by Wnt signaling in bone marrow. *Invest. Ophthalmol. Vis. Sci*. 54, 7386–7394. doi: 10.1167/iovs.13-13163

Majidinia, M., Aghazadeh, J., Jahanban-Esfahlani, R., and Yousefi, B. (2018). The roles of Wnt/beta-catenin pathway in tissue development and regenerative medicine. *J. Cell. Physiol*. 233, 5598–5612. doi: 10.1002/jcp.26265

Malinda, K. M. (2009). *In vivo* matrigel migration and angiogenesis assay. *Methods Mol. Biol*. 467, 287–294. doi: 10.1007/978-1-59745-241-0_17

Maul, T. M., Chew, D. W., Nieponice, A., and Vorp, D. A. (2011). Mechanical stimuli differentially control stem cell behavior: morphology, proliferation, and differentiation. *Biomech. Model Mechanobiol*. 10, 939–953. doi: 10.1007/s10237-010-0285-8

Miyake, Y., Furumatsu, T., Kubota, S., Kawata, K., Ozak, T., and Takigawa, M. (2011). Mechanical stretch. increases CCN2/CTGF expression in anterior cruciate ligament-derived cells. *Biochem. Biophys. Res. Commun*. 409, 247–252. doi: 10.1016/j.bbrc.2011.04.138

Murasawa, S., Kawamoto, A., Horii, M., Nakamori, S., and Asahara, T. (2005). Niche-dependent translineage commitment of endothelial progenitor cells, not cell fusion in general, into myocardial lineage cells. *Arterioscler Thromb. Vasc. Biol*. 25, 1388–1394. doi: 10.1161/01.ATV.0000168409.69960.e9

Murillo-Garzon, V., Gorrono-Etxebarria, I., and Akerfelt, M. (2018). Frizzled-8 integrates Wnt-11 and transforming growth factor-beta signaling in prostate cancer. *Nat. Commun*. 9:1747. doi: 10.1038/s41467-018-04042-w

Ostriker, A., Horita, H. N., Poczobutt, J., Weiser-Evans, M. C., and Nemenoff, R. A. (2014). Vascular smooth muscle cell-derived transforming growth factor-beta promotes maturation of activated, neointima lesion-like macrophages. *Arterioscler Thromb. Vasc. Biol*. 34, 877–886. doi: 10.1161/ATVBAHA.114.303214

Qi, Y. X., Jiang, J., Jiang, X. H., Wang, X. D., Ji, S. Y., Han, Y., et al. (2011). PDGF-BB and TGF-β1 on cross-talk between endothelial and smooth muscle cells in vascular remodeling induced by low shear stress. *Proc. Natl. Acad. Sci. U.S.A*. 108, 1908–1913. doi: 10.1073/pnas.1019219108

Qi, Y. X., Qu, M. J., Long, D. K., Liu, B., Yao, Q. P., Chien, S., et al. (2008). Rho-GDP dissociation inhibitor alpha downregulated by low shear stress promotes vascular smooth muscle cell migration and apoptosis: a proteomic analysis. *Cardiovasc. Res*. 80, 114–122. doi: 10.1093/cvr/cvn158

Qi, Y. X., Qu, M. J., Yan, Z. Q., Zhao, D., Jiang, X. H., Shen, B. R., et al. (2010). Cyclic strain modulates migration and proliferation of vascular smooth muscle cells via Rho-GDIalpha, Rac1, and p38 pathway. *J. Cell. Biochem*. 109, 906–914. doi: 10.1002/jcb.22465

Qi, Y. X., Yao, Q. P., Huang, K., Shi, Q., Zhang, P., Wang, G. L., et al. (2016). Nuclear envelope proteins modulate proliferation of vascular smooth muscle cells during cyclic stretch application. *Proc. Natl. Acad. Sci. U.S.A*. 113, 5293–5298. doi: 10.1073/pnas.1604569113

Shudo, Y., Cohen, J. E., Macarthur, J. W., Atluri, P., Hsiao, P. F., Yang, E. C., et al. (2013). Spatially oriented, temporally sequential smooth muscle cell-endothelial progenitor cell bi-level cell sheet neovascularizes ischemic myocardium. *Circulation* 128(11 Suppl. 1), S59–S68. doi: 10.1161/CIRCULATIONAHA.112.000293

Tripurani, S. K., Wang, Y., Fan, Y. X., Rahimi, M., Wong, L., Lee, M. H., et al. (2018). Suppression of Wnt/beta-catenin signaling by EGF receptor is required for hair follicle development. *Mol. Biol. Cell*. 29, 2784–2799. doi: 10.1091/mbc.E18-08-0488

Tu, J., Yang, F., Wan, J., Liu, Y., Zhang, J., Wu, B., et al. (2014). Light-controlled. astrocytes promote human mesenchymal stem cells toward neuronal differentiation and improve the neurological deficit in stroke rats. *Glia* 62, 106–121. doi: 10.1002/glia.22590

Wachowiak, M. P., Hay, D. C., and Johnson, M. J. (2016). Assessing heart rate variability through wavelet-based. statistical measures. *Comput. Biol. Med*. 77, 222–230. doi: 10.1016/j.compbiomed.2016.07.008

Wang, W. B., Li, H. P., Yan, J., Zhuang, F., Bao, M., Liu, J. T., et al. (2019). CTGF regulates cyclic stretch-induced vascular smooth muscle cell proliferation via microRNA-19b-3p. *Exp. Cell. Res*. 376, 77–85. doi: 10.1016/j.yexcr.2019.01.015

Wei, S., Huang, J., Li, Y., Zhao, J., Luo, Y., Meng, X., et al. (2015). Novel zinc finger transcription factor ZFP580 promotes differentiation of bone marrow-derived endothelial progenitor cells into endothelial cells via eNOS/NO pathway. *J. Mol. Cell. Cardiol.* 87, 17–26. doi: 10.1016/j.yjmcc.2015.08.004

Yan, J., Bao, H., Fan, Y. J., Jiang, Z. L., Qi, Y. X., and Han, Y. (2020). Platelet-derived microvesicles promote endothelial progenitor cell proliferation in intimal injury by delivering TGF-β1. *FEBS J.* doi: 10.1111/febs.15293. [Epub ahead of print].

Yao, Q. P., Xie, Z. W., Wang, K. X., Zhang, P., Han, Y., Qi, Y. X., et al. (2017). Profiles of long. noncoding RNAs in hypertensive rats: long noncoding RNA XR007793 regulates cyclic strain-induced proliferation and migration of vascular smooth muscle cells. *J. Hypertens*. 35, 1195–1203. doi: 10.1097/HJH.0000000000001304

Yu, Y., Gao, Y., Qin, J., Kuang, C. Y., Song, M. B., Yu, S. Y., et al. (2010). CCN1 promotes the differentiation of endothelial progenitor cells and reendothelialization in the early phase after vascular injury. *Basic Res. Cardiol*. 105, 713–724. doi: 10.1007/s00395-010-0117-0

Zhang, M., Malik, A. B., and Rehman, J. (2014). Endothelial progenitor cells and vascular repair. *Curr. Opin. Hematol*. 21, 224–228. doi: 10.1097/MOH.0000000000000041

Conflict of Interest: The authors declare that the research was conducted in the absence of any commercial or financial relationships that could be construed as a potential conflict of interest.

frontiers
in Cell and Developmental Biology

ORIGINAL RESEARCH
published: 12 February 2021
doi: 10.3389/fcell.2021.635307

RAMP2-AS1 Regulates Endothelial Homeostasis and Aging

Chih-Hung Lai[1,2,3], Aleysha T. Chen[1], Andrew B. Burns[1], Kiran Sriram[1,4], Yingjun Luo[1], Xiaofang Tang[1], Sergio Branciamore[1], Denis O'Meally[5], Szu-Ling Chang[1,2], Po-Hsun Huang[3], John Y-J. Shyy[6], Shu Chien[6,7], Russell C. Rockne[4,8]* and Zhen Bouman Chen[1,4]*

[1] Department of Diabetes Complications and Metabolism, City of Hope, Duarte, CA, United States, [2] Cardiovascular Center, Taichung Veterans General Hospital, Taichung, Taiwan, [3] Institute of Clinical Medicine, National Yang-Ming University, Taipei, Taiwan, [4] Irell and Manella Graduate School of Biological Sciences, City of Hope, Duarte, CA, United States, [5] Center for Gene Therapy, City of Hope, Duarte, CA, United States, [6] Department of Medicine, University of California, San Diego, La Jolla, CA, United States, [7] Department of Bioengineering, University of California, San Diego, La Jolla, CA, United States, [8] Division of Mathematical Oncology, Department of Computational and Quantitative Medicine, City of Hope, Duarte, CA, United States

OPEN ACCESS

Edited by:
Jing Zhou,
Peking University, China

Reviewed by:
Yingxin Qi,
Shanghai Jiao Tong University, China
Ding Yu Lee,
China University of Science and Technology, Taiwan

***Correspondence:**
Zhen Bouman Chen
zhenchen@coh.org
Russell C. Rockne
rrockne@coh.org

Specialty section:
This article was submitted to Cell Adhesion and Migration, a section of the journal Frontiers in Cell and Developmental Biology

Received: *30 November 2020*
Accepted: *22 January 2021*
Published: *12 February 2021*

Citation:
Lai C-H, Chen AT, Burns AB, Sriram K, Luo Y, Tang X, Branciamore S, O'Meally D, Chang S-L, Huang P-H, Shyy JY-J, Chien S, Rockne RC and Chen ZB (2021) RAMP2-AS1 Regulates Endothelial Homeostasis and Aging. Front. Cell Dev. Biol. 9:635307. doi: 10.3389/fcell.2021.635307

The homeostasis of vascular endothelium is crucial for cardiovascular health and endothelial cell (EC) aging and dysfunction could negatively impact vascular function. Leveraging transcriptome profiles from ECs subjected to various stimuli, including time-series data obtained from ECs under physiological pulsatile flow vs. pathophysiological oscillatory flow, we performed principal component analysis (PCA) to identify key genes contributing to divergent transcriptional states of ECs. Through bioinformatics analysis, we identified that a long non-coding RNA (lncRNA) RAMP2-AS1 encoded on the antisense of RAMP2, a determinant of endothelial homeostasis and vascular integrity, is a novel regulator essential for EC homeostasis and function. Knockdown of RAMP2-AS1 suppressed RAMP2 expression and caused EC functional changes promoting aging, including impaired angiogenesis and increased senescence. Our study demonstrates an integrative approach to quantifying EC aging based on transcriptome changes, which also identified a number of novel regulators, including protein-coding genes and many lncRNAs involved EC functional modulation, exemplified by RAMP2-AS1.

Keywords: endothelial function, aging, RAMP2-AS1, RAMP2, lncRNA, transcriptome, PCA, shear stress

INTRODUCTION

Vascular endothelium constitutes the vital interface between circulating blood and the vascular wall. The homeostasis of vascular endothelial cells (ECs), including their vasodilatory function and anti-inflammatory, anti-coagulatory, and anti-thrombotic properties, is crucial to vascular health (Fisher et al., 2001). In the process of aging, ECs undergo functional declines, which is manifested by a constellation of cellular and molecular changes, e.g., attenuated endothelium-dependent vasodilation, increased reactive oxygen species (ROS) production, and impaired angiogenic and regenerative capacities. This process of EC aging has been reviewed and discussed and various genes and pathways have been proposed to be important players (Brandes et al., 2005; Donato et al., 2015; Ungvari et al., 2018). However, the rate and the extent of EC aging have not been experimentally investigated at the transcriptome level using quantitative measurements.

In order to address this question, one approach would be to use a longitudinal time-series transcriptome data collected from ECs undergoing an aging-related process. One such process is EC response to flow, evident by the focal distribution of atherosclerotic lesions that are aggravated by aging (Wang and Bennett, 2012; Gimbrone and Garcia-Cardena, 2016). For example, the laminar and pulsatile shear stress (PS) in the straight parts of the artery not only causes an elevated expression of anti-oxidative and anti-inflammatory genes, but also suppresses pro-oxidative and pro-inflammatory genes, thus contributing to a potential anti-aging effect. Indeed, several key regulators in aging, e.g., Sirtuins 1 and 3 and genes supporting the mitochondrial antioxidant defense systems, e.g., PGC1α and Nrf1, are upregulated by laminar flow or PS (Chen et al., 2010; Tseng et al., 2014; Wu et al., 2018). In contrast, the oscillatory shear stress (OS) due to disturbed flow in the curvatures and bifurcations strongly induces these pro-oxidative and pro-inflammatory genes while suppressing the antioxidative and anti-inflammatory genes that cause EC dysfunction and predispose vascular disease (see Malek et al., 1999; Harrison et al., 2003; Chiu and Chien, 2011 for review).

Using a parallel-plate flow system, we have previously profiled the transcriptomes using RNA-sequencing (RNA-seq) in cultured human ECs subject to PS and OS in a time-course encompassing transient and chronic transcriptional changes (Ajami et al., 2017; Miao et al., 2018; He et al., 2019). Consistent with the well documented divergent effects, compared to OS, PS induced an anti-inflammatory, anti-oxidative, and anti-fibrotic gene expression program. In addition, leveraging these RNA-seq data, we have also identified several novel EC regulators, including several long non-coding RNAs (lncRNAs) as essential epigenetic components of EC response to flow (Huang et al., 2017; Miao et al., 2018).

In this study, we propose that PS deters EC aging by regulation of a transcriptional program underlying an anti-EC aging effect. We first leveraged temporal measurements of transcriptome (i.e., shear stress time-course RNA-seq) data to model a compressed aging trajectory associated with PS or OS through principal component analysis (PCA). Next, through exploring the key genes engaged in the distinct effects of PS vs. OS, as well as other stimuli known to regulate EC function, i.e., pro-inflammatory cytokine tumor necrosis factor alpha (TNFα) and endothelial protective drug statins, we identified receptor activity-modifying protein 2 (*RAMP2*, a known key regulator in EC function) and *RAMP2-AS1* (a lncRNA transcribed from the anti-sense of RAMP2) as a putative pair of genes that contribute to the divergence in EC aging trajectories. We further investigated the functional importance of RAMP2-AS1 in the regulation of RAMP2 and EC function. Together, our study demonstrates an integrative approach to unraveling novel crucial regulators and regulatory mechanisms in EC aging.

MATERIALS AND METHODS

Aging Trajectory and Eigengene Analysis

We have previously published the PS and OS EC RNA-sequencing (RNA-seq) data (GSE103672) (Ajami et al., 2017; Miao et al., 2018), consisting of 10 timepoints (i.e., 0, 1, 2, 3, 4, 6, 9, 12, 16, and 24 h), each with two biological replicates for both the PS and OS conditions. We constructed a data matrix (X) of log2 transformed counts per million reads (CPM) and performed PCA on the mean-centered data matrix with the singular value decomposition method so that $X = U\Sigma V^*$. Matrices were created for protein-coding genes (PCGs) and non-coding genes (NCGs) and were analyzed separately. Through an analysis of all principal components, we identified components which resulted in the most separation, and hence explained most of the variance, between the PS and OS conditions. These components were identified as PC3 for PCGs and PC2 for NCGs. We then constructed aging trajectories by plotting these components over time as performed in our previous study (Rockne et al., 2020; **Supplementary Figure 1**).

Genes associated with aging were defined by the principal component loadings (right singular vectors in the matrix V^*) corresponding to the aging trajectories, referred to as eigengenes. The eigengenes were ranked in descending order by absolute value (**Supplementary Table 1**) and were used to project additional RNA-seq data (X') into the component space by the transformation X'V. Coding and non-coding eigengenes were also ranked by mutual information with respect to the flow condition using a method for combining discrete and continuous data (Gao et al., 2017). Mutual information measures the mutual dependence between variables and quantifies the amount of information obtained about one variable by observing the other, in this case between genes and the flow conditions. The top 50-ranked protein-coding and non-coding eigengenes are listed in **Supplementary Table 3**.

EC Culture, Treatment, and Transfection

HUVECs (Cell Applications Inc., San Diego, CA) (Passages 4–8) from pooled donors were cultured in HUVEC growth medium containing EC growth supplements (Cell Applications Inc.), based on the manufacturer's recommendations, at 37°C in an atmosphere of 95% air and 5% CO_2. HUVECs were treated with atorvastatin (ATV) at 1 or 5 mM, or TNFα at 100 ng/ml for 24 h. Antisense LNA GapmeRs specifically targeting two different regions of RAMP2-AS1 (LG00116686, LG00226723) and scramble control designed and purchased from Qiagen were transfected into ECs with Lipofectamine 3000 following the protocol provided by the manufacturer and as described previously (Miao et al., 2018).

Intima Samples From Human Mesenteric Arteries

Intimal RNA was isolated from deidentified human mesenteric arteries obtained from the organ donors of Southern California Islet Cell Resource Center at City of Hope. The research consents for the use of postmortem human tissues were obtained from the donors' next of kin and ethical approval for this study was granted by the Institutional Review Board of City of Hope (IRB #01046). Intimal RNA was collected by flushing once the inner lumen with TRIzol following an established method (Nam et al., 2009) and as previously described (Tang et al., 2020).

RNA Extraction, Quantitative PCR, Library Preparation

RNA was extracted from cells and tissues using TRIzol (Invitrogen) following the manufacturer's instructions as described previously (Miao et al., 2018; Tang et al., 2020). The total RNA was reverse transcribed using the PrimeScript^{TM} RT Master Mix (Cat# RR036A-1, Takara), and cDNAs were used for PCR and qPCR analyses using Biorad CFX96. Each qPCR sample was performed in triplicate, with iTaq Universal SYBR Green Supermix (BioRad). β-actin (ACTB) was used as the internal control. For RNA-seq, 500 ng of total RNA per sample was used and the libraries were prepared using the KAPA mRNA HyperPrep Kit (Roche Diagnostics) following the manufacturer's manual. The libraries were sequenced with HiSeq2500 using the SR50 mode.

Immunoblotting

Upon collection, total cell protein was extracted with a NP40 Cell Lysis Buffer (Thermo Fisher Scientific) in the presence of a protease inhibitor (Cat#8340; Sigma-Aldrich) and a phosphatase inhibitor cocktail (Cat# 5870; Cell Signaling). Protein extracts (30 μg), along with a protein ladder, were loaded onto a 15% SDS-PAGE gel followed by transferring onto a PVDF membrane. The membranes were blocked with 5% skim milk and then incubated with primary antibodies in 3% BSA overnight at 4°C. The primary antibodies used were mouse anti-RAMP2 (sc-365240, Santa Cruz 1:100 dilution) and rabbit anti-β-actin (8457S, Cell Signaling, 1:1,000 dilution), which was used as a loading control. After washing with TBST (containing 0.1% Tween-20), the membranes were then incubated with HRP-conjugated anti-rabbit (7074S, Cell Signaling) or anti-mouse (7076S, Cell Signaling) secondary antibodies at room temperature for 1 h and developed using ECL substrate (Cat# WBKLS0500, Millipore). The densitometry was analyzed with use of Image J.

RNA-Seq Data Analysis

STAR (Dobin et al., 2013) was used to align raw sequencing data to the GRCh38 reference using GENCODE annotation Release 33. Each library was subjected to extensive quality control, including estimation of library complexity, gene body coverage, and duplication rates, among other metrics detailed in the pipeline repository. Reads were counted across genomic features using Subread featureCounts (Liao et al., 2013) and merged into a matrix of counts per gene for each sample. DESeq2 (Love et al., 2014) was then used to perform differential expression analysis with default parameters. Gene ontology enrichment analysis was performed through the Gene Ontology Consortium platform (Ashburner et al., 2000) and Benjamini-Hochberg corrected $P < 0.05$ were considered significantly enriched pathways.

Senescence-Associated β-gal (SA β-gal) Staining

Cytochemical staining for SA-β-galactosidase was performed using the Senescence β-Galactosidase Staining Kit (Cell Signaling Technology) following the manufacturer's manual. Briefly, the ECs following transfection were washed once with freshly prepared 1 × PBS, fixed in 1X Fixative solution for 10–15 min at room temperature, and then rinsed twice with 1 × PBS. The cells were stained for 48 h in a dry incubator before viewing under an Olympus JP/1 × 71 fluorescence microscope (Olympus, Japan) with digital camera output. The percentage of SA-β-galactosidase positive cells was determined by counting the number of blue cells under bright field illumination. The positively stained cells in three randomly selected low-power fields per well were counted by an independent observer in a blind fashion. The average was taken from the three fields.

Apoptosis Analysis

EC apoptosis was assayed using the FITC Annexin V Apoptosis Detection Kit II (BD Pharmingen, Cat # 556570) following the manufacturer-recommended protocol. Briefly, cells were collected using 0.05% Trypsin-EDTA, washed once with PBS and resuspended in the binding buffer. Cells were then stained with 5 μL Propodium Iodide Staining solution and 5 μL FITC Annexin V and incubated in the dark at room temperature of 20 min. Following incubation, cells were immediately analyzed on Accuri C6 flow cytometry (BD Biosciences).

Hanging Drop Cell Aggregation and 3D Sprouting Assay

Three-dimensional (3D) spheroid sprouting assay was performed following a published protocol (Heiss et al., 2015) with modifications. ECs cultured to confluency were trypsinized for 5 min at 37°C using 0.25% Trypsin/0.53 mM EDTA (ATCC 30-2101) and counted. The cell suspension was neutralized with M199 media and centrifuged at 200 rcf for 5 min. The media was aspirated, and the cells were resuspended at 10^6 cells/mL in fresh media. To form homogeneous aggregates of 500 cell per aggregate, 125 μl of the resuspended cells were added to 3.875 mL of M199 media. One mL of 0.3% (W/V) methylcellulose (Sigma M0512-100G) in M199 media was then added to the suspension to bring the total volume to 5 mL, resulting in a final density of 500 cells per 20 μL. The cell suspension was then distributed onto the inside lid of a petri dish using a multichannel pipette to form rows of 20 μL droplets. The dish was then inverted, and 5 mL of PBS was added to the bottom of the dish. Cells were incubated overnight. On the next day, cell aggregates were collected, washed, and centrifuged at 100 rcf for 2.5 min. The aggregates were resuspended in pre-chilled Matrigel (Corning 356234) to allow for two aggregates per 20 μL. Aggregates were distributed in 20 μL droplets onto the bottom of the plate. The plate was then turned upside down to form hanging drops and placed into a larger petri dish (to maintain sterility), which was then placed in incubator for 30 min. After the Matrigel has begun to gel, the plate was removed from the larger dish and turned upright to allow another hour to fully set. The gelled aggregates were then overlaid with M199 media containing 50 ng/mL of VEGF (Sigma V7259-10UG) and incubated for 3 days and monitored for sprouting.

Brightfield images of the sprouts were taken using an Amscope MU1000 camera and an Olympus IX50 microscope at 10× magnification. The images were then analyzed in FIJI (ImageJ) using the Sprout Morphology analysis tool (Eglinger et al., 2017). The images were first converted to 8-bit binary masks. Threshold values were then globally adjusted across all images to uniformly darken the background and highlight the aggregates and their sprouts. The images were then manually assessed for bubbles or other artifacts in the gel that the software could misconstrue as an aggregate. Pixel scale was determined using a hemocytometer, and this was applied globally to all images. Then the images were batch-run through the analysis package, where the software measured the aggregate and the sprout network. Data was exported from FIJI for statistical analysis.

Statistical Analysis

Statistical analysis was performed using Student's *t*-test (two-sided) between two groups or ANOVA followed by Tukey's post-test for multiple-group comparisons. If variances between two groups were significantly different (F-test), non-parametric Mann–Whitney *U*-test was applied. $P < 0.05$ was considered as statistically significant. For all the experiments, at least three independent experiments were performed unless otherwise specified.

RESULTS

ECs Under PS and OS Show Divergent Aging Trajectories Through Transcriptome Analysis

To construct an aging trajectory in ECs responding to PS and OS, we leveraged the RNA-seq data previously obtained from ECs subject to the PS (12 ± dyne/cm^2) and OS (1 ± 5 dyne/cm^2) for 10 time points (i.e., 0, 1, 2, 3, 4, 6, 9, 12, 16, and 24 h) (Ajami et al., 2017; Miao et al., 2018). For PCGs, PCA identified that the majority of the variance in these data was contained in the first 8 PCs (**Supplementary Figure 1A**).

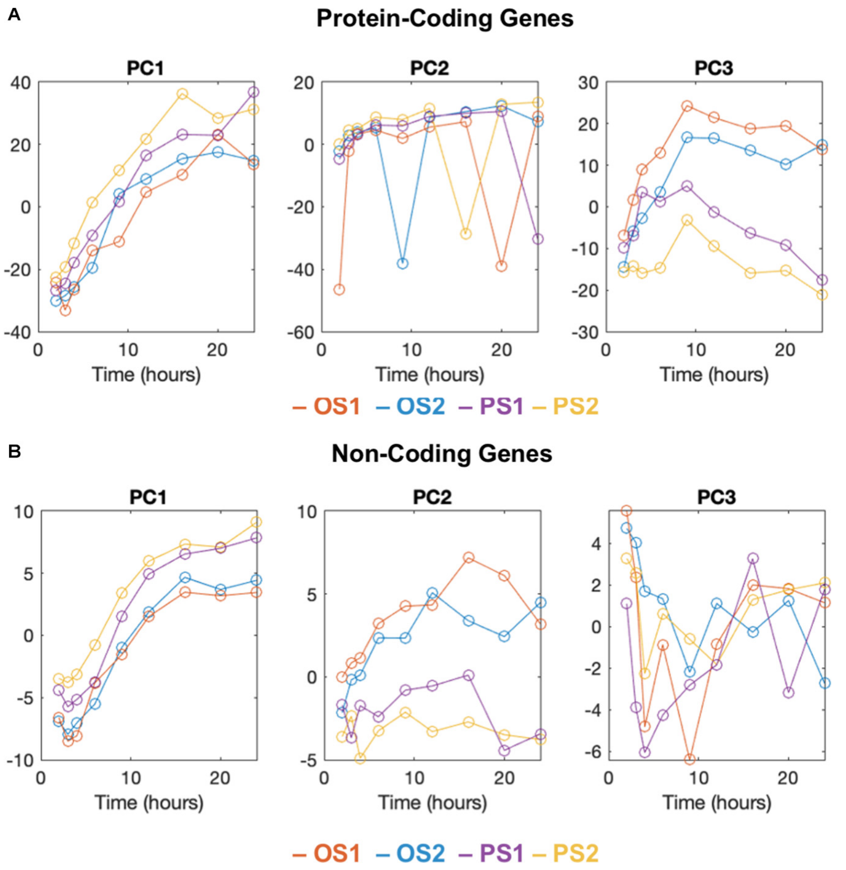

FIGURE 1 | PCA analysis and aging trajectory of ECs subject to PS and OS. The first 3 principal components of time-series RNA-sequencing data plotted against time (hours) for protein coding genes **(A)** and non-coding genes **(B)** of two replicates (OS 1, 2; PS 1, 2). **(A)** The first principal component (PC1) is correlated with time. The second component (PC2) includes intermittent spiking signals associated with the expression of mitochondrial genes, and the third component (PC3) shows divergent trajectories between OS and PS conditions. **(B)** Same as A except for non-coding genes. Divergent trajectories are shown in the second component (PC2). The third component is not clearly interpretable.

When plotting the first 8 PCs *vs.* time, we found that PC1 correlated with time, PC2 exhibited intermittent spiking signals associated with the expression of mitochondrial genes, and PC3 showed divergent trajectories between OS and PS (**Figure 1A** and **Supplementary Figures 1B,C**). In contrast, PC4 to PC8 were not clearly interpretable (**Supplementary Figure 1C**). Similarly, we performed PCA for the NCGs, particularly long intergenic non-coding RNAs (lincRNAs), which revealed divergent trajectories of PS *vs.* OS over time in PC2. To this end, we identified PC3 in PCGs and PC2 in NCGs to be reflective of divergent aging trajectories between PS and OS conditions.

To evaluate the potential of using PCA of PCGs in assessing the aging state of ECs, we used the PC3 eigengenes to project RNA-seq data obtained from HUVECs-treated with atorvastatin (ATV) that has been shown to exert EC protective effects (Sun et al., 2006; Chen et al., 2009; He et al., 2017) and those stimulated by TNFα that causes EC dysfunction (Zhang et al., 2009) (GSE163433). The PCA revealed that atorvastatin (ATV)-treated cells were similar to PS-imposed cells, whereas those treated with TNFα were more like those under OS (**Supplementary Figure 2A**). We also used RNA-seq data from hypoxia-treated human microvascular ECs we have published (GSE136912) (Tang et al., 2020), which appeared to be in-between of PS and OS regardless of the duration (**Supplementary Figure 2B**). This result is in line with a lack of clearly expected effect of hypoxia in EC aging.

LncRNA RAMP2-AS1 Is a Candidate Gene Contributing to Divergent Aging Trajectories

To evaluate the relative contribution of various genes to the aging trajectory and identify novel EC regulators, we ranked both PCGs and NCGs using PCA (**Supplementary Tables 1**, **2**).

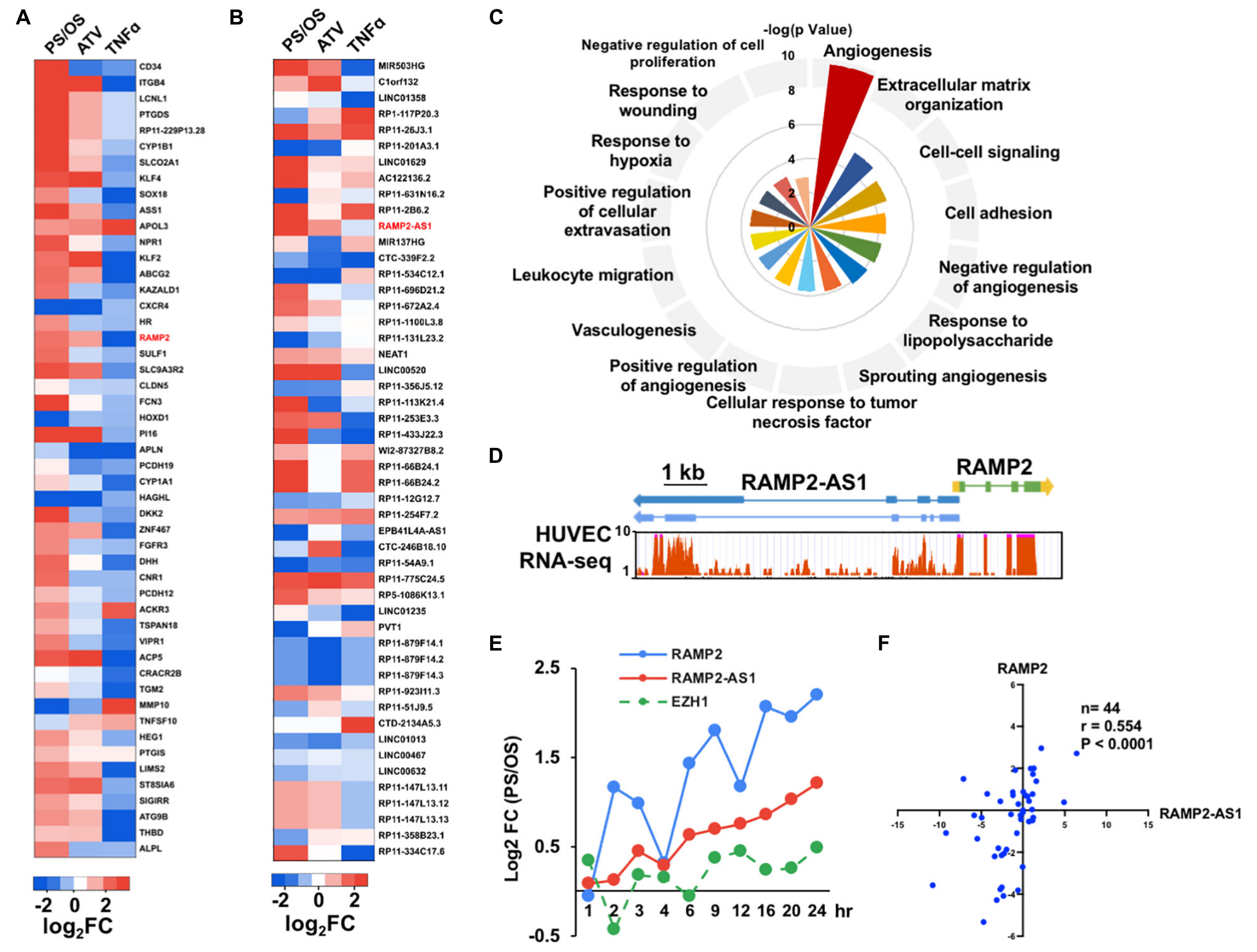

FIGURE 2 | Identification of RAMP2 and RAMP2-AS1 as top candidates. **(A,B)** PS/OS, ATV/control, and TNFα/control log2 fold changes in expression of top 50 protein-coding genes (PCGs), ranked by absolute values of PC3; non-coding genes (NCGs), ranked by absolute values of PC2. RAMP2 and RAMP2-AS1 are labeled in red showing induction by PS and ATV and suppression by TNFα. **(C)** Top 15 Biological Pathway terms from pathway enrichment analysis of top 200 PCGs, plotted with $-\log_{10}$ *P*-value. **(D)** Genomic structures of RAMP2-AS1 and RAMP2, wherein blocks depict exons, horizontal lines resemble introns, and arrowheads indicate the opposite transcriptional directions of RAMP2-AS1 and RAMP2; aligned with RNA-seq measurements along RAMP2 and RAMP2-AS1 in HUVECs. **(E)** RNA levels of RAMP2, RAMP2-AS1, and EZH1, plotted with PS/OS log2 fold changes across 10 time points, from 1 to 24 h under PS or OS. **(F)** Spearman correlation between RAMP2-AS2 and RAMP2 RNA levels in 44 human mesenteric arterial intimae quantified by qPCR, plotted with log2-transformed relative gene expression.

Among the top ranked PCGs, several are well characterized to be crucial for EC responses to PS, e.g., *KLF4* (ranked #8), *ASS1* (ranked #10), *KLF2* (ranked #13), *THBD* (ranked #49), and *eNOS* (ranked #63) (Dekker et al., 2002; Lin et al., 2005; Parmar et al., 2006; Hamik et al., 2007; Fang and Davies, 2012; **Figure 2A**). Pathway enrichment analysis of the top 200 ranked PCGs from PC3 indicated that they are involved in key functions of ECs, including angiogenesis, extracellular matrix organization, and cell adhesion (**Figure 2C**). Among the top-ranked NCGs (**Figure 2B**), MIR503HG (host gene of miR-503, ranked #1) has been shown to be important for cell cycle control and angiogenic function in ECs (Fiedler et al., 2015) and Clorf132 (ranked #2) is the host gene of miR-29b and miR-29c of which DNA methylation has been identified as a marker for prediction of chronological age (Zbieæ-Piekarska et al., 2015; Cho et al., 2017). Noticeably, LINC00520 (aka LEENE), which we previously identified as a PS-induced lncRNA that enhances eNOS expression (Miao et al., 2018), ranked #20. These data suggest that the PCA indeed identified genes known to be important for EC function or have been implicated in aging.

Next, we focused on identifying novel lncRNA regulators in EC biology because there is much less known about lncRNA functions. To further prioritize the lncRNAs candidates, we cross-referenced the shear stress data with those derived from ECs-treated with ATV or TNFα.

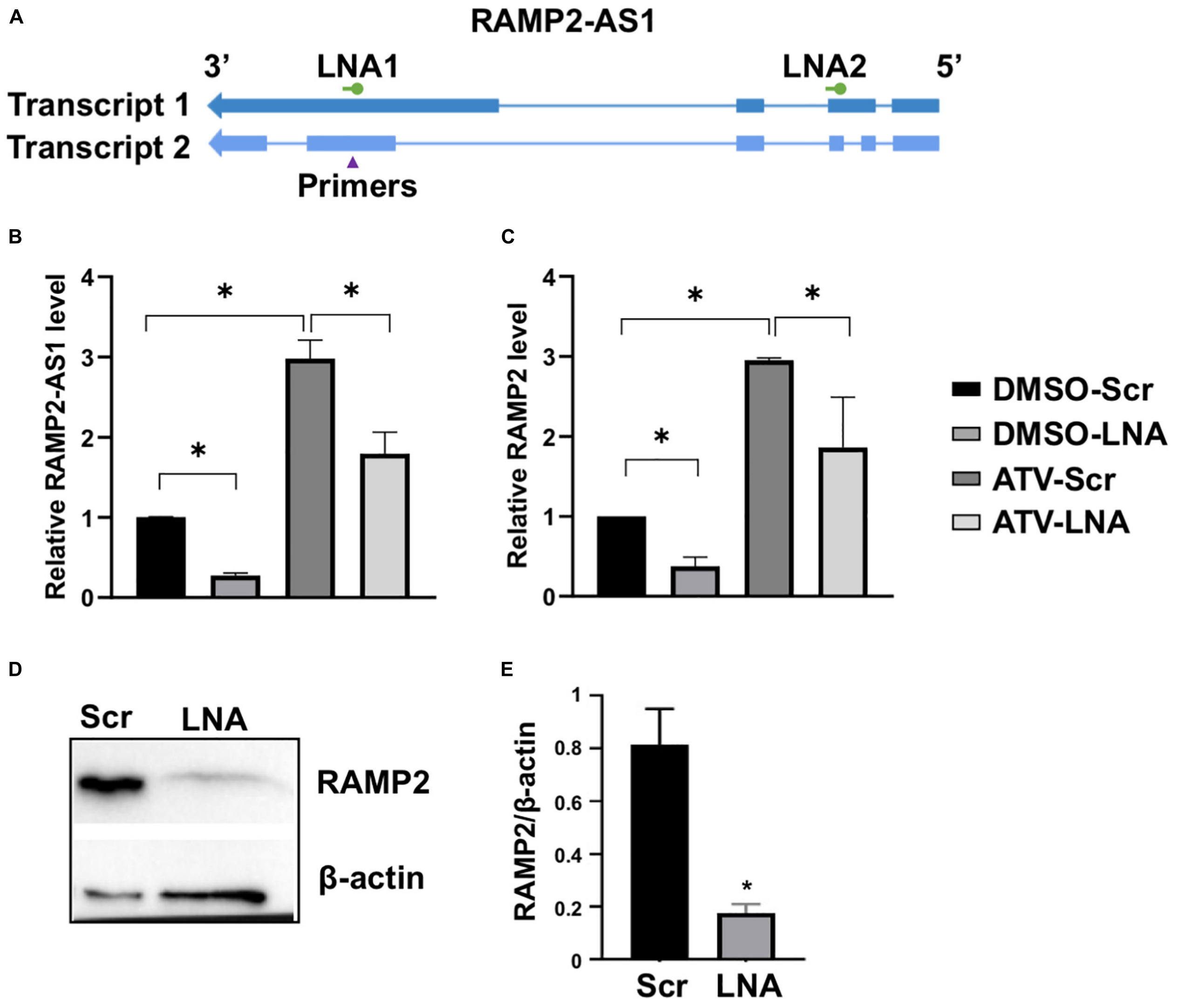

FIGURE 3 | RAMP2-AS1 inhibition suppresses RAMP2 expression. **(A)** Design of LNAs and qPCR primers for RAMP2-AS1 transcripts. **(B,C)** HUVECs were transfected with scramble (Scr) or locked nucleic acid (LNA) GapmeRs against RAMP2-AS1 (LNA1, hereafter labeled "LNA") at 25 nM, before treatment with ATV (5 μM) or DMSO. RAMP2-AS1 and RAMP2 mRNA levels were analyzed by qPCR. **(D,E)** Baseline HUVEC transfected with Scr and LNA were subjected to immunoblotting with specific antibodies as indicated. Representative blots **(D)** and densitometry analysis based on three experiments **(E)**. Data are representative of mean ± SEM from 5 **(B,C)** and 3 **(D,E)** independent experiments with each experiment performed in duplicates. $^*P < 0.05$ based on ANOVA, followed by Tukey's *post hoc* test **(B,C)** and two-tailed *t*-test **(E)**.

Specifically, we screened for the top NCGs from the PCA of shear stress datasets with the following criteria: fold change (FC) showing (1) positive association between PS/OS and ATV/control and (2) negative association between PS/OS and TNFα/control. The top three lncRNAs were the two miRNA host genes MIR503HG and C1orf132, and RAMP2-AS1 (**Supplementary Figure 3**).

Co-expression Pattern of RAMP2-AS1 and RAMP2 in ECs

The *RAMP2-AS1* gene is located on the antisense strand of the *RAMP2* gene (chr 17:40, 894, 172-40, 919, 137), which encodes receptor activity-modifying protein 2 (RAMP2), an adrenomedullin (ADM)-receptor accessory protein. *RAMP2-AS1* is transcribed divergently from *RAMP2,* with its transcription start site immediately upstream to that of *RAMP2* (**Figure 2D**). Interestingly, following the initial PCA, both RAMP2 and RAMP2-AS1 are highly ranked (#19 for RAMP2 in the PCG list and #11 for RAMP2-AS1 in the NCG list). Furthermore, RAMP2 has been demonstrated to be essential for EC function and vascular integrity as EC deletion of RAMP2 led to impaired angiogenic capacity as well as accelerated vascular senescence (Ichikawa-Shindo et al., 2008; Koyama et al., 2013).

Examining data available in Genotype-Tissue Expression (GTEX) project, we found similar tissue-specific gene expression patterns of RAMP2 and RAMP2-AS1 (**Supplementary Figure 4**). Both RAMP2 and RAMP2-AS1 mRNA levels were increased by PS in a time-dependent manner, when compared with OS (**Figure 2E**). Furthermore, based on multiple EC RNA-seq datasets (including shear stress, ATV, and TNFα), the mRNA levels of *RAMP2* and *RAMP2-AS1* showed a strong positive correlation ($R = 0.87$, $P < 0.001$), which was not observed for *RAMP2-AS1* and *EZH1* encoded less than 9 kb downstream of RAMP2-AS1 ($R = 0.36$, $P = 0.302$) (**Figure 2E**). We also used qPCR to confirm the co-regulatory pattern of RAMP2 and RAMP2-AS1 in HUVECs. For initial trial, we designed 4 sets of primers flanking 4 different exons of RAMP2-AS1 transcripts, which produced consistent data (**Supplementary Figures 5A,B**). For the rest of the experiments, we used the primer set that specifically amplifies a fragment in Exon 4 common to both RAMP2-AS1 mature transcripts. Consistent with the RNA-seq data, qPCR confirmed that ATV increased, whereas TNFα substantially decreased RAMP2 and RAMP2-AS1 RNA levels in ECs (**Supplementary Figures 5B–D**). Importantly, in mesenteric arterial endothelium isolated from 44 human donors (see donor characteristics in **Supplementary Figure 6**), RAMP2-AS1 and RAMP2 were also positively correlated ($r = 0.55$,

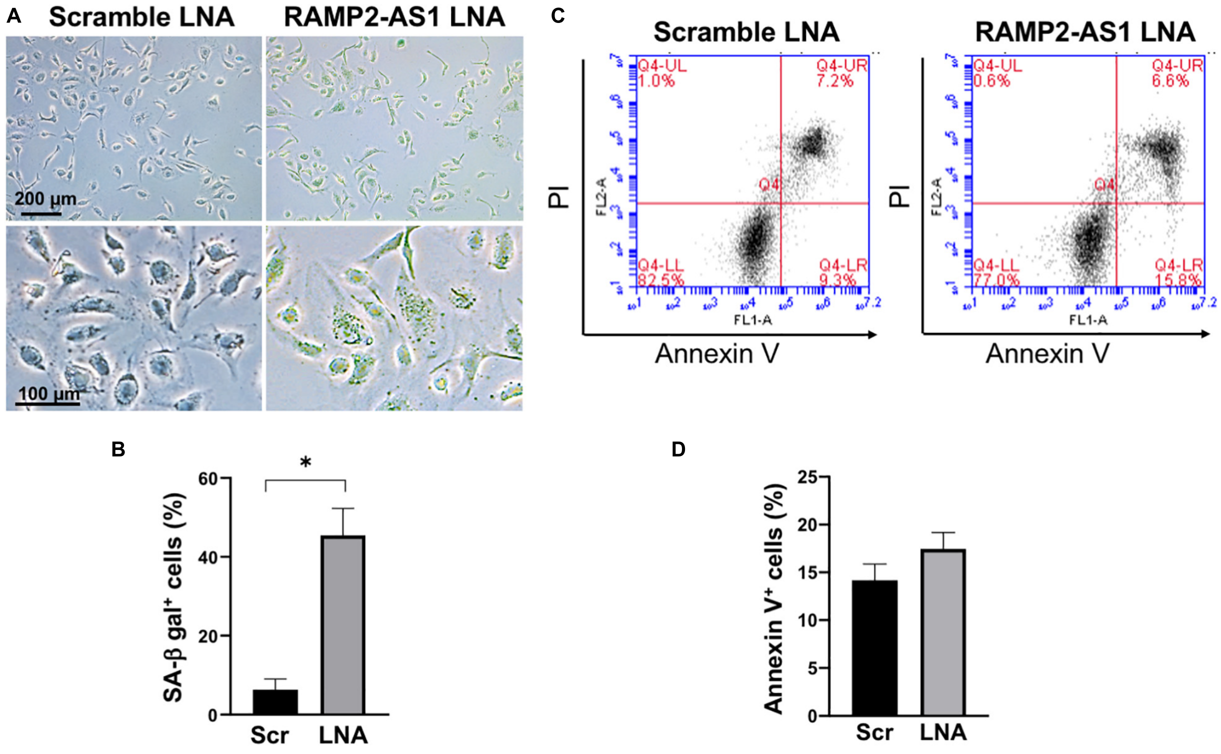

FIGURE 4 | RAMP2-AS1 inhibition promotes cell senescence. HUVECs were transfected with scramble or RAMP2-AS1 LNA GapmeRs and then used for SA-β-gal staining and apoptosis assay. **(A)** Representative images of SA-β-gal staining (green indicates positive staining) of ECs transfected with scramble or RAMP2-AS1 LNA GapmeRs. Scale bars: 200 μm (upper images) and 100 μm (lower images). **(B)** Three randomly selected views were captured from each of the duplicates per condition per experiment and percentage of ECs with SA-β-gal positive staining were calculated. $^*P < 0.05$ based on Student's *t*-test. Data represent mean ± SEM from five independent experiments. **(C,D)** Apoptotic cells were quantified by Annexin V staining using flow cytometry. Representative scatter plots show in **(C)** and quantification of Annexin V^+ cells expressed in percentage (%) in **(D)**. Data represent mean ± SEM based on three independent experiments.

$P < 0.001$, **Figure 2F**). Together, these data underscored a potential regulatory link between RAMP2 and RAMP2-AS1.

RAMP2-AS1 Regulates RAMP2 in ECs

Because lncRNAs can modulate the expression of nearby PCGs (Batista and Chang, 2013; Uchida and Dimmeler, 2015), we tested the possibility that RAMP2-AS1 regulates RAMP2 expression in ECs. To inhibit RAMP2-AS1, we designed two locked nucleic acid (LNA) GapmeRs targeting two specific regions in Exons 2 and 4 of the Transcript 1, which are shared by Transcript 2 (**Figure 3A**). While the Exon 4-targeting LNA (LNA1) significantly reduced the RAMP2-AS1 RNA level, the other LNA (LNA2) did not result in consistent data (**Supplementary Figure 5E**). Therefore, we used LNA1, and hereafter simplified as LNA, to inhibit RAMP2-AS1 in the rest of the experiments. In ECs treated with vehicle control (DMSO) or ATV, LNA inhibition of RAMP2-AS1 led to a significant decrease in RAMP2 mRNA level (**Figures 3B,C**). The suppressive effect of RAMP2-AS1 was more profound and consistent in the DMSO-treated than ATV-treated ECs. Therefore, we focused on examining the effect of RAMP2-AS1 knockdown on RAMP2 and EC functions at baseline condition. In line with the changes at the RNA level, RAMP2-AS1 knockdown also caused a significant suppression in RAMP2 protein level (**Figures 3D,E**). These data suggest that RAMP2-AS1 regulates the expression of RAMP2 in ECs. Interestingly, RAMP-AS1 knockdown did not suppress the ratio of induction by ATV, for either RAMP2-AS1 or RAMP2 (**Supplementary Figures 5F,G**), suggesting the residual RAMP2-AS1 was still able to respond to ATV and RAMP2-AS1 suppression may activate other compensatory pathways contributing to ATV-induced RAMP2.

Knock-Down of RAMP2-AS1 Increases EC Senescence and Decreases Angiogenic Capacity

Next, we investigated the effect of RAMP2-AS1 knockdown on EC functions, specifically cell senescence, apoptosis, and angiogenesis, all of which have been shown to be regulated by RAMP2 and related to vascular aging (Ichikawa-Shindo et al., 2008; Koyama et al., 2013). Senescence-associated β-galactosidase (SA-β-gal) staining, a marker of senescent cells, was increased in ECs with RAMP2-AS1 knockdown, as compared to ECs transfected with scramble control (**Figures 4A,B**). EC apoptosis,

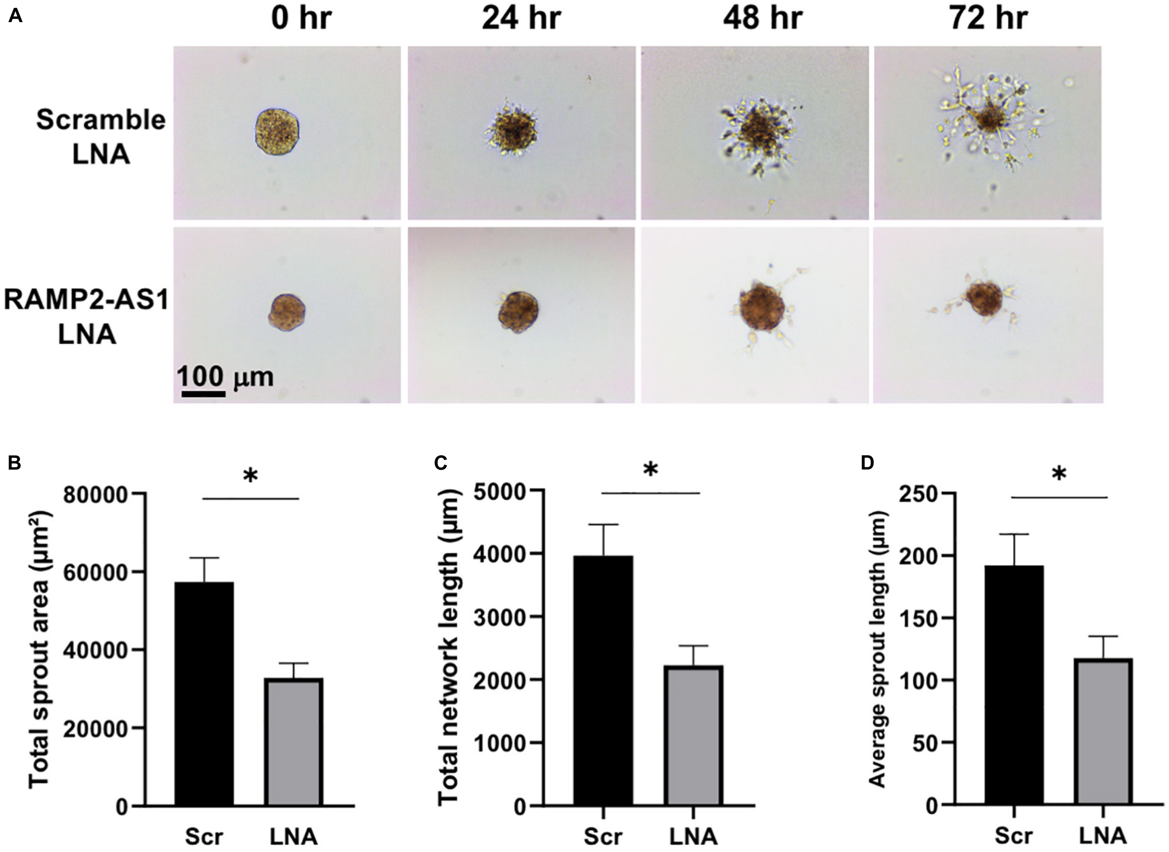

FIGURE 5 | RAMP2-AS1 inhibition impairs EC angiogenic capacity. HUVECs were transfected with scramble or RAMP2-AS1 LNA GapmeRs for 48 h and then used in 3D spheroid sprouting assay. **(A)** Representative images showing the sprouting from the EC aggregates. **(B–D)** Quantitative analysis of EC sprouts after 72 h in hydrogel using three parameters as indicated. Ten aggregates were analyzed per condition in each experiment. *$p < 0.05$ based on Student's *t*-test. Data are represented as mean ± SEM from three independent experiments.

as assayed by Annexin V staining, was not significantly altered but showed a trend toward increase in ECs with RAMP2-AS1 knockdown (**Figures 4C,D**). When these cells were subjected to 3D spheroid sprouting assay, ECs transfected with scramble LNA began to sprout by 24 h and infiltrated into the surrounding hydrogel uniformly to form networks by 48 h. In contrast, ECs transfected with RAMP2-AS1 LNA show almost no sprouting by 24 h, very few stalks of cells extending from the central aggregate by 48 h, and no network formed by 72 h (**Figure 5A**). Quantitative analysis revealed that the total sprout area, total network length, and average sprout length were all significantly lower in the ECs with RAMP2-AS1 knockdown (**Figures 5B–D**). Taken together, these data support that RAMP2-AS1 is essential for EC homeostasis and the mechanisms involve the suppression of senescence and promotion of angiogenesis.

Gene Network Regulated by RAMP2-AS1 in ECs

To gain additional information for RAMP2-AS1-regulated transcriptome, we performed RNA-seq in ECs transfected with scramble control or LNA inhibiting RAMP2-AS1. RNA-seq analysis identified 252 differential expressed genes (DEGs) with $P < 0.05$ and 585 DEGs with $P < 0.1$ in ECs with RAMP2-AS1 knockdown vs. scramble control, without a fold change cutoff (**Figure 6A**). To obtain an overview of cellular pathways affected by RAMP2-AS1 inhibition, we used the 585 DEGs with $P < 0.1$ for the subsequent pathway enrichment analysis. These included 232 upregulated and 353 downregulated genes. GO-based pathway enrichment analysis of these DEGs revealed their involvement in angiogenesis, inflammatory response, apoptosis, unfolded protein response, extracellular matrix (ECM) organization, and amino acid transportation (**Figure 6B**). In line with the impaired sprouting capacity (**Figure 5**), the inhibition of RAMP2-AS1 led to an overall downregulation of pro-angiogenic genes, including *VEGFA*, *PDGFA*, *FGF*, and *ADM2* (**Figure 6C**), supporting the effect observed with spheroid sprouting assay (**Figure 5**). In contrast, several genes encoding pro-inflammatory and coagulatory cytokines, e.g., *VWF*, *CXCL11*, *CCL14*, and *MIF*, were upregulated under RAMP2-AS1 knockdown, although some others are downregulated in the same condition. This

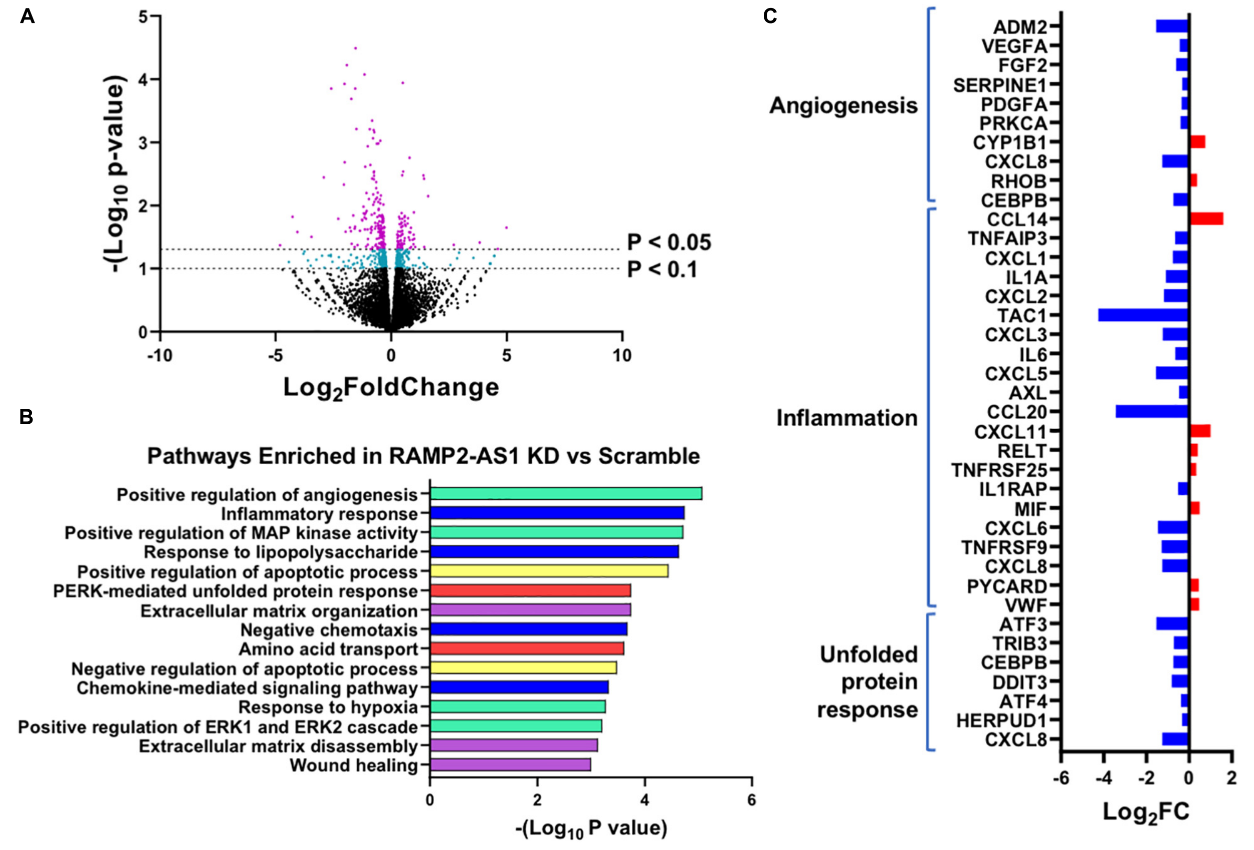

FIGURE 6 | RNA-seq profiling of transcriptome change caused by RAMP2-AS1 knockdown. HUVECs were transfected with RAMP2-AS1 LNA or scramble control in biological replicates. **(A)** Number of genes showing DE in RNA-seq with indicated *P*-value cutoffs. Genes showing DE with $P < 0.1$ are in cyan and those with $P < 0.05$ are in purple. **(B)** Top 15 enriched pathways ranked by -log$_{10}$ (*p*-value). Pathways belonging to the same family are grouped into similar colors; angiogenesis in cyan, inflammatory response in blue, unfolded protein response pathways in red, apoptosis in yellow, and ECM remodeling in purple. **(C)** Log2 FC (RAMP2-AS1 LNA vs. scramble control) of select genes involved in angiogenesis, inflammation, or unfolded protein response in RAMP2-AS1 knockdown vs. scramble control.

lack of a clear direction in inflammation was in line with the insignificant effect of RAMP2-AS1 LNA in monocyte adhesion to ECs (data not shown). Interestingly, RAMP2-AS1 knockdown also caused a list of genes involved in unfolded protein response (UPR) to be downregulated (**Figure 6C**), which provides possible explanation to the increased EC senescence (**Figure 4**). Other genes differentially expressed due to RAMP2-AS1 inhibition are listed in **Supplementary Table 2**. Collectively, inhibition of RAMP2-AS1 affect multiple pathways essential for EC homeostasis.

DISCUSSION AND CONCLUSION

In the current study, we employed PCA to identify crucial genes for divergent EC transcriptional states under PS vs. OS over time. Admittedly, EC aging encompasses many aspects of molecular and cellular changes, mediated through multiple levels of regulation other than transcriptional regulation. For example, DNA methylation has been used to calculate and predict epigenetic aging in several tissues and organs (Horvath and Raj, 2018). Furthermore, the relevance of using *in vitro* EC culture subjected to flow for up to 24 h to model the *in vivo* vascular aging that occurs in decades is another limitation. Nonetheless, the EC aging trajectories we have identified herein are an attempt to quantify EC transcriptional state over time in an unbiased manner by considering the genome-wide transcriptome changes, rather than a select set of genes.

PCA maximally preserves information and allows deconvolution of transcriptional profiles into interpretable components associated with the divergence in cells under various conditions. In particular, using PC3 of PCGs and PC2 of NCGs, we observed divergent trajectories of ECs under the PS vs. OS conditions. The divergence was supported by RNA-seq data from ATV and TNFα-treated EC, which, respectively, mapped close to PS and OS on PC3. Many of the genes identified from the PC3 of PCGs are well characterized as flow-responsive and essential for EC homeostasis, e.g., KLF2 and KLF4, the key transcription factors in ECs, and eNOS, the hallmark for EC homeostasis. Furthermore, many genes that have not been previously identified to be important regulators in flow-modulated EC function were also revealed by PC3, e.g., RAMP2. We also used mutual information-based statistics to analyze genes that may explain the flow-modulated distinct EC transcriptome profiles (**Supplementary Table 3**). Notably, many highly ranked genes derived from PCA, such as KLF2 and KLF4, are also highly ranked by mutual information (KLF ranked #1 and KLF2 ranked #12). Therefore, the PCA-identified PCGs and NCGs whose differential expressions under PS vs. OS contribute to the divergent aging trajectories are likely novel and important molecules regulating EC function.

Following a series of integrative bioinformatics analyses, we identified RAMP2-AS1 as a candidate novel lncRNA for further investigation. This is based on its top ranking in the degree of DE in ECs under various stimuli, as well as its highly correlated expression pattern with a key EC-regulator RAMP2 in cultured ECs and in human donor-derived arterial ECs. With respect to EC function, RAMP2-AS1 inhibition resulted in increased EC senescence and suppressed angiogenic sprouting function. At the molecular level, RAMP2-AS1 inhibition caused profound changes in a number of pathways, including angiogenesis, innate immune, and pro-inflammation activation, ECM organization, cell apoptosis, UPR, and amino acid transport. Of note, *ADM2* is also greatly downregulated by RAMP2-AS1 knockdown, suggesting that RAMP2-AS1 regulates ADM-RAMP2 signaling and EC homeostasis. On the other hand, we did not observe a significant effect in apoptosis and monocyte adhesion by RAMP2-AS1 knockdown. This is likely due to the baseline and static condition used in the present work. Future study is warranted to elucidate the role of RAMP2-AS1 in EC function in response to specific stimuli, such as different flow patterns and TNFα.

Given the genomic proximity of RAMP2-AS1 and RAMP2, and the nuclear localization of RAMP2-AS1 determined by the recently developed APEX-seq (Fazal et al., 2019), it is plausible that RAMP2-AS1 RNA acts *in cis* as a transcriptional activator for RAMP2, which is reminiscent of other lncRNAs (Kopp and Mendell, 2018). In support of this hypothesis, RAMP2-AS1 and RAMP2 are regulated in a highly correlational pattern. Moreover, RAMP2-AS1 knockdown strongly suppressed RAMP2 both at mRNA and protein levels. Importantly, EC functions previously identified to be regulated by RAMP2, e.g., angiogenesis and senescence (Ichikawa-Shindo et al., 2008; Koyama et al., 2013), were affected in a similar fashion by the RAMP2-AS1 knockdown. However, it is also possible that RAMP2-AS1 can function *in trans* to affect the transcription of other genes, as demonstrated for other nuclear-localized lncRNAs in ECs (Miao et al., 2018; Calandrelli et al., 2020). The molecular mechanisms involving RAMP2-AS1 with expanded scope of EC biology are of interest for future studies.

In conclusion, herein we exploited PCA to dissect the temporal and transcriptomic changes underlying the distinct effects elicited by physiological *vs.* pathophysiological flow in ECs. Integrative analysis of the divergent aging trajectories of ECs subject to PS *vs.* OS, TNFα, and ATV revealed RAMP2 and RAMP2-AS1 as novel regulators in EC aging and function. Suppression of RAMP2-AS1 leads to decreased RAMP2 expression, impaired EC sprouting, and increased EC senescence. Our study presents a novel systems biology approach to identify potential regulators in EC aging, as exemplified by RAMP2-AS1.

DATA AVAILABILITY STATEMENT

The datasets presented in this study can be found in online repositories. The names of the repository/repositories and accession number(s) can be found below: https://www.ncbi.nlm.nih.gov/geo/, Accession IDs: GSE103672, GSE136912, and GSE163433.

ETHICS STATEMENT

The research consents for the use of postmortem human tissues were obtained from the donors' next of kin and ethical approval for this study was granted by the Institutional Review Board of City of Hope (IRB #01046).

AUTHOR CONTRIBUTIONS

C-HL, RR, and ZC conceived the research. C-HL, AC, AB, RR, KS, YL, XT, SB, S-LC, and DO'M designed and performed experiments and analyzed the data. ZC, RR, and P-HH supervised experiments and interpreted results. C-HL, AC, AB, KS, RR, and ZC wrote the manuscript. SC and JS revised the manuscript. ZC and RR obtained funding for this study. All authors contributed to the article and approved the submitted version.

FUNDING

This study was in part funded by grants from the National Institutes of Health (NIH) (R01 HL145170 to ZC, R01 HL106570 and HL108735 to SC and JS, and U01CA250046 to RR), Ella Fitzgerald Foundation (to ZC), City of Hope Center for Cancer and Aging (to ZC and RR) at City of Hope. Research reported in this publication included work performed in the Integrative Genomics Core at City of Hope supported by the National Cancer Institute of the National Institutes of Health under award number P30CA033572.

SUPPLEMENTARY MATERIAL

The Supplementary Material for this article can be found online at: https://www.frontiersin.org/articles/10.3389/fcell.2021.635307/full#supplementary-material

REFERENCES

Ajami, N. E., Gupta, S., Maurya, M. R., Nguyen, P., Li, J. Y., Shyy, J. Y., et al. (2017). Systems biology analysis of longitudinal functional response of endothelial cells to shear stress. *Proc. Natl. Acad. Sci. U S A.* 114, 10990–10995. doi: 10.1073/pnas.1707517114

Ashburner, M., Ball, C. A., Blake, J. A., Botstein, D., Butler, H., Cherry, J. M., et al. (2000). Gene ontology: tool for the unification of biology. The Gene Ontology Consortium. *Nat. Genet.* 25, 25–29. doi: 10.1038/75556

Batista, P. J., and Chang, H. Y. (2013). Long noncoding RNAs: cellular address codes in development and disease. *Cell* 152, 1298–1307. doi: 10.1016/j.cell.2013.02.012

Brandes, R. P., Fleming, I., and Busse, R. (2005). Endothelial aging. *Cardiovasc. Res.* 66, 286–294. doi: 10.1016/j.cardiores.2004.12.027

Calandrelli, R., Xu, L., Luo, Y., Wu, W., Fan, X., Nguyen, T., et al. (2020). Stress-induced RNA–chromatin interactions promote endothelial dysfunction. *Nat. Commun.* 11:5211. doi: 10.1038/s41467-020-18957-w

Chen, Z., Peng, I. C., Cui, X., Li, Y. S., Chien, S., and Shyy, J. Y. (2010). Shear stress. SIRT1, and vascular homeostasis. *Proc. Natl. Acad. Sci. U S A.* 107, 10268–10273. doi: 10.1073/pnas.1003833107

Chen, Z., Peng, I.-C., Sun, W., Su, M.-I., Hsu, P.-H., Fu, Y., et al. (2009). AMP-Activated protein kinase functionally phosphorylates endothelial nitric oxide synthase Ser633. *Circul. Res.* 104, 496–505. doi: 10.1161/CIRCRESAHA.108.187567

Chiu, J. J., and Chien, S. (2011). Effects of disturbed flow on vascular endothelium: pathophysiological basis and clinical perspectives. *Physiol. Rev.* 91, 327–387. doi: 10.1152/physrev.00047.2009

Cho, S., Jung, S. E., Hong, S. R., Lee, E. H., Lee, J. H., Lee, S. D., et al. (2017). Independent validation of DNA-based approaches for age prediction in blood. *Forensic Sci. Int. Genet.* 29, 250–256. doi: 10.1016/j.fsigen.2017.04.020

Dekker, R. J., van Soest, S., Fontijn, R. D., Salamanca, S., de Groot, P. G., VanBavel, E., et al. (2002). Prolonged fluid shear stress induces a distinct set of endothelial cell genes, most specifically lung Krüppel-like factor (KLF2). *Blood* 100, 1689–1698. doi: 10.1182/blood-2002-01-0046

Dobin, A., Davis, C. A., Schlesinger, F., Drenkow, J., Zaleski, C., Jha, S., et al. (2013). STAR: ultrafast universal RNA-seq aligner. *Bioinformatics* 29, 15–21. doi: 10.1093/bioinformatics/bts635

Donato, A. J., Morgan, R. G., Walker, A. E., and Lesniewski, L. A. (2015). Cellular and molecular biology of aging endothelial cells. *J. Mol. Cell Cardiol.* 89(Pt B), 122–135. doi: 10.1016/j.yjmcc.2015.01.021

Eglinger, J., Karsjens, H., and Lammert, E. (2017). Quantitative assessment of angiogenesis and pericyte coverage in human cell-derived vascular sprouts. *Inflamm. Regenerat.* 37:2. doi: 10.1186/s41232-016-0033-32

Fang, Y., and Davies, P. F. (2012). Site-specific microRNA-92a regulation of Kruppel-like factors 4 and 2 in atherosusceptible endothelium. *Arterioscler. Thromb. Vasc. Biol.* 32, 979–987. doi: 10.1161/atvbaha.111.244053

Fazal, F. M., Han, S., Parker, K. R., Kaewsapsak, P., Xu, J., Boettiger, A. N., et al. (2019). Atlas of subcellular RNA localization revealed by APEX-Seq. *Cell* 178, 473–490.e26. doi: 10.1016/j.cell.2019.05.027

Fiedler, J., Breckwoldt, K., Remmele, C. W., Hartmann, D., Dittrich, M., Pfanne, A., et al. (2015). Development of long noncoding RNA-Based strategies to modulate tissue vascularization. *J. Am. College Cardiol.* 66, 2005–2015. doi: 10.1016/j.jacc.2015.07.081

Fisher, A. B., Chien, S., Barakat, A. I., and Nerem, R. M. (2001). Endothelial cellular response to altered shear stress. *Am. J. Physiol. Lung. Cell Mol. Physiol.* 281, L529–L533. doi: 10.1152/ajplung.2001.281.3.L529

Gao, W., Kannan, S., Oh, S., and Viswanath, P. (2017). "Estimating mutual information for discrete-continuous mixtures," in *Proceedings of the 31st International Conference on Neural Information Processing Systems*, (Long Beach, CA: Curran Associates Inc.).

Gimbrone, M. A. Jr., and Garcia-Cardena, G. (2016). Endothelial cell dysfunction and the pathobiology of atherosclerosis. *Circ. Res.* 118, 620–636. doi: 10.1161/CIRCRESAHA.115.306301

Hamik, A., Lin, Z., Kumar, A., Balcells, M., Sinha, S., Katz, J., et al. (2007). Kruppel-like factor 4 regulates endothelial inflammation. *J. Biol. Chem.* 282, 13769–13779. doi: 10.1074/jbc.M700078200

Harrison, D., Griendling, K. K., Landmesser, U., Hornig, B., and Drexler, H. (2003). Role of oxidative stress in atherosclerosis. *Am. J. Cardiol.* 91, 7A–11A. doi: 10.1016/s0002-9149(02)03144-3142

He, M., Chen, Z., Martin, M., Zhang, J., Sangwung, P., Woo, B., et al. (2017). miR-483 targeting of CTGF suppresses endothelial-to-mesenchymal transition. *Circul. Res.* 120, 354–365. doi: 10.1161/CIRCRESAHA.116.310233

He, M., Huang, T.-S., Li, S., Hong, H.-C., Chen, Z., Martin, M., et al. (2019). Atheroprotective flow upregulates ITPR3 (Inositol 1,4,5-Trisphosphate Receptor 3) in vascular endothelium via KLF4 (Krüppel-Like Factor 4)-mediated histone modifications. *Arteriosclerosis Thrombosis Vascular Biol.* 39, 902–914. doi: 10.1161/ATVBAHA.118.312301

Heiss, M., Hellström, M., Kalén, M., May, T., Weber, H., Hecker, M., et al. (2015). Endothelial cell spheroids as a versatile tool to study angiogenesis in vitro. *FASEB J.* 29, 3076–3084. doi: 10.1096/fj.14-267633

Horvath, S., and Raj, K. (2018). DNA methylation-based biomarkers and the epigenetic clock theory of ageing. *Nat. Rev. Genet.* 19, 371–384. doi: 10.1038/s41576-018-0004-3

Huang, T. S., Wang, K. C., Quon, S., Nguyen, P., Chang, T. Y., Chen, Z., et al. (2017). LINC00341 exerts an anti-inflammatory effect on endothelial cells by repressing VCAM1. *Physiol. Genom.* 49, 339–345. doi: 10.1152/physiolgenomics.00132.2016

Ichikawa-Shindo, Y., Sakurai, T., Kamiyoshi, A., Kawate, H., Iinuma, N., Yoshizawa, T., et al. (2008). The GPCR modulator protein RAMP2 is essential for angiogenesis and vascular integrity. *J. Clin. Invest.* 118, 29–39. doi: 10.1172/JCI33022

Kopp, F., and Mendell, J. T. (2018). Functional classification and experimental dissection of long noncoding RNAs. *Cell* 172, 393–407. doi: 10.1016/j.cell.2018.01.011

Koyama, T., Ochoa-Callejero, L., Sakurai, T., Kamiyoshi, A., Ichikawa-Shindo, Y., Iinuma, N., et al. (2013). Vascular endothelial adrenomedullin-RAMP2 system is essential for vascular integrity and organ homeostasis. *Circulation* 127, 842–853. doi: 10.1161/CIRCULATIONAHA.112.000756

Liao, Y., Smyth, G. K., and Shi, W. (2013). Featurecounts: an efficient general purpose program for assigning sequence reads to genomic features. *Bioinformatics* 30, 923–930. doi: 10.1093/bioinformatics/btt656

Lin, Z., Kumar, A., SenBanerjee, S., Staniszewski, K., Parmar, K., Vaughan, D. E., et al. (2005). Kruppel-like factor 2 (KLF2) regulates endothelial thrombotic function. *Circ. Res.* 96, e48–e57. doi: 10.1161/01.RES.0000159707.05637.a1

Love, M. I., Huber, W., and Anders, S. (2014). Moderated estimation of fold change and dispersion for RNA-seq data with DESeq2. *Genome Biol.* 15:550. doi: 10.1186/s13059-014-0550-558

Malek, A. M., Alper, S. L., and Izumo, S. (1999). Hemodynamic shear stress and its role in atherosclerosis. *JAMA* 282, 2035–2042. doi: 10.1001/jama.282.21.2035

Miao, Y., Ajami, N. E., Huang, T. S., Lin, F. M., Lou, C. H., Wang, Y. T., et al. (2018). Enhancer-associated long non-coding RNA LEENE regulates endothelial nitric oxide synthase and endothelial function. *Nat. Commun.* 9:292. doi: 10.1038/s41467-017-02113-y

Nam, D., Ni, C. W., Rezvan, A., Suo, J., Budzyn, K., Llanos, A., et al. (2009). Partial carotid ligation is a model of acutely induced disturbed flow, leading to rapid endothelial dysfunction and atherosclerosis. *Am. J. Physiol. Heart Circ. Physiol.* 297, H1535–H1543. doi: 10.1152/ajpheart.00510.2009

Parmar, K. M., Larman, H. B., Dai, G., Zhang, Y., Wang, E. T., Moorthy, S. N., et al. (2006). Integration of flow-dependent endothelial phenotypes by Kruppel-like factor 2. *J. Clin. Invest.* 116, 49–58. doi: 10.1172/jci24787

Rockne, R. C., Branciamore, S., Qi, J., Frankhouser, D. E., O'Meally, D., Hua, W. K., et al. (2020). State-Transition analysis of time-sequential gene expression identifies critical points that predict development of acute myeloid leukemia. *Cancer Res.* 80, 3157–3169. doi: 10.1158/0008-5472.Can-20-0354

Sun, W., Lee, T.-S., Zhu, M., Gu, C., Wang, Y., Zhu, Y., et al. (2006). Statins activate AMP-Activated protein kinase in vitro and in vivo. *Circulation* 114, 2655–2662. doi: 10.1161/CIRCULATIONAHA.106.630194

Tang, X., Miao, Y., Luo, Y., Sriram, K., Qi, Z., Lin, F.-M., et al. (2020). Suppression of endothelial AGO1 promotes adipose tissue browning and improves metabolic dysfunction. *Circulation* 142, 365–379. doi: 10.1161/CIRCULATIONAHA.119.041231

Tseng, A. H., Wu, L. H., Shieh, S. S., and Wang, D. L. (2014). SIRT3 interactions with FOXO3 acetylation, phosphorylation and ubiquitinylation mediate endothelial cell responses to hypoxia. *Biochem. J.* 464, 157–168. doi: 10.1042/bj20140213

Uchida, S., and Dimmeler, S. (2015). Long noncoding RNAs in cardiovascular diseases. *Circ. Res.* 116, 737–750. doi: 10.1161/circresaha.116.302521

Ungvari, Z., Tarantini, S., Kiss, T., Wren, J. D., Giles, C. B., Griffin, C. T., et al. (2018). Endothelial dysfunction and angiogenesis impairment in the ageing vasculature. *Nat. Rev. Cardiol.* 15, 555–565. doi: 10.1038/s41569-018-0030-z

Wang, J. C., and Bennett, M. (2012). Aging and atherosclerosis: mechanisms, functional consequences, and potential therapeutics for cellular senescence. *Circ. Res.* 111, 245–259. doi: 10.1161/CIRCRESAHA.111.261388

Wu, L. H., Chang, H. C., Ting, P. C., and Wang, D. L. (2018). Laminar shear stress promotes mitochondrial homeostasis in endothelial cells. *J. Cell Physiol.* 233, 5058–5069. doi: 10.1002/jcp.26375

Zbieæ-Piekarska, R., Spólnicka, M., Kupiec, T., Parys-Proszek, A., Makowska, Ż, Pałeczka, A., et al. (2015). Development of a forensically useful age prediction method based on DNA methylation analysis. *Forensic Sci. Int. Genet.* 17, 173–179. doi: 10.1016/j.fsigen.2015.05.001

Zhang, H., Park, Y., Wu, J., Chen, X., Lee, S., Yang, J., et al. (2009). Role of TNF-alpha in vascular dysfunction. *Clin. Sci. (Lond)* 116, 219–230. doi: 10.1042/cs20080196

Conflict of Interest: The authors declare that the research was conducted in the absence of any commercial or financial relationships that could be construed as a potential conflict of interest.

frontiers
in Cell and Developmental Biology

ORIGINAL RESEARCH
published: 15 February 2021
doi: 10.3389/fcell.2021.639509

Cardiac Gq Receptors and Calcineurin Activation Are Not Required for the Hypertrophic Response to Mechanical Left Ventricular Pressure Overload

Ze-Yan Yu[1,2,3†], *Hutao Gong*[1†], *Jianxin Wu*[1], *Yun Dai*[1], *Scott H. Kesteven*[1], *Diane Fatkin*[1,2,3], *Boris Martinac*[1,3], *Robert M. Graham*[1,2,3] and *Michael P. Feneley*[1,2,3*]

[1] Victor Chang Cardiac Research Institute, Darlinghurst, NSW, Australia, [2] Cardiology Department, St Vincent's Hospital, Darlinghurst, NSW, Australia, [3] Faculty of Medicine, University of New South Wales, Sydney, NSW, Australia

Edited by:
Jing Zhou,
Peking University, China

Reviewed by:
Ekhtear Hossain,
Southern University and A&M College,
United States
Han Xiao,
Peking University Third Hospital,
China

***Correspondence:**
Michael P. Feneley
michael.feneley@svha.org.au

†These authors have contributed equally to this work

Specialty section:
This article was submitted to
Cell Adhesion and Migration,
a section of the journal
Frontiers in Cell and Developmental
Biology

Received: 09 December 2020
Accepted: 26 January 2021
Published: 15 February 2021

Citation:
Yu Z-Y, Gong H, Wu J, Dai Y,
Kesteven SH, Fatkin D, Martinac B,
Graham RM and Feneley MP (2021)
Cardiac Gq Receptors
and Calcineurin Activation Are Not
Required for the Hypertrophic
Response to Mechanical Left
Ventricular Pressure Overload.
Front. Cell Dev. Biol. 9:639509.
doi: 10.3389/fcell.2021.639509

Rationale: Gq-coupled receptors are thought to play a critical role in the induction of left ventricular hypertrophy (LVH) secondary to pressure overload, although mechanosensitive channel activation by a variety of mechanisms has also been proposed, and the relative importance of calcineurin- and calmodulin kinase II (CaMKII)-dependent hypertrophic pathways remains controversial.

Objective: To determine the mechanisms regulating the induction of LVH in response to mechanical pressure overload.

Methods and Results: Transgenic mice with cardiac-targeted inhibition of Gq-coupled receptors (GqI mice) and their non-transgenic littermates (NTL) were subjected to neurohumoral stimulation (continuous, subcutaneous angiotensin II (AngII) infusion for 14 days) or mechanical pressure overload (transverse aortic arch constriction (TAC) for 21 days) to induce LVH. Candidate signaling pathway activation was examined. As expected, LVH observed in NTL mice with AngII infusion was attenuated in heterozygous ($GqI^{+/-}$) mice and absent in homozygous ($GqI^{-/-}$) mice. In contrast, LVH due to TAC was unaltered by either heterozygous or homozygous Gq inhibition. Gene expression of atrial natriuretic peptide (ANP), B-type natriuretic peptide (BNP) and α-skeletal actin (α-SA) was increased 48 h after AngII infusion or TAC in NTL mice; in GqI mice, the increases in ANP, BNP and α-SA in response to AngII were completely absent, as expected, but all three increased after TAC. Increased nuclear translocation of nuclear factor of activated T-cells c4 (NFATc4), indicating calcineurin pathway activation, occurred in NTL mice with AngII infusion but not TAC, and was prevented in GqI mice infused with AngII. Nuclear and cytoplasmic CaMKIIδ levels increased in both NTL and GqI mice after TAC but not AngII infusion, with increased cytoplasmic phospho- and total histone deacetylase 4 (HDAC4) and increased nuclear myocyte enhancer factor 2 (MEF2) levels.

Conclusion: Cardiac Gq receptors and calcineurin activation are required for neurohumorally mediated LVH but not for LVH induced by mechanical pressure overload (TAC). Rather, TAC-induced LVH is associated with activation of the CaMKII-HDAC4-MEF2 pathway.

Keywords: pressure overload induced hypertrophy, Gq receptors, calcineurin, CaMKIIδ, neurohumoral stimulation

INTRODUCTION

Pathological left ventricular hypertrophy (LVH) is the single strongest predictor of cardiovascular mortality and heart failure (Levy et al., 1990; Mudd and Kass, 2008), stimulating extensive research efforts to identify the molecular signaling pathways responsible for its induction as potential therapeutic targets (Mudd and Kass, 2008; Tamargo and Lopez-Sendon, 2011). Gq-coupled receptors are thought to play a central role in the induction of pathological LVH in response to agonists, such as angiotensin II (AngII), catecholamines and endothelin-1, or increased mechanical stress associated with hypertension, aortic stenosis and pathological ventricular remodeling after myocardial injury (D'Angelo et al., 1997; Adams et al., 1998; Akhter et al., 1998; Paradis et al., 2000; Frey and Olson, 2003).

At the sub-receptor level, an increase in intracellular calcium and activation of calcium-calmodulin dependent pathways has been thought to be necessary for the induction of pathological LVH (Bers, 2008; Zarain-Herzberg et al., 2011). Activation of the calcium-calmodulin dependent phosphatase, calcineurin, dephosphorylates the transcriptional regulator, nuclear factor of activated T cells (NFAT), resulting in its translocation to the nucleus to initiate hypertrophic gene transcription in pathological but not physiological hypertrophy (Molkentin et al., 1998; Molkentin, 2000, 2013; Wilkins and Molkentin, 2004; Wilkins et al., 2004; Kehat and Molkentin, 2010). Activation of calcium-calmodulin dependent kinase II (CaMKII) phosphorylates histone deacetylase 4 (HDAC4), promoting its nuclear export and relieving its inhibition of the critical nuclear transcriptional regulator, myocyte enhancer factor 2 (MEF2), thus enhancing hypertrophic gene transcription (Passier et al., 2000; Backs et al., 2006, 2009). Both the calcineurin-NFAT and the CaMKII-HDAC-MEF2 pathways have been claimed to be both sufficient and *necessary* for the induction of pathological LVH, although not without considerable controversy (Ding et al., 1999; Zhang et al., 1999, 2003, 2005, 2007; Molkentin, 2000, 2013; Zou et al., 2001; Frey and Olson, 2003; Ling et al., 2009). The question of the relative importance of calcineurin and CaMKII activation in pathological hypertrophy remains under active investigation (Kreusser et al., 2014; Lehmann et al., 2018).

Transient receptor potential canonical (TRPC) channels have been identified as a likely mechanism by which calcium enters through the myocyte cell membrane to trigger calcium-dependent activation of LVH signaling pathways (Watanabe et al., 2009; Wu et al., 2010; Eder and Molkentin, 2011). While activation of Gq-coupled receptors by agonists or mechanical membrane deformation is thought to cause receptor-operated TRPC channel activation by generating diacylglycerol (DAG), and also increased TRPC expression, some TRPC channels have been reported to be activated by membrane stretch (Bush et al., 2006; Kuwahara et al., 2006; Onohara et al., 2006; Spassova et al., 2006; Ohba et al., 2007; Seth et al., 2009; Koitabashi et al., 2010; Eder and Molkentin, 2011), but this remains controversial (Nikolaev et al., 2019). TRPCs might also promote calcium entry by functional interaction with other calcium entry mechanisms, including the sodium-calcium exchanger, Orai or L-type calcium channels (Eder and Molkentin, 2011). Alternatively, L-type calcium channels have been strongly implicated as a source of the triggering calcium by a different, protein-binding mechanism that anchors calcineurin to create a microdomain with L-type calcium channels at the sarcolemma (Heineke et al., 2010). Ca(v)3.2 T-type calcium channels (T-channels) have also been claimed to be required for pressure overload-induced cardiac hypertrophy in mice (Chiang et al., 2009). Syndecan-4, a transmembrane proteoglycan that connects extracellular matrix proteins to the cardiomyocyte cytoskeleton, has been reported to be necessary to directly mediate calcineurin activation in response to mechanical deformation and pressure overload (Finsen et al., 2011).

Thus, it is now apparent that there are a variety of mechanisms whereby pathological LVH could be triggered that do not necessarily depend on activation of cardiac Gq-coupled receptors. These mechanisms may be more important when mechanical loading is the predominant stimulus to LVH rather than neurohumoral activation. It is timely, therefore, to revisit the role of Gq-coupled receptors in the induction of LVH in response to left ventricular pressure overload. We show here that in mice with cardiac-targeted transgenic inhibition of Gq (Akhter et al., 1998), LVH in response to continuous AngII infusion was markedly inhibited in heterozygous mice and completely abolished in homozygous mice, as expected. In contrast, heterozygous or homozygous inhibition of Gq had *no effect* on LVH induced by LV pressure overload caused by transverse aortic arch constriction (TAC), the most

---

Abbreviations: α-SA, α-skeletal actin; AngII, angiotensin II; ANP, atrial natriuretic peptide; BNP, B-type natriuretic peptide; CaMKII, calmodulin kinase II; HDAC4, histone deacetylase 4; LVH, left ventricular hypertrophy; LVW/BW, left ventricular weight normalized to body weight; LVW/TL, left ventricular weight normalized to tibia length; MEF2, myocyte enhancer factor 2; NFAT, nuclear factor of activated T-cells; TAC, transverse aortic arch constriction.

commonly employed experimental model of pressure overload LVH (Rockman et al., 1994; Frey and Olson, 2003; Molkentin, 2013). Moreover, while AngII infusion caused activation of the calcineurin-NFAT pathway, as expected, it did not activate the CaMKII-HDAC4-MEF2 pathway. Conversely, TAC activated the CaMKII-HDAC4-MEF2 pathway but did not activate the calcineurin-NFAT pathway.

These findings have significant implications for the mechanistic understanding of LVH secondary to pressure overload but may also have important clinical and therapeutic implications for the optimal management of hypertensive heart disease.

MATERIALS AND METHODS

Generation of Transgenic Mice

Transgenic mice with endogenous, cardiac-restricted inhibition of Gq receptors (GqI mice; kindly provided by Dr. W. Koch), described previously in the heterozygous state (GqI$^{+/-}$) (Akhter et al., 1998), were employed. To ensure robust endogenous inhibition of cardiac Gq receptors, homozygous (GqI$^{-/-}$) mice were also bred. Male GqI$^{-/-}$, GqI$^{+/-}$ and non-transgenic littermate (NTL) mice aged 12 weeks were used. All experimental procedures were approved by the Garvan/St Vincent's Hospital Animal Ethics Committee, in accordance with the guidelines of the Australian Code of Practice for the Care and Use of Animals for Scientific Purposes. All animals were entered into the study in a randomized order.

Induction of Left Ventricular Hypertrophy

Transgenic and NTL mice were subjected to either continuous subcutaneous infusion of the Gq-coupled receptor agonist AngII or transverse aortic arch constriction (TAC) to induce pressure overload.

For AngII or saline infusion, mice were anaesthetized with 1.5–2% isoflurane, and a small incision was made in the skin between the scapulae. An osmotic mini-pump (Alzet) was inserted subcutaneously, and the incision closed. Angiotensin II (1.5 mg/kg/day, Sigma, Australia) was dissolved in 0.9% NaCI and delivered continuously until sacrifice at 48 h or 14 days. This dose was selected after dose-response testing to find the minimum dose necessary to produce a mild increase in systolic pressure (≈25 mmHg) for 14 days treatment, with the aim of achieving primarily humoral stimulation of LVH. Control mice underwent the same procedure with mini-pumps filled with 0.9% NaCI only.

For TAC, mice were anesthetized with 5% isoflurane and ventilated at 120 breaths/min (Harvard Apparatus Rodent Ventilator). The transverse aortic arch was accessed via an incision in the second intercostal space, and constricted with a ligature tied around a 25-gauge needle between the left and the right arteries, which was then removed (Rockman et al., 1994). TAC does not activate the renin-angiotensin system (Wiesner et al., 1997). Sham mice underwent the same procedure but the ligature was not tied. Simultaneous direct pressure recordings (1.4 F pressure catheter, AD Instruments, P/L) from both the right carotid artery and the aorta distal to the ligature (n = 20 mice) indicated a TAC pressure gradient of 60 ± 8 mmHg with this technique. Animals were sacrificed after 48 h or 21 days.

Invasive Hemodynamic Measurements

After 14 days of AngII infusion or 21 days of TAC, mice were anesthetized by inhalation of isoflurane (1.5%) and a 1.4F micro-tip pressure catheter (Millar Instruments Inc., Houston, TX, United States) was inserted into the LV via the right carotid artery. The heart rate, systolic aortic pressure, LV systolic pressure, + dP/dt, and –dP/dt were recorded (LabChart 6 Reader, AD Instruments, P/L). Animals were sacrificed, and the LV weights (LVW) normalized to body weight (BW) and to tibial length (TL) were measured as indicators of LVH.

Quantitative Real-Time Polymerase Chain Reaction (RT-PCR)

Gene expression was determined by quantitative RT-PCR. Total RNA was extracted and purified from LV tissue with a QIAGEN RNeasy Fibrous Tissue Mini Kit (QIAGEN, Cat#74704). RNA (500 ng) was reverse transcribed into cDNA using SuperScript III First-Strand Synthesis SuperMix system (Invitrogen, Cat#11752-250). cDNA was subjected to PCR amplification to detect ANP, BNP, α-SA and myocyte-enriched calcineurin-interacting protein 1 (MCIP1 [RCAN1]) gene expression, quantified by the LightCycler 480 Probes master (Roche, Cat#047049001). Probes for quantitative PCR were purchased from ABI: hypoxanthine-guanine phosphoribosyl transferase 1 (HPRT) (Mm00446968.m1), ANP (Mm01255748_g1), BNP (Mm01255770_g1), α-SA (Acta1, Mm00808218.g1), and MCIP1.4 (Mm1213407__m1). Samples were run in triplicate and mRNA levels were normalized to those of HPRT.

Western Blotting

Left ventricular tissue was lysed using NE-PER nuclear and cytoplasmic extraction reagents (Pierce Biotechnology, Rockford, IL, United States) and Protease Inhibitor Cocktail Kit and Halt Phosphatase Inhibitor Cocktail (Pierce Biotechnology), homogenized and proteins quantified using the Pierce BCA Protein Assay Kit. Protein (40 μg) was separated by SDS-PAGE, transferred to PVDF membranes (Bio-Rad Laboratories), and blocked with 5% bovine serum albumin (BSA, Sigma).

Primary antibodies included: NFATc4 (1:1500 final dilution; Abcam), phosphorylated (p-) GSK3β (Ser9, 1:1500; Cell Signaling), total GSK3β (1:500; Cell Signaling), GATA4 (1:1000; Santa Cruz Biotechnology), CaMKIIδ (1:1000; Santa Cruz Biotechnology), p-HDAC4 (1:1500; Cell Signaling), total HDAC4 (1:1500; Cell Signaling), MEF2A (1:3000; Cell Signaling). Glyceraldehyde-3-phosphate dehydrogenase (GAPDH, 1:5000; Abcam), and histone H2B (1:5000; Abcam) were used to standardize for loading. Horseradish peroxidase-conjugated goat anti-mouse (1:5000) or anti-rabbit (1:10000) secondary antibodies (Abcam, MA) were used at room temperature for 1 h. Immunologic detection was accomplished using Amersham ECL Western blotting detection reagents (GE Healthcare). Protein levels were quantified by densitometry using NIH ImageJ analysis software. Protein levels were normalized to relative changes in histone H2B for the nuclear fraction (Histone) and GAPDH for the cytoplasmic fraction and expressed as fold changes relative to those of control animals.

Statistical Analysis

All experiments and analyses were blinded. Data are presented as mean ± SEM. Paired two-tailed Student's test was applied to determine the statistical significance between two groups. One-way ANOVA was used to compare differences among multiple groups, followed by Tukey's *post hoc* test for significance. $P < 0.05$ was considered significant.

RESULTS

Inhibition of Cardiac Gq-Coupled Receptors Causes No Abnormal Cardiac Phenotype Under Baseline Conditions

To ensure robust endogenous inhibition of cardiac Gq receptors, we bred not only heterozygous ($\text{GqI}^{+/-}$) but also homozygous ($\text{GqI}^{-/-}$) mice. $\text{GqI}^{+/-}$ and $\text{GqI}^{-/-}$ mice at 12 weeks of age were healthy, with no apparent cardiac morphological or pathological abnormalities compared with their NTLs, suggesting that complete inhibition of cardiac Gq receptors did not appreciably alter the baseline phenotype of the heart.

Inhibition of Cardiac Gq-Coupled Receptors Inhibits the Induction of Left Ventricular Hypertrophy in Response to AngII Infusion

We next examined the role of cardiac Gq receptors in the induction of LVH in response to either AngII infusion (a predominantly humoral stimulus) or TAC (a mechanical stimulus) in transgenic ($\text{GqI}^{+/-}$ and $\text{GqI}^{-/-}$) and NTL mice.

Angiotensin II infusion for 14 days induced significant LVH in NTL mice, evidenced by a 31% increase in LVW/BW and a 28% increase in LVW/TL ($p < 0.001$, **Figure 1A**). As expected, the degree of LVH induced by AngII was significantly reduced in $\text{GqI}^{+/-}$ mice (19% and 17% increases in LVW/BW and LVW/TL, respectively, $p < 0.001$), and LVH was prevented in $\text{GqI}^{-/-}$ mice (**Figure 1A**).

The aortic systolic pressure was 20 mmHg higher, on average, with AngII infusion than with saline infusion (**Figure 1B**), indicating the small pressor effect of the dose of AngII selected (see section "Materials and Methods"), but this effect was the same in NTL, $\text{GqI}^{+/-}$ and $\text{GqI}^{-/-}$ mice. The complete abolition of the hypertrophic response to AngII in $\text{GqI}^{-/-}$ mice despite the same pressor effect seen in NTL mice confirms that humoral activation of the Gq-coupled AngII type 1 (AT1) receptor by AngII was the major mechanism of LVH induction, as distinct from a secondary effect of the small pressor response. There were no significant differences in dP/dt_{max} or dP/dt_{min} between mice treated with AngII or saline in transgenic or NTL mice (**Figure 1B**).

Inhibition of Cardiac Gq-Coupled Receptors Has No Effect on the Induction of Left Ventricular Hypertrophy in Response to TAC

After 21 days, TAC induced very significant LVH in NTL mice, evidenced by a mean 56% increase in LVW/BW and a mean 48% increase in LVW/TL relative to sham-operated animals (both $p < 0.001$, **Figure 2A**). Remarkably, the hypertrophic response to TAC observed in NTL mice was the *same* in $\text{GqI}^{+/-}$ and $\text{GqI}^{-/-}$ mice, evidenced by 58 and 61% mean increases, respectively, in LVW/BW and 52 and 51% mean increases, respectively, in LVW/TL (all $p < 0.001$, **Figure 2A**).

Aortic pressure proximal to the constriction and LV systolic pressure increased by 60–70 mmHg with TAC (**Figure 2B**). Importantly, the increase in the pressure load on the LV with TAC was the same in NTL, $\text{GqI}^{+/-}$ and $\text{GqI}^{-/-}$ mice. A statistically non-significant and equal reduction in dP/dt_{max} and dP/dt_{min} was observed with TAC in all three groups. There was no difference in lung weight normalized to body weight in TAC mice and sham-operated mice in any of the three groups (data not shown), indicating that this TAC model at 21 days remains a model of compensated LVH rather than heart failure.

Early Markers of Induction of Left Ventricular Hypertrophy

Although there was no significant LVH after 48 h of either AngII infusion or TAC, as indexed by the ratios of LVW/BW or LVW/TL, the early induction of hypertrophic pathways was evidenced by dramatic (3–8-fold) increases in gene expression of ANP, BNP, and α-SA in NTL mice with both AngII and TAC (**Figure 3**). In contrast, in both $\text{GqI}^{+/-}$ and $\text{GqI}^{-/-}$ mice, there was no increase in gene expression of ANP, BNP or α-SA with AngII infusion, but the increases in gene expression of ANP, BNP, and α-SA with TAC in transgenic GqI mice were similar to those observed in NTL mice. These results mirror those described above regarding LVH measured after 14 days or 21 days of AngII infusion or TAC, respectively.

Angiotensin II Infusion Activates the Calcineurin-NFAT Hypertrophic Signaling Pathway, and This Activation Is Inhibited by Inhibition of Cardiac Gq-Coupled Receptors

Infusion of AngII for 48 h in the NTL mice led to increased NFATc4 translocation to the nucleus, evidenced by a 66% mean increase in nuclear NFATc4 ($p < 0.01$) without change in cytoplasmic NFATc4, with a consequent 68% mean increase in the nuclear/cytoplasmic NFAT ratio ($p < 0.01$) when compared with saline-treated controls (**Figure 4**). These data indicate calcineurin activation by AngII infusion. The increase in NFATc4 nuclear translocation in NTL hearts was accompanied by a

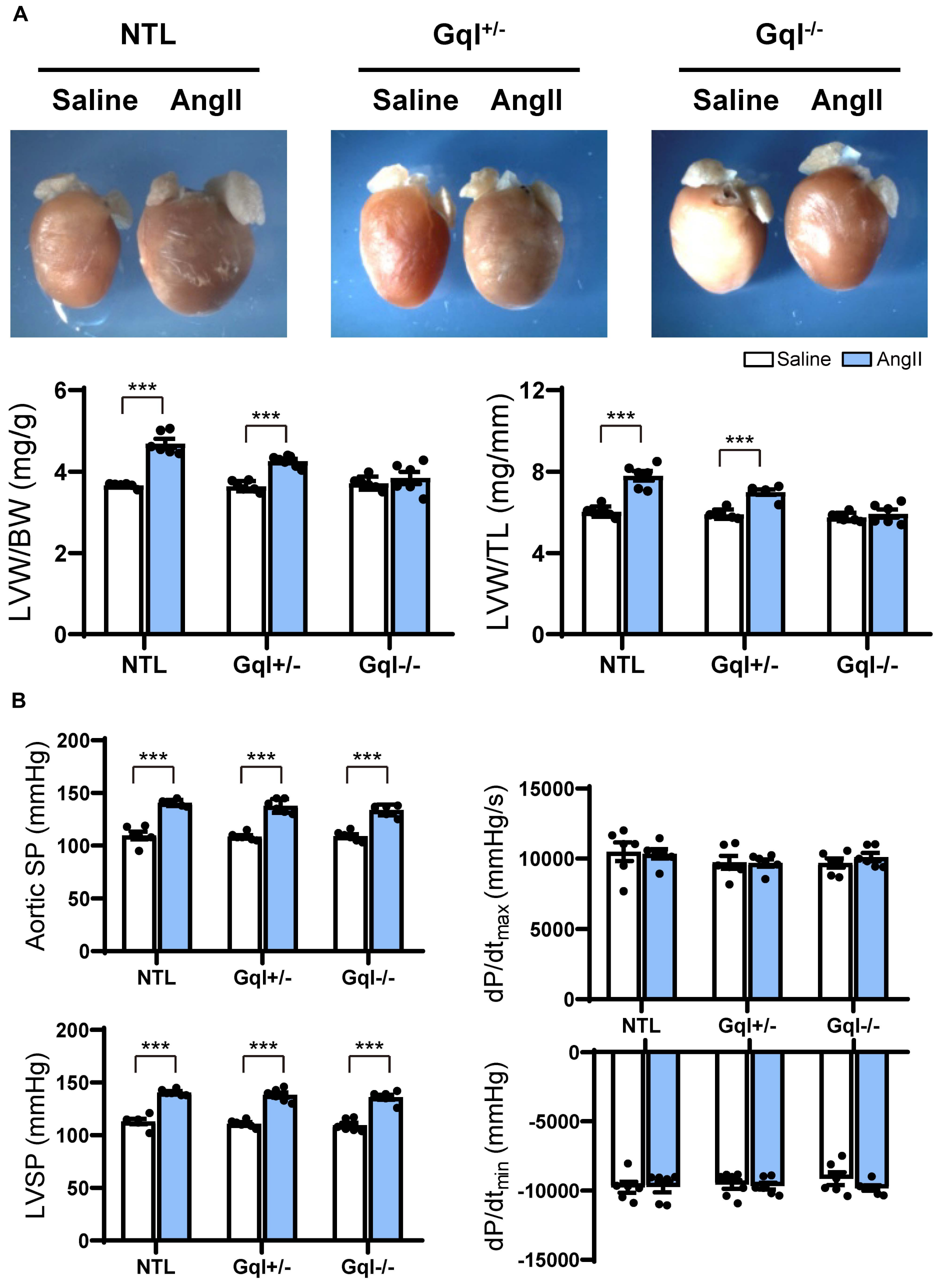

FIGURE 1 | The hypertrophic response to angiotensin II (AngII) infusion after 14 days. **(A)** Representative hearts and developed LVH indexed by the ratios of LVW/BW and LVW/TL in mice treated with AngII infusion versus saline infusion controls ($n = 7$–9/group); **(B)** Hemodynamic measurements. All values are mean ± SEM. $^{***}p < 0.001$ vs. saline-treated controls; NS: not significant. LVW/BW: LV weight to body weight ratio; LVW/TL: LV weight to tibia length ratio; SP: systolic pressure; dP/dt: first derivative of pressure with respect to time.

significant increase in the level of the nuclear transcription factor GATA4 ($p < 0.05$). Calcineurin activation by AngII infusion in NTL hearts was also accompanied by an increase in the nuclear fraction of the serine 9 phosphorylated form of glycogen synthase kinase-3 beta (GSK3β, $p < 0.01$) but no change in total nuclear GSK3β and no change in the total or phosphorylated form of GSK3β in the cytoplasm. These data are consistent with calcineurin's inhibition of the nuclear export of NFAT by GSK3β.

Importantly, all of these manifestations of the activation of the calcineurin-NFAT pathway with AngII infusion in NTL mice were completely absent in both the $\text{GqI}^{+/-}$ and the $\text{GqI}^{-/-}$ mice (**Figure 4**), consistent with the inhibition of the hypertrophic response to AngII in the transgenic hearts (**Figure 1A**).

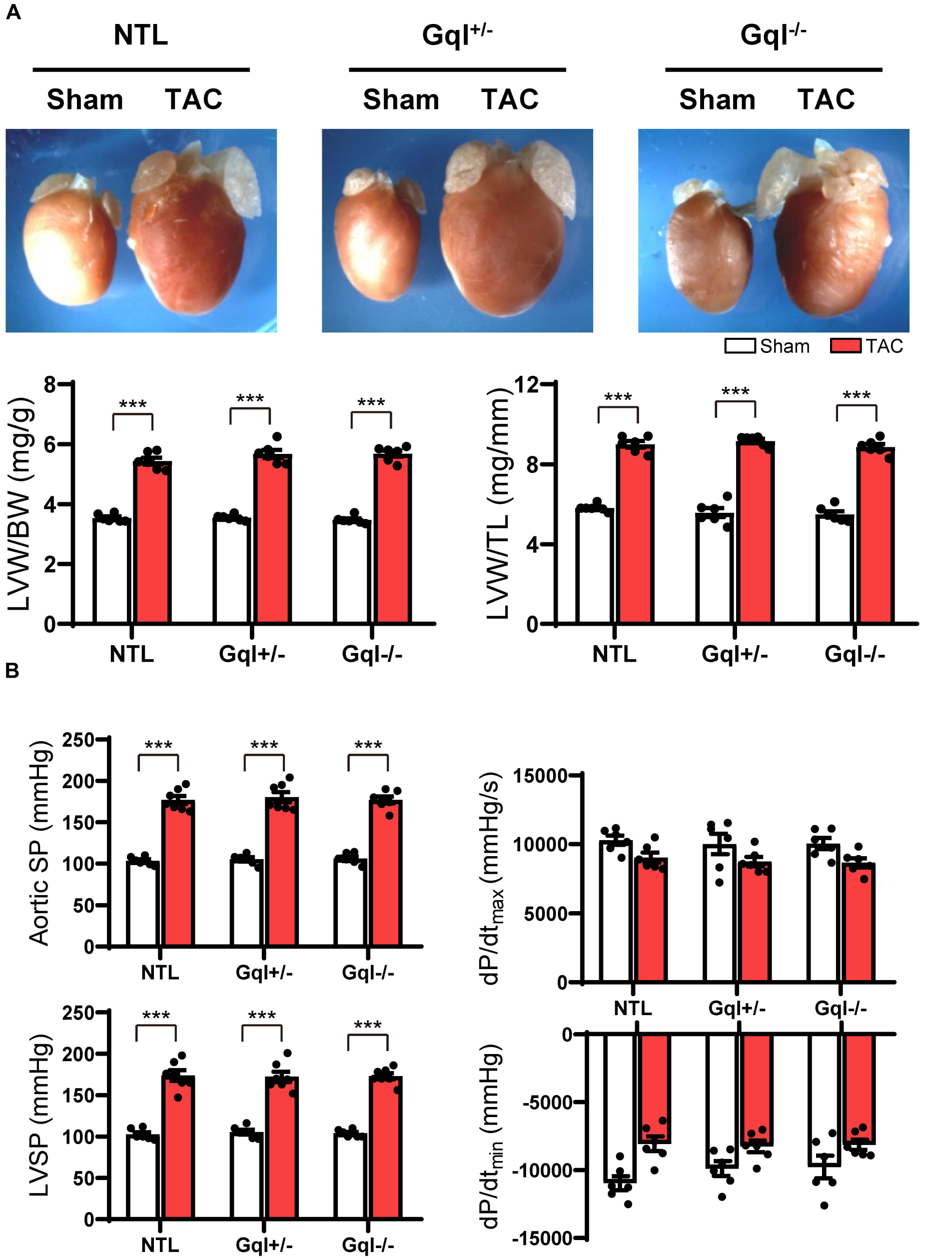

FIGURE 2 | The hypertrophic response to TAC for 21 days. **(A)** Representative hearts **(upper)** and developed LVH indexed by the ratios of LVW/BW and LVW/TL **(lower)** in mice subjected to TAC versus sham-operated controls ($n = 7–9$/group); **(B)** Hemodynamic measurements. All values are mean ± SEM. $^{**}p < 0.01$, $^{***}p < 0.001$ vs. sham-operated controls; LVW/BW: LV weight to body weight ratio; LVW/TL: LV weight to tibia length ratio; SP: systolic pressure; dP/dt: first derivative of pressure with respect to time.

TAC Does Not Activate the Calcineurin-NFAT Hypertrophic Signaling Pathway

In contrast to the effects of AngII infusion, TAC for 48 h did not cause any significant change in the levels of NFATc4, GATA4, total GSK3β or phosphorylated GSK3β in the nucleus or the cytoplasm in NTL hearts, nor in $GqI^{+/-}$ or $GqI^{-/-}$ hearts (**Figure 5**), indicating that TAC does not activate the calcineurin-NFAT hypertrophic signaling pathway.

Angiotensin II Does Not Activate the CaMKII-HDAC4-MEF2 Signaling Pathway

The infusion of AngII for 48 h did not cause any significant change in the levels of CaMKIIδ, total HDAC4 or phosphorylated HDAC4 (p-HDAC4) in the nucleus or the cytoplasm in

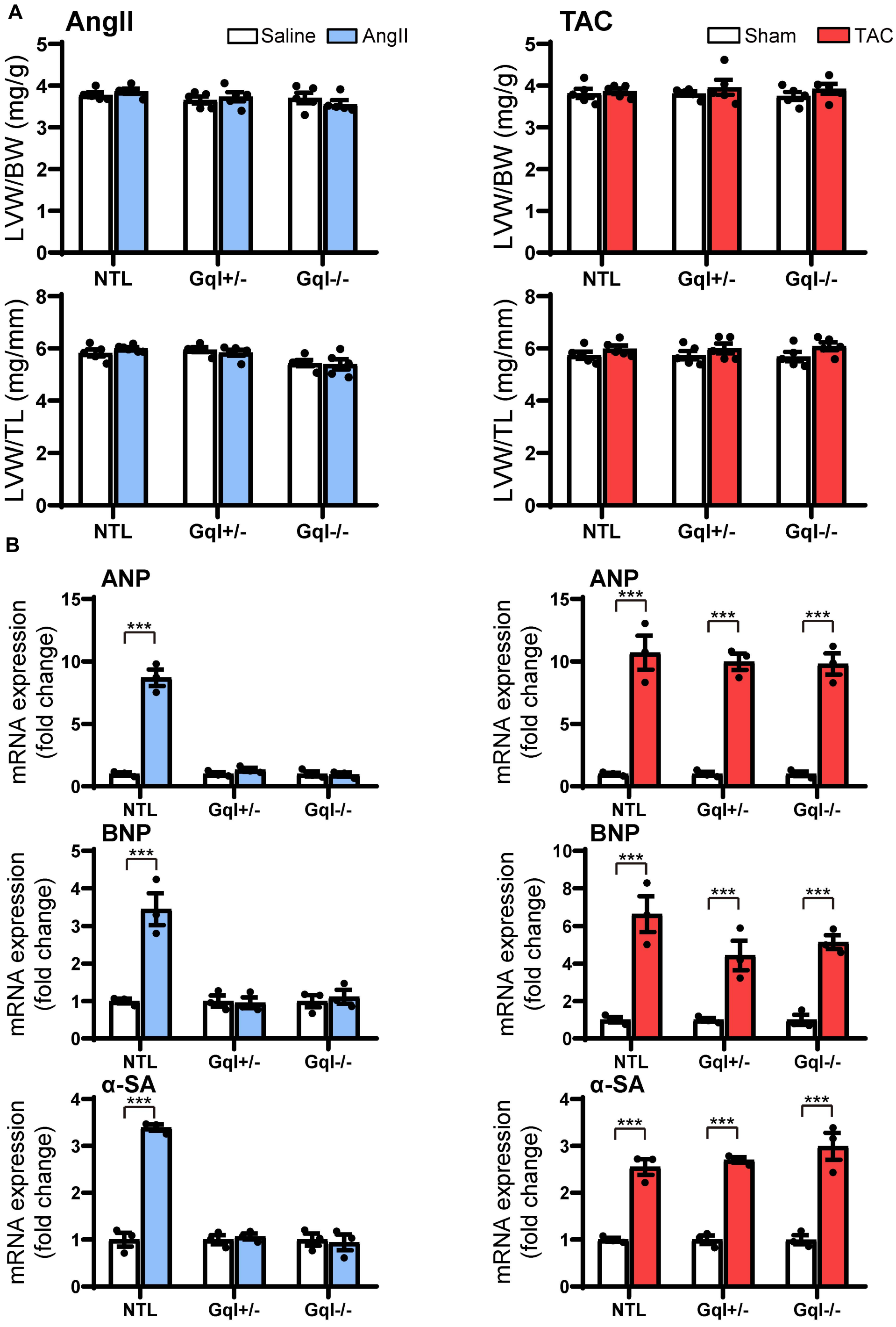

FIGURE 3 | Markers of the early induction of hypertrophy in response to angiotensin II infusion (AngII) **(left panels)** or TAC **(right panels)** after 48 h. **(A)** Ratios of LVW/BW and LVW/TL, *n* = 6–8/group. **(B)** Gene expression of ANP, BNP and α-skeletal actin, *n* = 3/group. All values are mean ± SEM. ****p* < 0.001 vs. saline treated or sham-operated controls, respectively; NS: not significant. LVW/BW: LV weight to body weight ratio; LVW/TL: LV weight to tibia length ratio; ANP: atrial natriuretic peptide; BNP: B-type natriuretic peptide; α-SA: α-skeletal actin.

NTL hearts, nor in $GqI^{+/-}$ or $GqI^{-/-}$ hearts (**Figure 6** and **Supplementary Figure 1**). Nor was there any change in nuclear levels of MEF2A with AngII infusion in NTL or transgenic hearts. These findings indicate that AngII does not activate the CaMKII-HDAC4-MEF2 hypertrophic signaling pathway.

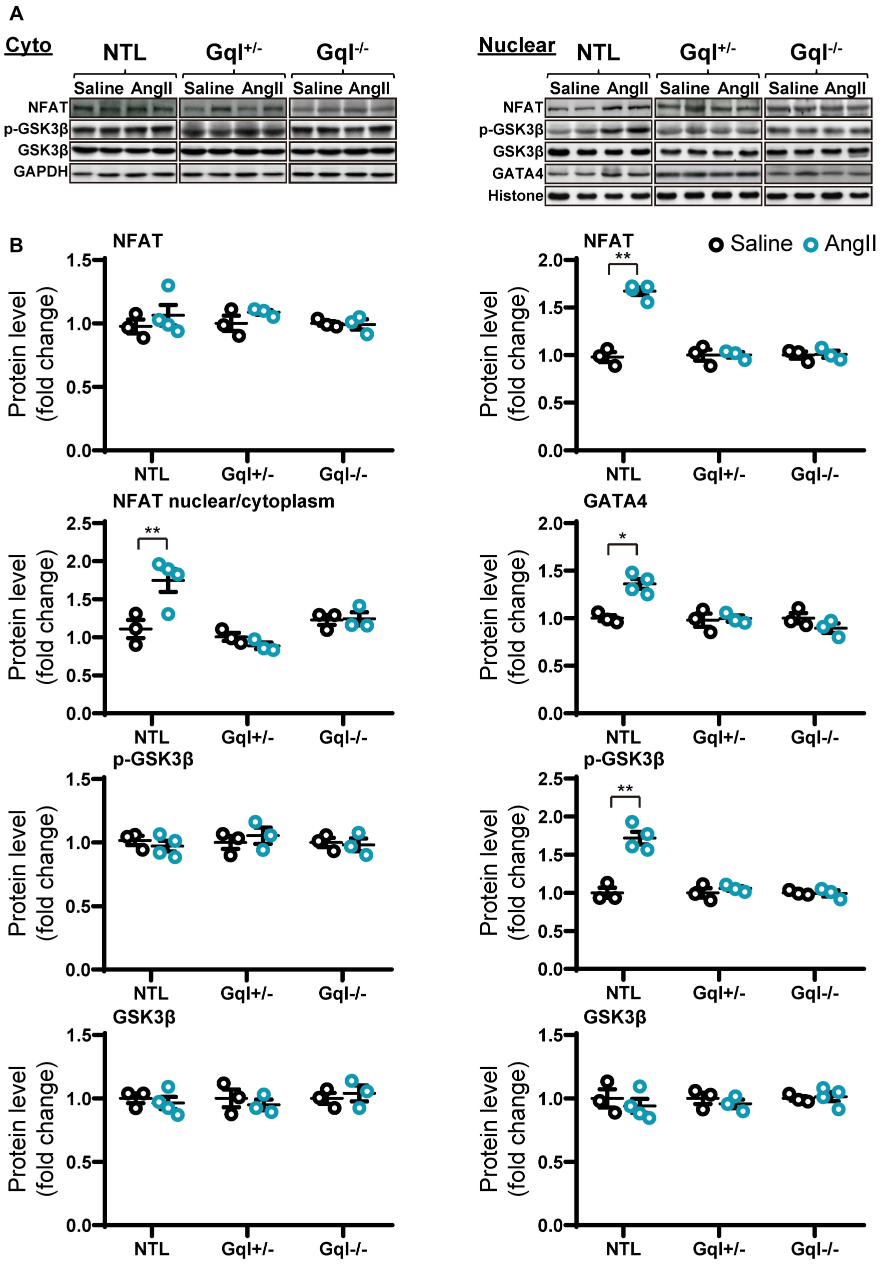

FIGURE 4 | NFAT-GATA4 signaling in response to angiotensin II infusion after 48 h. **(A)** Representative Western blots of NFATc4, phosphorylated glycogen synthase kinase-3 beta (GSK3β) and total GSK3β protein expression in the cytoplasm **(upper left panel)** and nucleus **(upper right panel)**. GATA4 blots are shown for the nucleus. **(B)** Cytoplasmic and nuclear data are normalized with GAPDH and histone, respectively **(bottom panels)**. All Western blot runs were performed in duplicate or triplicate. Results are presented as the mean value of 3–4 hearts per group ± SEM. *$p < 0.05$, **$p < 0.01$, vs. saline treated controls.

TAC Activates the CaMKII-HDAC4-MEF2 Hypertrophic Signaling Pathway, and This Activation Is Not Inhibited by Inhibition of Cardiac Gq-Coupled Receptors

Non-transgenic littermates hearts subjected to TAC for 48 h exhibited a significant increase in the levels of CaMKIIδ in both the cytoplasm and the nucleus (both $p < 0.01$, **Figure 7**). This TAC-induced increase in CaMKIIδ in NTL hearts was accompanied by increased levels of both total HDAC4 ($p < 0.05$) and p-HDAC4 ($p < 0.01$) in the cytoplasm, but there was no change in the nuclear HDAC4 or p-HDAC4 levels. Consequently, there was a significant increase in the cytoplasmic/nuclear ratio of HDAC4 ($p < 0.05$) in NTL hearts, indicating increased nuclear export of HDAC4, and this was associated with a significant

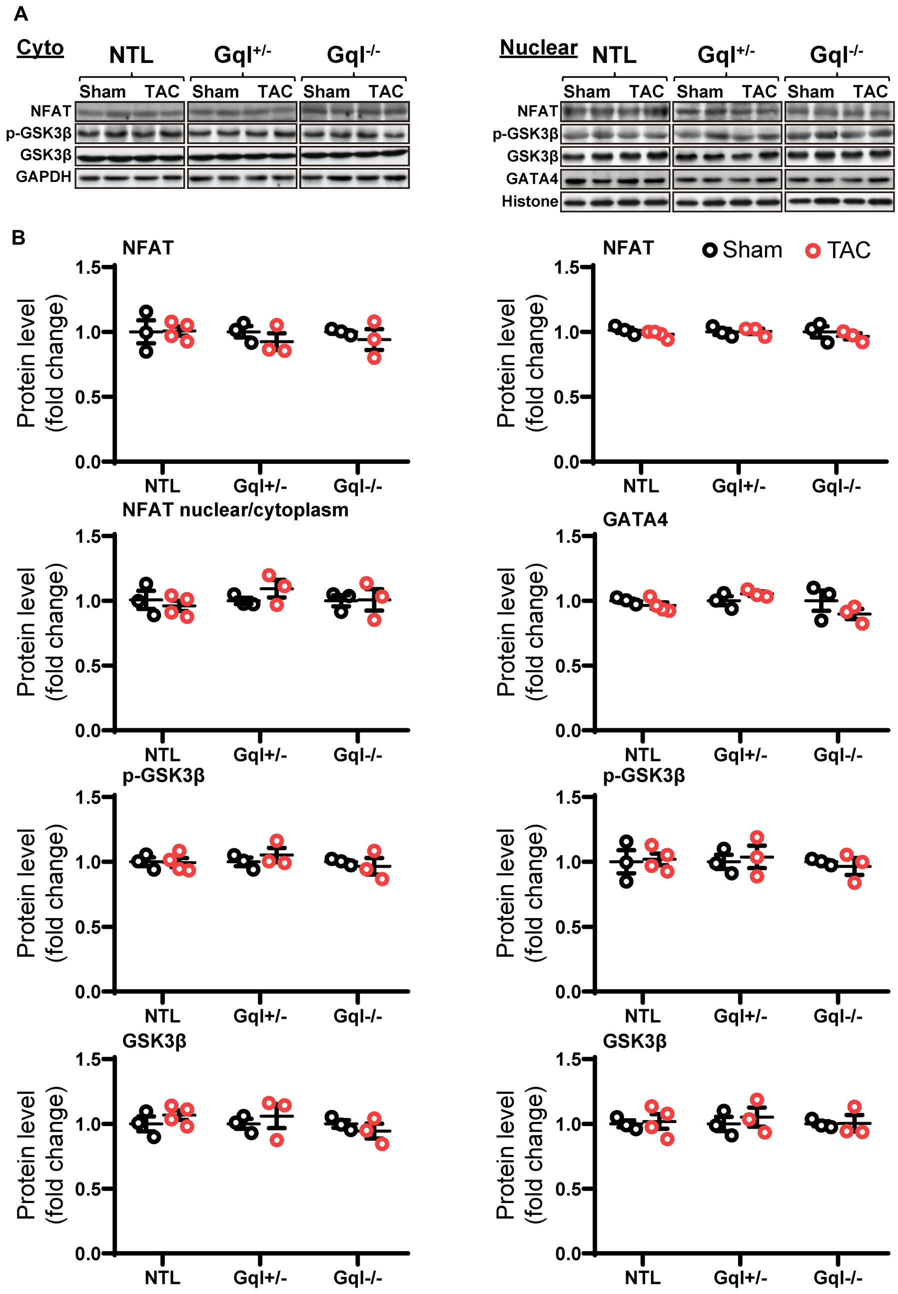

FIGURE 5 | NFAT-GATA4 signaling in response to TAC after 48 h. **(A)** Representative Western blots of NFATc4, phosphorylated glycogen synthase kinase-3 beta (GSK3β) and total GSK3β protein expression in the cytoplasm **(upper left panel)** and nucleus **(upper right panel)**. GATA4 blots are shown for the nucleus. **(B)** Cytoplasmic and nuclear data are normalized with GAPDH and histone, respectively **(bottom panels)**. All Western blot runs were performed in duplicate or triplicate. Results are presented as the mean value of 3–4 hearts per group ± SEM. None of the statistical comparisons between TAC mice and sham-operated controls were significant.

increase in the nuclear levels of MEF2A ($p < 0.001$). These findings indicate that TAC activates the CaMKII-HDAC4-MEF2 hypertrophic pathway, resulting in nuclear export of HDAC4, relieving its repression of MEF2A.

Importantly, all of these manifestations of the activation of the CaMKII-HDAC4-MEF2 hypertrophic pathway with TAC in NTL mice were also present in the GqI$^{+/-}$ and the GqI$^{-/-}$ mice, indicating that inhibition of cardiac Gq-coupled receptors has no effect on the activation of the CaMKII-HDAC4-MEF2 pathway with TAC. These findings are consistent with the complete absence of any inhibition of the hypertrophic response to TAC in the transgenic GqI hearts (**Figure 2A**).

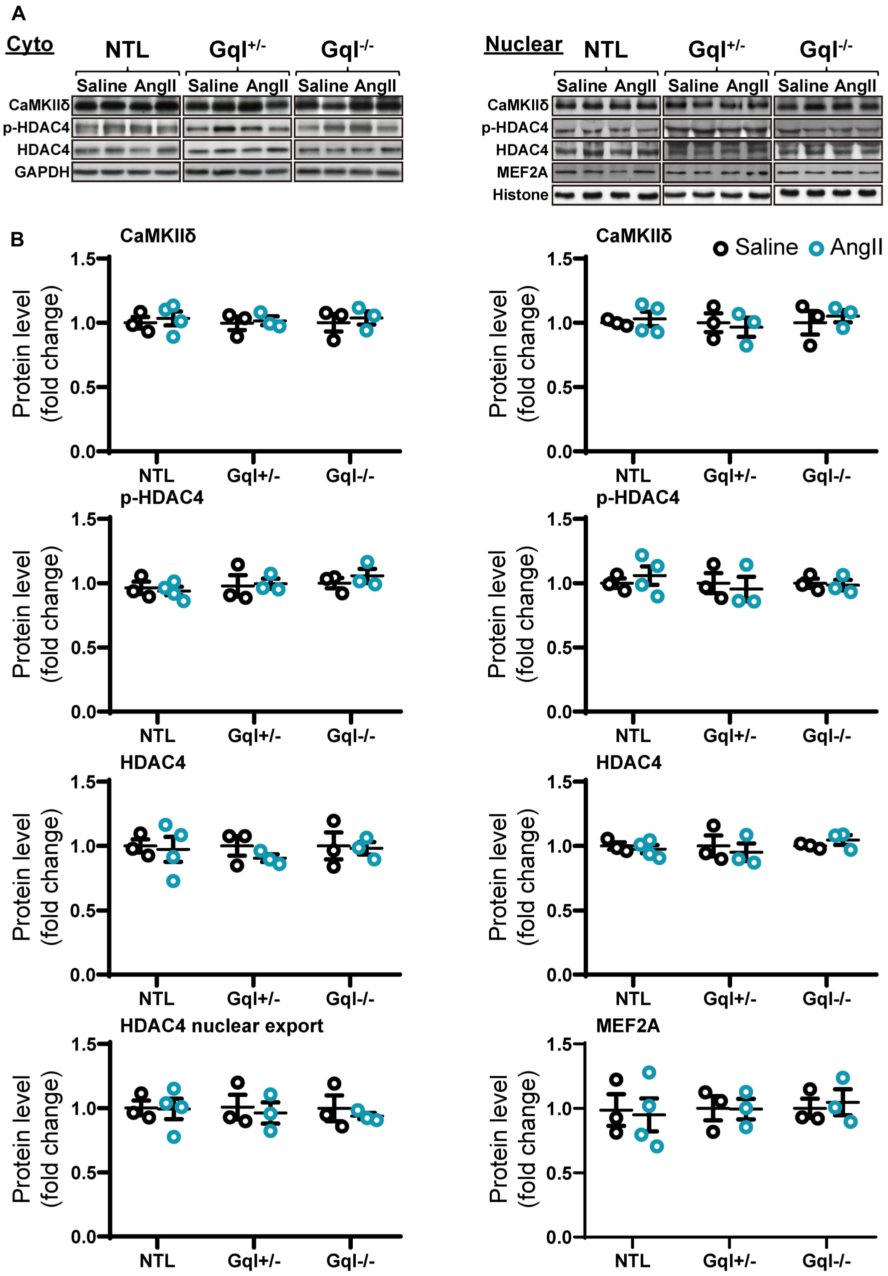

FIGURE 6 | CaMKIIδ, HDAC4 and MEF2A signaling in response to angiotensin II after 48 h. **(A)** Representative Western blots of CaMKIIδ, phosphorylated HDAC4 and total HDAC4 protein expression in the cytoplasm **(upper left panel)** and in the nucleus **(upper right panel)**. MEF2A blots are shown for the nucleus. **(B)** Cytoplasmic and nuclear data are normalized with GAPDH and histone, respectively **(bottom panels)**. The HDAC4 cytoplasmic/nuclear (cyto/nuclear) ratio was used as an indicator of HDAC4 nuclear export. All Western blot runs were performed in duplicate or triplicate. Results are presented as the mean value of 3–4 hearts per group ± SEM. None of the statistical comparisons between mice receiving AngII and saline were significant.

MCIP1 Is a Marker of Activation of Both the Calcineurin-NFAT and CaMKII-HDAC4-MEF2 Hypertrophic Signaling Pathways

Because MCIP1 gene expression is activated downstream of the nuclear translocation of NFATc4, it is often measured as an *in vivo* marker of calcineurin-NFAT hypertrophic pathway activation. Gene expression of the MCIP1.4 isoform was significantly and similarly elevated 48 h after *both* AngII infusion and TAC when compared with their respective saline infusion and sham controls (**Table 1**), despite the fact that calcineurin activation was evident with AngII infusion but not TAC (**Figures 4**, **5**). These findings indicate that MCIP1 gene expression is increased not only by

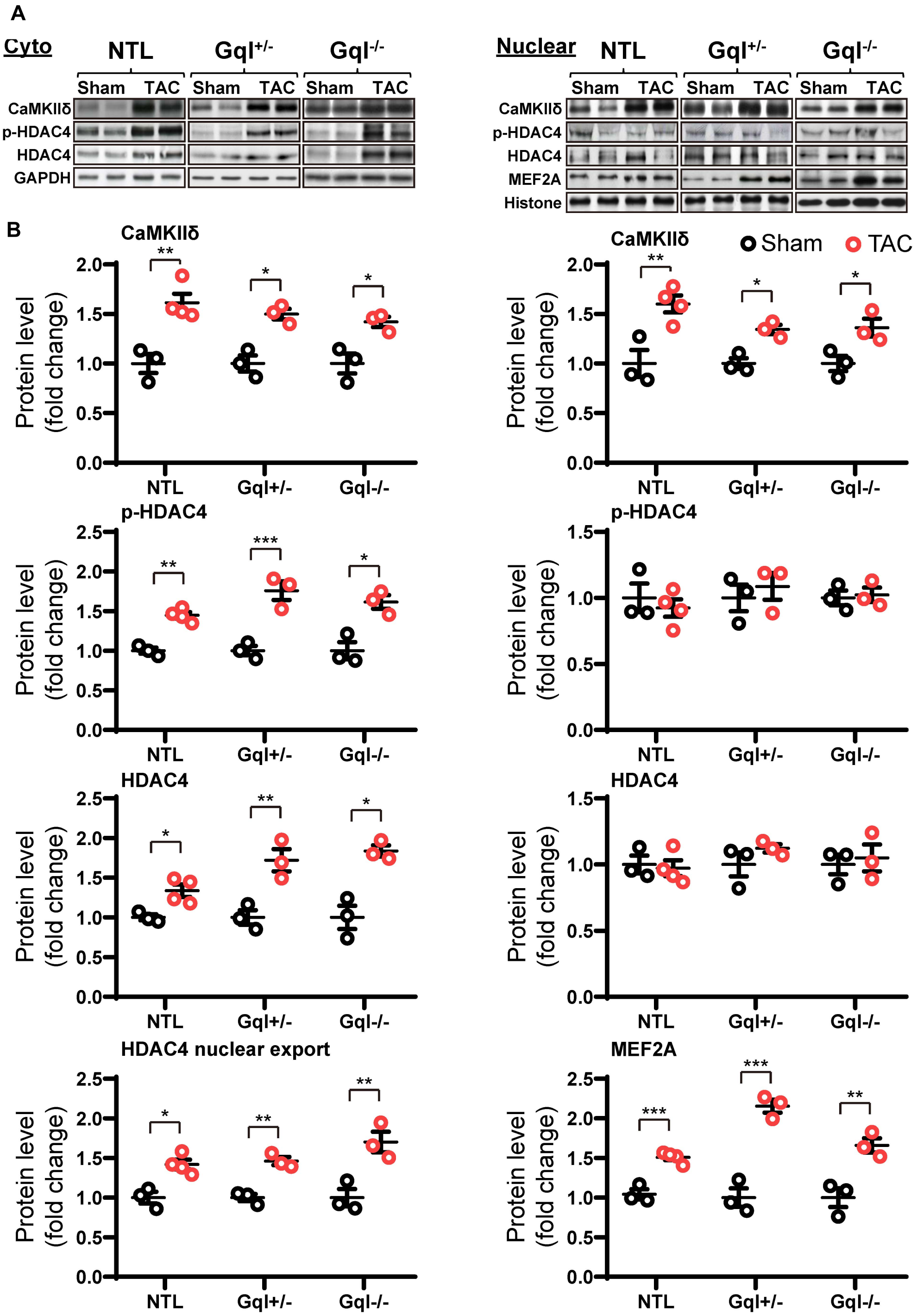

FIGURE 7 | CaMKIIδ, HDAC4 and MEF2A signaling in response to TAC after 48 h. **(A)** Representative Western blots of CaMKIIδ, phosphorylated (p-) HDAC4 and total HDAC4 protein expression in the cytoplasm **(upper left panel)** and in the nucleus **(upper right panel)**. MEF2A blots are shown for the nucleus. **(B)** Cytoplasmic and nuclear data are normalized with GAPDH and histone, respectively **(bottom panels)**. The HDAC4 cytoplasmic/nuclear (cyto/nuclear) ratio was used as an indicator of HDAC4 nuclear export. All Western blot runs were performed in duplicate or triplicate. Results are presented as the mean value of 3–4 hearts per group ± SEM. *$p < 0.05$, **$p < 0.01$, ***$p < 0.001$ vs. sham-operated controls.

TABLE 1 | MCIP1.4 isoform mRNA expression after angiotensin II (Ang II) or saline infusion for 48 h and 48 h after TAC or sham surgery in non-transgenic mice.

	MCIP1.4 mRNA
Saline	1.63 ± 0.06
Ang II	5.62 ± 0.26***
Sham	1.81 ± 0.1
TAC	4.48 ± 0.29***

*Results are presented as the mean value of six hearts per group ± SEM. MCIP1.4 isoform mRNA expression increased significantly with angiotensin II and TAC relative to their saline and sham controls, respectively (***$p < 0.001$).*

calcineurin-NFAT pathway activation but also by activation of the CaMKII-HDAC4-MEF2 hypertrophic pathway.

DISCUSSION

The Role of Cardiac Gq-Coupled Receptors in the Induction of LVH Secondary to Pressure Overload

The major finding of this investigation is that cardiac Gq-coupled receptors were not required for the induction of LVH after TAC, the most commonly employed experimental model of LVH secondary to LV pressure overload.

Although our results are very clear, and consistent with findings in mice with a global AT1a knockout after TAC (Harada et al., 1998b), they differ from those in the initial report of the phenotype of heterozygous GqI mice, which were reported to exhibit partial inhibition of TAC-induced LVH (Akhter et al., 1998). It is important to emphasize, therefore, that we took two steps in the current study to ensure that we achieved a robust inhibition of Gq. First, we bred both heterozygous (GqI$^{+/-}$) and homozygous (GqI$^{-/-}$) Gq-inhibited mice for this study. Second, the main purpose of the AngII infusion experiments in this study was to demonstrate that the Gq-inhibited mice used in this study did indeed exhibit effective Gq inhibition phenotypes. We demonstrated significant inhibition of AngII-induced LVH in mice with heterozygous Gq inhibition and complete inhibition of LVH in mice with homozygous Gq inhibition. Similarly, transgenic Gq inhibition prevented the increased gene expression of the hypertrophic markers ANP, BNP, and α-SA with AngII infusion. Finally, the activation of the calcineurin-NFAT hypertrophic signaling pathway by AngII was inhibited by transgenic Gq inhibition. These results demonstrate clearly and in a "dose-dependent" manner the effectiveness of the transgenic inhibition of Gq. The same results would be anticipated with other agonists of Gq-coupled receptors, including endothelin and catecholamines.

In contrast to the results obtained with AngII infusion, we showed that the transgenic inhibition of cardiac Gq-coupled receptors had *no effect* on the amount of TAC-induced LVH after 21 days, even with homozygous Gq inhibition. Consistent with this finding, transgenic Gq inhibition did not prevent the increased gene expression of ANP, BNP, and α-SA with TAC. Finally, the activation of the CaMKII-HDAC4-MEF2 pathway by TAC was not inhibited by transgenic Gq inhibition.

Our results do not exclude a role for cardiac Gq-receptors in the induction of LVH in situations where a variety of humoral stimuli may be important. For example, the systemic renin-angiotensin system is activated in hypertension secondary to renal artery stenosis, and activation of Gq-coupled cardiac receptors by circulating AngII would be expected to play an important role in the induction of LVH in this situation. Similarly, elevated circulating catecholamine levels can induce LVH via their Gq-coupled α-adrenergic receptors, as can elevated endothelin levels acting via their Gq-coupled endothelin receptors.

Differential Role of Two Calcium-Calmodulin Dependent Mechanisms in the Induction of Pressure Overload LVH

The second major finding of this investigation is the remarkable *segregation* of the roles of two calcium-calmodulin dependent hypertrophic pathways in mediating LVH secondary to a humoral stimulus (AngII) acting via Gq-coupled receptors, on one hand, and LVH secondary to a mechanical increase in proximal aortic pressure (TAC), on the other. It is generally believed that because activation of both pathways is calcium-calmodulin dependent, they are activated together by a variety of pathological signals that increase intracellular calcium, and that there is significant cross-talk between these pathways (Zarain-Herzberg et al., 2011). These segregated hypertrophic pathways are shown schematically in **Figure 8**. Gq-coupled receptor activation by a ligand drives LVH via the calcium-calmodulin dependent activation of calcineurin, which dephosphorylates NFAT, resulting in increased NFAT translocation to the nucleus, inhibition of GSK3β-mediated export of NFAT from the nucleus, increased GATA4 and combinatorial interaction with MEF2 that initiates transcription of hypertrophic genes. On the other hand, a mechanical stimulus (TAC) drives LVH via calcium-calmodulin dependent activation of CaMKII, resulting in increased nuclear export of HDAC4, which relieves the repression of MEF2, permitting its combinatorial interaction with NFAT and GATA4 to initiate hypertrophic gene transcription.

Although we found no evidence of CaMKII/MEF2 activation by AngII in the normal adult heart *in vivo*, AngII activates this pathway in vascular smooth muscle cells to induce growth and hypertrophy (Li et al., 2010; Ginnan et al., 2012). While AngII activation of calcineurin in the heart is very well documented, evidence supporting CaMKII/MEF2 activation by AngII and other ligands of Gq-coupled receptors in the heart is limited, and has been obtained mainly with *in vitro* stimulation of isolated neonatal cardiac myocytes (Zhu et al., 2000; Backs et al., 2006; Tang et al., 2016). This approach avoids the potentially confounding effect of increased blood pressure associated with vasoactive agonists like AngII *in vivo* (Fielitz et al., 2008), which our data suggest could activate CaMKII/MEF2 independent of cardiac Gq-coupled receptor activation. Like vascular smooth muscle cells, however, which are not terminally differentiated

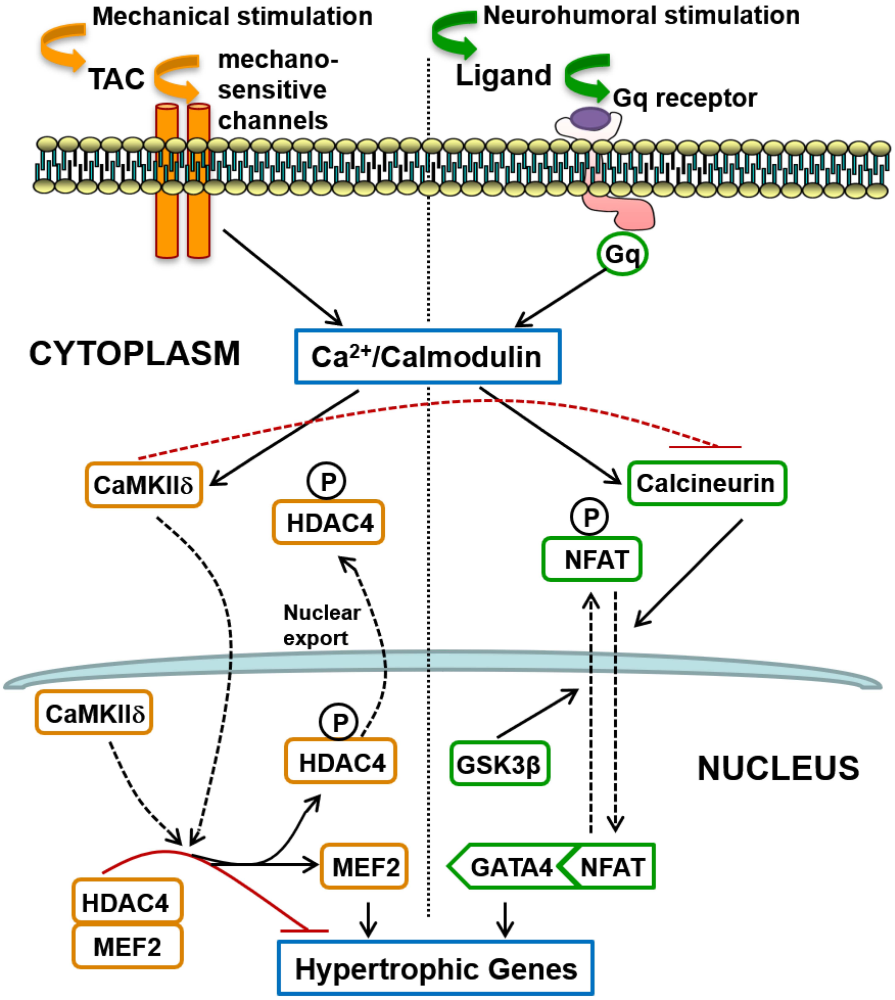

FIGURE 8 | Schematic summary of two distinct signaling pathways involved in the induction of cardiac hypertrophy in response to pressure overload: (1) The calcineurin-NFAT pathway is activated by Gq-coupled receptors in response to neurohumoral stimulation, not only by AngII but possibly also by endothelin and by catecholamines (acting on alpha-adrenergic receptors); (2) Mechanical loading, such as transverse aortic constriction (TAC), does not activate the systemic renin-angiotensin system but induces hypertrophy mediated by CaMKII-HDAC4-MEF2 signaling that does not require Gq-coupled receptor activation, but is presumably activated by calcium entry controlled by mechano-sensitive channels. Differences in the mode of intracellular calcium elevation in response to different stimuli (mechanical versus neuro-humoral) may account for the differential activation of calcineurin versus CaMKII, but CaMKII also directly inhibits activation of calcineurin, as indicated by the broken red inhibitory path (see section "Discussion").

(Ginnan et al., 2012), neonatal cardiac myocytes differ from their adult counterparts, retaining the capacity for cell replication (Naqvi et al., 2014). It is not yet clear whether this difference can explain the observed differences in CaMKII activation by AngII. One *in vivo* study reported increased MEF2 (mRNA and protein) in response to AngII infusion (Tang et al., 2016) in the adult mouse heart, but these measurements were made after hypertrophy was established and the potentially confounding blood pressure response to AngII and evidence of CaMKII activation were not reported. Others reported that the MEF2 target gene, *Xirp2*, mediated AngII-induced cardiac remodeling *in vivo*, but the AngII infusion increased the systolic blood pressure to approximately 170 mmHg and no assessment was made of CaMKII-HDAC4-MEF2 pathway activation or calcineurin pathway-activation *in vivo* (McCalmon et al., 2010). Moreover, given the convergence of these two pathways onto a common intra-nuclear transcriptional complex that includes MEF2 (see above and **Figure 8**), it would seem likely that calcineurin activation by sub-pressor doses of AngII may be sufficient to regulate *Xirp2 in vivo* without CaMKII activation.

MCIP1 Is a Marker of Both Calcineurin and CaMKII Activation

The third important finding of this investigation is that MCIP1 gene expression is increased not only with calcineurin pathway activation, as expected, but also with CaMKII pathway activation (**Table 1**). This is a consequence of the convergence of these two distinct signaling pathways onto a common intra-nuclear complex to initiate hypertrophic transcription (**Figure 8**) and the fact that nuclear export of HDAC4 relieves the repression not only of MEF2 but also of NFAT (McKinsey, 2007; Backs et al., 2011). Derepression of both MEF2 and NFAT by CaMKII activation results in gene transcription downstream of intranuclear NFAT, including expression of MCIP1 (**Figure 8**). It follows that increased MCIP1 gene expression cannot be regarded as a specific marker of calcineurin activation. For the same reason, a similar caveat should apply to conclusions regarding calcineurin activation drawn from experiments based on the NFAT luciferase reporter (Wilkins et al., 2004; Molkentin, 2013).

Mechanisms of Differential Activation of Calcineurin and CaMKII

The interesting question is the mechanism of differential activation of calcineurin and CaMKII in response to TAC given that both depend on calcium-calmodulin activation. It is known that calcineurin activation requires a sustained increase in the resting intracellular calcium level (Dolmetsch et al., 1997). Sustained Gq-coupled receptor activation by its humoral ligand (angiotensin II, endothelin or catecholamines), with activation and increased expression of TRPC6 receptors (Eder and Molkentin, 2011), for example, could provide the mechanism for this tonic calcium signal. In contrast, CaMKII activation is more sensitive to high-frequency, high-amplitude calcium oscillations (De Koninck and Schulman, 1998), and it is known that aortic constriction provides this type of calcium signal (Colella et al., 2008), possibly initiated directly by mechano-sensitive channels given our new findings regarding Gq (**Figure 8**), although the initial mechano-transduction could then trigger secondary sources of calcium entry (see section "Introduction").

In addition, activated CaMKII has been shown to directly inhibit the regulatory subunit of calcineurin (Kreusser et al., 2014), providing an additional explanation for the differential signaling pathway activation with TAC. This direct inhibition of calcineurin by CaMKII is also consistent with our finding that Gq inhibition has no impact on the hypertrophic response to TAC despite the fact that TAC increases DAG, which indicates Gq activation (Niizeki et al., 2008).

While there is consensus that activation of the CaMKII-HDAC4-MEF2 pathway causes the adverse left ventricular remodeling and heart failure that is associated with TAC-induced LVH (Ling et al., 2009; Kreusser et al., 2014), it has been less clear to some that this pathway induces the hypertrophy *per se*. A CaMKIIδ knockout (KO) in the mouse heart was clearly shown to inhibit TAC-induced LVH in 2009 (Backs et al., 2009), but a subsequent study by others of a CaMKIIδ KO mouse in the same year showed no inhibition of LVH 2 weeks after TAC, despite protection from adverse remodeling and heart failure 6 weeks after TAC (Ling et al., 2009). In the latter study, however, there was clear inhibition of LVH with CaMKIIδ KO 6 weeks after TAC. This was interpreted by the authors as secondary to the protection from adverse LV remodeling and dilatation, but others have noted the possibility that the design of this CaMKIIδ KO model might have allowed an incomplete KO (truncated protein transcription) whereas the previous KO model exhibited null transcription, possibly explaining the different hypertrophy phenotypes observed (Kreusser and Backs, 2014). A subsequent study of a double CaMKII isoform KO model presented a more complex picture of the hypertrophic response (Kreusser et al., 2014). In that latter study, a single KO of *either* CaMKIIδ or CaMKIIγ in the mouse heart did significantly inhibit the hypertrophic response to TAC (Kreusser et al., 2014), while a double KO of *both* CaMKII isoforms inhibited the adverse left ventricular remodeling and cardiac dysfunction but the hypertrophic response to TAC *increased* when compared with the single KO experiments, and was similar to control animals. This was explained by the loss of the direct inhibitory effect of CaMKII on calcineurin with the CaMKII double isoform KO (see above), so that the resultant increase in calcineurin activation explained the increased hypertrophy in the double KO animals when compared with the single KO animals (Kreusser et al., 2014).

It would be a mistake to infer from the CaMKII isoform double KO experiments above (Kreusser et al., 2014), however, that calcineurin activation induces the hypertrophic response to TAC in the normal heart while CaMKII activation induces only the adverse remodeling and heart failure. If that were the case, the CaMKII single isoform KO experiments would not have demonstrated the very significant reduction of LVH with TAC when compared with control animals (Backs et al., 2009; Kreusser et al., 2014). The alternative CaMKII isoform was shown to compensate for the loss of the direct inhibitory effect of the missing CaMKII isoform on calcineurin in the single isoform KO animals (Kreusser et al., 2014), with the consequence that the hypertrophic response to TAC in single KO animals should have equaled that in control animals unless CaMKII activation is pro-hypertrophic *per se*.

It is relevant to note here also the recent observation that gene therapy with the N-terminal proteolytic fragment of HDAC4, HDAC4-NT, overcomes CaMKII-induced cytoplasmic accumulation of HDAC4 and subsequent MEF2 activation after TAC, inhibiting not just the adverse LV remodeling after TAC but also the LVH (Lehmann et al., 2018), which clearly indicates a pro-hypertrophic role of CaMKII activation via HDAC4, independent of calcineurin. In addition, the significant reduction in HDAC4-NT levels observed after TAC may play a significant role in TAC-induced LVH and adverse LV remodeling (Lehmann et al., 2018).

Our findings here are consistent with this evidence of a pro-hypertrophic effect of CaMKII activation. Although we did not block the pathway to confirm the causal link, we observed activation of the CaMKII-HDAC4-MEF2 pathway preceding TAC-induced LVH in the normal adult mouse heart, but no evidence of calcineurin activation.

Previous Studies of Calcineurin Activation as the Cause of Pressure Overload LVH

The large body of conflicting data concerning the importance of calcineurin activation in pressure overload LVH has been reviewed extensively elsewhere (Molkentin, 2000, 2013). In addition to the previously acknowledged limitations of early studies based on pharmacological inhibitors of calcineurin, such as cyclosporin A and FK506, and the limitations of early calcineurin activity assays (Molkentin, 2000), it is important to consider the experimental pressure overload model employed in evaluating the results of previous studies. Most studies based on pressure overload induced by abdominal aortic constriction (AAC), for example, have reported that calcineurin-NFAT pathway activation accounts for the LVH observed, and this is consistent with our current results obtained with AngII infusion because AAC activates the systemic renin-angiotensin system (RAS) when the aorta is constricted between the renal arteries (Wiesner et al., 1997). For example, consistent with our AngII data in GqI mice, mice with conditional inactivation of Gαq/Gα11 in cardiac myocytes were shown not to develop LVH secondary to pressure overload induced by AAC (Wettschureck et al., 2001). When supra-renal AAC is used, however, there is little or no evidence of RAS activation (Nicks et al., 2020), which is consistent with the absence of any reduction in the amount of LVH induced by this model in mice with a global AT1a receptor knockout (Harada et al., 1998a). Of those studies based on TAC, which does not cause systemic RAS activation and has become the dominant experimental model of pressure overload, the results with regard to calcineurin activation are much more variable (Frey and Olson, 2003; Molkentin, 2013). Many of these TAC studies have relied on MCIP1 or the NFAT luciferase reporter as the only *in vivo* evidence for calcineurin activation with TAC (Wilkins et al., 2004; Molkentin, 2013). For the reasons noted above, neither of these indices is a specific marker of calcineurin activation because CaMKII activation causes derepression of intra-nuclear NFAT as well as MEF2. The only incontrovertible evidence of calcineurin-NFAT pathway activation is direct measurement of nuclear translocation of NFAT based on measurements of the nuclear and cytoplasmic NFAT fractions (Molkentin, 2013), as was done in our current study. We observed similar elevations of MCIP1 with calcineurin activation alone and with CaMKII activation in the absence of calcineurin activation (**Table 1**).

Transgenic inhibition/inactivation/overexpression of calcineurin by a variety of approaches was important in highlighting the potential role of calcineurin in cardiac growth and hypertrophy, but there are some limitations to these methods (Molkentin, 2013). For example, mice with an inducible loss of all cardiac myocyte calcineurin activity showed early lethality, reduced myocyte proliferation rates with fewer myocytes, greater myocyte apoptosis rates with acute pressure overload, and greater cell death and injury after ischaemia-reperfusion injury (Molkentin, 2013). Similarly, mice with transgenic overexpression of the calcineurin inhibitory domains of Cain or A-kinase anchoring protein 79 exhibited reduced heart weights with thinner left ventricular walls and reduced myofibrillar cross-sectional areas relative to controls (Molkentin, 2013). These findings indicate that calcineurin is important for normal myocyte development and functioning, so that transgenic models that inhibit calcineurin early in life may exhibit a non-specific impairment of growth and hypertrophic responses to a variety of stimuli. Such models may be unreliable indicators of the specific role of calcineurin activation in response to pressure overload in the normal adult heart. Similarly, much of the evidence that calcineurin induces pathological cardiac hypertrophy with adverse remodeling and heart failure comes from studies that used forced overexpression of a truncated CnA construct that was deficient in the regulatory domain that CaMKII phosphorylates to inhibit calcineurin (Molkentin, 2013). Due to their lack of calcineurin inhibition with CaMKII activation, such models likely overstate the calcineurin-related hypertrophic response and the adverse remodeling response to various stimuli, including TAC (Kreusser et al., 2014). One advantage of the data presented here regarding the role of calcineurin in pressure overload hypertrophy is that there was no genetic manipulation of the calcineurin pathway.

Clinical Implications

Our results may help explain why angiotensin converting enzyme inhibitors and angiotensin receptor blockers, although effective and frequently prescribed anti-hypertensive therapies, have not been shown to be more effective in reducing the morbidity and mortality of hypertensive heart disease than less specific anti-hypertensive agents, including diuretics (Psaty et al., 2003; Xue et al., 2015). This evidence suggests that for an equivalent blood pressure lowering effect, there is no convincing difference between anti-hypertensive therapies despite the putative anti-hypertrophic effects of newer and more expensive agents that target angiotensin and its receptors. Our results suggest that if the therapeutic aim is to prevent pressure-overload induced LVH and adverse remodeling, members of the CaMKII-HDAC4-MEF2 pathway, or its upstream activators, may be more effective targets for the development of new therapies. For example, the novel molecule 8MI, designed to interfere with MEF2-coregulator binding, not only prevents LVH and adverse LV remodeling after TAC but also reverses established LVH and adverse remodeling when commenced 5 weeks after TAC (Wei et al., 2017).

DATA AVAILABILITY STATEMENT

The raw data supporting the conclusion of this article will be made available by the authors, without undue reservation.

ETHICS STATEMENT

The animal study was reviewed and approved by The Garvan/St Vincent's Hospital Animal Ethics Committee.

AUTHOR CONTRIBUTIONS

Z-YY, HG, JW, YD, and SK conducted the experiments and analyzed the results. DF, BM, and RG contributed to the experimental protocols and critically reviewed the experimental results and the manuscript. MF conceived and designed the experiments and supervised their conduct. Z-YY and MF wrote the manuscript. All authors contributed to the article and approved the submitted version.

FUNDING

This research was supported by National Health and Medical Research Council of Australia Program Grants # 354400, 573732, and 526622.

SUPPLEMENTARY MATERIAL

The Supplementary Material for this article can be found online at: https://www.frontiersin.org/articles/10.3389/fcell.2021.639509/full#supplementary-material

REFERENCES

Adams, J. W., Sakata, Y., Davis, M. G., Sah, V. P., Wang, Y., Liggett, S. B., et al. (1998). Enhanced Galphaq signaling: a common pathway mediates cardiac hypertrophy and apoptotic heart failure. *Proc. Natl. Acad. Sci. U.S.A.* 95, 10140–10145. doi: 10.1073/pnas.95.17.10140

Akhter, S. A., Luttrell, L. M., Rockman, H. A., Iaccarino, G., Lefkowitz, R. J., and Koch, W. J. (1998). Targeting the receptor-Gq interface to inhibit in vivo pressure overload myocardial hypertrophy. *Science* 280, 574–577. doi: 10.1126/science.280.5363.574

Backs, J., Backs, T., Neef, S., Kreusser, M. M., Lehmann, L. H., Patrick, D. M., et al. (2009). The delta isoform of CaM kinase II is required for pathological cardiac hypertrophy and remodeling after pressure overload. *Proc. Natl. Acad. Sci. U.S.A.* 106, 2342–2347. doi: 10.1073/pnas.0813013106

Backs, J., Song, K., Bezprozvannaya, S., Chang, S., and Olson, E. N. (2006). CaM kinase II selectively signals to histone deacetylase 4 during cardiomyocyte hypertrophy. *J. Clin. Invest.* 116, 1853–1864. doi: 10.1172/jci27438

Backs, J., Worst, B. C., Lehmann, L. H., Patrick, D. M., Jebessa, Z., Kreusser, M. M., et al. (2011). Selective repression of MEF2 activity by PKA-dependent proteolysis of HDAC4. *J. Cell Biol.* 195, 403–415. doi: 10.1083/jcb.201105063

Bers, D. M. (2008). Calcium cycling and signaling in cardiac myocytes. *Annu. Rev. Physiol.* 70, 23–49. doi: 10.1146/annurev.physiol.70.113006.100455

Bush, E. W., Hood, D. B., Papst, P. J., Chapo, J. A., Minobe, W., Bristow, M. R., et al. (2006). Canonical transient receptor potential channels promote cardiomyocyte hypertrophy through activation of calcineurin signaling. *J. Biol. Chem.* 281, 33487–33496. doi: 10.1074/jbc.m605536200

Chiang, C. S., Huang, C. H., Chieng, H., Chang, Y. T., Chang, D., Chen, J. J., et al. (2009). The Ca(v)3.2 T-type Ca(2+) channel is required for pressure overload-induced cardiac hypertrophy in mice. *Circ. Res.* 104, 522–530. doi: 10.1161/circresaha.108.184051

Colella, M., Grisan, F., Robert, V., Turner, J. D., Thomas, A. P., and Pozzan, T. (2008). Ca2+ oscillation frequency decoding in cardiac cell hypertrophy: role of calcineurin/NFAT as Ca2+ signal integrators. *Proc. Natl. Acad. Sci. U.S.A.* 105, 2859–2864. doi: 10.1073/pnas.0712316105

D'Angelo, D. D., Sakata, Y., Lorenz, J. N., Boivin, G. P., Walsh, R. A., Liggett, S. B., et al. (1997). Transgenic Galphaq overexpression induces cardiac contractile failure in mice. *Proc. Natl. Acad. Sci. U.S.A.* 94, 8121–8126. doi: 10.1073/pnas.94.15.8121

De Koninck, P., and Schulman, H. (1998). Sensitivity of CaM kinase II to the frequency of Ca2+ oscillations. *Science* 279, 227–230. doi: 10.1126/science.279.5348.227

Ding, B., Price, R. L., Borg, T. K., Weinberg, E. O., Halloran, P. F., and Lorell, B. H. (1999). Pressure overload induces severe hypertrophy in mice treated with cyclosporine, an inhibitor of calcineurin. *Circ. Res.* 84, 729–734. doi: 10.1161/01.res.84.6.729

Dolmetsch, R. E., Lewis, R. S., Goodnow, C. C., and Healy, J. I. (1997). Differential activation of transcription factors induced by Ca2+ response amplitude and duration. *Nature* 386, 855–858. doi: 10.1038/386855a0

Eder, P., and Molkentin, J. D. (2011). TRPC channels as effectors of cardiac hypertrophy. *Circ. Res.* 108, 265–272. doi: 10.1161/circresaha.110.225888

Fielitz, J., Kim, M. S., Shelton, J. M., Qi, X., Hill, J. A., Richardson, J. A., et al. (2008). Requirement of protein kinase D1 for pathological cardiac remodeling. *Proc. Natl. Acad. Sci. U.S.A.* 105, 3059–3063. doi: 10.1073/pnas.0712265105

Finsen, A. V., Lunde, I. G., Sjaastad, I., Ostli, E. K., Lyngra, M., Jarstadmarken, H. O., et al. (2011). Syndecan-4 is essential for development of concentric myocardial hypertrophy via stretch-induced activation of the calcineurin-NFAT pathway. *PLoS One* 6:e28302. doi: 10.1371/journal.pone.0028302

Frey, N., and Olson, E. N. (2003). Cardiac hypertrophy: the good, the bad, and the ugly. *Annu. Rev. Physiol.* 65, 45–79. doi: 10.1146/annurev.physiol.65.092101.142243

Ginnan, R., Sun, L. Y., Schwarz, J. J., and Singer, H. A. (2012). MEF2 is regulated by CaMKIIdelta2 and a HDAC4-HDAC5 heterodimer in vascular smooth muscle cells. *Biochem. J.* 444, 105–114. doi: 10.1042/bj20120152

Harada, K., Komuro, I., Shiojima, I., Hayashi, D., Kudoh, S., Mizuno, T., et al. (1998a). Pressure overload induces cardiac hypertrophy in angiotensin II type 1A receptor knockout mice. *Circulation* 97, 1952–1959. doi: 10.1161/01.cir.97.19.1952

Harada, K., Komuro, I., Zou, Y., Kudoh, S., Kijima, K., Matsubara, H., et al. (1998b). Acute pressure overload could induce hypertrophic responses in the heart of angiotensin II type 1a knockout mice. *Circ. Res.* 82, 779–785. doi: 10.1161/01.res.82.7.779

Heineke, J., Auger-Messier, M., Correll, R. N., Xu, J., Benard, M. J., Yuan, W., et al. (2010). CIB1 is a regulator of pathological cardiac hypertrophy. *Nat. Med.* 16, 872–879. doi: 10.1038/nm.2181

Kehat, I., and Molkentin, J. D. (2010). Molecular pathways underlying cardiac remodeling during pathophysiological stimulation. *Circulation* 122, 2727–2735. doi: 10.1161/circulationaha.110.942268

Koitabashi, N., Aiba, T., Hesketh, G. G., Rowell, J., Zhang, M., Takimoto, E., et al. (2010). Cyclic GMP/PKG-dependent inhibition of TRPC6 channel activity and expression negatively regulates cardiomyocyte NFAT activation Novel mechanism of cardiac stress modulation by PDE5 inhibition. *J. Mol. Cell Cardiol.* 48, 713–724. doi: 10.1016/j.yjmcc.2009.11.015

Kreusser, M. M., and Backs, J. (2014). Integrated mechanisms of CaMKII-dependent ventricular remodeling. *Front. Pharmacol.* 5:36. doi: 10.3389/fphar.2014.00036

Kreusser, M. M., Lehmann, L. H., Keranov, S., Hoting, M. O., Oehl, U., Kohlhaas, M., et al. (2014). Cardiac CaM Kinase II genes delta and gamma contribute to adverse remodeling but redundantly inhibit calcineurin-induced myocardial hypertrophy. *Circulation* 130, 1262–1273. doi: 10.1161/circulationaha.114.006185

Kuwahara, K., Wang, Y., Mcanally, J., Richardson, J. A., Bassel-Duby, R., Hill, J. A., et al. (2006). TRPC6 fulfills a calcineurin signaling circuit during pathologic cardiac remodeling. *J. Clin. Invest.* 116, 3114–3126. doi: 10.1172/jci27702

Lehmann, L. H., Jebessa, Z. H., Kreusser, M. M., Horsch, A., He, T., Kronlage, M., et al. (2018). A proteolytic fragment of histone deacetylase 4 protects the heart from failure by regulating the hexosamine biosynthetic pathway. *Nat. Med.* 24, 62–72. doi: 10.1038/nm.4452

Levy, D., Garrison, R. J., Savage, D. D., Kannel, W. B., and Castelli, W. P. (1990). Prognostic implications of echocardiographically determined left ventricular mass in the Framingham Heart Study. *N. Engl. J. Med.* 322, 1561–1566. doi: 10.1056/nejm199005313222203

Li, H., Li, W., Gupta, A. K., Mohler, P. J., Anderson, M. E., and Grumbach, I. M. (2010). Calmodulin kinase II is required for angiotensin II-mediated vascular smooth muscle hypertrophy. *Am. J. Physiol. Heart Circ. Physiol.* 298, H688–H698.

Ling, H., Zhang, T., Pereira, L., Means, C. K., Cheng, H., Gu, Y., et al. (2009). Requirement for Ca2+/calmodulin-dependent kinase II in the transition from pressure overload-induced cardiac hypertrophy to heart failure in mice. *J. Clin. Invest.* 119, 1230–1240. doi: 10.1172/jci38022

McCalmon, S. A., Desjardins, D. M., Ahmad, S., Davidoff, K. S., Snyder, C. M., Sato, K., et al. (2010). Modulation of angiotensin II-mediated cardiac remodeling by the MEF2A target gene Xirp2. *Circ. Res.* 106, 952–960. doi: 10.1161/circresaha.109.209007

McKinsey, T. A. (2007). Derepression of pathological cardiac genes by members of the CaM kinase superfamily. *Cardiovasc. Res.* 73, 667–677. doi: 10.1016/j.cardiores.2006.11.036

Molkentin, J. D. (2000). Calcineurin and beyond: cardiac hypertrophic signaling. *Circ. Res.* 87, 731–738. doi: 10.1161/01.res.87.9.731

Molkentin, J. D. (2013). Parsing good versus bad signaling pathways in the heart: role of calcineurin-nuclear factor of activated T-cells. *Circ. Res.* 113, 16–19. doi: 10.1161/circresaha.113.301667

Molkentin, J. D., Lu, J. R., Antos, C. L., Markham, B., Richardson, J., Robbins, J., et al. (1998). A calcineurin-dependent transcriptional pathway for cardiac hypertrophy. *Cell* 93, 215–228. doi: 10.1016/s0092-8674(00)81573-1

Mudd, J. O., and Kass, D. A. (2008). Tackling heart failure in the twenty-first century. *Nature* 451, 919–928. doi: 10.1038/nature06798

Naqvi, N., Li, M., Calvert, J. W., Tejada, T., Lambert, J. P., Wu, J., et al. (2014). A proliferative burst during preadolescence establishes the final cardiomyocyte number. *Cell* 157, 795–807. doi: 10.1016/j.cell.2014.03.035

Nicks, A. M., Kesteven, S. H., Li, M., Wu, J., Chan, A. Y., Naqvi, N., et al. (2020). Pressure overload by suprarenal aortic constriction in mice leads to left ventricular hypertrophy without c-Kit expression in cardiomyocytes. *Sci. Rep.* 10:15318.

Niizeki, T., Takeishi, Y., Kitahara, T., Arimoto, T., Ishino, M., Bilim, O., et al. (2008). Diacylglycerol kinase-epsilon restores cardiac dysfunction under chronic pressure overload: a new specific regulator of Galpha(q) signaling cascade. *Am. J. Physiol. Heart Circ. Physiol.* 295, H245–H255.

Nikolaev, Y. A., Cox, C. D., Ridone, P., Rohde, P. R., Cordero-Morales, J. F., Vasquez, V., et al. (2019). Mammalian TRP ion channels are insensitive to membrane stretch. *J. Cell Sci.* 132:238360.

Ohba, T., Watanabe, H., Murakami, M., Takahashi, Y., Iino, K., Kuromitsu, S., et al. (2007). Upregulation of TRPC1 in the development of cardiac hypertrophy. *J. Mol. Cell Cardiol.* 42, 498–507. doi: 10.1016/j.yjmcc.2006.10.020

Onohara, N., Nishida, M., Inoue, R., Kobayashi, H., Sumimoto, H., Sato, Y., et al. (2006). TRPC3 and TRPC6 are essential for angiotensin II-induced cardiac hypertrophy. *EMBO J.* 25, 5305–5316. doi: 10.1038/sj.emboj.7601417

Paradis, P., Dali-Youcef, N., Paradis, F. W., Thibault, G., and Nemer, M. (2000). Overexpression of angiotensin II type I receptor in cardiomyocytes induces cardiac hypertrophy and remodeling. *Proc. Natl. Acad. Sci. U.S.A.* 97, 931–936. doi: 10.1073/pnas.97.2.931

Passier, R., Zeng, H., Frey, N., Naya, F. J., Nicol, R. L., McKinsey, T. A., et al. (2000). CaM kinase signaling induces cardiac hypertrophy and activates the MEF2 transcription factor in vivo. *J. Clin. Invest.* 105, 1395–1406. doi: 10.1172/jci8551

Psaty, B. M., Lumley, T., Furberg, C. D., Schellenbaum, G., Pahor, M., Alderman, M. H., et al. (2003). Health outcomes associated with various antihypertensive therapies used as first-line agents: a network meta-analysis. *JAMA* 289, 2534–2544. doi: 10.1001/jama.289.19.2534

Rockman, H. A., Wachhorst, S. P., Mao, L., and Ross, J. Jr. (1994). ANG II receptor blockade prevents ventricular hypertrophy and ANF gene expression with pressure overload in mice. *Am. J. Physiol.* 266, H2468–H2475.

Seth, M., Zhang, Z. S., Mao, L., Graham, V., Burch, J., Stiber, J., et al. (2009). TRPC1 channels are critical for hypertrophic signaling in the heart. *Circ. Res.* 105, 1023–1030. doi: 10.1161/circresaha.109.206581

Spassova, M. A., Hewavitharana, T., Xu, W., Soboloff, J., and Gill, D. L. (2006). A common mechanism underlies stretch activation and receptor activation of TRPC6 channels. *Proc. Natl. Acad. Sci. U.S.A.* 103, 16586–16591. doi: 10.1073/pnas.0606894103

Tamargo, J., and Lopez-Sendon, J. (2011). Novel therapeutic targets for the treatment of heart failure. *Nat. Rev. Drug Discov.* 10, 536–555. doi: 10.1038/nrd3431

Tang, C. M., Liu, F. Z., Zhu, J. N., Fu, Y. H., Lin, Q. X., Deng, C. Y., et al. (2016). Myocyte-specific enhancer factor 2C: a novel target gene of miR-214-3p in suppressing angiotensin II-induced cardiomyocyte hypertrophy. *Sci. Rep.* 6:36146.

Watanabe, H., Murakami, M., Ohba, T., Ono, K., and Ito, H. (2009). The pathological role of transient receptor potential channels in heart disease. *Circ. J.* 73, 419–427. doi: 10.1253/circj.cj-08-1153

Wei, J., Joshi, S., Speransky, S., Crowley, C., Jayathilaka, N., Lei, X., et al. (2017). Reversal of pathological cardiac hypertrophy via the MEF2-coregulator interface. *JCI Insight* 2:e91068.

Wettschureck, N., Rutten, H., Zywietz, A., Gehring, D., Wilkie, T. M., Chen, J., et al. (2001). Absence of pressure overload induced myocardial hypertrophy after conditional inactivation of Galphaq/Galpha11 in cardiomyocytes. *Nat. Med.* 7, 1236–1240. doi: 10.1038/nm1101-1236

Wiesner, R. J., Ehmke, H., Faulhaber, J., Zak, R., and Ruegg, J. C. (1997). Dissociation of left ventricular hypertrophy, beta-myosin heavy chain gene expression, and myosin isoform switch in rats after ascending aortic stenosis. *Circulation* 95, 1253–1259. doi: 10.1161/01.cir.95.5.1253

Wilkins, B. J., Dai, Y. S., Bueno, O. F., Parsons, S. A., Xu, J., Plank, D. M., et al. (2004). Calcineurin/NFAT coupling participates in pathological, but not physiological, cardiac hypertrophy. *Circ. Res.* 94, 110–118. doi: 10.1161/01.res.0000109415.17511.18

Wilkins, B. J., and Molkentin, J. D. (2004). Calcium-calcineurin signaling in the regulation of cardiac hypertrophy. *Biochem. Biophys. Res. Commun.* 322, 1178–1191. doi: 10.1016/j.bbrc.2004.07.121

Wu, X., Eder, P., Chang, B., and Molkentin, J. D. (2010). TRPC channels are necessary mediators of pathologic cardiac hypertrophy. *Proc. Natl. Acad. Sci. U.S.A.* 107, 7000–7005. doi: 10.1073/pnas.1001825107

Xue, H., Lu, Z., Tang, W. L., Pang, L. W., Wang, G. M., Wong, G. W., et al. (2015). First-line drugs inhibiting the renin angiotensin system versus other first-line antihypertensive drug classes for hypertension. *Cochrane Database Syst. Rev.* 1:CD008170.

Zarain-Herzberg, A., Fragoso-Medina, J., and Estrada-Aviles, R. (2011). Calcium-regulated transcriptional pathways in the normal and pathologic heart. *IUBMB Life* 63, 847–855. doi: 10.1002/iub.545

Zhang, R., Khoo, M. S., Wu, Y., Yang, Y., Grueter, C. E., Ni, G., et al. (2005). Calmodulin kinase II inhibition protects against structural heart disease. *Nat. Med.* 11, 409–417. doi: 10.1038/nm1215

Zhang, T., Kohlhaas, M., Backs, J., Mishra, S., Phillips, W., Dybkova, N., et al. (2007). CaMKIIdelta isoforms differentially affect calcium handling but similarly regulate HDAC/MEF2 transcriptional responses. *J. Biol. Chem.* 282, 35078–35087. doi: 10.1074/jbc.m707083200

Zhang, T., Maier, L. S., Dalton, N. D., Miyamoto, S., and Ross, J. Jr. (2003). The deltaC isoform of CaMKII is activated in cardiac hypertrophy and induces dilated cardiomyopathy and heart failure. *Circ. Res.* 92, 912–919. doi: 10.1161/01.res.0000069686.31472.c5

Zhang, W., Kowal, R. C., Rusnak, F., Sikkink, R. A., Olson, E. N., and Victor, R. G. (1999). Failure of calcineurin inhibitors to prevent pressure-overload left ventricular hypertrophy in rats. *Circ. Res.* 84, 722–728. doi: 10.1161/01.res.84.6.722

Zhu, W., Zou, Y., Shiojima, I., Kudoh, S., Aikawa, R., Hayashi, D., et al. (2000). Ca2+/calmodulin-dependent kinase II and calcineurin play critical roles in endothelin-1-induced cardiomyocyte hypertrophy. *J. Biol. Chem.* 275, 15239–15245. doi: 10.1074/jbc.275.20.15239

Zou, Y., Hiroi, Y., Uozumi, H., Takimoto, E., Toko, H., Zhu, W., et al. (2001). Calcineurin plays a critical role in the development of pressure overload-induced cardiac hypertrophy. *Circulation* 104, 97–101. doi: 10.1161/01.cir.104.1.97

Conflict of Interest: The authors declare that the research was conducted in the absence of any commercial or financial relationships that could be construed as a potential conflict of interest.

frontiers
in Cell and Developmental Biology

REVIEW
published: 26 February 2021
doi: 10.3389/fcell.2021.642840

Sensing and Responding of Cardiomyocytes to Changes of Tissue Stiffness in the Diseased Heart

Juliane Münch[1] and Salim Abdelilah-Seyfried[1,2]*

[1] Institute of Biochemistry and Biology, University of Potsdam, Potsdam, Germany, [2] Institute of Molecular Biology, Hannover Medical School, Hannover, Germany

Cardiomyocytes are permanently exposed to mechanical stimulation due to cardiac contractility. Passive myocardial stiffness is a crucial factor, which defines the physiological ventricular compliance and volume of diastolic filling with blood. Heart diseases often present with increased myocardial stiffness, for instance when fibrotic changes modify the composition of the cardiac extracellular matrix (ECM). Consequently, the ventricle loses its compliance, and the diastolic blood volume is reduced. Recent advances in the field of cardiac mechanobiology revealed that disease-related environmental stiffness changes cause severe alterations in cardiomyocyte cellular behavior and function. Here, we review the molecular mechanotransduction pathways that enable cardiomyocytes to sense stiffness changes and translate those into an altered gene expression. We will also summarize current knowledge about when myocardial stiffness increases in the diseased heart. Sophisticated *in vitro* studies revealed functional changes, when cardiomyocytes faced a stiffer matrix. Finally, we will highlight recent studies that described modulations of cardiac stiffness and thus myocardial performance *in vivo*. Mechanobiology research is just at the cusp of systematic investigations related to mechanical changes in the diseased heart but what is known already makes way for new therapeutic approaches in regenerative biology.

Keywords: mechanobiology, tissue stiffness, cardiomyocyte, heart regeneration, titin, collagen, agrin, extracellular matrix

Edited by:
Jing Zhou,
Peking University, China

Reviewed by:
Nazha Hamdani,
Ruhr University Bochum, Germany
Xiaohai Zhou,
University of California, San Diego,
United States

***Correspondence:**
Salim Abdelilah-Seyfried
salim.seyfried@uni-potsdam.de

Specialty section:
This article was submitted to Cell Adhesion and Migration, a section of the journal Frontiers in Cell and Developmental Biology

Received: *16 December 2020*
Accepted: *09 February 2021*
Published: *26 February 2021*

Citation:
Münch J and Abdelilah-Seyfried S (2021) Sensing and Responding of Cardiomyocytes to Changes of Tissue Stiffness in the Diseased Heart. Front. Cell Dev. Biol. 9:642840. doi: 10.3389/fcell.2021.642840

INTRODUCTION

The heart is both an electrical and mechanical organ. A heartbeat is initiated when pacemaker cells at the sinus venosus produce action potentials. This triggers the contraction of cardiomyocytes, which generates the mechanical force required to move blood throughout the body. During each contractile cycle of the heart, cardiomyocytes experience various types of forces, including the hemodynamic pressure by blood, contraction-induced elongation/shortening, and passive elasticity/stiffness from the surrounding extracellular matrix (ECM). Sensitivity of cardiomyocytes to changes in these physical parameters is critical and the mechanical work of the heart has to be adjusted to the levels needed for the physiological blood-based transport of nutrients, gases, and metabolic waste products. Myocardial infarction and cardiomyopathies are characterized by cardiac remodeling, a process that includes increases of cardiomyocyte cell size (hypertrophy), fibroblast proliferation, and the deposition of ECM proteins. These changes alter tissue stiffness and extracellular mechanical stimulation of cardiomyocytes, which affects their biomechanical signaling and heart function. Although cardiomyocytes possess the machinery to sense those mechanical alterations in the diseased heart, ultimately, this does not prevent a reduced cardiac function. However, we are just beginning to understand how biomechanical signaling changes in the diseased heart affect cardiomyocytes. This knowledge promises the development of regenerative cardiac therapies. Many of the proteins covered in this review have been linked to various types of cardiomyopathies. This clearly demonstrates the relevance of cardiac mechanobiology for both normal physiology and for understanding the etiology of cardiomyopathies. Due to the brevity of this review article, we refer to other review articles that cover the disease aspects of these proteins (Zemljic-Harpf et al., 2009; Kamdar and Garry, 2016; Singh and Robbins, 2018).

Here, we review the current state and rapid advances in the field of cardiomyocyte mechanobiology. These have also contributed to a better understanding of myocardial diseases and led to the discovery that cardiac regenerative processes can be modulated by changing mechanical properties of the heart. First, we focus on cytoskeletal and extracellular factors that determine physiological myocardial stiffness. Understanding how changes of tissue stiffness affect the diseased heart requires a clear understanding of which cellular components sense alterations of extracellular mechanical stimuli and transduce these into biochemical signaling and gene expression. For instance, mechanosensitive YAP signaling is highly responsive to matrix stiffness changes in cardiomyocytes and potently regulates cardiomyocyte proliferation (Mosqueira et al., 2014; Bassat et al., 2017; Wang et al., 2020). We will report about the effects of stiffness changes on cardiomyocyte performance, such as sarcomere assembly and contraction, and discuss biomechanical cellular signaling that causes abnormal cardiomyocyte behaviors. Then, we integrate this information and discuss what approaches have been taken to modulate the ECM to improve cardiac healing. Although cardiac mechanobiology research is emerging rapidly, we only have a limited knowledge about how to modulate the ECM in the diseased heart. Our review discusses molecular mechanisms that determine and sense stiffness changes in the heart and highlights disease-related alterations.

INTRA- AND EXTRACELLULAR COMPONENTS DETERMINE MYOCARDIAL STIFFNESS

Cardiac conduction imposes a constant mechanical deformation on the myocardium. Intra- and extracellular factors contribute to tissue stiffness, a cardiac mechanical property that allows cardiomyocytes to withstand constant mechanical impact. Stiffness is defined as the resistance of an object to elongation or shortening. The measure of stiffness is the elastic modulus or Young's modulus E, which describes the relation between tensile stress and axial strain of a material (unit in Pa). During the cardiac contractile cycle, the passive stiffness of the myocardium determines its maximal diastolic capacity/volume.

Cardiac stiffness changes dramatically during early life. In a comparative study, the murine heart was found to stiffen progressively between embryonic development day E2 with values of < 1 kPa until E14 with a 10-fold increase in stiffness, which is a value that was measured also in neonate and adult myocardium (Majkut et al., 2013). Concomitantly, there are comparable increases of cardiac actomyosin contractile proteins, adhesion proteins, and the calcium pump sarcoendoplasmic reticulum calcium transport ATPase (SERCA), which are all involved in the excitation and contraction coupling system of the heart (Majkut et al., 2013).

Other studies revealed that Young's modulus values vary in different vertebrate hearts (Ward and Iskratsch, 2020). Berry et al. reported an elastic modulus of adult rat hearts of around 18 ± 2 kPa (Berry et al., 2006). Similarly, Bhana et al. revealed tissue stiffness values of 4–11.4 kPa for native neonatal rat myocardium and 11.9–46.2 kPa for adult rat myocardium. Cardiomyocytes derived from human-induced pluripotent stem cells exhibited a stiffness with a Young's modulus of about 1.25 kPA, which decreased upon cytochalasin D-induced filamentous actin depolymerization (Pires et al., 2019).

The maintenance of physiological levels of cardiac stiffness not only determines overall ventricular diastolic function but also ensures proper cardiomyocyte functionality. When neonatal rat myocardium was cultured on substrates with a stiffness value of an adult heart, cardiomyocytes acquired cell morphologies and functions that were characteristic of a differentiated myocardium (Bhana et al., 2010). Similarly, Engler et al. found embryonic cardiomyocytes had an optimal contractility on matrices with stiffness values similar to the developing myocardium (Engler et al., 2008) and neonatal rat cardiomyocytes matured best on substrates with stiffness values of native, uninjured myocardium (Jacot et al., 2008). Hence, physiological stiffness of cardiac tissues is a crucial environmental mechanical cue that affects the development and mechanical properties of myocardial cells.

Extra- and intracellular components contribute to myocardial stiffness. On its extracellular side, cardiomyocytes are embedded within an ECM with a characteristic composition of glycosaminoglycans, proteoglycans, collagens, laminins, and fibronectins. These ECM proteins determine cell adhesion, cell motility, and contribute to outside-in signaling into cardiomyocytes (Chin et al., 2019). Strikingly, protein composition and levels of cross-linking change during development or disease, which affects the physiological stiffness of the heart (Ward and Iskratsch, 2020). Collagens are particularly important players in this context due to their ability to form thick, stiff and long fibrils, that can be densely packed to contribute to tissue stiffness in many organs (Tang, 2020). Changes in cardiac stiffness that occur during transition from neonatal to adult hearts have been attributed to the total amount of collagen and to the ratio of collagen type I versus collagen type III. Collagen type I provides rigidity while collagen type III increases elasticity (Marijianowski et al., 1994). Also, high levels of collagen crosslinking by the enzyme lysyl oxidase and high ratios of glycosylated lysine or hydroxylysine residues contribute to a reduced myocardial compliance (Ward and Iskratsch, 2020). Interestingly, lysyl oxidase upregulation and increased crosslinking enhanced cardiac stiffness and resulted in diastolic dysfunction (López et al., 2010).

Intracellular properties of cardiomyocytes also contribute to cardiac stiffness. The main regulator of intracellular stiffness of cardiomyocytes is titin, a giant protein that spans half of the sarcomere (Gregorio et al., 1999) and that underlies the myofibrillar passive tension response to stretch in striated muscle cells (Cazorla et al., 2000). Genetic alterations of the titin gene or developmental/disease-triggered posttranslational modifications affect passive myocardial stiffness. This has been extensively reviewed elsewhere (Granzier and Labeit, 2004; Krüger et al., 2009; LeWinter and Granzier, 2014; Tharp et al., 2019).

Titin comes in two isoforms within the mammalian heart (Freiburg et al., 2000). The more compliant isoform N2BA (>3.2 MDa) is predominant in the developing heart of several mammalian species and chick while the smaller and stiffer isoform N2B (3.0 MDa) is present shortly after birth. It has been suggested that titin isoform switching, together with isoform switching of troponin I and myosin, determines passive stiffness changes and functional transitions of the heart after birth (Lahmers et al., 2004; Opitz et al., 2004; Warren et al., 2004; Opitz and Linke, 2005). Direct triggers of these changes are genetic, species-specific (Krüger et al., 2006) or altered humoral factors (reviewed in Krüger and Linke, 2009).

While the overall amount of titin in cardiomyocytes is similar, the ratio of both isoforms varies in the myocardium of different mammalian species (Cazorla et al., 2000). Wu et al. examined the titin subtypes within the myocardium of the mouse ventricular wall, as well as the bovine left atrium and left ventricle, and found different ratios of N2BA and N2B. This study demonstrated that, under physiological conditions, a higher ratio of the shorter N2B isoform together with increases of collagen levels resulted in higher myocardial stiffness (Wu et al., 2000).

Microtubule networks and intermediate filaments also contribute to myocardial elasticity. Microtubules are supramolecular assemblies of α/β-tubulin heterodimers that are organized as highly dynamic filaments with multiple roles in mitosis, cell motility, or intracellular molecular transport. Within cardiomyocytes, microtubules generate resistance to the compressive load of the heart, which does not only depend on microtubule density but also on specific de-tyrosinations, which allow crosslinking with intermediate filaments. This affects myocardial stiffness and viscoelasticity (Robison et al., 2016; Ward and Iskratsch, 2020). In cardiac muscle, desmin is the predominant intermediate filament, which contributes to passive stiffness of cardiomyocytes and provides a link from the Z-disk to costameres (Ward and Iskratsch, 2020). Its filaments form a network surrounding myofibrils at the Z-band and in the intermyofibrillar space (Tokuyasu, 1983). During cardiac diseases, desmin is modified by phosphorylation or in expression levels (Ward and Iskratsch, 2020). The cytoskeletal components actin and myosin are required in cardiomyocytes to generate contractile force but play only a minor role in contributing to myocardial passive stiffness. Hence, several extra- and intracellular components, including titin and collagens, enable cardiomyocytes to maintain the physiological stiffness, which is required to sustain the mechanical pressure upon heart beating.

PATHOLOGICAL CHANGES IN CARDIAC STIFFNESS IMPAIR THE FUNCTION OF THE DISEASED HEART

The etiology of many cardiac pathologies has remained unresolved. However, increasing evidence points at a contribution of defective biomechanics in these diseases. These findings raise the question whether changes in mechanical properties of cardiomyocytes are causative to cardiac pathologies or whether pathologies affect biomechanical properties of cardiomyocytes. While it has been difficult to resolve the causality of events in many cardiac pathologies, increasing evidence suggests that physiological levels of cardiac stiffness are disturbed in many instances of cardiac diseases. Both, the cardiac ECM and intracellular components (titin) contribute to physiological levels of cardiac stiffness, which is disturbed in many cardiac diseases (Tharp et al., 2019). The roles of biomechanics-related cardiomyocyte gene mutations in the etiologies of cardiomyopathies have extensively been reviewed elsewhere (Brodehl et al., 2018; Ware and Cook, 2018; Tharp et al., 2019). Here, we mainly focus on cardiac diseases due to myocardial stiffness changes resulting from ischemic heart diseases, hypertension, or cardiac hypertrophy. Myocardial infarction caused by an obstruction of coronary vessels results in the massive death of cardiomyocytes. This triggers an immense inflammatory response. The adult mammalian heart lacks the capacity of myocardial regeneration. Instead, the loss of myocardium in the infarcted ischemic region causes a permanent replacement by a rigid fibrotic scar. This is crucial to preserve the structure of the heart and prevent ventricular rupture (Frangogiannis, 2019). However, fibrotic tissue also accumulates in other conditions of the heart such as pressure overload, metabolic dysfunction, and aging (Hinderer and Schenke-Layland, 2019). Cardiac fibrosis is characterized by increased expression and crosslinking of ECM proteins, which dramatically change myocardial stiffness. The main contributors to fibrotic tissue are cardiac fibroblasts, which secrete ECM proteins including collagens, fibronectin, laminin, elastin, fibrillin, proteoglycans, and glycoproteins. But fibroblasts also release enzymes such as matrix metalloproteases (MMPs) and tissue inhibitors of metalloproteinases (TIMPs), which modulate the ECM (Fan et al., 2012). Similarly, macrophages are gaining increased attention as an ECM-producing and -modulating cell type. Macrophages not only possess a crucial role in secreting MMPs but also secrete ECM proteins (O'Rourke et al., 2019; Simões et al., 2020). Different reports showed that fibrosis increases cardiac tissue stiffness. Coronary artery ligation-induced myocardial infarction in rat hearts resulted in fibrotic tissue with a Young's modulus of 55 ± 15 kPA (Berry et al., 2006). Infarcted myocardium in sheep hearts showed increased stiffness within 1–2 weeks upon myocardial infarction but later returned to physiological levels (Gupta et al., 1994). Yamamoto et al. (2002)

examined hearts from rats fed on a high-salt diet that had died from heart failure, which included hypertension, left ventricular hypertrophy, and fibrosis. Increased cardiac stiffness in those hearts was attributed to collagen accumulation and increased collagen-crosslinking rather than to hypertrophic cardiomyocytes (Yamamoto et al., 2002).

The giant molecule titin is the main intracellular regulator of passive tension in cardiomyocytes. Beside the ratio of N2B/N2BA isoforms, passive resistance of cardiomyocytes also depends on posttranslational titin modifications. Most studies reported important phosphosites within the "spring-like" I-band domain (Hidalgo et al., 2009; Hamdani et al., 2017; Tharp et al., 2019.). Increasing phosphorylations by PKCα at the proline-glutamate-valine-lysine (PEVK) spring element within the I-band domain cause increased myocardial stiffness (Hidalgo et al., 2009). In contrast, phosphorylation at the elastic I-band domain N2B-unique sequence (N2Bus) reduces titin tension and passive stiffness of cardiomyocytes (Hidalgo et al., 2009; Krüger et al., 2009, Kötter et al., 2013; Hamdani et al., 2017). In a rat model of concentric hypertrophy following pressure-overload, cardiac stiffness increased due to alterations in both aberrant extracellular collagen and reduced titin phosphorylation at the N2Bus domain. This resulted in diastolic dysfunction (Røe et al., 2017). Kötter et al. also revealed a crucial function for titin in the infarcted heart. Passive tension of cardiomyocytes, a contributor to myocardial stiffness, was increased as early as 3 days post myocardial infarction. Although the ratio of N2B/N2BA titin isoforms was unchanged at 3 days post myocardial infarction, phosphorylation on the PEVK spring element increased and phosphorylation of the N2Bus region decreased (Kötter et al., 2016). Interestingly, these titin modifications in the infarcted hearts were mediated by the inflammatory cytokine interleukin-6 (IL-6) (Kötter et al., 2016), which is expressed in the early inflammatory phase 3–72 h post myocardial infarction (Frangogiannis, 2006). Hence, the immune system contributes to the adaptation of myocardial stiffness in the infarcted heart.

The intracellular stiffness factors desmin and α-actinin are additional players in cardiac diseases. In a mouse model of diastolic dysfunction, levels of desmin and α-actinin increased at Z-disks. The authors suggested this to be a response to the increased strain to cardiomyocytes in this pathologic condition (Sheng et al., 2016), which points at a potential involvement of desmin in the cardiomyocyte response to mechanical changes. This would be a role in addition to its main function in sarcomere integrity and cell survival in several cardiac diseases (Hein et al., 2000). Indeed, the loss of desmin resulted in increased passive tissue stiffness in soleus muscle (Anderson et al., 2001). Further studies are required to understand the different roles of desmin in modulating myocardial passive stiffness versus adjusting myofibril and sarcomere integrity. In addition to the study of Sheng et al., also Sumita Yoshikawa et al. implicated actomyosin in pathological stiffness changes. Residual actin-myosin cross-bridge formation lead to increased passive cardiomyocyte stiffness in hypertrophic hearts (Sumita Yoshikawa et al., 2013). This is interesting because actomyosin networks play a rather minor role in influencing passive myocardial stiffness under physiological conditions.

The importance of physiological cardiac stiffness was also reported in zebrafish mutants that lacked caveolin-1, the main structural protein of caveolae. Caveolae are small membrane invaginations and are protective to mechanical stress by providing a membrane buffer when cells become stretched. The loss of caveolin-1 diminished caveolae formation in mice and also in the zebrafish heart (Grivas et al., 2020). Hearts that lacked caveolae showed an increased stiffness compared to control hearts and were functionally impaired (Grivas et al., 2020). This study further revealed a transient reduction in injury-induced cardiomyocyte proliferation in *caveolin-1* mutant hearts. However, overall regeneration was not affected. This was in contrast with previous observations, based on a different *caveolin-1* mutant, in which cardiomyocyte proliferation and cardiac regeneration were disturbed. Yet, mechanical properties and cardiac function were not examined in those animals (Cao et al., 2016). Findings of both studies raised the intriguing question, how modifications of physiological stiffness and/or reduced cardiac function *per se* influence regenerative capacities in zebrafish and mammalian hearts.

Changes in cardiac stiffness are hallmark characteristics of various cardiac diseases. Hearts of patients suffering from cardiac hypertrophy by pressure overload showed increased stiffness at the level of cardiomyocytes and ECM. This study demonstrated that both intra- and extracellular changes of biomechanical properties of the heart were affected in this condition (Chaturvedi et al., 2010).

Similarly, hearts of patients with hypertension and heart failure with a preserved ejection fraction (HFpEF), one of the main causes of heart failure, presented with increased myocardial passive stiffness together with ventricular remodeling and abnormalities in left ventricular diastolic function (Zile et al., 2004, 2011, 2015). This correlated with a decrease in titin phosphorylation on its PEVK spring and N2B elements and augmented total collagen deposition.

To date, we are lacking treatment options to avoid the detrimental changes in cardiac stiffness However, studies in mouse demonstrated that cardiac stiffness can be limited by exercise. In a mouse model with HFpEF, the authors examined the effects of free wheel running exercise on diastolic stiffness. This revealed a beneficial effect that was caused by beneficial phosphorylation changes in the PEVK and N2B spring elements of titin, which control stiffness properties of this important mechanical sarcomeric protein. In comparison, exercise did not decrease stiffness of the ECM. In pharmacological experiments, the authors used the drug ivabradine to lower the heart rate, which mimics one of the physiological effects of effective exercise. However, this treatment did not change the passive stiffness of the heart in the HFpEF mouse model. Taken together, this study demonstrated a beneficial effect of exercise-induced regulatory phosphorylations in titin that softens cardiac stiffness (Slater et al., 2017).

In conclusion, several reports showed that cardiac stiffness increases and cardiac functionality is severely impaired within the diseased heart (Gupta et al., 1994; Chaturvedi et al., 2010; Kötter et al., 2016; Sheng et al., 2016; Røe et al., 2017). These findings point at a vicious cycle in which increased passive stiffness of the heart impairs beneficial exercise, which again worsens cardiac stiffness due to pathological changes in ECM composition (mainly collagen) or negative regulatory modifications of titin.

Unlike most cardiac diseases characterized by increased tissue stiffness, patients suffering from dilated cardiomyopathy (DCM) present with reduced myocardial passive tension causing ventricular enlargement and impaired systolic function. DCM frequently results from genetic defects in the titin gene (reviewed in Tharp et al., 2019). However, lowered myocardial stiffness of end-stage heart failure patients suffering from non-ischemic DCM has also been attributed to an increased N2B-to-N2BA ratio. Hence, the more compliant large isoform of titin (N2BA) was augmented at the expense of the stiffer (N2B) isoform (Nagueh et al., 2004). Similarly, an increased N2B-to-N2BA protein ratio has been reported in failing human DCM hearts (Makarenko et al., 2004). This resulted in reduced passive stiffness of isolated myofibrils. The authors further showed that, in DCM hearts, the contribution of titin to passive stiffness of cardiomyocytes was strongly reduced. This finding suggests that the dominance of the compliant titin isoform counteracts stiffness increases within the whole ventricle caused by increased fibrosis (Makarenko et al., 2004).

We still lack a detailed time course of stiffness changes under different cardiac pathological conditions. In contrast to the previous studies, research in a canine model revealed that the passive elastic modulus decreased by 41% shortly (1 h) after myocardial infarction. Unfortunately, this study lacked data from later timepoints (Forrester et al., 1972). These studies suggest that changes to myocardial stiffness need to be considered in the context of the progression state of a pathology. Hence, detailed studies are required to understand myocardial stiffness changes during the initiation and progression of specific cardiac diseases. Altogether, much will be learned from understanding the exact roles of intra- and extracellular molecular modifiers of tissue compliance and from characterizing different cardiac cell types modulating ECM stiffness to which collagen deposition strongly contributes. Functional studies are required to modulate different regions within diseased or injured cardiac tissue to better understand the extracellular mechanical changes that face the affected myocardium.

FORCE SENSING AND TRANSMISSION WITHIN CARDIOMYOCYTES

The heartbeat constantly exposes cardiomyocytes to physical forces by stress and strain. In the previous chapter, we discussed changes of ECM composition, titin phosphorylation, and cardiac tissue elasticity that occur within the diseased heart. These tissue stiffness changes are detected by cardiomyocytes and converted into gene expression changes. Here, we will focus on the machinery that is involved in these mechanosensitive signal transduction processes.

The mechanotransduction processes which translate mechanical stimuli into cellular signals are sensitive to changes in shear stress, cell adhesion forces, substrate rigidity, membrane or cytoskeletal stretching, and compression due to pressure. Focal adhesion integrin-based multi-protein complexes are crucial for these processes and mediate inside-out and outside-in signaling in response to mechanical stimuli or signals from the ECM or neighboring cells. Focal adhesions also couple the mechanical tension between ECM and the cytoskeleton (Iskratsch et al., 2014; Petridou et al., 2017). Within the heart, mechanical coupling of the extracellular space with the sarcomere is established by costameres, which are specialized focal adhesion protein complexes that connect the sarcolemma of cardiomyocytes to sarcomeric cytoskeletal components (**Figure 1A**) (Ervasti, 2003). Costameres are sites of adhesion and force transmission between cardiomyocytes and stabilize those sites that are impacted by lateral forces, thereby protecting the labile sarcolemma (Hersch et al., 2013). Costameres transmit cytoskeletal contractile forces that are passing across the sarcolemma, the ECM, and finally to neighboring cells. It has been hypothesized that this could be crucial for the uniform contraction of adjacent cardiomyocytes (Samarel et al., 2013). Similar to focal adhesion complexes in other cell types, costameres of the striated muscle contain structural proteins and vinculin is a main component together with talin, α-actinin, β1-integrin, and desmin, which is the physical link between Z-line and sarcolemma (Ervasti, 2003). Integrins are crucial for transmitting mechanical cues from the ECM to intracellular structures, via their adapter proteins talin, α-actinin, and vinculin (**Figure 1A**). These proteins act in a clutch-like manner and the outside-in transmission of mechanical forces depends on the composition and amount of these adaptor proteins (Elosegui-Artola et al., 2016). Interestingly, the presence of vinculin and β-integrins and their association with costameres is directly influenced by mechanical forces (Sharp et al., 1997). Costameres also include structural proteins of the dystrophin-glycoprotein complex, which includes dystrophin, sarcoglycans, dystroglycans, and syntrophins (**Figure 1A**). The dystrophin-glycoprotein complex physically links the ECM with the cytoskeleton (actomyosin networks). α-dystroglycan directly connects with the ECM protein laminin, whereas β-dystroglycan spans the membrane and is linked to the intracellular components of the dystrophin-glycoprotein complex (Peter et al., 2011) (**Figure 1A**).

Upon force transmission into cardiomyocytes, different biochemical downstream signaling pathways are involved in the induction of gene expression changes. At the costamere, integrins recruit and activate different signaling kinases, including focal adhesion kinase (FAK), Rho-associated coiled-coil containing protein kinases (ROCKs), and mitogen-activated protein kinases (MAPKs) (Samarel, 2005) (**Figure 1B**). *In vitro* studies on neonatal rat ventricular myocytes revealed the importance of FAK complex signaling for the response of cardiomyocytes to mechanical stretching. FAK became more strongly phosphorylated and changed its subcellular localization when cardiomyocytes were stretched (Torsoni et al., 2003). Signaling by FAK also regulated the activation of MEF2 and Jun-C in a model of mechanical stress within isolated rat ventricular myocytes (Nadruz et al., 2005). Mef2 and Jun-C had already been shown to activate a hypertrophic genetic program. As a response to mechanical stress, FAK signaling coordinated the activity of NF-kB in cardiomyocytes (Crosara-Alberto et al., 2009).

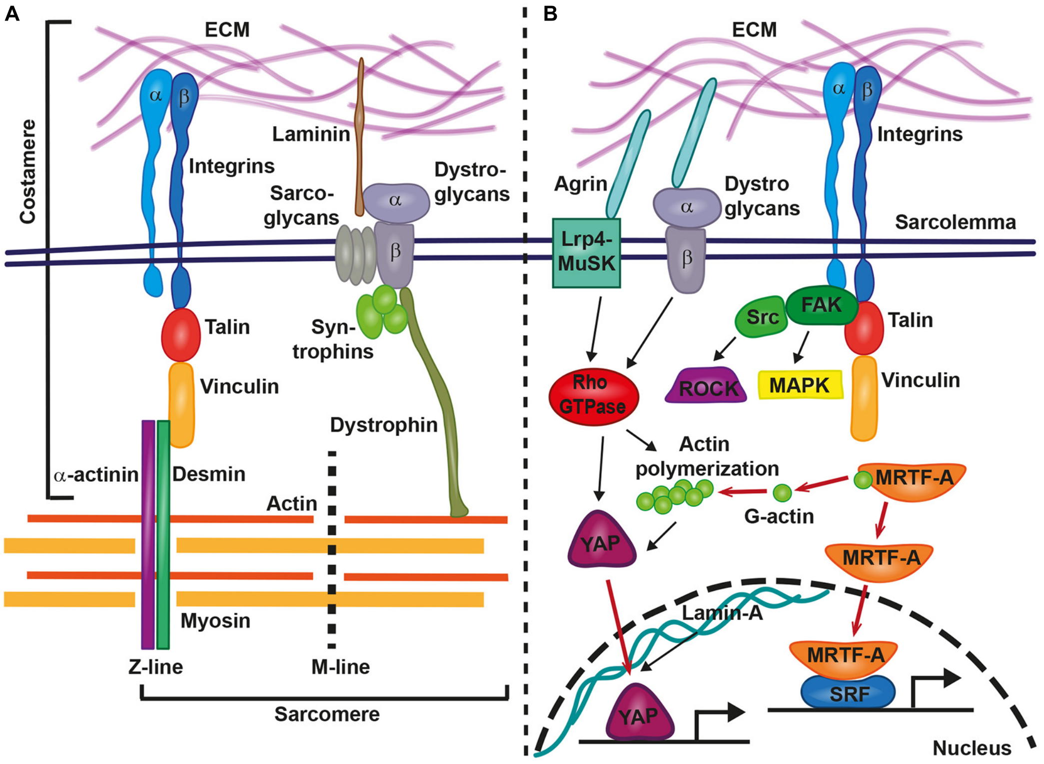

FIGURE 1 | Involvement of costameres in mechanotransduction in cardiomyocytes. Costameres are composed of structural and signaling proteins. These structures provide the link between extracellular matrix (ECM) and the sarcomere **(A)** or result in the activation of various signaling cascades, that lead to the translocation of transcription factors to the nucleus and gene transcription changes **(B)**. Inside-out and outside-in signaling is mediated by integrins and the structural proteins talin, vinculin, α-actinin, and desmin provide the linkage from the sarcolemma to the sarcomere (actin, myosin, M-line, and Z-line). Similarly, The ECM-bound laminin connects via the dystrophin-glycoprotein complex with sarcomeric cytoskeletal components. Agrin acts via the Lrp4-MuSK or the dystrophin-glycoprotein complex on intracellular signaling cascades. Integrins recruit the focal adhesion kinase (FAK)-steroid receptor coactivator (Src)-complex, Rho-associated coiled-coil containing protein kinases (ROCKs) and mitogen-activated protein kinases (MAPKs). Rho-GTPase-induced actin polymerization liberates myocardin-related transcription factor A (MRTF-A) for nuclear translocation and supports the transport of YAP into the nucleus. Other relevant signaling cascades and proteins are described in the main text.

An involvement in mechanotransduction has also been described for the myocardin-related transcription factor A (MRTF-A/MKL1/MAL). Cellular and biochemical studies showed that the inactive form of MRTF-A is bound to cytoplasmatic globular actin (G-actin). It is released and translocated to the nucleus in a Rho-dependent manner when G-actin polymerizes to form actomyosin (**Figure 1B**) (Miralles et al., 2003; Kuwahara et al., 2010). There it acts as a co-transcription factor together with serum response factor (SRF) (Kuwahara et al., 2010). Hadden et al. (2017) showed that MRTF-A nuclear translocation depends on substrate stiffness and was highest at 20 kPa, which is near the physiological level of cardiac stiffness. Also, mechanical stretching of cardiomyocytes increased the nuclear presence of MRTF-A and mutations in MRTF-A attenuated the hypertrophic response to chronic pressure overload or angiotensin II infusion. This further revealed the importance of MRTF-A in mediating mechanical signaling in the hypertrophic heart (Kuwahara et al., 2010). A complete loss of both homologs, MRTF-A and MRTF-B, in mice caused a range of cardiac defects, including reduced contractility, sarcomere disarray and adult onset heart failure (Mokalled et al., 2015). In epicardial cells, MRTF-A translocation to the nucleus activated a cell motility program required for cell migration. The ablation of *Mrtfa* and *Mrtfb* impaired the development of the coronary microvasculature (Trembley et al., 2015).

The Hippo signaling pathway controls organ size and cell proliferation in response to mechanical tension (Meng et al., 2016). Two key players in this pathway are the transcriptional activator Yes-associated protein (YAP) and its interaction partner WW domain containing transcription regulator 1 (WWTR1; also known as TAZ). These proteins are involved in sensing and transmitting mechanical signals to the nucleus to regulate specific gene expression. Mechanotransduction via YAP/TAZ occurs through Rho GTPase activity and tension of the actomyosin cytoskeleton (Dupont et al., 2011) (**Figure 1B**). Dupont et al. (2011) showed that YAP/TAZ was nuclear on stiff substrates whereas it became cytoplasmic on softer substrates. This activation of the YAP pathway was dose-dependent. The levels of YAP nuclear localization increased following a sigmoidal curve in human adipose-derived stem cells that had been plated on hydrogels with stiffness gradients ranging from 2 to

40 kPa (Hadden et al., 2017). This finding was conflicting with the previous study that had reported a switch-like manner of YAP nuclear localization depending on specific stiffness values (Dupont et al., 2011). YAP localization to the nucleus increased in a linear manner when stiffness was in the range between 12 and 20 kPa, whereas a plateau of YAP nuclear localization was reached when substrate stiffness was 20–40 kPa (Hadden et al., 2017). Hence, further studies are required to elucidate the precise regulatory mechanism of YAP localization in response to tissue stiffness.

While YAP is an important regulator and inducer of cardiomyocyte proliferation in the embryonic and postnatal heart, it does not induce hypertrophic growth of the myocardium. Strikingly, nuclear YAP/TAZ localizes to the nucleus of the infarcted murine myocardium at 3, 5, 14, and 36 days post myocardial infarction but not in remote, non-injured regions (Mosqueira et al., 2014). In human cardiomyocyte progenitor cells, localization of YAP depended on the cytoskeleton and on myosin contractility. YAP nuclear localization strongly increased in human cardiomyocyte progenitor cells that were cultured on collagen- and fibronectin-coated polyacrylamide gels with a Young's modulus higher than 10 kPa when compared to low stiffness gels (0.5–0.7 kPA). When YAP/TAZ was silenced, human cardiomyocyte progenitor cells adhered less to stiff substrates (>10 kPa), expression of genes involved in cell matrix interactions changed, and their migration capacity was reduced. Yet, no differences of these parameters were observed when YAP/TAZ-silenced human cardiomyocyte progenitor cells were cultured on soft gels. Human cardiomyocyte progenitor cells cultured on fibronectin-coated polyacrylamide gels with standard heart stiffness (10kPa) expressed the cardiac differentiation program (GATA-4, NKX2.5). However, this was prevented by YAP/TAZ silencing and cells instead expressed genes that indicated a commitment to the endothelial lineage (Mosqueira et al., 2014). Similarly, in fibroblasts, YAP-signaling was activated upon myocardial infarction and enabled differentiation and ECM gene expression via MRTF-A (Francisco et al., 2020). This pointed at the potent role of YAP/TAZ in progenitor cells to induce specific cellular fates in response to extracellular mechanical stimuli. This may have major implications on the healing capacity of injured tissues when mechanical properties have changed.

The mode by which YAP/TAZ becomes activated by mechanical stiffness has raised much interest. This led to the discovery of the ECM protein agrin as a stiffness sensor involved in YAP pathway activation. Its function is directly dependent on matrix stiffness and mediates YAP signaling in cells surrounded by hard but not soft matrices. While this has only been shown in mouse hepatocarcinoma cells (Chakraborty et al., 2017), it is conceivable that agrin may act in a similar manner in cardiomyocytes. In tune with such a model, agrin is required for cardiomyocyte proliferation and cardiac regeneration in the neonatal mouse heart in a way that involves YAP- and ERK signaling. A very exciting finding related to agrin is its involvement in the regeneration of adult murine cardiomyocytes. In a model of myocardial infarction, adult mice treated with recombinant agrin showed cardiomyocyte proliferation, a reduction in scarring, and improved cardiac function at 35 days post infarction. When treated with agrin, sarcomere disassembly was induced in P7 cardiomyocytes in culture and the expression of the sarcomeric protein cardiac troponin T was prevented. Interestingly, agrin application led to increased nuclearization of YAP in cardiomyocytes 1 day after myocardial infarction and the inhibition of YAP prevented agrin-induced cardiomyocyte proliferation (Bassat et al., 2017). This suggested a role of agrin as a modulator of cardiomyocyte differentiation, proliferation, and regeneration in a way that involves YAP signaling. The implications of this exciting discovery have been discussed in more detail in a recent review (Bigotti et al., 2020). Altogether the YAP/TAZ pathway plays a crucial role in cardiac mechanotransduction and is a potent regulator of cell fate and function.

The nuclear envelope has received much attention for its role in mediating mechanical stress into the nucleus. The structural nuclear envelope protein lamin A is stiffness-dependent and regulates chromatin organization, gene expression, and DNA replication (Carmosino et al., 2014). It has been suggested that lamins determine lineage specification toward contractile and hard tissues (Carmosino et al., 2014). Indeed, protein levels of lamin A are higher when organ stiffness increases in mice and men (Swift et al., 2013). Increasing substrate stiffness caused an exponential increase of lamina A in human adipose-derived stem cells (Hadden et al., 2017). One way by which lamin A affected mechanosensitive signaling was by promoting the translocation of YAP to the nucleus and by positively regulating the SRC pathway, which controls genes related to sarcomeric assembly and function (Balza and Misra, 2006; Carmosino et al., 2014). Patients and mice with mutations in lamin A suffer from cardiac diseases, including DCM. In murine knockout models, cardiomyocytes were less resistant to mechanical tension with reduced nuclear stability and increased rates of apoptosis (Nikolova et al., 2004).

These findings highlight the complex regulation involved in cardiac mechanotransduction. The sensation of physical changes and mechanotransduction within cardiomyocytes involves the costamere, a specialized complex of focal adhesion proteins, which mediates inside-out and outside-in signaling. Also, several downstream mechanosensitive signaling pathways become activated in cardiomyocytes in response to changes of matrix stiffness. These include the nuclear sensors YAP/TAZ, lamin A, and MRTF. These studies showed that general mechanisms of mechanotransduction signaling also function in cardiomyocytes and are required for adequate responses to physical changes and during differentiation.

CONSEQUENCES OF STIFFNESS CHANGES ON CARDIOMYOCYTE PERFORMANCE

Changes of the cardiac ECM affect the compliance of the cardiac ventricle, which impacts the diastolic volume (**Figure 2**). What are the consequences on cardiomyocytes when such tissue stiffness changes occur due to cardiac injury or disease? It has been a hallmark discovery that changes in substrate stiffness

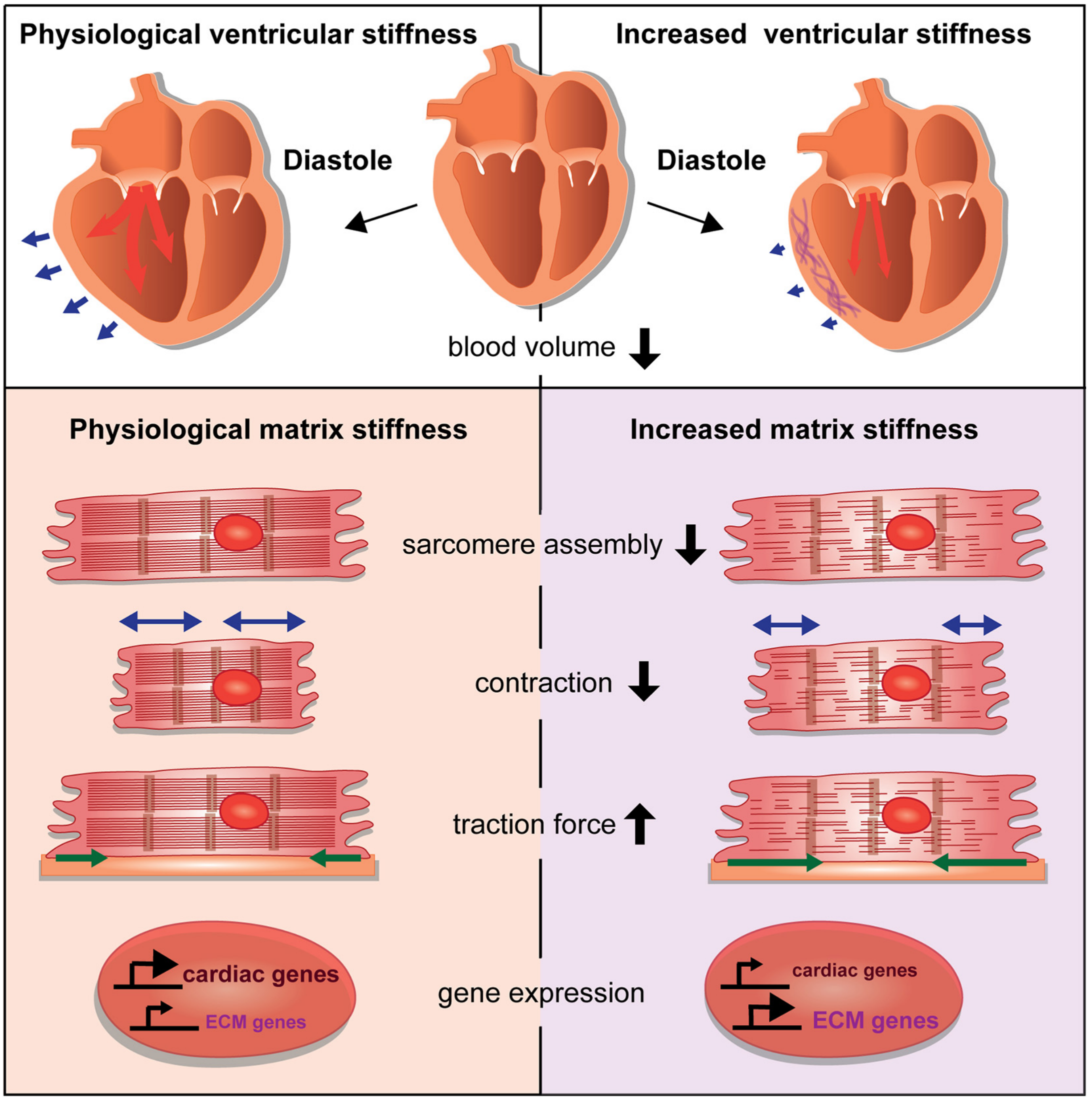

FIGURE 2 | Consequences of stiffness changes for cardiomyocytes. The increase of ventricular cardiac stiffness results in reduced diastolic blood volume. Blue arrows indicate the ventricular diastolic expansion. A stiffer matrix can interfere with sarcomere assembly and leads to changes in cardiomyocyte behavior by affecting cellular contraction and traction forces. Changes in matrix stiffness also cause aberrant gene expression that alters the balance of cardiac versus ECM genes.

can trigger dramatic changes in the morphology, behavior, and differentiation state of cells. Mesenchymal stem cells were differentiated into a range of divergent neurogenic, myogenic, or osteogenic tissues simply by modulating their substrate stiffness on which they had been plated (Engler et al., 2006). These experiments revealed the importance of biomechanical signaling for cell fate determination and raised increasing interest in the responses of cardiomyocytes to extracellular stiffness changes. Cardiomyocytes cultured on substrates with elasticity values representing physiological and diseased cardiac stiffness or with gradients of stiffness developed differently (Hadden et al., 2017; Chin et al., 2019). For instance, cardiomyocytes cultured on a stiff, fibrotic tissue-like matrix lacked striated myofibrils and failed to beat properly (Engler et al., 2008).

Heras-Bautista et al. used polyacrylamide (PAA) hydrogel matrices with ranges of stiffness corresponding with embryonic (12 kPA), adult (30 kPA), or fibrotic (123 kPA) cardiac tissue as substrates for murine induced pluripotent stem cell-derived cardiomyocytes. Cardiomyocytes that were grown on a stiff matrix had an impaired contractile function with disarranged sarcomeres whereas cardiomyocytes grown on soft and medium matrices had highly organized sarcomeres. Soft matrix conditions also resulted in comparative transcriptomes in contrast to cardiomyocytes exposed to a stiff hydrogel. Gene expression analyses of cardiomyocytes grown on stiff matrices revealed many deregulated genes, especially of genes related to developmental programs (Heras-Bautista et al., 2019). In addition, cardiomyocytes grown under stiff matrix conditions also upregulated different ECM-components or modulators, such as the collagens Col1a1, Col1a2, Col4a2, Col6a3, and Col8a2, matrix metalloproteinases, inhibitors of matrix metalloproteinases, and tenascinC, (Heras-Bautista et al., 2019). Similarly, bovine and murine adult cardiac side population progenitor cells were cultured on substrates with a stiffness corresponding with that of physiological or fibrotic myocardium. This study revealed that increased tissue stiffness not only augmented proliferation and cell cycling, reduced myocardial differentiation based on the levels of α-actinin expression, and accelerated cell aging as indicated by a reduction in telomere length, but also caused an increased expression of genes encoding for ECM and adhesion proteins (Qiu et al., 2015). Hence, stiff matrix conditions induced cardiomyocytes and progenitors to further change the matrix composition.

Culturing embryonic rat cardiomyocytes on substrates representing physiological or fibrotic stiffness values revealed that most cells were angular in shape on stiff substrates and roundish on soft substrates. However, neither myofibril organization and function, nor costamere numbers were affected by substrate stiffness (Hersch et al., 2013). Traction force microscopy of cells cultured on substrates with different stiffness values revealed an increased force generation by cardiomyocytes that corresponded with increasing substrate stiffness. This suggested a potent mechanism of force generation by cardiomyocytes, which ensures the stable cell contraction independently of substrate stiffness (Hersch et al., 2013).

Ribeiro et al. examined human pluripotent stem cell-derived cardiomyocyte behaviors when cultured on substrates with a stiffness ranging from 4 to 100 kPA. Contractile forces increased on very stiff matrices (90 kPA), which was in agreement with a previously mentioned study (Hersch et al., 2013). In contrast, cell shortening was reduced in cardiomyocytes compared to that of cells grown on substrates with a physiological stiffness (21 kPa). Hence, the authors suggested that very stiff matrices restrain cell shortening (Ribeiro et al., 2020).

Those studies revealed the importance of a cardiac matrix with physiological stiffness values. Aberrations can dramatically change cardiomyocyte behavior and performance by influencing differentiation, contractile function, gene expression, cell morphology, and force generation (**Figure 2**). How mechanotransductive pathways induce such molecular changes has raised increasing attention. Santos et al. utilized rat ring-shaped engineered connective tissue comprised of cardiac fibroblasts and collagen I while using ROCK signaling inhibitors. This resulted in reduced tissue stiffness, and also reduced TGF-β signaling-driven tissue stiffening (Santos et al., 2019). In this context, the inhibitory effect of ROCK inhibitors on stiffness was mediated by the regulation of lysyl oxidase, the collagen cross-linking enzyme and involved the activation of the actin-dependent MRTF/SRF pathway. This study also showed, that ROCK inhibitors similarly decreased stiffness of human engineered connective tissue and rat engineered cardiac muscle (Santos et al., 2019).

In a related study, Pandey et al. sought to address how cardiomyocytes probe and sense their environment. For this, they cultured neonatal rat cardiomyocytes on nanopillar arrays with different levels of stiffness. This revealed that the induction of cardiomyocyte hypertrophy on a stiff matrix was dependent on protein kinase C (PKC). PKC regulated the non-receptor tyrosine kinase Src, which activated non-muscle myosin contractions at cell edges that are involved in sensing of cell rigidity. By using a tension sensor for the costamere adaptor protein talin, the authors revealed that cyclic stretching of talin is induced downstream of PKC and Src under conditions of physiological stiffness but is continuously induced on matrices representing fibrotic stiffness. In infarcted mouse hearts, a model for DCM, PKCδ and PKCα localized to integrin adhesion sites at costameres together with non-muscle myosin light chain. This suggested an involvement of PKC- and Src-induced non-muscle myosin contractility for rigidity sensing in the diseased myocardium (Pandey et al., 2018).

Another recent study provided further insights into the complex relationship, upon cardiac infarction, between ventricular stiffness, ECM protein availability, YAP signaling activation, and induction of cardiomyocyte proliferation (Wang et al., 2020). The authors applied fetal ECM proteins and modified the stiffness of neonatal mouse hearts after myocardial infarction at day 5. Cardiac function improved three weeks post-surgery in comparison to non-treated hearts when they applied fetal ECM and decreased tissue stiffness by inhibiting lysyl oxidase-induced collagen crosslinking (inhibition by BAPN). Reduced stiffness due to lysyl oxidase inhibition also significantly diminished scarring. In a comparable experiment, mouse cardiac explants were cultured from day 1 under conditions of BAPN- or ribose-treatment to reduce or increase stiffness, respectively (Wang et al., 2020). These experiments revealed that a reduction of stiffness together with fetal ECM treatment increased cardiomyocyte proliferation, reduced collagen deposition, and augmented vascularization. A softer matrix increased the number of cardiomyocytes that exhibited nuclear YAP. This observation apparently contrasts with the study by Mosqueira et al., which reported increased levels of nuclear YAP in human cardiomyocyte progenitor cells grown on stiff matrices. These differences may result from using cardiomyocyte progenitor cells versus explants of infarcted cardiac tissue. Hence, additional studies are required to clarify the effects of stiffness changes on YAP nuclear localization. However, both studies reported an increase of cardiomyocyte proliferation upon nuclear YAP localization (Mosqueira et al., 2014; Wang et al., 2020). Softer matrix conditions in addition to a fetal ECM treatment led to an increased expression of agrin (Wang et al., 2020). Agrin promotes cardiomyocyte proliferation as described above and this may contribute to regenerative effects as well (Bassat et al., 2017). Hence, a softer matrix in combination with embryonic soluble ECM factors had positive effects on cardiomyocyte proliferation, which involved YAP-signaling and actin stability (Wang et al., 2020). These findings impressively illustrated the importance of mechanical cues in regulating regenerative processes of the heart.

Much of our knowledge related to the cellular changes in cardiomyocytes in response to increased tissue stiffness has come from *in vitro* studies. These enabled researchers to use well-defined experimental modulations. Several recent studies revealed direct cellular effects due to matrix stiffness changes. Yet, we are far from understanding the detailed interplay between cardiac stiffness and mechanotransduction in the context of the diseased or regenerating heart.

DISCUSSION

Cardiac diseases often result in fibrotic tissue deposition or cardiomyocyte hypertrophy, two irreversible physiological changes that have a major impact on cardiac function. In this review, we focused on changes of cardiac stiffness that occur in diseased hearts. Myocardial stiffness, which is the potential of cardiomyocytes to resist contraction-induced elongation or shortening, relies on intra- and extracellular components. Stiffness increases in diseased hearts often result from alterations of ECM components. For instance, ECM becomes deposited during fibrosis after myocardial infarction (Frangogiannis, 2019). Fibroblasts are the main players that cause an enhanced ECM deposition. Currently, the roles of other cardiac cell types in depositing and modeling the fibrotic ECM and thus influencing cardiac stiffness have not systematically been addressed. A recent study revealed that macrophages contribute to collagen deposition in the injured mouse and zebrafish heart (Simões et al., 2020). Yet, how macrophages impact myocardial tissue stiffness upon cardiac insult still needs to be resolved.

When the diseased heart turns less compliant, stiffness of the ventricular myocardium prevents that the required physiological volume during diastole is reached and blood flow throughout the body is insufficient. However, besides the global impact that an increase of myocardial stiffness has on heart physiology, there are also crucial cellular changes that occur within the affected myocardium. Here, we reviewed the sophisticated molecular machinery that senses stiffness changes in the environment of cardiomyocytes and mediates appropriate responses (**Figure 1**). Mechanotransductive signaling cascades activate gene expression changes with wide consequences for cardiomyocyte function, differentiation, and contractility (**Figure 2**). This may directly affect intracellular components such as titin that are required for cardiomyocyte passive stiffness. We still need a better understanding why cardiomyocytes show such prominent responses to biomechanical changes. What are short- and long-term consequences of such functional modifications? Answers to these questions may have relevance for a better understanding of cardiac diseases. We need to know, what occurs to cardiomyocytes suddenly facing a different, stiffer environment. Here, we reported that this can cause changes in sarcomere assembly and contractility, aberrant ECM production, cell shape changes, and modifications in force generation. Moreover, stiffness changes also affect the differentiation state of cardiomyocytes. This means, that beside the immense loss of cardiomyocytes after myocardial infarction, remaining cardiomyocytes may lose functionality with further debilitating consequences on heart performance. Although, recent advances showed that cardiomyocytes can sense and respond to those changes, we actually lack detailed studies of such mechanisms. What are the consequences of fibroblast-driven fibrotic tissue deposition and could this even worsen cardiac function after a myocardial infarction? While the deposition of a rigid fibrotic scar is fatal for long-term ventricular functionality, it is indispensable to prevent the heart from ventricular rupture and for maintaining the structure of the heart shortly after a myocardial infarction (Frangogiannis, 2019).

Knowledge about how cardiomyocytes respond to pathological tissue stiffness changes is crucial when it comes to the development of regenerative therapies. External factors that modulate the ECM and tissue stiffness in the diseased heart represent an excellent source for drug and treatment development. They are more easily applicable as part of a therapy than drugs that directly target an intracellular signaling cascade. *In vitro* studies have potently shown that changing substrate stiffness affects cardiomyocyte function. However, there are only few reports about how stiffness changes may lead to cardiomyocyte de-differentiation and increased proliferation, which is required for cardiac repair. We are just beginning to discover powerful molecules for inducing cardiomyocyte proliferation and to test their potential *in vivo* in the diseased heart. One pioneering study involved the discovery of the ECM protein agrin, a stiffness sensor in the mechanotransduction cascade regulating cardiomyocyte proliferation (Bassat et al., 2017; Chakraborty et al., 2017). Its potential to improve fibrosis, cardiac function and adverse remodeling after myocardial infarction was recently even shown in big animal models (Baehr et al., 2020).

Another promising approach based on modulating isoforms of the basement membrane protein laminin interfered with myocardial stiffness in HFpEF patients (Hochman-Mendez et al., 2020). Laminin is part of the costamere (**Figure 1A**) and involved in transmitting extracellular biomechanical signals to the contractile apparatus. Altering the ECM laminin content affected titin isoform expression, which regulates passive stiffness of cardiomyocytes (Hochman-Mendez et al., 2020). Such novel approaches promise the development of cardiac therapies after myocardial infarction.

However, besides this amplitude of recent discoveries about the mechanotransduction machinery in cardiomyocytes and the consequences of aberrant tissue stiffness, many questions still remain unanswered. Little is known about the prospects of therapeutic modifications of cardiac ECM and its stiffness, in order to improve cardiomyocyte performance and induce regenerative processes without softening of the ventricular wall. And how exactly can costamere proteins detect substrate stiffness? How does aberrant mechanical signaling due to a stiff matrix interfere with cell migration, intercellular communication, and ligand availability for cardiomyocytes and other cardiac cell types? Several studies have shown the importance of the ECM for cytokine- and growth factor-mediated signaling (Frangogiannis, 2017). It also needs to be addressed, whether other cell types respond to tissue stiffness changes in the heart and how this affects myocardial regeneration. For example macrophages are highly responsive to matrix stiffness changes (Sridharan et al., 2019) and also cause stiffness increases and diastolic dysfunction (Hulsmans et al., 2018). Many of those questions have only been addressed to a limited extent. However, their answers are crucial when it comes to the development of novel regenerative therapies that target tissue stiffness changes in the heart.

AUTHOR CONTRIBUTIONS

JM established a plan for this manuscript and designed the figures. JM and SA-S wrote the draft and approved the submitted manuscript. Both authors contributed to the article and approved the submitted version.

FUNDING

Our group was supported by a Deutsche Forschungsgemeinschaft (DFG) network grant for SFB958 and projects SE2016/7-2, SE2016/10-1, and SE2016/13-1.

ACKNOWLEDGMENTS

We thank the lab members for critical reading of the manuscript. Certainly, there are further, important studies and reviews on this research topic that we could not mention due to the briefness of this review. We apologize for their omissions.

REFERENCES

Anderson, J., Li, Z., and Goubel, F. (2001). Passive stiffness is increased in soleus muscle of desmin knockout mouse. *Muscle Nerve* 24, 1090–1092. doi: 10.1002/mus.1115

Baehr, A., Umansky, K. B., Bassat, E., Jurisch, V., Klett, K., Bozoglu, T., et al. (2020). Agrin promotes coordinated therapeutic processes leading to improved cardiac repair in pigs. *Circulation* 142, 868–881. doi: 10.1161/CIRCULATIONAHA.119.045116

Balza, R. O., and Misra, R. P. (2006). Role of the serum response factor in regulating contractile apparatus gene expression and sarcomeric integrity in cardiomyocytes. *J. Biol. Chem.* 281, 6498–6510. doi: 10.1074/jbc.M509487200

Bassat, E., Mutlak, Y. E., Genzelinakh, A., Shadrin, I. Y., Baruch Umansky, K., Yifa, O., et al. (2017). The extracellular matrix protein agrin promotes heart regeneration in mice. *Nature* 547, 179–184. doi: 10.1038/nature22978

Berry, M. F., Engler, A. J., Woo, Y. J., Pirolli, T. J., Bish, L. T., Jayasankar, V., et al. (2006). Mesenchymal stem cell injection after myocardial infarction improves myocardial compliance. *Am. J. Physiol. Heart Circ. Physiol.* 290, H2196–H2203. doi: 10.1152/ajpheart.01017.2005

Bhana, B., Iyer, R. K., Chen, W. L. K., Zhao, R., Sider, K. L., Likhitpanichkul, M., et al. (2010). Influence of substrate stiffness on the phenotype of heart cells. *Biotechnol. Bioeng.* 105, 1148–1160. doi: 10.1002/bit.22647

Bigotti, M. G., Skeffington, K. L., Jones, F. P., Caputo, M., and Brancaccio, A. (2020). Agrin-Mediated cardiac regeneration: some open questions. *Front. Bioeng. Biotechnol.* 8:594. doi: 10.3389/fbioe.2020.00594

Brodehl, A., Gaertner-Rommel, A., and Milting, H. (2018). Molecular insights into cardiomyopathies associated with desmin (DES) mutations. *Biophys. Rev.* 10, 983–1006. doi: 10.1007/s12551-018-0429-0

Cao, J., Navis, A., Cox, B. D., Dickson, A. L., Gemberling, M., Karra, R., et al. (2016). Single epicardial cell transcriptome sequencing identifies Caveolin 1 as an essential factor in zebrafish heart regeneration. *Development* 143, 232–243. doi: 10.1242/dev.130534

Carmosino, M., Torretta, S., Procino, G., Gerbino, A., Forleo, C., Favale, S., et al. (2014). Role of nuclear Lamin A/C in cardiomyocyte functions. *Biol. Cell* 106, 346–358. doi: 10.1111/boc.201400033

Cazorla, O., Freiburg, A., Helmes, M., Centner, T., McNabb, M., Wu, Y., et al. (2000). Differential expression of cardiac titin isoforms and modulation of cellular stiffness. *Circ. Res.* 86, 59–67. doi: 10.1161/01.res.86.1.59

Chakraborty, S., Njah, K., Pobbati, A. V., Lim, Y. B., Raju, A., Lakshmanan, M., et al. (2017). Agrin as a mechanotransduction signal regulating YAP through the Hippo pathway. *Cell Rep.* 18, 2464–2479. doi: 10.1016/j.celrep.2017.02.041

Chaturvedi, R. R., Herron, T., Simmons, R., Shore, D., Kumar, P., Sethia, B., et al. (2010). Passive stiffness of myocardium from congenital heart disease and implications for diastole. *Circulation* 121, 979–988. doi: 10.1161/CIRCULATIONAHA.109.850677

Chin, I. L., Hool, L., and Choi, Y. S. (2019). A review of in vitro platforms for understanding cardiomyocyte mechanobiology. *Front. Bioeng. Biotechnol.* 7:133. doi: 10.3389/fbioe.2019.00133

Crosara-Alberto, D. P., Inoue, R. Y., and Costa, C. R. C. (2009). FAK signalling mediates NF-kappaB activation by mechanical stress in cardiac myocytes. *Clin. Chim. Acta* 403, 81–86. doi: 10.1016/j.cca.2009.01.023

Dupont, S., Morsut, L., Aragona, M., Enzo, E., Giulitti, S., Cordenonsi, M., et al. (2011). Role of YAP/TAZ in mechanotransduction. *Nature* 474, 179–183. doi: 10.1038/nature10137

Elosegui-Artola, A., Oria, R., Chen, Y., Kosmalska, A., Pérez-González, C., Castro, N., et al. (2016). Mechanical regulation of a molecular clutch defines force transmission and transduction in response to matrix rigidity. *Nat. Cell Biol.* 18, 540–548. doi: 10.1038/ncb3336

Engler, A. J., Carag-Krieger, C., Johnson, C. P., Raab, M., Tang, H.-Y., Speicher, D. W., et al. (2008). Embryonic cardiomyocytes beat best on a matrix with heart-like elasticity: scar-like rigidity inhibits beating. *J. Cell Sci.* 121, 3794–3802. doi: 10.1242/jcs.029678

Engler, A. J., Sen, S., Sweeney, H. L., and Discher, D. E. (2006). Matrix elasticity directs stem cell lineage specification. *Cell* 126, 677–689. doi: 10.1016/j.cell.2006.06.044

Ervasti, J. M. (2003). Costameres: the Achilles' heel of Herculean muscle: the Achilles' heel of Herculean muscle. *J. Biol. Chem.* 278, 13591–13594. doi: 10.1074/jbc.R200021200

Fan, D., Takawale, A., Lee, J., and Kassiri, Z. (2012). Cardiac fibroblasts, fibrosis and extracellular matrix remodeling in heart disease. *Fibrogenesis Tissue Repair* 5:15. doi: 10.1186/1755-1536-5-15

Forrester, J. S., Diamond, G., Parmley, W. W., and Swan, H. J. (1972). Early increase in left ventricular compliance after myocardial infarction. *J. Clin. Invest.* 51, 598–603. doi: 10.1172/JCI106849

Francisco, J., Zhang, Y., Im Jeong, J., Mizushima, W., Ikeda, S., Ivessa, A., et al. (2020). Blockade of fibroblast YAP attenuates cardiac fibrosis and dysfunction through MRTF-A inhibition. *JACC Basic Transl. Sci.* 5, 931–945. doi: 10.1016/j.jacbts.2020.07.009

Frangogiannis, N. G. (2006). The mechanistic basis of infarct healing. *Antioxid. Redox Signal.* 8, 1907–1939. doi: 10.1089/ars.2006.8.1907

Frangogiannis, N. G. (2017). The extracellular matrix in myocardial injury, repair, and remodeling. *J. Clin. Invest.* 127, 1600–1612. doi: 10.1172/JCI87491

Frangogiannis, N. G. (2019). Cardiac fibrosis: cell biological mechanisms, molecular pathways and therapeutic opportunities. *Mol. Aspects Med.* 65, 70–99. doi: 10.1016/j.mam.2018.07.001

Freiburg, A., Trombitas, K., Hell, W., Cazorla, O., Fougerousse, F., Centner, T., et al. (2000). Series of exon-skipping events in the elastic spring region of titin as the structural basis for myofibrillar elastic diversity. *Circ. Res.* 86, 1114–1121. doi: 10.1161/01.res.86.11.1114

Granzier, H. L., and Labeit, S. (2004). The giant protein titin: a major player in myocardial mechanics, signaling, and disease. *Circ. Res.* 94, 284–295. doi: 10.1161/01.RES.0000117769.88862.F8

Gregorio, C. C., Granzier, H., Sorimachi, H., and Labeit, S. (1999). Muscle assembly: a titanic achievement? *Curr. Opin. Cell Biol.* 11, 18–25. doi: 10.1016/s0955-0674(99)80003-9

Grivas, D., González-Rajal, Á, Guerrero Rodríguez, C., Garcia, R., and de La Pompa, J. L. (2020). Loss of Caveolin-1 and caveolae leads to increased cardiac cell stiffness and functional decline of the adult zebrafish heart. *Sci. Rep.* 10:12816. doi: 10.1038/s41598-020-68802-9

Gupta, K. B., Ratcliffe, M. B., Fallert, M. A., Edmunds, L. H., and Bogen, D. K. (1994). Changes in passive mechanical stiffness of myocardial tissue with aneurysm formation. *Circulation* 89, 2315–2326. doi: 10.1161/01.cir.89.5.2315

Hadden, W. J., Young, J. L., Holle, A. W., McFetridge, M. L., Du Kim, Y., Wijesinghe, P., et al. (2017). Stem cell migration and mechanotransduction on linear stiffness gradient hydrogels. *Proc. Natl. Acad. Sci. U.S.A.* 114, 5647–5652. doi: 10.1073/pnas.1618239114

Hamdani, N., Herwig, M., and Linke, W. A. (2017). Tampering with springs: phosphorylation of titin affecting the mechanical function of cardiomyocytes. *Biophys. Rev.* 9, 225–237. doi: 10.1007/s12551-017-0263-9

Hein, S., Kostin, S., Heling, A., Maeno, Y., and Schaper, J. (2000). The role of the cytoskeleton in heart failure. *Cardiovasc. Res.* 45, 273–278. doi: 10.1016/s0008-6363(99)00268-0

Heras-Bautista, C. O., Mikhael, N., Lam, J., Shinde, V., Katsen-Globa, A., Dieluweit, S., et al. (2019). Cardiomyocytes facing fibrotic conditions re-express extracellular matrix transcripts. *Acta Biomater.* 89, 180–192. doi: 10.1016/j.actbio.2019.03.017

Hersch, N., Wolters, B., Dreissen, G., Springer, R., Kirchgeßner, N., Merkel, R., et al. (2013). The constant beat: cardiomyocytes adapt their forces by equal contraction upon environmental stiffening. *Biol. Open* 2, 351–361. doi: 10.1242/bio.20133830

Hidalgo, C., Hudson, B., Bogomolovas, J., Zhu, Y., Anderson, B., Greaser, M., et al. (2009). PKC phosphorylation of titin's PEVK element: a novel and conserved pathway for modulating myocardial stiffness. *Circ. Res.* 105, 631–638.

Hinderer, S., and Schenke-Layland, K. (2019). Cardiac fibrosis – A short review of causes and therapeutic strategies. *Adv. Drug Deliv. Rev.* 146, 77–82. doi: 10.1016/j.addr.2019.05.011

Hochman-Mendez, C., Curty, E., and Taylor, D. A. (2020). Change the laminin, change the cardiomyocyte: improve untreatable heart failure. *Int. J. Mol. Sci.* 21:6013. doi: 10.3390/ijms21176013

Hulsmans, M., Sager, H. B., Roh, J. D., Valero-Muñoz, M., Houstis, N. E., Iwamoto, Y., et al. (2018). Cardiac macrophages promote diastolic dysfunction. *J. Exp. Med.* 215, 423–440. doi: 10.1084/jem.20171274

Iskratsch, T., Wolfenson, H., and Sheetz, M. P. (2014). Appreciating force and shape—the rise of mechanotransduction in cell biology. *Nat. Rev. Mol. Cell Biol.* 15, 825–833. doi: 10.1038/nrm3903

Jacot, J. G., McCulloch, A. D., and Omens, J. H. (2008). Substrate stiffness affects the functional maturation of neonatal rat ventricular myocytes. *Biophys. J.* 95, 3479–3487. doi: 10.1529/biophysj.107.124545

Kamdar, F., and Garry, D. J. (2016). Dystrophin-Deficient cardiomyopathy. *J. Am. Coll. Cardiol.* 67, 2533–2546. doi: 10.1016/j.jacc.2016.02.081

Kötter, S., Gout, L., Von Frieling-Salewsky, M., Müller, A. E., Helling, S., Marcus, K., et al. (2013). Differential changes in titin domain phosphorylation increase myofilament stiffness in failing human hearts. *Cardiovasc. Res.* 99, 648–656. doi: 10.1093/cvr/cvt144

Kötter, S., Kazmierowska, M., Andresen, C., Bottermann, K., Grandoch, M., Gorressen, S., et al. (2016). Titin-Based cardiac myocyte stiffening contributes to early adaptive ventricular remodeling after myocardial infarction. *Circ. Res.* 119, 1017–1029. doi: 10.1161/CIRCRESAHA.116.309685

Krüger, M., Kohl, T., and Linke, W. A. (2006). Developmental changes in passive stiffness and myofilament Ca2+ sensitivity due to titin and troponin-I isoform switching are not critically triggered by birth. *Am. J. Physiol. Heart Circ. Physiol.* 291, H496–H506. doi: 10.1152/ajpheart.00114.2006

Krüger, M., Kötter, S., Grützner, A., Lang, P., Andresen, C., Redfield, M. M., et al. (2009). Protein kinase G modulates human myocardial passive stiffness by phosphorylation of the titin springs. *Circ. Res.* 104, 87–94. doi: 10.1161/CIRCRESAHA.108.184408

Krüger, M., and Linke, W. A. (2009). Titin-based mechanical signalling in normal and failing myocardium. *J. Mol. Cell. Cardiol.* 46, 490–498. doi: 10.1016/j.yjmcc.2009.01.004

Kuwahara, K., Kinoshita, H., Kuwabara, Y., Nakagawa, Y., Usami, S., Minami, T., et al. (2010). Myocardin-related transcription factor A is a common mediator of mechanical stress- and neurohumoral stimulation-induced cardiac hypertrophic signaling leading to activation of brain natriuretic peptide gene expression. *Mol. Cell. Biol.* 30, 4134–4148. doi: 10.1128/MCB.00154-10

Lahmers, S., Wu, Y., Call, D. R., Labeit, S., and Granzier, H. (2004). Developmental control of titin isoform expression and passive stiffness in fetal and neonatal myocardium. *Circ. Res.* 94, 505–513. doi: 10.1161/01.RES.0000115522.52554.86

LeWinter, M. M., and Granzier, H. L. (2014). Cardiac titin and heart disease. *J. Cardiovasc. Pharmacol.* 63, 207–212. doi: 10.1097/FJC.0000000000000007

López, B., González, A., Hermida, N., Valencia, F., de Teresa, E., and Díez, J. (2010). Role of lysyl oxidase in myocardial fibrosis: from basic science to clinical aspects. *Am. J. Physiol. Heart Circ. Physiol.* 299, H1–H9. doi: 10.1152/ajpheart.00335.2010

Majkut, S., Idema, T., Swift, J., Krieger, C., Liu, A., and Discher, D. E. (2013). Heart-specific stiffening in early embryos parallels matrix and myosin expression to optimize beating. *Curr. Biol.* 23, 2434–2439. doi: 10.1016/j.cub.2013.10.057

Makarenko, I., Opitz, C. A., Leake, M. C., Neagoe, C., Kulke, M., Gwathmey, J. K., et al. (2004). Passive stiffness changes caused by upregulation of compliant titin isoforms in human dilated cardiomyopathy hearts. *Circ. Res.* 95, 708–716. doi: 10.1161/01.RES.0000143901.37063.2f

Marijianowski, M. M. H., van der Loos, C. M., Mohrschladt, M. F., and Becker, A. E. (1994). The neonatal heart has a relatively high content of total collagen and type I collagen, a condition that may explain the less compliant state. *J. Am. Coll. Cardiol.* 23, 1204–1208. doi: 10.1016/0735-1097(94)90612-2

Meng, Z., Moroishi, T., and Guan, K.-L. (2016). Mechanisms of Hippo pathway regulation. *Genes Dev.* 30, 1–17. doi: 10.1101/gad.274027.115

Miralles, F., Posern, G., Zaromytidou, A.-I., and Treisman, R. (2003). Actin dynamics control SRF activity by regulation of its coactivator MAL. *Cell* 113, 329–342. doi: 10.1016/s0092-8674(03)00278-2

Mokalled, M. H., Carroll, K. J., Cenik, B. K., Chen, B., Liu, N., Olson, E. N., et al. (2015). Myocardin-related transcription factors are required for cardiac development and function. *Dev. Biol.* 406, 109–116. doi: 10.1016/j.ydbio.2015.09.006

Mosqueira, D., Pagliari, S., Uto, K., Ebara, M., Romanazzo, S., Escobedo-Lucea, C., et al. (2014). Hippo pathway effectors control cardiac progenitor cell fate by acting as dynamic sensors of substrate mechanics and nanostructure. *ACS Nano* 8, 2033–2047. doi: 10.1021/nn4058984

Nadruz, W., Corat, M. A. F., Marin, T. M., Guimarães Pereira, G. A., and Franchini, K. G. (2005). Focal adhesion kinase mediates MEF2 and c-Jun activation by stretch: role in the activation of the cardiac hypertrophic genetic program. *Cardiovasc. Res.* 68, 87–97. doi: 10.1016/j.cardiores.2005.05.011

Nagueh, S. F., Shah, G., Wu, Y., Torre-Amione, G., King, N. M., Lahmers, S., et al. (2004). Altered titin expression, myocardial stiffness, and left ventricular function in patients with dilated cardiomyopathy. *Circulation* 110, 155–162. doi: 10.1161/01.CIR.0000135591.37759.AF

Nikolova, V., Leimena, C., McMahon, A. C., Tan, J. C., Chandar, S., Jogia, D., et al. (2004). Defects in nuclear structure and function promote dilated cardiomyopathy in lamin A/C-deficient mice. *J. Clin. Invest.* 113, 357–369. doi: 10.1172/JCI19448

Opitz, C. A., Leake, M. C., Makarenko, I., Benes, V., and Linke, W. A. (2004). Developmentally regulated switching of titin size alters myofibrillar stiffness in the perinatal heart. *Circ. Res.* 94, 967–975. doi: 10.1161/01.RES.0000124301.48193.E1

Opitz, C. A., and Linke, W. A. (2005). Plasticity of cardiac titin/connectin in heart development. *J. Muscle Res. Cell Motil.* 26, 333–342. doi: 10.1007/s10974-005-9040-7

O'Rourke, S. A., Dunne, A., and Monaghan, M. G. (2019). The role of macrophages in the infarcted myocardium: orchestrators of ECM remodeling. *Front. Cardiovasc. Med.* 6:101. doi: 10.3389/fcvm.2019.00101

Pandey, P., Hawkes, W., Hu, J., Megone, W. V., Gautrot, J., Anilkumar, N., et al. (2018). Cardiomyocytes sense matrix rigidity through a combination of muscle and non-muscle myosin contractions. *Dev. Cell* 44, 326–336.e3. doi: 10.1016/j.devcel.2017.12.024

Peter, A. K., Cheng, H., Ross, R. S., Knowlton, K. U., and Chen, J. (2011). The costamere bridges sarcomeres to the sarcolemma in striated muscle. *Prog. Pediatr. Cardiol.* 31, 83–88. doi: 10.1016/j.ppedcard.2011.02.003

Petridou, N. I., Spiró, Z., and Heisenberg, C. P. (2017). Multiscale force sensing in development. *Nat. Cell Biol.* 19, 581–588. doi: 10.1038/ncb3524

Pires, R. H., Shree, N., Manu, E., Guzniczak, E., and Otto, O. (2019). Cardiomyocyte mechanodynamics under conditions of actin remodelling. *Philos. Trans. R. Soc. Lond. B Biol. Sci.* 374, 20190081. doi: 10.1098/rstb.2019.0081

Qiu, Y., Bayomy, A. F., Gomez, M. V., Bauer, M., Du, P., Yang, Y., et al. (2015). A role for matrix stiffness in the regulation of cardiac side population cell function. *Am. J. Physiol. Heart Circ. Physiol.* 308, H990–H997. doi: 10.1152/ajpheart.00935.2014

Ribeiro, M. C., Slaats, R. H., Schwach, V., Rivera-Arbelaez, J. M., Tertoolen, L. G. J., van Meer, B. J., et al. (2020). A cardiomyocyte show of force: a fluorescent alpha-actinin reporter line sheds light on human cardiomyocyte contractility versus substrate stiffness. *J. Mol. Cell. Cardiol.* 141, 54–64. doi: 10.1016/j.yjmcc.2020.03.008

Robison, P., Caporizzo, M. A., Ahmadzadeh, H., Bogush, A. I., Chen, C. Y., Margulies, K. B., et al. (2016). Detyrosinated microtubules buckle and bear load in contracting cardiomyocytes. *Science* 352:aaf0659. doi: 10.1126/science.aaf0659

Røe, ÅT., Aronsen, J. M., Skårdal, K., Hamdani, N., Linke, W. A., Danielsen, H. E., et al. (2017). Increased passive stiffness promotes diastolic dysfunction despite improved Ca2+ handling during left ventricular concentric hypertrophy. *Cardiovasc. Res.* 113, 1161–1172. doi: 10.1093/cvr/cvx087

Samarel, A. M. (2005). Costameres, focal adhesions, and cardiomyocyte mechanotransduction. *Am. J. Physiol. Heart Circ. Physiol.* 289, H2291–H2301. doi: 10.1152/ajpheart.00749.2005

Samarel, A. M., Koshman, Y. E., Swanson, E. R., and Russell, B. (2013). "Biophysical forces modulate the costamere and Z-Disc for sarcomere remodeling in heart failure," in *Biophysics of the Failing Heart Biological and Medical Physics, Biomedical Engineering*, eds R. Solaro and J. Tardiff (New York, NY: Springer), 141–174.

Santos, G. L., Hartmann, S., Zimmermann, W.-H., Ridley, A., and Lutz, S. (2019). Inhibition of Rho-associated kinases suppresses cardiac myofibroblast function in engineered connective and heart muscle tissues. *J. Mol. Cell. Cardiol.* 134, 13–28. doi: 10.1016/j.yjmcc.2019.06.015

Sharp, W. W., Simpson, D. G., Borg, T. K., Samarel, A. M., and Terracio, L. (1997). Mechanical forces regulate focal adhesion and costamere assembly in cardiac myocytes. *Am. J. Physiol.* 273, H546–H556. doi: 10.1152/ajpheart.1997.273.2.H546

Sheng, J.-J., Feng, H.-Z., Pinto, J. R., Wei, H., and Jin, J.-P. (2016). Increases of desmin and α-actinin in mouse cardiac myofibrils as a response to diastolic dysfunction. *J. Mol. Cell. Cardiol.* 99, 218–229. doi: 10.1016/j.yjmcc.2015.10.035

Simões, F. C., Cahill, T. J., Kenyon, A., Gavriouchkina, D., Vieira, J. M., Sun, X., et al. (2020). Macrophages directly contribute collagen to scar formation during zebrafish heart regeneration and mouse heart repair. *Nat. Commun.* 11:600. doi: 10.1038/s41467-019-14263-2

Singh, S. R., and Robbins, J. (2018). Desmin and cardiac disease: an unfolding story. *Circ. Res.* 122, 1324–1326. doi: 10.1161/CIRCRESAHA.118.312965

Slater, R. E., Strom, J. G., and Granzier, H. (2017). Effect of exercise on passive myocardial stiffness in mice with diastolic dysfunction. *J. Mol. Cell. Cardiol.* 108, 24–33. doi: 10.1016/j.yjmcc.2017.04.006

Sridharan, R., Cavanagh, B., Cameron, A. R., Kelly, D. J., and O'Brien, F. J. (2019). Material stiffness influences the polarization state, function and migration mode of macrophages. *Acta Biomater.* 89, 47–59. doi: 10.1016/j.actbio.2019.02.048

Sumita Yoshikawa, W., Nakamura, K., Miura, D., Shimizu, J., Hashimoto, K., Kataoka, N., et al. (2013). Increased passive stiffness of cardiomyocytes in the transverse direction and residual actin and myosin cross-bridge formation in hypertrophied rat hearts induced by chronic β-adrenergic stimulation. *Circ. J.* 77, 741–748. doi: 10.1253/circj.cj-12-0779

Swift, J., Ivanovska, I. L., Buxboim, A., Harada, T., Dingal, P. C. D. P., Pinter, J., et al. (2013). Nuclear lamin-A scales with tissue stiffness and enhances matrix-directed differentiation. *Science* 341, 1240104. doi: 10.1126/science.1240104

Tang, V. W. (2020). Collagen, stiffness, and adhesion: the evolutionary basis of vertebrate mechanobiology. *Mol. Biol. Cell* 31, 1823–1834. doi: 10.1091/mbc.E19-12-0709

Tharp, C. A., Haywood, M. E., Sbaizero, O., Taylor, M., and Mestroni, L. (2019). The giant protein titin's role in cardiomyopathy: genetic, transcriptional, and post-translational modifications of TTN and their contribution to cardiac disease. *Front. Physiol.* 10:1436. doi: 10.3389/fphys.2019.01436

Tokuyasu, K. T. (1983). Visualization of longitudinally-oriented intermediate filaments in frozen sections of chicken cardiac muscle by a new staining method. *J. Cell Biol.* 97, 562–565. doi: 10.1083/jcb.97.2.562

Torsoni, A. S., Constancio, S. S., Nadruz, W., Hanks, S. K., and Franchini, K. G. (2003). Focal adhesion kinase is activated and mediates the early hypertrophic response to stretch in cardiac myocytes. *Circ. Res.* 93, 140–147. doi: 10.1161/01.RES.0000081595.25297.1B

Trembley, M. A., Velasquez, L. S., de Mesy Bentley, K. L., and Small, E. M. (2015). Myocardin-related transcription factors control the motility of epicardium-derived cells and the maturation of coronary vessels. *Development* 142, 21–30. doi: 10.1242/dev.116418

Wang, X., Senapati, S., Akinbote, A., Gnanasambandam, B., Park, P. S.-H., and Senyo, S. E. (2020). Microenvironment stiffness requires decellularized cardiac extracellular matrix to promote heart regeneration in the neonatal mouse heart. *Acta Biomater.* 113, 380–392. doi: 10.1016/j.actbio.2020.06.032

Ward, M., and Iskratsch, T. (2020). Mix and (mis-)match – The mechanosensing machinery in the changing environment of the developing, healthy adult and diseased heart. *Biochim. Biophys. Acta Mol. Cell Res.* 1867:118436. doi: 10.1016/j.bbamcr.2019.01.017

Ware, J. S., and Cook, S. A. (2018). Role of titin in cardiomyopathy: from DNA variants to patient stratification. *Nat. Rev. Cardiol.* 15, 241–252. doi: 10.1038/nrcardio.2017.190

Warren, C. M., Krzesinski, P. R., Campbell, K. S., Moss, R. L., and Greaser, M. L. (2004). Titin isoform changes in rat myocardium during development. *Mech. Dev.* 121, 1301–1312. doi: 10.1016/j.mod.2004.07.003

Wu, Y., Cazorla, O., Labeit, D., Labeit, S., and Granzier, H. (2000). Changes in titin and collagen underlie diastolic stiffness diversity of cardiac muscle. *J. Mol. Cell. Cardiol.* 32, 2151–2162. doi: 10.1006/jmcc.2000.1281

Yamamoto, K., Masuyama, T., Sakata, Y., Nishikawa, N., Mano, T., Yoshida, J., et al. (2002). Myocardial stiffness is determined by ventricular fibrosis, but not by compensatory or excessive hypertrophy in hypertensive heart. *Cardiovasc. Res.* 55, 76–82. doi: 10.1016/s0008-6363(02)00341-3

Zemljic-Harpf, A., Manso, A. M., and Ross, R. S. (2009). Vinculin and talin: focus on the myocardium. *J. Invest. Med.* 57, 849–855. doi: 10.2310/JIM.0b013e3181c5e074

Zile, M. R., Baicu, C. F., and Gaasch, W. H. (2004). Diastolic heart failure–abnormalities in active relaxation and passive stiffness of the left ventricle. *New Engl. J. Med.* 350, 1953–1959. doi: 10.1056/NEJMoa032566

Zile, M. R., Baicu, C. F., Ikonomidis, J. S., Stroud, R. E., Nietert, P. J., Bradshaw, A. D., et al. (2015). Myocardial stiffness in patients with heart failure and a preserved ejection fraction: contributions of collagen and titin. *Circulation* 131, 1247–1259. doi: 10.1161/CIRCULATIONAHA.114.013215

Zile, M. R., Gottdiener, J. S., Hetzel, S. J., McMurray, J. J., Komajda, M., McKelvie, R., et al. (2011). Prevalence and significance of alterations in cardiac structure and function in patients with heart failure and a preserved ejection fraction. *Circulation* 124, 2491–2501. doi: 10.1161/CIRCULATIONAHA.110.011031

Conflict of Interest: The authors declare that the research was conducted in the absence of any commercial or financial relationships that could be construed as a potential conflict of interest.

frontiers
in Cell and Developmental Biology

ORIGINAL RESEARCH
published: 02 March 2021
doi: 10.3389/fcell.2021.641763

Platelet-Derived Extracellular Vesicles Increase Col8a1 Secretion and Vascular Stiffness in Intimal Injury

Han Bao[1,2], Zi-Tong Li[1], Lei-Han Xu[3,4], Tong-Yue Su[3,4], Yue Han[1], Min Bao[1], Ze Liu[1], Yang-Jing Fan[1], Yue Lou[1], Yi Chen[1], Zong-Lai Jiang[1], Xiao-Bo Gong[1,2] and Ying-Xin Qi[1,3,4]*

[1] Institute of Mechanobiology & Medical Engineering, School of Life Sciences & Biotechnology, Shanghai Jiao Tong University, Shanghai, China, [2] Key Laboratory of Hydrodynamics (Ministry of Education), Department of Engineering Mechanics, School of Naval Architecture, Ocean and Civil Engineering, Shanghai Jiao Tong University, Shanghai, China, [3] Key Laboratory for Biomechanics and Mechanobiology of Ministry of Education, School of Biological Science and Medical Engineering, Beihang University, Beijing, China, [4] Beijing Advanced Innovation Center for Biomedical Engineering, Beihang University, Beijing, China

OPEN ACCESS

Edited by:
Jing Zhou,
Peking University, China

Reviewed by:
Wei Chen,
Zhejiang University, China
An Ouyang,
Harvard Medical School,
United States

***Correspondence:**
Ying-Xin Qi
qiyx@sjtu.edu.cn

Specialty section:
This article was submitted to Cell Adhesion and Migration, a section of the journal Frontiers in Cell and Developmental Biology

Received: *14 December 2020*
Accepted: *09 February 2021*
Published: *02 March 2021*

Citation:
Bao H, Li Z-T, Xu L-H, Su T-Y, Han Y, Bao M, Liu Z, Fan Y-J, Lou Y, Chen Y, Jiang Z-L, Gong X-B and Qi Y-X (2021) Platelet-Derived Extracellular Vesicles Increase Col8a1 Secretion and Vascular Stiffness in Intimal Injury. Front. Cell Dev. Biol. 9:641763. doi: 10.3389/fcell.2021.641763

The arterial mechanical microenvironment, including stiffness, is a crucial pathophysiological feature of vascular remodeling, such as neointimal hyperplasia after carotid endarterectomy and balloon dilatation surgeries. In this study, we examined changes in neointimal stiffness in a Sprague-Dawley rat carotid artery intimal injury model and revealed that extracellular matrix (ECM) secretion and vascular stiffness were increased. Once the endothelial layer is damaged *in vivo*, activated platelets adhere to the intima and may secrete platelet-derived extracellular vesicles (pEVs) and communicate with vascular smooth muscle cells (VSMCs). *In vitro*, pEVs stimulated VSMCs to promote collagen secretion and cell adhesion. MRNA sequencing analysis of a carotid artery intimal injury model showed that ECM factors, including col8a1, col8a2, col12a1, and elastin, were upregulated. Subsequently, ingenuity pathway analysis (IPA) was used to examine the possible signaling pathways involved in the formation of ECM, of which the Akt pathway played a central role. *In vitro*, pEVs activated Akt signaling through the PIP_3 pathway and induced the production of Col8a1. MicroRNA (miR) sequencing of pEVs released from activated platelets revealed that 14 of the top 30 miRs in pEVs targeted PTEN, which could promote the activation of the Akt pathway. Further research showed that the most abundant miR targeting PTEN was miR-92a-3p, which promoted Col8a1 expression. Interestingly, knockdown of Col8a1 expression *in vivo* abrogated the increase in carotid artery stiffness and simultaneously increased the degree of neointimal hyperplasia. Our results revealed that pEVs may deliver miR-92a-3p to VSMCs to induce the production and secretion of Col8a1 *via* the PTEN/PIP3/Akt pathway, subsequently increasing vascular stiffness. Therefore, pEVs and key molecules may be potential therapeutic targets for treating neointimal hyperplasia.

Keywords: intimal injury, vascular stiffness, platelet-derived extracellular vesicles, vascular smooth muscle cell, col8a1

INTRODUCTION

Extracellular matrix (ECM) stiffness can directly influence many aspects of physiological and pathological processes, including intestine and lung morphogenesis (Rabelink et al., 2017), blood cell development (Leiva et al., 2018), tumor invasion (Schedin and Keely, 2011) and vascular aging (Lacolley et al., 2017). At the cellular level, the stiffness of the extracellular environment plays roles in orienting cell division, directing cell migration, and driving cell differentiation (Handorf et al., 2015). In the cardiovascular system, arterial stiffness associated with cardiovascular diseases has been explored extensively and has been indicated to have a huge impact (Harvey et al., 2016). In hypertension, ECM remodeling, including increasing collagen deposition, cross-linking collagen, and breaking down elastic laminae, affects arterial stiffness and promotes the proliferation of endothelial cells (ECs) and vascular smooth muscle cells (VSMCs) (Thenappan et al., 2018). In addition, in atherosclerosis, the elastic modulus of the thoracic aorta reaches 15 kPa in comparison with 5 kPa in normal mice and increases VSMC proliferation, apoptosis and osteochondrogenic transformation (Xie et al., 2018). Moreover, arterial stiffness could become an important marker to characterize vascular damage (Duprez and Cohn, 2007).

Injury of the arterial endothelial lamina, also called intimal injury, usually occurs after carotid endarterectomy (Budincevic et al., 2015), peripheral artery brachytherapy (Fokkema et al., 2012), stent placement for arterial occlusive disease (Dangas and Kuepper, 2002) and balloon dilatation surgeries (Quencer and Arici, 2015). After intimal injury, VSMC accumulation and extracellular matrix deposition result in intimal hyperplasia and vessel or stent occlusion (Cai et al., 2015). During this process, VSMCs change from a quiescent contractile phenotype to an active synthetic phenotype, which can migrate, proliferate and secrete ECM (Rudijanto, 2007). Subsequently, ECM remodeling changes the mechanical properties of the artery, including vascular elasticity (Stephan et al., 1997) and stiffness (Jaminon et al., 2019). For example, in mechanically injured iliac artery segments in rabbits, collagen types I and III and vascular stiffness were increased, which could induce plaque vulnerability (Kanshana et al., 2018). Although ECM remodeling and vascular stiffness play important roles in regulating intimal injury and intimal hyperplasia, the changes in ECM components and the factors regulating these changes are not fully understood.

There are many factors that can cause VSMC phenotypic transformation to remodel the ECM, such as multiple growth factors (Rudijanto, 2007; Guo et al., 2014), noncoding RNAs (Zeng et al., 2019), lipoproteins (Greig et al., 2015) and chemical compounds (Guo et al., 2019). In addition, platelets, a cellular debris shed by megakaryocytes, was originally thought to be components of coagulation, and now have been proven to play crucial roles in VSMC dysfunction. During intimal injury, platelets are activated, adhere to the intima and participate in intercellular communication with VSMCs (Pang et al., 2019; Zeng et al., 2019). Activated platelets secrete multiple agents, such as thromboxane and PDGF (Pang et al., 2019), leading to the migration and proliferation of VSMCs and promoting the formation of plaques. In recent years, research has shown that platelet-derived extracellular vesicles (pEVs), which are released by activated platelets, can transport molecules and participate in intercellular communication (Laffont et al., 2013). For example, pEVs containing serotonin and TXA2 could induce rabbit VSMC proliferation at the sites of vascular injury (Pakala, 2004).

Extracellular vesicles (EVs), which range in size from 40 nm to 5 μm, include small EVs (exosomes, arrestin-domain-containing protein 1-mediated microvesicles, etc.) and large EVs (microvesicles, apoptotic bodies, etc.) (Jeppesen et al., 2019). Previous studies showed that there were many bioactive molecules delivered by pEVs, including lipids, proteins, nucleic acids, and organelles involved in numerous biological processes (Puhm et al., 2020). For example, pEV-derived TGF-β can induce the differentiation of naïve $CD4^+$ T cells into $Foxp3^+$ regulatory T cells, which can influence T lymphocytes that are recruited to atherosclerotic lesions (Vajen et al., 2015). In addition, pEVs can deliver small noncoding RNAs, such as miR-223, to ECs and repress the expression of target mRNAs, such as FBXW7 and EFNA1 (Laffont et al., 2013). Although pEVs can participate in the regulation of VSMC proliferation (Pakala, 2004) and migration (Shan et al., 2015) through the delivery of a variety of molecules, it is still unclear whether pEVs can affect VSMC-induced ECM remodeling and arterial stiffness in the context of intimal injury.

In the present study, we examined vascular stiffness in intimal injury and the regulatory mechanisms of pEVs in ECM remodeling mediated by VSMCs. This study may provide new insight into the changes in vascular stiffness in intimal injury and may provide novel mechanoresponsive targets for the maintenance of vascular homeostasis.

Abbreviations: 3′ UTRs, 3′ untranslated regions; Col8a1, Collagen type VIII alpha 1 chain; CS, cyclic stretch; ECM, extracellular matrix; ECs, endothelial cells; HE staining, hematoxylin-eosin staining; IPA, ingenuity pathway analysis; MMP, matrix metalloproteinase; NTA, nanoparticle tracking analysis; OSS, oscillatory shear stress; pEVs, platelet-derived extracellular vesicles; pMPs, platelet-derived microparticles; SD rats, Sprague-Dawley rats; siRNA, small interfering RNA; VSMCs, vascular smooth muscle cells.

MATERIALS AND METHODS

The main methods are described in the text, and additional methods are detailed in the Supporting Information (**Supplementary Materials and Methods**).

Rat Carotid Artery Intimal Injury Model

The animal care and experimental protocols were conducted in accordance with the Animal Management Rules of China (55, 2001, Ministry of Health, China), and the study was approved by the Animal Research Committee of Shanghai Jiao Tong University.

Male Sprague-Dawley (SD) rats with an average weight of 400 g were anesthetized with isoflurane inhalation (MATRX VIP 3000, United States). The left carotid arteries were exposed, and a percutaneous transluminal angioplasty balloon dilatation catheter (2 F, 0.67 mm, Edwards Lifesciences, United States) was used to establish vascular intimal injury (Raugi et al., 1990). The arteries were then harvested after 2 weeks, and the undamaged right carotid artery served as the self-control.

Immunofluorescence Staining

The carotid arteries samples were fixed in 4% paraformaldehyde, dehydrated in 30% sucrose solution, and then cut into 6-μm sections. The frozen sections were washed three times with PBS, permeabilized with 0.3% Triton X-100 for 30 min, and immersed in a solution of 10% goat serum for 30 min at room temperature to block nonspecific binding. Subsequently, the sections were incubated with the primary antibodies against Col8a1 (1:400, Proteintech Group, United States), Col8a2 (1:400, Abcepta, United States), SMA (1:500, Invitrogen, United States), vWF (1:500, Cell Signaling Technology, United States), CD41 (1:500, Cell Signaling Technology, United States) at 4°C overnight. After incubated with secondary antibody (1:1000. Abcam, United Kingdom) for 2 h, DAPI was used for nuclei staining for 15 min at room temperature. Staining at the cellular level, paraformaldehyde was used to fix VSMCs for 30 min and then followed the above method. Photographs were taken by confocal microscopy (LV1000; Olympus).

FISH Analysis

Six-μm frozen-sections of carotid artery samples were treated with 0.3% H_2O_2 to block endogenous peroxide activity and proteinase K (5 $\mathrm{mg \cdot mL^{-1}}$) for permeabilization. The samples were then hybridized with a miR-92a-3p biotinylated probe or a NC probe (Shanghai GenePharma, China) (200 nM) overnight at 56°C. The FISH signals were amplified with Tyramide SuperBoost Kits (Thermo Fisher Scientific, United States) followed by an Alexa Fluor Tyramide Kit (Thermo Fisher Scientific, United States), and photographed under confocal microscopy (LV1000; Olympus). The sequences of the RNA oligos were listed in **Supplementary Table 1**.

Ultrasound Imaging

Multi-mode Ultrasound Imaging System (Fujifilm VisualSonics, United States) was used to detect the change in arterial diameter (%) of the carotid artery in rats after intimal injury. SD rats were anesthetized with isoflurane (MATRX VIP 3000, United States) and signals were collected using 20 MHz MX Series transducer (MX250S) in "M-Mode". Data analysis were performed on FUJIFILM VisualSonics Measurement software.

Vascular Stiffness Measurement

Piuma Nanoindenter (Optics11, Netherlands) was used to detect the stiffness of the carotid artery after intimal injury (Xie et al., 2018). A probe with a 0.49 $\mathrm{N \cdot m^{-1}}$ spring constant and a 31 μm spherical indentation radius was used. All measurements were performed with the carotid artery flattened onto the bottom of a dish and submerged in PBS at room temperature. The indents were depth controlled (10 μm), and the loading and unloading period was set to be 2 s. Based on the load-displacement curves, the Young's modulus was calculated using the Hertz spherical indentation model in Piuma Software (version: V3.3.0). For vascular stiffness analysis, 5-10 measurements were made on each carotid artery.

Nanoparticle Tracking Analysis

Nanoparticle tracking analysis was used to analyze the number and diameter of pEVs (Szatanek et al., 2017). The obtained pEVs were diluted with PBS and loaded into the NanoSight module (NanoSight NS300, United Kingdom) for measurement. The module was washed with PBS after each measurement.

Transcriptome Sequencing and miR Sequencing

The intimal injury arteries harvested after 2 weeks, and the undamaged right carotid artery served as the self-control, then performed transcriptome sequencing (GEO accession numbers: GSE164050). And the miR sequencing used by activated platelets and platelets released pEVs. Differentially expressed mRNAs or miRs were analyzed utilizing DESeq with the following criteria: fold change > 2 and false discovery rate (FDR) < 0.05. Afterwards, the ClustVis. web tool[1] was used to upload raw data and create heatmaps.

Ingenuity Pathway Analysis

The possible biological processes and functional classifications were obtained with Ingenuity Pathway Analysis (IPA) software[2] (Content version: 57662101, Qiagen, Germany). "Formation of extracelluar matirx" related genes in "Diseases and Functions model" were fist selected based on transcriptome sequencing data. Besides, the most abundant 30 miRs expressed in pEVs were uploaded into IPA to analyze their downstream target genes and main functions involved in. IPA integrated the available knowledge on genes, drugs, chemicals, protein families, processes, and pathways based on the interactions and functions derived from the Ingenuity Pathways Knowledge Database Literature, and understands the complex biological and chemical systems at the core of life science research based on lectures or predicated analysis (Dai et al., 2009).

---

[1] https://biit.cs.ut.ee/clustvis/

[2] https://www.qiagenbioinformatics.com

Stimulation of VSMCs With LY294002

LY294002 (10 μM), a highly selective inhibitor of phosphatidylinositol 3 (PI3) kinase, was preincubated with VSMCs for 1 h before adding pEVs. The same volume of DMSO was used as control.

PIP_3 ELISA

The concentration of PIP_3 in VSMCs was determined by ELISA using a rat PIP_3 ELISA kit (Shanghai FanTai Biotechnology, China). The kit used bi-antibody sandwich method to determine the level of PIP_3. First of all, the sample added to the microwells of the coated PIP_3 monoclonal antibody, and then it is combined with HRP-labeled PIP_3 antibody to form an antibody-antigen-enzyme-labeled antibody complex. After 3 times washing by PBS, the substrate TMB and acid were added for chromogenic reaction. The absorbance (OD value) was measured with the microplate reader (Bio-Rad 680, Bio-Rad, United States) at a wavelength of 450 nm.

Dual Luciferase Reporter Assay

The 3′ untranslated regions (UTRs) of PTEN including the predicted miR-92a-3p binding sequences, and the mutation segment were all obtained by gene synthesis. The segments were inserted into the downstream of the luciferase reporter gene (psiCheck-2, Promega, United States), respectively. To determine the suppressing efficiency of miR-92a-3p, HEK-293T cells were transfected with the reporter plasmid or the mutated vectors together with miR-92a-3p mimic or NC. Twenty-four h later, firefly and renilla luciferase activities were measured consecutively using a dual luciferase reporter assay system (Promega, United States).

Local Injection of Col8a1 SiRNA

After carotid artery intimal injury surgery, the rats were randomly assigned to two groups: subcutaneous injections of 300 μl of anti-col8a1 siRNA (1 μM) or negative control (Pillé et al., 2005). Subcutaneous injections were repeated every 2 days for a total of 2 weeks.

Statistical Analysis

Each experiment was performed at least in quadruplicate of biological replicates. Statistical analysis was performed and figures were prepared with the GraphPad Prism 6.0 (GraphPad Software, CA, United States). All values are expressed as the mean ± SD. The Gaussian distribution of values was analyzed by the Kolmogorov-Smirnov test. A paired *t*-test was used for paired data with a Gaussian distribution; A Wilcoxon matched-pairs signed rank test was used for paired data that lacked a Gaussian distribution or a sample size that was less than 5. In addition, the Friedman test was used for multiple comparisons with a single reference group whose sample size was less than 5. An unpaired *t*-test was used for unpaired data with a Gaussian distribution. Differences with values of $P < 0.05$ were regarded as statistically significant.

RESULTS

Intimal Injury Increases Vascular Stiffness and Promotes Collagen Accumulation

To explore the mechanical properties of the carotid artery after injury, we used ultrasound imaging to measure the deformation of the carotid artery following cardiac pulsation (**Figure 1A**) and a Piuma Nanoindenter to measure the stiffness of the carotid artery (**Figure 1B**) at 2 weeks after injury. Compared with that of the self-contralateral common carotid artery, the change in arterial diameter (%) (Safar et al., 1981) at 2 weeks after intimal injury surgery was significantly decreased (**Figure 1A**). Moreover, compared with that of the control, the stiffness of the carotid artery increased from an average of 13.45 kPa to an average of 20.98 kPa (**Figure 1B**).

To address the progression of vascular remodeling after intimal injury, elastin-van Gieson, hematoxylin-eosin (HE), and picrosirius red staining were used to examine the neointima, vascular morphology and collagen levels in the common carotid artery at 2 weeks after injury (**Figure 1D**). Compared with that of the self-contralateral common carotid artery, the neointima and VSMCs were significantly thickened and increased in the injured carotid artery (**Figures 1C,D**). Collagen accumulated in the vessel wall, especially in areas of neointimal hyperplasia (**Figure 1D**). These results suggested that in the intimal injury model, the stiffness of the injured vessel was increased at approximately 2 weeks. The main component in areas of hyperplasia was VSMCs, and there was a large amount of collagen in the neointima, which may affect the mechanical properties of the injured artery.

pEVs Interact With VSMCs to Promote the Secretion of Collagen

Immunofluorescence staining revealed that CD41-positive pEVs were closely adjacent to VSMCs in the injured carotid artery *in vivo* (**Figure 2A**). Then, Nanoparticle Tracking Analysis (NTA) was used to examine the concentration and size distribution of the circulating EVs after intimal injury surgery. The results showed that compared with the control group, the number and size of circulating EVs did not change significantly after intimal injury surgery (**Supplementary Figure 1**). This may because that the activation of platelets and the release of pEVs mainly occur in the injured area, and cannot significantly affect the number of pEVs in the entire blood.

In vitro, Electron microscopy imaging and NTA indicated that the size of most pEVs secreted by activated platelets was between 100 to 200 nm (**Figures 2B,C** and **Supplementary Figure 2**). Moreover, nanoparticle tracking analysis (NTA) indicated that the size a peak was at 164 nm. In addition, there was a small peak at 36 nm, indicating that there might be a small amount of exosomes in the extracted pEVs (**Figures 2B,C**).

To investigate the adhesion of pEVs to VSMCs *in vitro*, pEVs were labeled with the red fluorescent cell linker PKH26. The immunofluorescence staining results showed that PKH26-positive pEVs adhered to VSMCs after pEV stimulation for 1 h

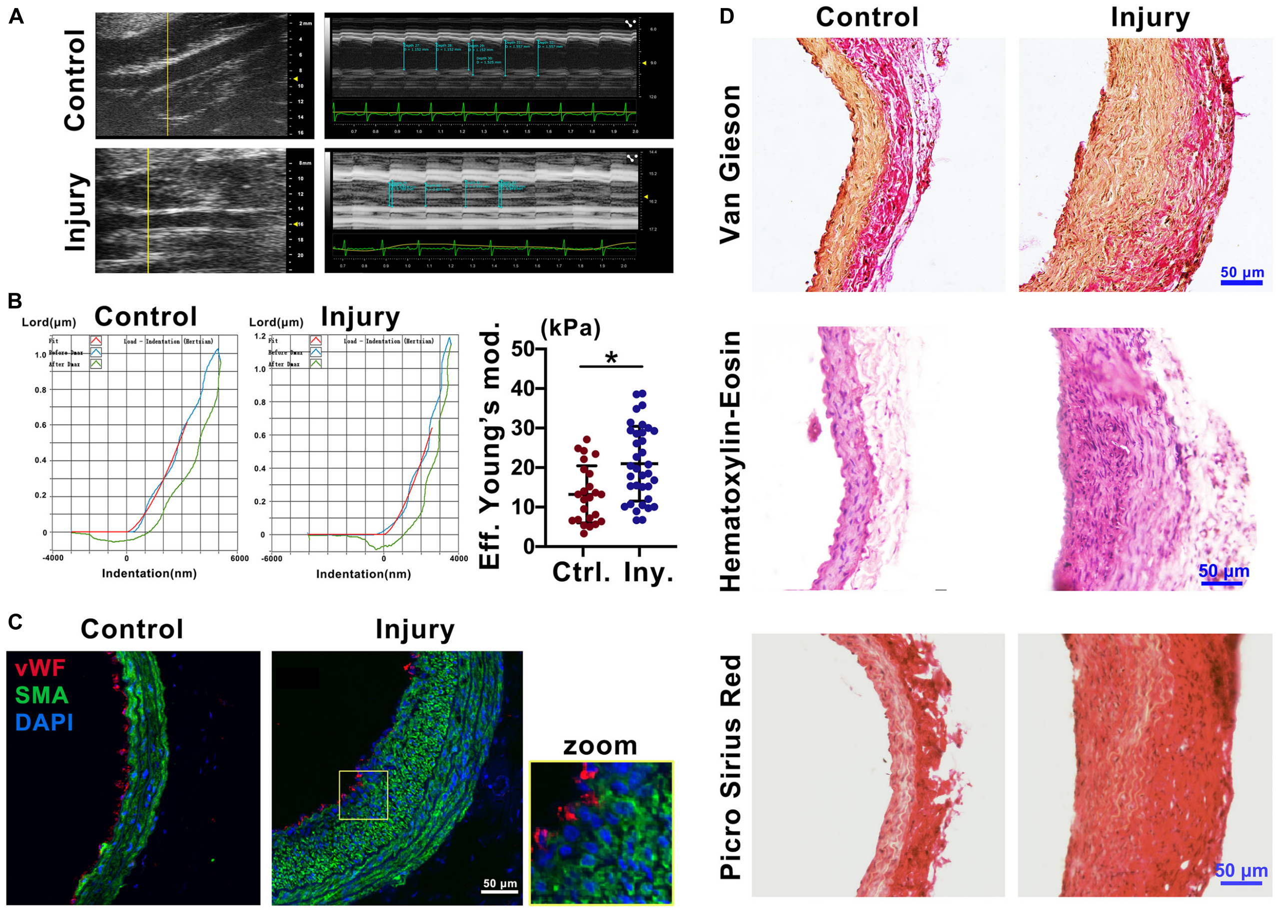

FIGURE 1 | Intimal injury promoted neointimal hyperplasia and increased vascular stiffness. **(A)** Ultrasound imaging was used to measure the change in arterial diameter (%). At 2 weeks after intimal injury surgery, the change in arterial diameter was significantly decreased. **(B)** The Piuma nanoindenter was used to determine vascular stiffness, and the stiffness of the carotid artery increased from an average of 13.45 kPa to an average of 20.98 kPa after intimal injury surgery. **(C)** Immunofluorescence was used to determine the type of cells in areas of neointimal hyperplasia, and most of the hyperplasia involved VSMCs. Green indicates SMA staining (VSMCs), red indicates vWF staining (ECs), and nuclear staining is shown in blue by DAPI (bar = 50 μm). **(D)** Elastin-van Gieson, hematoxylin-eosin (HE), and picrosirius red staining revealed that the area of neointimal hyperplasia was significantly thickened and collagen accumulated 2 weeks after intimal injury compared with those of the contralateral common carotid artery (control) (bar = 50 μm). The values are shown as the mean ± SD, $^{*}P < 0.05$ vs. control ($n = 4$ biological replicates).

(**Figure 2F**). When pEVs and newly digested and suspended VSMCs were mixed and seeded on an uncoated glass plate, more VSMCs adhered and spread on the glass surface than in the control group (**Figures 2D,E**), indicating that pEVs promoted VSMC adhesion. In addition, increased bundles of long microtubules were present in VSMCs stimulated by pEVs (**Figures 2G,H**), which might be because VSMCs secrete large amounts of extracellular matrix (ECM), and VSMCs have improved focal adhesion on a smooth glass plate (Humphries, 2009). Subsequently, picrosirius red staining was used to analyze whether collagen secretion by VSMCs was changed after pEV stimulation. Compared with unstimulated VSMCs, VSMCs stimulated by pEVs secreted more collagen (**Figure 2I**). These results suggested that during vascular intimal injury, pEVs could interact with VSMCs and cause VSMCs to secrete increased ECM, thereby inducing vascular ECM remodeling. Then, we focused on the ECM, expecially the members of collagen to determine their roles in the process of endometrial injury.

Intimal Injury and pEVs Upregulate Col8a1 Expression

To explore the ECM and ECM regulatory factors involved in neointimal hyperplasia in an intimal injury model, we used mRNA sequencing to analyze the changes in mRNA expression in the injured carotid artery at 2 weeks after surgery. Among the differentially expressed genes, 237 genes were identified as "extracellular space" by IPA (**Supplementary Table 2**). Subsequently, we used UniProt[3] and GO "molecular function" analyses to distinguish these "extracellular space" molecules into the "extracellular matrix structural constituent" and "extracellular matrix organization and metalloendopeptidase

---

[3] https://www.uniprot.org

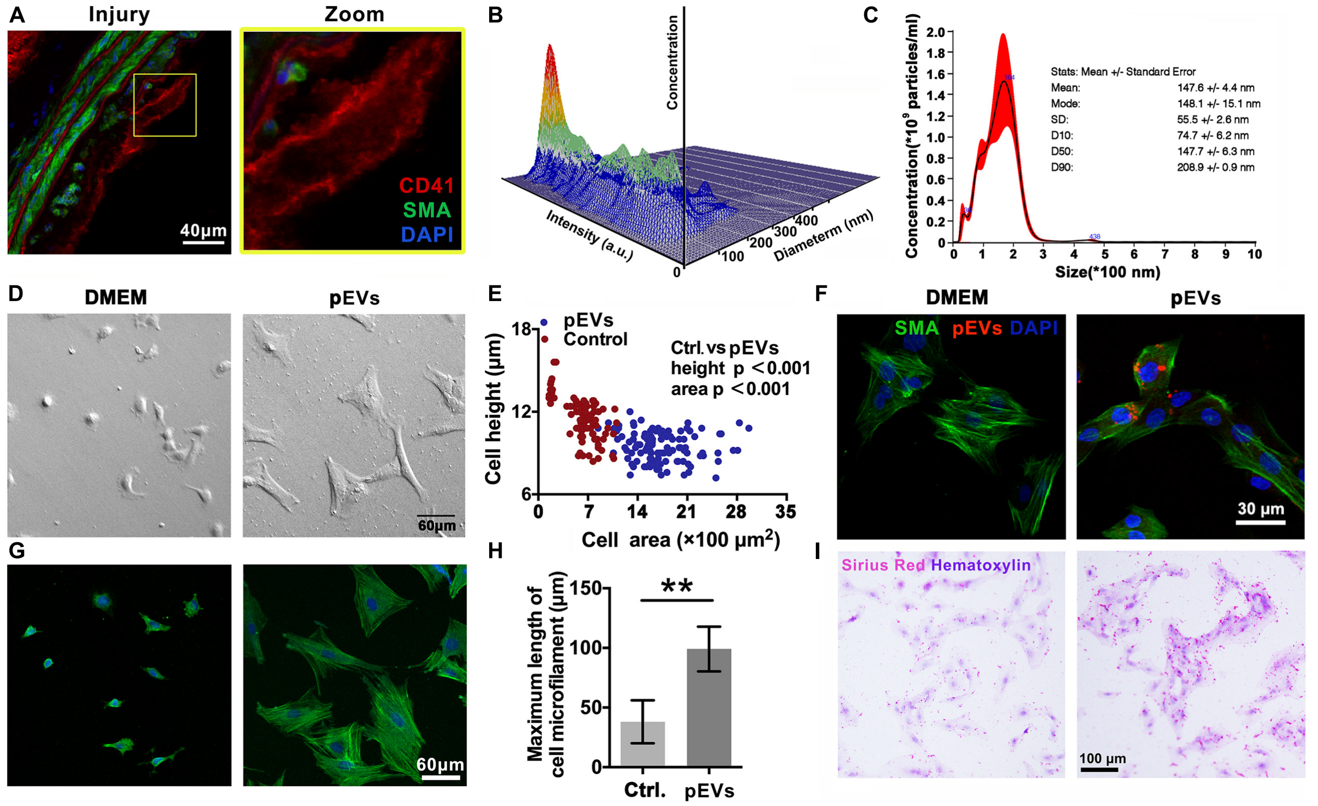

FIGURE 2 | pEVs interacted with VSMCs to promote collagen secretion. **(A)** Immunofluorescence staining was used to examine the adhesion of VSMCs *in situ* compared with that in the control group. Green indicates SMA staining (VSMCs), red indicates CD41 staining (pEVs), and nuclear staining is shown in blue by DAPI (bar = 40 μm). **(B,C)** Nanoparticle tracking analysis (NTA) was used to examine the concentration and size distribution of the pEVs. The results revealed that most of the pEVs were between 100 and 300 nm in size. **(D,E)** Cell morphological analysis revealed the adhesion of VSMCs to glass culture dishes after pEV stimulation. The area and height of cell adhesion were measured by the confocal microscope. After pEV stimulation, more VSMCs adhered and spread on the surface of the glass plate compared with the control (bar = 60 μm). **(F)** pEVs significantly adhered to VSMCs at 1 h. Red fluorescence shows the pEV membranes, which were labeled with the fluorescent cell linker PKH26, green fluorescence shows SMA staining (VSMCs), and blue fluorescence shows DAPI-labeled nuclei (bar = 30 μm). **(G,H)** Microtubule staining showed changes in microtubule length, and more bundles of long microtubules were present in the VSMCs stimulated by pEVs than in unstimulated cells (bar = 60 μm). **(I)** Picrosirius red staining was used to analyze whether VSMC collagen secretion changed after pEV stimulation. Compared with unstimulated VSMCs, VSMCs stimulated with pEVs secreted more collagen (bar = 100 μm). The values are shown as the mean ± SD, *$P < 0.05$, **$P < 0.01$ vs. control ($n = 4$ biological replicates).

activity" categories (**Supplementary Table 3**). Among them, the "extracellular matrix structural constituent" category contained 20 molecules, and the "extracellular matrix organization and metalloendopeptidase activity" category contained 43 molecules (**Supplementary Table 3** and **Figure 3A**).

We selected the 10 molecules with the highest abundance and greater than 2-fold differential expression in the "extracellular matrix structural constituent" category for subsequent analysis. As shown in **Figure 3B**, real-time RT-PCR analysis validated that col8a1, col12a1, col8a2, elastin, col6a3, acan and tenascin expression levels were significantly upregulated at 2 weeks after intimal injury surgery compared with those of the self-contralateral common carotid artery. *In vitro*, after pEV stimulation for 12 h, qPCR analysis showed that col8a1, elastin, col16a1, col8a2 and col12a1 expression levels were significantly upregulated compared with those of the control (**Figure 3C**). The expression levels of col8a1, col8a2, col12a1, and elastin changed in response to both stimuli. Among these molecules, the Col VIII family has been proven to play an important role in changes in the stiffness of atherosclerotic plaques (Merei et al., 2017). Therefore, we performed immunofluorescence and western blotting analyses of Col8a1 and Col8a2.

The immunofluorescence staining results showed that in the neointima after intimal injury *in vivo* and in VSMCs stimulated with pEVs *in vitro*, the fluorescence intensities of Col8a1 and Col8a2 increased significantly (**Figures 3D,E** and **Supplementary Figure 3**). Col8a1 was mostly located in the cytoplasm, as shown immunofluorescence staining, and the qPCR and western blotting results revealed that col8a1 mRNA and protein expression also significantly increased (**Figures 3F,G**). However, Col8a2 was mostly located in the nucleus (**Supplementary Figure 3B**), which was different from the traditional understanding of VSMCs (Stephan et al., 2004; Adiguzel et al., 2006). These results suggest that pEV-induced VSMCs produce and secrete Col8a1, which may contribute to ECM remodeling during vascular intimal injury.

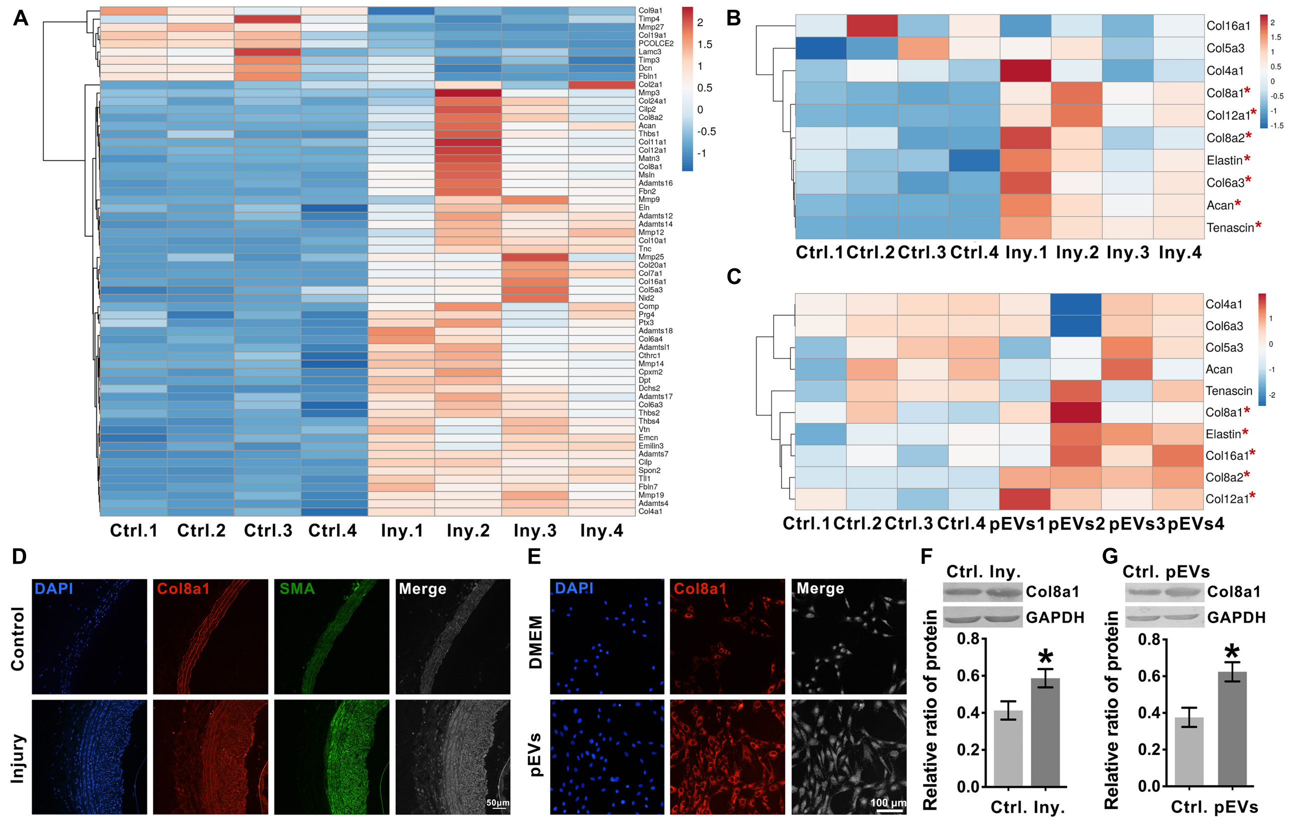

FIGURE 3 | Intimal injury and pEVs regulated the increase in Col8a1 expression. **(A)** Bioinformatics analysis revealed 63 distinct molecules related to ECM remodeling in the intimal injury model by mRNA sequencing. **(B,C)** Real-time RT-PCR was used to measure the expression of the 10 molecules with the highest abundance and differential expression, as determined by mRNA sequencing of extracellular matrix structural components. **(B)** Thee intimal injury group was compared with the self-contralateral common carotid artery, and **(C)** the pEV stimulation group was compared with the control group. **(D,E)** Immunofluorescence staining was used to measure Col8a1 accumulation in response to intimal injury or pEV stimulation *in vitro*. The results showed that in response to either intimal injury **(D)** or pEV stimulation **(E)**, the fluorescence intensity of Col8a1 increased significantly. **(F,G)** Western blotting was used to measure the expression of Col8a1. The results showed that in response to either intimal injury **(F)** or pEV stimulation **(G)**, the expression of Col8a1 increased significantly. The values are shown as the mean ± SD, **P* < 0.05 vs. control (*n* = 4 biological replicates).

PIP$_3$/Akt Signaling Regulates the Production of Col8a1

To investigate the molecules transported by pEVs that are involved in regulating the production of Col8a1, IPA software was used to analyze related molecules that may participate in the regulation of "formation of extracellular matrix" (**Figure 4A**). The results revealed that 36 molecules correlated with the formation of extracellular matrix (**Figure 4A** and **Supplementary Table 4**). Among them, we focused on Akt signaling, which is the core signaling pathway that participates in this network (**Figure 4B**). Western blotting was used to measure the expression of phosphorylated Akt in VSMCs after pEV stimulation, and we found that Akt was significantly activated (**Figure 4C**). In order to detect whether the Akt carried by pEVs contribute to the Akt changes in VSMCs, which subsequently increased the phosphorylation of Akt, the expression of total Akt in VSMCs after pEVs stimulation was analyzed (**Supplementary Figure 4**). The results showed that the expression of total Akt was similar between the control group and pEVs stimulation group, which indicated that the increased pAkt may be activated by pEVs but not via the direct delivery.

Since multiple molecules, such as PIP$_3$, PDK1 and mTORC2, have been reported to be involved in the activation of Akt (Xu et al., 2015), western blotting and ELISA were further performed (**Figures 4D–F**). Among these three molecules, only the expression of PIP$_3$ increased significantly in VSMCs stimulated with pEVs. The stimulation of pEVs was complicated, and using IPA software the potential interleaving of multiple signal networks which may lead to the activation of Akt and inactivation of PDK1 and mTOR were analyzed (**Supplementary Figure 5**). Therefore, Akt activation may be due to the activation of upstream PIP$_3$ induced by pEVs.

To further verify the effect of PIP$_3$/Akt signaling on the production of Col8a1 by VSMCs, cells were pretreated with LY294002, a specific inhibitor of PIP$_3$/Akt signaling, for 1 h and then treated with pEVs. LY294002 significantly abrogated the expression level of p-Akt induced by pEVs (**Figure 4G**). After treatment with pEVs for 12 h, LY294002 also had the same effect on the repression of col8a1 mRNA (**Figure 4I**).

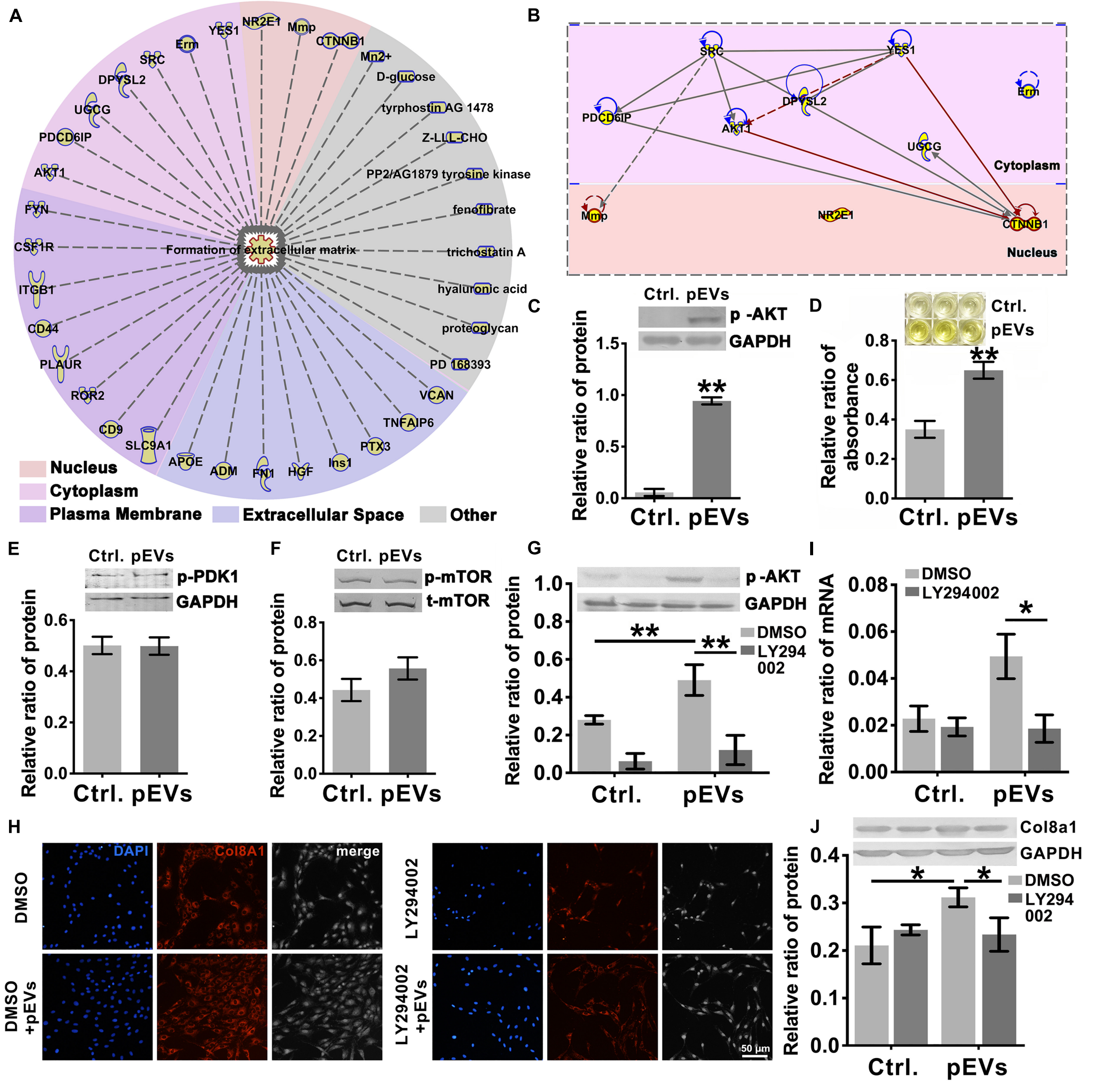

FIGURE 4 | PIP$_3$/Akt signaling regulated the production of Col8a1. **(A)** IPA software was used to analyze related molecules that can participate in the regulation of "formation of extracellular matrix" and **(B)** the core signaling pathways in the cytoplasm and nucleus participated in this network. **(C)** Western blotting was used to measure the expression of phosphorylated Akt in VSMCs, and the results showed that Akt was significantly activated after pEV stimulation. **(D–F)** ELISA and western blotting were used to analyze molecules involved in the activation of Akt. Only the level of PIP$_3$ increased significantly in VSMCs after pEV stimulation, **(D)** while PDK1 **(E)** and mTORC **(F)** were unchanged. **(G–J)** The specific PIP$_3$/Akt signaling inhibitor LY294002 was used to examine the effect of PIP$_3$/Akt signaling on the production of Col8a1. **(G)** LY294002 significantly abrogated the expression of p-Akt induced by pEVs and blocked the mRNA **(I)** and protein expression of col8a1 **(H,J)**. The values are shown as the mean ± SD, $^{*}P < 0.05$, $^{**}P < 0.01$ vs. control ($n = 4$ biological replicates).

Immunofluorescence staining and western blotting showed that the addition of LY294002 blocked the protein expression of Col8a1 in VSMCs stimulated with pEVs (**Figures 4H,J**). These results suggested that PIP$_3$/Akt signaling participated in the production of Col8a1 by VSMCs stimulated with pEVs.

miR-92a-3p Delivered by pEVs Induces the Production of Col8a1 by Inhibiting PTEN

Recent studies have shown that pEVs can deliver a variety of miRs (Laffont et al., 2013). MiR sequencing was used to identify the top 30 miRs expressed in pEVs secreted from activated platelets (**Figure 5A**). The functions of the downstream target molecules (82 in total) of these 30 miRs were analyzed by IPA software, and we found that the downstream molecules were mainly related to "cellular movement" and "cardiovascular system development" (**Figure 5B** and **Supplementary Table 5**). A total of 41 of the 82 molecules formed a core network structure, of which 7 key molecules were involved in the Akt signaling pathway (**Figure 5C** and **Supplementary Table 6**).

Among the 30 miRs, 19 core seed sequences could bind to the 3'UTRs of different target gene mRNAs (**Supplementary Table 7**). Among the 30 miRs, 14 miRs targeted the same

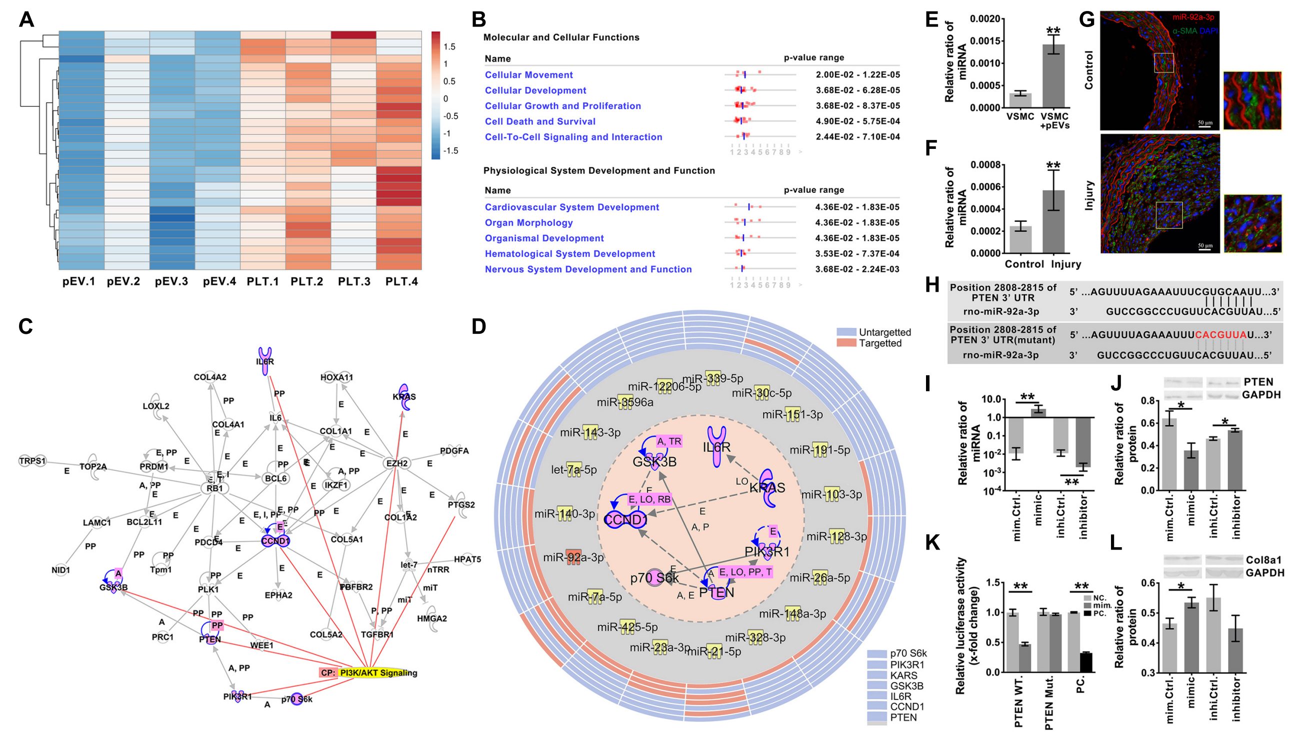

FIGURE 5 | miR-92a-3p upregulated the production of Col8a1 by inhibiting the expression of PTEN. **(A)** mRNA sequencing was used to analyze activated platelets and their secreted pEVs, and the top 30 miRs in pEVs are shown. **(B)** IPA software was used to analyze the downstream target molecules of the top 30 miRs in pEVs, and these molecules were mainly related to "cellular movement" and "cardiovascular system development." **(C)** IPA software was used to analyze the core downstream network that intersected PI3K/AKT signaling and identified 7 key molecules involved in the Akt signaling pathway. **(D)** IPA software and a literature search were used to analyze miRs and their target mRNAs. Among the 30 miRs, 14 miRs targeted the same molecule, PTEN. **(E,F)** Real-time RT-PCR was used to measure miR-92a-3p expression in response to intimal injury or pEV stimulation *in vitro*. The results showed that in response to either pEV stimulation **(E)** or intimal injury **(F)**, miR-92a-3p expression increased significantly. **(G)** In the intimal injury model, FISH was used to measure miR-92a-3p expression *in situ*. The results validated that miR-92a-3p expression levels were significantly upregulated in VSMCs compared with the self-contralateral carotid artery. **(H)** The PTEN 3'UTR has a binding site for miR-92a-3p. **(I)** The qPCR results showed that the miR-92a-3p mimic or inhibitor significantly increased or decreased miR-92a-3p expression in VSMCs, respectively. **(J)** Western blotting indicated that in VSMCs, the miR-92a-3p mimic reduced the protein expression of PTEN, while the miR-92a-3p inhibitor increased PTEN expression compared with that of the control. **(K)** A dual luciferase reporter gene system was used to examine the luciferase activity in wild-type (WT) and mutant PTEN 3'UTRs in negative control and miR-92a-3p mimic-treated HEK-293T cells. miR-92a-3p significantly reduced the luciferase activity of the wild-type PTEN 3'UTR compared with the negative control in three culture replicates. **(L)** Western blotting indicated that in VSMCs, miR-92a-3p mimics increased the protein expression of Col8a1, which was mediated by PTEN. The values are shown as the mean ± SD, *$P < 0.05$, **$P < 0.01$ vs. control ($n = 4$ biological replicates).

molecule, PTEN, which was the most common of all 7 targeted molecules associated with PI3K/Akt signaling (**Figure 5D** and **Supplementary Table 8**). Therefore, miR-92a-3p, which targeted PTEN and was the most highly expressed in pEVs, was selected for follow-up studies.

After pEV stimulation for 12 h *in vitro*, the qPCR results verified that miR-92a-3p expression in VSMCs was significantly upregulated in comparison with that of the control (**Figure 5E**). To detect whether the increased miR- 92a-3p was produced by VSMCs or was delivered by pEVs to VSMCs, the precursor of miR-92a-3p (pre-miR-92a-3p) in VSMCs was detected. If the miR-92a-3p was produced by VSMCs, pre-miR-92a-3p would increase in VSMCs (**Supplementary Figure 6**). The results showed that the expression of pre-miR-92a-3p were similar between the control group and pEVs stimulation group, which indicated that the increased miR-92a-3p was transferred by pEVs. Moreover, western blotting showed that PTEN expression in VSMCs was significantly downregulated after pEV stimulation for 24 h (**Supplementary Figure 7**). *In vivo*, qPCR and FISH results verified that miR-92a-3p expression levels were significantly upregulated in VSMCs 2 weeks after intimal injury surgery in comparison with those of the self-contralateral carotid artery (**Figures 5F,G**). There was a predicted binding site for miR-92a-3p at the PTEN 3'UTR site 2808-2815 (**Figure 5H** and **Supplementary Table 9**), indicating that miR-92a-3p may negatively regulate PTEN protein expression.

Subsequently, miR-92a-3p was overexpressed or knocked down in VSMCs with a specific mimic or inhibitor, respectively (**Figure 5I**). Western blotting indicated that the miR-92a-3p mimic significantly reduced the protein expression of PTEN, whereas the inhibitor increased PTEN levels compared with those of the respective NC (**Figure 5J**). These results indicate that miR-92a-3p plays an important role in the regulation of PTEN expression.

Dual luciferase reporter gene analysis was then used to assess the binding and inhibitory capacity of miR-92a-3p for the target sites of the PTEN 3′UTR. Compared with the NC, cotransfection of the miR-92a-3p mimic with the wild-type 3′UTR of PTEN significantly decreased the luciferase activity in HEK-293T cells (**Figure 5K**). In contrast, there was no significant change when miR-92a-3p was cotransfected with the mutant PTEN 3’UTR compared to the NC (**Figures 5H,K**).

Then, we evaluated the impact of miR-92a-3p changes on Col8a1. The qPCR and western blot results indicated that the miR-92a-3p mimic significantly increased the mRNA and protein expression of col8a1 (**Figure 5L** and **Supplementary Figure 8**). These results indicated that miR-92a-3p negatively regulated the expression of PTEN and subsequently promoted the production of Col8a1 in VSMCs.

Knockdown of Col8a1 Downregulates Vascular Stiffness

To further elucidate the effects of Col8a1 on vascular stiffness in the intimal injury model, col8a1 small interfering RNA (siRNA) was injected locally to knockdown Col8a1 expression (**Supplementary Figure 9**). Three pairs of specific siRNAs were designed, and the most efficient siRNA, si-#2, was identified (**Figure 6A** and **Supplementary Table 1**). In intimal injury, the siRNA significantly reduced the mRNA and protein expression of col8a1 compared with that of the NC (**Figures 6B,C**). Vascular morphological analysis revealed that the vessel wall was thickened, but the collagen density was reduced after col8a1 siRNA injection (**Figures 6D,E**).

Regarding the mechanical properties of the carotid artery, compared with that of NC injection after intimal injury, siRNA injection significantly decreased the change in arterial diameter (%) at 2 weeks after intimal injury surgery from an average of 13.93% to an average of 4.82% (**Figure 6F**). Moreover, the stiffness of the carotid artery decreased from an average of 20.31 kPa to an average of 16.28 kPa compared with that of the NC group (**Figure 6G**). These results suggested that Col8a1 knockdown could alleviate the increase in vascular stiffness in the intimal injury model.

DISCUSSION

Mechano-homeostasis plays a key role in maintaining the biological functions of the cardiovascular system and the pathological development of cardiovascular disease (Chien, 2007; Haga et al., 2007). A variety of mechanical stresses change, coordinate and control a variety of vascular cells, including ECs and vascular smooth muscle cells (VSMCs) (Tanaka et al., 2019; Zhang et al., 2020; Ngai et al., 2020). Therefore, exploring the changes in the mechanical stress that arterial cells are subjected to is crucial to understanding the mechanobiological mechanisms underlying vascular cell dysfunction. Here, we found that pEVs target VSMCs and effectively promote the production of Col8a1, an important component of the ECM that participates in vascular stiffness.

In the pathogenesis of many cardiovascular diseases, ECM remodeling is closely related to vascular stiffness. Alterations in extracellular matrix composition and arterial geometry result in structural arterial stiffness (Namba et al., 2019). In a murine femoral wire injury model associated with intimal hyperplasia, there is substantial collagen and proteoglycan deposition (Fu et al., 2014), which may cause changes in vascular stiffness. In addition, collagen type I (Lee et al., 2009; Kanshana et al., 2018), type III (Kanshana et al., 2018), type VIII (Plenz et al., 1999) and fibronectin (Yao et al., 2009) are upregulated in different animal intimal injury models. For example, in mechanically injured iliac artery segments in rabbits, collagen types I and III and VSMCs are increased, and there is a reduction in the immunolabeling of macrophage markers (CD68) (Kanshana et al., 2018). In addition, the matrix metalloproteinase (MMP) family, is also essential for arterial stiffening (Liu et al., 2015). MMPs can lead to degradation and remodeling of the arterial ECM and affect arterial stiffening (Liu et al., 2015). In mechanical intimal injury, MMP2 (Tummers et al., 2010) and MMP9 (Cho and Reidy, 2002) are significantly elevated. After acute vascular injury, MMP12 is induced in VSMCs and influences elastin degradation and arterial stiffening (Liu et al., 2015).

Col8a1 is a short chain member of type VIII collagen (Greenhill et al., 2000). In the vessel wall, Col8a1 is mainly located in the subendothelial space, subendothelium and media of arteries, and is secreted by ECs and VSMCs (Plenz et al., 2003). It has been reported that the increased expression of Col8a1 promotes proliferation and migration of ECs and VSMCs (Plenz et al., 2003). At earlier stages of atherogenesis, endothelial derived Col8a1 has been proved to be a key factor in EC proliferation which may play a positive role in endothelial repair and the integrity of neointima (Plenz et al., 1999, 2003). Whereas, VSMC derived Col8a1 mainly takes part in the atherosclerotic plaque development at later stages (Yasuda et al., 2000), and increases VSMC proliferation in ApoE$^{-/-}$ atherosclerotic mice (Yasuda et al., 2000; Lopes et al., 2013). In rat carotid artery balloon injury model, Col8a1secreted by VSMC is overexpressed in the luminal part of carotids after endothelial denudation, and strongly promotes migration of VSMCs (Sibinga et al., 1997). In our study, silencing Col8a1 induced the neointimal hyperplasia which suggested the increased contents of VSMCs, meanwhile, reduced the stiffness of the carotid artery. These studies suggest that although the indiscriminate repression of Col8a1 in all vascular cells could alleviate the increased vascular stiffness, it may also block EC repair which causes excessive proliferation of VSMCs. Whether the VSMC specific knockdown of Col8a1 will be a potential therapeutic target for treating neointimal hyperplasia induced by vascular intima injury and carotid surgery is still unclear and should be further studied in the future.

After vascular intima injury and carotid surgery, the adhesion and aggregation of circulating platelets on the injured intima was an important pathological process (Zaldivia et al., 2017). The activation of platelets and pEV secretion at the intima injury and atherosclerotic plaque could cause VSMC phenotypic switching, migration and proliferation, and subsequent facilitate vascular calcification (Schurgers et al., 2018). Hence, the antiplatelet agents could significantly reduce the risk of carotid stenosis recurrence by reducing platelets deposited at the site of the injured endothelium and vascular inflammation (Dharmakidari et al., 2017; Liu et al., 2018). However, the antiplatelet agent

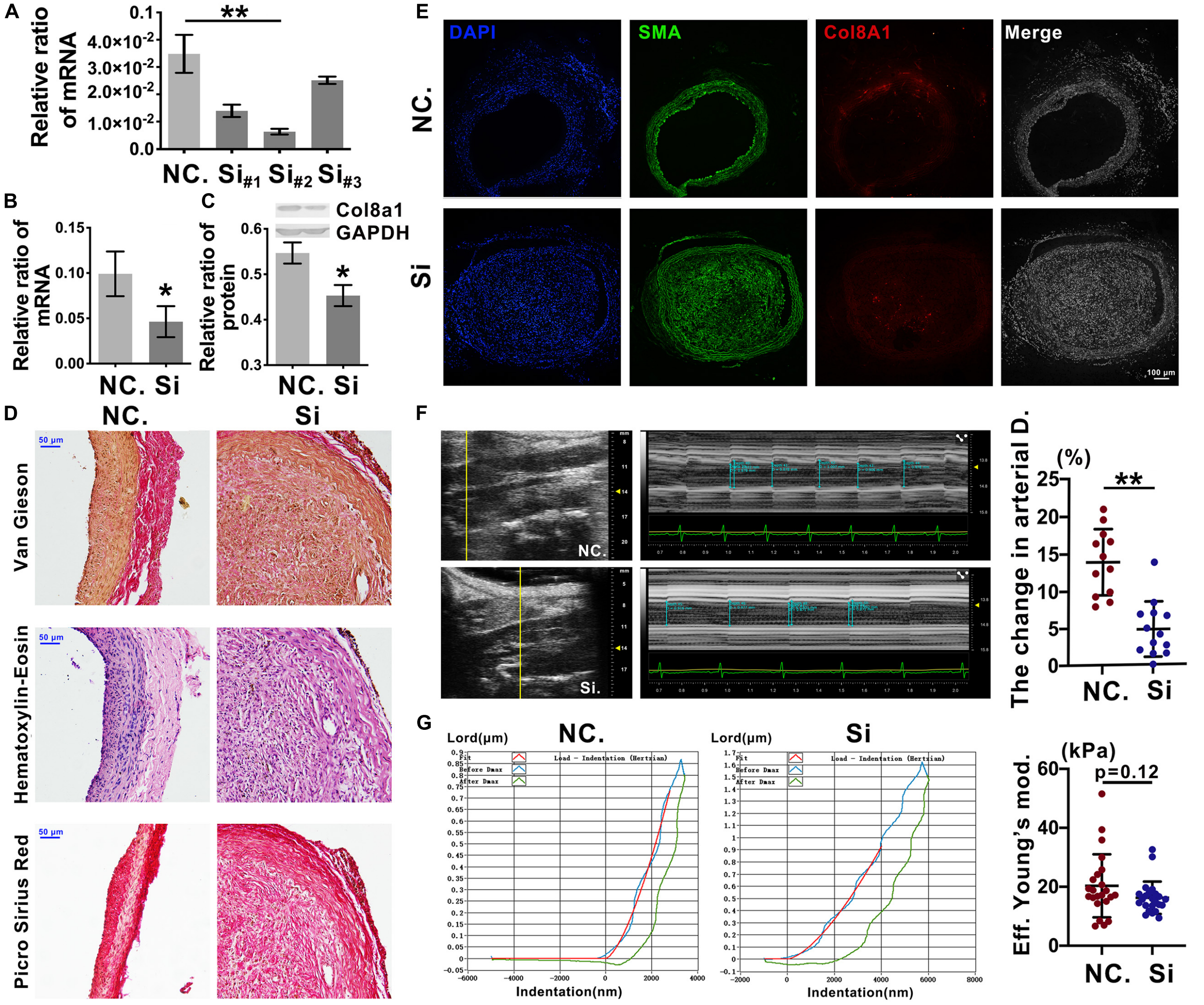

FIGURE 6 | Knockdown of Col8a1 downregulated vascular stiffness. **(A)** Real-time RT-PCR results showed the interference efficiencies of 3 col8a1 siRNA sequences, and si#2 was the most efficient siRNA. **(B,C)** Real-time RT-PCR and western blotting were used to determine the efficiency of si#2 *in vivo*. Compared with the NC, si#2 significantly reduced the mRNA **(B)** and protein **(C)** expression of col8a1. **(D)** Elastin-van Gieson, hematoxylin-eosin (HE), and picrosirius red staining revealed that compared with that of NC administration, neointimal hyperplasia and vascular morphology were thickened after Col8a1 knockdown, but the collagen density was reduced (bar = 50 μm). **(E)** Immunofluorescence was used to examine Col8a1 accumulation in the col8a1 siRNA and control injection groups. Green indicates SMA staining (VSMCs), red indicates Col8a1 staining, and nuclear staining is shown in blue by DAPI (bar = 100 μm). **(F)** Ultrasound imaging was used to measure the change in arterial diameter (%). After col8a1 siRNA injection, at 2 weeks after intimal injury surgery, the change in arterial diameter was significantly increased. **(G)** The Piuma nanoindenter was used to determine vascular stiffness, and the stiffness of the carotid artery decreased from an average of 20.31 kPa to an average of 16.28 kPa compared with that of the NC group. The values are shown as the mean ± SD, *$P < 0.05$, **$P < 0.01$ vs. control ($n = 4$ biological replicates).

still has its limitations in the treatment of intimal injury. For example, despite the widespread application of drug-eluting stents and anti-platelet therapy, instent restenosis remains a major clinical issue in percutaneous coronary interventions (Waksman and Steinvil, 2016; Liu et al., 2018). In terms of basic research, antiplatelet agent–acetylsalicylic acid (ASA; aspirin), has no significant effect on vascular remodeling in response to denudation injury to rat carotid arteries (Yang et al., 2004). Rosińska's research also reported that despite the ani-aggregation role of aspirin in platelet, it has no significant effect on microvesicle parameters, including pEVs (Rosińska et al., 2019). Hence, further understanding the platelet and pEVs relative mechanisms in intimal injury may provide novel targets to prevent intimal hyperplasia and vessel or stent occlusion.

In 1967, platelet-derived microparticles (pMPs), which are now called pEVs, were first identified during blood coagulation research and were called platelet dust (Wolf, 1967). We now know that pEVs contain abundant genetic materials and bioactive molecules and transfer these contents from platelets to recipient cells in the circulatory system (Puhm et al., 2020). In our study, pEVs activated PIP_3/Akt signaling to promote Col8a1 production. Interestingly, several inflammatory factors, oxidative stress-related factors were also changed by pEVs (**Supplementary Figure 10**). In fact, based on the results reported by Dean et al. (2009), we analyzed 449 proteins present in pEVs and examined their relationship with PIP_3/Akt signaling. Functional analysis of these molecules by IPA software showed that these 449 molecules were mainly related to "inflammatory response" and "cellular compromise" (**Supplementary Figure 11A**), and among them, OCRL, ITGB3, and RAP1A. may be involved in the activation of the Akt pathway (**Supplementary Figure 11B**). The molecular mechanism by which pEVs activate VSMCs is quite complicated and still requires further research.

Many miRs are involved in the development of cardiovascular disease (Wojciechowska et al., 2017). The different miRs, including miR-92a, have different effects in the occurrence and development of cardiovascular diseases. In vascular ECs, up-regulated miR-92a in neointimal lesions caused by wire-induced injury, impairs cell proliferation and migration *via* repressing integrin α5 and sirtuin1, which subsequently reduces eNOS (Daniel et al., 2014). In VSMCs, increased expression of miR-92a, induced by PDGF-BB during the formation of atherosclerosis plaque in mice, promotes cell proliferation and migration via targeting KLF4 (Wang et al., 2019). These results indicate that miR-92a induces the dysfunctions of vascular cells and participates in the pathological process of intimal injury or atherosclerosis. On the other hand, a protective effect of miR-92a on vascular homeostasis was also reported. In older adults and old B6D2F1 mice (an established model of vascular aging), miR-92a expression is reduced which contributes to age-related endothelial dysfunction and increased large artery stiffness (Hazra et al., 2016). In our present work, miR-92a-3p delivered by pEVs targets to PTEN, which then activates the Akt signaling and causes Col8a1 deposition at the intimal injury arteries. These works revealed a varied of functions of miR-92a in different cardiovascular diseases and in different types of cells. This may due to the difference in the pathogenesis of cardiovascular diseases and the complexity of the biological signaling networks caused by miR-92a.

In summary, the current study revealed that during intimal injury, pEVs are located at the injury site, contact VSMCs, and may deliver miR-92a-3p, which in turn represses PTEN and promotes the activation of the Akt pathway and Col8a1 production in VSMCs. Knockdown of Col8a1 expression abrogated the increase in carotid artery stiffness. Therefore, pEVs and the key molecules involved in stiffness modulation may be potential therapeutic targets for neointimal hyperplasia.

DATA AVAILABILITY STATEMENT

The datasets presented in this study can be found in online repositories. The names of the repository/repositories and accession number(s) can be found below: NCBI Gene Expression Omnibus, accession no: GSE164050.

ETHICS STATEMENT

The animal study was reviewed and approved by Animal Research Committee of Shanghai Jiao Tong University.

AUTHOR CONTRIBUTIONS

HB and Y-XQ designed the research. HB, Z-TL, L-HX, T-YS, YH, MB, ZL, Y-JF, YL, and YC performed the research. HB and Z-TL analyzed the data. HB, Z-LJ, X-BG, and Y-XQ wrote the manuscript. All authors contributed to the article and approved the submitted version.

FUNDING

This research was supported by grants from the National Natural Science Foundation of China, Nos. 11972232 and 11625209.

SUPPLEMENTARY MATERIAL

The Supplementary Material for this article can be found online at: https://www.frontiersin.org/articles/10.3389/fcell.2021.641763/full#supplementary-material

REFERENCES

Adiguzel, E., Hou, G., Mulholland, D., Hopfer, U., Fukai, N., Olsen, B., et al. (2006). Migration and growth are attenuated in vascular smooth muscle cells with type VIII collagen-null alleles. *Arterioscler. Thromb. Vasc. Biol.* 26, 56–61.doi: 10.1161/01.ATV.0000194155.96456.b7

Budincevic, H., Ivkosic, A., Martinac, M., Trajbar, T., Bielen, I., and Csiba, L. (2015). Asymptomatic dissecting intimal lesions of common carotid arteries after carotid endarterectomy. *Surg. Today* 45, 1227–1232.doi: 10.1007/s00595-014-1018-x

Cai, J., Yuan, H., Wang, Q., Yang, H., Al-Abed, Y., Hua, Z., et al. (2015). HMGB1-driven inflammation and intimal hyperplasia after arterial injury involves cell-specific actions mediated by TLR4. *Arterioscler. Thromb. Vasc. Biol.* 35, 2579–2593. doi: 10.1161/ATVBAHA.115.305789

Chien, S. (2007). Mechanotransduction and endothelial cell homeostasis: the wisdom of the cell. *Am. J. Physiol. Heart Circ. Physio*l. 292, H1209–H1224. doi: 10.1152/ajpheart.01047.2006

Cho, A., and Reidy, M. A. (2002). Matrix metalloproteinase-9 is necessary for the regulation of smooth muscle cell replication and migration after arterial injury. *Circ. Res.* 91, 845–851.doi: 10.1161/01.res.0000040420.17366.2e

Dai, L., Li, C., Shedden, K. A., Misek, D. E., and Lubman, D. M. (2009). Comparative proteomic study of two closely related ovarian endometrioid adenocarcinoma cell lines using cIEF fractionation and pathway analysis. *Electrophoresis* 30, 1119–1131.doi: 10.1002/elps.200800505

Dangas, G., and Kuepper, F. (2002). Cardiology patient page. Restenosis: repeat narrowing of a coronary artery: prevention and treatment. *Circulation* 105, 2586–2587.doi: 10.1161/01.cir.0000019122.00032.df

Daniel, J. M., Penzkofer, D., Teske, R., Dutzman, N. J., Koch, A., Bielenberg, W., et al. (2014). Inhibition of miR-92a improves re-endothelialization and prevents neointima formation following vascular injury. *Cardiovasc. Res.* 103, 564–572.doi: 10.1093/cvr/cvu162

Dean, W. L., Lee, M. J., Cummins, T. D., Schultz, D. J., and Powell, D. W. (2009). Proteomic and functional characterisation of platelet microparticle size classes. *Thromb. Haemost*. 102, 711–718.doi: 10.1160/TH09-04-243

Dharmakidari, S., Bhattacharya, P., and Chaturvedi, S. (2017). Carotid artery stenosis: medical therapy, surgery, and stenting. *Curr. Neurol. Neurosci. Rep*. 17:77. doi: 10.1007/s11910-017-0786-2

Duprez, D. A., and Cohn, J. N. (2007). Arterial stiffness as a risk factor for coronary atherosclerosis. *Curr. Atheroscler. Rep*. 9, 139–144.doi: 10.1007/s11883-007-0010-y

Fokkema, M., den Hartog, A. G., Bots, M. L., van der Tweel, I., Moll, F. L., and de Borst, G. J. (2012). Stenting versus surgery in patients with carotid stenosis after previous cervical radiation therapy: systematic review and meta-analysis. *Stroke* 43, 793–801.doi: 10.1161/STROKEAHA.111.633743

Fu, Y., Duru, E. A., and Davies, M. G. (2014). Effect of metabolic syndrome on the response to arterial injury. *J. Surg. Res*. 191, 33–41.doi: 10.1016/j.jss.2014.05.051

Greenhill, N. S., Rüger, B. M., Hasan, Q., and Davis, P. F. (2000). The alpha1(VIII) and alpha2(VIII) collagen chains form two distinct homotrimeric proteins *in vivo*. *Matrix Biol.* 19, 19–28.doi: 10.1016/s0945-053x(99)00053-0

Greig, F. H., Hutchison, L., Spickett, C. M., and Kennedy, S. (2015). Differential effects of chlorinated and oxidized phospholipids in vascular tissue: implications for neointima formation. *Clin. Sci. (Lond)* 128, 579–592.doi: 10.1042/CS20140578

Guo, L., Ning, W., Tan, Z., Gong, Z., and Li, X. (2014). Mechanism of matrix metalloproteinase axis-induced neointimal growth. *J. Mol. Cell Cardiol*. 66, 116–125.doi: 10.1016/j.yjmcc.2013.11.014

Guo, S., Zhang, R., Liu, Q., Wan, Q., Wang, Y., Yu, Y., et al. (2019). 2,3,7,8-Tetrachlorodibenzo-p-dioxin promotes injury-induced vascular neointima formation in mice. *FASEB J*. 33, 10207–10217.doi: 10.1096/fj.201900546R

Haga, J. H., Li, Y. S., and Chien, S. (2007). Molecular basis of the effects of mechanical stretch on vascular smooth muscle cells. *J. Biomech*. 40, 947–960.doi: 10.1016/j.jbiomech.2006.04.011

Handorf, A. M., Zhou, Y., Halanski, M. A., and Li, W. J. (2015). Tissue stiffness dictates development, homeostasis, and disease progression. *Organogenesis* 11, 1–15.doi: 10.1080/15476278.2015.1019687

Harvey, A., Montezano, A. C., Lopes, R. A., Rios, F., and Touyz, R. M. (2016). Vascular fibrosis in aging and hypertension: molecular mechanisms and clinical implications. *Can. J. Cardiol*. 32, 659–668.doi: 10.1016/j.cjca.2016.02.070

Hazra, S., Henson, G. D., Morgan, R. G., Breevoort, S. R., Ives, S. J., Richardson, R. S., et al. (2016). Experimental reduction of miR-92a mimics arterial aging. *Exp. Gerontol.* 83, 165–170.doi: 10.1016/j.exger.2016.08.007

Humphries, M. J. (2009). Cell adhesion assays. *Methods Mol. Biol.* 522, 203–210.doi: 10.1007/978-1-59745-413-1_14

Jaminon, A., Reesink, K., Kroon, A., and Schurgers, L. (2019). The role of vascular smooth muscle cells in arterial remodeling: focus on calcification-related processes. *Int. J. Mol. Sci*. 20:5694.doi: 10.3390/ijms20225694

Jeppesen, D. K., Fenix, A. M., Franklin, J. L., Higginbotham, J. N., Zhang, Q., Zimmerman, L. J., et al. (2019). Reassessment of exosome composition. *Cell* 177, 428–445.e18. doi: 10.1016/j.cell.2019.02.029

Kanshana, J. S., Rebello, S. C., Pathak, P., Kanuri, B. N., Aggarwal, H., Srivastava, V., et al. (2018). Standardized fraction of Xylocarpus moluccensis fruits improve vascular relaxation and plaque stability in dyslipidemic models of atherosclerosis. *J. Ethnopharmacol*. 213, 81–91. doi: 10.1016/j.jep.2017.11.004

Lacolley, P., Regnault, V., Segers, P., and Laurent, S. (2017). Vascular smooth muscle cells and arterial stiffening: relevance in development, aging, and disease. *Physiol. Rev*. 97, 1555–1617.doi: 10.1152/physrev.00003.2017

Laffont, B., Corduan, A., Plé, H., Duchez, A. C., Cloutier, N., Boilard, E., et al. (2013). Activated platelets can deliver mRNA regulatory Ago2microRNA complexes to endothelial cells via microparticles. *Blood* 122, 253–261.doi: 10.1182/blood-2013-03-492801

Lee, M. Y., San Martin, A., Mehta, P. K., Dikalova, A. E., Garrido, A. M., Datla, S. R., et al. (2009). Mechanisms of vascular smooth muscle NADPH oxidase 1 (Nox1) contribution to injury-induced neointimal formation. *Arterioscler. Thromb. Vasc. Biol*. 29, 480–487.doi: 10.1161/ATVBAHA.108.181925

Leiva, O., Leon, C., Kah Ng, S., Mangin, P., Gachet, C., and Ravid, K. (2018). The role of extracellular matrix stiffness in megakaryocyte and platelet development and func. *Am. J. Hematol*. 93, 430–441. doi: 10.1002/ajh.25008

Liu, G., Gong, Y., Zhang, R., Piao, L., Li, X., Liu, Q., et al. (2018). Resolvin E1 attenuates injury-induced vascular neointimal formation by inhibition of inflammatory responses and vascular smooth muscle cell migration. *FASEB J*. 32, 5413–5425.doi: 10.1096/fj.201800173R

Liu, S. L., Bae, Y. H., Yu, C., Monslow, J., Hawthorne, E. A., Castagnino, P., et al. (2015). Matrix metalloproteinase-12 is an essential mediator of acute and chronic arterial stiffening. *Sci. Rep*. 5:17189. doi: 10.1038/srep17189

Lopes, J., Adiguzel, E., Gu, S., Liu, S. L., Hou, G., Heximer, S., et al. (2013). Type VIII collagen mediates vessel wall remodeling after arterial injury and fibrous cap formation in atherosclerosis. *Am. J. Pathol*. 182, 2241–2253.doi: 10.1016/j.ajpath.2013.02.011

Merei, B., Badel, P., Davis, L., Sutton, M. A., Avril, S., and Lessner, S. M. (2017). Atherosclerotic plaque delamination: Experiments and 2D finite element model to simulate plaque peeling in two strains of transgenic mice. *J. Mech. Behav. Biomed. Mater*. 67, 19–30.doi: 10.1016/j.jmbbm.2016.12.001

Namba, T., Masaki, N., Takase, B., and Adachi, T. (2019). Arterial stiffness assessed by cardio-ankle vascular index. *Int. J. Mol. Sci*. 20:3664.doi: 10.3390/ijms20153664

Ngai, D., Lino, M., Rothenberg, K. E., Simmons, C. A., Fernandez-Gonzalez, R., and Bendeck, M. P. (2020). DDR1 (Discoidin Domain Receptor-1)-RhoA (Ras Homolog Family Member A) axis senses matrix stiffness to promote vascular calcification. *Arterioscler. Thromb. Vasc. Biol*. 40, 1763–1776.doi: 10.1161/ATVBAHA.120.314697

Pakala, R. (2004). Serotonin and thromboxane A2 stimulate platelet-derived microparticle-induced smooth muscle cell proliferation. *Cardiovasc. Radiat. Med*. 5, 20–26.doi: 10.1016/j.carrad.2003.12.002

Pang, J., Hu, P., Wang, J., Jiang, J., and Lai, J. (2019). Vorapaxar stabilizes permeability of the endothelial barrier under cholesterol stimulation via the AKT/JNK and NF−κB signaling pathways. *Mol. Med. Rep*. 19, 5291–5300. doi: 10.3892/mmr.2019.10211

Pillé, J. Y., Denoyelle, C., Varet, J., Bertrand, J. R., Soria, J., Opolon, P., et al. (2005). Anti-RhoA and anti-RhoC siRNAs inhibit the proliferation and invasiveness of MDA-MB-231 breast cancer cells *in vitro* and *in vivo*. *Mol. Ther*. 11, 267–274.doi: 10.1016/j.ymthe.2004.08.029

Plenz, G., Dorszewski, A., Breithardt, G., and Robenek, H. (1999). Expression of type VIII collagen after cholesterol diet and injury in the rabbit model of atherosclerosis. *Arterioscler. Thromb. Vasc. Biol*. 19, 1201–1209.doi: 10.1161/01.atv.19.5.1201

Plenz, G. A., Deng, M. C., Robenek, H., and Völker, W. (2003). Vascular collagens: spotlight on the role of type VIII collagen in atherogenesis. *Atherosclerosis* 166, 1–11.doi: 10.1016/s0021-9150(01)00766-3

Puhm, F., Boilard, E., and Machlus, K. R. (2020). Platelet extracellular vesicles: beyond the blood. *Arterioscler. Thromb. Vasc. Biol.* 41, 87–96. doi: 10.1161/ATVBAHA.120.314644

Quencer, K. B., and Arici, M. (2015). Arteriovenous fistulas and their characteristic sites of stenosis. AJR. *AJR Am. J. Roentgenol.* 205, 726–734.doi: 10.2214/AJR.15.14650

Rabelink, T. J., van den Berg, B. M., Garsen, M., Wang, G., Elkin, M., and van der Vlag, J. (2017). Heparanase: roles in cell survival, extracellular matrix remodelling and the development of kidney disease. *Nat. Rev. Mol. Cell Biol*. 13, 201–212.doi: 10.1038/nrneph.2017.6

Raugi, G. J., Mullen, J. S., Bark, D. H., Okada, T., and Mayberg, M. R. (1990). Thrombospondin deposition in rat carotid artery injury. *Am. J. Pathol*. 137, 179–185.

Rosińska, J., Maciejewska, J., Narożny, R., Kozubski, W., and Łukasik, M. (2019). Association of platelet-derived microvesicles with high on-treatment platelet reactivity in convalescent ischemic stroke patients treated with acetylsalicylic acid. *Wiad Lek*. 72, 1426–1436. doi: 10.36740/wlek201908102

Rudijanto, A. (2007). The role of vascular smooth muscle cells on the pathogenesis of atherosclerosis. *Acta Med. Indones*. 39, 86–93.

Safar, M. E., Peronneau, P. A., Levenson, J. A., Toto-Moukouo, J. A., and Simon, A. C. (1981). Pulsed Doppler: diameter, blood flow velocity and volumic flow of the brachial artery in sustained essential hypertension. *Circulation* 63, 393–400.doi: 10.1161/01.cir.63.2.393

Schedin, P., and Keely, P. J. (2011). Mammary gland ECM remodeling, stiffness, and mechanosignaling in normal development and tumor progression. *Cold Spring Harb. Perspect. Biol*. 3:a003228.doi: 10.1101/cshperspect.a003228

Schurgers, L. J., Akbulut, A. C., Kaczor, D. M., Halder, M., Koenen, R. R., and Kramann, R. (2018). Initiation and propagation of vascular calcification is regulated by a concert of platelet- and smooth muscle cell-derived extracellular vesicles. *Front. Cardiovasc. Med*. 5:36. doi: 10.3389/fcvm.2018.00036

Shan, Z., Qin, S., Li, W., Wu, W., Yang, J., Chu, M., et al. (2015). An endocrine genetic signal between blood cells and vascular smooth muscle cells: role of MicroRNA-223 in smooth muscle function and atherogenesis. *J. Am. Coll. Cardio*l. 65, 2526–2537. doi: 10.1016/j.jacc.2015.03.570

Sibinga, N. E., Foster, L. C., Hsieh, C. M., Perrella, M. A., Lee, W. S., Endege, W. O., et al. (1997). Collagen VIII is expressed by vascular smooth muscle cells in response to vascular injury. *Circ. Res*. 80, 532–541.doi: 10.1161/01.res.80.4.532

Stephan, D., San, H., Yang, Z. Y., Gordon, D., Goelz, S., Nabel, G. J., et al. (1997). Inhibition of vascular smooth muscle cell proliferation and intimal hyperplasia by gene transfer of beta-interferon. *Mol. Med*. 3, 593–599.

Stephan, S., Sherratt, M. J., Hodson, N., Shuttleworth, C. A., and Kielty, C. M. (2004). Expression and supramolecular assembly of recombinant alpha1(viii) and alpha2(viii) collagen homotrimers. *J. Biol. Chem*. 279, 21469–21477.doi: 10.1074/jbc.M305805200

Szatanek, R., Baj-Krzyworzeka, M., Zimoch, J., Lekka, M., Siedlar, M., and Baran, J. (2017). The methods of choice for extracellular vesicles (EVs) characterization. *Int. J. Mol. Sci*. 18:1153.doi: 10.3390/ijms18061153

Tanaka, L. Y., Araujo, T., Rodriguez, A. I., Ferraz, M. S., Pelegati, V. B., Morais, M., et al. (2019). Peri/epicellular protein disulfide isomerase-A1 acts as an upstream organizer of cytoskeletal mechanoadaptation in vascular smooth muscle cells. *Am. J. Physiol. Heart Circ. Physiol*. 316, H566–H579. doi: 10.1152/ajpheart.00379.2018

Thenappan, T., Chan, S. Y., and Weir, E. K. (2018). Role of extracellular matrix in the pathogenesis of pulmonary arterial hypertension. *Am. J. Physiol. Heart Circ. Physiol*. 315, H1322–H1331. doi: 10.1152/ajpheart.00136.2018

Tummers, A. M., Mountain, D. J., Mix, J. W., Kirkpatrick, S. S., Cassada, D. C., Stevens, S. L., et al. (2010). Serum levels of matrix metalloproteinase-2 as a marker of intimal hyperplasia. *J. Surg. Res*. 160, 9–13.doi: 10.1016/j.jss.2009.04.003

Vajen, T., Mause, S. F., and Koenen, R. R. (2015). Microvesicles from platelets: novel drivers of vascular inflammation. *Thromb. Haemost*. 114, 228–236.doi: 10.1160/TH14-11-0962

Waksman, R., and Steinvil, A. (2016). In-stent restenosis? the raiders of the magic remedy. *Circ. Cardiovasc. Interv*. 9:e004150. doi: 10.1161/CIRCINTERVENTIONS.116.004150

Wang, J., Zhang, C., Li, C., Zhao, D., Li, S., Ma, L., et al. (2019). MicroRNA-92a promotes vascular smooth muscle cell proliferation and migration through the ROCK/MLCK signalling pathway. *J. Cell Mol. Med*. 23, 3696–3710.doi: 10.1111/jcmm.14274

Wojciechowska, A., Braniewska, A., and Kozar-Kamińska, K. (2017). MicroRNA in cardiovascular biology and disease. *Adv. Clin. Exp. Med*. 26, 865–874. doi: 10.17219/acem/62915

Wolf, P. (1967). The nature and significance of platelet products in human plasma. *Br. J. Haematol*. 13, 269–288. doi: 10.1111/j.1365-2141.1967.tb08741.x

Xie, S. A., Zhang, T., Wang, J., Zhao, F., Zhang, Y. P., Yao, W. J., et al. (2018). Matrix stiffness determines the phenotype of vascular smooth muscle cell *in vitro* and *in vivo*: role of DNA methyltransferase1. *Biomaterials* 155, 203–216.doi: 10.1016/j.biomaterials.2017.11.033

Xu, W., Yang, Z., and Lu, N. (2015). A new role for the PI3K/Akt signaling pathway in the epithelial-mesenchymal transition. *Cell Adh. Migr*. 9, 317–324.doi: 10.1080/19336918.2015.1016686

Yang, H. M., Kim, H. S., Park, K. W., You, H. J., Jeon, S. I., Youn, S. W., et al. (2004). Celecoxib, a cyclooxygenase-2 inhibitor, reduces neointimal hyperplasia through inhibition of Akt signaling. *Circulation* 110, 301–308.doi: 10.1161/01.CIR.0000135467.43430.16

Yao, E. H., Fukuda, N., Ueno, T., Matsuda, H., Nagase, H., Matsumoto, Y., et al. (2009). A pyrrole-imidazole polyamide targeting transforming growth factor-beta1 inhibits restenosis and preserves endothelialization in the injured artery. *Cardiovasc. Res*. 81, 797–804.doi: 10.1093/cvr/cvn355

Yasuda, O., Zhang, S. H., Miyamoto, Y., and Maeda, N. (2000). Differential expression of the alpha1 type VIII collagen gene by smooth muscle cells from atherosclerotic plaques of apolipoprotein-E-deficient mice. *J. Vasc. Res*. 37, 158–169.doi: 10.1159/000025727

Zaldivia, M. T. K., McFadyen, J. D., Lim, B., Wang, X., and Peter, K. (2017). Platelet-derived microvesicles in cardiovascular diseases. *Front. Cardiovasc. Med*. 4:74. doi: 10.3389/fcvm.2017.00074

Zeng, Z., Xia, L., Fan, X., Ostriker, A. C., Yarovinsky, T., Su, M., et al. (2019). Platelet-derived miR-223 promotes a phenotypic switch in arterial injury repair. *J. Clin. Invest*. 129, 1372–1386.doi: 10.1172/JCI124508

Zhang, C., Zhou, T., Chen, Z., Yan, M., Li, B., Lv, H., et al. (2020). Coupling of integrin α5 to annexin A2 by flow drives endothelial activation. *Circ. Res*. 127, 1074–1090. doi: 10.1161/CIRCRESAHA.120.316857

Conflict of Interest: The authors declare that the research was conducted in the absence of any commercial or financial relationships that could be construed as a potential conflict of interest.

frontiers
in Cell and Developmental Biology

ORIGINAL RESEARCH
published: 04 March 2021
doi: 10.3389/fcell.2021.641382

The Combined Contribution of Vascular Endothelial Cell Migration and Adhesion to Stent Re-endothelialization

Xiaoli Wang, Fei Fang, Yinghao Ni, Hongchi Yu, Jia Ma, Li Deng, Chunli Li, Yang Shen* and Xiaoheng Liu*

West China School of Basic Medical Sciences and Forensic Medicine, Institute of Biomedical Engineering, Sichuan University, Chengdu, China

Edited by:
Jing Zhou,
Peking University, China

Reviewed by:
Weijuan Yao,
Peking University Health Science Centre, China
Tieying Yin,
Chongqing University, China

***Correspondence:**
Yang Shen
shenyang@scu.edu.cn
Xiaoheng Liu
liuxiaohg@scu.edu.cn

Specialty section:
This article was submitted to Cell Adhesion and Migration, a section of the journal Frontiers in Cell and Developmental Biology

Received: 14 December 2020
Accepted: 08 February 2021
Published: 04 March 2021

Citation:
Wang X, Fang F, Ni Y, Yu H, Ma J, Deng L, Li C, Shen Y and Liu X (2021) The Combined Contribution of Vascular Endothelial Cell Migration and Adhesion to Stent Re-endothelialization. Front. Cell Dev. Biol. 9:641382. doi: 10.3389/fcell.2021.641382

Coronary stent placement inevitably causes mechanical damage to the endothelium, leading to endothelial denudation and in-stent restenosis (ISR). Re-endothelialization depends mainly on the migration of vascular endothelial cells (VECs) adjacent to the damaged intima, as well as the mobilization and adhesion of circulating VECs. To evaluate the combined contribution of VEC migration and adhesion to re-endothelialization under flow and the influence of stent, *in vitro* models were constructed to simulate various endothelial denudation scales (2 mm/5 mm/10 mm) and stent deployment depths (flat/groove/bulge). Our results showed that (1) in 2 mm flat/groove/bulge models, both VEC migration and adhesion combined completed the percentage of endothelial recovery about 27, 16, and 12%, and migration accounted for about 21, 15, and 7%, respectively. It was suggested that the flat and groove models were in favor of VEC migration. (2) With the augmentation of the injury scales (5 and 10 mm), the contribution of circulating VEC adhesion on endothelial repair increased. Taken together, endothelial restoration mainly depended on the migration of adjacent VECs when the injury scale was 2 mm. The adhered cells contributed to re-endothelialization in an injury scale-dependent way. This study is helpful to provide new enlightenment for surface modification of cardiovascular implants.

Keywords: in-stent restenosis, re-endothelialization, fluid shear stress, cell migration, cell adhesion

INTRODUCTION

Cardiovascular disease remains the leading cause of death globally (Kivimaki and Steptoe, 2018). Stent implantation reconstructs stenotic arteries by expanding the vascular wall and restoring blood flow perfusion. However, stent deployment inevitably causes endothelial denudation, which promotes in-stent restenosis (ISR) and late thrombosis (Krankenberg et al., 2015). Rapid re-endothelialization is an important therapeutic goal to avoid ISR and thrombosis (Liang et al., 2016; Bedair et al., 2017).

Endothelium restoration after stenting has been widely investigated (Tesfamariam, 2016). The repair of impaired vascular endothelium involves the migration of vascular endothelial cells (VECs) from adjacent uninjured sites and homing and adhesion of circulating VECs. However, the cell source of re-endothelialization is still being disputed (Van der Heiden et al., 2013). Since endothelial progenitor cells (EPCs) were found in peripheral blood, circulating EPCs were regarded as the primary cell source for reconstructing the damaged endothelium (Zhang et al., 2014). On the other hand, mounting evidence indicated that circulating EPCs (most likely monocytic) could not directly contribute to endothelial regeneration by forming part of the regenerating endothelium (Evans et al., 2020). As a marker of endothelial injury, circulating endothelial cells detached from impaired vessels, sloughed into the circulation, and contributed to vascular repair (Quilici et al., 2004; Blann et al., 2005). Hagensen et al. (2011) indicated that endothelial restoration mainly depended on the migration of VECs from the adjacent healthy endothelium. Douglas et al. (2013) found that both migration of VECs and adhesion of circulating cells participated in endothelial repair in stented arteries. Therefore, the contribution of adjacent VEC migration and circulating VEC adhesion to re-endothelialization needs further study.

There are several factors that can potentially influence endothelium recovery post stenting, including stent deployment depth, the scale of endothelial denudation, hemodynamic changes, and the structure and material properties of the stent (Kakinoki et al., 2018; Wang et al., 2018; Torii et al., 2020). Due to differences in individual vessel diameter and atherosclerotic plaque type, stent placement causes endothelium injury of various depths and scales (O'Brien et al., 2016). However, the effects of stent deployment depth and injury scales on adjacent VEC migration and circulating VEC adhesion remain poorly understood. Of note, if the diameter of the vessel is mismatched with stent expansion, stent strut is deeply embedded in a vessel well to form a "groove," or part of the stent strut is exposed in the vessel lumen forming a "bulge" (insufficient expansion). In addition, the dilation of stent leads to almost complete endothelial loss of the stented segment, and only few endothelial cells remained at the edge of the stent (Douglas et al., 2013; Du et al., 2018). The average available stent length is longer than 10 mm, and the diameter of the stent ranges from 1 to 3 mm (Kalapatapu et al., 2007; Byrne et al., 2017). Accordingly, models with various scales were designed: (1) the thickness of a single stent strut (2 mm), (2) half of endothelial denudation at stent segment (5 mm), and (3) whole length of stented damaged to the vessel well (10 mm).

The presence of stent markedly alters vascular mechanics, especially blood flow patterns and fluid shear stress (FSS) (Gijsen et al., 2019; Torii et al., 2020). Under physiological conditions, endothelial cells are exposed to laminar FSS ranging from 10 to 20 dyn/cm^2 (Kwak et al., 2014). Atherosclerotic plaque leads to arterial stenosis or occlusion, which increases FSS in the upstream and central plaque areas, while the downstream areas of plaque are exposed to low FSS (Michail et al., 2018). Implanted stent restores stenotic vessels and converts sharply elevated wall shear stress to relatively low level, but induces geometric changes of vascular wall and local turbulence (Van der Heiden et al., 2013). However, the influence of stent deployment depth and injury scales on local hemodynamics is still unclear.

In the present study, *in vitro* models were constructed to explore the effects of stent deployment depth and injury scales on local hemodynamics. Using these models, we further investigated the combined contribution of VEC migration and adhesion to re-endothelialization under flow. Our study will provide new inspiration for exploring the mechanism about stent re-endothelialization upon vascular biomechanical stimuli and modifying the surface of cardiovascular stent.

MATERIALS AND METHODS

Construction of *in vitro* Injury Models After Stent Implantation

To explore the influence of stent on local hemodynamics and the combined contribution of VEC migration and adhesion to re-endothelialization, we constructed *in vitro* injury models to simulate various endothelial denudation scales (2 mm/5 mm/10 mm) and stent deployment depths (groove/flat/bulge). First, glass slides (7.5 × 2.5 × 1.0 cm) were used to build 2 mm/5 mm/10 mm embedment/protrusion, respectively (referred to as groove$_{2\ \mathrm{mm}}$/groove$_{5\ \mathrm{mm}}$/groove$_{10\ \mathrm{mm}}$, bulge$_{2\ \mathrm{mm}}$/bulge$_{5\ \mathrm{mm}}$/Bulge$_{10\ \mathrm{mm}}$, respectively).

Characterization of Groove/Bulge Slide Models by SEM

The slides were dipped in a mixture of concentrated sulfuric acid and potassium dichromate overnight, cleaned to remove surface contaminants, dried, and then autoclaved. Sprayed with Au, the constructed groove, and bulge slide models were observed under a scanning electron microscope (SEM, Hitachi Company, Japan).

Computational Fluid Dynamic Simulation

In this study, the straight left coronary artery was selected as the geometric structure of the vascular model based on the finite element method to calculate the hemodynamic and flow distribution of the coronary artery. ANSYS 16.0 (ANSYS, Inc., United States) was applied to divide finite element mesh and generate the finite element model. The input–output boundary of each finite element model was applied with the physiological boundary condition of the left coronary artery, and the control condition was set. The mean of the physiological parameters was applied in the numerical simulation. In detail, the vessel diameter was set as 4 mm, the inlet velocity was 0.5 m/s, the density of blood was 1,050 g/cm^3, and the viscosity coefficient was 0.003 mPa s, respectively. Groove/bulge with a width of 2 mm/5 mm/10 mm and 0.085 mm/0.17 mm in depth was set in the vessels to simulate the different injury scales and stent deployment depths. Finally, the finite element method was used to solve the divided finite element model. After the solution was completed, the hemodynamic and flow distribution in different injury models after stent implantation were numerically analyzed.

Cell Culture

Human umbilical vein endothelial cells (HUVECs) were chosen in the present study, which were purchased from Jiangsu Blood Research Institute. HUVECs were maintained in RPMI-1640 complete growth medium (Invitrogen Company, United States) with 10% fetal bovine serum (FBS, Gibco BRL, United States), 2 mM L-glutamine, 100 U/ml penicillin, 20 mmol/L HEPES (Sigma, United States), 2% $NaHCO_3$, and 50 mg/ml streptomycin (Beyotime Institute of Biotechnology).

Lentivirus-GFP/Lentivirus-mCherry Transfection of HUVECs

Lentivirus-GFP/Lentivirus-mCherry (Heyuan Biotechnology Co., Ltd., China) was used to transfect HUVECs with green fluorescent (GFP) and red fluorescent mCherry protein markers, respectively. HUVECs were grown in 24-well plates at a density of 7×10^4 cells/well, then added with 500 μl RPMI-1640 complete growth medium and cultured at 37°C, in 5% CO_2 incubator (Heraeus Company, Germany) for 24 h. Next, the culture medium was replaced with DMEM high-glucose complete medium (Gibco BRL, United States) with 5 μg/ml polybrene (Heyuan Biotechnology Co., Ltd., China) and preconfigured virus solution with MOI = 40. Polybrene is a cationic polymer, which can neutralize the electric charge to promote binding between the lentivirus and cell membrane. After 72 h of infection, the infection efficiency was evaluated by a fluorescence microscope (Olympus, Japan); 0.5 μg/ml purinomycin was selected to maintain HUVECs labeled with green fluorescent protein (GFP-HUVECs) or red fluorescent protein (mCherry-HUVECs). In the following experiments, GFP-HUVECs were used to characterize the migration of adjacent VECs, and mCherry-HUVECs to indicate the adhesion of circulating VECs.

Cell Migration and Adhesion Assays

As shown in **Figure 1A**, the scratch-wound assay was used to measure the migration ability of HUVECs. (GFP-)HUVECs were cultured to approximately 90% confluence, and then a cell-free area was constructed at the embedment/protrusion part of $\text{groove}_{2\ \text{mm}}$/$\text{bulge}_{2\ \text{mm}}$ models and 2 mm scratches on flat slides ($\text{flat}_{2\ \text{mm}}$). Static culture or slides were placed into a parallel plate flow chamber to load 15.27 dyn/cm^2 FSS for 24 h. The migrated distance/area of the cell was determined and calculated. As shown in **Figure 1B**, the adhesion assay was used to evaluate the adhesion ability of circulated HUVECs under static condition and FSS stimulation. The blank groove/bulge models were placed into static or circulated mCherry-HUVEC suspension (1×10^5 cells/ml) for 24 h. The number/area of red fluorescent spots in each field of vision was analyzed. For the combined effect of cell migration and adhesion, the cell-free area on the embedment/protrusion part of the groove/bulge models after 90% confluence of (GFP-)HUVECs was constructed, and the mCherry-HUVEC suspension (1×10^5 cells/ml) under static or dynamic condition for 24 h was introduced (as shown in **Figure 1C**). The cell migration distance/area and the adhesion number/area were quantitatively analyzed through ImageJ 1.44p software (National Institutes of Health, United States).

F-Actin Staining

HUVECs on the $\text{groove}_{2\ \text{mm}}$ model were loaded with 15.27 dyn/cm^2 FSS for 24 h and fixed with 4% paraformaldehyde (Biosharp Company, China) for 10 min at 37°C and then with 0.5% Triton X-100 for 5 min and 1% BSA block for 30 min. Then, the TRITC-labeled antibody F-actin (Solarbio Science & Technology Co., Ltd., China) with 1:200 dilution was added and co-incubated for 20 min at 37°C, followed by 1:800 diluted DAPI (4′,6′-diamidino-2-phenylindole) staining for 10 min at 37°C and washed with phosphate buffered saline (PBS). The samples sealed with glycerol were observed by laser scanning confocal microscopy (Leica TCS SP5, Germany).

Cell Morphology by SEM

HUVECs were seeded onto 2 mm flat/groove/bulge models and cultured to approximately 90% confluence. Cells at the embedment/protrusion part of the groove/bulge models were removed. Then, cells were loaded with 15.27 dyn/cm^2 laminar FSS for 24 h, followed by 0.1 M, pH 7.35, sodium arsenate solution (Budweiser Biotechnology Co., Ltd., China) containing 2% glutaraldehyde (Amerso Company, China) and 2% paraformaldehyde (Biosharp Company, China) fixation for 15 min, and washed for 5 min with PBS and distilled deionized water (ddH_2O), respectively. The samples were dehydrated by 30, 50, 70, 90, and 100% ethanol solution and placed in a freeze dryer (Yaxing Yike Technology Co., Ltd., China). SEM (Hitachi Company, Japan) was used to observe the morphology of HUVECs.

Statistical Analysis

All statistics were analyzed using statistical software SPSS 11.5 (SPSS, Inc., Chicago, Illinois). Data obtained from different treatment groups were statistically compared and reported as mean ± SD. To reveal differences among the groups, one-way ANOVA followed by Tukey's test was used. Differences were considered significant at $P < 0.05$.

RESULTS

Establishment of *in vitro* Vascular Injury Models After Stent Placement

To simulate sufficient/insufficient expansion of stent *in vitro*, glass slides with embedment (thereafter referred to as groove) and protrusion (thereafter referred to as bulge) in injured scales of 2 mm/5 mm/10 mm were designed and constructed (**Figures 2A,B**). We verified that the depth of the groove model (2 mm) was 197.0 ± 6.8 μm. The left-edge angle (29.7 ± 1.2°) and the right-edge angle (29.9 ± 0.8°) were measured by SEM (**Figure 2C**, up panel). In the bulge model, the height

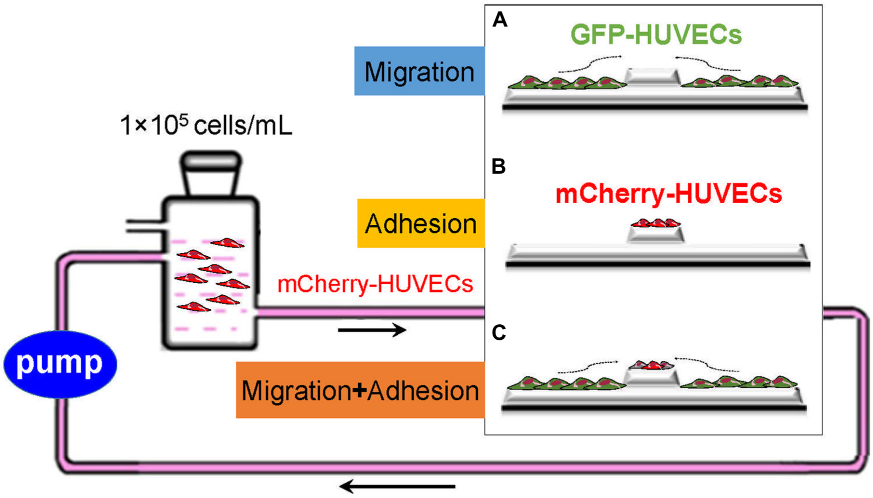

FIGURE 1 | Schematic of exploring the cell sources of re-endothelialization and their contribution. GFP-HUVECs (green) and mCherry-HUVECs (red) were used to characterize adjacent VEC migration and adhesion of circulating VECs: **(A)** The migration of adjacent VECs contributed to re-endothelialization. **(B)** Circulatory VECs adhered to complete endothelium restoration. **(C)** The combined effect of adjacent VEC migration and circulatory VEC adhesion on stent re-endothelialization.

of protrusion was 185.9 ± 2.8 μm, and the left- and right-edge angles were 30.0 ± 0.4° and 28.9 ± 1.0°, respectively (**Figure 2C**, down panel).

Numerical Simulation of Hemodynamics and Flow Distribution

ANSYS 16.0 was used to simulate and calculate the effects of different stent deployment depth and injury scales on hemodynamics and flow distribution. The straight left main coronary artery was selected as the geometric structure of the vascular model. According to the physiology parameter of the left coronary artery, the vessel diameter was set as 4 mm, the inlet velocity was 0.5 m/s, the blood density was 1,050 g/cm^3, and the viscosity coefficient was 0.003 mPa s, respectively.

It could be found that the overall flow distribution was not affected by stent placement (**Figure 3**). In the groove models simulating sufficient stent dilation, the scale of vascular damage was set as 2, 5, and 10 mm with 0.085 mm in depth (**Figure 3A**). There was no flow disturbance in the upstream and downstream of the damaged vessel segment. In the models simulating stent expansion with proper pressure, the height of the stent protrusion was 0.085 mm. An obvious disturbance appeared in the downstream of 2 mm width; when the damage scale was up to 5 and 10 mm, the disturbance flow disappeared (**Figure 3B**). In the bulge models simulating insufficient stent expansion, the scale of vascular damage was set as 2, 5, and 10 mm with 0.17 mm in height. The downstream of 2 and 5 mm width caused fluid separation area and obvious flow turbulence. When the injury scale increased to 10 mm, the flow disturbance disappeared (**Figure 3C**). These results implied that stent-induced injury had no obvious influence on the upstream flow distribution but had a significant influence on the downstream flow, depending on the injury scales and height of the stent.

Cell Sources and the Respective Contribution to Re-endothelialization Under Static Conditions

Using scratch-wound assays, we investigated the effects of groove/bulge models with 2 mm width (referred to as groove$_{2\ \mathrm{mm}}$/bulge$_{2\ \mathrm{mm}}$) on the adjacent VEC migration and re-endothelialization under static conditions. The 2 mm scratch on glass slides (flat$_{2\ \mathrm{mm}}$) was constructed as the control group. Under static condition, 90% of wound was healed in the flat$_{2\ \mathrm{mm}}$/groove$_{2\ \mathrm{mm}}$/bulge$_{2\ \mathrm{mm}}$ models at 8, 16, and 24 days, respectively (**Figure 4A**, left panel), suggesting that the migration velocity of VECs in the flat$_{2\ \mathrm{mm}}$ model was faster than that in the groove$_{2\ \mathrm{mm}}$ model and the bulge$_{2\ \mathrm{mm}}$ model (**Figure 4A**, right panel). The number of adhesive VECs per unit area in flat$_{2\ \mathrm{mm}}$/groove$_{2\ \mathrm{mm}}$/bulge$_{2\ \mathrm{mm}}$ was 126 ± 5, 142 ± 7, and 68 ± 11 after 24 h, which was groove$_{2\ \mathrm{mm}}$ > flat$_{2\ \mathrm{mm}}$ > bulge$_{2\ \mathrm{mm}}$ (**Figure 4B**).

Additionally, we further examined the combined effect of VEC migration and adhesion and analyzed their respective contribution to re-endothelialization. The results indicated that the adhesion of mCherry-HUVECs was the main cell source for damaged endothelium repair under static condition. In the flat$_{2\ \mathrm{mm}}$/groove$_{2\ \mathrm{mm}}$/bulge$_{2\ \mathrm{mm}}$ model, endothelium recovery in flat$_{2\ \mathrm{mm}}$ was 41%, adjacent VEC migration accounted for 11%, and the percentage of adherent VECs was 30%. In the groove$_{2\ \mathrm{mm}}$ model, approximately 59% endothelium restoration was completed, the migrated cells accounted for 6%, while the adherent cells contributed 29%. In the bulge$_{2\ \mathrm{mm}}$ model, the percentage of re-endothelialization was 23%, the migration was 4%, and the adhesion was 19% (**Figure 5A**).

With increased injury scales (5 and 10 mm), more adherent circulating VECs contributed to endothelial repair. In the groove model with widths of 5 and 10 mm, endothelium recovery was up to approximately 48 and 61%, and adhesion was about 43

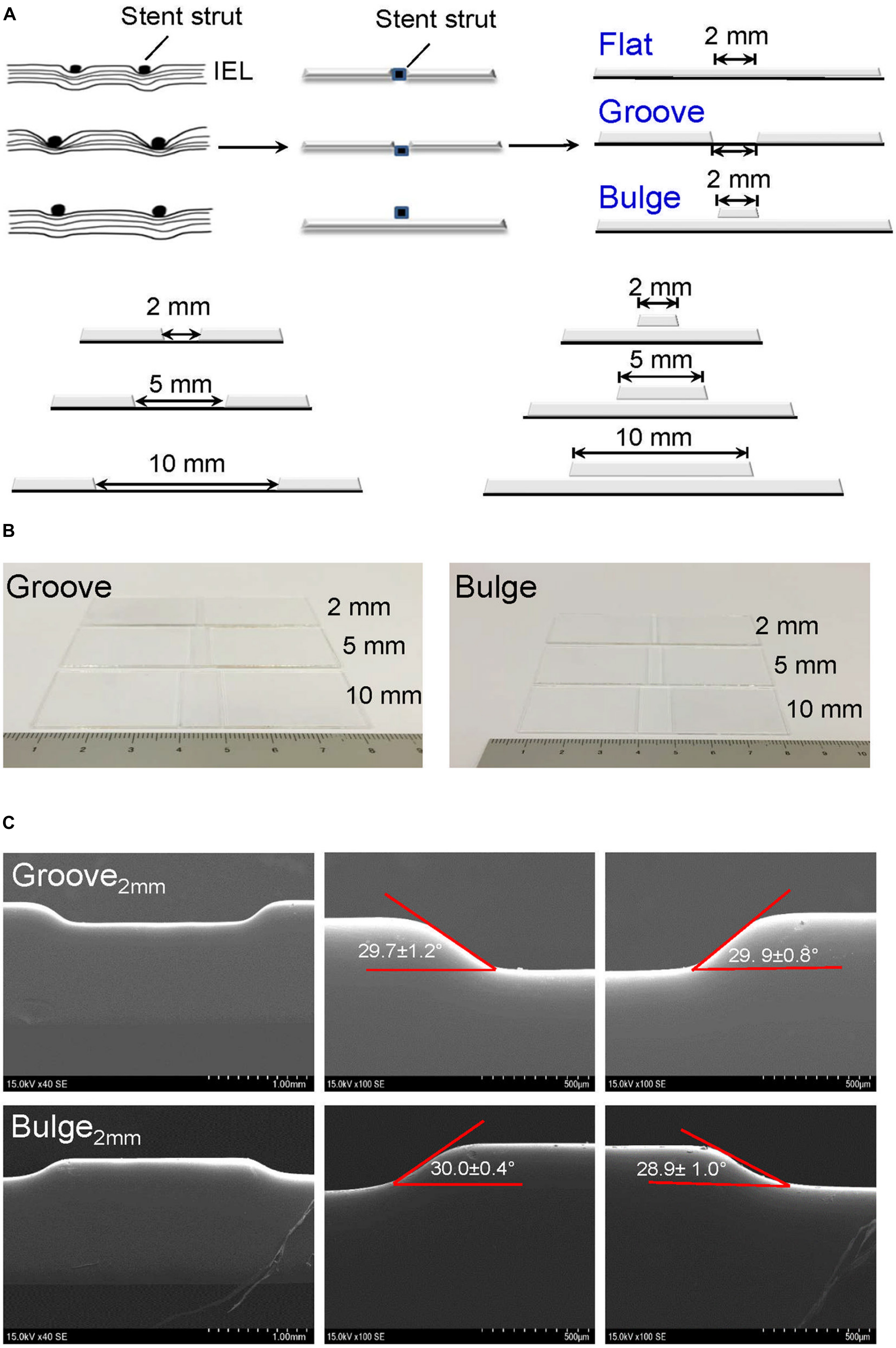

FIGURE 2 | Construction of glass slide models to simulate vascular injury after stent implantation. **(A)** Design of vascular injury scales with 2 mm (the thickness of a single stent strut), 5 mm (half of endothelial denudation at stent segment), and 10 mm width (whole length of stent). The stent is embedded in the vessel wall with a horizontal line (flat model) or deeply embedded into the vessel wall (groove model); the stent is protruded from the vessel wall (bulge model). The black dots and squares represent stent struts embedded in the vessel wall. The curved lines indicate internal elastic lamina (IEL). **(B)** Typical digital images of groove/bulge models with widths of 2 mm/5 mm/10 mm. **(C)** Observation of edge angles at groove/bulge models with the width of 2 mm by SEM. Scale bars = 1 mm and 500 µm.

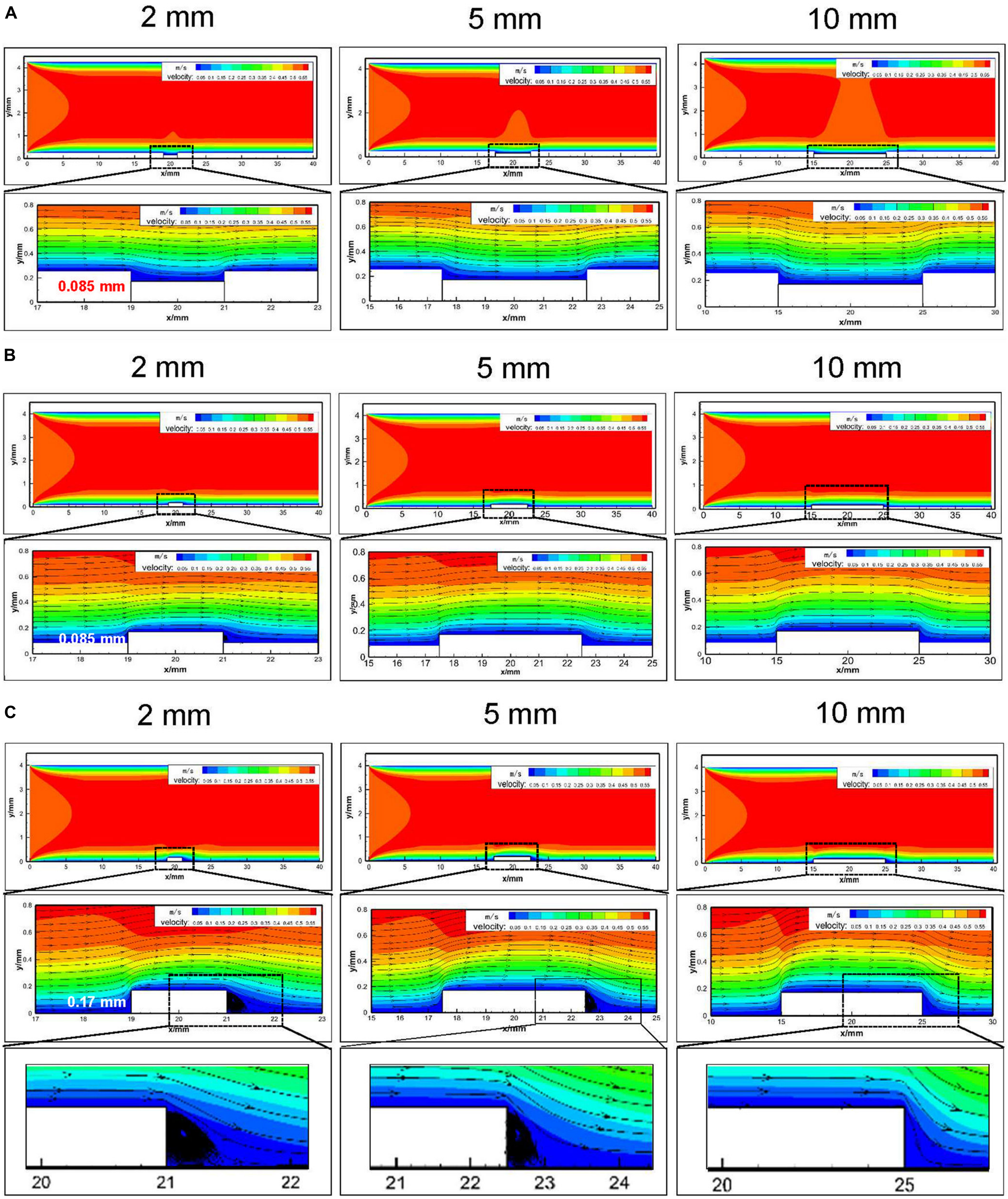

FIGURE 3 | Numerical analysis of hemodynamics and flow distribution in embedment models with different injury scales (2 mm/5 mm/10 mm). **(A)** Embedment with 0.085 mm in depth and the hemodynamics and flow distribution of the injured blood vessels; **(B)** protrusion with 0.085 mm in height in the vessel lumen and the hemodynamics and flow distribution of the injured vessel segment; **(C)** protrusion with 0.17 mm in height in the vessel lumen and the hemodynamics and flow distribution of the injured blood vessels. The enlarged black area indicated that downstream of the 2 and 5 mm bulge model caused fluid separation area and flow turbulence.

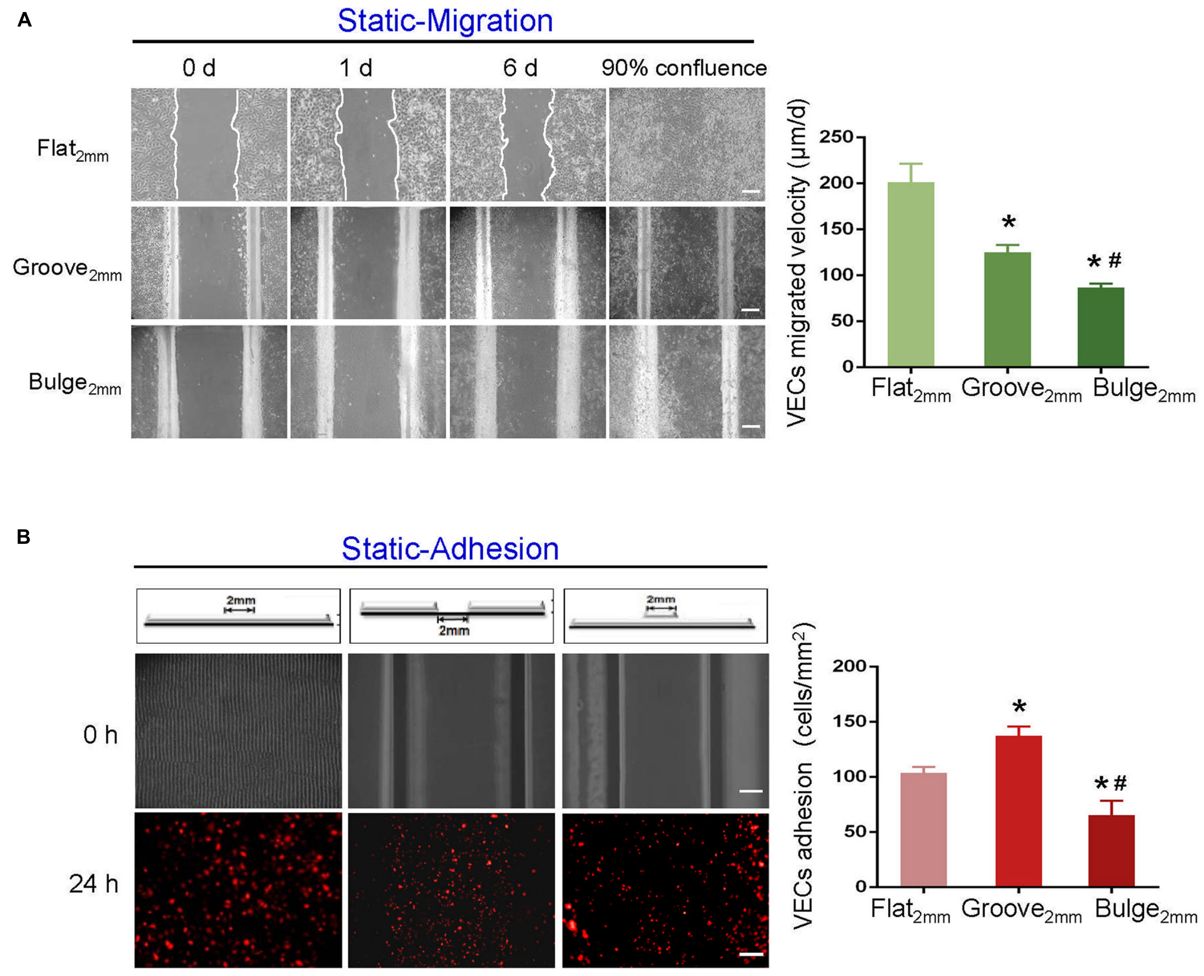

FIGURE 4 | Effects of groove/bulge models on VEC migration or adhesion under static condition. Under static condition, **(A)** $\text{groove}_{2\,mm}$/$\text{bulge}_{2\,mm}$ models were cultured until 90% confluence, and then cells were removed on the embedment/protrusion part, investigating the effects of stent embedment/protrusion on VEC migration and its statistical results. **(B)** Blank $\text{groove}_{2\,mm}$/$\text{bulge}_{2\,mm}$ models were placed into 1 × 10^5 cells/ml mCherry-HUVEC suspension for 24 h, determining the effects of stent embedment/protrusion on VEC adhesion and its statistical results. $^*P < 0.05$ vs. $\text{flat}_{2\,mm}$; $\#P < 0.05$ vs. $\text{groove}_{2\,mm}$, the difference was statistically significant ($n = 3$). Scale bar = 500 μm.

and 56%, respectively (**Figure 5B**). In the $\text{bulge}_{5\text{ mm}}$/$\text{bulge}_{10\text{ mm}}$ models, the percentage of re-endothelialization was 33 and 45%, and adhesion accounted for 30 and 42%, respectively (**Figure 5C**). The results demonstrated that circulating VECs contributed to re-endothelialization in an endothelial denudation scale-dependent way under the static condition.

Effects of Vascular Injury Model on VEC Morphology Under Flow

The influence of $\text{flat}_{2\text{ mm}}$/$\text{groove}_{2\text{ mm}}$/$\text{bulge}_{2\text{ mm}}$ on VEC morphology under flow was observed by SEM. As shown in **Figure 6A**, compared with static control, FSS promoted endothelial cells to arrange along the shear direction. In response to FSS exposure, endothelial cells spread out with obvious parapodium in $\text{groove}_{2\text{ mm}}$ models in favor of directed cell locomotion, while VECs accumulated in clusters on the edge of $\text{bulge}_{2\text{ mm}}$ models. Additionally, in the $\text{groove}_{2\text{ mm}}$ model, the distribution of F-actin in VECs exposed to FSS was examined. The confocal images indicated that VECs upstream showed longer filopodia and more bundles of filaments at the leading edge of the cells. By contrast, VECs downstream displayed disordered actin stress fibers (**Figure 6B**).

Cell Sources of Re-endothelialization and Their Contribution Under Flow

To explore the combined contribution of VEC migration and adhesion to re-endothelialization under flow, the labeled GFP-HUVECs and circulating mCherry-HUVECs were placed in a flow chamber together. The GFP-HUVECs were firstly cultured onto $\text{flat}_{2\text{ mm}}$/$\text{groove}_{2\text{ mm}}$/$\text{bulge}_{2\text{ mm}}$ models until confluence, and subsequently, the cell-free area of the embedment/protrusion part was constructed. These models were then placed in the parallel plate flow chamber with circulated mCherry-HUVEC suspension (1 × 10^5 cells/ml) in the perfusion system for 24 h.

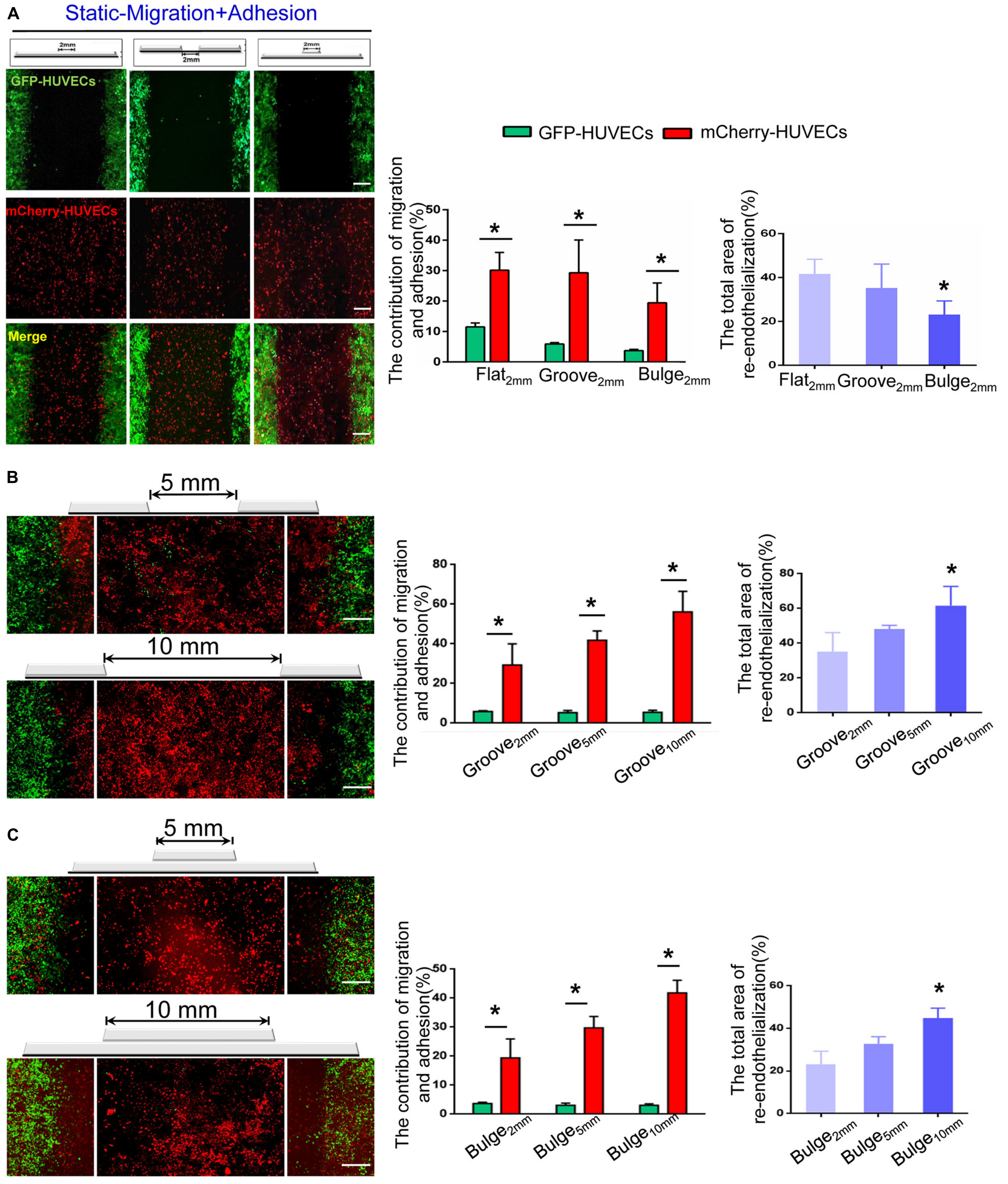

FIGURE 5 | The combined effect of VEC migration and adhesion on re-endothelialization under static condition. **(A)** In the flat$_{2\ mm}$/groove$_{2\ mm}$/bulge$_{2\ mm}$ models, the endothelial cell source of endothelium recovery and their respective contributions were analyzed. *$P < 0.05$ vs. flat$_{2\ mm}$, the difference was statistically significant ($n = 3$). **(B,C)** With the augmentation of the injury scales to 5 and 10 mm in the groove/bulge models, the endothelial cell sources of re-endothelialization were analyzed. *$P < 0.05$ vs. groove$_{2\ mm}$ or bulge$_{2\ mm}$, the difference was statistically significant ($n = 3$). Scale bar = 500 μm.

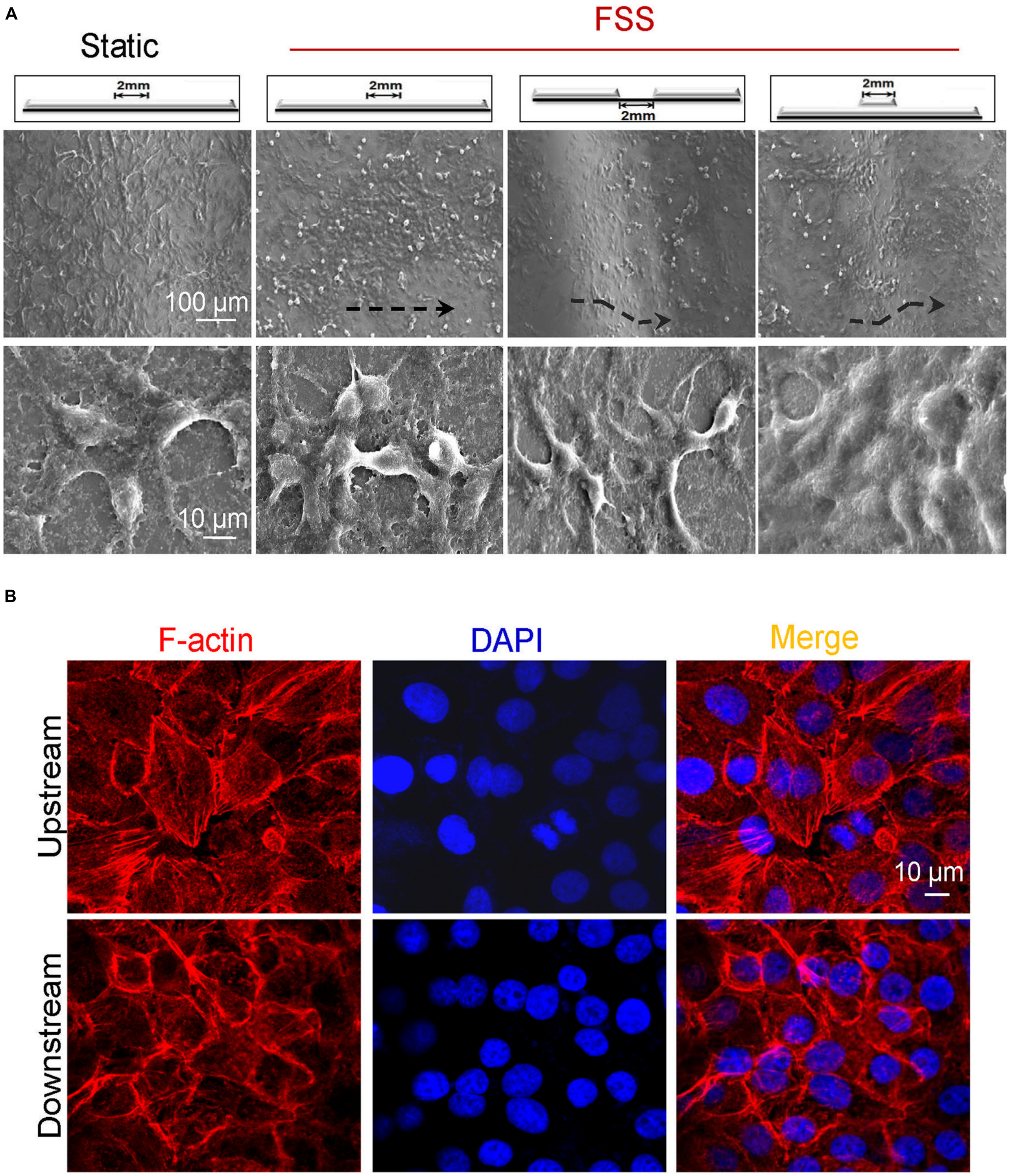

FIGURE 6 | Morphology of endothelial cells in vascular injury models under flow. **(A)** Exposed to FSS, endothelial cells spread out with obvious parapodium in the groove models in favor of directed cell locomotion, while they accumulated in clusters on the edge of the bulge models. Scale bars = 100 and 10 µm. The black dashed lines indicated the flow direction. **(B)** Exposed to FSS, the distribution of F-actin arrays in VECs upstream and downstream of the groove$_{2\ mm}$ model. Scale bar = 10 µm.

It could be found that approximately 27% (flat$_{2\ mm}$), 16% (groove$_{2\ mm}$), and 12% (bulge$_{2\ mm}$) of re-endothelialization were completed. The migrated VECs (GFP-HUVECs) accounted for 21% (flat$_{2\ mm}$), 15% (groove$_{2\ mm}$), and 7% and the adhered VECs (mCherry-HUVECs) were 6% (flat$_{2\ mm}$), 1% (groove$_{2\ mm}$), and 5% (bulge$_{2\ mm}$), respectively (**Figure 7A**). These results indicated that the flat and groove models promoted VEC migration under flow, while the bulge model facilitated cell adhesion.

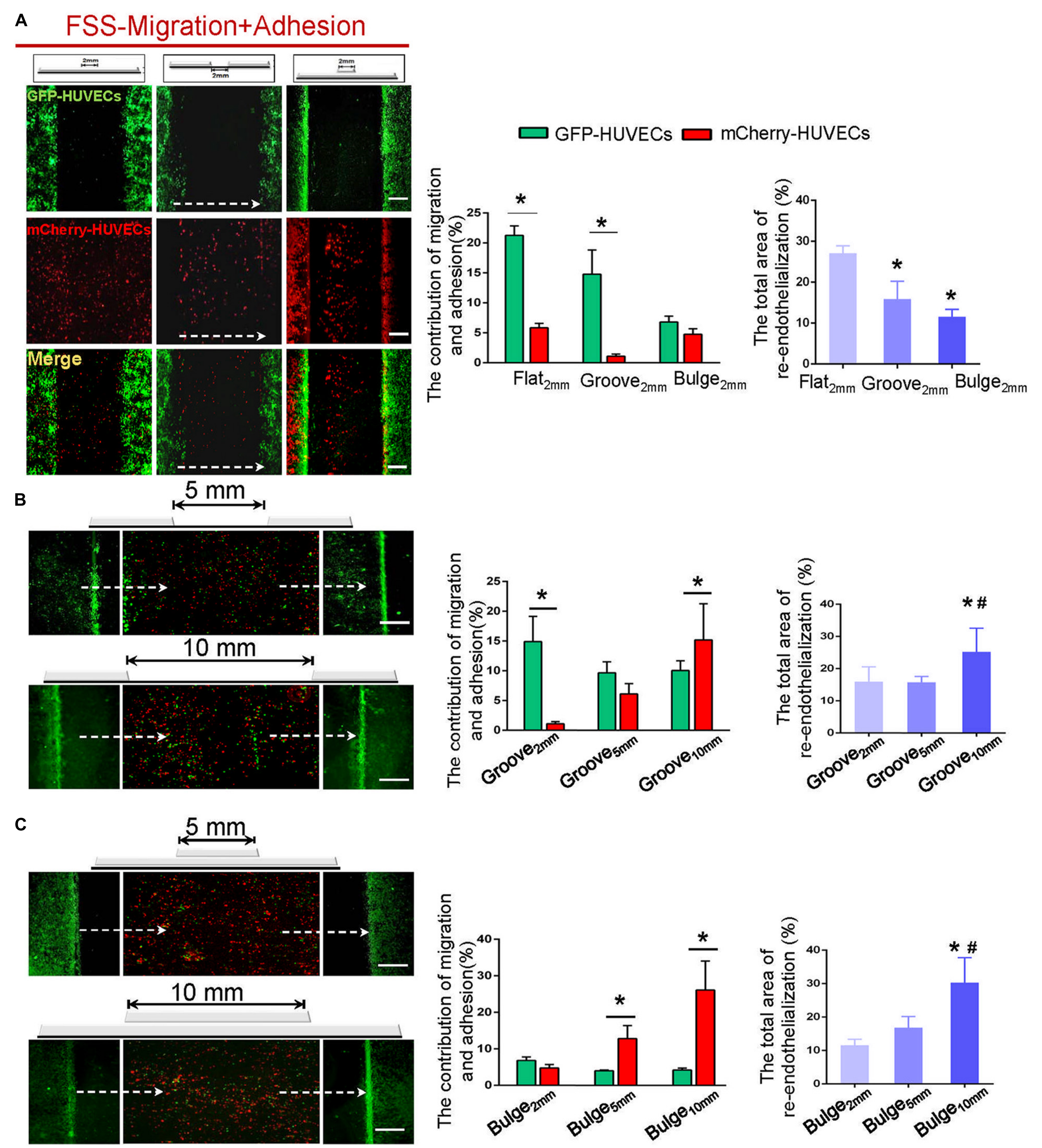

FIGURE 7 | The combined contribution of VEC migration and adhesion to re-endothelialization under flow. **(A)** In the flat$_{2\ mm}$/groove$_{2\ mm}$/bulge$_{2\ mm}$ models, the endothelial cell source of endothelial restoration and their respective contribution under flow were analyzed. **(B,C)** With the augmentation of the injury scales to 5 and 10 mm in the groove/bulge models, the endothelial cell source of re-endothelialization under flow was analyzed. The white dashed lines indicated the flow direction. $^{*}P < 0.05$ vs. flat$_{2\ mm}$ or groove$_{2\ mm}$ or bulge$_{2\ mm}$; $^{\#}P < 0.05$ vs. groove$_{5\ mm}$ or bulge$_{5\ mm}$, the difference was statistically significant ($n = 3$). Scale bar = 500 μm.

With increased injury scales (5 and 10 mm), more adherent circulating VECs could be found, in turn largely contributing to endothelial repair in an endothelial denudation scale-dependent way. In the groove model with widths of 5 and 10 mm, impaired endothelium recovered approximately 16 and 25%, and the adhesion was about 6 and 15%, respectively (**Figure 7B**). In the bulge$_{5\ mm}$/bulge$_{10\ mm}$ models, the percentage of re-endothelialization was 17 and 30%, and the adhesion was 13 and 26% (**Figure 7C**). The results indicated that adjacent VEC migration was the main contributor of endothelial restoration under flow in models with 2 mm injury width. The increased injury scale promoted the adherent cells to contribute to endothelial regeneration.

DISCUSSION

Interventions including balloon angioplasty and stent implantation inevitably cause mechanical damage to the endothelium, leading to endothelial denudation and subsequent ISR and late thrombosis. The pathophysiological mechanism of ISR has not been fully elucidated, but it is considered to include inflammation, proliferation, and matrix remodeling. Rapid restoration of functional vascular endothelium is an important therapeutic goal to avoid ISR, late thrombosis, and other postoperative complications (Bedair et al., 2017; Chang et al., 2018).

Factors including stent deployment depth, the scale of endothelial denudation, hemodynamic changes, and the structure and material properties of the stent potentially regulate re-endothelialization in stented vessels (Conway and Schwartz, 2015; Kang et al., 2015; Liang et al., 2016; Ostrowski et al., 2016). Due to the lack of effective *in vivo* and *in vitro* models, the cell sources of endothelial repair after stent implantation have not been fully understood. In this study, we developed an *in vitro* vascular injury model to mimic various endothelial denudation scales (2 mm/5 mm/10 mm) and stent deployment depths (groove/flat/bulge) (**Figures 2A,B**). The models of vascular injury *in vitro* were validated by SEM, and our results revealed that in the groove model, the deployment depth was 197.0 ± 6.8 μm, and the left- and right-edge angles were $29.7 \pm 1.2°$ and $29.9 \pm 0.8°$, respectively. In the bulge model, the protrusion height was 185.9 ± 2.8 μm, and the left- and right-edge angles were $30.0 \pm 0.4°$ and $28.9 \pm 1.0°$, respectively (**Figure 2C**).

The presence of stent inside the blood vessel causes changes in the local flow environment (Ng et al., 2017; Tenekecioglu et al., 2017). To evaluate the influence of different deployment depths and endothelial denudation scales on flow distribution, computational fluid dynamics simulation analysis was carried out. Our results suggested that groove/bulge models did not alter the hemodynamics in the upstream of stent segment, while they generated flow separation in the downstream and led to turbulence, depending on the injury scales and stent deployment depth (**Figure 3**). Consistent with our results, Jiang et al. (2019) revealed that stent deployment led to local flow turbulence and fluid separation area at the distal end of stent struts, which was characterized by flow recirculation, low shear rate, and long particle residence time. Of note, it is hard to simulate all physiological parameters at the same time in numerical simulation, and some conditions may be simplified. In the present study, we performed a two-dimensional simulation, which neglected some details that could be observed in three-dimensional simulation, such as blood vessel wall pressure, wall shear stress (WSS), and other hemodynamic parameters. Therefore, the changes of WSS in the groove and bulge models were not calculated and analyzed. By placing undersized stent at the lesion site or insufficient expansion, it was found that upstream of the stent induced high shear stress while the downstream produced low shear stress (Rikhtegar et al., 2014). Wang et al. (2018) indicated that low WSS was usually observed at the distal of the stent struts as compared with the proximal end of the struts. Using an *in vitro* flow chamber that contained ridges, Hsiao et al. (2016) indicated that flow rate of 21.6 ml/min medium would generate flow velocities that were the highest through the center (0.25 m/s). Additionally, the ridges created local flow disturbances including a region of very high unidirectional WSS (>100 dyn/cm^2) at the top of the ridge and recirculating bidirectional flow with low-average WSS downstream from the ridge.

Increasing evidence pointed out that the degree of stent-induced arterial injury was correlated to re-endothelialization rate (Gunn et al., 2002; Gao et al., 2015). However, the effect of stent deployment depth and injury scales on endothelial restoration remains unclear. Based on the constructed flat$_{2\ \mathrm{mm}}$/groove$_{2\ \mathrm{mm}}$/bulge$_{2\ \mathrm{mm}}$ models, we investigated the effects of stent deployment depth on adjacent VEC migration, circulating VEC adhesion, and their combined effect on re-endothelialization under static condition. As shown in **Figures 4**, **5**, our results indicated that the groove model was in favor of VEC migration and adhesion, and re-endothelialization was mainly derived from the adhesion of VECs under static condition. Consistently, Palmaz et al. (1999) found that grooved surfaces significantly increased the migration rate of endothelial cells. A novel micro/nanopatterned scaffold surface with a typical geometry of groove, ranging from 0.5 to 50 μm, was developed to evaluate cell reactions. Their results revealed that groove could selectively promote endothelial repair and inhibit the proliferation of SMCs in a width-dependent manner (Ding et al., 2014). Additionally, with stent deployment depths of 90, 110, and 130 μm, Tahir et al. (2013) showed that the deeper penetration of stent struts resulted in a late endothelial recovery and higher neointimal growth. Further, they qualitatively compared the restoration of damaged intima at a deployment depth of 110 μm, which found approximately 59% endothelium presented from the third day after stenting, and endothelium recovery was 100% after 15 days.

Stent application results in geometric changes of vascular wall and disturbed flow, which regulate the physiology of VECs. VECs showed resistance to vascular injury under high laminar FSS, while they expressed proinflammatory and prothrombotic genes and adopt an athero-prone phenotype when exposed to low and oscillating flow (Souilhol et al., 2020). Here, we explored the effects of the vascular injury model on VEC morphology under flow. It was found that VECs spread out with obvious parapodium in groove models in favor of directed cell locomotion, while they accumulated in clusters on the edge of bulge models (**Figure 6A**). Additionally, endothelial cells exposed to FSS exhibited stress filament formation upstream of groove$_{2\ \mathrm{mm}}$, while they displayed disordered actin stress fibers downstream of groove$_{2\ \mathrm{mm}}$ (**Figure 6B**). The difference in the morphologies of VECs upstream and downstream may be caused by the changes of flow distribution and wall shear stress. Yoshino et al. (2017) showed that a higher WSS flow needed a higher WSS gradient to be able to affect the cell's morphological change.

Instead, on lower uniform WSS without WSS gradient flow, EC elongation and reorientation to the flow direction occurred.

Re-endothelialization is a complex mechanobiological process, which is modulated by the proliferation and migration of resident endothelial cells from uninjured intima (Evans et al., 2020; Li et al., 2021) and by the adhesion of circulating endothelial cells (Tesfamariam, 2016; Hu et al., 2019). Increased circulating endothelial cells in the peripheral blood have been reported in various pathologic conditions involving severe endothelial perturbation, including inflammatory disease, acute myocardial infarction, unstable angina, and critical limb ischemia (Makin et al., 2004; Lee et al., 2005). Using different pathological animal models and mechanical damage models in various studies, the cell source of endothelial repair after vascular injury has been controversial. By grafting the common carotid artery of transgenic mice with fluorescent endothelium (Tie2-GFP) into wild-type mice, Hagensen et al. (2011) illustrated that the migration but not the adhesion of endothelial cells contributed to the regeneration of the endothelium. However, using mice that received either aortic or bone marrow grafts from transgenic mice with Tie2-LacZ-labeled endothelial cell, another study revealed that both local VEC migration and circulating cell adhesion participated in endothelium restoration, although the respective contribution varied between animals (Douglas et al., 2013).

Combining stent-induced vascular injury with mechanical factors, we further explored the combined effect of VEC migration and adhesion on re-endothelialization and their contribution. It could be seen from **Figure 7** that endothelial repair mainly depended on the migration of adjacent VECs at an injury scale of 2 mm, while the quantity of circulating VEC adhesion increased and largely contributed to endothelial repair with the increase of the injury scale, showing an injury scale dependence. A possible explanation for this phenomenon is the different WSS in the groove and bulge models. Alterations in flow patterns and WSS induced by stent application have been correlated with VEC migration and adhesion (Putra et al., 2018; Wang et al., 2018). Consistently, using a ridged flow chamber, Hsiao et al. (2016) demonstrated that VECs migrated in the direction of flow upstream from the ridges but subsequently accumulated downstream from ridges at sites of bidirectional flow. Localized bidirectional flow in the downstream of the stent trapped migrating VECs, which involved reduced migratory polarity associated with altered actin dynamics. Ostrowski et al. (2014) observed that human microvascular ECs were stimulated to migrate toward the region of high WSS and against the flow direction under the influence of WSS gradient distribution created by the impinging flow. Additionally, employing a lab-on-a-chip system, Stamp et al. (2016) systematically investigated cell adhesion under static, dynamic, and physiologically relevant conditions. They found increased detachment with increasing surface roughness under dynamic conditions, which involved shear flow-induced activation of focal adhesions, leading to an enhancement of stress fibers.

In conclusion, we successfully constructed an *in vitro* injury model to simulate various endothelial denudation scales and stent deployment depths. Flow distribution analysis revealed that the injury models did not alter the hemodynamics in the upstream of stent segment but generated flow separation in the downstream and led to turbulence, depending on the injury scales and stent deployment depth. Furthermore, this study preliminarily clarified the endothelial cell sources of re-endothelialization mainly derived from the migration of adjacent VECs when the injury scale was 2 mm; with the increase of the injury scale, the contribution of VEC adhesion to endothelium restoration increased in an injury scale-dependent way. Our study will provide new enlightenment for researchers engaged in vascular biomechanics and surface modification of cardiovascular implants.

DATA AVAILABILITY STATEMENT

The original contributions presented in the study are included in the article/supplementary material, further inquiries can be directed to the corresponding author/s.

ETHICS STATEMENT

This article does not contain any studies with human participants or animals performed by the any of the authors.

AUTHOR CONTRIBUTIONS

XW, YS, and XL were responsible for the conception and design, acquisition, analysis, and interpretation of data, and drafting of the manuscript. FF and YN were responsible for SEM and numerical simulation data acquisition. HY was responsible for statistics. JM, LD, and CL were responsible for cell migration and adhesion assay data acquisition. YS and XL were responsible for revising the manuscript critically for important intellectual content and for the final approval of the version to be published. All authors read and approved the final manuscript.

FUNDING

This study was supported by the National Natural Science Foundation of China (31870939, 31570948, and 11932014).

REFERENCES

Bedair, T. M., ElNaggar, M. A., Joung, Y. K., and Han, D. K. (2017). Recent advances to accelerate re-endothelialization for vascular stents. *J. Tissue Eng.* 8, 1–14. doi: 10.1177/2041731417731546

Blann, A. D., Woywodt, A., Bertolini, F., Bull, T. M., Buyon, J. P., Clancy, R. M., et al. (2005). Circulating endothelial cells. *Biomarker Vasc. Dis. Thromb. Haemost* 93, 228–235. doi: 10.1160/TH04-09-0578

Byrne, R. A., Stone, G. W., Ormiston, J., and Kastrati, A. J. T. L. (2017). Coronary balloon angioplasty, stents, and scaffolds. *Lancet* 390, 781–792. doi: 10.1016/S0140-6736(17)31927-X

Chang, H. K., Kim, P. H., Kim, D. W., Cho, H. M., Jeong, M. J., Kim, D. H., et al. (2018). Coronary stents with inducible VEGF/HGF-secreting UCB-MSCs reduced restenosis and increased re-endothelialization in a swine model. *Exp. Mol. Med.* 50:114. doi: 10.1038/s12276-018-0143-9

Conway, D. E., and Schwartz, M. A. (2015). Mechanotransduction of shear stress occurs through changes in VE-cadherin and PECAM-1 tension: implications for cell migration. *Cell Adhes. Migr.* 9, 335–339. doi: 10.4161/19336918.2014.968498

Ding, Y., Yang, Z., Bi, C. W., Yang, M., Xu, S. L., Lu, X., et al. (2014). Directing vascular cell selectivity and hemocompatibility on patterned platforms featuring variable topographic geometry and size. *ACS Appl. Mater. Interfaces* 6, 12062–12070. doi: 10.1021/am502692k

Douglas, G., Van Kampen, E., Hale, A. B., McNeill, E., Patel, J., Crabtree, M. J., et al. (2013). Endothelial cell repopulation after stenting determines in-stent neointima formation: effects of bare-metal vs. drug-eluting stents and genetic endothelial cell modification. *Eur. Heart J.* 34, 3378–3388. doi: 10.1093/eurheartj/ehs240

Du, R., Wang, Y., Huang, Y., Zhao, Y., Zhang, D., Du, D., et al. (2018). Design and testing of hydrophobic core/hydrophilic shell nano/micro particles for drug-eluting stent coating. *NPG Asia Mater.* 10, 642–658. doi: 10.1038/s41427-018-0064-z

Evans, C. E., Iruela-Arispe, M. L., and Zhao, Y.-Y. (2020). Mechanisms of endothelial regeneration and vascular repair and their application to regenerative medicine. *Am. J. Pathol.* 191, 52–65. doi: 10.1016/j.ajpath.2020.10.001

Gao, M., Yao, Q., Liu, Y., Sun, F., Ma, Y., and Sun, G. (2015). Association between mobilization of circulating endothelial progenitor cells and time or degree of injury from angioplasty in patients with exertional angina: a prospective study. *Exp. Ther. Med.* 10, 809–815. doi: 10.3892/etm.2015.2571

Gijsen, F., Katagiri, Y., Barlis, P., Bourantas, C., Collet, C., Coskun, U., et al. (2019). Expert recommendations on the assessment of wall shear stress in human coronary arteries: existing methodologies, technical considerations, and clinical applications. *Eur. Heart J.* 40, 3421–3433. doi: 10.1093/eurheartj/ehz551

Gunn, J., Arnold, N., Chan, K. H., Shepherd, L., Cumberland, D. C., and Crossman, D. C. (2002). Coronary artery stretch versus deep injury in the development of in-stent neointima. *Heart* 88, 401–405. doi: 10.1136/heart.88.4.401

Hagensen, M. K., Raarup, M. K., Mortensen, M. B., Thim, T., Nyengaard, J. R., Falk, E., et al. (2011). Circulating endothelial progenitor cells do not contribute to regeneration of endothelium after murine arterial injury. *Cardiovasc. Res.* 93, 223–231.

Hsiao, S. T., Spencer, T., Boldock, L., Prosseda, S. D., Xanthis, I., Tovar-Lopez, F. J., et al. (2016). Endothelial repair in stented arteries is accelerated by inhibition of Rho-associated protein kinase. *Cardiovasc. Res.* 112, 689–701. doi: 10.1093/cvr/cvw210

Hu, Q., Ke, X., Zhang, T., Chen, Y., Huang, Q., Deng, B., et al. (2019). Hydrogen sulfide improves vascular repair by promoting endothelial nitric oxide synthase-dependent mobilization of endothelial progenitor cells. *J. Hypertens.* 37, 972–984. doi: 10.1097/HJH.0000000000001983

Jiang, B., Thondapu, V., Poon, E., Barlis, P., and Ooi, A. (2019). Numerical study of incomplete stent apposition caused by deploying undersized stent in arteries with elliptical cross-sections. *J. Biomech. Eng.* 141:054501. doi: 10.1115/1.4042899

Kakinoki, S., Takasaki, K., Mahara, A., Ehashi, T., Hirano, Y., and Yamaoka, T. (2018). Direct surface modification of metallic biomaterials via tyrosine oxidation aiming to accelerate the re-endothelialization of vascular stents. *J. Biomed. Mater. Res. A* 106, 491–499. doi: 10.1002/jbm.a.36258

Kalapatapu, K., Dilmanian, H., Aronow, W. S., Mundia, M., Pucillo, A. L., Weiss, M. B., et al. (2007). The average stent length is longer and the average stent diameter is shorter in patients with drug-eluting stents vs bare-metal stents during percutaneous coronary intervention. *Am. J. Ther.* 14, 277–279. doi: 10.1097/MJT.0b013e3180653377

Kang, T.-Y., Lee, J. H., Kim, B. J., Kang, J.-A., Hong, J. M., Kim, B. S., et al. (2015). In vivo endothelization of tubular vascular grafts through in situ recruitment of endothelial and endothelial progenitor cells by RGD-fused mussel adhesive proteins. *Biofabrication* 7:015007. doi: 10.1088/1758-5090/7/1/015007

Kivimaki, M., and Steptoe, A. (2018). Effects of stress on the development and progression of cardiovascular disease. *Nat. Rev. Cardiol.* 15, 215–229. doi: 10.1038/nrcardio.2017.189

Krankenberg, H., Tübler, T., Ingwersen, M., Schlüter, M., Scheinert, D., Blessing, E., et al. (2015). Drug-coated balloon versus standard balloon for superficial femoral artery in-stent restenosis: the randomized femoral artery in-stent restenosis (FAIR) trial. *Circulation* 132, 2230–2236. doi: 10.1161/CIRCULATIONAHA.115.017364

Kwak, B. R., Magnus, B. C., Marie-Luce, B. P., Giuseppina, C., Daemen, M. J. A. P., Davies, P. F., et al. (2014). Biomechanical factors in atherosclerosis: mechanisms and clinical implications. *Eur. Heart J.* 35, 3013–3020. doi: 10.1093/eurheartj/ehu353

Lee, K. W., Lip, G. Y., Tayebjee, M., Foster, W., and Blann, A. D. (2005). Circulating endothelial cells, von Willebrand factor, interleukin-6, and prognosis in patients with acute coronary syndromes. *Blood* 105, 526–532. doi: 10.1182/blood-2004-03-1106

Li, J., Chen, Y., Gao, J., Chen, Y., Zhou, C., Lin, X., et al. (2021). Eva1a ameliorates atherosclerosis by promoting re-endothelialization of injured arteries via Rac1/Cdc42/Arpc1b. *Cardiovasc. Res.* 117, 450–461. doi: 10.1093/cvr/cvaa011

Liang, C., Hu, Y., Wang, H., Xia, D., Li, Q., Zhang, J., et al. (2016). Biomimetic cardiovascular stents for in vivo re-endothelialization. *Biomaterials* 103, 170–182. doi: 10.1016/j.biomaterials.2016.06.042

Makin, A. J., Blann, A. D., Chung, N. A., Silverman, S. H., and Lip, G. Y. (2004). Assessment of endothelial damage in atherosclerotic vascular disease by quantification of circulating endothelial cells. Relationship with von Willebrand factor and tissue factor. *Eur. Heart J.* 25, 371–376. doi: 10.1016/j.ehj.2003.04.001

Michail, M., Davies, J. E., Cameron, J. D., Parker, K. H., and Brown, A. J. (2018). Pathophysiological coronary and microcirculatory flow alterations in aortic stenosis. *Nat. Rev. Cardiol.* 15, 420–431. doi: 10.1038/s41569-018-0011-2

Ng, J., Bourantas, C. V., Torii, R., Ang, H. Y., Tenekecioglu, E., Serruys, P. W., et al. (2017). Local hemodynamic forces after stenting: implications on restenosis and thrombosis. *Arterioscler. Thromb. Vasc. Biol.* 37, 2231–2242. doi: 10.1161/ATVBAHA.117.309728

O'Brien, C. C., Lopes, A. C., Kolandaivelu, K., Kunio, M., Brown, J., Kolachalama, V. B., et al. (2016). Vascular response to experimental stent malapposition and under-expansion. *Ann. Biomed. Eng.* 44, 2251–2260. doi: 10.1007/s10439-015-1518-x

Ostrowski, M. A., Huang, E. Y., Surya, V. N., Poplawski, C., Barakat, J. M., Lin, G. L., et al. (2016). Multiplexed fluid flow device to study cellular response to tunable shear stress gradients. *Ann. Biomed. Eng.* 44, 2261–2272. doi: 10.1007/s10439-015-1500-7

Ostrowski, M. A., Huang, N. F., Walker, T. W., Verwijlen, T., Poplawski, C., Khoo, A. S., et al. (2014). Microvascular endothelial cells migrate upstream and align against the shear stress field created by impinging flow. *Biophys. J.* 106, 366–374. doi: 10.1016/j.bpj.2013.11.4502

Palmaz, J. C., Benson, A., and Sprague, E. A. (1999). Influence of surface topography on endothelialization of intravascular metallic material. *J. Vasc. Interv. Radiol.* 10, 439–444. doi: 10.1016/S1051-0443(99)70063-1

Putra, N. K., Wang, Z., Anzai, H., and Ohta, M. (2018). "Computational fluid dynamics analysis to predict endothelial cells migration during flow exposure experiment with placement of two stent wires," in *Proceedings of the 2018 40th Annual International Conference of the IEEE Engineering in Medicine and Biology Society (EMBC)*, (Piscataway, NJ: IEEE), 5454–5457.

Quilici, J., Banzet, N., Paule, P., Meynard, J. B., Mutin, M., Bonnet, J. L., et al. (2004). Circulating endothelial cell count as a diagnostic marker for non-ST-elevation acute coronary syndromes. *Circulation* 110, 1586–1591. doi: 10.1161/01.CIR.0000142295.85740.98

Rikhtegar, F., Wyss, C., Stok, K. S., Poulikakos, D., Muller, R., and Kurtcuoglu, V. (2014). Hemodynamics in coronary arteries with overlapping stents. *J. Biomech.* 47, 505–511. doi: 10.1016/j.jbiomech.2013.10.048

Souilhol, C., Serbanovic-Canic, J., Fragiadaki, M., Chico, T. J., Ridger, V., Roddie, H., et al. (2020). Endothelial responses to shear stress in atherosclerosis: a novel role for developmental genes. *Nat. Rev. Cardiol.* 17, 52–63. doi: 10.1038/s41569-019-0239-5

Stamp, M. E., Jotten, A. M., Kudella, P. W., Breyer, D., Strobl, F. G., Geislinger, T. M., et al. (2016). Exploring the limits of cell adhesion under shear stress within physiological conditions and beyond on a chip. *Diagnostics* 6:38. doi: 10.3390/diagnostics6040038

Tahir, H., Bona-Casas, C., and Hoekstra, A. G. (2013). Modelling the effect of a functional endothelium on the development of in-stent restenosis. *PLoS One* 8:e66138. doi: 10.1371/journal.pone.0066138

Tenekecioglu, E., Torii, R., Sotomi, Y., Collet, C., Dijkstra, J., Miyazaki, Y., et al. (2017). The effect of strut protrusion on shear stress distribution: hemodynamic insights from a prospective clinical trial. *JACC Cardiovasc. Interv.* 10, 1803–1805. doi: 10.1016/j.jcin.2017.06.020

Tesfamariam, B. (2016). Endothelial repair and regeneration following intimal injury. *J. Cardiovasc. Transl. Res.* 9, 91–101. doi: 10.1007/s12265-016-9677-1

Torii, R., Tenekecioglu, E., Katagiri, Y., Chichareon, P., Sotomi, Y., Dijkstra, J., et al. (2020). The impact of plaque type on strut embedment/protrusion and shear stress distribution in bioresorbable scaffold. *Eur. Heart J. Cardiovasc. Imaging* 21, 454–462. doi: 10.1093/ehjci/jez155

Van der Heiden, K., Gijsen, F. J., Narracott, A., Hsiao, S., Halliday, I., Gunn, J., et al. (2013). The effects of stenting on shear stress: relevance to endothelial injury and repair. *Cardiovasc. Res.* 99, 269–275. doi: 10.1093/cvr/cvt090

Wang, J., Jin, X., Huang, Y., Ran, X., Luo, D., Yang, D., et al. (2018). Endovascular stent-induced alterations in host artery mechanical environments and their roles in stent restenosis and late thrombosis. *Regen. Biomater.* 5, 177–187. doi: 10.1093/rb/rby006

Yoshino, D., Sakamoto, N., and Sato, M. J. I. B. (2017). Fluid shear stress combined with shear stress spatial gradients regulates vascular endothelial morphology. *Integr. Biol.* 9, 584–594. doi: 10.1039/c7ib00065k

Zhang, M., Rehman, J., and Malik, A. B. J. C. (2014). Endothelial progenitor cells and vascular repair. *Curr. Opin. Hematol.* 21, 224–228. doi: 10.1097/MOH.0000000000000041

Conflict of Interest: The authors declare that the research was conducted in the absence of any commercial or financial relationships that could be construed as a potential conflict of interest.

frontiers
in Cell and Developmental Biology

MINI REVIEW
published: 06 April 2021
doi: 10.3389/fcell.2021.640781

Shear-Regulated Extracellular Microenvironments and Endothelial Cell Surface Integrin Receptors Intertwine in Atherosclerosis

Fan-E Mo[1,2]*

[1]*Department of Cell Biology and Anatomy, College of Medicine, National Cheng Kung University, Tainan, Taiwan,* [2]*Institute of Basic Medical Sciences, College of Medicine, National Cheng Kung University, Tainan, Taiwan*

Mechanical forces imposed by blood flow shear stress directly modulate endothelial gene expression and functional phenotype. The production of extracellular matrix proteins and corresponding cell-surface integrin receptors in arterial endothelial cells is intricately regulated by blood flow patterns. Laminar blood flow promotes mature and atheroresistant endothelial phenotype, while disturbed flow induces dysfunctional and atheroprone endothelial responses. Here, we discuss how hemodynamic changes orchestrate the remodeling of extracellular microenvironments and the expression profile of the integrin receptors in endothelial cells leading to oxidative stress and inflammation. Targeting the interaction between matrix proteins and their corresponding integrins is a potential therapeutic approach for atherosclerosis.

Keywords: disturbed flow atherosclerosis, extracellular matrix, integrin, matricellular proteins, endothelial dysfunction, atheroprotection

OPEN ACCESS

Edited by:
Jing Zhou,
Peking University, China

Reviewed by:
Orest William Blaschuk,
McGill University, Canada
Myeongwoo Lee,
Baylor University, United States

***Correspondence:**
Fan-E Mo
femo@mail.ncku.edu.tw;
fanemo@gmail.com

Specialty section:
This article was submitted to
Cell Adhesion and Migration,
a section of the journal
Frontiers in Cell and Developmental Biology

Received: *12 December 2020*
Accepted: *18 March 2021*
Published: *06 April 2021*

Citation:
Mo F-E (2021) Shear-Regulated Extracellular Microenvironments and Endothelial Cell Surface Integrin Receptors Intertwine in Atherosclerosis.
Front. Cell Dev. Biol. 9:640781.
doi: 10.3389/fcell.2021.640781

INTRODUCTION

Though risk factors, such as hyperlipidemia, hypertension, and hyperglycemia, pose a threat to the entire arterial system, atherosclerosis preferentially occurs at arterial branches or curvatures, where the local blood flow is disturbed (Chiu and Chien, 2011). Blood flow imposes fictional drag, called sheer stress, directly to the inner lining endothelial cells (ECs). Laminar blood flow found at the straight part of artery generates unidirectional shear stress and promotes functional endothelial phenotype (atheroprotective). By contrast, disturbed flow generates low and oscillatory sheer stress, and induces EC activation and maladaptive alterations in endothelial functional phenotype (atheroprone; Hsu et al., 2019). Low endothelial shear stress correlates with increased plaque burden and risks of rupture in patients with coronary artery disease (Chatzizisis et al., 2008; Stone et al., 2012). Endothelial dysfunction by disturbed flow is manifested by the lack of nitric oxide production, and chronic inflammatory response mediated through the pleiotropic transcription factor nuclear factor-κB (NF-κB; Gimbrone and Garcia-Cardena, 2016). These atheroprone genes include cell-surface adhesion molecules (such as vascular cell adhesion molecule-1; Korenaga et al., 1997), secreted cytokines (such as interleukin-1 and monocyte chemoattractant protein 1; Hsu et al., 2019), and prothrombotic mediators (such as von Willebrand factor; Zhu et al., 2020). Recent studies using systems biology approaches have demonstrated that low endothelial shear stress causes aberrant reactivation of vascular developmental signaling pathways, such as BMP-TGFβ, WNT, Notch, HIF1α, TWIST1, and HOX family genes, leading to increased inflammation and vascular permeability (Souilhol et al., 2020).

Consequently, the infiltration of monocytes/macrophages rises, the uptake of lipid elevates, local inflammation and oxidative stress intensifies, and the number of vascular smooth muscle cells increases in the intima, leading to the formation of atherosclerotic plaques. Emerging evidence suggests that local microenvironment also plays a major role in regulating endothelial cell function and regional susceptibility to atherosclerosis (Yurdagul et al., 2016). Hemodynamics may affect endothelial remodeling and change subendothelial matrix composition. Concurrently, the expression profile of cell-surface integrin receptors responsible for interacting with the extracellular matrix (ECM) is adjusted in the ECs to accommodate the changing microenvironment. The signaling induced by the engagement of ECM proteins and corresponding integrin receptors regulates endothelial cell functional phenotype. The critical role in atherogenesis and the accessibility of matrix/integrin engagement makes it an attractive therapeutic target for atherosclerosis. This minireview summarizes recent findings on the shear-induced ECM remodeling and integrin expression, and their roles in atherosclerosis (**Figure 1**).

BASEMENT MEMBRANE

The basement membrane is the subendothelial ECM largely secreted by and closely interacting with ECs. The major components of the basement membrane in normal vessels include laminin and type IV collagen (Yurchenco and O'Rear, 1994). Both laminin and collagen IV promote homeostasis of ECs, and prevent disturbed flow-induced NF-κB activation and inflammation (Orr et al., 2005). The composition of basement membrane is regulated by hemodynamic patterns. Disturbed flow induces subendothelial matrix remodeling to a "provisional" matrix rich in fibronectin at atheroprone sites prior to other signs of atherosclerosis (Orr et al., 2005). The provisional ECM is initially named with regard to the transient ECM (enriched with fibronectin, vitronectin, and fibrinogen) that is deposited and subsequently cleared during wound healing (Stupack and Cheresh, 2002). A fibronectin-rich ECM primes ECs to activation by oxidized low-density lipoprotein (Yurdagul et al., 2014) and hyperglycemia (Green et al., 2014). Onset of atheroprotective laminar shear stress induces a transient fibronectin upregulation compared to static control *in vitro*, whereas atheroprone oscillatory shear stress initiates a steady increase in fibronectin expression through the activation of NF-κB. Furthermore, because fibronectin promotes NF-κB activation, disturbed flow creates positive feedback to sustain endothelial inflammation (Feaver et al., 2010). Whereas disturbed shear activates p21-activated kinase in ECs on fibronectin leading to enhanced NF-κB and inflammation, ECs on native basement proteins inhibits shear-induced p21-activated kinase activation through a protein kinase A-dependent pathway.

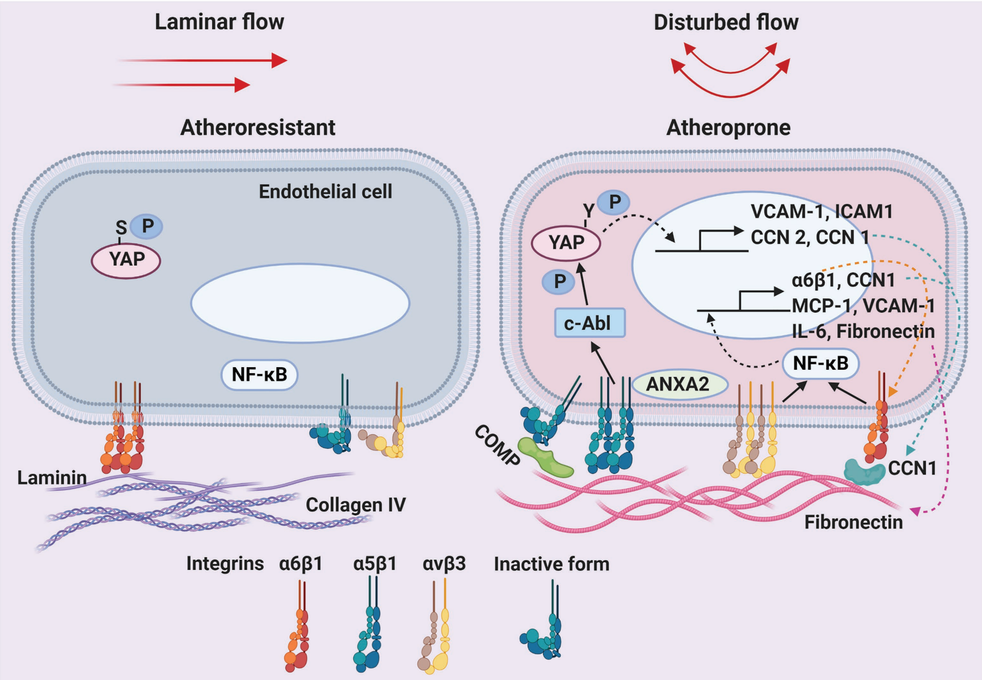

FIGURE 1 | Shear-regulated extracellular microenvironments and endothelial integrin receptors in atherosclerosis. Schematic of the dynamic changes in the composition of the endothelial basement membrane and cell-surface integrin receptors by unidirectional laminar blood flow or oscillatory disturbed flow. Solid arrows: activation of downstream effectors. Dashed arrows: translocation of proteins. ANXA2, annexin A2; COMP, cartilage oligomeric matrix protein; ICAM1, intercellular adhesion molecule 1; IL-6, interleukin-6; MCP-1, monocyte chemoattractant protein 1; NF-κB, nuclear factor-κB; P, phosphorylation; S, serine; VCAM-1, vascular cell adhesion molecule 1; Y, tyrosine; YAP, yes-associated protein.

INTEGRINS

Integrins are transmembrane heterodimeric proteins consisting of α and β subunits, responsible for cell adhesion to ECM and transducing environmental cues and internal cell signals in both directions. There are at least 18 α subunits and eight β subunits through different combinations to form 24 distinct integrins (Hynes, 2002). ECs express a repertoire of integrins to mediate dynamic interactions between cells and ECM. Endothelium on a native ECM expresses the collagen-binding (α1β1 and α2β1) and laminin-binding (α3β1, α6β1, and α6β4) integrins for mediating EC anchorage within quiescent blood vessels. ECs on a provisional matrix express RGD-binding integrins (including α5β1 and αvβ3), resulting in EC activation for angiogenesis or in pathologic conditions (Stupack and Cheresh, 2002). αvβ3 critically mediates EC interactions with provisional matrix proteins and disturbed flow-induced pro-inflammatory signaling (NF-κB and p21-activated kinase activation) in early atherogenic stages. However, inhibiting αvβ3 does not affect all the shear-induced signaling, as Akt, endothelial nitric oxide synthase, and extracellular regulated kinase remain responsive (Chen et al., 2015). Endothelial α5β1 binding with fibronectin under low oscillatory shear stress phosphorylates (activates) the cytosolic nonreceptor protein kinase c-Abl, which then induces tyrosine phosphorylation (at Y^{357}) and nuclear translocation of yes-associated protein (YAP), leading to pro-atherogenic gene expression and EC activation. The phosphorylation of c-Abl and YAP^{Y357} is significantly higher in atherosclerotic plaques of *Apoe*$^{-/-}$ mice and in patients (Li et al., 2019). Of note, YAP can also be serine phosphorylated at S127 (for 14-3-3 binding and cytoplasmic retention) and at S381 (for ubiquitination and degradation), thus inactivated by the Hippo pathway (Yu et al., 2015). As such, unidirectional shear flow sustains the cytoplasmic levels of $YAP^{S127,S381}$ phosphorylation and suppression in ECs for atheroprotection through RhoA inhibition (Wang et al., 2016b). Endothelial α5β1 upon binding with fibronectin also recruits phosphodiesterase 4D5 at adhesion sites, which subsequently connects with phosphatase PP2A and its regulatory subunit B55α. Fibronectin-induced PP2A holoenzyme assembly triggers YAP^{S127}-dephosphorylation and facilitates YAP activation (Yun et al., 2019). Although no direct evidence, increased levels of YAP by disturbed flow in ECs is consistent with the possibility of YAP^{S381}-dephosphorylation (lower ubiquitination and degradation; Wang et al., 2016a). Furthermore, to effectively transduce outside-in signaling, inactive integrins require inside-out signaling to make a conformational change and promote their binding with permissive ligands. Disturbed flow activates endothelial α5β1 by increasing calcium influx through the cation channel Piezo1, which activates PTP1B-dependent dephosphorylation of annexin A2. Annexin A2 then binds to integrin α5 and facilitates translocation to lipid rafts to induce integrin activation and ligation (Zhang et al., 2020). Integrin α5β1 activation is essential for fibronectin deposition and proinflammatory responses by atheroprone shear or oxidized low-density-lipoproteins (Yurdagul et al., 2014; Al-Yafeai et al., 2018). Interestingly, laminin-binding integrin α6β1 is also induced by disturbed flow (Hsu et al., 2019). α6β1 binds to other ECM molecules in addition to laminin, which will be discussed below.

MATRICELLULAR PROTEINS

Matricellular proteins are a group of extracellular proteins that do not directly serve structural roles, but rather function contextually as regulators of cell-matrix interactions and cell function (Bornstein and Sage, 2002). A number of matricellular proteins have been implicated in atherosclerosis. Among them, CCN1/CYR61 is the most well-characterized example of how matricellular proteins may regulate the formation of atherosclerosis. CCN1, a member of the CCN matricellular protein family, binds to at least seven integrin receptors, including α6β1 and αvβ3 on ECs (Kireeva et al., 1998; Leu et al., 2003; Chen and Lau, 2009), thus regulating diverse cellular activities including cell adhesion, migration, differentiation, proliferation, and survival/apoptosis/senescence (Lau, 2016). CCN1 is expressed in atherosclerotic lesions in patients (Hilfiker et al., 2002) and in the *Apoe*$^{-/-}$ mouse models (Hsu et al., 2019). CCN1 expression is upregulated by oscillatory shear stress, and downregulated by laminar shear stress in ECs (Wang et al., 2016a,b; Hsu et al., 2019). Shear-induced CCN1 binds to α6β1 and causes atheroprone phenotypic changes in EC *via* NF-κB activation, which further increases the expression of CCN1, α6, and β1 in a vicious circle. A peptide antagonist selectively targeting CCN1-α6β1 engagement has been tested and effectively inhibits disturbed flow-induced atherogenesis *in vitro* and *in vivo* (Hsu et al., 2019). α6β1 is expressed at basal levels in quiescent ECs and binds to basement membrane protein laminin at focal adhesion sites (Seano et al., 2014). A fibronectin-rich provisional matrix under disturbed flow releases α6β1 from focal adhesions (Chen et al., 2015). The combination of α6β1 upregulation and disassembly by disturbed flow results in more accessible receptor integrins for CCN1 action.

CCN2/connective tissue growth factor and CCN1 share similar integrin receptors and are co-expressed in advanced atherosclerotic lesions in mice (Schober et al., 2002). Both CCN1 and CCN2 are directly induced by YAP/TAZ in ECs under oscillatory shear stress (Wang et al., 2016a,b). CCN2 has been demonstrated to increase neointimal thickening in a rat carotid artery angioplasty model (Kundi et al., 2009). However, the role of CCN2 in atherosclerosis remains elusive.

Interestingly, the matricellular protein cartilage oligomeric matrix protein (COMP)/thrombospondin-5 inhibits disturbed flow-induced inflammatory EC activation and atherogenesis through inactivating integrin α5, thus preventing α5β1-fibronectin engagement (Lv et al., 2021). COMP deficiency leads to accelerated atherosclerosis, plaque calcification, and post injury restenosis (Wang et al., 2010). The degradation of COMP has been associated with atherosclerosis progression in patients with symptomatic carotid stenosis by measuring circulating levels of COMP and its fragments (Sandstedt et al., 2021). It is worth noting that COMP is mostly secreted by vascular smooth muscle cells in the arterial wall, not by ECs (Fu et al., 2016).

It is likely that intimal smooth muscle cells are responsible for producing and distributing COMP protein to the basement membrane of endothelium.

DISCUSSION

Current therapy for atherosclerosis primarily targets hyperlipidemia, thrombosis, and more recently vascular inflammation (Libby and Hansson, 2018). No available treatments directly target the dysfunctional endothelium in atherosclerosis. Patients with the conditions, such as existing atherosclerotic plaque, in-stent restenosis, bypass graft occlusion, transplant vasculopathy, or aortic valve calcification, are prone to further development of atherosclerotic lesion due to endothelial dysfunction caused by disturbed blood flow in the affected vascular segments (Chiu and Chien, 2011). The interaction between ECM and endothelial integrin receptors becomes a favorable therapeutic target for its accessibility and its critical role in atherosclerosis discussed in this review. The caveat of blocking provisional matrix proteins, such as fibronectin, poses a threat of complications because of the diverse and indispensable functions of fibronectin (George et al., 1993; Liu et al., 2010). Alternatively, integrin α5 can be considered as a target. Though α5-null mutation causes embryonic lethality in mice (Yang et al., 1993), $\alpha5^{+/-}$ mice are viable and display significant resistance to disturbed flow-induced EC dysfunction and atherosclerosis (Sun et al., 2016), suggesting a benefit from lowering α5 activities. An integrin α5β1-blocking peptide (ATN161) successfully abolishes disturbed flow-induced YAP activation and atherogenesis in *Apoe*$^{-/-}$ mice (Li et al., 2019). Additionally, CCN1-α6β1 engagement is proven a promising therapeutic target for atherosclerosis (Hsu et al., 2019). Because laminin-α6β1 signaling is important for endothelial homeostasis and function, targeting α6β1 may be at risk of losing the atheroprotective effect from the native ECM. The antagonistic peptide T1 (derived from an α6β1-binding sequence of CCN1) preferentially blocks α6β1 binding with CCN1, without affecting binding with laminin. T1 peptide effectively blocks flow-induced atheroprone activation in ECs and atherogenesis in mice (Hsu et al., 2019). Moreover, a COMP-derived peptidomimetics (CCPep24), designed as an agonist for the specific COMP-α5 interaction, provides atheroprotection against flow-induced EC activation and atherogenesis in mice (Lv et al., 2021). Together, synthetic peptides or peptidomimetics have been successfully used to offer selective inhibition on interactions between specific provisional matrix components and their integrin receptors, and validate the approach targeting the pairing between matrix proteins and integrins for atherosclerosis therapy.

AUTHOR CONTRIBUTIONS

The author confirms being the sole contributor of this work and has approved it for publication.

FUNDING

This work was supported by grants MOST 1092320B006044-MY3 from the Ministry of Science and Technology of Taiwan.

REFERENCES

Al-Yafeai, Z., Yurdagul, A. Jr., Peretik, J. M., Alfaidi, M., Murphy, P. A., and Orr, A. W. (2018). Endothelial FN (Fibronectin) deposition by α5β1 Integrins drives atherogenic inflammation. *Arterioscler. Thromb. Vasc. Biol.* 38, 2601–2614. doi: 10.1161/ATVBAHA.118.311705

Bornstein, P., and Sage, E. H. (2002). Matricellular proteins: extracellular modulators of cell function. *Curr. Opin. Cell Biol.* 14, 608–616. doi: 10.1016/s0955-0674(02)00361-7

Chatzizisis, Y. S., Jonas, M., Coskun, A. U., Beigel, R., Stone, B. V., Maynard, C., et al. (2008). Prediction of the localization of high-risk coronary atherosclerotic plaques on the basis of low endothelial shear stress: an intravascular ultrasound and histopathology natural history study. *Circulation* 117, 993–1002. doi: 10.1161/CIRCULATIONAHA.107.695254

Chen, J., Green, J., Yurdagul, A. Jr., Albert, P., Mcinnis, M. C., and Orr, A. W. (2015). alphavbeta3 Integrins mediate flow-induced NF-kappaB activation, proinflammatory gene expression, and early atherogenic inflammation. *Am. J. Pathol.* 185, 2575–2589. doi: 10.1016/j.ajpath.2015.05.013

Chen, C. C., and Lau, L. F. (2009). Functions and mechanisms of action of CCN matricellular proteins. *Int. J. Biochem. Cell Biol.* 41, 771–783. doi: 10.1016/j.biocel.2008.07.025

Chiu, J. J., and Chien, S. (2011). Effects of disturbed flow on vascular endothelium: pathophysiological basis and clinical perspectives. *Physiol. Rev.* 91, 327–387. doi: 10.1152/physrev.00047.2009

Feaver, R. E., Gelfand, B. D., Wang, C., Schwartz, M. A., and Blackman, B. R. (2010). Atheroprone hemodynamics regulate fibronectin deposition to create positive feedback that sustains endothelial inflammation. *Circ. Res.* 106, 1703–1711. doi: 10.1161/CIRCRESAHA.109.216283

Fu, Y., Gao, C., Liang, Y., Wang, M., Huang, Y., Ma, W., et al. (2016). Shift of macrophage phenotype due to cartilage oligomeric matrix protein deficiency drives atherosclerotic calcification. *Circ. Res.* 119, 261–276. doi: 10.1161/CIRCRESAHA.115.308021

George, E. L., Georges-Labouesse, E. N., Patel-King, R. S., Rayburn, H., and Hynes, R. O. (1993). Defects in mesoderm, neural tube and vascular development in mouse embryos lacking fibronectin. *Development* 119, 1079–1091.

Gimbrone, M. A. Jr., and Garcia-Cardena, G. (2016). Endothelial cell dysfunction and the pathobiology of atherosclerosis. *Circ. Res.* 118, 620–636. doi: 10.1161/CIRCRESAHA.115.306301

Green, J., Yurdagul, A. Jr., Mcinnis, M. C., Albert, P., and Orr, A. W. (2014). Flow patterns regulate hyperglycemia-induced subendothelial matrix remodeling during early atherogenesis. *Atherosclerosis* 232, 277–284. doi: 10.1016/j.atherosclerosis.2013.11.052

Hilfiker, A., Hilfiker-Kleiner, D., Fuchs, M., Kaminski, K., Lichtenberg, A., Rothkotter, H. J., et al. (2002). Expression of CYR61, an angiogenic immediate early gene, in arteriosclerosis and its regulation by angiotensin II. *Circulation* 106, 254–260. doi: 10.1161/01.CIR.0000021426.87274.62

Hsu, P. L., Chen, J. S., Wang, C. Y., Wu, H. L., and Mo, F. E. (2019). Shear-induced CCN1 promotes atheroprone endothelial phenotypes and atherosclerosis. *Circulation* 139, 2877–2891. doi: 10.1161/CIRCULATIONAHA.118.033895

Hynes, R. O. (2002). Integrins: bidirectional, allosteric signaling machines. *Cell* 110, 673–687. doi: 10.1016/S0092-8674(02)00971-6

Kireeva, M. L., Lam, S. C., and Lau, L. F. (1998). Adhesion of human umbilical vein endothelial cells to the immediate-early gene product Cyr61 is mediated through integrin αvβ3. *J. Biol. Chem.* 273, 3090–3096. doi: 10.1074/jbc.273.5.3090

Korenaga, R., Ando, J., Kosaki, K., Isshiki, M., Takada, Y., and Kamiya, A. (1997). Negative transcriptional regulation of the VCAM-1 gene by fluid shear stress in murine endothelial cells. *Am. J. Phys.* 273, C1506–C1515. doi: 10.1152/ajpcell.1997.273.5.c1506

Kundi, R., Hollenbeck, S. T., Yamanouchi, D., Herman, B. C., Edlin, R., Ryer, E. J., et al. (2009). Arterial gene transfer of the TGF-beta signalling protein Smad3 induces adaptive remodelling following angioplasty: a role for CTGF. *Cardiovasc. Res.* 84, 326–335. doi: 10.1093/cvr/cvp220

Lau, L. F. (2016). Cell surface receptors for CCN proteins. *J. Cell Commun. Signal.* 10, 121–127. doi: 10.1007/s12079-016-0324-z

Leu, S. J., Liu, Y., Chen, N., Chen, C. C., Lam, S. C., and Lau, L. F. (2003). Identification of a novel integrin alpha 6beta 1 binding site in the angiogenic inducer CCN1 (CYR61). *J. Biol. Chem.* 278, 33801–33808. doi: 10.1074/jbc.M305862200

Li, B., He, J., Lv, H., Liu, Y., Lv, X., Zhang, C., et al. (2019). c-Abl regulates YAPY357 phosphorylation to activate endothelial atherogenic responses to disturbed flow. *J. Clin. Invest.* 129, 1167–1179. doi: 10.1172/JCI122440

Libby, P., and Hansson, G. K. (2018). Taming immune and inflammatory responses to treat atherosclerosis. *J. Am. Coll. Cardiol.* 71, 173–176. doi: 10.1016/j.jacc.2017.10.081

Liu, K., Cheng, L., Flesken-Nikitin, A., Huang, L., Nikitin, A. Y., and Pauli, B. U. (2010). Conditional knockout of fibronectin abrogates mouse mammary gland lobuloalveolar differentiation. *Dev. Biol.* 346, 11–24. doi: 10.1016/j.ydbio.2010.07.001

Lv, H., Wang, H., Quan, M., Zhang, C., Fu, Y., Zhang, L., et al. (2021). Cartilage oligomeric matrix protein fine-tunes disturbed flow-induced endothelial activation and atherogenesis. *Matrix Biol.* 95, 32–51. doi: 10.1016/j.matbio.2020.10.003

Orr, A. W., Sanders, J. M., Bevard, M., Coleman, E., Sarembock, I. J., and Schwartz, M. A. (2005). The subendothelial extracellular matrix modulates NF-kappaB activation by flow: a potential role in atherosclerosis. *J. Cell Biol.* 169, 191–202. doi: 10.1083/jcb.200410073

Sandstedt, J., Vargmar, K., Björkman, K., Ruetschi, U., Bergström, G., Hultén, L. M., et al. (2021). COMP (cartilage oligomeric matrix protein) neoepitope: a novel biomarker to identify symptomatic carotid stenosis. *Arterioscler. Thromb. Vasc. Biol.* 41, 1218–1228. doi: 10.1161/ATVBAHA.120.314720

Schober, J. M., Chen, N., Grzeszkiewicz, T. M., Jovanovic, I., Emeson, E. E., Ugarova, T. P., et al. (2002). Identification of integrin alpha(M)beta(2) as an adhesion receptor on peripheral blood monocytes for Cyr61 (CCN1) and connective tissue growth factor (CCN2): immediate-early gene products expressed in atherosclerotic lesions. *Blood* 99, 4457–4465. doi: 10.1182/blood.V99.12.4457

Seano, G., Chiaverina, G., Gagliardi, P. A., Di Blasio, L., Puliafito, A., Bouvard, C., et al. (2014). Endothelial podosome rosettes regulate vascular branching in tumour angiogenesis. *Nat. Cell Biol.* 16, 931–941. doi: 10.1038/ncb3036

Souilhol, C., Serbanovic-Canic, J., Fragiadaki, M., Chico, T. J., Ridger, V., Roddie, H., et al. (2020). Endothelial responses to shear stress in atherosclerosis: a novel role for developmental genes. *Nat. Rev. Cardiol.* 17, 52–63. doi: 10.1038/s41569-019-0239-5

Stone, P. H., Saito, S., Takahashi, S., Makita, Y., Nakamura, S., Kawasaki, T., et al. (2012). Prediction of progression of coronary artery disease and clinical outcomes using vascular profiling of endothelial shear stress and arterial plaque characteristics: the PREDICTION study. *Circulation* 126, 172–181. doi: 10.1161/CIRCULATIONAHA.112.096438

Stupack, D. G., and Cheresh, D. A. (2002). ECM remodeling regulates angiogenesis: endothelial integrins look for new ligands. *Sci. STKE* 2002:E7. doi: 10.1126/stke.2002.119.pe7

Sun, X., Fu, Y., Gu, M., Zhang, L., Li, D., Li, H., et al. (2016). Activation of integrin α5 mediated by flow requires its translocation to membrane lipid rafts in vascular endothelial cells. *Proc. Natl. Acad. Sci. U. S. A.* 113, 769–774. doi: 10.1073/pnas.1524523113

Wang, L., Luo, J. Y., Li, B., Tian, X. Y., Chen, L. J., Huang, Y., et al. (2016b). Integrin-YAP/TAZ-JNK cascade mediates atheroprotective effect of unidirectional shear flow. *Nature* 540, 579–582. doi: 10.1038/nature20602

Wang, K. C., Yeh, Y. T., Nguyen, P., Limqueco, E., Lopez, J., Thorossian, S., et al. (2016a). Flow-dependent YAP/TAZ activities regulate endothelial phenotypes and atherosclerosis. *Proc. Natl. Acad. Sci. U. S. A.* 113, 11525–11530. doi: 10.1073/pnas.1613121113

Wang, L., Zheng, J., Du, Y., Huang, Y., Li, J., Liu, B., et al. (2010). Cartilage oligomeric matrix protein maintains the contractile phenotype of vascular smooth muscle cells by interacting with alpha(7)beta(1) integrin. *Circ. Res.* 106, 514–525. doi: 10.1161/CIRCRESAHA.109.202762

Yang, J. T., Rayburn, H., and Hynes, R. O. (1993). Embryonic mesodermal defects in alpha 5 integrin-deficient mice. *Development* 119, 1093–1105.

Yu, F. X., Zhao, B., and Guan, K. L. (2015). Hippo pathway in organ size control, tissue homeostasis, and cancer. *Cell* 163, 811–828. doi: 10.1016/j.cell.2015.10.044

Yun, S., Hu, R., Schwaemmle, M. E., Scherer, A. N., Zhuang, Z., Koleske, A. J., et al. (2019). Integrin α5β1 regulates PP2A complex assembly through PDE4D in atherosclerosis. *J. Clin. Invest.* 129, 4863–4874. doi: 10.1172/JCI127692

Yurchenco, P. D., and O'Rear, J. J. (1994). Basal lamina assembly. *Curr. Opin. Cell Biol.* 6, 674–681. doi: 10.1016/0955-0674(94)90093-0

Yurdagul, A. Jr., Finney, A. C., Woolard, M. D., and Orr, A. W. (2016). The arterial microenvironment: the where and why of atherosclerosis. *Biochem. J.* 473, 1281–1295. doi: 10.1042/BJ20150844

Yurdagul, A. Jr., Green, J., Albert, P., Mcinnis, M. C., Mazar, A. P., and Orr, A. W. (2014). alpha5beta1 integrin signaling mediates oxidized low-density lipoprotein-induced inflammation and early atherosclerosis. *Arterioscler. Thromb. Vasc. Biol.* 34, 1362–1373. doi: 10.1161/ATVBAHA.114.303863

Zhang, C., Zhou, T., Chen, Z., Yan, M., Li, B., Lv, H., et al. (2020). Coupling of integrin α5 to annexin A2 by flow drives endothelial activation. *Circ. Res.* 127, 1074–1090. doi: 10.1161/CIRCRESAHA.120.316857

Zhu, J. J., Jiang, Z. T., Liu, C., Xi, Y. F., Wang, J., Yang, F. F., et al. (2020). VAMP3 and SNAP23 as potential targets for preventing the disturbed flow-accelerated thrombus formation. *Front. Cell Dev. Biol.* 8:576826. doi: 10.3389/fcell.2020.576826

Conflict of Interest: The author declares that the research was conducted in the absence of any commercial or financial relationships that could be construed as a potential conflict of interest.

frontiers
in Cell and Developmental Biology

ORIGINAL RESEARCH
published: 09 April 2021
doi: 10.3389/fcell.2021.642150

Maintenance of HDACs and H3K9me3 Prevents Arterial Flow-Induced Venous Endothelial Damage

Ting-Yun Wang[1†], Ming-Min Chang[1†], Yi-Shuan Julie Li[2], Tzu-Chieh Huang[1], Shu Chien[2,3] and Chia-Ching Wu[1,4,5,6*]

[1] Department of Cell Biology and Anatomy, College of Medicine, National Cheng Kung University, Tainan, Taiwan, [2] Department of Bioengineering, University of California, San Diego, La Jolla, CA, United States, [3] Institute of Engineering in Medicine, University of California, San Diego, La Jolla, CA, United States, [4] Institute of Basic Medical Sciences, College of Medicine, National Cheng Kung University, Tainan, Taiwan, [5] International Center for Wound Repair and Regeneration, National Cheng Kung University, Tainan, Taiwan, [6] Department of Biomedical Engineering, National Cheng Kung University, Tainan, Taiwan

Edited by:
Jing Zhou,
Peking University, China

Reviewed by:
Lingfang Zeng,
King's College London,
United Kingdom
Ding Ai,
Tianjin Medical University, China

***Correspondence:**
Chia-Ching Wu
joshccwu@mail.ncku.edu.tw

† These authors have contributed equally to this work

Specialty section:
This article was submitted to
Cell Adhesion and Migration,
a section of the journal
Frontiers in Cell and Developmental
Biology

Received: 15 December 2020
Accepted: 09 March 2021
Published: 09 April 2021

Citation:
Wang T-Y, Chang M-M, Li Y-SJ,
Huang T-C, Chien S and Wu C-C
(2021) Maintenance of HDACs
and H3K9me3 Prevents Arterial
Flow-Induced Venous Endothelial
Damage.
Front. Cell Dev. Biol. 9:642150.
doi: 10.3389/fcell.2021.642150

The transition of flow microenvironments from veins to arteries in vein graft surgery induces "peel-off" of venous endothelial cells (vECs) and results in restenosis. Recently, arterial laminar shear stress (ALS) and oscillatory shear stress (OS) have been shown to affect the cell cycle and inflammation through epigenetic controls such as histone deacetylation by histone deacetylases (HDACs) and trimethylation on lysine 9 of histone 3 (H3K9me3) in arterial ECs. However, the roles of H3K9me3 and HDAC in vEC damage under ALS are not known. We hypothesized that the different responses of HDACs and H3K9me3 might cause vEC damage under the transition of venous flow to arterial flow. We found that arterial ECs showed high expression of H3K9me3 protein and were retained in the G0 phase of the cell cycle after being subjected to ALS. vECs became round under ALS with a decrease in the expression of H3K9me3, HDAC3, and HDAC5, and an increase in the expression of vascular cell adhesion molecule 1 (VCAM-1). Inhibition of HDACs activity by a specific inhibitor, phenylbutyrate, in arterial ECs caused similar ALS-induced inflammation and cell loss as observed in vECs. Activation of HDACs and H3K9me3 by ITSA-1, an HDAC activator, could prevent ALS-induced peel-off and reduced VCAM-1 expression in vECs. Moreover, shear stress modulates EC morphology by the regulation of focal adhesion kinase (FAK) expression. ITSA-1 or EGF could increase phosphorylated (p)-FAK expression in vECs under ALS. We found that perturbation of the activity of p-FAK and increase in p-FAK expression restored ALS-induced H3K9me3 expression in vECs. Hence, the abnormal mechanoresponses of H3K9me3 and HDAC in vECs after being subjected to ALS could be reversed by ITSA-1 or EGF treatment: this offers a strategy to prevent vein graft failure.

Keywords: shear stress, venous endothelial cell, HDACs, H3K9me3, FAK, ITSA-1, EGF, vein graft failure

INTRODUCTION

Autologous saphenous veins are the most commonly used conduits in coronary artery bypass grafts for the treatment of coronary artery stenosis (De Vries et al., 2016; McKavanagh et al., 2017; Caliskan et al., 2020). Unfortunately, low efficacy of grafting can occur due to vascular inflammation, thrombosis, intimal hyperplasia, and subsequent accelerated atherosclerosis, *viz.* "vein graft failure" (VGF) or "vein graft disease" (VGD) (De Vries et al., 2016; de Vries and Quax, 2018; Ruiter and Pesce, 2018). Moreover, failure of grafts increases the frequency of adverse cardiovascular outcomes and death. Another type of VGF can be seen in arteriovenous grafts for hemodialysis. A radiocephalic arteriovenous fistula (AVF) at the wrist is the first choice for hemodialysis access. In radiocephalic AVFs, the A-V angle between the vein and the proximal artery of juxta-anastomotic region wider than 46.5° leads to disturbed blood flow, which is the most common site of venous stenosis (Yang et al., 2020).

Endothelial cells (ECs) line the inner wall of vessels. They have a crucial role in the maintenance of vessel structure and homeostasis (Shimokawa and Satoh, 2014; Peng et al., 2019). ECs can sense mechanical forces ("mechanosensing") and convert them into intracellular signals for cell remodeling by transmitting the signal across the transmembrane adhesion receptors (e.g., cadherin, syndecan, and integrin) (Chien, 2007; Garoffolo and Pesce, 2019; Peng et al., 2019). Therefore, maintenance of a physiologic, laminar shear stress is crucial for normal vascular function, including regulation of vascular caliber as well as inhibition of cell proliferation, thrombosis, and inflammation of vessel walls (Frosen et al., 2019). Venous endothelial cells (vECs) are physiologically adapted to chronic low shear stress. When vECs are implanted into the arterial circulation, they are exposed suddenly to arterial laminar shear stress (ALS). ALS can induce the molecular cascades of autophagy and apoptosis in vECs to cause endothelial dysfunction and stenosis recurrence (Chang et al., 2016). Endothelial dysfunction is associated with cardiovascular risk factors and can initiate atherosclerosis (Hadi et al., 2005; Garoffolo and Pesce, 2019). Several factors can cause endothelial dysfunction. Nitric oxide acts as a vasodilator, and it has been reported that reduced expression of nitric oxide damages EC function (Gimbrone and Garcia-Cardena, 2016; Tajadura et al., 2020). Loss of anchorage also results in endothelial dysfunction. Integrin receptors in focal adhesions (FA) mediate cell adhesion and contribute to the integrity of the endothelial barrier. Laminar shear stress induces FA remodeling by forming peripheral "actin bundles" on the basal side of the cell and subsequently causes cell disassociation. Disruption of FA signaling leads to loss of cell adhesion and triggers cell death (Kirchenbuechler et al., 2014; Verma et al., 2015; Driscoll et al., 2020).

Several studies have shown that shear stress can regulate homeostasis, proliferation, apoptosis, migration, and remodeling in ECs, as well as gene expression (Li et al., 2005; Peng et al., 2019). Proper laminar shear stress stimulates cellular responses (e.g., secretion of cytokines and growth factors) to promote antithrombosis and antigrowth, and further maintain cell function. However, a sudden change in shear stress can cause EC apoptosis by increasing secretion of proinflammatory factors [e.g., monocyte chemoattractant protein 1 and vascular cell adhesion molecule 1 (VCAM-1)] and is associated with several pathophysiological conditions (e.g., atherosclerosis). Cell cycle is an ordered set of events that leads to duplication of a cell's DNA and cell division to produce two daughter cells. The cell cycle comprises four phases: two gap phases (G1 and G2), an S phase (for DNA synthesis), and an M phase (which consists of genetic material), followed by cell division. There is increasing evidence for the importance of cell cycle dysregulation in the pathogenesis of cancer, atherosclerosis, inflammation, and neurodegenerative disorders (Zhivotovsky and Orrenius, 2010; Peng et al., 2019). Several investigations have indicated that shear stress inhibits DNA synthesis in ECs by inhibiting transition from the G0/G1 to S phase (Akimoto et al., 2000). However, it has been reported that disturbed flow promotes cell cycle progression and maintains cells in the S + G2/M phase (Guo et al., 2007). Therefore, derangement of steady shear stress leads to cell proliferation, which may cause atherosclerosis through disruption of EC stability (Akimoto et al., 2000). The stages of the cell cycle are regulated by epigenetic modification (Dominguez and Berger, 2008), but the mechanism of assembly and dynamics of histone modification in cell cycle regulation are not known.

Post-translational modification (PTM) includes DNA methylation, histone modifications, and RNA interference. PTM can also modulate the actin cytoskeleton to affect cell functions (e.g., cell adhesion) (Yan et al., 2010; Kottakis et al., 2011). Recent studies have shown that KDM2B (a histone demethylase for H3K4me3 and H3K36me2) regulates the expression of focal adhesion kinase (FAK), phosphoinositide 3 kinase (PI3K), and protein kinase B (Akt) (Zacharopoulou et al., 2018). Luo et al. (2011) have shown that interaction between FAK and methyl CpG-binding protein 2 (MeCP2) can modify heterochromatin reorganization and suppress the association between MeCP2 and histone deacetylase 1 (HDAC1) during oxidative stress. FA dynamics are important for survival and spread of ECs and are associated with actin organization (Carragher and Frame, 2004). Therefore, disruption of FA signaling may lead to loss of cell adhesion and trigger cell death (Caltagarone et al., 2007). FA, a macromolecular complex comprising talin, α-actinin, vinculin, zyxin, paxillin, Src, and FAK, is the connection between the extracellular matrix and actin cytoskeleton (Kuo, 2013). FA mediates the adhesion, migration, mechanosensing, and signaling of cells (Case et al., 2015). FAK is a cytoplasmic tyrosine kinase that mediates the dynamics and signaling of FA in response to growth factors and integrin-ligand binding (Li et al., 2002). Phosphorylation of FAK at Tyr-397 is important for recruitment of Src to promote the formation and maturation of FA. Also, FAK drives FA turnover through control of targeted proteolysis of FA proteins (Romer et al., 2006). FAK is required to maintain EC function, and knockdown of FAK in ECs increases the apoptosis and permeability of cells (Zhao et al., 2010). Therefore, the different responses of FAK between arterial and venous ECs under ALS may be one of the reasons for EC damage. However, the mechano-transduction pathway between arterial and venous ECs under ALS is not known.

Here, we compared the differences in HDACs and trimethylation of lysine 9 on histone 3 (H3K9me3) in arterial ECs and venous ECs under ALS. We speculated that FAs-mediated epigenetic regulation may also cause the vEC damage under ALS.

MATERIALS AND METHODS

Cell Lines

The human umbilical vein endothelial cells (HUVECs) (BCRC no. H-UV001) and the human saphenous vein endothelial cells (HSVECs) (cat. no. C-12231) were purchased from Bioresource Collection and Research Center (Hsinchu, Taiwan) and PromoCell (Heidelberg, Germany), respectively. All cells were cultured in Medium 199 (M199) containing 20% fetal bovine serum (FBS), 100 U/ml penicillin, 100 μg/ml streptomycin (P/S), and 25% endothelial cell growth medium (EGM) in an atmosphere of 5% CO_2 at 37°C. When cells reached a 90% confluent monolayer, cell passaging was performed by trypsinization using 0.05% trypsin-EDTA. The cells used in experiments were from passages 3 to 7.

Shear Stress *in vitro*

The shear stress experiments were conducted based on our previous study (Wu et al., 2007). Cells were seeded on fibronectin (10 μg/ml)-coated slides for 24 h and then starved in M199 medium containing 2% FBS. After 24 h, the starved ECs were transferred to M199 medium containing 20% FBS and 25% EGM and maintained under static (ST) condition or subjected to ALS or oscillatory shear stress (OS). For the ALS or OS group, the slides with ECs were assembled into the flow chamber, in which a flow channel was created by "sandwiching" a silicone gasket between the slide and an acrylic plate. The CO_2-equilibrated medium flew across the flow chamber in response to the pressure difference between the inlet and outlet of the chamber. Cells were subjected to ALS at 12 dynes/cm2 or OS at 0.5 ± 4 dynes/cm2 for 12 h or 24 h. The total area subjected to shearing was 1.5 cm in width (W) and 5.0 cm in length (L). The channel height (h) was 0.025 cm, and the shear flow in this narrow gap was laminar with a parabolic velocity. The wall shear stress (τ wall) was calculated as: $\tau \text{ wall} = \Delta P\,(h/2L) = 6Q\mu/Wh^2$, where ΔP is the pressure difference between the inlet and the outlet of the flow channel, Q is the volumetric flow rate, and μ is the fluid viscosity. Protein samples were collected for Western blotting analysis.

Western Blot Analysis

The ECs were washed twice with ice-cold phosphate-buffered saline and then lysed by using ice-cold lysis buffer containing Tris (50 mM, pH 7.4), NaCl (150 mM), and a protease inhibitor cocktail. The protein concentration was determined using a protein assay kit based on the Bradford method. Total protein (25 μg) in cell lysates was separated by sodium dodecyl sulfate–polyacrylamide gel electrophoresis using 10% gels and transferred to nitrocellulose membranes. The latter were blocked by 5% skimmed milk Tris-buffered saline with Tween 20 (TBST) for 2 h at room temperature and then immunoblotted with primary specific antibodies overnight at 4°C. The primary antibodies are as follows: H3K9me3 (1:1000, Abcam), cyclin A1 (1:1000, Cell Signaling), cyclin B1 (1:1000, Cell Signaling), HDAC1 (1:1000, Abcam), HDAC2 (1:1000, Abcam), HDAC3 (1:500, Santa Cruz), HDAC4 (1:500, Santa Cruz), HDAC5 (1:500, Santa Cruz), phosphor-HDAC3 (p-HDAC3, 1:1000, Cell Signaling), phosphor-HDAC4,5,7 (p-HDAC4,5,7, 1:1000, Cell Signaling), VCAM-1 (1:1000, Santa Cruz), phosphor-FAK Y397 (p-FAK, 1:1000, BD Biosciences), and total FAK (t-FAK, 1:1000, BD Biosciences). Thereafter, the membrane was hybridized with secondary antibodies conjugated with horseradish peroxidase (HRP) (Sigma-Aldrich). Signals were developed with the ECL Ultra Western HRP Substrate (Immobilon^{TM}; Merck, Whitehouse Station, NJ, United States) and X-ray films (Fujifilm; Tokyo, Japan).

Transfection by Electroporation

A total of 1×10^6 ECs were suspended in electroporation buffer (0.1 ml of Opti-MEM, Gibco) and mixed with plasmids (5 μg). This mixture of ECs and plasmid was added into 2-mm gap cuvettes. Electroporation was carried out with a poring pulse of 175 V for a pulse length of 5 ms and a transfer pulse of 20 V for 50 ms. After electroporation, the cells were seeded in a 6-mm fibronectin-coated slide with 0.5 ml of M199 medium supplemented with 20% FBS without antibiotics. After 24 h of serum starvation, the slides were assembled in the flow chamber and subjected to fluid shear.

Fluorescence Resonance Energy Transfer

Fluorescence Resonance Energy Transfer (FRET) is a distance-dependent physical process in which energy is transferred from one fluorophore (donor) to another (acceptor). Donor leakage is determined from cyan fluorescent protein (CFP)-transfected cells. Cross-excitation of acceptors is obtained from yellow fluorescent protein (YFP)-transfected cells. FRET is dependent on the distance and relative orientation between the two fluorophores (CFP and YFP) (Wang and Wang, 2009). FRET maps and the pixel-wise FRET Index for the sensors were determined using the FRET ratio (= FRET channel/CFP channel).

To monitor the dynamics of H3K9 trimethylation, a FRET-based H3K9me3 biosensor kindly provided by Dr. YingXiao Wang (University of California, San Diego, La Jolla, United States) was used (Lin et al., 2004). The FRET-based H3K9me3 biosensor comprised a YFP tag, HP1, CFP tag, and H3 N-terminus. When the H3K9me3 biosensor was activated, the YFP-tagged HP1 interacted with the K9 methylation from the CFP-tagged H3 N-terminus. This action led to the proximation of CFP to YFP, resulting in an increase in the FRET signal. In contrast, the FRET ratio was reduced by the removal of YFP-HP1 from CFP-H3K9 when H3K9me3 was deactivated. The time-lapse images were collected by confocal microscopy with a 44DF20 excitation filter, a 455DRLP dichroic mirror, and two emission filters controlled by a filter changer (480DF30 for CFP and 535DF25 for YFP) with a time interval of 1 h. To achieve high-quality fluorescence images of living cells, a 60 × oil objective lens was used in a confocal microscope with environmental control for supplementation with 5% CO_2 at 37°C. Images were analyzed by FluoCell (Liu et al., 2014), which has been developed by the research team of Dr. YingXiao Wang. The FRET ratio was calculated based on the FRET/CFP signal using MATLAB software[1].

Phalloidin F-actin Staining

Arterial laminar shear stress-treated vECs were washed with PBS and fixed in 4% paraformaldehyde in PBS at room temperature for 10 min. Then, the fixation solution was aspirated and the cells were washed twice. Alexa fluor 546-Phalloidin working solution was added for 60 min. Cells were washed with PBS and fixed by using mounting media with DAPI. Samples were examined using the Olympus FluoView FV1000 confocal microscope (Olympus, Tokyo, Japan). Images were analyzed using the Olympus FluoView FV10-ASW software (Olympus).

Statistical Analysis

Statistical analysis was carried out using Prism 6 software (GraphPad, La Jolla, CA, United States). $p < 0.05$ was considered to be statistically significant in this study. The specific statistical methods are indicated in each figure legend.

RESULTS

Flow-Modulated H3K9me3 Expression Plays an Important Role in Cell Cycle Regulation

Several reports have revealed that ALS plays a critical role in inhibiting the cell cycle event from the G0/G1 phase to the S phase, which maintains cell quiescence (Ehsan et al., 2002; Luo et al., 2011). To investigate the role of H3K9me3 in the ALS-induced cell quiescence, first, we examined the effect of different shear stresses in modulating H3K9me3 expression in ECs. The HUVECs, which are more like arterial ECs, were cultured under ST (no flow), ALS, or OS conditions for 12 or 24 h; the expressions of cyclin A1 (which is involved in the control of the transition from G1 to S phase and mitosis), cyclin B1 (which is required for entry into and progression through mitosis), and H3K9me3 were measured by Western blotting (**Figure 1A**). ALS increased H3K9me3 expression and inhibited cyclin A1 expression in HUVECs, indicating that ECs could not enter DNA synthesis and were retained in the G0 phase. In contrast, OS did not alter H3K9me3 expression and caused HUVEC proliferation.

To explore the real-time status of H3K9me3 in arterial ECs under different conditions, we transfected the CFP-YPet H3K9me3 FRET biosensor into HUVECs and utilized the time-lapse confocal microscopy to monitor H3K9me3 in HUVECs under different conditions. In HUVECs subjected to ALS, time-lapse images showed that the FRET density of H3K9me3 biosensor in nuclei increased gradually from 2 to 12 h after (**Figure 1B**). However, there was no change in the FRET ratio for H3K9me3 in ST- or OS-treated HUVECs (**Figure 1B**). The quantified mean ratio for normalized FRET intensity showed a significant increase under ALS in comparison with that under ST or OS. These results suggested that H3K9me3 expression was induced by ALS, but not ST or OS, in arterial ECs. We also demonstrated correlation between cell cycle and H3K9me3 in arterial ECs by synchronization under ST (**Figure 1C**). After 24 h of serum starvation, HUVECs were cultured in normal medium, and protein was collected at 0, 3, 6, 12, and 24 h under ALS stimulation. The expression of H3K9me3 in HUVECs was negatively correlated with that of cyclin A. Taken together, these data suggested that ALS could induce H3K9me3 expression and quiescence in arterial ECs.

ALS Induced Distinct Effects in Arterial and Venous ECs

Next, we examined the relation between the expression of H3K9me3 under ALS and inflammatory response in vECs, with the aim of comparing the responses of arterial and venous ECs under ALS. HUVECs and HSVECs were subjected to ALS for 0, 1, 3, and 6 h. Phase images showed that ALS triggered arterial ECs to become elongated and align parallel to the flow direction (**Figure 2A**). In contrast, vECs became rounded and were lost upon ALS stimulation. Western blotting results showed that ALS resulted in sustained increases in H3K9me3 expression in arterial ECs, but not in vECs (**Figure 2B**). These results demonstrated that H3K9me3 expression in response to ALS was different between arterial and venous ECs. To confirm this finding, we transfected the H3K9 FRET biosensor into HUVECs or HSVECs to explore the status of H3K9me3. Time-lapse images were recorded 0, 1, 2, 3, and 4 h after ALS. The H3K9me3 FRET ratio of HUVECs increased in response to ALS stimulation. In contrast, the H3k9me3 FRET ratio decreased after ALS in HSVECs (**Figure 2C**).

Several studies have demonstrated that HDACs have crucial roles in EC inflammation and atherosclerosis (Zhou et al., 2011; Lee and Chiu, 2019). Hence, we examined the expressions of HDAC1, HDAC2, HDAC3, HDAC4, and HDAC5 and an inflammation marker (VCAM-1) in these two cell types following ALS treatment. ALS reduced the expressions of HDAC4 and HDAC5 in HSVECs, while it increased the expressions of HDAC3, HDAC4, HDAC5, phosphorylated (p)-HDAC3, and p-HDAC4/5/7 in HUVECs (**Figure 2D**). The expression of VCAM-1 in HSVECs after ALS was higher than that in HUVECs. Taken together, these results indicate that ALS induced different effects in arterial and venous ECs. In addition, the results suggest the involvement of H3K9me3 and HDAC in the ALS-induced inflammatory response in vECs.

Inhibition of HDAC Activity Reversed an Atheroprotective Morphology and Induced Inflammation in ALS-Treated Arterial ECs

To further assess the role of HDACs in the responses of arterial ECs under ALS, we perturbed HDACs expression by treating HUVECs with a HDAC inhibitor, sodium phenylbutyrate (PBA), and subjected PBA-treated HUVECs to ALS for 0, 1, 3, and

---

[1] www.mathworks.com/

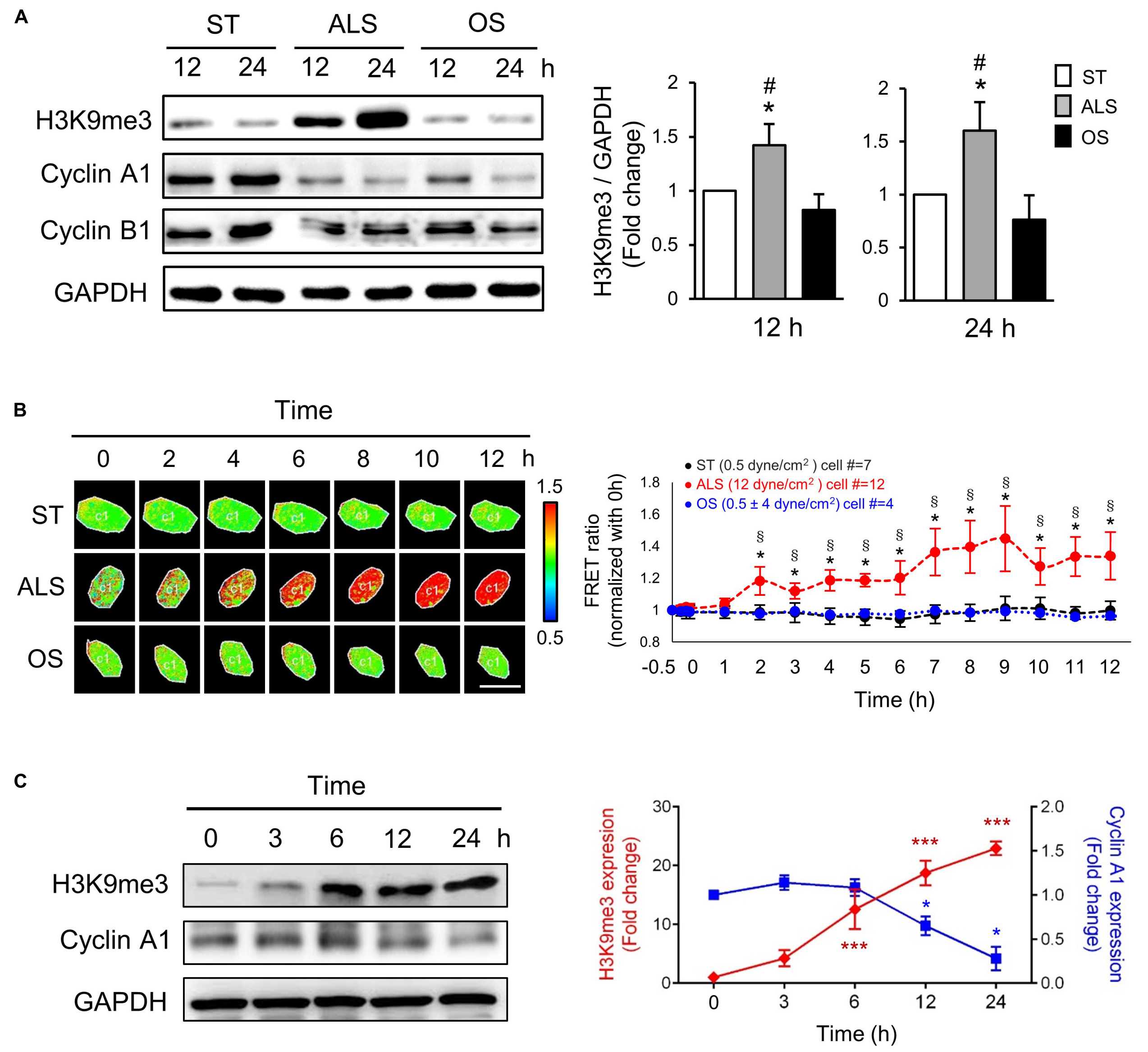

FIGURE 1 | ALS increased the expression of H3K9me3 and promoted the cell quiescence in arterial ECs. **(A)** Western blotting analysis for the expression of H3K9me3, cyclin A1, and cyclin B1 in HUVECs, which were subjected to ST, ALS, or OS treatment for 12 and 24 h. ALS increased the H3K9me3 expression and decreased the cyclin A1 expression, whereas OS did not change the H3K9me3 at 12 and 24 h. **(B)** The time-lapse FRET ratio images of arterial ECs expressing the H3K9me3 biosensors were recorded to track the status of H3K9me3 every 2 h under ST, ALS, or OS over the time course of 12 h. The results were normalized to 0 h for each experiment. Scale bar in the phase image: 20 μm. **(C)** Western blotting analysis for the expression of H3K9me3 and cyclin A1 in synchronized HUVECs at 0, 3, 6, 12, and 24 h under ALS stimulation. The low expression of cyclin A1 was accompanied by the high level of H3K9me3. Data were represented as mean ± SEM, $n = 3$. p-values were calculated using one-way ANOVA in **(A)** and **(C)** and using two-way ANOVA in **(B)** with Tukey's multiple comparisons post-tests. In **(A)** and **(B)**, $^{*}p < 0.05$, ALS-treated HUVECs compared to the ST group; $^{\#}p < 0.05$, ALS-treated HUVECs compared to the OS group. **(C)** $^{*}p < 0.05$, $^{***}p < 0.001$ with different color indicates a statistically significant difference at each time point compared to their corresponding control group (0 h).

6 h. Many PBA-treated HUVECs were lost as comparison with the vehicle group (**Figure 3A**). Western blot results revealed that the phosphorylation of HDAC3 and HDAC4/5/7 and the expression of HADC3, HDAC4, and HDAC5 were decreased by PBA treatment under ALS (**Figure 3B**). H3K9me3 expression was not increased in PBA-treated HUVECs after being subjected to ALS. An increase in VCAM-1 expression suggests that the abolishment of HDACs and H3K9me3 by PBA treatment caused inflammation in HUVECs under ALS. Using the H3K9 FRET biosensor, the status of H3K9me3 was investigated in PBA-treated HUVECs under ALS. The H3K9me3 FRET biosensor result showed a suppression of H3K9me3 expression in ALS-stimulated HUVECs upon PBA treatment (**Figure 3C**). These findings suggest that the inhibition of HDACs expression by PBA in arterial ECs suppressed the ALS-induced H3K9me3 expression and led to cell inflammation.

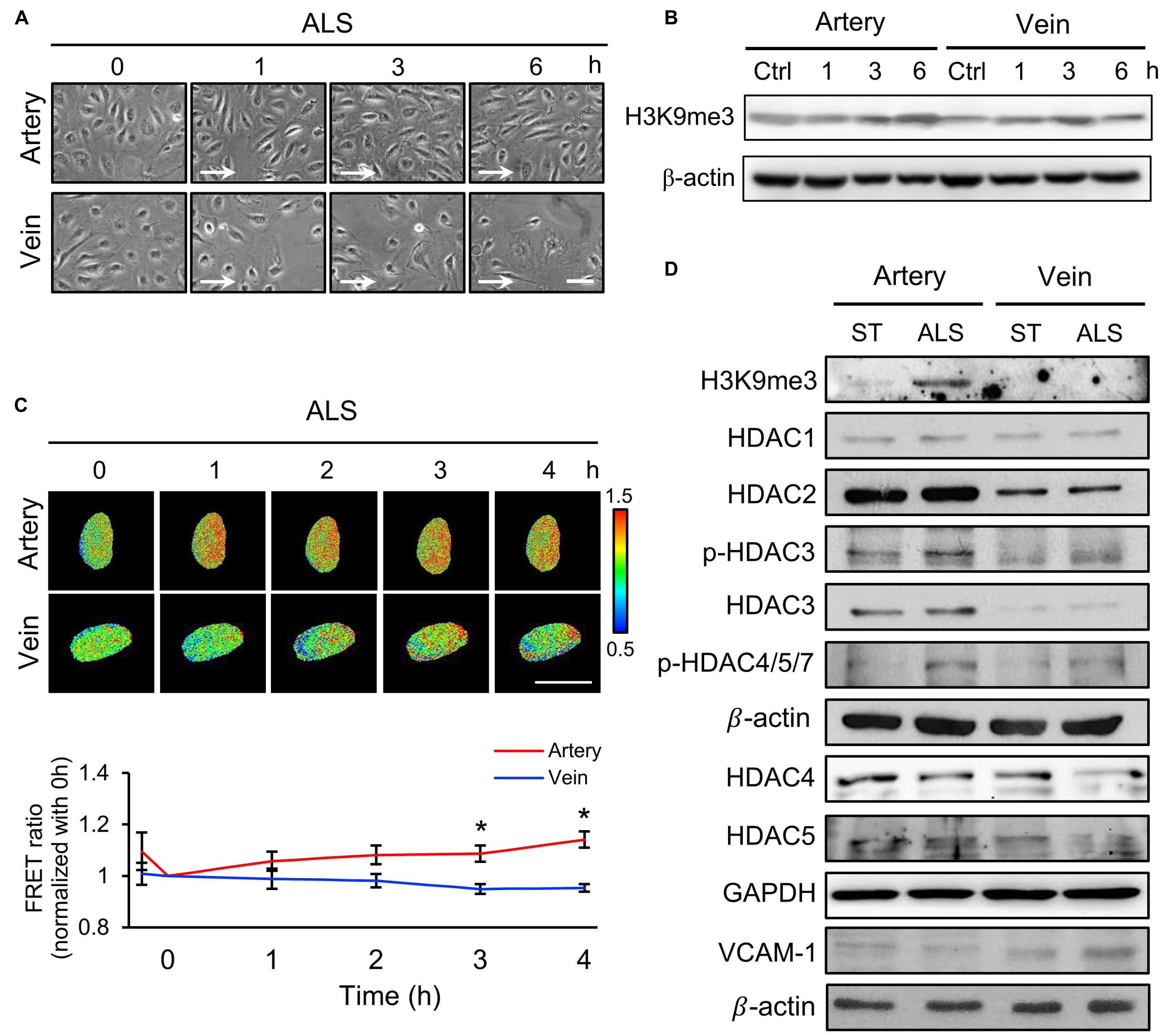

FIGURE 2 | The different effect of arterial and venous ECs under ALS. **(A)** Morphology observations of arterial ECs (HUVECs) and venous ECs (HSVECs) after being subjected to ALS for 0, 1, 3, and 6 h. **(B)** The Western blot analysis for the expression of H3K9me3 and β-actin in total cell lysates from **(A)**. The expression of H3K9me3 was time-dependent increase in arterial ECs but not in vECs. **(C)** The time-lapse FRET ratio images of HUVECs and HSVECs expressing the H3K9me3 biosensors were recorded to track the status of H3K9me3 every 2 h under ALS for 12 h. Compared to HUVECs, no FRET ratio of activated H3K9me3 was observed in vECs upon ALS stimulation at different time points (0, 1, 3, and 6 h). **(D)** Protein expressions were examined by using Western blotting analysis. HUVECs and HSVECs were subjected to ST or ALS condition for 24 h. Lower expression of H3K9me3 in ALS-treated HSVECs compared to ALS-treated HUVECs was shown. ALS decreased the HDAC4 and HDAC5 and increased VCAM-1 in ALS-treated HSVECs. The increases of HDAC3, HDAC4, HDAC5, p-HDAC3, and p-HDAC4,5,7 were observed in ALS-treated HUVSCs at 24 h. Scale bar in **(A)** = 200 μm. Arrow indicated the flow direction of ALS (left to right). Scale bar in **(C)** = 20 μm. Data were represented as mean ± SEM. **p*-values were calculated using one-way ANOVA with Tukey's multiple comparisons post-tests. **p* < 0.05 compared to the vECs group.

Activation of HDACs Rescued vECs From the ALS-Induced Pathological Responses

Since we observed a decrease of HDACs expression in ALS-induced vEC inflammation (**Figure 2D**), we induced HDACs expression in HSVECs under ALS by initiating ITSA-1 (150 μM) treatment and measured H3K9me3 expression and cell inflammation in ISTA-1 and ALS treatments. Cell morphology was aligned parallel to the flow direction of ALS after ITSA-1 treatment in HSVECs (**Figure 4A**), indicating that ITSA-1 reverted the pathological responses to ALS in vECs. Western blotting showed that ITSA-1 increased the expressions of H3K9me3, pHDAC3, HDAC3, and p-HDAC4/5/7 in ALS-treated HSVECs (**Figure 4B**). A decrease in VCAM-1 expression was found after ITSA-1 treatment in HSVECs under ALS.

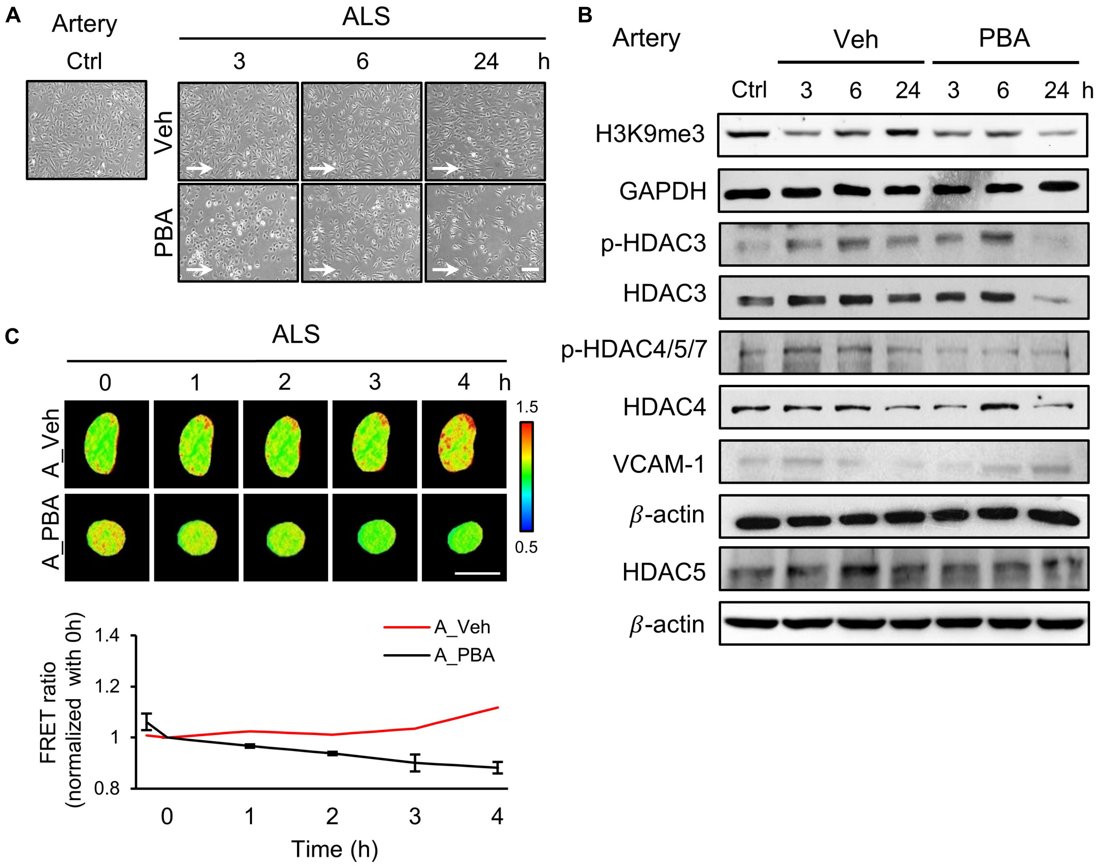

FIGURE 3 | PBA inhibited the expression of H3K9me3 in arterial ECs. **(A)** The images were presented the cell morphology of PBA (150 μM) or vehicle-treated arterial ECs (HUVECs) under ALS at 3, 6, and 24 h. PBA-induced arterial ECs had gradually increased the number of round-up damage morphology after subjected to ALS at 3, 6, and 24 h. **(B)** Protein expressions were examined by using Western blotting analysis. The decreases of H3K9me3, p-HDAC3, p-HDAC4,5,7, HDAC3, HDAC4, and HDAC5 and the increase of VCAM-1 were observed after treating PBA under ALS in HUVECs compared to vehicle group. **(C)** By utilizing the H3K9me3 FRET biosensor to examine the H3K9me3 status, the FRET ratio of H3K9me3 was declined in PBA-treated HUVECs under ALS condition compared to the vehicle group **(C)**. Scale bar in **(A)** = 200 μm. Scale bar in **(C)** = 20 μm. Data were represented as mean ± SEM. Arrow indicated the flow direction of ALS (left to right).

These results suggested that the increases in expressions of HDACs and H3K9me3 through HDAC activation rescued vECs from ALS-induced inflammation. We used the H3K9me3 FRET biosensor to measure H3K9me3 expression in ITSA-1-treated HSVECs upon ALS stimulation. The normalized FRET ratio revealed that H3K9me3 expression was increased in the ITSA-1 group as compared with that in the vehicle group under ALS in HSVECs (**Figure 4C**). The FRET results are in accordance with the Western blotting results. Taken together, these data suggest that the increased expressions of HDACs and H3K9me3 by ITSA-1 could reverse inflammation in ALS-induced vECs.

Effects of FAK on H3K9me3 Expression Under ALS

It has been reported that ECs undergo cell death if they become detached from the extracellular matrix (Ruoslahti and Reed, 1994). Moreover, FAK is involved in the regulation of FA structures (Sieg et al., 1999) and the increase of integrin activation to strengthen FA (Michael et al., 2009). We explored whether p-FAK was involved in ALS-mediated H3K9me3 expression in arterial ECs. Western blotting showed that FAK phosphorylation in PBA-treated arterial ECs was decreased compared to the vehicle group under ALS (**Figure 5A**). We also examined the role of FAK in H3K9me3 expression under ALS by using a FAK inhibitor (FI14) and a FAK activator [epidermal growth factor (EGF)] in HUVECs and HSVECs. Arterial ECs became round and lost after using FI14 (5 μM) to inhibit the phosphorylation site (Y397) of FAK under ALS (**Figure 5B**). Cell images showed that FI14 treatment caused arterial ECs to peel off after exposure to ALS. Expressions of p-FAK, t-FAK, and H3K9me3 were measured by Western blotting (**Figure 5C**). A decrease of p-FAK was found upon FI14 treatment in HUVECs under ALS. H3K9me3 expression also declined after being subjected to ALS in FI14-treated HUVECs, indicating that the blockage of p-FAK expression could suppress ALS-induced H3K9me3 expression in arterial ECs. To confirm this result, we utilized the H3K9me3 FRET biosensor to detect the activation status of H3K9me3. The normalized FRET ratio was decreased after

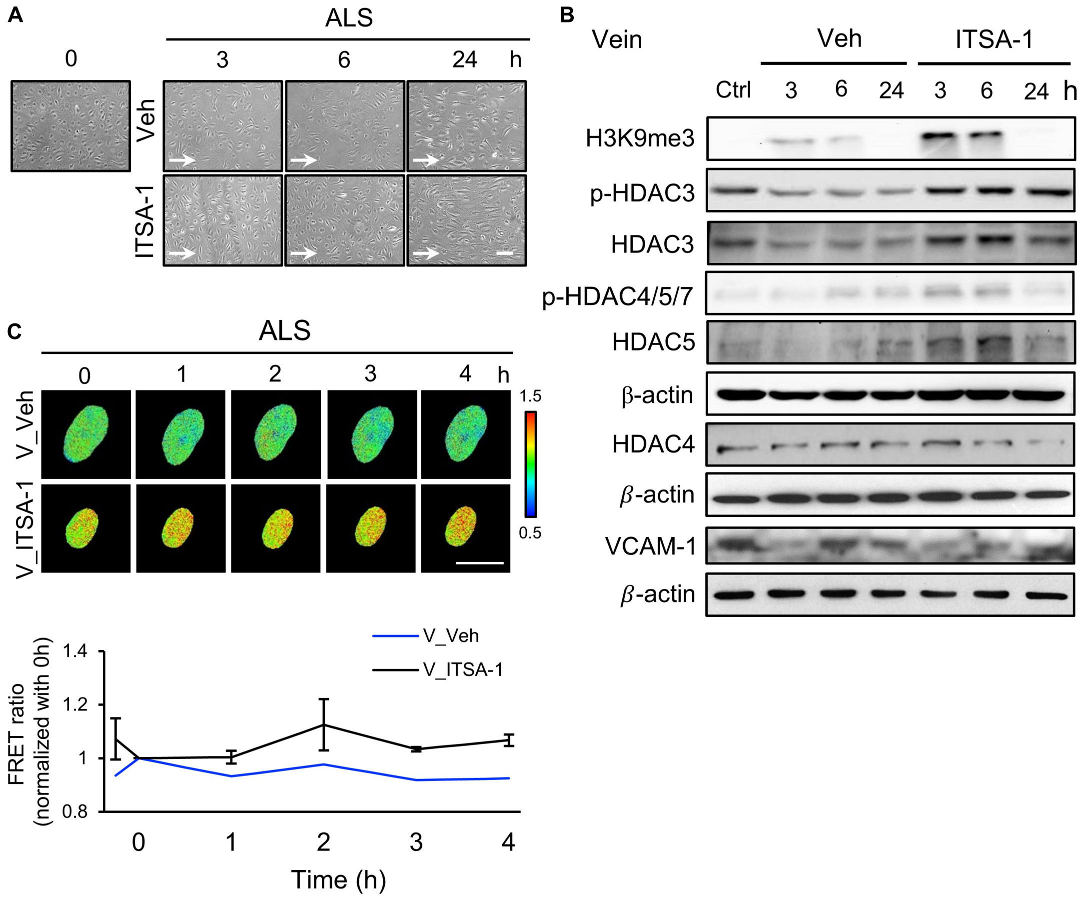

FIGURE 4 | Reverse the ALS-induced inflammation by ITSA-1 in vEC. **(A)** The cell images of 150 μM ITSA-1- or vehicle-treated vECs (HSVECs) were shown under ALS for 0, 3, 6, and 24 h. The ITSA-1-treated HSVECs were significantly aligned parallel to the flow direction of ALS at 24 h. **(B)** Protein expression was analyzed by using Western blotting assay against H3K9me3, p-HDAC3, p-HDAC4,5,7, HDAC3, HDAC4, HDAC5, and VCAM-1. ITSA-1-treated HSVECs reduced the VCAM-1 expression by increasing the HDAC3, p-HDAC4, 5, 7, and H3K9me3 as compared to the vehicle group after exposed to ALS at 3 and 6 h. **(C)** The level of H3K9me3 was raised in the ITSA-1 group but not in vehicle group under ALS in H3K9me3 FRET biosensor-transfected HSVECs. Scale bar in **(A)** = 200 μm. Scale bar in **(C)** = 20 μm. Data were represented as mean ± SEM. Arrow indicated the flow direction of ALS (left to right).

FI14 treatment in arterial ECs. During ALS stimulation, the results for the FRET biosensor of FI14-treated arterial ECs showed a similar trend to those for the Western blotting data (**Figure 5D**).

We also assessed the expression of p-FAK upon ITSA-1 treatment in ALS-stimulated HSVECs. FAK phosphorylation was increased by applying ITSA-1 in HSVECs under ALS (**Figure 6A**). We used EGF (100 ng/ml) to activate p-FAK expression in HSVECs; the morphology of EGF-treated HSVECs showed alignment with the ALS direction, and the peel-off of HUVECs was reduced after ALS stimulation over 24 h (**Figure 6B**). Western blotting showed that HSVECs upon EGF treatment could activate p-FAK and cause sustained increases in H3K9me3 expression after being subjected to ALS (**Figure 6C**). In addition, H3K9me3 activation was demonstrated by transfecting the H3K9me3 FRET biosensor into HSVECs under ALS. The normalized H3K9me3 FRET ratio of HSVECs was increased in the EGF group compared with that in the vehicle group after ALS stimulation. These data indicated that an increase in p-FAK activity by EGF treatment could increase H3K9me3 expression in vECs in response to the arterial flow stimuli under ALS (**Figure 6D**). Immunofluorescent staining of actin using phalloidin revealed a decrease in F-actin expression in vECs following ALS treatment. The supplementation of EGF rescued the effect of ALS treatment on F-actin expression and led to the formation of aligned stress fibers in parallel to the flow direction (**Figure 6E**). Taken together, these data indicate the involvement of FAK in H3K9me3 mediated ALS-induced vEC inflammation.

DISCUSSION

In the current study, we demonstrated that ALS inhibited the expressions of cyclin A1 and cyclin B1 to keep the ECs in the G0 phase, but OS did not. The responses of arterial and venous ECs to ALS stimulation were very different. Expressions of HDACs and H3K9me3 decreased in ALS-treated vECs, whereas

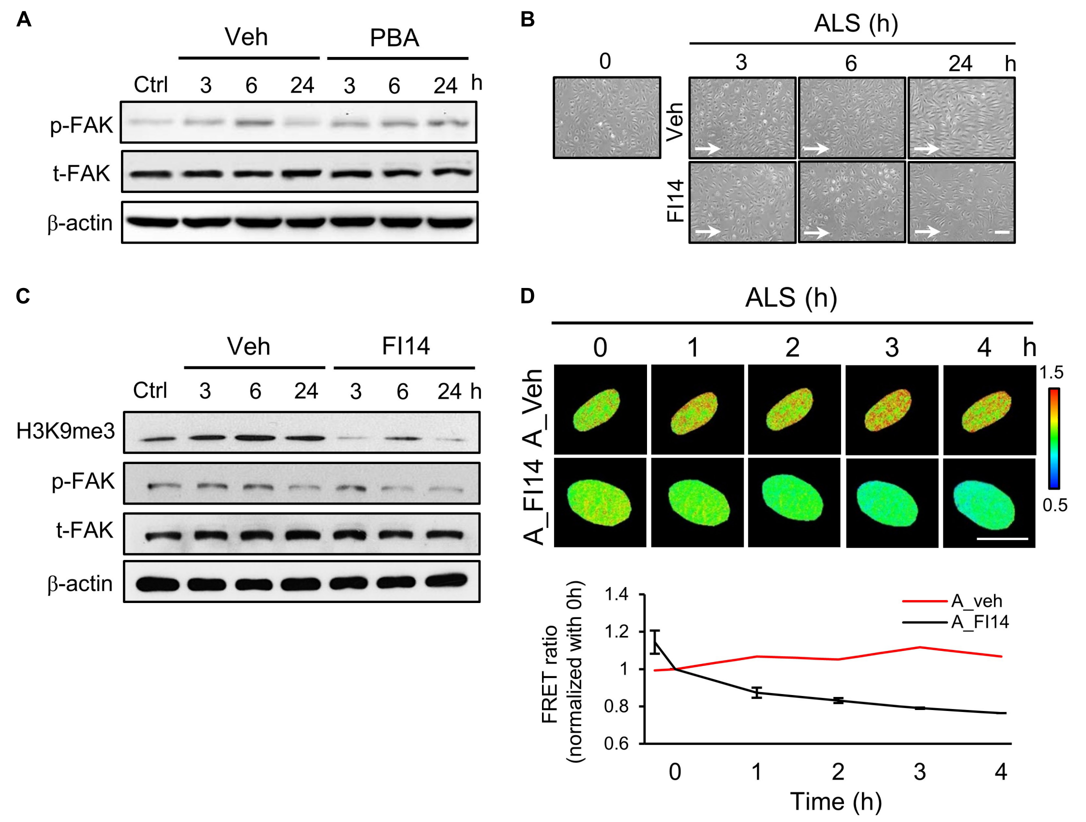

FIGURE 5 | Inhibition of FAK decreased the ALS-induced H3K9 methylation in arterial ECs. **(A)** The expression of p-FAK was decreased in PBA (150 μM)-treated arterial ECs (HUVECs) by Western blotting assay after being subjected to ALS at 0, 3, 6, and 24 h. **(B)** ALS significantly triggered the cell peel-off in FI14-treated HUVECs at 24 h. **(C)** Protein expression was analyzed by using Western blotting assay against H3K9me3, p-FAK, and t-FAK. Blocking the phosphorylation of FAK by FI14 treatment decreased the expression of H3K9me3 in ALS-stimulated HUVECs. **(D)** The normalized H3K9me3 FRET ratio was declined in FI14-treated HUVECs after being subjected to ALS by transfecting the H3K9me3 FRET biosensor. Scale bar in **(B)** = 200 μm. Scale bar in **(D)** = 20 μm. Data were represented as mean ± SEM. Arrow indicated the flow direction of ALS (left to right).

expressions of these proteins increased in ALS-treated arterial ECs (**Figure 7**). It has been shown that steady laminar flow reduces EC proliferation, with cells arrested in the G0/G1 phase, whereas disturbed flow patterns increase EC turnover (Guo et al., 2007). Laminar shear stress activates the PI3K-Akt pathway and the antiproliferative adenosine monophosphate-activated protein kinase (AMPK), but in oscillatory flow, only Akt activation is found. Several studies have indicated that AMPK counteracts Akt to mediate the downstream signal of mammalian target of rapamycin (mTOR)-p70S6 kinase (S6K), which is important for the regulation of the EC cell cycle. In addition, laminar shear stress leads arterial ECs to align in the direction of flow and exhibit low turnover or activation (Givens and Tzima, 2016). The transcription factor Krüppel-like factor-2 (KLF-2), an anti-inflammatory gene, shows high expression in arterial ECs under laminar shear stress (Givens and Tzima, 2016). In contrast, disturbed flow induces activation of nuclear factor-kappa B (NFκB), VCAM-1 expression, reactive oxygen species (ROS) production, and inflammatory responses in HUVEC (Go et al., 2014). Increases of senescence-associated β-galactosidase activity and p53 expression have been documented after exposure of arterial EC to disturbed flow. These results indicate that disturbed flow upregulates the p53-p21-dependent pathway to promote senescence or apoptosis of ECs (Warboys et al., 2014). We found that laminar shear stress induced arterial ECs alignment parallel to the flow direction and reduced cell inflammation. In contrast, vECs became round and inflamed after ALS exposure.

Recent studies have demonstrated that the effects of laminar shear stress on histone modification provide the molecular basis for laminar shear stress-mediated gene regulation in ECs (Illi et al., 2003). Laminar shear stress (12 dynes/cm2) induces the phosphorylation of HDAC5 and the disassociation of p-HDAC5 and myocyte enhancer factor-2 (MEF2) in HUVECs (Wang and Wang, 2009). Upregulation of MEF2 transcriptional activity leads to the expression of KLF-2 and endothelial nitric oxide synthase (eNOS) to maintain EC functions. These studies suggested that H3K9me3 and HDACs are important factors that regulate EC function. Arterial ECs had higher expression of HDACs than vECs after ALS stimulation. Disturbed flow in arterial ECs leads to different proatherogenic phenotypes, inflammation, proliferation, apoptosis, and reduction of vascular reactivity of ECs (Heo et al., 2015). PTM and epigenetic events are

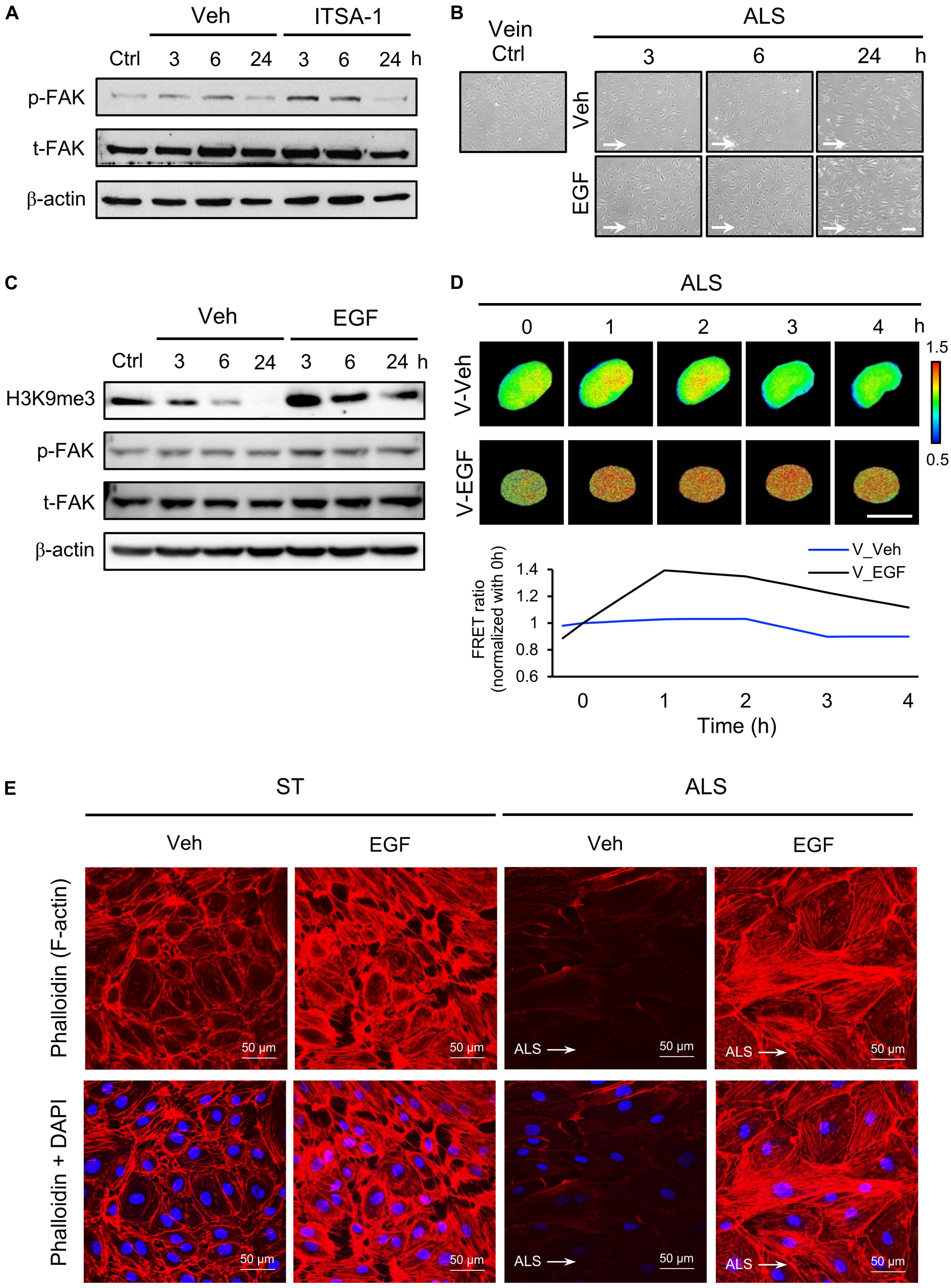

FIGURE 6 | Protective effect of EGF on preventing ALS-induced EC inflammation. **(A)** Western blotting analysis for activating H3K9me3 by treating ITSA-1 in vEC (HSVECs); the expression of p-FAK was increased after ALS stimulation. **(B)** Treating EGF (100 ng/ml) in HSUVEs prevented the cell peel-off and the cells were parallel to the flow direction under ALS. **(C)** Protein expression was analyzed by using conventional Western blotting assay against H3K9me3, p-FAK, and t-FAK. The expression of H3K9me3 was gradually increased by raising the expression of p-FAK in EGF-treated HSVECs under ALS. **(D)** To validate the flow regulation of H3K9me3 in EGF-treated HUVECs, the results also confirmed that EGF induced H3K9me3 over the time course of 4 h in H3K9me3 biosensor-transfected HSVECs under ALS. **(E)** Alexa fluor 546-Phalloidin staining was used to determine the expression of F-actin on vECs with or without EGF treatment under ALS for 24 h. Nuclei were stained with DAPI (blue). Scale bar in cell phase images = 200 μm. Scale bar in FRET images = 20 μm. Data were represented as mean ± SEM. Arrow indicated the flow direction of ALS (left to right).

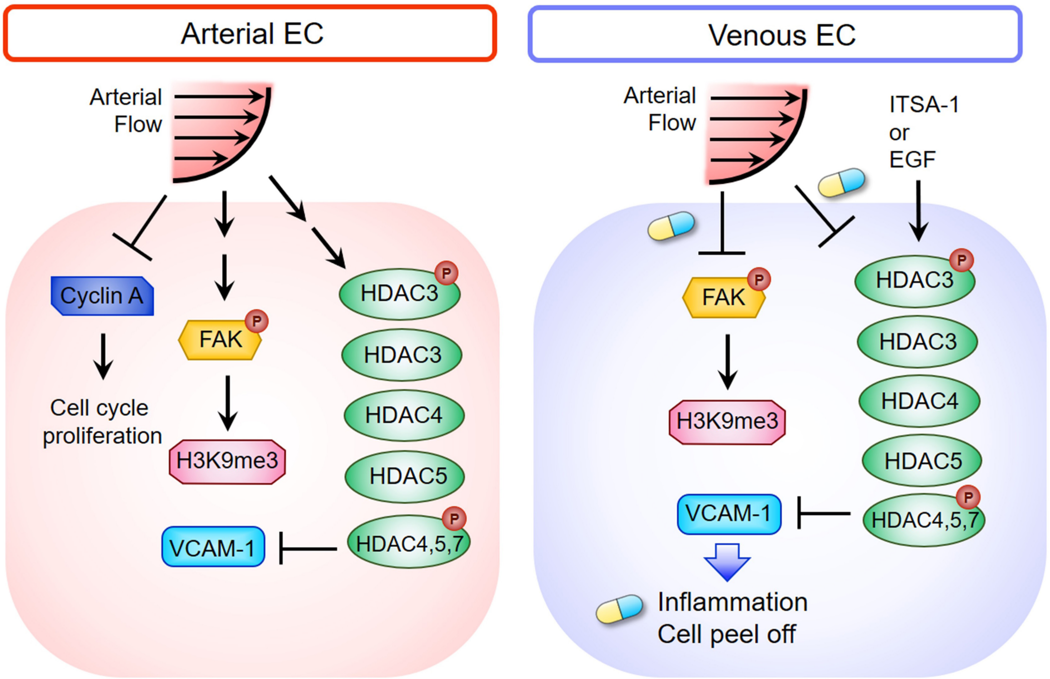

FIGURE 7 | Schematic diagram depicting the mechanism of HDACs and H3K9me3-mediated inflammation in triggering vEC damage under ALS stimulation. The blue and yellow capsule symbol means that the ALS-induced damages were rescued by treating with ITSA-1 or EGF.

involved in disturbed flow-induced endothelial proatherogenic phenotypes. Disturbed flow mediates several specific-signaling events including kinase activation (such as activation of p90ROS-sensitive kinases and inflammasome) (Heo et al., 2015), SUMOylation-related enzyme activity (Heo et al., 2013), DNA methylation (Jiang et al., 2014), and histone modification (Illi et al., 2003). Studies have indicated that laminar shear stress (10 dynes/cm^2) promotes phosphorylation of H3S10 and acetylation of H3K14 by the formation of the cAMP-responsive element-binding protein (Illi et al., 2003; Beldjoud et al., 2015). Histone methylation is also a crucial PTM that affects a wide variety of biological processes (Heo et al., 2016). However, the specific site of histone methylation in disturbed flow has not been sufficiently investigated. We found that arterial ECs in ALS induced H3K9me3 expression, but OS and ST did not. Moreover, the increase in VCAM-1 expression was associated with a decrease in H3K9me3 expression in vECs under ALS. These results indicate that H3K9me3 expression is important in the vEC damage during transition from venous to arterial flow. H3K9me3 and HDACs may serve as critical mechanosensitive molecules to modulate inflammation and EC peel-off during transition from venous to arterial flow in vECs.

It has been shown that there is a correlation between H3K9me3 expression and tumor progression in multiple cancer types (e.g., colorectal cancer) and that global H3K9 methylation upregulates tumorigenesis through the enzymatic activity of SUV39h1 (Yokoyama et al., 2013). Dysregulation of H3K9 methylation is found in various diseases such as neurodegenerative diseases. In hepatocellular carcinoma cells, knockdown of SUV39h1 expression has been shown to decrease H3K9me3 expression and disturb cell proliferation and sphere formation (Chiba et al., 2015). Villeneuve and coworkers demonstrated that H3K9me3 and SUV39h1 have pivotal roles in repressing the expression of inflammatory genes in vascular smooth muscle cells (Villeneuve et al., 2008). It has been reported that the increase of inflammatory genes in vascular cells cultured with high glucose was accompanied with the decrease of H3K9me3, which is known to protect against the biochemical state of diabetic inflammation (Abi Khalil, 2014). In addition, studies have shown that MeCP2 suppresses cell proliferation via recruiting HDAC activity and the subsequent activation of H3K9me3 (Fuks et al., 2003). These results are consistent with our observations, which demonstrate that the upregulation of H3K9me3 can repress the inflammation and proliferation of cell, and that H3K9me3 and HDACs could reverse ALS-induced vein graft pathogenesis.

It has been revealed that short hairpin RNA-mediated knockdown of HDAC3 suppresses H3K9 methylation (Huang et al., 2011). In Hdac3-null mice, the loss of H3K9me3 was found to coincide with the failure to maintain chromatin structure (Bhaskara et al., 2010). In investigating the relationship between H3K9me3 and inflammation when ECs were subjected to ALS, we discovered that peel-off and a decrease in H3K9me3 expression occurred in vECs after subjecting them to arterial flow. Surprisingly, we observed that vECs had low expression of HDAC3 in the arterial flow-induced inflammatory response. Next, we applied ITSA-1 to vECs to induce HDAC expression. We found that the high H3K9me3 expression in vECs reduced the inflammation responses in vECs. ITSA-1 (a small molecule for HDAC activator) has been used for screening chemical genetic suppressors and could become a valuable probe of many biological processes (Koeller et al., 2003). ITSA-1 has not been applied widely in clinical studies, but it could be used to uncover new therapeutical approaches to vascular diseases. We found that H3K9me3 and HDAC could participate in the arterial flow-induced inflammatory response in vECs, but the exact mechanism is not completely understood. Further studies are needed to reveal how H3K9me3 and HDAC3 regulate ALS-induced vEC damage.

Epidermal growth factor (which is part of a complex network of growth factors and receptors) facilitates cell growth (Goodsell, 2003). In our study, EGF upregulated H3K9 methylation in vECs after ALS stimulation. Several studies have shown that EGF interacts with the epidermal growth factor receptor (EGFR) to induce its kinase activity and autophosphorylation on tyrosine residues (Ge et al., 2002). However, overexpression of EGFR engenders constitutive activation of the EGFR and has been shown to correlate with tumor proliferation, tumor metastasis, and resistance to chemotherapy (Mendelsohn and Baselga, 2000). In this regard, the clinical application of EGF treatment may be a possible approach to reduce the excessive activity of EGFR in inducing tumor proliferation.

We have provided evidence that losses of HDACs and H3K9me3 expressions might cause vEC damage under the transition of venous flow to arterial flow. Inhibition of HDAC activities in arterial ECs by a specific inhibitor caused ALS-induced inflammation and cell loss similar to that observed in vECs. Activation of HDACs and H3K9me3 by ITSA-1 treatment could prevent ALS-induced vEC peel-off and reduce VCAM-1 expression in vECs. The abnormal mechanoresponses of H3K9me3 and HDAC in vECs after ALS exposure can be reversed by ITSA-1 treatment, which could be a strategy to prevent vascular graft failure.

DATA AVAILABILITY STATEMENT

The raw data supporting the conclusions of this article will be made available by the authors, without undue reservation.

AUTHOR CONTRIBUTIONS

C-CW and SC conceived and supervised this project. T-YW and M-MC contributed equally to this work. T-YW, M-MC, and T-CH performed the experiments and interpreted data. T-YW, M-MC, and C-CW wrote the manuscript. SC and Y-SJL helped with data analysis and the manuscript editing. M-MC and T-CH revised the manuscript. All authors contributed to the article and approved the submitted version.

FUNDING

This work was funded by grants from the Ministry of Science and Technology, Taiwan, Republic of China (ROC) (MOST 105-2314-B-006-041-MY5, MOST 104-2320-B-006-003, MOST 105-2320-B-006-003, MOST 106-2320-B-006-003, MOST 109-2311-B-006-005, and MOST 109-2811-B-006-555) and the National Health Research Institutes of Taiwan (NHRI-EX106-10525EI, NHRI-EX109-10925EI, and NHRI-EX110-10925EI).

ACKNOWLEDGMENTS

We thank YingXiao Wang (University of California, San Diego, United States) for providing the FRET-based H3K9me3 biosensor plasmids and FluoCell image system in this study. We also thank Da-Ming Huang, a candidate of NCKU, for modifying the MATLAB code to analyze the FRET data.

REFERENCES

Abi Khalil, C. (2014). The emerging role of epigenetics in cardiovascular disease. *Ther. Adv. Chronic Dis.* 5, 178–187. doi: 10.1177/2040622314529325

Akimoto, S., Mitsumata, M., Sasaguri, T., and Yoshida, Y. (2000). Laminar shear stress inhibits vascular endothelial cell proliferation by inducing cyclin-dependent kinase inhibitor p21(Sdi1/Cip1/Waf1). *Circ. Res.* 86, 185–190. doi: 10.1161/01.res.86.2.185

Beldjoud, H., Barsegyan, A., and Roozendaal, B. (2015). Noradrenergic activation of the basolateral amygdala enhances object recognition memory and induces chromatin remodeling in the insular cortex. *Front. Behav. Neurosci.* 9:108. doi: 10.3389/fnbeh.2015.00108

Bhaskara, S., Knutson, S. K., Jiang, G., Chandrasekharan, M. B., Wilson, A. J., Zheng, S., et al. (2010). Hdac3 is essential for the maintenance of chromatin structure and genome stability. *Cancer Cell* 18, 436–447. doi: 10.1016/j.ccr.2010.10.022

Caliskan, E., De Souza, D. R., Boning, A., Liakopoulos, O. J., Choi, Y. H., Pepper, J., et al. (2020). Saphenous vein grafts in contemporary coronary artery bypass graft surgery. *Nat. Rev. Cardiol.* 17, 155–169. doi: 10.1038/s41569-019-0249-3

Caltagarone, J., Jing, Z., and Bowser, R. (2007). Focal adhesions regulate Abeta signaling and cell death in Alzheimer's disease. *Biochim. Biophys. Acta* 1772, 438–445. doi: 10.1016/j.bbadis.2006.11.007

Carragher, N. O., and Frame, M. C. (2004). Focal adhesion and actin dynamics: a place where kinases and proteases meet to promote invasion. *Trends Cell Biol.* 14, 241–249. doi: 10.1016/j.tcb.2004.03.011

Case, L. B., Baird, M. A., Shtengel, G., Campbell, S. L., Hess, H. F., Davidson, M. W., et al. (2015). Molecular mechanism of vinculin activation and nanoscale spatial organization in focal adhesions. *Nat. Cell Biol.* 17, 880–892. doi: 10.1038/ncb3180

Chang, Y. J., Huang, H. C., Hsueh, Y. Y., Wang, S. W., Su, F. C., Chang, C. H., et al. (2016). Role of excessive autophagy induced by mechanical overload in vein graft neointima formation: prediction and prevention. *Sci. Rep.* 6:22147. doi: 10.1038/srep22147

Chiba, T., Saito, T., Yuki, K., Zen, Y., Koide, S., Kanogawa, N., et al. (2015). Histone lysine methyltransferase SUV39H1 is a potent target for epigenetic therapy of hepatocellular carcinoma. *Int. J. Cancer* 136, 289–298. doi: 10.1002/ijc.28985

Chien, S. (2007). Mechanotransduction and endothelial cell homeostasis: the wisdom of the cell. *Am. J. Physiol. Heart Circ. Physiol.* 292, H1209–H1224. doi: 10.1152/ajpheart.01047.2006

de Vries, M. R., and Quax, P. H. A. (2018). Inflammation in vein graft disease. *Front. Cardiovasc. Med.* 5:3. doi: 10.3389/fcvm.2018.00003

De Vries, M. R., Simons, K. H., Jukema, J. W., Braun, J., and Quax, P. H. (2016). Vein graft failure: from pathophysiology to clinical outcomes. *Nat. Rev. Cardiol.* 13, 451–470. doi: 10.1038/nrcardio.2016.76

Dominguez, M., and Berger, F. (2008). Chromatin and the cell cycle meet in Madrid. *Development* 135, 3475–3480. doi: 10.1242/dev.000844

Driscoll, T. P., Ahn, S. J., Huang, B., Kumar, A., and Schwartz, M. A. (2020). Actin flow-dependent and -independent force transmission through integrins. *Proc. Natl. Acad. Sci. U.S.A.* 117, 32413–32422. doi: 10.1073/pnas.2010292117

Ehsan, A., Mann, M. J., Dell'acqua, G., Tamura, K., Braun-Dullaeus, R., and Dzau, V. J. (2002). Endothelial healing in vein grafts: proliferative burst unimpaired by genetic therapy of neointimal disease. *Circulation* 105, 1686–1692.

Frosen, J., Cebral, J., Robertson, A. M., and Aoki, T. (2019). Flow-induced, inflammation-mediated arterial wall remodeling in the formation and progression of intracranial aneurysms. *Neurosurg. Focus* 47:E21. doi: 10.3171/2019.5.FOCUS19234

Fuks, F., Hurd, P. J., Wolf, D., Nan, X., Bird, A. P., and Kouzarides, T. (2003). The methyl-CpG-binding protein MeCP2 links DNA methylation to histone methylation. *J. Biol. Chem.* 278, 4035–4040. doi: 10.1074/jbc.M210256200

Garoffolo, G., and Pesce, M. (2019). Mechanotransduction in the cardiovascular system: from developmental origins to homeostasis and pathology. *Cells* 8:1607. doi: 10.3390/cells8121607

Ge, G., Wu, J., Wang, Y., and Lin, Q. (2002). Activation mechanism of solubilized epidermal growth factor receptor tyrosine kinase. *Biochem. Biophys. Res. Commun.* 290, 914–920. doi: 10.1006/bbrc.2001.6285

Gimbrone, M. A. Jr., and Garcia-Cardena, G. (2016). Endothelial cell dysfunction and the pathobiology of atherosclerosis. *Circ. Res.* 118, 620–636. doi: 10.1161/CIRCRESAHA.115.306301

Givens, C., and Tzima, E. (2016). Endothelial mechanosignaling: does one sensor fit all? *Antioxid. Redox Signal.* 25, 373–388. doi: 10.1089/ars.2015.6493

Go, Y. M., Son, D. J., Park, H., Orr, M., Hao, L., Takabe, W., et al. (2014). Disturbed flow enhances inflammatory signaling and atherogenesis by increasing thioredoxin-1 level in endothelial cell nuclei. *PLoS One* 9:e108346. doi: 10.1371/journal.pone.0108346

Goodsell, D. S. (2003). The molecular perspective: epidermal growth factor. *Oncologist* 8, 496–497. doi: 10.1634/theoncologist.8-5-496

Guo, D., Chien, S., and Shyy, J. Y. (2007). Regulation of endothelial cell cycle by laminar versus oscillatory flow: distinct modes of interactions of AMP-activated protein kinase and Akt pathways. *Circ. Res.* 100, 564–571. doi: 10.1161/01.RES.0000259561.23876.c5

Hadi, H. A., Carr, C. S., and Al Suwaidi, J. (2005). Endothelial dysfunction: cardiovascular risk factors, therapy, and outcome. *Vasc. Health Risk Manag.* 1, 183–198.

Heo, K. S., Berk, B. C., and Abe, J. (2016). Disturbed flow-induced endothelial proatherogenic signaling via regulating post-translational modifications and epigenetic events. *Antioxid. Redox Signal.* 25, 435–450. doi: 10.1089/ars.2015.6556

Heo, K. S., Chang, E., Le, N. T., Cushman, H., Yeh, E. T., Fujiwara, K., et al. (2013). De-SUMOylation enzyme of sentrin/SUMO-specific protease 2 regulates disturbed flow-induced SUMOylation of ERK5 and p53 that leads to endothelial dysfunction and atherosclerosis. *Circ. Res.* 112, 911–923. doi: 10.1161/CIRCRESAHA.111.300179

Heo, K. S., Le, N. T., Cushman, H. J., Giancursio, C. J., Chang, E., Woo, C. H., et al. (2015). Disturbed flow-activated p90RSK kinase accelerates atherosclerosis by inhibiting SENP2 function. *J. Clin. Invest.* 125, 1299–1310. doi: 10.1172/JCI76453

Huang, P. H., Chen, C. H., Chou, C. C., Sargeant, A. M., Kulp, S. K., Teng, C. M., et al. (2011). Histone deacetylase inhibitors stimulate histone H3 lysine 4 methylation in part via transcriptional repression of histone H3 lysine 4 demethylases. *Mol. Pharmacol.* 79, 197–206. doi: 10.1124/mol.110.067702

Illi, B., Nanni, S., Scopece, A., Farsetti, A., Biglioli, P., Capogrossi, M. C., et al. (2003). Shear stress-mediated chromatin remodeling provides molecular basis for flow-dependent regulation of gene expression. *Circ. Res.* 93, 155–161. doi: 10.1161/01.RES.0000080933.82105.29

Jiang, Y. Z., Jimenez, J. M., Ou, K., Mccormick, M. E., Zhang, L. D., and Davies, P. F. (2014). Hemodynamic disturbed flow induces differential DNA methylation of endothelial Kruppel-Like Factor 4 promoter in vitro and in vivo. *Circ. Res.* 115, 32–43. doi: 10.1161/CIRCRESAHA.115.303883

Kirchenbuechler, I., Guu, D., Kurniawan, N. A., Koenderink, G. H., and Lettinga, M. P. (2014). Direct visualization of flow-induced conformational transitions of single actin filaments in entangled solutions. *Nat. Commun.* 5:5060. doi: 10.1038/ncomms6060

Koeller, K. M., Haggarty, S. J., Perkins, B. D., Leykin, I., Wong, J. C., Kao, M. C., et al. (2003). Chemical genetic modifier screens: small molecule trichostatin suppressors as probes of intracellular histone and tubulin acetylation. *Chem. Biol.* 10, 397–410. doi: 10.1016/s1074-5521(03)00093-0

Kottakis, F., Polytarchou, C., Foltopoulou, P., Sanidas, I., Kampranis, S. C., and Tsichlis, P. N. (2011). FGF-2 regulates cell proliferation, migration, and angiogenesis through an NDY1/KDM2B-miR-101-EZH2 pathway. *Mol. Cell* 43, 285–298. doi: 10.1016/j.molcel.2011.06.020

Kuo, J. C. (2013). Mechanotransduction at focal adhesions: integrating cytoskeletal mechanics in migrating cells. *J. Cell. Mol. Med.* 17, 704–712. doi: 10.1111/jcmm.12054

Lee, D. Y., and Chiu, J. J. (2019). Atherosclerosis and flow: roles of epigenetic modulation in vascular endothelium. *J. Biomed. Sci.* 26:56. doi: 10.1186/s12929-019-0551-8

Li, S., Butler, P., Wang, Y., Hu, Y., Han, D. C., Usami, S., et al. (2002). The role of the dynamics of focal adhesion kinase in the mechanotaxis of endothelial cells. *Proc. Natl. Acad. Sci. U.S.A.* 99, 3546–3551. doi: 10.1073/pnas.052018099

Li, Y. S., Haga, J. H., and Chien, S. (2005). Molecular basis of the effects of shear stress on vascular endothelial cells. *J. Biomech.* 38, 1949–1971. doi: 10.1016/j.jbiomech.2004.09.030

Lin, C. W., Jao, C. Y., and Ting, A. Y. (2004). Genetically encoded fluorescent reporters of histone methylation in living cells. *J. Am. Chem. Soc.* 126, 5982–5983. doi: 10.1021/ja038854h

Liu, B., Lu, S., Hu, Y. L., Liao, X., Ouyang, M., and Wang, Y. (2014). RhoA and membrane fluidity mediates the spatially polarized Src/FAK activation in response to shear stress. *Sci. Rep.* 4:7008. doi: 10.1038/srep07008

Luo, W., Xiong, W., Zhou, J., Fang, Z., Chen, W., Fan, Y., et al. (2011). Laminar shear stress delivers cell cycle arrest and anti-apoptosis to mesenchymal stem cells. *Acta Biochim. Biophys. Sin. (Shanghai)* 43, 210–216. doi: 10.1093/abbs/gmr004

McKavanagh, P., Yanagawa, B., Zawadowski, G., and Cheema, A. (2017). Management and prevention of saphenous vein graft failure: a review. *Cardiol. Ther.* 6, 203–223. doi: 10.1007/s40119-017-0094-6

Mendelsohn, J., and Baselga, J. (2000). The EGF receptor family as targets for cancer therapy. *Oncogene* 19, 6550–6565. doi: 10.1038/sj.onc.1204082

Michael, K. E., Dumbauld, D. W., Burns, K. L., Hanks, S. K., and Garcia, A. J. (2009). Focal adhesion kinase modulates cell adhesion strengthening via integrin activation. *Mol. Biol. Cell* 20, 2508–2519. doi: 10.1091/mbc.E08-01-0076

Peng, Z., Shu, B., Zhang, Y., and Wang, M. (2019). Endothelial response to pathophysiological stress. *Arterioscler. Thromb. Vasc. Biol.* 39, e233–e243. doi: 10.1161/ATVBAHA.119.312580

Romer, L. H., Birukov, K. G., and Garcia, J. G. (2006). Focal adhesions: paradigm for a signaling nexus. *Circ. Res.* 98, 606–616. doi: 10.1161/01.RES.0000207408.31270.db

Ruiter, M. S., and Pesce, M. (2018). Mechanotransduction in Coronary Vein Graft Disease. *Front. Cardiovasc. Med.* 5:20. doi: 10.3389/fcvm.2018.00020

Ruoslahti, E., and Reed, J. C. (1994). Anchorage dependence, integrins, and apoptosis. *Cell* 77, 477–478. doi: 10.1016/0092-8674(94)90209-7

Sieg, D. J., Hauck, C. R., and Schlaepfer, D. D. (1999). Required role of focal adhesion kinase (FAK) for integrin-stimulated cell migration. *J. Cell Sci.* 112, 2677–2691.

Shimokawa, H., and Satoh, K. (2014). Vascular function. *Arterioscler. Thromb. Vasc. Biol.* 34, 2359–2362. doi: 10.1161/ATVBAHA.114.304119

Tajadura, V., Hansen, M. H., Smith, J., Charles, H., Rickman, M., Farrell-Dillon, K., et al. (2020). beta-catenin promotes endothelial survival by regulating eNOS activity and flow-dependent anti-apoptotic gene expression. *Cell Death Dis.* 11:493. doi: 10.1038/s41419-020-2687-6

Verma, D., Meng, F., Sachs, F., and Hua, S. Z. (2015). Flow-induced focal adhesion remodeling mediated by local cytoskeletal stresses and reorganization. *Cell Adh. Migr.* 9, 432–440. doi: 10.1080/19336918.2015.1089379

Villeneuve, L. M., Reddy, M. A., Lanting, L. L., Wang, M., Meng, L., and Natarajan, R. (2008). Epigenetic histone H3 lysine 9 methylation in metabolic memory and inflammatory phenotype of vascular smooth muscle cells in diabetes. *Proc. Natl. Acad. Sci. U.S.A.* 105, 9047–9052. doi: 10.1073/pnas.0803623105

Wang, Y., and Wang, N. (2009). FRET and mechanobiology. *Integr. Biol. (Camb.)* 1, 565–573. doi: 10.1039/b913093b

Warboys, C. M., De Luca, A., Amini, N., Luong, L., Duckles, H., Hsiao, S., et al. (2014). Disturbed flow promotes endothelial senescence via a p53-dependent pathway. *Arterioscler. Thromb. Vasc. Biol.* 34, 985–995. doi: 10.1161/ATVBAHA.114.303415

Wu, C. C., Li, Y. S., Haga, J. H., Kaunas, R., Chiu, J. J., Su, F. C., et al. (2007). Directional shear flow and Rho activation prevent the endothelial cell apoptosis induced by micropatterned anisotropic geometry. *Proc. Natl. Acad. Sci. U.S.A.* 104, 1254–1259. doi: 10.1073/pnas.0609806104

Yan, M. S., Matouk, C. C., and Marsden, P. A. (2010). Epigenetics of the vascular endothelium. *J. Appl. Physiol. (1985)* 109, 916–926. doi: 10.1152/japplphysiol.00131.2010

Yang, C. Y., Li, M. C., Lan, C. W., Lee, W. J., Lee, C. J., Wu, C. H., et al. (2020). The anastomotic angle of hemodialysis arteriovenous fistula is associated with flow disturbance at the venous stenosis location on angiography. *Front. Bioeng. Biotechnol.* 8:846. doi: 10.3389/fbioe.2020.00846

Yokoyama, Y., Hieda, M., Nishioka, Y., Matsumoto, A., Higashi, S., Kimura, H., et al. (2013). Cancer-associated upregulation of histone H3 lysine 9 trimethylation promotes cell motility in vitro and drives tumor formation in vivo. *Cancer Sci.* 104, 889–895. doi: 10.1111/cas.12166

Zacharopoulou, N., Tsapara, A., Kallergi, G., Schmid, E., Tsichlis, P. N., Kampranis, S. C., et al. (2018). The epigenetic factor KDM2B regulates cell adhesion, small rho GTPases, actin cytoskeleton and migration in prostate cancer cells. *Biochim. Biophys. Acta Mol. Cell Res.* 1865, 587–597. doi: 10.1016/j.bbamcr.2018.01.009

Zhao, X., Peng, X., Sun, S., Park, A. Y., and Guan, J. L. (2010). Role of kinase-independent and -dependent functions of FAK in endothelial cell survival and barrier function during embryonic development. *J. Cell Biol.* 189, 955–965. doi: 10.1083/jcb.200912094

Zhivotovsky, B., and Orrenius, S. (2010). Cell cycle and cell death in disease: past, present and future. *J. Intern. Med.* 268, 395–409. doi: 10.1111/j.1365-2796.2010.02282.x

Zhou, B., Margariti, A., Zeng, L., and Xu, Q. (2011). Role of histone deacetylases in vascular cell homeostasis and arteriosclerosis. *Cardiovasc. Res.* 90, 413–420. doi: 10.1093/cvr/cvr003

Conflict of Interest: The authors declare that the research was conducted in the absence of any commercial or financial relationships that could be construed as a potential conflict of interest.

frontiers
in Cell and Developmental Biology

ORIGINAL RESEARCH
published: 20 April 2021
doi: 10.3389/fcell.2021.647714

Mechanoresponsive Smad5 Enhances MiR-487a Processing to Promote Vascular Endothelial Proliferation in Response to Disturbed Flow

Wei-Li Wang[1], Li-Jing Chen[1,2], Shu-Yi Wei[1], Yu-Tsung Shih[1], Yi-Hsuan Huang[1], Pei-Lin Lee[1], Chih-I Lee[1], Mei-Cun Wang[1], Ding-Yu Lee[3], Shu Chien[2] and Jeng-Jiann Chiu[1,4,5,6,7,8]*

[1] Institute of Cellular and System Medicine, National Health Research Institutes, Miaoli, Taiwan, [2] Departments of Bioengineering and Medicine and Institute of Engineering in Medicine, University of California, San Diego, San Diego, CA, United States, [3] Department of Biological Science and Technology, China University of Science and Technology, Taipei, Taiwan, [4] School of Medical Laboratory Science and Biotechnology, College of Medical Science and Technology, Taipei Medical University, Taipei, Taiwan, [5] Ph.D. Program in Medical Biotechnology, College of Medical Science and Technology, Taipei Medical University, Taipei, Taiwan, [6] Taipei Heart Institute, Taipei Medical University, Taipei, Taiwan, [7] Institute of Biomedical Engineering, National Tsing Hua University, Hsinchu, Taiwan, [8] Institute of Polymer Science and Engineering, National Taiwan University, Taipei, Taiwan

Edited by:
Dimitra Gkika,
INSERM UMR 1277 Hétérogénéité, Plasticité et Résistance aux Thérapies Anticancéreuses (CANTHER), France

Reviewed by:
Nanping Wang,
Dalian Medical University, China
Yun Fang,
University of Chicago, United States
Qingping Yao,
Shanghai Jiao Tong University, China

***Correspondence:**
Jeng-Jiann Chiu
jjchiu88@tmu.edu.tw;
jjchiu@nhri.org.tw
orcid.org/0000-0003-4071-7367

Specialty section:
This article was submitted to Cell Adhesion and Migration, a section of the journal Frontiers in Cell and Developmental Biology

Received: *06 January 2021*
Accepted: *16 March 2021*
Published: *20 April 2021*

Citation:
Wang W-L, Chen L-J, Wei S-Y, Shih Y-T, Huang Y-H, Lee P-L, Lee C-I, Wang M-C, Lee D-Y, Chien S and Chiu J-J (2021) Mechanoresponsive Smad5 Enhances MiR-487a Processing to Promote Vascular Endothelial Proliferation in Response to Disturbed Flow. Front. Cell Dev. Biol. 9:647714. doi: 10.3389/fcell.2021.647714

MicroRNAs (miRs) and bone morphogenetic protein receptor–specific Smads are mechano-responsive molecules that play vital roles in modulating endothelial cell (EC) functions in response to blood flow. However, the roles of interplay between these molecules in modulating EC functions under flows remain unclear. We elucidated the regulatory roles of the interplay between miR-487a and Smad5 in EC proliferation in response to different flow patterns. Microarray and quantitative RT-PCR showed that disturbed flow with low and oscillatory shear stress (OS, 0.5 ± 4 dynes/cm^2) upregulates EC miR-487a in comparison to static controls and pulsatile shear stress (12 ± 4 dynes/cm^2). MiR-487a expression was higher in ECs in the inner curvature (OS region) than the outer curvature of the rat aortic arch and thoracic aorta and also elevated in diseased human coronary arteries. MiR-487a expression was promoted by nuclear phospho-Smad5, which bound to primary-miR-487a to facilitate miR-487a processing. Algorithm prediction and luciferase reporter and argonaute 2-immunoprecipitation assays demonstrated that miR-487a binds to 3′UTR of CREB binding protein (CBP) and p53. Knockdown and overexpression of miR-487a decreased and increased, respectively, phospho-Rb and cyclin A expressions through CBP and p53. A BrdU incorporation assay showed that miR-487a enhanced EC proliferation under OS *in vitro* and in disturbed flow regions of experimentally stenosed rat abdominal aorta *in vivo*.

These results demonstrate that disturbed flow with OS induces EC expression of miR-487a through its enhanced processing by activated-Smad5. MiR-487 inhibits its direct targets CBP and p53 to induce EC cycle progression and proliferation. Our findings suggest that EC miR-487 may serve as an important molecular target for intervention against disturbed flow–associated vascular disorders resulting from atherosclerosis.

Keywords: disturbed flow, endothelium, MicroRNA, shear stress, Smad

INTRODUCTION

Endothelial cell (EC) dysfunction is a critical step leading to vascular pathologies, including atherosclerosis, which develop preferentially in arterial branches and curvatures, where the local flow is disturbed with low and oscillatory shear stress (OS) (Chiu and Chien , 2011). In contrast, the straight part of the artery, which is exposed to sustained laminar flow with pulsatile shear stress (PS) having a clear direction, is generally spared from atherosclerotic lesions (Chiu and Chien , 2011). Recent studies show that disturbed flow with OS accelerates EC cycle progression and proliferation (Chiu and Chien , 2011) to promote atherogenesis (Obikane et al., 2010; Chiu and Chien , 2011). Bone morphogenetic protein (BMP)-4 and BMP receptor (BMPR)-specific Smads (i.e., Smad1/5/8) are shown to be activated in ECs by disturbed flow with OS (Sorescu et al., 2003). In our previous studies, we demonstrate that BMPR-specific Smad1/5 can be activated by OS to accelerate EC cycle progression and proliferation *in vitro* and *in vivo* (Zhou et al., 2012). Although BMPR-specific Smads are shown to regulate EC responses to OS, the detailed mechanisms by which BMPR-specific Smads regulate OS-induced EC cycle progression and proliferation remain unclear.

MicroRNAs (MiRs) are noncoding small RNAs, typically 18–22 nucleotides in length, which can regulate gene expression at the posttranscriptional level by interacting with the 3′ untranslated region (3′UTR) of the target message RNA (mRNA) (Bartel, 2009). More than 200 miRs have been found in human ECs, some of which can be regulated by different flow patterns and shear stresses to modulate vascular homeostasis and pathophysiological processes (Donaldson et al., 2018). Laminar shear stress (LS) and PS can upregulate a set of miRs, including miR-23b (Wang et al., 2010), miR-10a (Lee et al., 2017), miR-126 (Mondadori dos Santos et al., 2015), miR-30-5p (Demolli et al., 2015), miR-181b (Sun et al., 2014), miR-143/145 (Kohlstedt et al., 2013; Schmitt et al., 2014), and miR-146a (Chen et al., 2015) in ECs to inhibit their proliferation or inflammation and, hence, atherogenesis (Donaldson et al., 2018). In contrast, OS upregulates miR-92a (Wu et al., 2011), miR-663 (Ni et al., 2011), miR-712 (Son et al., 2013), and miR-21 (Zhou et al., 2011) to promote EC pro-inflammatory responses and atherogenesis. A recent study by Davis et al. (2010) demonstrates that Smads can bind to the consensus sequence, i.e., RNA-Smad binding element (R-SBE: 5′-CAGAC-3′ or 5′-CAGGG-3′) of the primary transcripts of transforming growth factor (TGF)-β/BMP-regulated miRs to promote their processing from primary transcript (pri-miR) to precursor form (pre-miR). Although there have been considerable studies on the roles of miRs in modulating EC responses to fluid flow and shear stress, the molecular mechanisms by which disturbed flow with OS induces the processing of miRs to modulate EC cell cycle and proliferation remain unclear. We postulated that disturbed flow with OS can activate BMPR-specific Smads to regulate the processing of TGF-β/BMP-regulated miRs to subsequently induce EC cycle progression and proliferation.

P53 is a tumor suppressor that plays vital roles in modulating cell cycle and proliferation (Levine, 1997). The relationship between p53 and miRs in vascular physiology and pathophysiology is not clear. It has been shown that p53 activity can be regulated by posttranslational modifications, such as acetylation (Kruse and Gu, 2009). P53 was shown to be acetylated by cAMP-responsive element-binding protein (CREB) (CBP)/p300, which is an acetyltransferase and transcriptional cofactor that serves as a tumor suppressor (Goodman and Smolik, 2000), and CBP/p300-associated factor (pCAF) in response to a variety of cellular stress signals (Brooks and Gu, 2011). The acetylation of p53 can enhance its stability by inhibiting ubiquitination (Li et al., 2002). LS has been shown to induce the upregulation of p53 (Lin et al., 2000) and its acetylation at Lys-382 in ECs (Zeng et al., 2003). Whether OS can modulate p53 expression and acetylation through miRs in ECs to promote their cell cycle progression and proliferation remains unclear.

In the present study, which ranges from *in vitro* cell culture research on effects of different flow patterns and shear stresses on molecular signaling to *in vivo* investigations on the experimentally stenosed rat abdominal aorta and clinical specimens from patients with coronary artery disease (CAD), we demonstrate that disturbed flow with OS induces EC expression of miR-487a, which contains the R-SBE sequence. This OS-induction of miR-487a is regulated by its association with BMPR-specific Smad5, which can promote the processing of pri-miR-487a to pre-miR-487a in EC nuclei. The OS-induction of miR-487a enhances EC proliferation *via* direct targeting of p53 and CBP to increase Rb phosphorylation and cyclin A expression. Our results suggest that miR-487a is a critical molecule for intervention against disturbed flow–induced EC dysfunction and its associated vascular disorders.

MATERIALS AND METHODS

Cell Culture and Flow Apparatus

Human aortic ECs obtained commercially (Clonetics, Palo Alto, CA, United States) (Tsai et al., 2009) were grown in medium 199 (M199; Gibco, Grand Island, NY, United States) supplemented with 20% fetal bovine serum (FBS; Gibco). Cells between passages four and seven were used in the experiments. Cultured ECs were subjected to PS at 12 ± 4 dynes/cm^2 or OS at 0.5 ± 4 dynes/cm^2 in a parallel-plate flow chamber as previously described (Lee et al., 2017). Detailed procedures are described in online **Supplementary Documents**.

RNA-Immunoprecipitation (IP) Assay

ECs subjected to flow or transfected with control miR or pre-miR-487a were lysed in a lysis buffer containing protease inhibitor cocktail (Schmitt et al., 2014). Detailed procedures are described in online **Supplementary Documents**.

Animal Model of Aortic Stenosis

A U-shaped titanium clip (Ethicon Endo-Surgery) was surgically applied to the rat abdominal aorta as previously described (Zhou et al., 2012). The animal experiments were performed in accordance with National Institutes of Health guidelines and with the approval of the Animal Research Committee of National Health Research Institutes. Detailed procedures are described in online **Supplementary Documents**.

En Face Staining

The formalin-fixed rat aorta tissues were washed with Tris-buffered saline (TBS). The aorta was longitudinally dissected with micro-dissecting scissors and pinned flat for *en face* staining as previously described (de Planell-Saguer et al., 2010). Detailed procedures are described in online **Supplementary Documents**.

RNA-electrophoretic mobility shift assay

RNA-electrophoretic mobility shift assay (EMSA) was conducted by using a bio-UTP-labeled pri-miR-487a probe (∼150 nt). The pri-miR-487a probe was heat-denatured at 65°C for 6 min and renatured prior to being added to the binding buffer containing EC nuclear proteins (10 μg). Detailed procedures are described in online **Supplementary Documents**.

Pri-miR-487a Processing Assay

The pri-miR-487a processing assay was performed as previously described (Guil and Caceres, 2007). In brief, the biotin-labeled, full-length pri-miR-487a containing 522 nucleotides was prepared by *in vitro* transcription with T7 RNA polymerase in the presence of biotin-UTP, using a human miR-487a gene cloned into a pcDNA3.1(+) vector as a template. Detailed procedures are described in online **Supplementary Documents**.

Generation of Luciferase Reporter Constructs

To generate reporter vectors bearing miR-487a binding sites and wild-type and mutant 3′UTR of CBP and p53, the sense and antisense strands of oligonucleotides bearing the predicted miR-487a binding sequences were commercially synthesized, annealed, and cloned into HindIII and MluI of the pMIR-REPORT luciferase vector (Ambion). Detailed procedures are described in online **Supplementary Documents**.

Statistics Analysis

Results are expressed as mean ± SEM. Statistical significance was determined using the Mann-Whitney rank sum test in the program SigmaStat 3.5 for two groups of data and a one-way analysis of variance (ANOVA), followed by Scheffe's test for multiple comparisons. The level of statistical significance was defined as $P < 0.05$ from three to five separate experiments.

An expanded Methods section is available in the online **Supplementary Documents**.

RESULTS

OS Induces miR-487a Expression in ECs *in vitro*

Because our previous studies demonstrate that BMPR-specific Smads can be activated by OS in ECs (Zhou et al., 2012) and that Smads may promote maturation of miRs containing Smad binding elements (Davis et al., 2008, 2010), we first identified the OS-responsive miRs whose expression could be regulated by BMPR-specific Smads in ECs. Three independent groups of experiments, i.e., ECs under static conditions and exposed to OS (0.5 ± 4 dynes/cm^2) or PS (12 ± 4 dynes/cm^2) for 24 h, were performed with TaqMan® Human MicroRNA array A, which contains 380 human miR probes. The results showed that nine of 380 human miRs are significantly upregulated by OS in ECs in comparison to PS-stimulated and static control cells (**Table 1** and online **Supplementary Table 1**). Among these miRs, miR-487a was most upregulated by OS (2.15-fold increase, $P < 0.05$) and contains the putative Smad binding elements (**Table 1**). This OS-induced miR-487a expression in ECs was confirmed by quantitative RT-PCR analysis of these cells (**Figure 1A**). Because the targeting of mRNA by an miR is dependent on its association with Argonaute (Ago) protein to form functional miR-induced silencing complex (miRISC) (Bartel., 2009), we investigated whether OS induces the association of Ago2 with miR-487a in ECs. The Ago2-IP assay showed that miR-487a is significantly enriched in the Ago2-containing miRISC in OS-stimulated ECs, as compared with PS-stimulated and static control cells (**Figure 1B**). Contrary to the mature miR-487a, the expression of pri-miR-487a was decreased in ECs under OS stimulation in comparison to PS (**Figure 1C**). These results indicate that OS promotes the progression of miR-487a from primary to mature form in ECs.

MiR-487a Is Upregulated in ECs in Athero-Susceptible, Disturbed Flow Regions of the Native Circulation and Diseased Human Coronary Arteries *in vivo*

To investigate whether the OS-induction of miR-487a found in cultured ECs *in vitro* also exists in the native circulation *in vivo*, we examined the aortic arch and the straight segment of thoracic aorta of normal rats by *en face in situ* hybridization of miR-487a and immunostaining for von Willebrand factor (vWF), with H33342 nuclear counterstaining. The results show that high levels

TABLE 1 | Disturbed flow–responsive miRs in ECs.

MiR names	Mean fold change (OS/CL)	*p*-value	Mean fold change (PS/CL)	*p*-value	RNA-Smad binding element
hsa-miR-487a	2.15	0.03	1.42	0.77	aaucauacagggacauccaguu
has-miR-92a	2.00	0.02	0.69	0.01	
hsa-miR-576	1.84	0.04	3.27	0.52	–
has-miR-21	1.6	<0.01	2.14	<0.01	uagcuuaucagacugauguuga
hsa-miR-181a	1.43	0.05	1.18	0.55	–
hsa-miR-125a-3p	1.34	0.04	2.27	0.04	
hsa-miR-181c	1.33	0.04	0.69	0.29	–
hsa-let-7g	1.27	0.05	0.94	0.75	–
hsa-let-7a	1.20	<0.01	1.05	0.79	–

ECs were kept under static conditions as controls (CL) or exposed to OS (0.5 ± 4 dynes/cm^2) or PS (12 ± 4 dynes/cm^2) for 24 h, and their total RNAs were collected and subjected to miR microarray analysis. Data represent triplicate experiments with similar results. Primary miR-487a and miR-21 contain RNA-Smad binding element sequence in their stem regions, where the Smad proteins are able to bind to regulate miR processing at the post-transcriptional level.

of miR-487a expression are present in the EC cytoplasm in the inner curvature of aortic arch, where disturbed flow with OS occurs (Chiu and Chien , 2011), but not in the outer curvature and the straight segment of the thoracic aorta, where laminar flow with PS prevails (Chiu and Chien , 2011; **Figure 1D**). To further assess miR-487a expression in atherosclerotic lesions, immunohistochemical examinations were made on diseased human coronary arteries with the use of internal thoracic arteries from the same patients as controls. The results showed that miR-487a is highly expressed in the EC layer (indicated by arrows) but not in the neointima in the lesion region (**Figure 1E**). In contrast, the control thoracic aorta showed virtually no detectable staining of miR-487a in the EC layer. These results demonstrate that EC miR-487a is specifically induced in athero-susceptible, disturbed flow regions in the native circulation *in vivo* and in diseased human coronary arteries. Thus, the OS-induction of EC miR-487a may play important roles in the formation and progression of atherosclerosis.

OS Induces Smad5 Activation in ECs to Promote miR-487a Processing

It has been reported that Smad proteins may not affect the transcription of miRs, but they may bind to Drosha and R-SBE of primary miRs to promote miR processing (Davis et al., 2008, 2010). Transfecting ECs with Smad5-specific siRNA abolished OS-induction of mature miR-487a (**Figure 2A**) with no significant influences on primary miR-487a expression in these ECs (**Figure 2B**). Moreover, application of shear stress to ECs did not affect Drosha expression in these ECs (**Figure 2F**). These results indicate that the OS-induction of EC mature miR-487a is attributable to the binding of Smad5 to primary miR-487a to promote miR-487a processing, but not due to the modulations in primary miR-487a and Drosha expression levels in these OS-stimulated cells.

To test this hypothesis, RNA-IP analysis was performed to investigate whether Smad5 can assemble with pri-miR-487a in ECs under flow. As shown in **Figure 2C**, application of OS to ECs for 24 h induced association of Smad5 with pri-miR-487a in these ECs as compared with static and PS-stimulated cells. We further investigated whether the R-SBE sequence of miR-487a is essential for the recruitment of Smad5. A 2-bp mutation was introduced into the R-SBE of pri-miR-487a (pri-miR-487a-mut), and the interaction between Smad5 and pri-miR-487a was examined by RNA electrophoretic mobility shift assay (RNA-EMSA) with pri-miR-487a-mut and pri-miR-487a-WT (wild type) as probes. The results show that use of the pri-miR-487a-WT probe resulted in the formation of RNA-protein complex, which was inhibited by R-SBE mutation (shift in **Figure 2D**). Application of OS to ECs for 24 h resulted in increases in the RNA-protein complex formation in ECs as compared with static and PS-stimulated cells (**Figure 2D**). This OS-induction of RNA-Smad5 protein complex was confirmed by the decrease in RNA-protein complex formation with the use of anti-Smad5 antibody (**Figure 2D**). To test whether OS can promote pre-miR-487a production, an *in vitro* pri-miR processing assay was performed by incubating biotin-labeled pri-miR487a substrates (544 nucleotides) with nuclear extracts from ECs subjected to OS, PS, or in a static condition. The results show that OS induced increases in pre-miR-487a expression in ECs in comparison to static and PS-stimulated cells, indicating that OS stimuli can facilitate the processing of pri-miR-487a in ECs (**Figure 2E**). We further used the fractionation assay to investigate whether OS induces Smad5 activation to interact with pri-miR-487a in the EC nuclei. The results show that application of OS to ECs results in significant induction of Smad5 phosphorylation in EC nuclei as compared with static and PS-stimulated cells (**Figure 2F**). The levels of Drosha proteins are not significantly different in ECs subjected to OS, PS, and the static condition. Taken together, these results indicate that application of OS to ECs induces Smad5 activation and its binding to the R-SBE of pri-miR-487a with Drosha in EC nuclei, which can consequently promote miR-487a processing in these ECs.

MiR-487a Inhibits CBP and p53 Expressions by Targeting Their 3′UTR

The use of bioinformatics databases miRanda, RNAhybrid, miRNAMap, and miRWALK predicted that human CBP and p53 are potential targets of miR-487a. Both CBP and p53 contain miR-487a binding sites in the 3′UTRs of their mRNAs

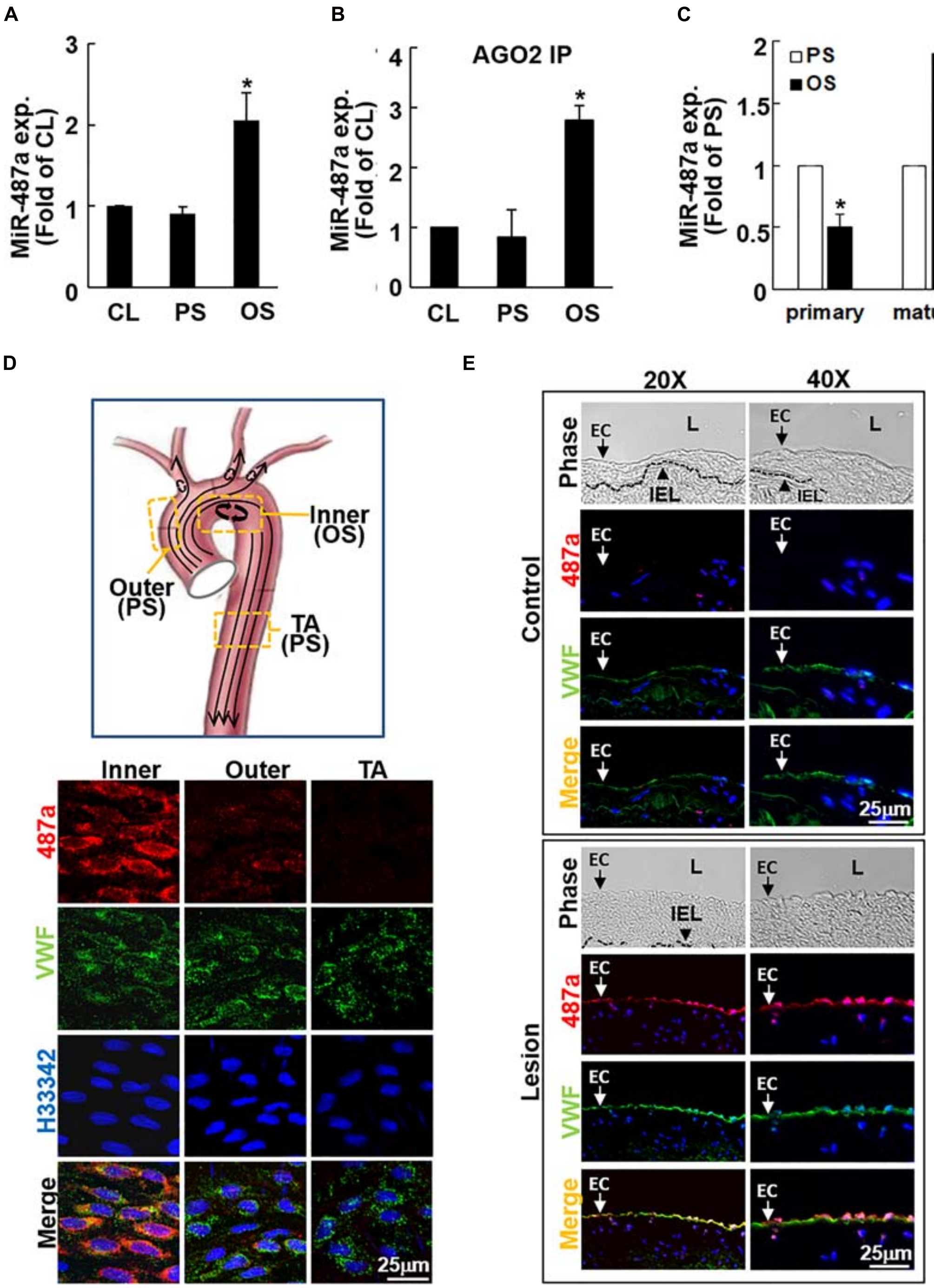

FIGURE 1 | OS induces mature miR-487a expression in ECs *in vitro* and *in vivo*. ECs were kept under static conditions as controls (CL) or exposed to OS or PS for 24 h, and the mature **(A)** Ago2-associated mature **(B)** and primary **(C)** miR-487a expressions of EC lysates were analyzed by quantitative RT-PCR. Data are mean ± SEM from three independent experiments. $^*P < 0.05$ vs. static or PS-stimulated cells. **(D)** The inner and outer curvatures of aortic arch and the straight segment of thoracic aorta of normal rats were examined by *en face* immunostaining for miR-487a and vWF with H33342 nuclear counterstains. **(E)** Serial cross-sections of diseased human coronary arteries were stained for human miR-487a and vWF and counterstained with H33342. IEL, internal elastic lamina. L, lumen. Arrow denotes the EC layer. Results are representative of five independent experiments with similar results.

(**Figure 3A**). To investigate whether miR-487a can directly target CBP and p53, we constructed a series of luciferase reporter plasmids containing predicted miR-487a recognition sequences in the 3′-UTRs of CBP and p53. The sequence that is a direct match of the miR-487a binding site was used as a positive control. Together with pre-miR-487a or a negative control

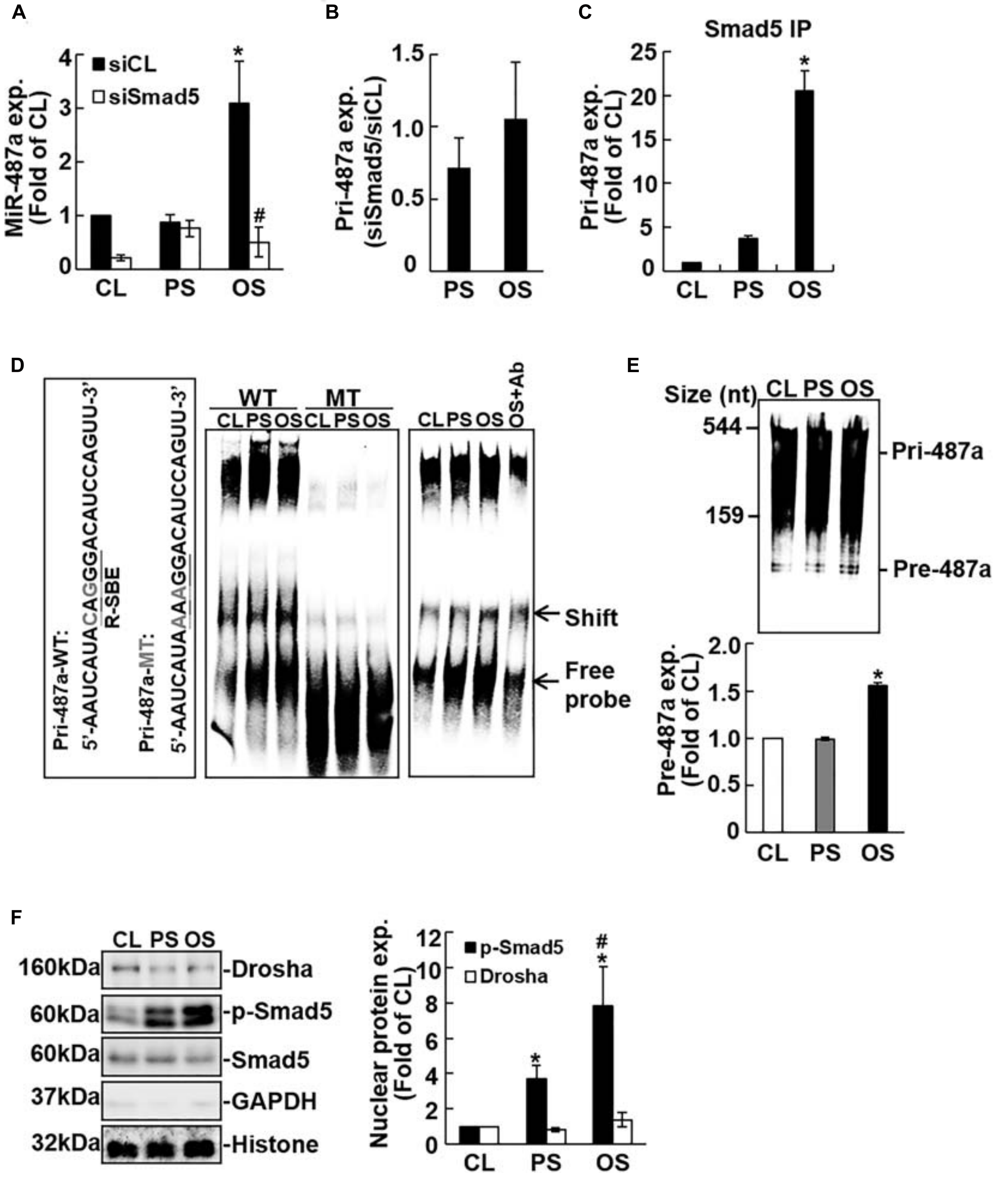

FIGURE 2 | Processing of EC pri-miR-487a is promoted by its association with nuclear phospho-Smad5 in response to OS. ECs were transfected with control (siCL) or Smad5-specific siRNA (siSmad5) (40 nM each) for 48 h before exposure to flow. The expression of the mature **(A)** primary **(B)** miR-487a and pri-miR-487a in Smad-immunoprecipitated complex **(C)** were analyzed by quantitative RT-PCR. Data are mean ± SEM from three independent experiments. $^{*}P < 0.05$ vs. static control cells. $^{\#}P < 0.05$ vs. siCL. **(D)** The nuclear fraction of conditioned ECs was extracted and subjected to EMSA using biotin-labeled WT or R-SBE mutant (mut) pri-miR-487a as the probe. **(E)** *In vitro* pri-miR-487a processing assay was performed by incubating nuclear extracts with biotin-labeled pri-miR-487a substrate. Results in panels **(D,E)** are representative of triplicate experiments with similar results. **(F)** Nuclear and cytosol localizations of the designated proteins were detected by Western blot analysis. Data are mean ± SEM from three independent experiments. $^{*}P < 0.05$ vs. static control cells. $^{\#}P < 0.05$ vs. PS-stimulated cells.

RNA, these constructed reporter plasmids were transfected into ECs. The results show that transfection with pre-miR-487a decreases the luciferase activity of the reporter vectors with an miR-487a binding site, CBP-3′UTR, and p53-3′UTR to 0. 63-, 0.66, and 0.69-fold, respectively, as compared with the control vector (**Figure 3B**). Mutations of the miR-487a binding site in CBP-3′UTR and p53-3′UTR returned the luciferase activity levels to 0.75 ($P < 0.05$) and 0.98 ($P < 0.01$) folds, respectively. The Ago2-immunoprecipitation assay showed enrichments of CBP- and p53-3′UTRs in miRISCs in ECs transfected with pre-miR-487a (**Figure 3C**) or subjected to OS (**Figure 3D**). Overexpression of pre-miR-487a in ECs under static conditions inhibited CBP

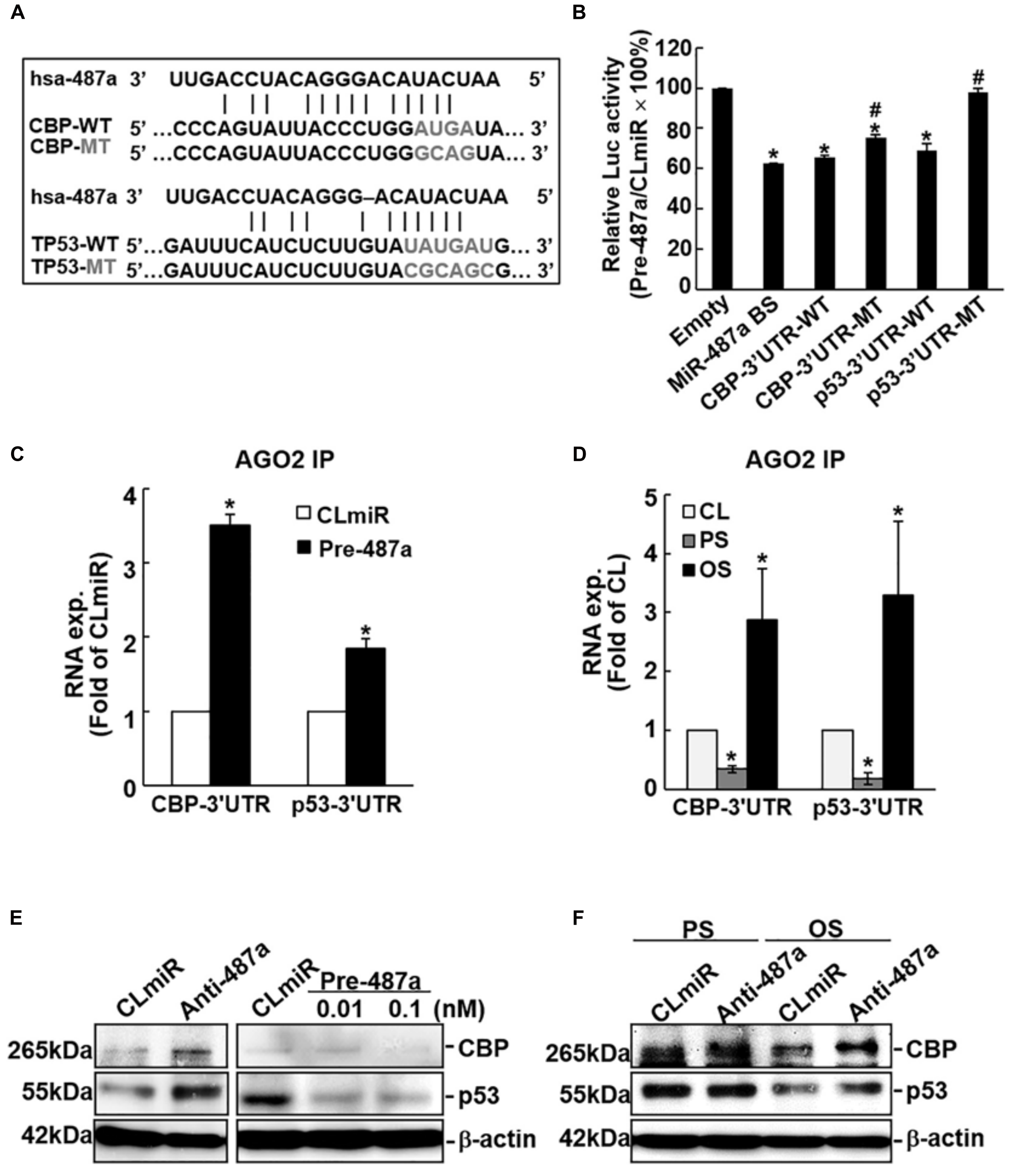

FIGURE 3 | MiR-487a targets 3′UTR of CBP and p53 to regulate their expressions. **(A)** The 3′UTRs of CBP and p53 genes contain miR-487a binding sites. **(B)** A series of pMIR-REPORT luciferase reporter plasmids, including empty vector only, consensus miR-487a binding sequences, wild-type and mutant 3′UTR of CBP and p53, were co-transfected with pre-miR-487a (Pre-487a) or control miR (CLmiR) into ECs for 48 h, and their luciferase (Luc) activity was measured and normalized to β-gal activity. **(C–F)** ECs were transfected with pre-miR-487a, anti-miR-487a (Anti-487a), or CLmiR. In some experiments, ECs were kept as static controls (CL) or exposed to OS or PS for 24 h. Ago2 pull-down assay was performed, and the transcription levels of CBP and p53 in Ago2-immunocomplexes were determined by quantitative RT-PCT **(C,D)**. Protein expressions of CBP and p53 were determined by Western blot analysis **(E,F)**. Data represent triplicate experiments with similar results. $^*P < 0.05$ vs. static control. Data in panels **(B,C,D)** are mean ± SEM from three independent experiments. Results in panels **(E,F)** are representative of triplicate experiments with similar results. $^*P < 0.05$ vs. empty vector **(B)**, CLmiR **(C)**, or static control cells **(D)**. $^\#P < 0.05$ vs. wild-type 3′UTR.

and p53 protein expressions in these ECs (**Figure 3E**). In contrast, transfection of ECs with anti-miR-487a increased CBP and p53 protein expressions in these ECs (**Figure 3E**). Application of OS to ECs for 24 h resulted in inhibitions in CBP and p53 expressions in ECs (**Figure 3F**). These OS-inhibitions in CBP and p53 expressions were rescued by transfecting ECs with anti-miR-487a. Taken together, our results indicate that both CBP and p53 are direct target molecules of miR-487a and that OS inhibits CBP and p53 expressions *via* upregulating miR-487a in ECs.

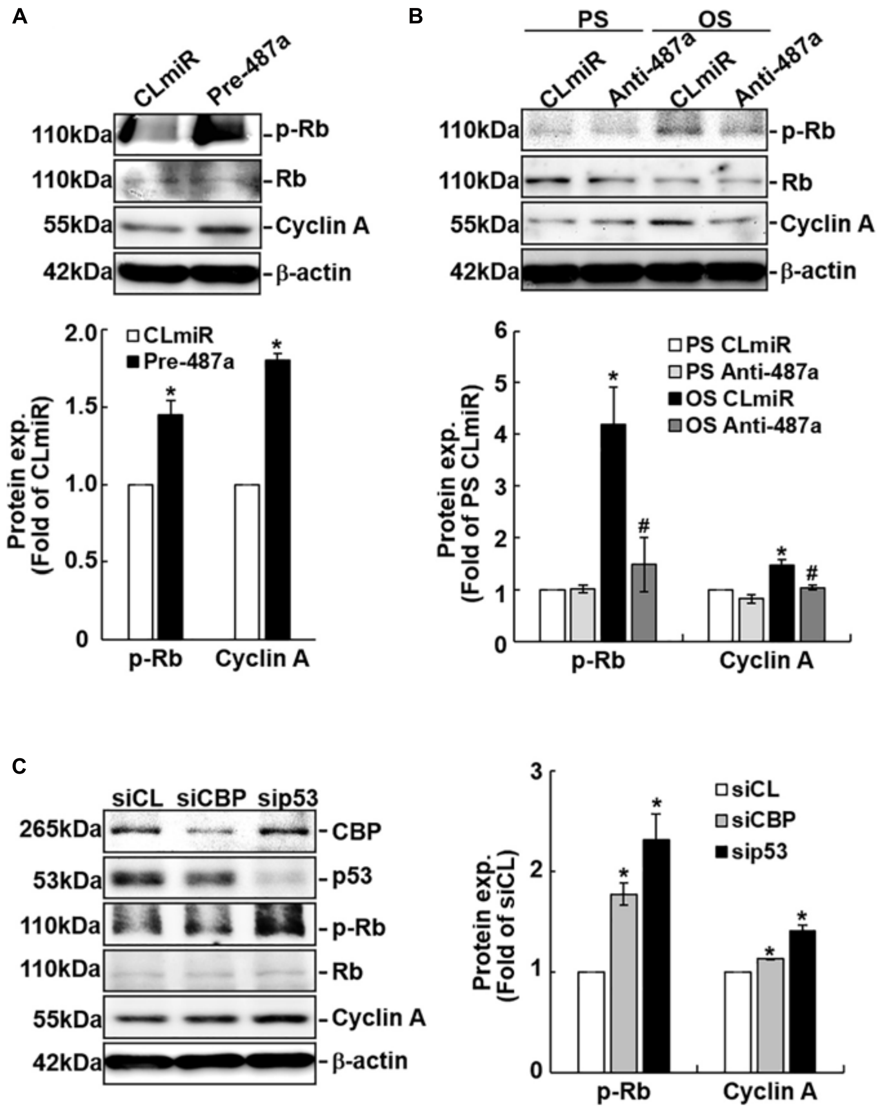

FIGURE 4 | MiR-487a regulates Rb phosphorylation and cyclin A expression through CBP and p53 in ECs. ECs were transfected with control miR (CLmiR), pre-miR-487a (Pre-487a) **(A)**, or anti-miR-487a (Anti-487a) **(B)** for 48 h, and then kept under static conditions (CL) or exposed to PS or OS. In some experiments, ECs were transfected with CBP- and p53-specific siRNAs (siCBP and sip53) **(C)** for 48 h, and then kept under static conditions as controls. Cell lysates were collected, and the cell cycle regulatory protein expressions were determined by Western blot analysis. Data are mean ± SEM from three independent experiments. $^{*}P < 0.05$ vs. CLmiR **(A)**, PS CLmiR **(B)**, or siCL **(C)**. $^{\#}P < 0.05$ vs. OS CLmiR **(B)**.

OS Induces Rb Phosphorylation and Cyclin A Expression Through Upregulating miR-487a and Downregulating CBP and p53 Expressions in ECs

To investigate whether cell cycle regulatory proteins are regulated by miR-487a in ECs in response to flow, ECs were transfected with pre-miR-487a or anti-miR-487a and then kept under the static condition or subjected to different flow patterns. Transfecting ECs with pre-miR-487a under the static condition induced Rb phosphorylation and cyclin A expression (**Figure 4A**). Application of OS to ECs for 24 h also induced these cell cycle regulatory proteins (**Figure 4B**). These OS-induced responses were inhibited by transfecting ECs with anti-miR-487a, indicating that OS induces Rb phosphorylation and cyclin A expression through upregulating miR-487a in ECs. Moreover, knockdown of CBP and p53 in ECs by their specific siRNAs resulted in increases in Rb phosphorylation and cyclin A expression in ECs (**Figure 4C**). Taken together, our data show that OS-induction of miR-487a downregulates CBP and p53 expressions to upregulate phospho-Rb and cyclin A, which may consequently promote cell cycle progression in ECs.

Because CBP has been shown to acetylate and, hence, stabilize p53 (Brooks and Gu, 2011) and our data show that knockdown of CBP decreases the protein levels of p53 (**Figure 4C**), we

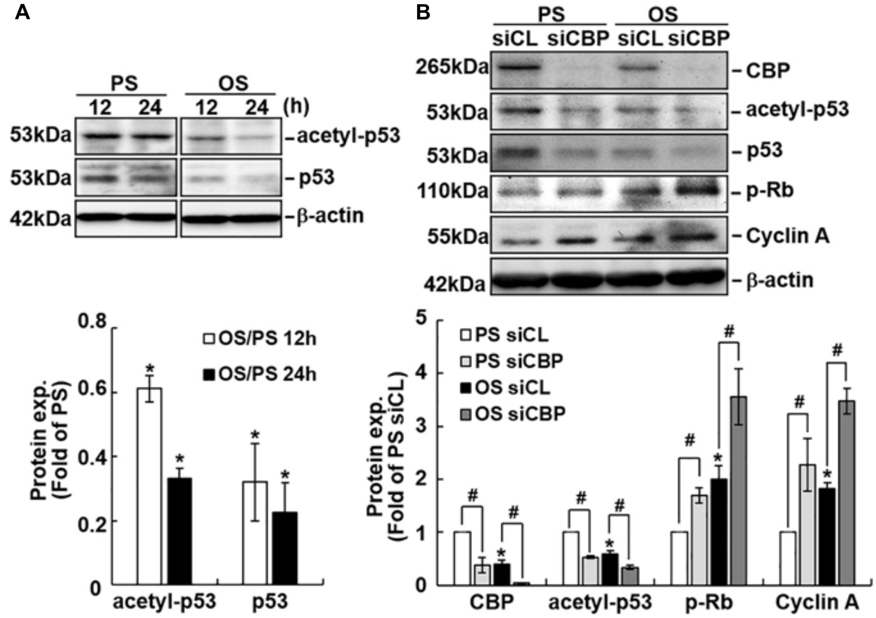

FIGURE 5 | CBP acetylates p53 in ECs in response to PS. ECs were subjected to OS vs. PS for the indicated times **(A)**. In some experiments, ECs were transfected with control (siCL) or CBP-specific siRNA (siCBP) for 48 h before subjecting to flows **(B)**. Protein expression was detected by Western blot analysis using the indicated antibodies. Data are mean ± SEM from three independent experiments. $^*P < 0.05$ vs. PS stimuli **(A)** or PS and siCL **(B)**. $^\#P < 0.05$ vs. siCL **(B)**.

investigated whether different flow patterns exert differential effects on EC p53 acetylation to regulate its expression. Exposure of ECs to OS for 12 or 24 h caused lower expression levels of acetylated-p53 and p53 proteins (**Figure 5A**) and higher levels of phospho-Rb and cyclin A proteins (**Figure 5B**) in these ECs in comparison to PS-stimulated cells. Knockdown of CBP by its specific siRNAs resulted in downregulation of acetylated-p53 and upregulation of phospho-Rb and cyclin A expressions in both PS- and OS-stimulated ECs (**Figure 5B**). These results suggest that the OS-mediated decreases in p53 expression in ECs may be attributable, at least in part, to the decreased expression of CBP, which resulted in reduction of p53 acetylation in ECs in response to OS.

MiR-487a Plays Important Roles in Modulating EC Proliferation in Response to OS *in vivo* and *in vitro*

To assess whether miR-487a is involved in OS-induced EC proliferation *in vivo*, we used a stenosis model in which the rat abdominal aorta was subjected to partial constriction by using a U-clip (**Figure 6A**; Zhou et al., 2012). This placement of the U-clip resulted in a 65% constriction of the aorta diameter, which induced an accelerated forward pulsatile flow pattern in the constricted region, followed by a pronounced oscillating flow with the existence of retrograde velocities in the downstream region of poststenotic dilatation (Zhou et al., 2012). Anti-miR-487a or control miR was locally injected into the affected aorta during 40 min of vascular occlusion and then removed before flow resumption. The cell proliferation marker bromodeoxyuridin (BrdU) was administered intravenously 24 h before sacrifice. *En face* immunostaining showed that miR-487a was highly expressed in ECs in the downstream OS region in control animals (**Figure 6B**). This upregulation of EC miR-487a in the downstream OS region was accompanied by significant increases in the BrdU uptake as compared with the upstream PS region (**Figures 6B,C**). *In vivo* administration with anti-miR-487a resulted in inhibitions in miR-487a expression and BrdU uptake in ECs in the downstream OS region. This miR-487a-mediated EC proliferation induced by disturbed flow with OS *in vivo* was substantiated by our *in vitro* flow assay, which shows that applications of OS and PS to ECs for 24 h result in upregulation and downregulation of BrdU uptake in ECs in comparison to control cells, respectively (**Figures 6D,E**). Transfecting ECs with anti-miR-487a inhibited OS-induced BrdU uptake in ECs, whereas overexpression of pre-miR-487a increased BrdU uptake in PS-stimulated and control cells. Taken together, our results indicate that miR-487a plays important roles in modulating EC proliferation in response to OS *in vivo* and *in vitro*.

DISCUSSION

This study has identified EC miR-487a as a novel mechanoresponsive miR, whose expression can be induced by disturbed flow with OS to promote EC proliferation *in vitro* and *in vivo*. This disturbed flow–induction of miR-487a was mediated by BMPR-specific Smad5, which promotes miR-487a processing in ECs in response to disturbed flow. Several lines of evidence support this conclusion (summarized in **Figure 7**). First, exposure of ECs to OS but not PS induced miR-487a

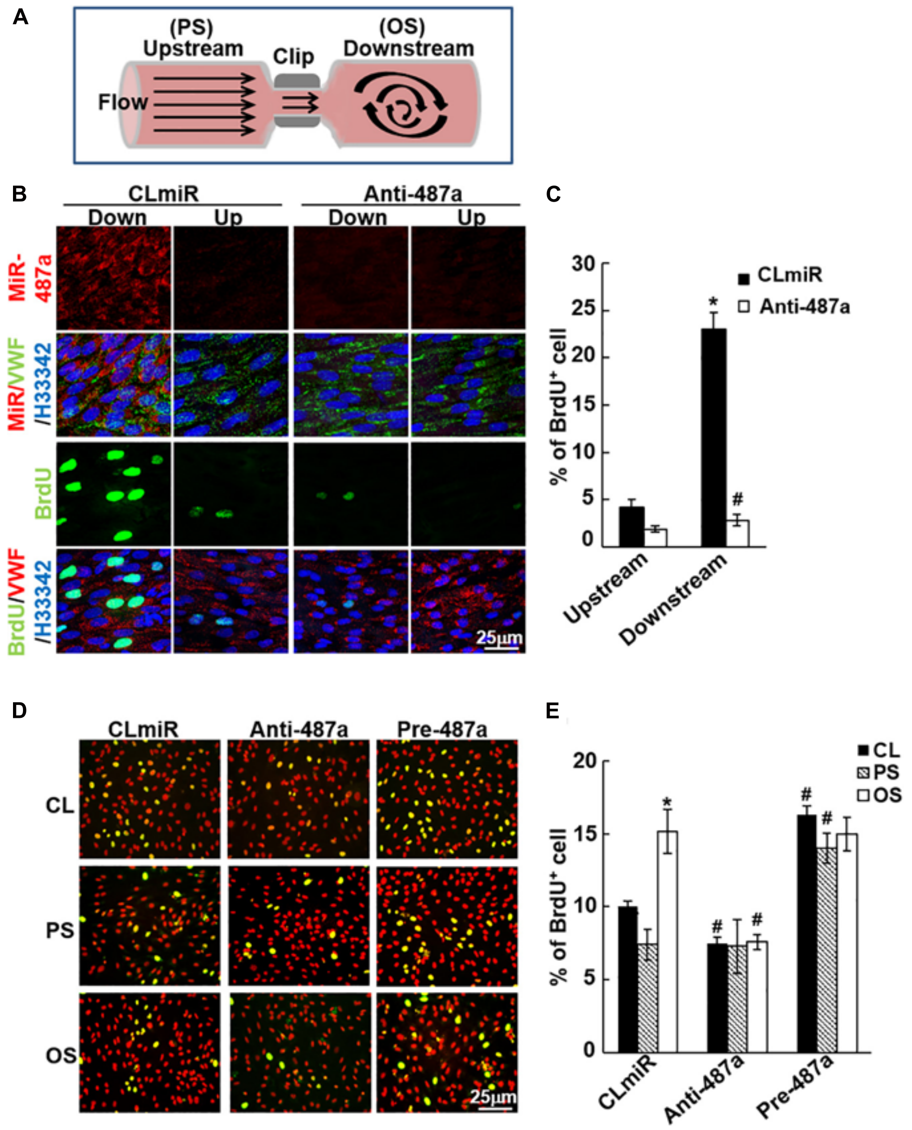

FIGURE 6 | MiR-487a enhances EC proliferation in response to OS *in vivo* and *in vitro*. **(A)** Schematic diagram showing the creation of stenosis in the rat abdominal aorta by using a U-shaped clip. **(B)** Anti-miR-487a or control saline ($n = 5$ each) was mixed with invivofectamine (Invitrogen) and injected into the rat abdominal aorta that had been subjected to stenosis using a U-clip. BrdU was injected i.v. into the rats 1 week after surgery and 1 day before sacrifice. *En face* staining of miR-487a, BrdU, vWF, and H33342 was performed on the luminal surfaces of the affected aortas. **(C)** Statistic data showing that anti-miR-487a administration inhibits disturbed flow-induced BrdU uptake in ECs in regions downstream to constricted areas. Data are mean ± SEM from three independent experiments. $^{*}P < 0.05$ vs. upstream area. $^{\#}P < 0.05$ vs. CLmiR. **(D,E)** ECs were transfected with anti-miR-487a (Anti-487a) or pre-miR-487a (Pre-487a) for 48 h and then were kept as static controls or exposed to OS or PS. BrdU incorporation assay was performed. Data are mean ± SEM from three independent experiments. $^{*}P < 0.05$ vs. static controls. $^{\#}P < 0.05$ vs. CLmiR.

expression in ECs with increased enrichment of miR-487a in the Ago2-containing miRISC. This OS-induction of miR-487a was also observed in the EC layer of athero-susceptible, disturbed flow regions in rat aortic arch *in vivo* and diseased human coronary arteries. Second, application of OS to ECs induced activation of Smad5, which bound to the R-SBE of primary miR-487a in EC nuclei to promote the processing and maturation of miR-487a. Third, miR-487a can bind to the 3′UTR of CBP and p53 to inhibit their expressions in ECs in response to OS. These OS-inhibitions of CBP and p53 expressions resulted in increases in Rb phosphorylation and cyclin A expression in ECs. Fourth, application of OS to ECs resulted in decreases in acetylation levels of p53. These responses were attributable, at least in part, to the OS-reduction of CBP, which is shown to acetylate and, hence, stabilize p53. Finally, knockdown of miR-487a by its antagomir inhibited OS-induced EC proliferation *in vitro* and *in vivo*, indicating the important roles of miR-487a in promoting EC proliferation in response to OS. Thus, our findings provide new insights into the mechanisms by which disturbed flow with OS activates Smad protein to induce the processing and maturation

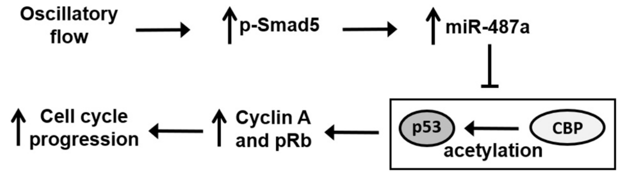

FIGURE 7 | Schematic diagram of miR-487a signaling and its modulation in gene expression and function in ECs in response to OS. OS activates Smad5 to promote miR-487a processing, which directly targets the 3′UTR of CBP and p53 to repress their expressions, thus inhibiting their anti-proliferative function through the inhibition in Rb phosphorylation and cyclin A expression, leading to cell cycle progression and proliferation.

of miR-487a in ECs, which can directly target CBP and p53 to induce Rb phosphorylation and cyclin A expression with the consequent promotion of EC proliferation.

MiRs have been shown to play pivotal roles in modulating signaling, gene expression, and functions in ECs and, hence, vascular biology and pathobiology in health and diseases (Donaldson et al., 2018). There is accumulating evidence that different flow patterns and shear stresses may play differential roles in modulating miR expression in ECs with the consequent modulation in EC function and atherogenesis. Although laminar or pulsatile flow with PS upregulates a set of EC miRs, including miR-23b (Wang et al., 2010), miR-10a (Lee et al., 2017), miR-126 (Mondadori dos Santos et al., 2015), miR-30-5p (Demolli et al., 2015), miR-181b (Sun et al., 2014), miR-143/145 (Kohlstedt et al., 2013; Schmitt et al., 2014), and miR-146a (Chen et al., 2015) to inhibit EC proliferation or inflammation, disturbed flow with OS upregulates miR-92a (Wu et al., 2011), miR-663 (Ni et al., 2011), miR-712 (Son et al., 2013), and miR-21 (Zhou et al., 2011) to promote EC pro-inflammatory responses and atherogenesis. In the present study, we demonstrated for the first time that miR-487a is a novel mechanoresponsive miR in ECs that can be induced by disturbed flow with OS. This disturbed flow–induction of EC miR-487a is attributable to the promotion of miR-487a processing but not primary miR-487a expression in ECs in response to disturbed flow. Several lines of evidence support this notion. First, application of OS to ECs reduced the expression of primary miR-487a in ECs. Second, mature miR-487a was significantly enriched in the Ago2-containing miRISC in OS-stimulated ECs, indicating that OS induces the expression of functional miR487a in ECs. Third, the *in vitro* pri-miR processing assay, in which biotin-labeled pri-miR487a substrates are incubated with nuclear extracts from sheared ECs, demonstrated that OS induces increases in EC pre-miR-487a expression. Fourth, *en face* immunostaining using an LNA-miR-487a probe to detect the mature form of miRs *in situ* (Nuovo, 2008) showed that mature miR-487a is highly expressed in the EC cytoplasm in the disturbed flow region of the rat aortic arch and experimentally stenosed abdominal aorta *in vivo*. Thus, our findings indicate that disturbed flow induces the processing and maturation, but not transcription, of miR-487a in ECs.

Smad proteins (Davis et al., 2008) and other cofactors, including KSRP (Trabucchi et al., 2009), FUS/TLS (Morlando et al., 2012), and YAP (Mori et al., 2014) are shown to be able to associate with microprocessor proteins Drosha and DGCR8 to regulate the processing of miRs in cells (Gregory et al., 2006; Han et al., 2006). Our previous studies demonstrate that disturbed flow with OS induces the activation of BMPR-specific Smad1/5 in ECs to contribute to their cell cycle progression and proliferation and, hence, atherogenesis (Zhou et al., 2012). Because miR-487a contains the putative RNA-Smad binding elements within the stem region of the primary transcript (Davis et al., 2010), we hypothesized that this OS-activation of BMPR-specific Smads may participate in the OS-induced processing of miR-487a in ECs. This hypothesis was confirmed by the following findings. First, knockdown of Smad5 abolished the OS-induction of mature miR-487a but had no effect on primary miR-487a expression in ECs. Second, the RNA-IP assay demonstrated that OS induces association of Smad5 with pri-miR-487a in ECs. Third, Smad5-IP, RNA-EMSA, and *in vitro* processing assays demonstrated that Smad5 can bind to the R-SBE element of pri-miR-487a to induce its processing in ECs in response to OS. It is known that primary miRs are transcribed and processed to precursor miRs in the nucleus (Kim et al., 2009) and that Smads' activation upon TGF-β/BMP stimulation is accompanied by their nuclear translocation to reach the regulatory targets (Chen and Xu, 2011). In the present study using a nuclear fractionation assay found that the levels of phospho-Smad5, but not Drosha, in the nucleus are much higher in ECs subjected to OS stimulation as compared with static control and PS-stimulated ECs. This fractionation assay further demonstrated that application of OS to ECs results in an increase in Smad5-pri-miR-487a complex formation in EC nuclei in comparison to static and PS-stimulated cells. Thus, our findings indicate that disturbed flow can activate Smad5 and increase its localization to EC nuclei to enhance its binding to pri-miR-487a, thereby promoting miR-487a processing in ECs.

As shown in **Table 1**, miR-21 is also upregulated by OS and has the RNA-Smad binding element. This result is in agreement with the results of our previous study, which shows that the transcriptional level of miR-21 could be upregulated by disturbed flow with OS *via* the c-Jun signaling pathway in ECs (Zhou et al., 2011). In addition, Smad1/5 are shown to modulate miR-21 processing in human pulmonary arterial smooth muscle cells in response to BMPs (Davis et al., 2008, 2010). Thus, it is possible that disturbed flow with OS could regulate the processing of miR-21 in ECs *via* the activated Smad5. However, Weber et al. (2010) found that application of prolonged unidirectional shear stress (15 dynes/cm^2) to ECs for 24 h could upregulate miR-21 expression in these ECs. These results implicate that the mechanisms underlying shear stress–regulated miR-21 expression in ECs are complicated and warrant further investigation.

Recent studies show that miR-487a is upregulated in several types of tumor cells to regulate genes involved in tumor progression, including sprouty-related EVH1 domain containing two (Chang et al., 2017), phosphoinositide-3-kinase regulatory subunit 1 (Chang et al., 2017), breast cancer resistance protein (Ma et al., 2013), and membrane-associated guanylate kinase inverted 2 (Ma et al., 2016). However, the role of miR-487a and its molecular mechanisms in modulating EC functions and vascular biology remained unclear. Our present study provides the first evidence that miR-487a can regulate cell cycle regulatory proteins in ECs and their proliferation in response to OS. *In silico* analysis predicted that miR-487a can directly target CBP and p53 in cells. The present study on ECs has validated this bioinformatics prediction by using the luciferase reporter and Ago2-IP assays to show that miR-487a can bind to the 3′UTR of CBP and p53 in ECs and that CBP- and p53-3′UTRs are enriched in miRISCs in ECs overexpressing miR-487a or subjected to OS. Knockdown and overexpression of miR-487a resulted in upregulation and downregulation of CBP and p53 in ECs, respectively. Moreover, subjection of ECs to OS resulted in downregulation of CBP and p53 in comparison to PS-stimulated ECs. This OS-mediated downregulation of CBP and p53 in ECs can be rescued by knockdown of miR-487a. The regulatory roles of miR-487a in EC cell cycle and proliferation through CBP and p53 were further substantiated by their regulations of Rb phosphorylation and cyclin A expression in ECs. Overexpression of miR-487a and knockdowns of CBP and p53 resulted in increases in Rb phosphorylation and cyclin A expression in ECs. Taken together, our data provide new insights into the mechanisms by which disturbed flow with OS induces EC cycle progression and proliferation by directly targeting CBP and p53 and their regulations in Rb phosphorylation and cyclin A expression in ECs.

The acetylation level of p53 is correlated to its activation and stabilization (Brooks and Gu, 2011). Zeng et al. (2003) found that laminar flow with LS increases the level of acetylation of p53 at lysine 382, which is recognized as the CBP/p300 acetylation site (Zeng et al., 2003). In the present study, we found that application of OS to ECs reduces the level of acetylation of p53 at lysine 382 as compared with PS-stimulated cells. Knockdown of CBP resulted in decreases in p53 acetylation at lysine 382 and its expression in ECs. These findings suggest that OS-reduction of p53 expression in ECs may be attributable, at least in part, to the downregulation of CBP, which leads to decreases in p53 acetylation and, hence, its expression in OS-stimulated ECs.

The present study has the following physiological and pathophysiological significance. We have characterized miR-487a as an important mechanoresponsive molecule that connects the chain of events of disturbed flow, mechanical sensing, and EC cycle progression and proliferation in the arterial wall. We also present evidence that the role of miR-487a in modulating OS-induced EC proliferation is mediated through its regulation of CBP and p53 expressions and downstream Rb phosphorylation and cyclin A expression. Our findings that OS induces bindings of Smad5 to the R-SBE element of pri-miR-487a to increase the Smad5-pri-miR-487a complex formation in EC nuclei indicate that OS induces the processing and maturation of miR-487a in ECs. In concert with the previous findings that the miR-487a level is upregulated in serum of patients with atypical coronary artery disease in comparison to healthy controls (Wang et al., 2014), our present data that miR-487a is highly expressed in the EC layer of athero-susceptible regions of the rat aortic arch and abdominal stenosed aorta and diseased human coronary arteries implicate that EC miR-487a may play important roles in the formation and progression of atherosclerosis.

In summary, the present study used a combination of cell culture, experimental animals, and clinical specimens to demonstrate that endothelial miR-487a expression is induced by disturbed flow with OS both *in vitro* and *in vivo* (including the endothelial layers of rat aorta subjected to different flow patterns and diseased human coronary arterial wall) with consequent promotion of EC proliferation. Our findings suggest that endothelial miR-487a may be a promising molecular target for therapeutic intervention against vascular disorders associated with disturbed flow-induced EC dysfunction, such as atherosclerosis.

DATA AVAILABILITY STATEMENT

The datasets presented in this study can be found in online repositories. The names of the repository/repositories and accession number(s) can be found in the article/**Supplementary Material**.

ETHICS STATEMENT

The studies involving human participants were reviewed and approved by The Hospital Human Subjects Review Committee and Ethics Review Board of the National Health Research Institutes (Number: EC1020901-E). The patients/participants provided their written informed consent to participate in this study. The animal study was reviewed and approved by National Institutes of Health guidelines and with the approval of the Animal Research Committee of National Health Research Institutes.

AUTHOR CONTRIBUTIONS

W-LW, L-JC, S-YW, Y-TS, Y-HH, P-LL, C-IL, M-CW carried out experimental work. W-LW, J-JC designed experiments. W-LW, D-YL, SC, and J-JC participated in discussion and wrote manuscript. J-JC supervised research work. All authors contributed to the article and approved the submitted version.

FUNDING

This work was supported by the grants MOST 109-2326-B-400-006, MOST 109-2320-B-400-010-MY3, and TMU 108-AE1-B51 (to J-JC).

SUPPLEMENTARY MATERIAL

The Supplementary Material for this article can be found online at: https://www.frontiersin.org/articles/10.3389/fcell.2021.647714/full#supplementary-material

REFERENCES

Bartel, D. P. (2009). MicroRNAs: target recognition and regulatory functions. *Cell* 136, 215–233. doi: 10.1016/j.cell.2009.01.002

Brooks, C. L., and Gu, W. (2011). The impact of acetylation and deacetylation on the p53 pathway. *Protein Cell* 2, 456–462. doi: 10.1007/s13238-011-1063-9

Chang, R. M., Xiao, S., Lei, X., Yang, H., Fang, F., and Yang, L. Y. (2017). MiRNA-487a promotes proliferation and metastasis in hepatocellular carcinoma. *Clin. Cancer Res.* 23, 2593–2604. doi: 10.1158/1078-0432.CCR-16-0851

Chen, L. J., Chuang, L., Huang, Y. H., Zhou, J., Lim, S. H., Lee, C. I., et al. (2015). MicroRNA mediation of endothelial inflammatory response to smooth muscle cells and its inhibition by atheroprotective shear stress. *Circ. Res.* 116, 1157–1169.

Chen, X., and Xu, L. (2011). Mechanism and regulation of nucleocytoplasmic trafficking of smad. *Cell Biosci.* 1, 40–47. doi: 10.1186/2045-3701-1-40

Chiu J. J., and Chien S. (2011). Effects of disturbed flow on vascular endothelium: pathophysiological basis and clinical perspectives. *Physiol. Rev.* 91, 327–387. doi: 10.1152/physrev.00047.2009

Davis, B. N., Hilyard, A. C., Lagna, G., and Hata, A. (2008). SMAD proteins control DROSHA-mediated microRNA maturation. *Nature* 454, 56–61. doi: 10.1038/nature07086

Davis, B. N., Hilyard, A. C., Nguyen, P. H., Lagna, G., and Hata, A. (2010). Smad proteins bind a conserved RNA sequence to promote microRNA maturation by Drosha. *Mol. Cell* 39, 373–384. doi: 10.1016/j.molcel.2010.07.011

de Planell-Saguer, M., Rodicio, M. C., and Mourelatos, Z. (2010). Rapid in situ codetection of noncoding RNAs and proteins in cells and formalin-fixed paraffin-embedded tissue sections without protease treatment. *Nat. Protoc.* 5, 1061–1073. doi: 10.1038/nprot.2010.62

Demolli, S., Doebele, C., Doddaballapur, A., Lang, V., Fisslthaler, B., Chavakis, E., et al. (2015). MicroRNA-30 mediates anti-inflammatory effects of shear stress and KLF2 via repression of angiopoietin 2. *J. Mol. Cell. Cardiol.* 88, 111–119. doi: 10.1016/j.yjmcc.2015.10.009

Donaldson, C. J., Lao, K. H., and Zeng, L. (2018). The salient role of microRNAs in atherogenesis. *J. Mol. Cell. Cardiol.* 122, 98–113. doi: 10.1016/j.yjmcc.2018.08.004

Goodman, R. H., and Smolik, S. (2000). CBP/p300 in cell growth, transformation, and development. *Genes Dev.* 14, 1553–1577. doi: 10.1101/gad.14.13.1553

Gregory, R. I., Chendrimada, T. P., and Shiekhattar, R. (2006). MicroRNA biogenesis: isolation and characterization of the microprocessor complex. *Methods Mol. Biol.*342, 33–47. doi: 10.1385/1-59745-123-1:33

Guil, S., and Caceres, J. F. (2007). The multifunctional RNA-binding protein hnRNP A1 is required for processing of miR-18a. *Nat. Struct. Mol. Biol.* 14, 591–596. doi: 10.1038/nsmb1250

Han, J., Lee, Y., Yeom, K. H., Nam, J. W., Heo, I., Rhee, J. K., et al. (2006). Molecular basis for the recognition of primary microRNAs by the Drosha-DGCR8 complex. *Cell* 125, 887–901. doi: 10.1016/j.cell.2006.03.043

Kim, V. N., Han, J., and Siomi, M. C. (2009). Biogenesis of small RNAs in animals. *Nat. Rev. Mol. Cell Biol.* 10, 126–139. doi: 10.1038/nrm2632

Kohlstedt, K., Trouvain, C., Boettger, T., Shi, L., Fisslthaler, B., and Fleming, I. (2013). AMP-activated protein kinase regulates endothelial cell angiotensin-converting enzyme expression via p53 and the post-transcriptional regulation of microRNA-143/145. *Circ. Res.* 112, 1150–1158. doi: 10.1161/CIRCRESAHA.113.301282

Kruse, J. P., and Gu, W. (2009). Modes of p53 regulation. *Cell* 137, 609–622. doi: 10.1016/j.cell.2009.04.0500

Lee, D. Y., Lin, T. E., Lee, C. I., Zhou, J., Huang, Y. H., Lee, P. L., et al. (2017). MicroRNA-10a is crucial for endothelial response to different flow patterns via interaction of retinoid acid receptors and histone deacetylases. *Proc. Natl. Acad. Sci. U.S.A.* 114, 2072–2077. doi: 10.1073/pnas.1621425114

Levine, A. J. (1997). p53, the cellular gatekeeper for growth and division. *Cell* 88, 323–331. doi: 10.1016/s0092-8674(00)81871-1

Li, M., Luo, J., Brooks, C. L., and Gu, W. (2002). Acetylation of p53 inhibits its ubiquitination by Mdm2. *J. Biol. Chem.* 277, 50607–50611. doi: 10.1074/jbc.C200578200

Lin, K., Hsu, P. P., Chen, B. P., Yuan, S., Usami, S., Shyy, J. Y., et al. (2000). Molecular mechanism of endothelial growth arrest by laminar shear stress. *Proc. Natl. Acad. Sci. U.S.A.* 97, 9385–9389. doi: 10.1073/pnas.170282597

Ma, M. T., He, M., Jiang, Q., Yan, Y., Guan, S., Zhang, J., et al. (2016). MiR-487a promotes TGF-β1-induced EMT, the migration and invasion of breast cancer cells by directly targeting MAGI2. *Int. J. Biol. Sci.* 12, 397–408. doi: 10.7150/ijbs.13475

Ma, M. T., He, M., Wang, Y., Jiao, X. Y., Zhao, L., Bai, X. F., et al. (2013). MiR-487a resensitizes mitoxantrone (MX)-resistant breast cancer cells (MCF-7/MX) to MX by targeting breast cancer resistance protein (BCRP/ABCG2). *Cancer Lett.* 339, 107–115. doi: 10.1016/j.canlet.2013.07.016

Mondadori dos Santos, A., Metzinger, L., Haddad, O., M'baya-Moutoula, E., Taïbi, F., Charnaux, N., et al. (2015). miR-126 is involved in vascular remodeling under laminar shear stress. *Biomed. Res. Int.* 2015, 497280. doi: 10.1155/2015/497280

Mori, M., Triboulet, R., Mohseni, M., Schlegelmilch, K., Shrestha, K., Camargo, F. D., et al. (2014). Hippo signaling regulates microprocessor and links cell-density-dependent miRNA biogenesis to cancer. *Cell* 156, 893–906. doi: 10.1016/j.cell.2013.12.043

Morlando, M., Dini, M. S., Torrelli, G., Rosa, A., Di, C. V., Caffarelli, E., et al. (2012). FUS stimulates microRNA biogenesis by facilitating co-transcriptional Drosha recruitment. *EMBO J.* 31, 4502–4510. doi: 10.1038/emboj.2012.319

Ni, C. W., Qiu, H., and Jo, H. (2011). MicroRNA-663 upregulated by oscillatory shear stress plays a role in inflammatory response of endothelial cells. *Am. J. Physiol. Heart Circ. Physiol.* 300, H1762–H1769. doi: 10.1152/ajpheart.00829.2010

Nuovo, G. J. (2008). In situ detectio of precursor andd mature microRNAs in paraffin embedded, formalin fixed tissues and cell preparations. *Methods* 44, 39–46. doi: 10.1016/j.ymeth.2007.10.008

Obikane, H., Abiko, Y., Ueno, H., Kusumi, Y., Esumi, M., and Mitsumata, M. (2010). Effect of endothelial cell proliferation on atherogenesis: a role of p21 (Sdi/Cip/Waf1) in monocyte adhesion to endothelial cells. *Atherosclerosis* 212, 116–122.

Schmitt, M. M., Megens, R. T., Zernecke, A., Bidzhekov, K., van den Akker, N. M., Rademakers, T., et al. (2014). Endothelial junctional adhesion molecule-a guides monocytes into flow-dependent predilection sites of atherosclerosis. *Circulation* 129, 66–76. doi: 10.1161/CIRCULATIONAHA.113.004149

Son, D. J., Kumar, S., Takabe, W., Kim, C. W., Ni, C. W., Alberts-Grill, N., et al. (2013). The atypical mechanosensitive microRNA-712 derived from pre-ribosomal RNA induces endothelial inflammation and atherosclerosis. *Nat. Commun.* 4:3000.

Sorescu, G. P., Sykes, M., Weiss, D., Platt, M. O., Saha, A., Hwang, J., et al. (2003). Bone morphogenic protein 4 produced in endothelial cells by oscillatory shear stress stimulates an inflammatory response. *J. Biol. Chem.* 278, 31128–31135. doi: 10.1074/jbc.M300703200

Sun, X., He, S., Wara, A. K. M., Icli, B., Shvartz, E., Tesmenitsky, Y., et al. (2014). Systemic delivery of microRNA-181b inhibits nuclear factor-kappaB activation, vascular inflammation, and atherosclerosis in apolipoprotein E-deficient mice. *Circ. Res.* 114, 32–40. doi: 10.1161/CIRCRESAHA.113.302089

Trabucchi, M., Briata, P., Garcia-Mayoral, M., Haase, A. D., Filipowicz, W., Ramos, A., et al. (2009). The RNA-binding protein KSRP promotes the biogenesis of a subset of microRNAs. *Nature* 459, 1010–1014. doi: 10.1038/nature08025

Tsai, M. C., Chen, L., Zhou, J., Tang, Z., Hsu, T. F., Wang, Y., et al. (2009). Shear stress induces synthetic-to-contractile phenotypic modulation in smooth muscle cells via peroxisome proliferator-activated receptor alpha/delta activations by prostacyclin released by sheared endothelial cells. *Circ. Res.* 105, 471–480. doi: 10.1161/CIRCRESAHA.109.193656

Wang, J., Pei, Y., Zhong, Y., Jiang, S., Shao, J., and Gong, J. (2014). Altered serum microRNAs as novel diagnostic biomarkers for atypical coronary artery disease. *PLoS One* 9:e107012. doi: 10.1371/journal.pone.0107012

Wang, K. C., Garmire, L. X., Young, A., Nguyen, P., Trinh, A., Subramaniam, S., et al. (2010). Role of microRNA-23b in flow-regulation of Rb phosphorylation and endothelial cell growth. *Proc. Natl. Acad. Sci. U.S.A.* 107, 3234–3239. doi: 10.1073/pnas.0914825107

Weber, M., Baker, M. B., Moore, J. P., and Searles, C. D. (2010). MiR-21 is induced in endothelial cells by shear stress and modulates apoptosis and eNOS activity. *Biochem. Biophys. Res. Commun.* 393, 643–648.

Wu, W., Xiao, H., Laguna-Fernandez, A., Villarreal, G. Jr., Wang, K. C., Geary, G. G., et al. (2011). Flow-dependent regulation of kruppel-like factor 2 is mediated by microRNA-92a. *Circulation* 124, 633–641. doi: 10.1161/CIRCULATIONAHA.110.005108

Zeng, L., Zhang, Y., Chien, S., Liu, X., and Shyy, J. Y. (2003). The role of p53 deacetylation in p21Waf1 regulation by laminar flow. *J. Biol. Chem.* 278, 24594–24599. doi: 10.1074/jbc.M301955200

Zhou, J., Lee, P. L., Tsai, C. S., Lee, C. I., Yang, T. L., Chuang, H. S., et al. (2012). Force-specific activation of Smad1/5 regulates vascular endothelial cell cycle progression in response to disturbed flow. *Proc. Natl. Acad. Sci. U.S.A.* 109, 7770–7775. doi: 10.1073/pnas.1205476109

Zhou, J., Wang, K. C., Wu, W., Subramaniam, S., Shyy, J. Y., Chiu, J. J., et al. (2011). MicroRNA-21 targets peroxisome proliferators-activated receptor-alpha in an autoregulatory loop to modulate flow-induced endothelial inflammation. *Proc. Natl. Acad. Sci. U.S.A.* 108, 10355–10360. doi: 10.1073/pnas.1107052108

Conflict of Interest: The authors declare that the research was conducted in the absence of any commercial or financial relationships that could be construed as a potential conflict of interest.

frontiers
in Cell and Developmental Biology

ORIGINAL RESEARCH
published: 13 May 2021
doi: 10.3389/fcell.2021.675562

Protein Phosphatase 2A Mediates YAP Activation in Endothelial Cells Upon VEGF Stimulation and Matrix Stiffness

Xiao Jiang[1†], Jiandong Hu[1†], Ziru Wu[1], Sarah Trusso Cafarello[2], Mario Di Matteo[2], Ying Shen[3], Xue Dong[1,4], Heike Adler[3], Massimiliano Mazzone[2], Carmen Ruiz de Almodovar[3*] and Xiaohong Wang[1,5*]

[1] Laboratory of Molecular Ophthalmology, Department of Pharmacology, Tianjin Key Laboratory of Inflammation Biology, School of Basic Medical Sciences, Tianjin Medical University, Tianjin, China, [2] Laboratory of Tumor Inflammation and Angiogenesis, Center for Cancer Biology, VIB, Leuven, Belgium, [3] European Center for Angioscience, Medicine Faculty Mannheim, Heidelberg University, Mannheim, Germany, [4] Department of Ophthalmology, Tianjin Medical University General Hospital, Tianjin, China, [5] Key Laboratory of Immune Microenvironment and Disease, Ministry of Education, School of Basic Medical Sciences, Tianjin Medical University, Tianjin, China

Angiogenesis is an essential process during development. Abnormal angiogenesis also contributes to many disease conditions such as tumor and retinal diseases. Previous studies have established the Hippo signaling pathway effector Yes-associated protein (YAP) as a crucial regulator of angiogenesis. In ECs, activated YAP promotes endothelial cell proliferation, migration and sprouting. YAP activity is regulated by vascular endothelial growth factor (VEGF) and mechanical cues such as extracellular matrix (ECM) stiffness. However, it is unclear how VEGF or ECM stiffness signal to YAP, especially how dephosphorylation of YAP occurs in response to VEGF stimulus or ECM stiffening. Here, we show that protein phosphatase 2A (PP2A) is required for this process. Blocking PP2A activity abolishes VEGF or ECM stiffening mediated YAP activation. Systemic administration of a PP2A inhibitor suppresses YAP activity in blood vessels in developmental and pathological angiogenesis mouse models. Consistently, PP2A inhibitor also inhibits sprouting angiogenesis. Mechanistically, PP2A directly interacts with YAP, and this interaction requires proper cytoskeleton dynamics. These findings identify PP2A as a crucial mediator of YAP activation in ECs and hence as an important regulator of angiogenesis.

Keywords: angiogenesis, YAP, PP2A, VEGF, matrix stiffness

OPEN ACCESS

Edited by:
Jing Zhou,
Peking University, China

Reviewed by:
Lei Chang,
Soochow University Medical College (SUMC), China
Stephan Huveneers,
Academic Medical Center, Netherlands

****Correspondence:***
Carmen Ruiz de Almodovar
carmen.ruizdealmodovar@medma.uni-heidelberg.de
Xiaohong Wang
xiaohongwang@tmu.edu.cn

[†] These authors have contributed equally to this work

Specialty section:
This article was submitted to Cell Adhesion and Migration, a section of the journal Frontiers in Cell and Developmental Biology

Received: *03 March 2021*
Accepted: *08 April 2021*
Published: *13 May 2021*

Citation:
Jiang X, Hu J, Wu Z, Cafarello ST, Di Matteo M, Shen Y, Dong X, Adler H, Mazzone M, Ruiz de Almodovar C and Wang X (2021) Protein Phosphatase 2A Mediates YAP Activation in Endothelial Cells Upon VEGF Stimulation and Matrix Stiffness. Front. Cell Dev. Biol. 9:675562. doi: 10.3389/fcell.2021.675562

INTRODUCTION

Extension of the vascular network is mediated by endothelial cell sprouting, migration, and proliferation. Recent studies have established Yes-associated protein (YAP), and its paralog transcriptional coactivator with PDZ-binding motif (TAZ; also known as WWTR1), as crucial regulators of angiogenesis (Kim et al., 2017; Wang et al., 2017). YAP/TAZ are the ultimate effectors of the Hippo signaling pathway. They shuttle between the cytoplasm and the nucleus, where they associate with transcriptional factor and regulate a set of target gene expression

(Yu et al., 2012; Moya and Halder, 2019). The activity of YAP/TAZ can be suppressed by the core components of hippo pathway, containing a kinase cascade including MST1/2 and LATS1/2. MST1/2 phosphorylate LATS1/2, which then phosphorylate YAP/TAZ, causing their cytoplasmic sequestration and subsequent degradation (Totaro et al., 2018).

The activity of YAP/TAZ can be regulated by soluble growth factors and physical signals (Panciera et al., 2017). During angiogenesis, both vascular endothelial growth factor (VEGF) and extracellular matrix (ECM) stiffening activate YAP/TAZ in endothelial cells (Shen et al., 2020). VEGF stimulus or high stiffness reduce phosphorylation of YAP, which further lead to YAP activation and nuclear translocation (Wang et al., 2017; Meng et al., 2018). Interestingly, phosphorylation of MST1 did not change in response to VEGF stimulus, suggesting a potential MST-independent regulation of YAP activity by VEGF (He et al., 2018). This raises the question of whether YAP/TAZ regulation involves phosphatase activity.

Multiple protein phosphatases are identified as YAP phosphatase, including protein phosphatase 1 (PP1), protein phosphatase 2A (PP2A), and PTPN14 in different cell types (Schlegelmilch et al., 2011; Wang et al., 2011, 2012). Interestingly, in dominant negative PP2A expressing cells, VEGF induced ECs migration was significantly abolished (Urbich et al., 2002), suggesting that PP2A activity might be required for a VEGF stimulated angiogenic response. As an abundant cellular serine/threonine phosphatase, PP2A is involved in numerous signaling pathways (Janssens and Goris, 2001). In endothelial cells, PP2A is involved in regulating angiogenesis, vascular permeability, vascular remodeling in development and disease conditions (Le Guelte et al., 2012; Martin et al., 2013; Yun et al., 2019; Ehling et al., 2020). A recent study showed that in endothelial cells, YAP was a direct target of PP2A, and PP2A was involved in disturbed flow mediated YAP activation via Integrinα5β1 (Yun et al., 2019). Based on these evidences, in this study we wondered whether PP2A mediates YAP dephosphorylation in response to VEGF or high stiffness during angiogenesis.

Here, we found that PP2A is required for VEGF or high stiffness stimulated angiogenic responses. We demonstrate that the integrity of cytoskeleton is required for this regulation. *In vivo* pharmacological inhibition of PP2A activity reduced EC proliferation and inhibited angiogenesis in developmental and pathological angiogenesis models. These results provide further insight into the regulatory mechanism of YAP in ECs during angiogenesis.

RESULTS

PP2A Regulates YAP Activity in ECs

We first determined whether PP2A regulates YAP activity in endothelial cells. For this, we used LB100, a pan-PP2A inhibitor that blocks the catalytic PP2A subunit (Hong et al., 2015). By checking the phosphorylation status of YAP, we found that LB100 treatment resulted in a hyper-phosphorylation of YAP in human umbilical vein endothelial cells (HUVECs) (**Figures 1A,B**). As the phosphorylation of YAP leads to cytoplasmic sequestration and inactivation, we further checked the subcellular localization of YAP. LB100 treatment time-dependently increased cytoplasmic localized YAP in HUVECs (**Figures 1C,D**). Analysis of mRNA levels of YAP/TAZ target genes *CTGF and CYR61* also showed a dose dependent decrease upon LB100 treatment (**Figures 1E,F**).

Next, we constructed an adenovirus vector expressing a dominant negative mutant form of the catalytic subunit C of PP2A, L199P (L199P and DN-PP2Ac), which is catalytically impaired (Evans et al., 1999). Wild-type (WT) PP2A catalytic C subunit (PP2Ac and WT-PP2Ac) were used as control. As Akt is known to be a PP2A substrate (Li et al., 2012; Tobisawa et al., 2017), we used phospho-Akt as a positive control. By infecting HUVECs with WT-PP2Ac or DN-PP2Ac adenovirus, we found that DN-PP2Ac indeed increased phospho-Akt (**Figure 1G**). Consistently, DN-PP2Ac also increased phospho-YAP, suggesting PP2A activity is required for YAP activation (**Figure 1G**).

PP2A Activity Is Required for VEGF or High Stiffness Mediated YAP Activation

Next, we aimed to understand whether PP2A is required for VEGF or high stiffness mediated YAP activation. For this, we used HUVECs transduced with WT-PP2Ac and DN-PP2Ac adenovirus and analyzed the subcellular localization of YAP. In WT-PP2Ac expressing cells, VEGF induced YAP nuclear translocation. However, in DN-PP2Ac expressing cells, VEGF failed to do so (**Figures 2A,B**). Similarly, high matrix stiffness increased nuclear localized YAP in WT-PP2Ac expressing cells, but not in DN-PP2Ac cells (**Figures 2C,D**). Additionally, DN-PP2Ac alone caused a significant reduction of nuclear localized YAP in all conditions (**Figures 2A–D**). Analysis of mRNA levels of *CTGF, CYR61*, and *ANGPT2* also revealed that YAP target genes upregulation induced by VEGF was only observed in WT-PP2Ac expressing ECs, but not in DN-PP2Ac ECs (**Figures 2E–G**). Again, with or without VEGF stimulation, DN-PP2Ac significantly reduced the gene expression of YAP target genes *CTGF, CYR61*, and *ANGPT2* compared with WT-PP2Ac (**Figures 2E–G**).

VEGF or High Stiffness-Mediated EC Proliferation and Angiogenesis Requires PP2A Activity

Yes-associated protein activity is required for multiple process during angiogenesis, including EC proliferation, migration and sprouting (Kim et al., 2017; Wang et al., 2017; Shen et al., 2020). To explore the biological consequences of PP2A mediated activation in response to VEGF or high stiffness, we performed a set of *in vitro* angiogenesis assays. To test whether PP2A has an effect on EC proliferation, we performed a BrdU incorporation assay in HUVECs infected by WT- or DN-PP2Ac expressing adenovirus. As expected, VEGF increased EC proliferation in WT-PP2Ac group, but had no obvious effect in DN-PP2Ac group (**Figures 3A,B**). To further understand the role of PP2A in stiffness regulated EC proliferation, we seeded HUVECs on polyacrylamide (PA) hydrogels with high or low stiffness.

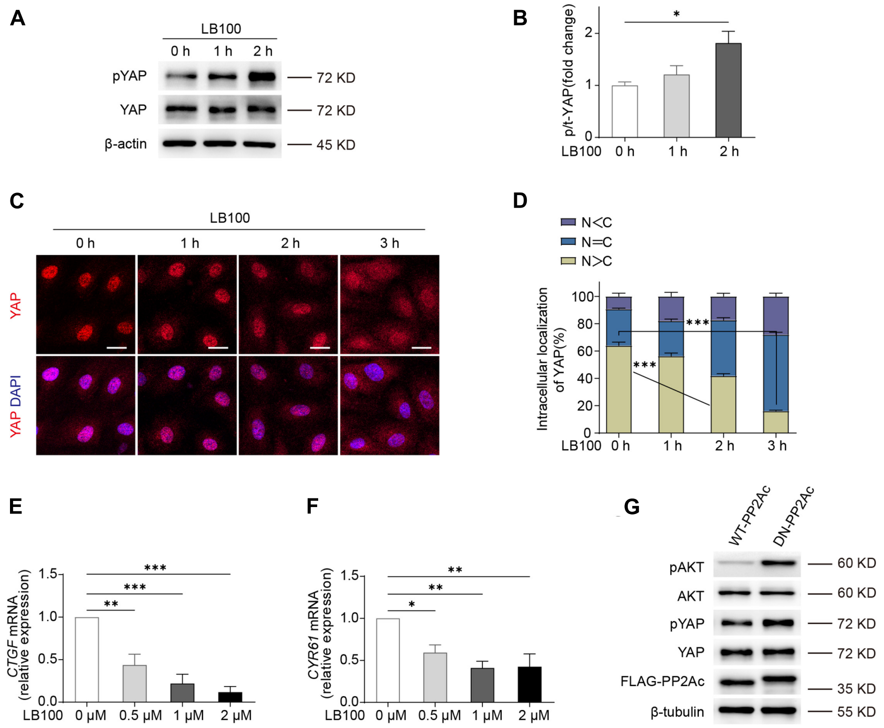

FIGURE 1 | PP2A regulate YAP activity in ECs. **(A)** Western blot detection YAP phosphorylation status treated with 2 μM LB100 for the indicated time points. **(B)** Quantification of western blot shown in **(A)**. $n = 4$ independent experiments. **(C)** Representative images of HUVECs stimulated with 2 μM LB100 for the indicated time points and stained for YAP and DAPI. **(D)** Quantification of YAP subcellular localization treated as in **(C)**. Data from approximately 200 cells from 12 random fields of view (at least three independent experiments). N, nucleus; C, cytosol. N < C, nuclear staining was weaker than cytoplasm; N = C, nuclear staining was equal to cytoplasm; N > C, nuclear staining is stronger than cytoplasm. **(E,F)** qPCR analysis the expression of YAP target genes *CTGF, CYR61* in HUVEC treated with indicated dose of LB100 for 24 h. **(G)** Representative western blot showing pYAP status in HUVECs infected with WT-PP2Ac and DN-PP2Ac adenovirus for 36 h, pAkt was used as a positive control. Data are shown as mean ± SEM, one-way ANOVA followed by Tukey's multiple comparisons test. $^{*}p < 0.05$, $^{**}p < 0.01$, $^{***}p < 0.001$, ns indicates not significant. Scale bars, 20 μm.

Similarly, while high stiffness increased proliferation in WT-PP2Ac expressing ECs, this effect was not observed in DN-PP2Ac expressing ECs (**Figures 3C,D**).

Expansion of the vasculature also requires ECs migration. *In vitro* scratch assay showed that while VEGF significantly induced EC migration and the closure of the gap in WT-PP2Ac expressing ECs, this effect was abolished in DN-PP2Ac ECs (**Figures 3E,F**). Consistently, DN-PP2Ac ECs failed to form *lamellipodia* after VEGF stimulation (**Supplementary Figures 1A,B**; Carvalho et al., 2019). Cell migration establishment also requires front-rear cell polarity. YAP/TAZ is required for cell polarity regulation, as depletion of YAP/TAZ impairs Golgi polarization in a wound scratch model (Mason et al., 2019). We therefore tested whether PP2A is also required for VEGF induced Golgi polarization. For this, we stained GM130 to label Golgi apparatus in the wound scratch model (**Figure 3G**), and quantified the polarity index of ECs (**Figure 3H**). VEGF increased significant Golgi polarization in both leading cells and following cells in WT-PP2Ac expressing ECs, but not in DN-PP2Ac ECs, suggesting that PP2A activity is also needed for cell polarity establishment (**Figures 3I–L**).

Yes-associated protein subcellular localization and activity are regulated by cell-cell interaction and cytoskeleton tension. In confluent endothelial monolayer, YAP nuclear enrichment increased preferentially in migrating cells beyond the wound edge in a wound scratch model (Mason et al., 2019), which contributes to the regulation of cell migration. However, in DN-PP2Ac expressing ECs, the nuclear enrichment of YAP in the wound edge was not observed, suggesting PP2A activity is required for YAP activation during cell migration (**Figures 3M,N**).

Cell geometry can be affected by matrix rigidity. High stiffness increases the spread cell area and elongation in ECs, and this morphological change could be regulated by YAP/TAZ (Dupont et al., 2011; Mason et al., 2019). By quantifying the spread cell area and elongation in WT-PP2Ac or DN-PP2Ac adenovirus infected ECs growing on soft or stiff matrix, we found that increasing the matrix stiffness significantly increased the cell spreading area and elongation in WT-PP2Ac ECs, however, this was not observed in DN-PP2Ac ECs (**Supplementary Figures 1C–E**). These data further suggest that PP2A is also involved in cell geometry change in response to matrix stiffness.

Yes-associated protein/TAZ is also crucial in regulating sprouting during angiogenesis (Wang et al., 2017). To evaluate the role of PP2A in vessel sprouting, we performed an *ex vivo* aortic ring assay. The quantification showed that inhibiting PP2A activity by LB100 significantly reduced vascularization

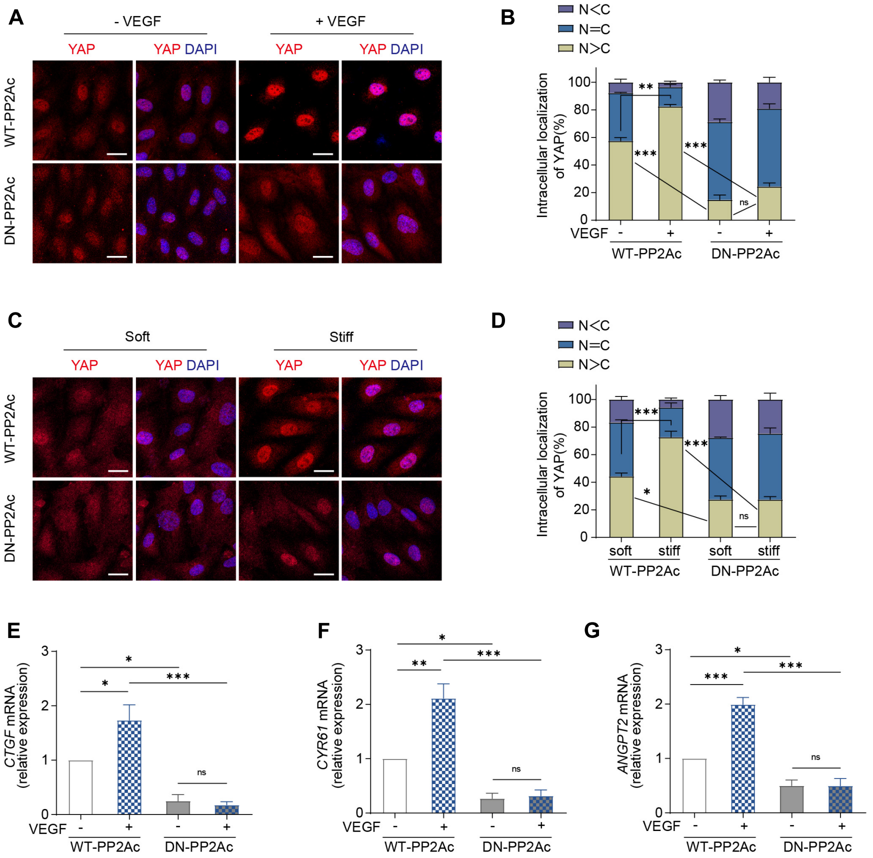

FIGURE 2 | VEGF or high stiffness activation of YAP requires PP2A activity. **(A)** Representative images of YAP localization in HUVECs infected with WT-PP2Ac, DN-PP2Ac adenovirus for 24 h, starved in 2% FBS medium for another 12 h, and treated with or without 50 ng/mL VEGF for 3 h. **(B)** Quantification of YAP cellular localization for HUVECs treated as in **(A)**. Approximately 200 cells from 12 random fields of view from three independent experiments were quantified. N, nucleus; C, cytosol. **(C)** HUVECs were infected with WT-PP2Ac, DN-PP2Ac adenovirus for 36 h. The cells were then trypsinized and seeded on soft (0.2 kpa) and stiff (20 kpa) hydrogels. After 3 h, the cells were fixed and stained for YAP and DAPI. **(D)** Quantification of YAP cellular localization in HUVECs treated as in **(C)**. N, nucleus; C, cytosol. **(E–G)** Relative mRNA level of *CTGF* **(E)**, *CYR61* **(F)**, and *ANGPT2* **(G)** in HUVECs infected with WT-PP2Ac, DN-PP2Ac adenovirus, serum starved and stimulated with 50 ng/mL VEGF. Data are shown as mean ± SEM, one-way ANOVA followed by Tukey's multiple comparisons test. $^{*}p < 0.05$, $^{**}p < 0.01$, $^{***}p < 0.001$, ns indicates not significant. Scale bars, 20 μm.

and sprouting in the aortic ring model (**Supplementary Figures 1F,G**).

PP2A Inhibition Impairs Developmental Angiogenesis *in vivo*

During embryonic mouse spinal cord development, VEGF expressed by the neuroepithelium activates YAP/TAZ in ECs and promotes vascularization (Wang et al., 2017). Thus, we explored whether PP2A activity is required for this process. For this, LB100 was administrated to pregnant females at embryonic day 11.5 (E11.5) and the embryos were dissected 4 h after injection (**Figure 4A**). Immunofluorescence showed that the nuclear localized YAP in ECs in LB100 treated group was significantly reduced (**Figures 4B,C**), suggesting that PP2A activity is required in ECs for YAP activation during developmental angiogenesis. Consistent with the inhibition of YAP activation, and the role of YAP in EC proliferation, we also detected reduced EC proliferation in spinal cords of LB100 (4 h) treated embryos (**Figures 4D,E**). We also dissected the embryos 24 h after LB100 injection (**Figure 4F**) and analyzed EC proliferation and vascularization. Consistently, LB100 treatment also reduced EC proliferation and blood vascular density in embryos 24 h after LB100 injection in pregnant females (**Figures 4G,I**). In addition, blood vessel density in the developing cortex also showed that LB100 treatment limited EC proliferation and impaired vascularization in another region of the central nervous system (**Figures 4J–L**).

PP2A Inhibition Suppresses Pathological Retinal Angiogenesis in the Oxygen-Induced Retinopathy Model

We next aimed to explore whether inhibiting PP2A activity is also necessary for pathological angiogenesis in the nervous system. For this, we deployed an oxygen-induced retinopathy (OIR) mouse model, which resembles human retinopathy of prematurity (ROP) and certain aspects of proliferative diabetic

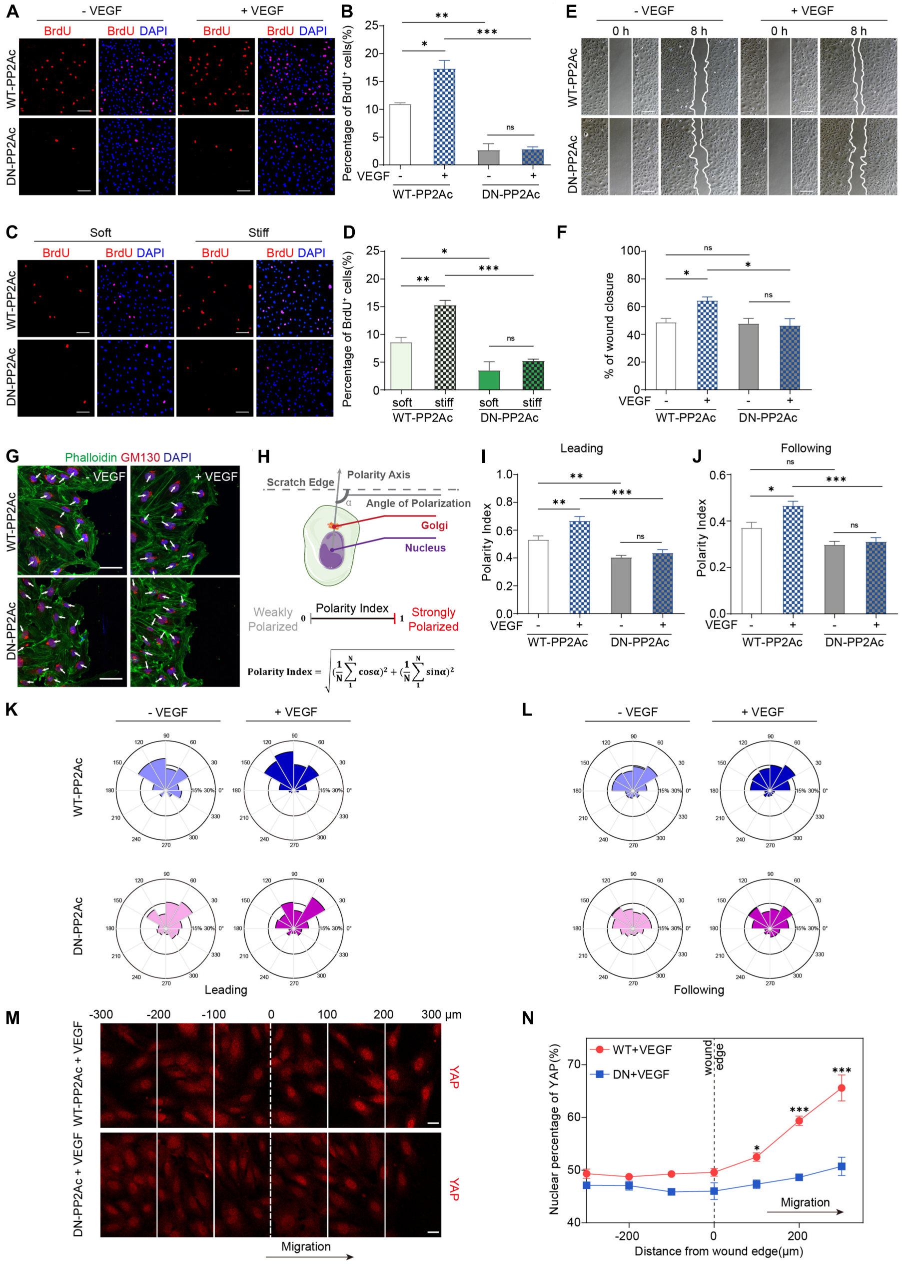

FIGURE 3 | PP2A activity is required for EC proliferation and migration. **(A)** BrdU incorporation of HUVECs infected with WT-PP2Ac or DN-PP2Ac adenovirus, serum starved and stimulated with 50 ng/mL VEGF. **(B)** Quantification of BrdU$^+$ cells of **(A)**. Data from 15 random fields of view (at least three independent experiments) were quantified. **(C)** HUVECs were infected with WT-PP2Ac orDN-PP2Ac adenovirus, trypsinized and seeded on soft (0.2 kpa) and stiff (20 kpa) hydrogels. After 6 h, the cells were fixed and stained for BrdU incorporation. **(D)** Quantification of BrdU$^+$ cells of **(C)**. Cells from 12 random fields of view, from at least three independent experiments were quantified. **(E)** HUVECs were infected with WT-PP2Ac or DN-PP2Ac and the wound scratch assay was performed. Representative bright field images of the scratch assay showing HUVECs migration after 50 ng/mL VEGF treatment for 8 h. **(F)** Quantification of wound closure from **(E)**. Approximately 40 fields of view from five independent experiments were quantified. **(G)** Representative images of the wound scratch assay showing the polarity angles of WT- PP2Ac or DN-PP2Ac HUVECs after 50 ng/mL VEGF treatment for 8 h. GM130 labels Golgi apparatus. **(H)** Schematic of the Polarity Index calculation. Polarity axis of each cell was defined as the angle (α) between the scratch edge and the cell polarity axis (nucleus-to-Golgi apparatus vector). The polarity index was calculated according to the formula. **(I,J)** Polarity index of WT-PP2Ac or DN-PP2Ac leading cells **(I)** and following cells **(J)**. *n* = 100–120 leading cells and 320–350 following cells from three independent experiments. **(K,L)** Angular histograms showing the distribution of polarization angles of leading cells **(K)** and following cells **(L)**. *n* = 100–120 leading cells and 320–350 following cells from three independent experiments. **(M)** HUVECs were infected with WT-PP2Ac or DN-PP2Ac adenovirus for 30 h, afterward, the cells were starved for 12 h and a wound was made by scraping the confluent monolayer. 50 ng/mL VEGF was added in the medium. After 8 h, the cells were fixed and stained for YAP and DAPI. Representative immunofluorescent images of YAP localization were subdivided into 100 μm region of interests. The original wound edge was labeled as "0." **(N)** Quantification of nuclear YAP fluorescence intensity of **(M)**. *n* = 7 fields from three independent experiments per condition. Data are shown as mean ± SEM, one-way ANOVA followed by Tukey's multiple comparisons test in **(B,D,F,I,J)**, two-way ANOVA followed by Sidak multiple comparisons test in **(N)**. *$p < 0.05$, **$p < 0.01$, ***$p < 0.001$, ns indicates not significant. Scale bars, 100 μm in **(A,C,E)** and 50 μm in **(G)**, 20 μm in **(M)**.

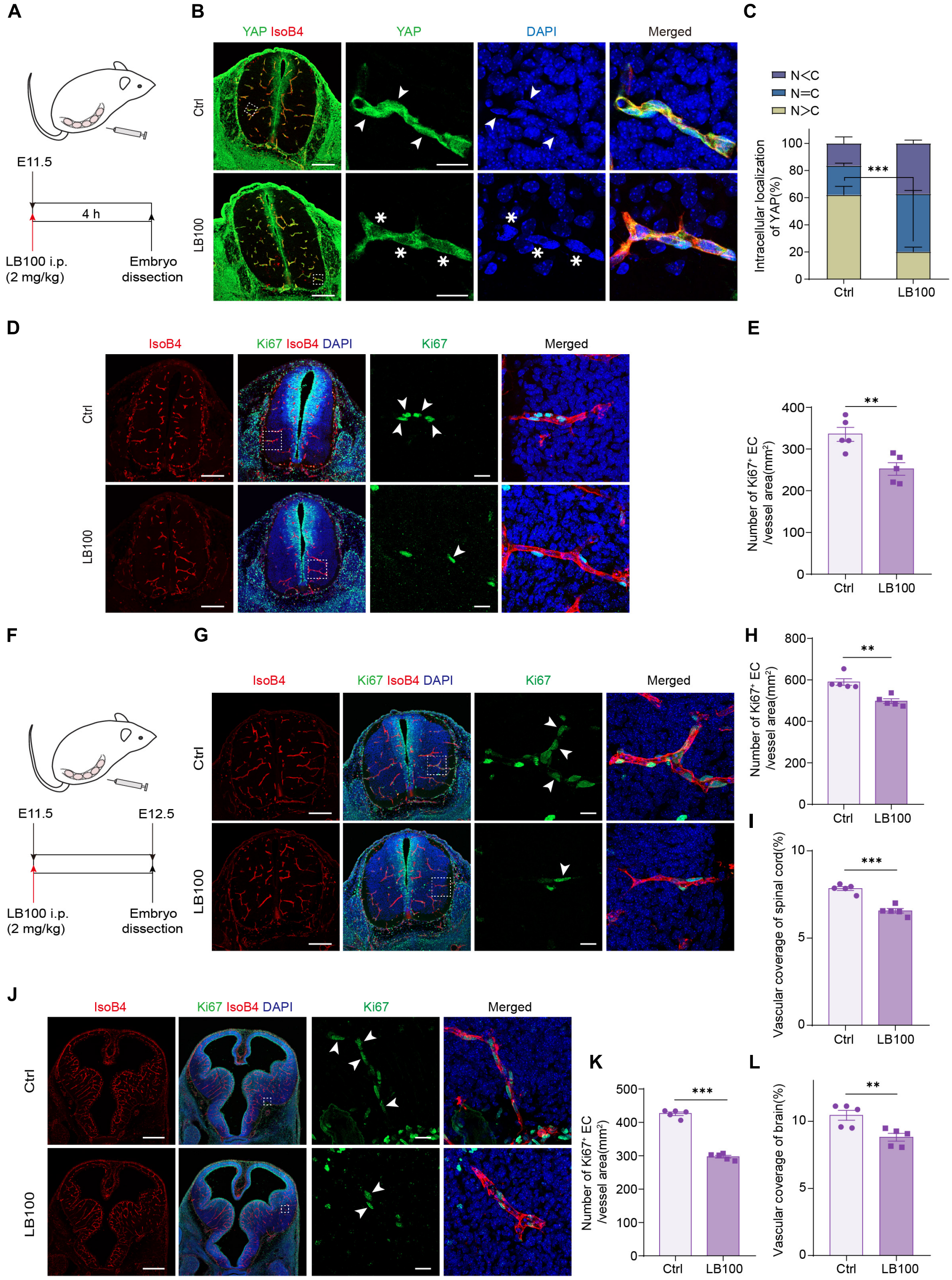

FIGURE 4 | PP2A inhibition impairs developmental vascularization in embryos. **(A)** Scheme of LB100 injection in pregnant females. **(B)** Representative confocal images of spinal cord from mouse embryos treated as in **(A)** and stained for YAP, ECs (IsoB4), and nuclei (DAPI). Images are representative of 3 litters per condition. Arrowhead indicate nuclear YAP and asterisk indicate cytosolic YAP in ECs. **(C)** Quantification of YAP cellular localization in the spinal cord from embryos treated with vehicle or LB100 of **(B)**. N, nucleus; C, cytosol. *n* = 5 Vehicle and 5 LB100 embryos per condition. **(D)** Representative confocal images of spinal cord from embryos treated as in **(A)** and stained for Ki67, ECs (IsoB4), and nuclei (DAPI). Arrowhead indicate Ki67 positive ECs. Images are representative of 3 litters per condition. **(E)** Quantification of Ki67 positive ECs in the embryo spinal cord of **(D)**. *n* = 5 Vehicle and 5 LB100 embryos per condition. **(F)** Scheme of LB100 injection in pregnant females. **(G)** Representative confocal images of spinal cord from mouse embryos treated as in **(G)** and stained for Ki67, ECs (IsoB4), and nuclei (DAPI). Arrowhead indicate Ki67 positive ECs. Images are representative of 3 litters per condition. **(H)** Quantification of Ki67 positive ECs in the embryo spinal cord of **(H)**. *n* = 5 Vehicle and 5 LB100 embryos per condition. **(I)** Quantification of vascular coverage of the embryo spinal cord of **(H)**. *n* = 5 Vehicle and 5 LB100 embryos per condition. **(J)** Representative confocal images of brains from embryos treated as in **(G)** and stained for Ki67, ECs (IsoB4), and nuclei (DAPI). Arrowhead indicate Ki67 positive ECs. Images are representative of 3 litters per condition. **(K)** Quantification of Ki67 positive in brains of **(K)**. *n* = 5 Vehicle and 5 LB100 embryos per condition. **(L)** Quantification of vascular coverage ECs of **(K)**. *n* = 5 Vehicle and 5 LB100 embryos per condition. Data are shown as mean ± SEM, two tailed Student's *t*-test. $^{**}p < 0.01$ and $^{***}p < 0.001$. Scale bars, 200 μm (lower magnification) and 20 μm (insets) in **(B,D,G)**, 500 μm (lower magnification) and 20 μm (insets) in **(J)**.

retinopathy (PDR) (Connor et al., 2009). For this, mouse pups were exposed to hyperoxia conditions (75% oxygen) from postnatal day 7 (P7) to P12, as previously described (Connor et al., 2009). Hyperoxia reduces the level of VEGF, which leads to vaso-obliteration. At P12, the pups were returned to ambient air, the relatively hypoxic environment led to high expression of VEGF, which in turn resulted in pathological neovascularization and formation of vascular tufts (**Figure 5A**). To test whether PP2A inhibition has an anti-angiogenic effect, which could be beneficial for preventing neovascularization, LB100 was retro-orbitally injected into the pups at P12. Saline vehicle injected in the same way served as control (Ctrl) (**Figure 5A**). Analysis of the avascular area revealed that LB100 did not significantly alter vaso-obliteration. However, by quantifying vascular tufts formation, we found that the neovascularization was significantly reduced in LB100 treated group (**Figures 5B–D**). We also analyzed whether EC proliferation was affected. We injected 5-ethynyl-2′-deoxyuridine (EdU) to label proliferating cells, and stained ERG to label the nucleus of endothelial cells. By quantifying the number of EdU$^+$ ERG$^+$ nuclei in the retina, we found that LB100 treatment significantly reduced the number of proliferating ECs (**Figures 5E,F**). As Angpt2 is a known YAP/target gene in endothelial cells (Choi et al., 2015; Wang et al., 2017; He et al., 2018), we determined the expression of *Angpt2* in the retinas by qPCR. The results showed that LB100 significantly reduced *Angpt2* expression, further proved an inhibitory effect of YAP by LB100 in the retinas (**Supplementary Figure 2A**).

The abnormal vascular growth in the OIR mice also results in impairment of vascular barrier, retinal hemorrhages and inflammation. Quantification of blood island showed that LB100 treatment significantly relieved retinal hemorrhages in the OIR model (**Supplementary Figures 2B,C**). Retinal inflammation also plays an important role in the pathogenesis of neovascular retinopathy. Consistently, the expression levels of monocyte chemotactic protein 1 (*Mcp-1*), intercellular adhesion molecule 1 (*Icam-1*), interleukin-1α (*Il-1a*), interleukin-1β (*Il-1b*), interleukin-6 (*Il-6*) and

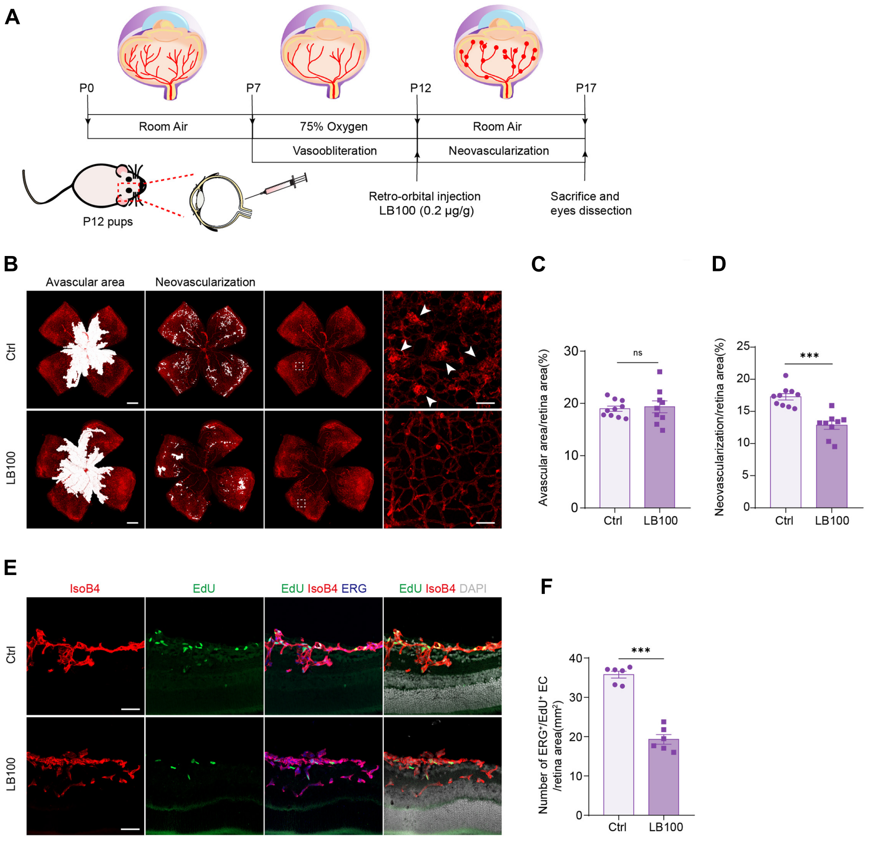

FIGURE 5 | PP2A inhibition suppresses pathological retinal angiogenesis in the OIR model. **(A)** Schematic depiction of the mouse OIR model. Pups were placed in 75% oxygen from P7 to P12, and then returned to normal oxygen conditions. Vehicle (Ctrl) or LB100 (0.2 μg/g body weight) were injected retro-orbitally at P12. Pups were sacrificed and eyes were dissected at P17. **(B)** Representative confocal images of retina vasculature stained with IsoB4 in OIR retinas from vehicle (Ctrl) or LB100 treated pups. The avascular area, neovascularization area, and high magnification images for showing the neovascular tufts (indicated by arrowheads) are presented, respectively. **(C,D)** Avascular area and neovascularization quantification of **(B)**. $n = 10$ Vehicle and 9 LB100 eyes per condition. **(E)** Representative confocal images of retina sagittal sections costained with IsoB4, EdU (labels proliferating cells), and ERG (labels EC nuclei) in pups treated as in **(A)**. **(F)** Quantitative analysis of EdU$^+$ ERG$^+$ cell number of **(E)**. $n = 6$ Vehicle and 6 LB100 eyes per condition. Data are shown as mean ± SEM, two tailed Student's *t*-test. $^{***}p < 0.001$, ns indicates not significant. Scale bars, 500 μm (lower magnification) and 50 μm (insets) in **(B)**, 50 μm in **(E)**.

Vegf of the retina was significantly decreased after LB100 treatment (**Supplementary Figures 2D–I**). Collectively, these results indicate that PP2A inhibition suppresses YAP, limits EC proliferation, and protects vascular leakage in pathological angiogenesis.

Cytoskeleton Dynamics Is Required for PP2A and YAP Interaction

We next aimed to investigate how PP2A is involved in the regulation of YAP activation. It was shown that PP2Ac directly bind to YAP, and this interaction is associated with cell density or presence of α-catenin in a human epidermal keratinocyte line (Schlegelmilch et al., 2011). In HEK293T cells, we transfected Flag-YAP or the control vector plasmid (vector). YAP, and its bounded protein patterns, were then immunoprecipitated by using anti-Flag M2 magnetic beads. Western blot showed that PP2Ac binds to Flag-YAP and confirmed a physical interaction of PP2Ac and YAP (**Figure 6A**). In HUVECs, we also performed co-IP for YAP/TAZ. Consistently, in ECs PP2Ac also was found associated with YAP/TAZ and this interaction was further enhanced by VEGF stimulation (**Figures 6B,C**). A previous study (He et al., 2018) showed that VEGF-mediated activation of YAP is independent of MST kinase, and our own data also showed that the binding of MST and PP2Ac was not changed by VEGF treatment (**Supplementary Figure 2J**). Altogether suggesting that an interaction between phosphatase PP2A and YAP is required YAP dephosphorylation and activation in response to VEGF stimulation.

By using an actin-disrupting agent, Latrunculin B (LatB) to interrupt actin polymerization in ECs, YAP/TAZ activity could not be activated by VEGF (Wang et al., 2017), suggesting YAP/TAZ activation requires an intact actin cytoskeleton. DN-PP2Ac suppressed expression of YAP target genes

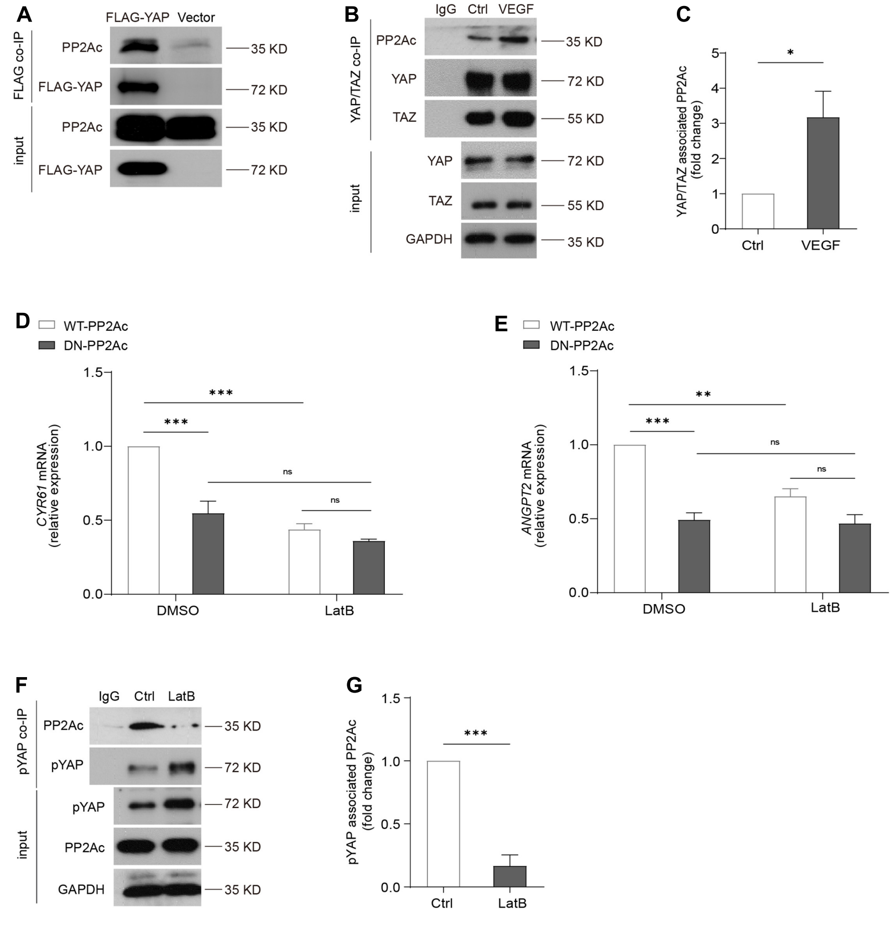

FIGURE 6 | Cytoskeleton dynamics is required for PP2A and YAP interaction. **(A)** HEK293T cells were transfected with a control plasmid or a plasmid encoding Flag-YAP. Cell lysate were incubated with anti-Flag affinity beads and eluted with 3X-Flag peptide. Representative blots of this co-Immunoprecipitation (co-IP) showed PP2Ac as an interacting protein with Flag-YAP. **(B)** Representative blots of the co-Immunoprecipitation (co-IP) of endogenous YAP/TAZ and PP2Ac in HUVECs stimulated with 50 ng/mL VEGF for 2 h. **(C)** Quantification of co-IP shown in **(B)**. $n = 3$ independent experiments. **(D,E)** HUVECs were infected with WT-PP2Ac or DN-PP2Ac adenovirus for 36 h, followed by LatB (0.05 μg/mL) treatment for 6 h. The expression of YAP target genes *CYR61 and ANGPT2* were analyzed by qPCR. **(F)** Representative blots of the co-Immunoprecipitation (co-IP) of pYAP and PP2Ac in HUVECs treated with LatB for 2 h. **(G)** Quantification of co-IP shown in **(F)**. $n = 3$ independent experiments. Data are shown as mean ± SEM, one-way ANOVA followed by Tukey's multiple comparisons test in **(D,E)**, two tailed Student's *t*-test in **(C,G)**. $^{*}p < 0.05$, $^{**}p < 0.01$, $^{***}p < 0.001$, ns indicates not significant.

including *CYR61* and *ANGPT2,* compared with WT-PP2Ac cells. Interestingly, in LatB treated ECs, no significant difference was observed between DN-PP2Ac and WT-PP2Ac expressing ECs, suggesting the regulation of PP2A on YAP requires actin cytoskeleton (**Figures 6D,E**). Next, we questioned whether LatB could affect the binding of PP2Ac to YAP. For this, we again performed co-IP experiment. The result showed that while phospho-YAP was increased upon LatB treatment, the binding of PP2Ac and pYAP was strongly reduced (**Figures 6F,G**). The above results further suggested that PP2A regulation of YAP requires cytoskeleton dynamics.

DISCUSSION

Proper control of angiogenesis is crucial for organ vascularization and growth. Recent studies have defined YAP/TAZ as essential factor in regulating angiogenesis. In response to pro-angiogenic stimuli such as VEGF or ECM rigidity, the phosphorylation of YAP/TAZ is reduced, which further leads to its nuclear translocation and activation. Although there are mounting evidences showing the important role of YAP/TAZ in angiogenesis in multiple model organisms, it is not clear why the pro-angiogenic stimulus result in hypo-phosphorylation of YAP/TAZ, as the canonical Hippo signaling upstream kinase MST is not involved in this regulation (He et al., 2018). In this study, we prove that PP2A mediates hypo-phosphorylation of YAP in ECs in response to pro-angiogenic stimulus, specifically, VEGF and high stiffness (**Figure 7**).

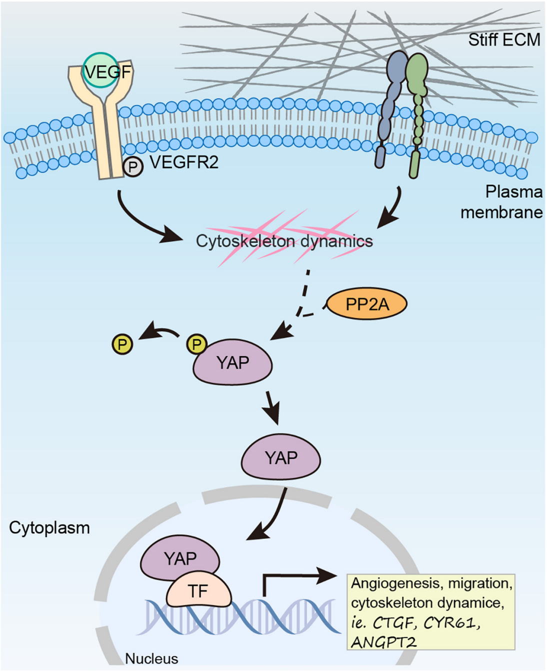

FIGURE 7 | Working model showing PP2A mediates dephosphorylation of YAP in response to VEGF and high stiffness to promote angiogenesis in ECs.

Protein phosphatase 2A is one of the major Ser/Thr phosphatases that regulates different biological processes such as cell proliferation, apoptosis and signaling transduction by dephosphorylating many critical molecular such as Akt, cMyc, P53, β-catenin (Seshacharyulu et al., 2013). Aberrant expression of PP2A is associated with various human malignancies, as loss of its phosphatase activity has been found in several type of tumors (Janssens et al., 2005; Mumby, 2007). In blood vessels, it has been reported that PP2A is involved in regulating multiple steps of angiogenesis, including endothelial tube formation, lumen stabilization, vascular remodeling, and vascular permeability (Le Guelte et al., 2012; Martin et al., 2013; Ehling et al., 2020). During atherogenesis, PP2A is also involved in inflammatory activation of the endothelium (Yun et al., 2016, 2019). These studies highlight the importance of PP2A in regulating blood vessel formation and homeostasis.

Protein phosphatase 2A holoenzyme consists a core enzyme composed of the structural A and catalytic C subunits, and regulatory B subunit (Schuhmacher et al., 2019). There are 2 A isoforms, 2 C isoforms, and four families of B subunit, each containing several isoforms, which mediate selective substrate binding and catalytic activity (Schuhmacher et al., 2019). Thus, the modulation of PP2A activity by different B subunit highlights the complexity. In endothelial cells, the important role of PP2A-B55α subunit have been recognized. Two studies have shown that B55α plays a crucial role in vessel stabilization in both zebrafish and mouse (Martin et al., 2013; Ehling et al., 2020). During mouse embryonic development, endothelial specific knockout of B55α leads to embryonic lethality, suggesting an essential role of B55α in the developing vasculature (Ehling et al., 2020). Importantly, another study also reported B55α subunit recruit PP2A to phosphodiesterase 4D5 (PDE4D5), and such interaction stabilize B55α-PP2A complex and then dephosphorylate and activate YAP. Due to the important role of B55α in ECs and its interaction with YAP, although in this study we did not focus on identifying the varying regulatory B subunit, it is tempting to speculate that B55α might be involved in this regulation.

The role of PP2A in regulating Hippo signaling pathway was reported by several studies. The canonical Hippo pathway consists of a core kinase cascade in which MST phosphorylates LATS, which further phosphorylates YAP/TAZ. In the MST-LATS-YAP/TAZ signaling axis, studies have shown that PP2A acts as a phosphatase and could dephosphorylate MST and YAP. Regulation of MST by PP2A has been observed in *Drosophila* and mammals, where PP2A directly interact with MST and dephosphorylate MST (Ribeiro et al., 2010; Couzens et al., 2013; Chen et al., 2019). Furthermore, PP2A inhibition reactivates Hippo signaling via targeting MST, which has anti-tumor effects (Tang et al., 2020). PP2A also interact with YAP to induce dephosphorylation of YAP, thereby disrupting the binding to 14-3-3 and leads to YAP activation (Schlegelmilch et al., 2011; Wang et al., 2011; Yun et al., 2019). However, PP1, but not PP2A, is responsible for dephosphorylation of TAZ (Liu et al., 2011). Thus, in this study, we mainly focused on investigating YAP. However, PP2A inhibitor LB100 or dominant negative form of PP2A treatment might also lead to TAZ activation via an upstream regulation of MST-LATS-TAZ axis. Interestingly, Akt, which is a known substrate of PP2A (Li et al., 2012; Tobisawa et al., 2017), could also be a regulator of YAP (Basu et al., 2003; Strano et al., 2005). It was reported that Akt could phosphorylate YAP, and such modification impairs YAP nuclear translocation and cotranscriptional activity (Basu et al., 2003; Strano et al., 2005). Thus, it would be interestingly to test whether a PP2A-Akt-YAP regulatory axis exists in ECs, as Akt is known to be a crucial regulator for EC migration and survival (Dimmeler and Zeiher, 2000; Lamalice et al., 2007).

ECs are influenced by the mechanical properties of the environment. Stiff matrix promotes EC proliferation and can lead to defects of vascular integrity (Huynh et al., 2011; Yeh et al., 2012). YAP/TAZ works as mechanotransducers to regulate cell behaviors. Various mechanical cues, such as ECM rigidity, shear stress and stretching regulate YAP/TAZ activity (Dupont et al., 2011; Benham-Pyle et al., 2015; Wang K.C. et al., 2016; Wang L. et al., 2016; Chang et al., 2018; Li et al., 2019). In the process of pathological angiogenesis in highly fibrotic solid tumor tissue, both VEGF and matrix stiffness trigger YAP/TAZ activation and lead to abnormal vessel growth and impaired vessel integrity (Shen et al., 2020). As we identified PP2A as a crucial mediator during this regulation, it might be valuable to consider PP2A as a target also for controlling solid tumor angiogenesis. Indeed, it was shown that LB100 treatment reduced tumor burden and tumor vascular density in a LLC lung cancer model (Ehling et al., 2020). Notably, LB100 as the pan-PP2A inhibitor, was approved for phase I clinical study in patients. There are also two phase II clinical studies on going (Chung et al., 2017) [1]. This further highlights the potential of PP2A inhibitors as an anti-pathological angiogenesis strategy.

In summary, in this study we show that PP2A mediates hypo-phosphorylation of YAP in ECs in response to VEGF or high stiffness. PP2A inhibition diminished VEGF or high stiffness triggered EC proliferation and angiogenesis. In a pathological angiogenesis model, blocking PP2A reduced abnormal vessel growth and inhibited vascular leakage. Thus, it provide new insight for considering the PP2A-YAP axis for therapeutic interventions in angiogenesis disorders.

MATERIALS AND METHODS

Animals

All study protocols involving the use of animals were approved by the Institutional Animal Care and Use Committee of Tianjin Medical University. Adult wild-type C57BL/6J and neonatal C57BL/6J mice with mothers were purchased from Model Animal Research Center of Nanjing University.

Cell Culture

Human umbilical vein endothelial cells were cultured with M199 (Gibco®, Life Technologies, United States) supplemented with 20% FBS, 100 U/mL penicillin and 100 μg/mL streptomycin (HyClone^{TM}, GE Healthcare Life Sciences, United States), glutamine, heparin, thymidine and endothelial cell growth factors (ECGF, Sigma-Aldrich, United States) as previously described (Fu et al., 2011) and were used from passage 2 to passage 5. For stimulation experiments, cells were starved overnight in ECGF free M199 medium supplemented with 2% FBS. HEK293T cells were cultured in Dulbecco Modified Eagle's Medium containing 10% FBS penicillin (100 U/mL) and streptomycin (100 μg/mL).

Antibodies and Reagents

Rabbit monoclonal antibody (mAb) against YAP (Cat No. 52771), rabbit mAb against Ki67 (Cat No. 15580), mouse mAb against human CD31 (Cat No. 9498), rabbit mAb against ERG (Cat No. 92513) and rat mAb against BrdU (Cat No. 6326) were purchased from Abcam (Cambridge, United Kingdom). Rabbit mAb against YAP (Cat No. 14074), Rabbit mAb against pYAP (Cat No. 4911) and rabbit mAb against MST1 (Cat No. 14946) were from Cell Signaling Technology (Boston, MA, United States). Mouse mAb against β-actin, Mouse mAb against GAPDH and Mouse mAb against β-tubulin were from Utibody (Tianjin, China). LB100 (Cat No. s7537) was from Selleck (Houston, TX, United States). LatB (Cat No. L5288) was from Sigma Aldrich (St. Louis, MO, United States). Recombinant Human VEGF (Cat No. 293-VE) was from R&D systems (Minneapolis, MN, United States).

PP2A Recombinant Adenovirus Construction and Infection

Generation of L199P (DN-PP2Ac) mutants was as previously described (with point mutations of leu 199 to pro). Adenovirus expressing green fluorescent protein (Ad-GFP), Ad-Flag-tagged human WT-PP2Ac and DN-PP2Ac mutants were from GeneChem (Shanghai, China). HUVECs were infected with adenovirus at multiplicity of infection (MOI) ≈100. A total of 36–48 h after infection, cells were used for analysis.

Mouse Embryos Processing

To analyze the vasculature of mouse embryos, LB100 was dissolved in saline solution (0.9% NaCl) and injected intraperitoneally with a concentration of 2 mg/kg body weight at E11.5. Embryos were then dissected at indicated time points and fixed by 4% paraformaldehyde/PBS at 4°C overnight. Afterward, they were transferred to 30% sucrose/PBS at 4°C overnight and subsequently embedded in optimal cutting temperature compound (OCT) (Sakura, Japan) and frozen at −80°C. Serial 20 μm (for spinal cord) and 60 μm (for brain) -thick sections were cut using a cryostat (CM1950, Leica, Germany).

Immunofluorescence

Cryosections were washed, permeabilized in PBS containing 0.3% TritonX-100 then blocked in PBS solution with 2% BSA, 0.3% TritonX-100 for 1 h, and incubated with primary antibodies (YAP, 1:200; ki67, 1:1000) at 4°C overnight. After washing, the cryosections were incubated with corresponding secondary antibodies for 2 h at RT. Images were collected on a confocal fluorescence microscope (LSM 800, Carl Zeiss, Germany). At least four images from each tissue were used for analyze.

---

[1] https://clinicaltrials.gov/ct2/results?cond=&term=LB100&cntry=&state=&city=&dist

Oxygen-Induced Retinopathy Model

Oxygen-induced retinopathy model was performed as previously described (Connor et al., 2009; Dong et al., 2021). Briefly, neonatal C57BL/6J mice with the nursing mother at day P7 were exposed to hyperoxia (75% O_2) for 5 days and then returned to room air at P12. For applying treatment, LB100 was dissolved in saline solution (0.9% NaCl) and injected retro-orbitally with a concentration of 0.2 μg/g body weight at P12. The retinas were collected at P17 for analysis.

Retina Dissection, Processing, and Staining

Mice were sacrificed and eyes were enucleated. The eyes were fixed in 4% PFA/PBS for 4 h at 4°C. Retinas were dissected, washed with PBS and permeabilized with PBS containing 1% TritonX-100 overnight at 4°C then blocked in PBS containing 5% BSA, 0.5% TritonX-100. After blocking, for visualization of retinal vasculature in OIR models, flat-mounted retinas were stained with isolectinGS-IB4 (Alexa Fluor 568-conjugated, 1:100, I21413, Invitrogen, United States) for 2 h at RT. Flat-mounted retinas were analyzed using a confocal fluorescence microscope (LSM 800, Carl Zeiss, Germany).

Morphometric Analyses

Morphometric analyses of the retinas were performed using ImageJ software and Adobe Photoshop software. To determine the amount of regression and neovascularization, the number of pixels in the avascular regression area and neovascular area was measured using the Lasso tool of Adobe Photoshop software as described (Connor et al., 2009), and divided by the number of pixels in the total retinal area and presented as a percentage.

EdU Injection in Pups

A total of 50 μg/g body weight EdU (E6032, US EVERBRIGHT INC., China) was i.p. injected into pups at P17 in OIR model 2.5 h before sacrifice. Eyes were enucleated and fixed in 4% PFA for 1 h at 4°C. Afterward, the eyes were transferred to 30% sucrose/PBS at 4°C overnight and embedded in OCT (Sakura, Japan) and stored at −80°C. Sagittal cryosections of the eyes were made for analysis. EdU^+ cells in the cryosections of retinas were detected by using YF® 488 Click-iT EdU Stain Kits (C6033, US EVERBRIGHT INC., China), according to the manufacturer's instructions. ECs were counterstained with ERG (1:400) and isolectinGS-IB4 (1:200). The numbers of EdU^+ERG^+ cells were counted from six sagittal eye sections. To ensure that similar areas were used for doing quantification for each eye, we always use sections intersect the optic nerve area to maintain consistency.

Mouse Aortic Ring Assay

The aortic ring assay was performed as previously described (Baker et al., 2011). Briefly, the thoracic aorta was sectioned into 1-mm long aortic rings and cultured in Opti-MEM^{TM} (Thermo Scientific, US) with 100 U/mL penicillin and 100 μg/mL streptomycin overnight. Aortic rings were encapsulated in growth factor reduced Matrigel (Corning, United States) in 24-well plates. The aortic ring was then cultured in Opti-MEM^{TM} supplemented with 2.5% FBS, 30 ng/mL VEGF with or without LB100 (4 μM) in a humidified 37°C, 5% CO_2 incubator for 5 days. Images were acquired by using a Nikon TI2-U microscope. Images were analyzed with NIH ImageJ software.

RNA Extraction and Quantitative Real-Time PCR Analysis

For animals, eyes were enucleated from pups at P17 in OIR model. Retinas were dissected and homogenized in TRIzol® reagent (Invitrogen, United States). For *in vitro* cultured cells, the cells were harvested for RNA extraction using TRIzol® reagent. RNA samples were reverse-transcribed to complementary DNA (cDNA) using TransScript One-Step gDNA Removal and cDNA Synthesis SuperMix (TransGen, China). qPCR was performed using *PerfectStart*^{TM} Green qPCR SuperMix (TransGen, China) and was processed with QuantStudio 5 Real-Time PCR system (Applied Biosystems, United States). GAPDH was used as internal control. All qPCR results were obtained from at least three biological repeats.

Immunoprecipitation and Immunoblotting

Co-IP assays were performed as previously described (Wang et al., 2017). Cells were lysed using mild lysis buffer [20 mM Tris at pH 7.5, 150 mM NaCl, 5 mM EDTA, 1% NP-40, 10% Glycerol, 1X protease inhibitor cocktail, and 1X phosphatase inhibitor (Roche)]. Cell lysates were centrifuged for 15 min, and supernatants were used for immunoprecipitation. Anti-YAP/TAZ antibody or anti-pYAP antibody (Cell Signaling Technology, United States) was incubated with the supernatant overnight on a rotor, and protein A/G–magnetic beads (Thermo Scientific, United States) were added in for 2 more hours. Immunoprecipitates were washed and proteins were eluted with SDS sample buffer. For analyzing the interaction of YAP and PP2Ac in HEK293T, the cells were transfected with Flag-tagged human YAP (Flag-YAP). Empty vector was used as control. After 36 h, cell lysate was collected and incubated with anti-Flag M2 magnetic beads (Sigma-Aldrich) to capture the Flag protein complex. After binding, the magnetic beads were washed, 3X-Flag peptide was applied to elute the Flag-protein complex.

Immunofluorescence of Cells in Culture

For YAP staining, HUVECs were cultured in collagen coated coverslips in 24-well plates or on PA hydrogels. After treatment, cells were fixed with 4% PFA/PBS for 15 min at RT. Afterward, cells were permeabilized with 0.2% Triton X-100 PBS, blocked in 2% BSA, 0.2% Triton X-100 PBS, and incubated with primary antibodies (YAP, 1:200; GM130, 1:50; human CD31, 1:100). After washing, cells were incubated with secondary antibodies. Phalloidin (1:100, CA1610, Solarbio, China) was used together with secondary antibodies. Images were acquired by confocal microscope (LSM 800, Carl Zeiss, Germany). More than 8 fields of view from at least three independent experiments were randomly chosen. Cells presenting preferential nuclear YAP localization, equal nuclear or cytoplasmic, or mainly cytoplasmic YAP localization were counted blindly.

Polyacrylamide Gel Manufacturing

Polyacrylamide gels were prepared as previously described (Yeh et al., 2012). Briefly, solutions were prepared by using acrylamide (40% w/v solution; Sigma-Aldrich, Germany; A4058) and bis-acrylamide crosslinker (2% w/v solution, Sigma-Aldrich, Germany; 111-26-9). Gels with different stiffness were prepared by varying the final concentrations of acrylamide and bis-acrylamide. To remove oxygen from the solutions, the mixtures were degassed for 15 min. To polymerize the mixtures, 30 μL of 10% w/v ammonium persulfate (Bio-Rad, United States; 1610700) and 20 μL of N,N,N9,N9-tetramethylethylenediamine (TEMED; Bio-Rad, United States; 1610800) were added to yield a final volume of 5 mL. Gel surfaces were then activated by exposing the heterobifunctional crosslinker Sulfo-SANPAH (Pierce, United States; 22589) at 0.5 mg/mL in 50 nM HEPES (Sigma-Aldrich, Germany; H3375) to UV light. After activation, the gels were washed with PBS to remove excess crosslinker. Gels were then coated with 0.1 mg/mL collagen (Sigma-Aldrich, Germany; F0895) at 37°C for 1 h or overnight at 4°C.

BrdU Incorporation in ECs

The BrdU incorporation assay was performed as previously described (Shen et al., 2020; Dong et al., 2021). Briefly, HUVECs were cultured in collagen coated coverslips in 24-well plates or on PA hydrogels. After indicated treatment, BrdU (10 μM) was added and incubation of the cultures continued for 4 h at 37°C. Cells were fixed in 4% PFA/PBS for 20 min and blocked in PBS containing 2% BSA, 0.3% TritonX-100 for 30 min at RT. Unmasking was done by adding ice-cold 0.1 M HCl for 20 min followed by 2 M HCl for 30 min. Neutralization was done prior to primary antibody incubation with sodium borate buffer (0.1 M Na_2B_4O7 in water, PH8.5) for 15 min. An anti-BrdU antibody (1:250) was incubated in blocking solution overnight at 4°C and corresponding secondary antibody was incubated for 2 h at RT. Nuclei were labeled with DAPI (1:1000, D1306, Invitrogen, United States). Images were obtained using a fluorescence microscope (Ti2-U, Nikon, Japan). Quantification was done blind to the experimental condition.

Scratch Assay

To analyze the EC migration, scratch assay was performed as previously described (Tisch et al., 2019).HUVECs were plated on 6-well plates and infected with adenoviruses for 30 h. After overnight starvation, a wound was made by scraping the cell monolayer with a 200 μL pipette tip, and cells were stimulated with or without VEGF (50 ng/mL). Pictures were acquired at time-point zero and 8 h after incubation at 37°C. The percentage of wound closure between 0 and 8 h was analyzed with ImageJ software. Results are from five independent experiments, for each treatment eight fields of view were analyzed.

Polarity Index Calculation

Cell polarity analysis was performed as previously described (Dubrac et al., 2016; Carvalho et al., 2019). Briefly, HUVECs were plated on coverslips and infected with adenoviruses for 30 h. After overnight starvation, a wound was made by scraping the cell monolayer with a 200 μL pipette tip, and cells were stimulated with or without VEGF (50 ng/mL). After 8 h, the culture was fixed and stained with GM130 (Alexa Fluor® 555-conjugated, 1:50, 560066, BD, United States), Phalloidin (1:100, CA1620, Solarbio, China) and DAPI (1:1000). Images were obtained by confocal microscope (LSM 900, Carl Zeiss, Germany) and analyzed by ImageJ software. Leader cells were identified as the first row of cell directly in contact with the scratch, the follower cells comprising the second to third rows of cells away from the scratch. The polarity of each cell was defined as the angle (α) between the Golgi-nuclei axis and the scratch line as shown in **Figure 3H**.The polarity index was calculated following the formula below.

$$\text{Polarity Index} = \sqrt{\Big(\frac{1}{N}\sum_{1}^{N}\cos^{2}\Big(\frac{1}{N}\sum_{1}^{N}\sin\Big)^{2}}$$

Statistical Analysis

Results were expressed as the mean ± SEM. To calculate statistical significance, the student's *t*-test (two-tailed), one-way ANOVA followed by Tukey's multiple comparisons test or two-way ANOVA followed by Sidak multiple comparisons test were used. p-value < 0.05 was considered significant. All calculations were performed using Prism software.

DATA AVAILABILITY STATEMENT

The original contributions presented in the study are included in the article/**Supplementary Material**, further inquiries can be directed to the corresponding author/s.

ETHICS STATEMENT

The animal study was reviewed and approved by the Institutional Animal Care and Use Committee of Tianjin Medical University.

AUTHOR CONTRIBUTIONS

CR and XW designed the project. XJ, JH, ZW, SC, MD, YS, XD, HA, and XW carried out the experiments. XJ, JH, ZW, and XW analyzed the data. MM, CR and XW supervised the study. XJ, CR, and XW wrote the manuscript with the input from all authors.

FUNDING

This study was supported by National Key R&D Program of China (2020YFA0803703), National Natural Science Foundation of China (31871184 and 81970828), the Postdoctoral Science Foundation of China (2019M651054), by DFG grants from SFB1366 ("Vascular control of Organ Function" project number 39404578), and RTG2099 (to CR).

SUPPLEMENTARY MATERIAL

The Supplementary Material for this article can be found online at: https://www.frontiersin.org/articles/10.3389/fcell.2021.675562/full#supplementary-material

Supplementary Figure 1 | PP2A activity is required for EC cytoskeleton change and sprouting. **(A)** Representative images of HUVECs stained with Phalloidin (actin) showing that *lamellipodia* formation upon VEGF (50 ng/mL for 30 min) treatment in WT-PP2Ac or DN-PP2Ac expressing HUVECs. **(B)** Quantification of the number of HUVECs with *lamellipodia* of **(A)**. Cells in nine random fields of view (≈120 cells) were quantified. **(C)** Representative images of WT-PP2Ac or DN–PP2Ac expressing HUVECs seeded on soft (0.2 kpa) and stiff (20 kpa) hydrogels stained for Phalloidin (actin). **(D,E)** Quantification of individual cell area and circularity in **(C)**. A, area; P, perimeter. Cells in 10 random fields of view (≈50 cells per condition) were quantified. **(F)** Representative images of mice aortic rings treated with vehicle (Ctrl) or LB100 (4 μM). **(G)** Quantification of microvascular sprouting area of **(F)**. (n = 3–5 aortic ring per condition.) Data are shown as mean ± SEM, one-way ANOVA followed by Tukey's multiple comparisons test in **(B,D,E)**, two tailed Student's t-test in G. *$p < 0.05$, **$p < 0.01$, and ***$p < 0.001$, ns indicates not significant. Scale bars, 50 μm (lower magnification) and 20 μm (insets) in **(A)**, 20 μm in **(C)**, 500 μm in **(F)**.

Supplementary Figure 2 | PP2A inhibition reduces vascular leakage in the OIR model. **(A)** qPCR analysis of the expression of YAP target gene *Angpt2* in retinas of vehicle or LB100 treated OIR pups. (n = 5 Vehicle and 9 LB100 mice per condition.) **(B)** Representative images of the outer surface of the OIR retinal cup at P17. Blood island formation indicates hemorrhages in the retinas. **(C)** Quantification of blood island area out of the total retinal area of **(B)**. (n = 5 Vehicle and 7 LB100 mice per condition). **(D–I)** qPCR analysis of the expression of *Mcp-1, Icam-1, Il-1a, Il-1b, Il-6,* and *Vegf* in retinas treated as in **(A)**. (n = 5 Vehicle and 9 LB100 mice per condition.) **(J)** Representative blots of the co-Immunoprecipitation (co-IP) of endogenous MST1 and PP2Ac in HUVECs stimulated with 50 ng/mL VEGF for 2 h. Data are shown as mean ± SEM, two tailed Student's t-test. *$p < 0.05$, **$p < 0.01$, and ***$p < 0.001$. Scale bars, 1 mm.

REFERENCES

Baker, M., Robinson, S. D., Lechertier, T., Barber, P. R., Tavora, B., D'Amico, G., et al. (2011). Use of the mouse aortic ring assay to study angiogenesis. *Nat. Protoc.* 7, 89–104. doi: 10.1038/nprot.2011.435

Basu, S., Totty, N. F., Irwin, M. S., Sudol, M., and Downward, J. (2003). Akt phosphorylates the Yes-associated protein, YAP, to induce interaction with 14-3-3 and attenuation of p73-mediated apoptosis. *Mol. Cell* 11, 11–23. doi: 10.1016/s1097-2765(02)00776-1

Benham-Pyle, B. W., Pruitt, B. L., and Nelson, W. J. (2015). Cell adhesion. Mechanical strain induces E-cadherin-dependent Yap1 and beta-catenin activation to drive cell cycle entry. *Science* 348, 1024–1027. doi: 10.1126/science.aaa4559

Carvalho, J. R., Fortunato, I. C., Fonseca, C. G., Pezzarossa, A., Barbacena, P., Dominguez-Cejudo, M. A., et al. (2019). Non-canonical Wnt signaling regulates junctional mechanocoupling during angiogenic collective cell migration. *Elife* 8:e45853.

Chang, L., Azzolin, L., Di Biagio, D., Zanconato, F., Battilana, G., Lucon Xiccato, R., et al. (2018). The SWI/SNF complex is a mechanoregulated inhibitor of YAP and TAZ. *Nature* 563, 265–269. doi: 10.1038/s41586-018-0658-1

Chen, R., Xie, R., Meng, Z., Ma, S., and Guan, K. L. (2019). STRIPAK integrates upstream signals to initiate the Hippo kinase cascade. *Nat. Cell Biol.* 21, 1565–1577. doi: 10.1038/s41556-019-0426-y

Choi, H. J., Zhang, H., Park, H., Choi, K. S., Lee, H. W., Agrawal, V., et al. (2015). Yes-associated protein regulates endothelial cell contact-mediated expression of angiopoietin-2. *Nat. Commun.* 6:6943.

Chung, V., Mansfield, A. S., Braiteh, F., Richards, D., Durivage, H., Ungerleider, R. S., et al. (2017). Safety, tolerability, and preliminary activity of LB-100, an inhibitor of protein phosphatase 2A, in patients with relapsed solid tumors: an open-label, dose escalation, first-in-human, phase I trial. *Clin. Cancer Res.* 23, 3277–3284. doi: 10.1158/1078-0432.ccr-16-2299

Connor, K. M., Krah, N. M., Dennison, R. J., Aderman, C. M., Chen, J., Guerin, K. I., et al. (2009). Quantification of oxygen-induced retinopathy in the mouse: a model of vessel loss, vessel regrowth and pathological angiogenesis. *Nat. Protoc.* 4, 1565–1573.

Couzens, A. L., Knight, J. D., Kean, M. J., Teo, G., Weiss, A., Dunham, W. H., et al. (2013). Protein interaction network of the mammalian Hippo pathway reveals mechanisms of kinase-phosphatase interactions. *Sci. Signal.* 6:rs15. doi: 10.1126/scisignal.2004712

Dimmeler, S., and Zeiher, A. M. (2000). Akt takes center stage in angiogenesis signaling. *Circ. Res.* 86, 4–5. doi: 10.1161/01.res.86.1.4

Dong, X., Lei, Y., Yu, Z., Wang, T., Liu, Y., Han, G., et al. (2021). Exosome-mediated delivery of an anti-angiogenic peptide inhibits pathological retinal angiogenesis. *Theranostics* 11, 5107–5126. doi: 10.7150/thno.54755

Dubrac, A., Genet, G., Ola, R., Zhang, F., Pibouin-Fragner, L., Han, J., et al. (2016). Targeting NCK-mediated endothelial cell front-rear polarity inhibits neovascularization. *Circulation* 133, 409–421. doi: 10.1161/circulationaha.115.017537

Dupont, S., Morsut, L., Aragona, M., Enzo, E., Giulitti, S., Cordenonsi, M., et al. (2011). Role of YAP/TAZ in mechanotransduction. *Nature* 474, 179–183.

Ehling, M., Celus, W., Martin-Perez, R., Alba, R., Willox, S., Di Conza, G., et al. (2020). B55alpha/PP2A limits endothelial cell apoptosis during vascular remodeling: a complementary approach to kill pathological vessels? *Circ. Res.* 127, 707–723. doi: 10.1161/circresaha.119.316071

Evans, D. R., Myles, T., Hofsteenge, J., and Hemmings, B. A. (1999). Functional expression of human PP2Ac in yeast permits the identification of novel C-terminal and dominant-negative mutant forms. *J. Biol. Chem.* 274, 24038–24046. doi: 10.1074/jbc.274.34.24038

Fu, Y., Hou, Y., Fu, C., Gu, M., Li, C., Kong, W., et al. (2011). A novel mechanism of gamma/delta T-lymphocyte and endothelial activation by shear stress: the role of ecto-ATP synthase beta chain. *Circ. Res.* 108, 410–417. doi: 10.1161/circresaha.110.230151

He, J., Bao, Q., Zhang, Y., Liu, M., Lv, H., Liu, Y., et al. (2018). Yes-associated protein promotes angiogenesis via signal transducer and activator of transcription 3 in endothelial cells. *Circ. Res.* 122, 591–605. doi: 10.1161/circresaha.117.311950

Hong, C. S., Ho, W., Zhang, C., Yang, C., Elder, J. B., and Zhuang, Z. (2015). LB100, a small molecule inhibitor of PP2A with potent chemo- and radio-sensitizing potential. *Cancer Biol. Ther.* 16, 821–833. doi: 10.1080/15384047.2015.1040961

Huynh, J., Nishimura, N., Rana, K., Peloquin, J. M., Califano, J. P., Montague, C. R., et al. (2011). Age-related intimal stiffening enhances endothelial permeability and leukocyte transmigration. *Sci. Transl. Med.* 3, 112ra122. doi: 10.1126/scitranslmed.3002761

Janssens, V., and Goris, J. (2001). Protein phosphatase 2A: a highly regulated family of serine/threonine phosphatases implicated in cell growth and signalling. *Biochem. J.* 353, 417–439. doi: 10.1042/0264-6021:3530417

Janssens, V., Goris, J., and Van Hoof, C. (2005). PP2A: the expected tumor suppressor. *Curr. Opin. Genet. Dev.* 15, 34–41. doi: 10.1016/j.gde.2004.12.004

Kim, J., Kim, Y. H., Kim, J., Park, D. Y., Bae, H., Lee, D. H., et al. (2017). YAP/TAZ regulates sprouting angiogenesis and vascular barrier maturation. *J. Clin. Invest.* 127, 3441–3461. doi: 10.1172/jci93825

Lamalice, L., Le Boeuf, F., and Huot, J. (2007). Endothelial cell migration during angiogenesis. *Circ. Res.* 100, 782–794. doi: 10.1161/01.res.0000259593.07661.1e

Le Guelte, A., Galan-Moya, E. M., Dwyer, J., Treps, L., Kettler, G., Hebda, J. K., et al. (2012). Semaphorin 3A elevates endothelial cell permeability through PP2A inactivation. *J. Cell Sci.* 125, 4137–4146. doi: 10.1242/jcs.108282

Li, B., He, J., Lv, H., Liu, Y., Lv, X., Zhang, C., et al. (2019). c-Abl regulates YAPY357 phosphorylation to activate endothelial atherogenic responses to disturbed flow. *J. Clin. Invest.* 129, 1167–1179. doi: 10.1172/jci122440

Li, G., Ji, X. D., Gao, H., Zhao, J. S., Xu, J. F., Sun, Z. J., et al. (2012). EphB3 suppresses non-small-cell lung cancer metastasis via a PP2A/RACK1/Akt signalling complex. *Nat. Commun.* 3:667.

Liu, C. Y., Lv, X., Li, T., Xu, Y., Zhou, X., Zhao, S., et al. (2011). PP1 cooperates with ASPP2 to dephosphorylate and activate TAZ. *J. Biol. Chem.* 286, 5558–5566. doi: 10.1074/jbc.m110.194019

Martin, M., Geudens, I., Bruyr, J., Potente, M., Bleuart, A., Lebrun, M., et al. (2013). PP2A regulatory subunit Balpha controls endothelial contractility and vessel lumen integrity via regulation of HDAC7. *EMBO J.* 32, 2491–2503. doi: 10.1038/emboj.2013.187

Mason, D. E., Collins, J. M., Dawahare, J. H., Nguyen, T. D., Lin, Y., Voytik-Harbin, S. L., et al. (2019). YAP and TAZ limit cytoskeletal and focal adhesion maturation to enable persistent cell motility. *J. Cell Biol.* 218, 1369–1389. doi: 10.1083/jcb.201806065

Meng, Z., Qiu, Y., Lin, K. C., Kumar, A., Placone, J. K., Fang, C., et al. (2018). RAP2 mediates mechanoresponses of the Hippo pathway. *Nature* 560, 655–660. doi: 10.1038/s41586-018-0444-0

Moya, I. M., and Halder, G. (2019). Hippo-YAP/TAZ signalling in organ regeneration and regenerative medicine. *Nat. Rev. Mol. Cell Biol.* 20, 211–226. doi: 10.1038/s41580-018-0086-y

Mumby, M. (2007). PP2A: unveiling a reluctant tumor suppressor. *Cell* 130, 21–24. doi: 10.1016/j.cell.2007.06.034

Panciera, T., Azzolin, L., Cordenonsi, M., and Piccolo, S. (2017). Mechanobiology of YAP and TAZ in physiology and disease. *Nat. Rev. Mol. Cell Biol.* 18, 758–770. doi: 10.1038/nrm.2017.87

Ribeiro, P. S., Josue, F., Wepf, A., Wehr, M. C., Rinner, O., Kelly, G., et al. (2010). Combined functional genomic and proteomic approaches identify a PP2A complex as a negative regulator of Hippo signaling. *Mol. Cell* 39, 521–534. doi: 10.1016/j.molcel.2010.08.002

Schlegelmilch, K., Mohseni, M., Kirak, O., Pruszak, J., Rodriguez, J. R., Zhou, D., et al. (2011). Yap1 acts downstream of alpha-catenin to control epidermal proliferation. *Cell* 144, 782–795. doi: 10.1016/j.cell.2011.02.031

Schuhmacher, D., Sontag, J. M., and Sontag, E. (2019). Protein phosphatase 2A: more than a passenger in the regulation of epithelial cell-cell junctions. *Front. Cell Dev. Biol.* 7:30. doi: 10.3389/fcell.2019.00030

Seshacharyulu, P., Pandey, P., Datta, K., and Batra, S. K. (2013). Phosphatase: PP2A structural importance, regulation and its aberrant expression in cancer. *Cancer Lett.* 335, 9–18. doi: 10.1016/j.canlet.2013.02.036

Shen, Y., Wang, X., Lu, J., Salfenmoser, M., Wirsik, N. M., Schleussner, N., et al. (2020). Reduction of liver metastasis stiffness improves response to bevacizumab in metastatic colorectal cancer. *Cancer Cell* 37, 800–817.e7.

Strano, S., Monti, O., Pediconi, N., Baccarini, A., Fontemaggi, G., Lapi, E., et al. (2005). The transcriptional coactivator Yes-associated protein drives p73 gene-target specificity in response to DNA Damage. *Mol. Cell* 18, 447–459. doi: 10.1016/j.molcel.2005.04.008

Tang, Y., Fang, G., Guo, F., Zhang, H., Chen, X., An, L., et al. (2020). Selective inhibition of STRN3-containing PP2A phosphatase restores Hippo tumor-suppressor activity in gastric cancer. *Cancer Cell* 38, 115–128.e9.

Tisch, N., Freire-Valls, A., Yerbes, R., Paredes, I., Porta, S. La, Wang, X., et al. (2019). Caspase-8 modulates physiological and pathological angiogenesis during retina development. *J. Clin. Invest.* 129, 5092–5107. doi: 10.1172/jci122767

Tobisawa, T., Yano, T., Tanno, M., Miki, T., Kuno, A., Kimura, Y., et al. (2017). Insufficient activation of Akt upon reperfusion because of its novel modification by reduced PP2A-B55alpha contributes to enlargement of infarct size by chronic kidney disease. *Basic Res. Cardiol.* 112:31.

Totaro, A., Panciera, T., and Piccolo, S. (2018). YAP/TAZ upstream signals and downstream responses. *Nat. Cell Biol.* 20, 888–899. doi: 10.1038/s41556-018-0142-z

Urbich, C., Reissner, A., Chavakis, E., Dernbach, E., Haendeler, J., Fleming, I., et al. (2002). Dephosphorylation of endothelial nitric oxide synthase contributes to the anti-angiogenic effects of endostatin. *FASEB J.* 16, 706–708. doi: 10.1096/fj.01-0637fje

Wang, K. C., Yeh, Y. T., Nguyen, P., Limqueco, E., Lopez, J., Thorossian, S., et al. (2016). Flow-dependent YAP/TAZ activities regulate endothelial phenotypes and atherosclerosis. *Proc. Natl. Acad. Sci. U.S.A.* 113, 11525–11530. doi: 10.1073/pnas.1613121113

Wang, L., Luo, J. Y., Li, B., Tian, X. Y., Chen, L. J., Huang, Y., et al. (2016). Integrin-YAP/TAZ-JNK cascade mediates atheroprotective effect of unidirectional shear flow. *Nature* 540, 579–582. doi: 10.1038/nature20602

Wang, P., Bai, Y., Song, B., Wang, Y., Liu, D., Lai, Y., et al. (2011). PP1A-mediated dephosphorylation positively regulates YAP2 activity. *PLoS One* 6:e24288. doi: 10.1371/journal.pone.0024288

Wang, W., Huang, J., Wang, X., Yuan, J., Li, X., Feng, L., et al. (2012). PTPN14 is required for the density-dependent control of YAP1. *Genes Dev.* 26, 1959–1971. doi: 10.1101/gad.192955.112

Wang, X., Freire Valls, A., Schermann, G., Shen, Y., Moya, I. M., Castro, L., et al. (2017). YAP/TAZ orchestrate VEGF signaling during developmental angiogenesis. *Dev. Cell* 42, 462–478.e7.

Yeh, Y. T., Hur, S. S., Chang, J., Wang, K. C., Chiu, J. J., Li, Y. S., et al. (2012). Matrix stiffness regulates endothelial cell proliferation through septin 9. *PLoS One* 7:e46889. doi: 10.1371/journal.pone.0046889

Yu, F. X., Zhao, B., Panupinthu, N., Jewell, J. L., Lian, I., Wang, L. H., et al. (2012). Regulation of the Hippo-YAP pathway by G-protein-coupled receptor signaling. *Cell* 150, 780–791. doi: 10.1016/j.cell.2012.06.037

Yun, S., Budatha, M., Dahlman, J. E., Coon, B. G., Cameron, R. T., Langer, R., et al. (2016). Interaction between integrin alpha5 and PDE4D regulates endothelial inflammatory signalling. *Nat. Cell Biol.* 18, 1043–1053. doi: 10.1038/ncb3405

Yun, S., Hu, R., Schwaemmle, M. E., Scherer, A. N., Zhuang, Z., Koleske, A. J., et al. (2019). Integrin alpha5beta1 regulates PP2A complex assembly through PDE4D in atherosclerosis. *J. Clin. Invest.* 130, 4863–4874. doi: 10.1172/jci127692

Conflict of Interest: The authors declare that the research was conducted in the absence of any commercial or financial relationships that could be construed as a potential conflict of interest.

frontiers
in Cell and Developmental Biology

ORIGINAL RESEARCH
published: 18 May 2021
doi: 10.3389/fcell.2021.648715

Substrate Stiffness Regulates Cholesterol Efflux in Smooth Muscle Cells

Xiuli Mao [1]***, Yiling Tan*** [1]***, Huali Wang*** [1]***, Song Li*** [2] ***and Yue Zhou*** [1]*

[1] *School of Biomedical Engineering, Shanghai Jiao Tong University, Shanghai, China,* [2] *Department of Bioengineering and Department of Medicine, University of California, Los Angeles, Los Angeles, CA, United States*

The infiltration and deposition of cholesterol in the arterial wall play an important role in the initiation and development of atherosclerosis. Smooth muscle cells (SMCs) are the major cell type in the intima. Upon exposure to cholesterol, SMCs may undergo a phenotype switching into foam cells. Meanwhile, the pathological processes of the blood vessel such as cholesterol deposition and calcification induce the changes in the substrate stiffness around SMCs. However, whether substrate stiffness affects the cholesterol accumulation in SMCs and the formation of foam cells is not well-understood. In this study, SMCs were cultured on the substrates with different stiffnesses ranging from 1 to 100 kPa and treated with cholesterol. We found that cholesterol accumulation in SMCs was higher on 1 and 100 kPa substrates than that on intermediate stiffness at 40 kPa; consistently, total cholesterol (TC) content on 1 and 100 kPa substrates was also higher. As a result, the accumulation of cholesterol increased the expression of macrophage marker CD68 and downregulated SMC contractile marker smooth muscle α-actin (ACTA2). Furthermore, the mRNA and protein expression level of cholesterol efflux gene ATP-binding cassette transporter A1 (ABCA1) was much higher on 40 kPa substrate. With the treatment of a liver X receptor (LXR) agonist GW3965, the expression of ABCA1 increased and cholesterol loading decreased, showing an additive effect with substrate stiffness. In contrast, inhibition of LXR decreased ABCA1 gene expression and increased cholesterol accumulation in SMCs. Consistently, when ABCA1 gene was knockdown, the cholesterol accumulation was increased in SMCs on all substrates with different stiffness. These results revealed that substrate stiffness played an important role on SMCs cholesterol accumulation by regulating the ABCA1 expression. Our findings on the effects of substrate stiffness on cholesterol efflux unravel a new mechanism of biophysical regulation of cholesterol metabolism and SMC phenotype, and provide a rational basis for the development of novel therapies.

Keywords: vascular smooth muscle cells, substrate stiffness, cholesterol, foam cells, cholesterol efflux

OPEN ACCESS

Edited by:
Jing Zhou,
Peking University, China

Reviewed by:
Tzong-Shyuan Lee,
National Taiwan University, Taiwan
Zhongkui Hong,
University of South Dakota,
United States

****Correspondence:***
Yue Zhou
yzhou2009@sjtu.edu.cn

Specialty section:
This article was submitted to Cell Adhesion and Migration, a section of the journal Frontiers in Cell and Developmental Biology

Received: *01 January 2021*
Accepted: *13 April 2021*
Published: *18 May 2021*

Citation:
Mao X, Tan Y, Wang H, Li S and Zhou Y (2021) Substrate Stiffness Regulates Cholesterol Efflux in Smooth Muscle Cells. Front. Cell Dev. Biol. 9:648715. doi: 10.3389/fcell.2021.648715

1. INTRODUCTION

Atherosclerosis is a multi-factorial process involving significant changes in microenvironment and vascular cell phenotypes (Falk, 2006; Libby et al., 2011). The disorder of lipid metabolism leads to the development of atherosclerotic plaque, which forms a necrotic core containing cells with lipid (foam cells). It has been generally accepted that most foam cells were originated from macrophages, which derives from the circulating monocytes (Yu et al., 2013). However, vascular smooth muscle cells (SMCs) have also been shown to participate in foam cell formation (Allahverdian et al., 2012). The uptake and accumulation of excess cholesterol in SMCs is an external driver to convert SMC phenotype. SMCs lose their contractile makers, such as smooth muscle α-actin (ACTA2), and increase the expression of markers of macrophage phenotype such as CD68 (Gomez and Owens, 2012; Chaabane et al., 2014). This conversion plays a critical role in the composition and stability of the plaque and contributes to the development and progress of atherosclerosis.

During the formation of atherosclerotic plaque, with the accumulation of cholesterol and calcification, the stiffness of the blood vessels changes. The stiffness of normal aorta in rabbit was about 40 kPa, while the local elastic modulus of atherosclerotic lesions of rabbit thoracic aortas decreased at the early stage and increased at later stage with the development of atherosclerosis (Matsumoto et al., 2002). In apolipoprotein E-deficient mice, the stiffness of lipid rich areas in the blood vessel was 5.5 ± 3.5 kPa while the stiffness of the fibrous caps was almost 59.4 ± 47.4 kPa, even rising to 250 kPa (Tracqui et al., 2011). The stiffness of aorta in monkeys was around 20–40 kPa (Sehgel et al., 2015). These findings suggest that the physiological stiffness of aorta is about 40 kPa and the pathological changes may decrease the stiffness to a level as low as 1 kPa and increase the stiffness to 100 kPa or higher. Meanwhile, vascular endothelial cells and SMCs can sense and respond to such stiffness changes in the vascular wall, causing phenotypic switching of these cells (Rudijanto, 2007; Tian et al., 2019). It has been reported that membrane cholesterol and substrate stiffness can synergistically affect the biomechanical properties and the remodeling of the cytoskeleton of SMCs. Atomic force microscopy revealed that substrate stiffness also regulated the stiffness of SMCs themselves, as well as their adhesion behavior mediated by $\alpha5\beta1$-integrin (Sanyour et al., 2019). However, it is not known whether the stiffness change in the microenvironment affects the cholesterol metabolism in SMCs and their phenotype change.

Cholesterol is an essential component of cell membrane to maintain the membrane integrity, fluidity, and metabolic function of the cells (Maxfield and Tabas, 2005; Gelissen and Brown, 2017). Cellular cholesterol homeostasis is controlled by the precise regulation of the uptake, synthesis, and efflux of cholesterol, where cholesterol efflux is a major part of reverse cholesterol transport (RCT) (Litvinov et al., 2016). RCT is the only way to remove excess cholesterol from the cells in peripheral tissues and transport it to liver and intestine, which can prevent cholesterol accumulation in vascular cells and inhibit the development of atherosclerosis (Simons and Ikonen, 2000; van der Wulp et al., 2013). The membrane cholesterol transporters, such as ATP-binding cassette transporter A1 (ABCA1), participates in RCT to transport the excessive phospholipids and cholesterol to the outside of the cells (Oram and Heinecke, 2005; Liao and McLachlan, 2018). On a high-cholesterol diet, ABCA1-deficient mice showed more cholesterol accumulation and more foam cells formation than wild-type mice (Choi et al., 2009). The sterol-responsive nuclear receptor, liver X receptor (LXR), is a vital transcription factor being activated in response to excess cellular cholesterol (Im and Osborne, 2011; Rasheed and Cummins, 2018). It has been reported that LXR agonists can facilitate RCT and protect mice against atherosclerosis (Joseph et al., 2002). Since the focus of cellular cholesterol homeostasis has been carried out in the monocyte-derived macrophages, little has been explored from the aspect of the cholesterol homeostasis in SMCs. There is evidence that the formation of SMC-derived foam cells in the human coronary arteries is partially due to their reduced ability to remove excess cholesterol through ABCA1 (Allahverdian et al., 2014). However, it is not clear whether substrate stiffness could regulate SMCs cholesterol accumulation and efflux in the pathogenesis of atherosclerosis.

To address this question, we varied the stiffness of extracellular substrate ranging between 1 and 100 kPa, and investigated the effects of substrate stiffness on cholesterol accumulation and efflux in SMCs and their interactions with LXR signaling pathway, demonstrating the crosstalk between biophysical and biochemical signaling in the regulation of SMC functions.

2. MATERIALS AND METHODS

2.1. Preparation of Substrates With Different Stiffness

Substrates with different stiffness were prepared as described previously by adjusting the ratio of 40% acrylamide to 2% bis-acrylamide (w/v) (Sangon Biotech, China) (Chen et al., 2019; Tian et al., 2019). Tetramethylethylenediamine (TEMED, Klamar, China) and 10% ammonium persulfate solution (APS, Sinopharm, China) were used as cross-linking reagent. Before polymerization, 200 μl mixture was added onto a glass slide pre-treated with gel slick (Lonza, Switzerland), and a piece of silicified cover slip was put upon the gel solution to make a sandwich. After 5 min, the substrates were treated with sulfo-SANPAH (Thermo Fisher, USA) and coated with 1 mg/mL collagen I (Corning, USA) to facilitate the cell adhesion. Finally, the substrate was sterilized by 75% alcohol and UV before cell culture.

2.2. Cell Culture

Human aortic smooth muscle cells (SMCs) were purchased from ScienCell Research Laboratories (ScienCell, USA) and used for experiments at passages 5–10. Cells were cultured in SMC medium (ScienCell, USA) supplemented with 2% fetal bovine serum, 1% penicillin/streptomycin, and 1% smooth muscle cell growth supplement (SMCGS) in a 37°C incubator (Corning, USA) with 5% CO_2.

To induce the foam cell state, SMCs were primed by Chol: MβCD complex (20 μg/ml) (Sigma, USA), a "water-soluble cholesterol" for 72 h.

In the inhibition experiments, SMCs were treated with GSK2033 (MedChemExpress, China), a liver X receptor (LXR) inhibitor, at a final concentration of 1 μM in the culture medium for 72 h. DMSO was used as control.

In the agonist experiments, SMCs were treated with GW3965 (Sigma, USA), a selective agonist of LXR, at a final concentration of 1 μM in the culture medium for 72 h. DMSO was used as control.

2.3. Cell Viability Test

To optimize the concentration of Chol: MβCD, SMCs were seeded in a 96-well plate and treated with a concentration gradient of Chol: MβCD (0, 10, 20, 40, and 80 μg/ml) for 72 h at standard culture condition. Then, the culture media was removed and the cell were incubated with CCK-8 reagent (DOJINDO, Japan) for 1 h. Optical density (OD) at 450 nm of each well was determined using a plate-reader (Bio Tek, Synergy 2, USA). The OD of the experiment and the control groups were both corrected by subtracting the OD of the blank. Cell viability was expressed as the percentage $OD_{450\ nm}$ of experimental group to that of the control group.

2.4. Cellular Cholesterol Uptake and Quantitation

Oil Red O staining was used to quantify the amount of cholesterol in the SMCs. Briefly, after cholesterol loading, SMCs were fixed in 4% (w/v) paraformaldehyde (PFA) and incubated in 60% isopropanol for 3 min. Then, cells were stained with Oil Red O and Harris' hematoxylin. Images were captured by a light-microscope (DMI3000B, Leica, Germany). The cellular cholesterol was extract by isopropanol and OD value at 520 nm was determined to represent the cholesterol concentration.

The cholesterol uptake by SMCs was identified by BODIPY 493/503 staining (Qiu and Simon, 2016). After 20 μg/ml cholesterol treatment for 72 h, SMCs were washed 3 times with Dulbecco's phosphate buffered saline (DPBS) and 2 μM BODIPY 493/503 was added (Cayman, USA) for 15 min at 37°C in dark. Then, cells were fixed in 4% (w/v) PFA for 15 min, and incubated with DAPI for 5 min to stain the nucleus. Images were captured by a laser scanning confocal microscope (Leica, TCS SP5 II, Germany). Cholesterol uptake was quantified by relative fluorescence intensity (FI).

2.5. Cellular Cholesterol and Protein Determination

Cellular total cholesterol (TC) was determined by TC assay kit (NanJing Jiancheng Bioengineering Institute, China) according to manufacturer's instructions. The cellular cholesterol concentration was normalized by total protein content determined by BCA Protein Assay Kit (Thermo Scientific, USA).

2.6. Cholesterol Efflux Determination

Cholesterol concentration is proportional to the intensity of the 20S-methyl-21-[(7-nitro-2,1,3β-benzoxadiazol-4-yl) amino]-pregn-5-en-3-ol (NBD cholesterol) (J&K Scientific, China) fluorescence signal. After cholesterol loading, the SMCs were incubated with NBD cholesterol for 8 h and Apoa1 for additional 8 h to induce cholesterol efflux. The culture medium comprised of the cholesterol efflux was collected and the SMCs were lysed with 2% Triton X-100 to release the cholesterol remained in the cells. Both the efflux and the supernatant from the lysed cells (non-efflux) were subject for fluorescence intensity (FI) measuring at 528±20 nm (with 485±20 nm excitation wavelength). Cholesterol efflux rate = efflux FI / (efflux FI + non-efflux FI) × 100%.

TABLE 1 | RT-qPCR primer sequences.

Primer name	Forward primer (5'-3')	Reverse primer (5'-3')
GAPDH	GGGAAGGTGAAGGTCGGAGT	GGGGTCATTGATGGCAACA
ABCA1	CAGGAGGTGATGTTTCTGACC	CGCAGACAATACGAGACACAG
ACTA2	GGACATCAAGGAGAAACTGTG	CCATCAGGCAACTCGTAACT
CD68	TGCTTCTCTCATTCCCCTATG	GGTAGACAACCTTCTGCTGGA
LGALS3	CATGCTGATAACAATTCTGGG	GGTTAAAGTGGAAGGCAACAT

2.7. Real-Time Quantitative Polymerase Chain Reaction (RT-qPCR)

Total RNA was extracted with the RNA simple Total RNA Extraction kit (TIANGEN, China) and reverse transcribed into cDNA by using the Fastking RT kit (with gDNase) (TIANGEN, China), following the manufacturer's instruction. The mRNA level was determined by RT-qPCR (Thermo Fisher Scientific, USA) using the Talent qPCR PreMix Kit (SYBR Green) (TIANGEN, China) and the specific primer pairs was listed in **Table 1**. All data were normalized to GAPDH and expressed as fold change over the controls.

2.8. Western Blotting

Total protein of SMCs was extracted by the plus RIPA lysis buffer (Beyotime Biotechnology, China) with protease inhibitor. BCA Protein Assay Kit (Thermo Scientific, USA) was used to quantify the protein concentration. Then, equal amount of the total cell lysates was loaded for SDS-PAGE electrophoresis, and transferred to PVDF membrane. After 10% BSA blocking, the membrane was incubated with primary antibody and incubated overnight at 4°C. The primary antibodies used in this research are ACTA2 (Abcam, UK), CD68 (Abcam, UK), ABCA1 (Novus, USA), α-Tubulin (Cell Signaling Technology, USA), and GAPDH (Cell Signaling Technology, USA). After removing the primary antibody, HRP-conjugated secondary antibodies (Cell Signaling Technology, USA) were added and incubated with the membrane for 1 h at room temperature and visualized by Immobilon western chemiluminescent HRP substrate (Merck Millipore, Germany). The protein expression was normalized by the expression of α-Tubulin or GAPDH in respective samples.

2.9. Immunofluorescence Staining

To characterize the SMCs phenotype, cells were fixed in 4% (w/v) PFA, and incubated with primary antibodies of ACTA2 or CD68 overnight at 4°C. Then, cells were washed by DPBS and incubated with the fluorescent labeled secondary antibodies accordingly for 1 h at room temperature. Finally, cell nucleus was stained with DAPI for 5 min. Images were captured under a laser scanning confocal microscope (Leica, TCS SP5 II).

2.10. siRNA Transfection

SMCs were seeded on substrates with different stiffness overnight to reach 50–70% confluency before transfection. The negative siRNA control (NC) or siRNA targeting ABCA1 (siABCA1) (Guangzhou RiboBio, China) was transfected into SMCs at a concentration of 50 nM in the culture medium according to manufacturer's instructions. Twenty-four hours after the transfection, cholesterol was added into the cell culture medium and the cells were treated by cholesterol for 24 h.

2.11. Statistical Analysis

Unless otherwise indicated, the results were shown as mean ± SEM ($n = 3$), and student t-test was used for pairwise comparisons for the same stiffness between groups and the different stiffness within groups. For all cases, $p < 0.05$ was considered statistically significant. Data were analyzed by GraphPad Prism 6.0 software.

3. RESULTS

3.1. Cholesterol Accumulation Induced SMCs Phenotype Switching to a Foam Cell-Like State

To confirm the effects of loading on SMCs phenotype switching, Chol: MβCD, a "water-soluble cholesterol" that can be efficiently and quickly uptaken by cells, was used to treat SMCs (Christian et al., 1997; Qin et al., 2006). The cholesterol concentration was titrated to show that little cytotoxicity was detected at 20 μg/ml (or lower) after 72 h (**Figure 1A**). Meanwhile, the cellular uptake of cholesterol was confirmed by Oil Red O staining and quantitation. After Chol: MβCD treatment for 72 h, 20 μg/ml group showed more cholesterol droplets than the other two groups (**Figure 1C**). In addition, Oil Red O stained cellular cholesterol was extracted by isopropanol and the OD values were compared (**Figure 1B**).

Furthermore, to characterize the SMCs phenotype switching from SMCs to foam cell-like state, the gene expression level of SMC maker (ACTA2) and macrophage marker gene (CD68 and LGALS3) were analyzed by RT-qPCR. The continuous cholesterol accumulation significantly reduced ACTA2 expression and promoted CD68 and LGALS3 expression (**Figures 1D,E**). Moreover, ACTA2 and CD68 expression was confirmed by immunostaining and Western blotting analysis (**Figures 1F,G**).

3.2. Substrate Stiffness Regulated Cholesterol Level in SMCs

To explore the possible influence of substrate stiffness on SMCs cholesterol level, a lipophilic fluorescent probe, BODIPY 493/503, was used to label cellular neutral lipid contents. SMCs were seeded on substrate of different stiffness and treated by cholesterol at indicated times points. The cholesterol accumulation in SMCs showed a time-dependent increase during 72 h and significant difference at different substrate stiffness (**Figures 2A,B**). At the substrate stiffness of 1 and 100 kPa, cholesterol levels in SMCs were significantly higher than other groups at all time points. This was further confirmed by the quantitation of total cholesterol (TC) level where 1, 40, and 100 kPa were selected as representative stiffnesses (**Figure 2C**). These results suggested that the stiffness of the substrate affected the accumulation of cholesterol in SMCs.

3.3. Substrate Stiffness Affected SMCs Phenotypic Transformation

We further determined whether the changes in substrate stiffness would affect the SMCs phenotype. ACTA2 was chosen to represent the contractile phenotype of the SMCs and CD68 as a marker for macrophage phenotype. RT-qPCR results showed that there was a decrease in gene expression of SMC contractile maker ACTA2 and an increase in macrophage marker CD68 (**Figures 3A,B**) upon cholesterol treatment. While ACTA2 expression increased with substrate stiffness, the suppressive effect of cholesterol was consistent for all stiffness (**Figure 3A**). The treatment of cholesterol demonstrated a very strong external force to drive SMCs to express stronger macrophage phenotype. However, consistent with the low cholesterol accumulation on 40 kPa substrate, cholesterol treatment demonstrated a significantly lower CD68 expression on 40 kPa compared with 1 and 100 kPa (**Figure 3B**), implying that substrate stiffness exerted a regulatory effect on SMC phenotype. The protein expression level of both ACTA2 and CD68 was consistent with the mRNA level (**Figures 3C,D**). SMCs on the 40 kPa substrate showed a relatively smaller change in macrophage marker expression (**Figures 3E,F**), suggesting less phenotypic change occurred on 40 kPa substrate.

3.4. Substrate Stiffness Affected Cholesterol Accumulation in SMCs by Regulating Cholesterol Efflux Through ABCA1

Although cellular cholesterol homeostasis is a combined outcome of the uptake, synthesis, and efflux of cholesterol, cholesterol efflux is the key event of RCT to remove excess cholesterol. Cholesterol uptake by SMCs is largely mediated by non-specific pinocytosis (Rivera et al., 2013); therefore, we focused on the effect of substrate stiffness on the regulation of cholesterol efflux. Cholesterol efflux is mediated by ABCA1, an active transmembrane transporter related to the transmembrane transport of cholesterol and phospholipids. Interestingly, we found that ABCA1 mRNA expression on 40 kPa substrate was significantly higher than 1 and 100 kPa substrates (**Figure 4A**). Immunostaining showed that the expression of ABCA1 is higher on 40 kPa substrate compared to that on 1 and 100 kPa ones (**Figure 4B**). Western blotting analysis confirmed the protein level of ABCA1 being consistent with the gene expression level (**Figures 4C,D**). Therefore, the regulatory effect of substrate stiffness on cholesterol accumulation in SMC is related to ABCA1 expression and cholesterol efflux.

3.5. LXR Signaling Pathway Converged With Stiffness to Regulate ABCA1 and Cholesterol Efflux in SMCs

To further understand the influence of substrate stiffness on SMCs cholesterol efflux, we modulated the LXR signaling pathway, the upstream regulator of ABCA1, to regulate the expression of ABCA1. LXR has been reported as a sterol-responsive nuclear receptor. GW3965 is a selective agonist to LXR and GSK2033 is a selective LXR antagonist (Collins et al., 2002; Delvecchio et al., 2007; Helder et al., 2020). The activation

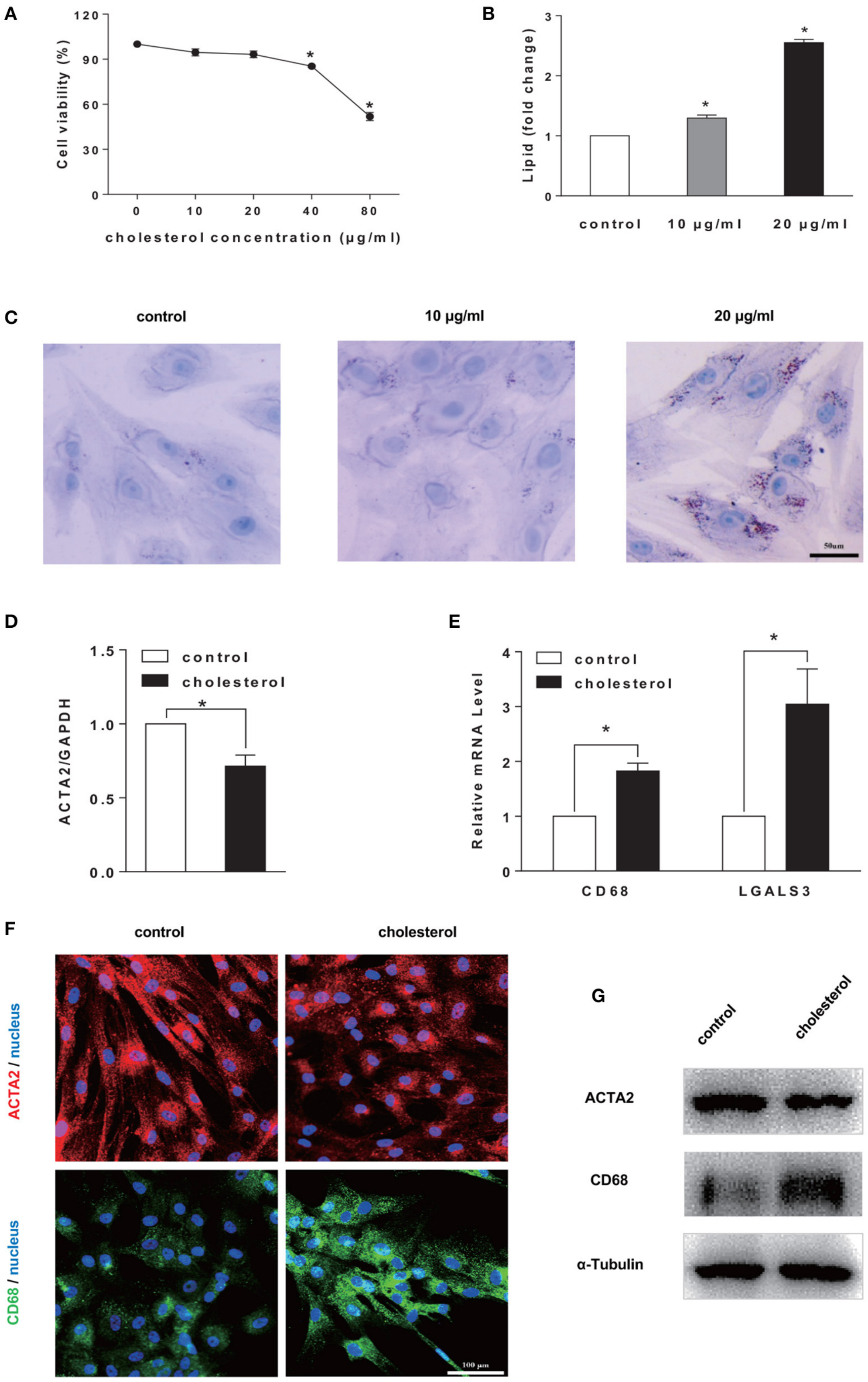

FIGURE 1 | Cholesterol accumulation induced SMCs phenotype switching to a foam cell-like state. **(A)** Cell viability test. SMCs were treated by Chol: MβCD at different concentrations for 72 h. CCK-8 was used to determine cell viability (*n* = 3). **(B,C)** Cellular cholesterol amount determination. Oil Red O staining (in **C**) (scale

(Continued)

FIGURE 1 | bar = 50 μm) and quantitation by colorimetric analysis ($n = 3$) (in **B**). **(D,E)** SMCs were treated with 20 μg/ml Chol: MβCD for 72 h, the mRNA expression level of SMC marker (ACTA2) and macrophage markers (CD68 and LGALS3) was measured by RT-qPCR. GAPDH was used as the internal control for normalization ($n = 3$). Fold change is the ratio of SMCs gene expression with and without (control) cholesterol treatment ($n = 3$). **(F)** ACTA2 (red) and CD68 (green) protein expression was examined by immunofluorescence staining (blue: DAPI staining of nucleus, scale bar = 100 μm). **(G)** ACTA2 and CD68 protein expression was analyzed by Western blotting analysis. The expression of α-Tubulin was used as the internal control ($n = 3$). *$p < 0.05$.

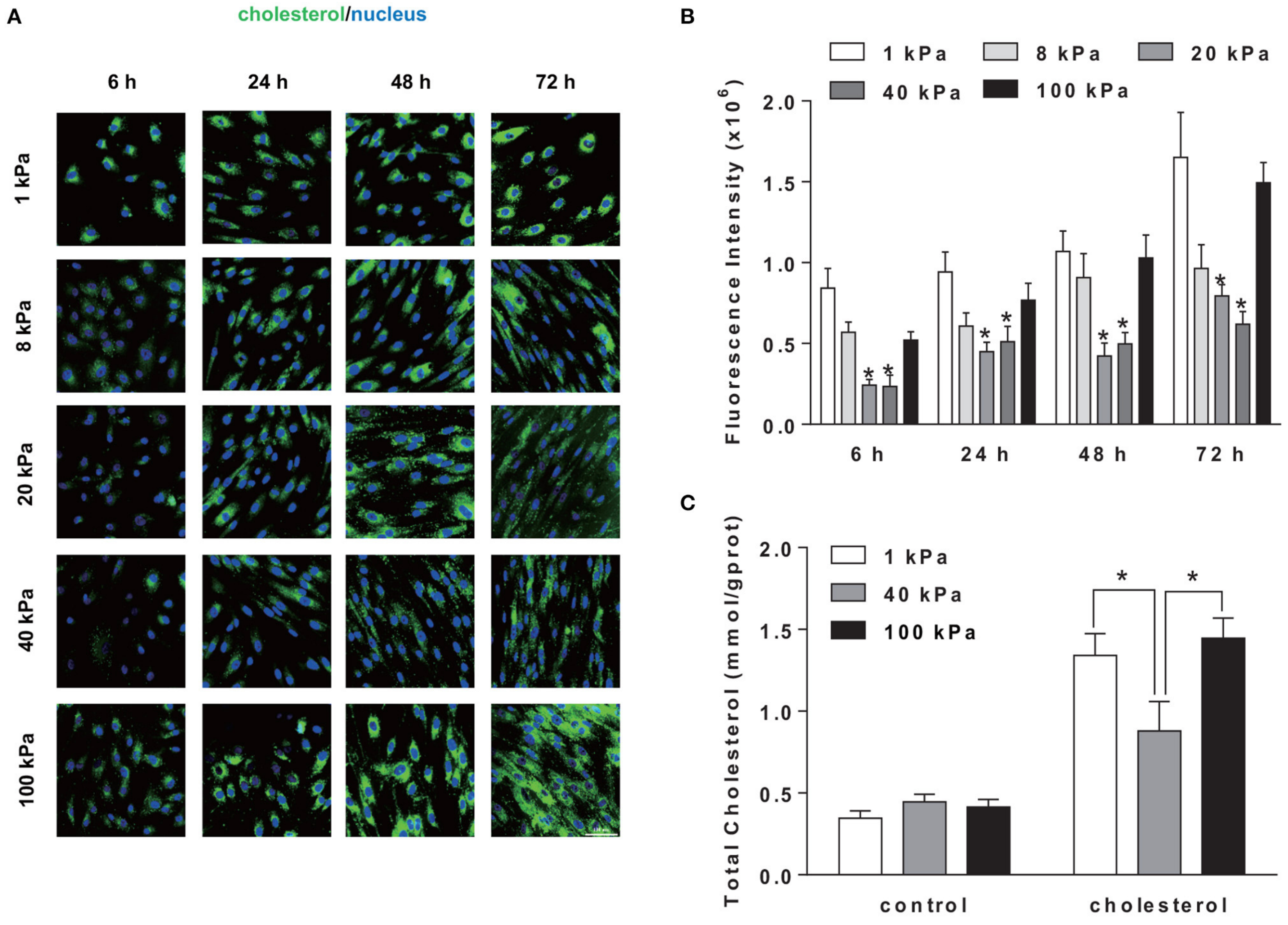

FIGURE 2 | Substrate stiffness regulated cholesterol level in SMCs. SMCs were seeded on substrate of different stiffness (1, 8, 20, 40, 100 kPa) at different time points (6, 24, 48, 72 h). **(A)** The cholesterol level in SMCs (green: BODIPY 493/503 staining of cholesterol; blue: DAPI staining of nucleus, scale bar = 100 μm). **(B)** The level of cholesterol quantified by the fluorescence intensity, which is the total green fluorescence intensity normalized by the number of the cell nucleus (determined by DAPI). *Indicates for comparison with 1 and 100 kPa $p < 0.05$. **(C)** After treated with 20 μg/ml of Chol: MβCD for 72 h, cellular total cholesterol (TC) was quantified by TC Kit and $OD_{510\ nm}$ was determined by a plate reader ($n = 3$). Cells without treatment were used as the control. *$p < 0.05$.

effect of GW3965 and the inhibition effect of GSK2033 on LXR expression was confirmed (**Figure 5A**). Activation of LXR by GW3965 treatment increased both the mRNA and protein expression of ABCA1 in SMCs (**Figures 5B,C**). Moreover, the expression level of LXR and ABCA1 on 40 kPa was higher than that on 1 and 100 kPa substrates. In contrast, inhibition of LXR by GSK2033 treatment almost abolished both the mRNA level and protein expression level of ABCA1 on all substrates with different stiffnesses (**Figures 5B,D**). As a result, with the upregulation of LXR and cholesterol treatment for 72 hours, SMC cholesterol efflux increased significantly ($p < 0.05$). In addition, compared with 1 and 100 kPa, 40 kPa stiffness induced the highest cholesterol efflux rate in SMCs, suggesting the additive effect of substrate stiffness and LXR signaling. In contrast, downregulating LXR by GSK2033 treatment blocked cholesterol efflux of SMCs, regardless of substrate stiffness (**Figure 5E**). Furthermore, change in cholesterol efflux resulted in the change of the cellular cholesterol content. BODIPY 493/503 staining demonstrated that LXR agonist GW3965 treatment led to very low cholesterol accumulation in SMCs, and there is no observable difference among the different substrate stiffness. However, inhibition of LXR resulted in the inhibition of cholesterol efflux. Consequently, the cellular cholesterol level was increased on all substrate stiffness (**Figure 5F**).

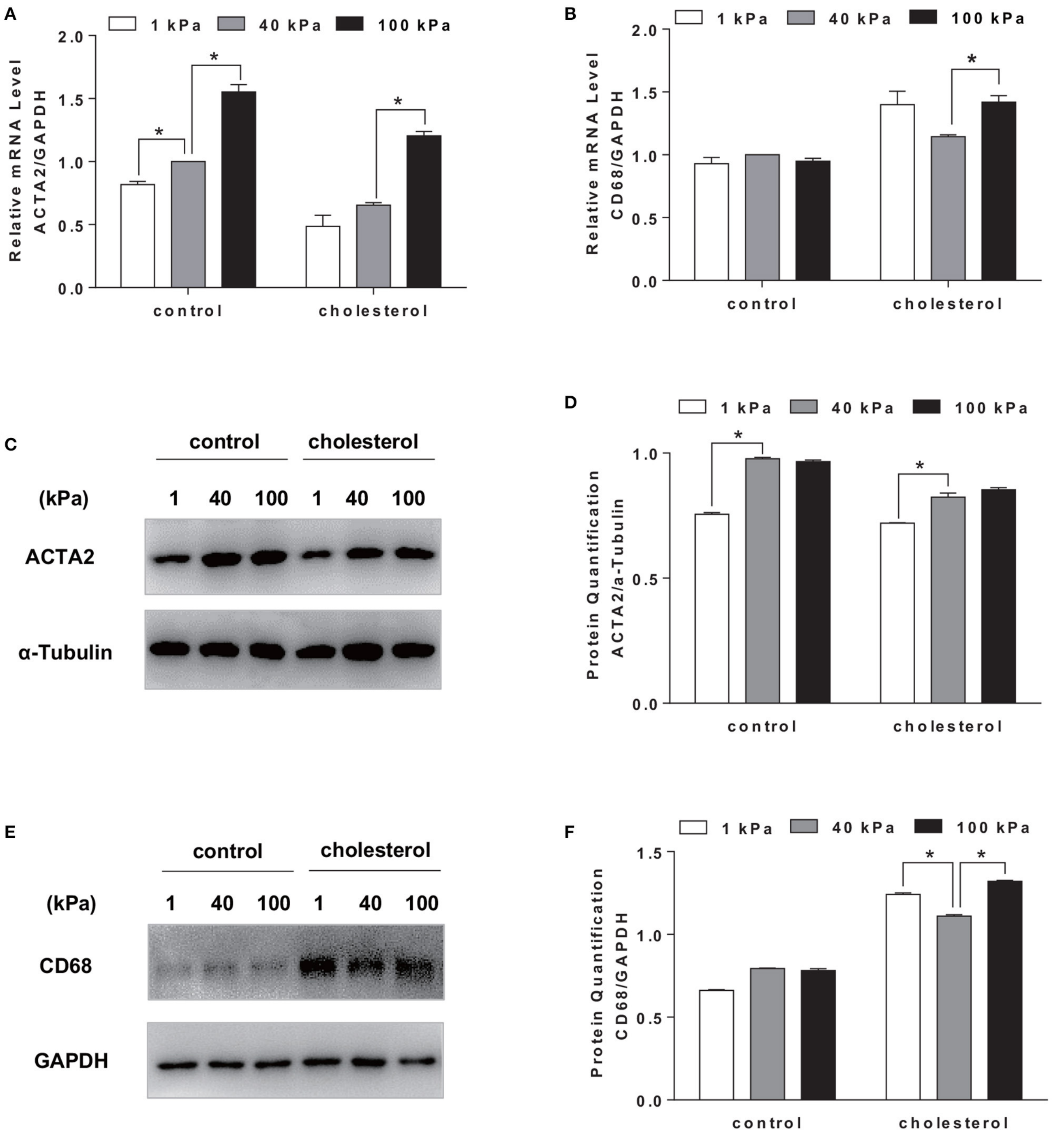

FIGURE 3 | Substrate stiffness affected SMCs phenotypic transformation. SMCs were seeded on substrate with different stiffness and treated with 20 μg/ml Chol: MβCD for 72 h. SMCs without treatment were used as control. **(A,B)** ACTA2 and CD68 gene expression level was measured by RT-qPCR. GAPDH was used as the internal control for normalization ($n = 3$). **(C,D)** ACTA2 protein expression was analyzed by Western blotting analysis. The expression of α-Tubulin was used as the internal control. Quantitation of the protein expression was calculated as the ratio of target protein to α-Tubulin ($n = 3$). **(E,F)** CD68 protein expression was analyzed by Western blotting analysis. The expression of GAPDH was used as the internal control. Quantitation of the protein expression was calculated as the ratio of target protein to GAPDH ($n = 3$). $^*p < 0.05$.

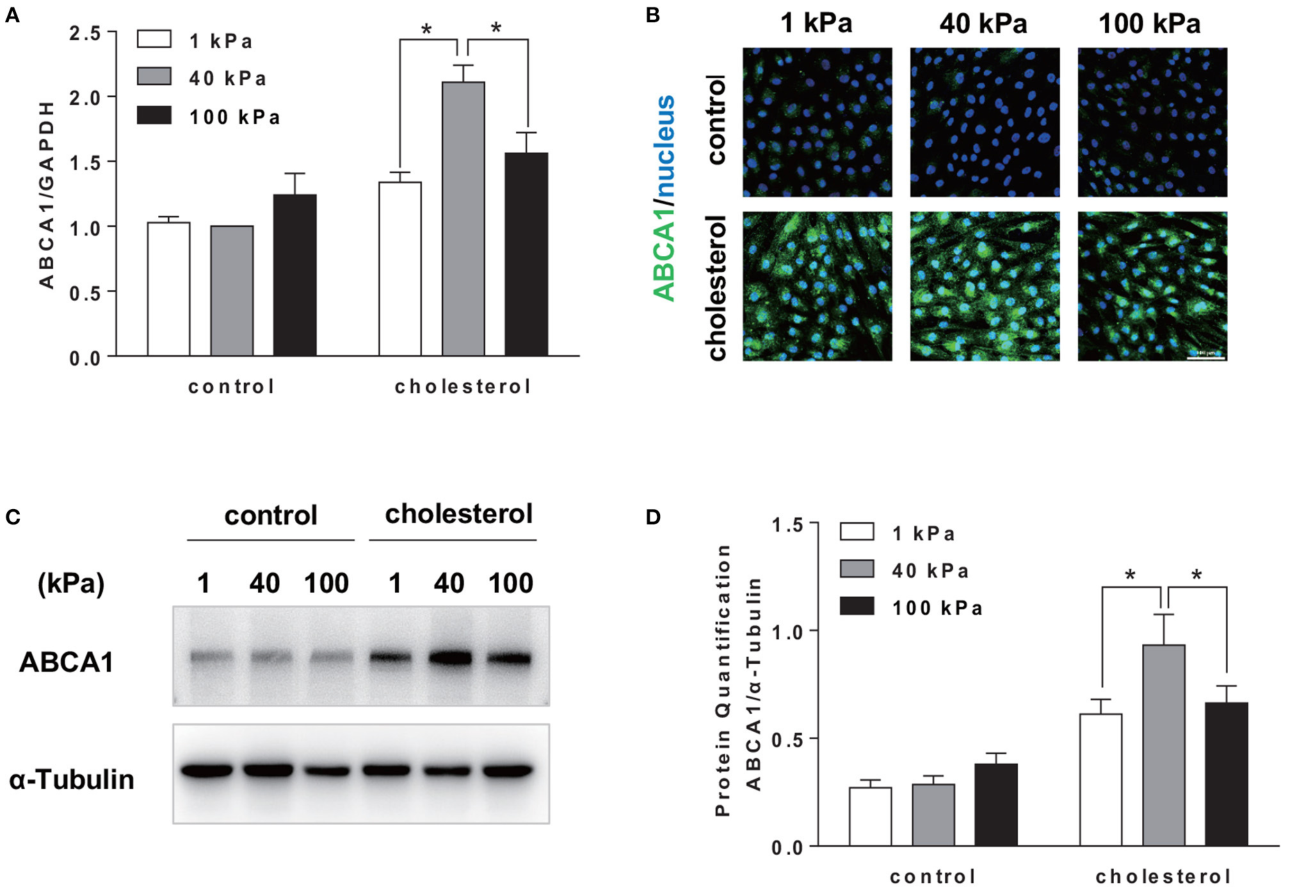

FIGURE 4 | Substrate stiffness affected cholesterol accumulation in SMCs by regulating cholesterol efflux through ABCA1. SMCs were seeded on substrate with different stiffness and treated with 20 μg/ml Chol: MβCD for 72 h. SMCs without treatment were used as control. **(A)** ABCA1 gene expression level was measured by RT-qPCR. GAPDH was used as the internal control for normalization ($n = 3$). **(B)** ABCA1 (green) expression in SMCs cultured on substrate with different stiffness without (control) or with cholesterol treatment (blue: DAPI staining of the nucleus, scale bar = 100 μm). **(C,D)** ABCA1 protein expression level was analyzed by Western blotting analysis. The expression of α-Tubulin was used as the internal control. Quantitation of the protein expression was calculated as the ratio of target protein to α-Tubulin ($n = 3$). $^{*}p < 0.05$.

3.6. Knockdown of ABCA1 Increased Cholesterol Accumulation in SMCs

To further verify that ABCA1 is a key mediator of substrate stiffness regulating cholesterol accumulation in SMCs, we knocked down cholesterol efflux gene ABCA1. The results showed that siABCA1 effectively reduced ABCA1 expression (**Figure 6A**). BODIPY 493/503 staining results showed that, compared with the control group, the cholesterol accumulation level in SMCs of each substrate stiffness was higher in the siABCA1 group (**Figures 6B,C**).

4. DISCUSSION AND CONCLUSION

SMCs are the main cell component to maintain the vascular wall structure and vascular tension. And their phenotypic transformation is essential to response to environment cues, including cytokines, mechanical influences, and extracellular cholesterol (Owens et al., 2004). In atherosclerosis, SMCs provide an initial location for the retention of cholesterol that facilitates the formation of thickened intimal layer. During this process, complex structural and functional changes occur in the SMCs, resulting in the development of the foam cells enclosing excess cholesterol (Rong et al., 2003; Feil et al., 2014). It has been reported that more than 50% of CD68^{+} foam cells are SMCs-derived in atherosclerotic lesion (Allahverdian et al., 2014). In addition, studies have shown that cholesterol load can induce the expression of macrophage marker CD68 in both mouse and human SMCs, meanwhile reducing the expression of the contractile marker ACTA2 (Rong et al., 2003; Vengrenyuk et al., 2015; Liu et al., 2017; Vendrov et al., 2019). Our results also showed that, cholesterol treatment reduced the expression of ACTA2 in SMCs although the gene and protein expression of ACTA2 still increased with substrate stiffness. On the other hand, the expression level of CD68 was lower at 40 kPa compared to the cells on and 100 kPa, suggesting a different mechanism of stiffness regulation. Taken together, these results suggested that substrate stiffness could regulate SMC phenotypic switching to

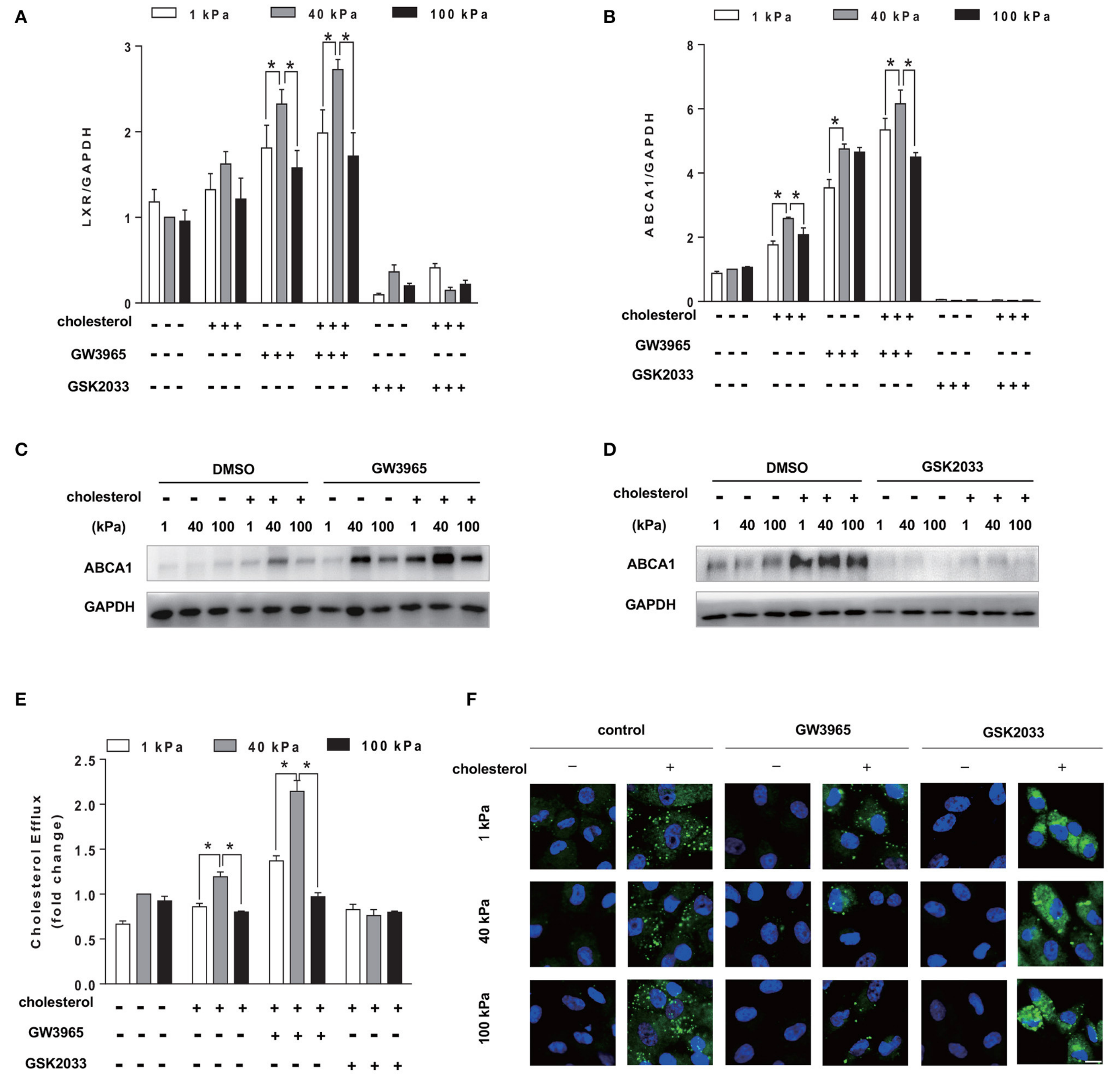

FIGURE 5 | Additive effect of substrate stiffness and LXR signaling pathway on ABCA1 expression and cholesterol efflux. SMCs were seeded on substrate with different stiffness and treated with 20 μg/ml Chol: MβCD and GW3965 (1 μM) or GSK2033 (1 μM) in the serum-free medium for 72 h. **(A,B)** LXR and ABCA1 gene expression level was measured by RT-qPCR. GAPDH was used as the internal control for normalization ($n = 3$). **(C,D)** ABCA1 protein expression was analyzed by Western blotting analysis after GW3965 or GSK2033 treatment. DMSO was used as control. The expression of GAPDH was used as the internal control ($n = 3$). **(E)** Cholesterol efflux rate. The results were expressed as fold change of all groups compared with the control group at 40 kPa ($n = 3$). **(F)** The cholesterol accumulation in SMCs after GW3965 or GSK2033 treatment (green: BODIPY 493/503 staining of cholesterol; blue: DAPI staining of nucleus, scale bar = 10 μm). $^*p < 0.05$.

foam cells and that the physiological level of substrate stiffness could suppress phenotypic changes.

Atherosclerosis is a chronic pathological process, in which the deposition of lipoproteins in the blood vessels leads to the softening of blood vessels and the formation of fat stripes. Subsequently, hyperplasia of fibrous tissue and calcareous deposition result in thickening and hardening of the arterial wall (Lemarié et al., 2010). Studies have shown that the stiffness of early lesion aortic was 10 times less than the normal aortic (Tian et al., 2019). In advanced atherosclerosis, vascular stiffness may increase to 100 kPa or more due to the calcification of arterial wall (Matsumoto et al., 2002). Our results showed that the

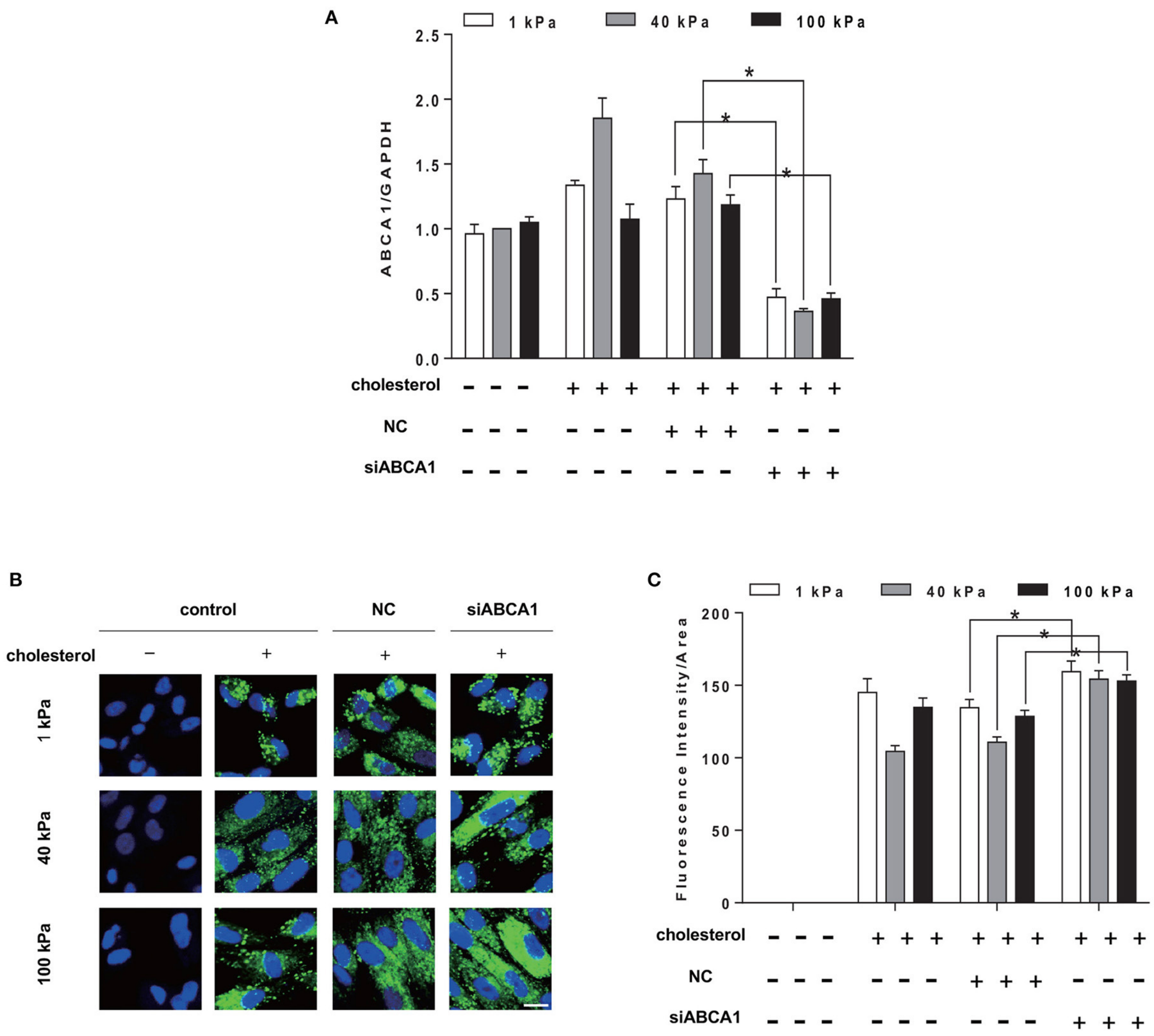

FIGURE 6 | Knockdown of ABCA1 promotes cholesterol accumulation in SMCs. SMCs were seeded on substrate with different stiffness and treated with 20 μg/ml Chol: MβCD and siABCA1 for 72 h. **(A)** ABCA1 gene expression level was measured by RT-qPCR. GAPDH was used as the internal control for normalization ($n = 3$) (NC, Negative siRNA control). **(B)** The cholesterol in SMCs after ABCA1 gene knockdown (green: BODIPY 493/503 staining of cholesterol; blue: DAPI staining of nucleus, scale bar = 10 μm). **(C)** The level of cholesterol quantified by the fluorescence intensity and normalized by the area of the green fluorescence. $*p < 0.05$.

substrate stiffness directly affected the cholesterol accumulation in SMCs. Among the stiffness range we tested (1, 8, 20, 40, 100 kPa), the cholesterol accumulation in SMCs on both softer (1 and 8 kPa) and harder substrates (100 kPa) demonstrated a significant trend of increase compared to those on substrates with moderate stiffness (20 and 40 kPa). Therefore, in the subsequent research, 1, 40, and 100 kPa substrate stiffness were selected as the experimental conditions. Interestingly, the result from cellular TC analysis confirmed this observation, that TC was also higher on 1 and 100 kPa substrates. This is a direct evidence that blood vessel stiffness within physiological to pathological range significantly affect SMCs cholesterol content.

Since cholesterol accumulation in the arterial wall is an important characteristic of atherosclerosis, RCT is considered to play a key role of anti-atherosclerosis. RCT can remove excess cholesterol from peripheral tissues to the liver (Liao and McLachlan, 2018). Specifically, apolipoprotein A1 (ApoA1) obtains free cholesterol through ABCA1 from peripheral cells and free cholesterol can be esterified into cholesterol ester by lecithin-cholesterol acyl transferase (LCAT) to mature high density lipoprotein (HDL). HDL can be selectively absorbed by liver. Finally, liver excretes cholesterol into feces or converted it into bile acid (Tall et al., 2008; Talbot et al., 2018). Studies have shown that the loss of ABCA1 and ABCG1 resulted in a significant decrease in the cholesterol efflux from macrophages (Yvan-Charvet et al., 2007). Consistently, our results demonstrated that the change in the expression level of ABCA1 resulted in the change in cholesterol content in the SMCs. Although ABCG1 is also responsible for cholesterol efflux, our results showed that there were only slight changes in the expression of ABCG1 among substrate stiffness compared to that of ABCA1 (**Supplementary Figure 1**). Moreover, substrate stiffness was directly responsible for the ABCA1 expression level change. Therefore, activation of RCT by enhancing ABCA1 expression through manipulating substrate stiffness may be an attractive strategy to alleviate cholesterol accumulation in the SMCs and prevent atherosclerosis.

LXR is the key regulator of lipid balance in mammals and plays an important role in regulating cholesterol transportation and lipid metabolism. Upon activation, LXR can induce the expression of membrane transporters, thereby promoting cholesterol efflux and preventing cholesterol overload (Choi et al., 2009; Hong and Tontonoz, 2014). It is reported that activation of LXR could induce the expression of ABCA1 in primary human airway SMCs, increasing cholesterol efflux. In addition, the RCT rate of macrophages increased after the treatment with synthetic LXR-RXR ligands T1317 (Delvecchio et al., 2007), which is in agreement with our results. Our results show that LXR agonist, GW3965, upregulated the expression level of ABCA1 and subsequently cholesterol efflux showing an additive effect with 40 kPa substrate stiffness. On the other hand, blocking cholesterol efflux by either using LXR antagonist GSK2033 or knocking down ABCA1 led to cholesterol retention inside SMCs. Although ABCA1 expression was higher at 40 kPa substrate stiffness, blocking ABCA1 expression by LXR abolished the stiffness effect, suggesting that ABCA1 is an important mediator of stiffness effect on cholesterol efflux.

In conclusion, our study demonstrates that different substrate stiffness regulates SMC phenotype switching in response to high extracellular cholesterol level. Both 1 and 100 kPa substrate stiffness increases cholesterol retention in SMCs by suppressing the cholesterol efflux, while intermediate substrate stiffness at 40 kPa results in the least cholesterol accumulation and helps maintain a contractile phenotype. Moreover, our results suggest that cholesterol efflux gene ABCA1 is a key mediator of substrate stiffness regulation of cholesterol accumulation in SMCs. These findings provide further insight into the biophysical regulation of cholesterol metabolism and SMC phenotype. In future studies, it would be interesting to explore how substrate stiffness transmits mechanical signals into SMCs and affects cholesterol accumulation or efflux.

DATA AVAILABILITY STATEMENT

The datasets presented in this study can be found in online repositories. The names of the repository/repositories and accession number(s) can be found at: https://www.ncbi.nlm.nih.gov/, NM 001256799.3; https://www.ncbi.nlm.nih.gov/, NM 005502; https://www.ncbi.nlm.nih.gov/, NM 001141945.2; https://www.ncbi.nlm.nih.gov/, NM 001040059; https://www.ncbi.nlm.nih.gov/, NM 001357678.

AUTHOR CONTRIBUTIONS

All authors have made significant contributions to the work and analysis and interpretation of data. SL, YZ, and XM conception or design of the work and manuscript writing. XM, YT, and HW acquisition of the data. All authors have approved the submitted version and have agreed both to be personally accountable for the author's own contributions and to ensure that questions related to the accuracy or integrity of any part of the work.

FUNDING

This work was supported by the National Key Research and Development Program of China (2016YFC1100202) to YZ, the Multidisciplinary Research Foundation of Shanghai Jiao Tong University, China (YG2021QN96) to YZ.

SUPPLEMENTARY MATERIAL

The Supplementary Material for this article can be found online at: https://www.frontiersin.org/articles/10.3389/fcell.2021.648715/full#supplementary-material

REFERENCES

Allahverdian, S., Chehroudi, A. C., McManus, B. M., Abraham, T., and Francis, G. A. (2014). Contribution of intimal smooth muscle cells to cholesterol accumulation and macrophage-like cells in human atherosclerosis. *Circulation* 129, 1551–1559. doi: 10.1161/CIRCULATIONAHA.113.005015

Allahverdian, S., Pannu, P. S., and Francis, G. A. (2012). Contribution of monocyte-derived macrophages and smooth muscle cells to arterial foam cell formation. *Cardiovasc. Res.* 95, 165–172. doi: 10.1093/cvr/cvs094

Chaabane, C., Coen, M., and Bochaton-Piallat, M.-L. (2014). Smooth muscle cell phenotypic switch: implications for foam cell formation. *Curr. Opin. Lipidol.* 25, 374–379. doi: 10.1097/MOL.0000000000000113

Chen, W., Tian, B., Liang, J., Yu, S., Zhou, Y., and Li, S. (2019). Matrix stiffness regulates the interactions between endothelial cells and monocytes. *Biomaterials* 221:119362. doi: 10.1016/j.biomaterials.2019.119362

Choi, H. Y., Rahmani, M., Wong, B. W., Allahverdian, S., McManus, B. M., Pickering, J. G., et al. (2009). ATP-binding cassette transporter A1 expression and apolipoprotein AI binding are impaired in intima-type arterial smooth muscle cells. *Circulation* 119:3223. doi: 10.1161/CIRCULATIONAHA.108.841130

Christian, A., Haynes, M., Phillips, M., and Rothblat, G. (1997). Use of cyclodextrins for manipulating cellular cholesterol content. *J. Lipid Res.* 38, 2264–2272. doi: 10.1016/S0022-2275(20)34940-3

Collins, J. L., Fivush, A. M., Watson, M. A., Galardi, C. M., Lewis, M. C., Moore, L. B., et al. (2002). Identification of a nonsteroidal liver x receptor agonist through parallel array synthesis of tertiary amines. *J. Med. Chem.* 45, 1963–1966. doi: 10.1021/jm0255116

Delvecchio, C. J., Bilan, P., Radford, K., Stephen, J., Trigatti, B. L., Cox, G., et al. (2007). Liver X receptor stimulates cholesterol efflux and inhibits expression of proinflammatory mediators in human airway smooth muscle cells. *Mol. Endocrinol.* 21, 1324–1334. doi: 10.1210/me.2007-0017

Falk, E. (2006). Pathogenesis of atherosclerosis. *J. Am. Coll. Cardiol.* 47(8 Suppl.), C7–C12. doi: 10.1016/j.jacc.2005.09.068

Feil, S., Fehrenbacher, B., Lukowski, R., Essmann, F., Schulze-Osthoff, K., Schaller, M., et al. (2014). Transdifferentiation of vascular smooth muscle cells to macrophage-like cells during atherogenesis. *Circ. Res.* 115, 662–667. doi: 10.1161/CIRCRESAHA.115.304634

Gelissen, I., and Brown, A. (2017). An overview of cholesterol homeostasis. *Methods Mol. Biol*. 1583, 1–6. doi: 10.1007/978-1-4939-6875-6

Gomez, D., and Owens, G. K. (2012). Smooth muscle cell phenotypic switching in atherosclerosis. *Cardiovasc. Res*. 95, 156–164. doi: 10.1093/cvr/cvs115

Helder, R. W., Boiten, W. A., van Dijk, R., Gooris, G. S., El Ghalbzouri, A., and Bouwstra, J. A. (2020). The effects of LXR agonist t0901317 and LXR antagonist gsk2033 on morphogenesis and lipid properties in full thickness skin models. *Biochim. Biophys. Acta* 1865:158546. doi: 10.1016/j.bbalip.2019.158546

Hong, C., and Tontonoz, P. (2014). Liver X receptors in lipid metabolism: opportunities for drug discovery. *Nat. Rev. Drug Discov*. 13, 433–444. doi: 10.1038/nrd4280

Im, S.-S., and Osborne, T. F. (2011). Liver x receptors in atherosclerosis and inflammation. *Circ. Res*. 108, 996–1001. doi: 10.1161/CIRCRESAHA.110.226878

Joseph, S. B., McKilligin, E., Pei, L., Watson, M. A., Collins, A. R., Laffitte, B. A., et al. (2002). Synthetic LXR ligand inhibits the development of atherosclerosis in mice. *Proc. Natl. Acad. Sci. U.S.A*. 99, 7604–7609. doi: 10.1073/pnas.112059299

Lemarié, C. A., Tharaux, P.-L., and Lehoux, S. (2010). Extracellular matrix alterations in hypertensive vascular remodeling. *J. Mol. Cell. Cardiol*. 48, 433–439. doi: 10.1016/j.yjmcc.2009.09.018

Liao, S., and McLachlan, C. S. (2018). Cholesterol efflux: does it contribute to aortic stiffening? *J. Cardiovasc. Dev. Dis*. 5:23. doi: 10.3390/jcdd5020023

Libby, P., Ridker, P. M., and Hansson, G. K. (2011). Progress and challenges in translating the biology of atherosclerosis. *Nature* 473, 317–325. doi: 10.1038/nature10146

Litvinov, D. Y., Savushkin, E. V., Garaeva, E. A., and Dergunov, A. D. (2016). Cholesterol efflux and reverse cholesterol transport: experimental approaches. *Curr. Med. Chem*. 23, 3883–3908. doi: 10.2174/0929867323666160809093009

Liu, Q., Zhang, H., Lin, J., Zhang, R., Chen, S., Liu, W., et al. (2017). C1Q/TNF-related protein 9 inhibits the cholesterol-induced vascular smooth muscle cell phenotype switch and cell dysfunction by activating amp-dependent kinase. *J. Cell. Mol. Med*. 21, 2823–2836. doi: 10.1111/jcmm.13196

Matsumoto, T., Abe, H., Ohashi, T., Kato, Y., and Sato, M. (2002). Local elastic modulus of atherosclerotic lesions of rabbit thoracic aortas measured by pipette aspiration method. *Physiol. Meas*. 23:635. doi: 10.1088/0967-3334/23/4/304

Maxfield, F. R., and Tabas, I. (2005). Role of cholesterol and lipid organization in disease. *Nature* 438, 612–621. doi: 10.1038/nature04399

Oram, J. F., and Heinecke, J. W. (2005). ATP-binding cassette transporter A1: a cell cholesterol exporter that protects against cardiovascular disease. *Physiol. Rev*. 85, 1343–1372. doi: 10.1152/physrev.00005.2005

Owens, G. K., Kumar, M. S., and Wamhoff, B. R. (2004). Molecular regulation of vascular smooth muscle cell differentiation in development and disease. *Physiol. Rev*. 84, 767–801. doi: 10.1152/physrev.00041.2003

Qin, C., Nagao, T., Grosheva, I., Maxfield, F. R., and Pierini, L. M. (2006). Elevated plasma membrane cholesterol content alters macrophage signaling and function. *Arterioscl. Thromb. Vasc. Biol*. 26, 372–378. doi: 10.1161/01.ATV.0000197848.67999.e1

Rasheed, A., and Cummins, C. L. (2018). Beyond the foam cell: the role of LXRs in preventing atherogenesis. *Int. J. Mol. Sci*. 19:2307. doi: 10.3390/ijms19082307

Rivera, J., Walduck, A. K., Thomas, S. R., Glaros, E. N., Hooker, E. U., Guida, E., et al. (2013). Accumulation of serum lipids by vascular smooth muscle cells involves a macropinocytosis-like uptake pathway and is associated with the downregulation of the ATP-binding cassette transporter A1. *Naunyn-Schmiedeberg's Arch. Pharmacol*. 386, 1081–1093. doi: 10.1007/s00210-013-0909-5

Rong, J. X., Shapiro, M., Trogan, E., and Fisher, E. A. (2003). Transdifferentiation of mouse aortic smooth muscle cells to a macrophage-like state after cholesterol loading. *Proc. Natl. Acad. Sci. U.S.A*. 100, 13531–13536. doi: 10.1073/pnas.1735526100

Rudijanto, A. (2007). The role of vascular smooth muscle cells on the pathogenesis of atherosclerosis. *Acta Med. Indones*. 39, 86–93.

Sanyour, H. J., Li, N., Rickel, A. P., Childs, J. D., Kinser, C. N., and Hong, Z. (2019). Membrane cholesterol and substrate stiffness co-ordinate to induce the remodelling of the cytoskeleton and the alteration in the biomechanics of vascular smooth muscle cells. *Cardiovasc. Res*. 115, 1369–1380. doi: 10.1093/cvr/cvy276

Sehgel, N. L., Vatner, S. F., and Meininger, G. A. (2015). "Smooth muscle cell stiffness syndrome"–revisiting the structural basis of arterial stiffness. *Front. Physiol*. 6:335. doi: 10.3389/fphys.2015.00335

Simons, K., and Ikonen, E. (2000). How cells handle cholesterol. *Science* 290, 1721–1726. doi: 10.1126/science.290.5497.1721

Talbot, C. P., Plat, J., Ritsch, A., and Mensink, R. P. (2018). Determinants of cholesterol efflux capacity in humans. *Prog. Lipid Res*. 69, 21–32. doi: 10.1016/j.plipres.2017.12.001

Tall, A. R., Yvan-Charvet, L., Terasaka, N., Pagler, T., and Wang, N. (2008). HDL, ABC transporters, and cholesterol efflux: implications for the treatment of atherosclerosis. *Cell Metab*. 7, 365–375. doi: 10.1016/j.cmet.2008.03.001

Tian, B., Ding, X., Song, Y., Chen, W., Liang, J., Yang, L., et al. (2019). Matrix stiffness regulates SMC functions via TGF-β signaling pathway. *Biomaterials* 221:119407. doi: 10.1016/j.biomaterials.2019.119407

Tracqui, P., Broisat, A., Toczek, J., Mesnier, N., Ohayon, J., and Riou, L. (2011). Mapping elasticity moduli of atherosclerotic plaque *in situ* via atomic force microscopy. *J. Struct. Biol*. 174, 115–123. doi: 10.1016/j.jsb.2011.01.010

van der Wulp, M. Y., Verkade, H. J., and Groen, A. K. (2013). Regulation of cholesterol homeostasis. *Mol. Cell. Endocrinol*. 368, 1–16. doi: 10.1016/j.mce.2012.06.007

Vendrov, A. E., Sumida, A., Canugovi, C., Lozhkin, A., Hayami, T., Madamanchi, N. R., et al. (2019). Noxa1-dependent nadph oxidase regulates redox signaling and phenotype of vascular smooth muscle cell during atherogenesis. *Redox Biol*. 21:101063. doi: 10.1016/j.redox.2018.11.021

Vengrenyuk, Y., Nishi, H., Long, X., Ouimet, M., Savji, N., Martinez, F. O., et al. (2015). Cholesterol loading reprograms the microrna-143/145-myocardin axis to convert aortic smooth muscle cells to a dysfunctional macrophage-like phenotype. *Arteriosc. Thromb. Vasc. Biol*. 35, 535–546. doi: 10.1161/ATVBAHA.114.304029

Yu, X.-H., Fu, Y.-C., Zhang, D.-W., Yin, K., and Tang, C.-K. (2013). Foam cells in atherosclerosis. *Clin. Chim. Acta* 424, 245–252. doi: 10.1016/j.cca.2013.06.006

Yvan-Charvet, L., Ranalletta, M., Wang, N., Han, S., Terasaka, N., Li, R., et al. (2007). Combined deficiency of ABCA1 and ABCG1 promotes foam cell accumulation and accelerates atherosclerosis in mice. *J. Clin. Invest*. 117, 3900–3908. doi: 10.1172/JCI33372

Conflict of Interest: The authors declare that the research was conducted in the absence of any commercial or financial relationships that could be construed as a potential conflict of interest.

frontiers
in Cell and Developmental Biology

ORIGINAL RESEARCH
published: 01 June 2021
doi: 10.3389/fcell.2021.642108

Shear Stress Accumulation Enhances von Willebrand Factor-Induced Platelet P-Selectin Translocation in a PI3K/Akt Pathway-Dependent Manner

Jinhua Fang[1], Xiaoxi Sun[1], Silu Liu[1], Pu Yang[1], Jiangguo Lin[1,2], Jingjing Feng[1], Miguel A. Cruz[3], Jing-fei Dong[4], Ying Fang[1] and Jianhua Wu[1]**

[1] Institute of Biomechanics/School of Biology and Biological Engineering, South China University of Technology, Guangzhou, China, [2] Research Department of Medical Sciences, Guangdong Provincial People's Hospital, Guangdong Academy of Medical Sciences, Guangzhou, China, [3] Cardiovascular Research Section, Department of Medicine, Baylor College of Medicine/Center for Translational Research on Inflammatory Diseases (CTRID), Michael E. DeBakey Veterans Affairs Medical Center, Houston, TX, United States, [4] Bloodworks Research Institute and Hematology Division, Department of Medicine, University of Washington, Seattle, WA, United States

Edited by:
Jing Zhou,
Peking University, China

Reviewed by:
Hans Deckmyn,
KU Leuven Kulak, Belgium
Georgy Guria,
National Research Center for Hematology, Russia

***Correspondence:**
Jianhua Wu
wujianhua@scut.edu.cn
Ying Fang
yfang@scut.edu.cn

Specialty section:
This article was submitted to Cell Adhesion and Migration, a section of the journal Frontiers in Cell and Developmental Biology

Received: *15 December 2020*
Accepted: *21 April 2021*
Published: *01 June 2021*

Citation:
Fang J, Sun X, Liu S, Yang P, Lin J, Feng J, Cruz MA, Dong J-f, Fang Y and Wu J (2021) Shear Stress Accumulation Enhances von Willebrand Factor-Induced Platelet P-Selectin Translocation in a PI3K/Akt Pathway-Dependent Manner. Front. Cell Dev. Biol. 9:642108. doi: 10.3389/fcell.2021.642108

Platelet adhesion and activation through the interaction of von Willebrand factor (VWF) with platelet glycoprotein (GP) Ibα are the early key events in hemostasis and thrombosis especially under high blood shear stress. P-selectin translocation from α granule to the cell surface is a typical platelet function phenotype, which makes the platelet-induced inflammatory response of flowing leukocytes possible and can be induced by either chemical agonists (thrombin, ADP, etc.) or high blood shear stress, but regulations of VWF mutation and blood shear stress on VWF-induced P-selectin translocation remain unclear. With flow cytometry, parallel plate flow chamber, and immunofluorescence staining techniques, we examined the P-selectin translocation of platelets on immobilized wild-type (WT) VWF-A1 domain and its two mutants, the gain-of-function (GOF) mutant R1308L and the loss-of-function (LOF) mutant G1324S, respectively. The results showed that the VWF-A1-induced platelet P-selectin translocation was triggered, accelerated, and enhanced by fluid shear stress and could be correlated with shear stress accumulation (SSA, the product of fluid shear stress and mechanical stimulus time), and the PI3K/Akt axis was involved in the platelet P-selectin translocation. The force-triggered P-selectin translocation occurred quickly on partial platelet surface first and then extended gradually to the whole platelet surface as SSA increased. The P-selectin translocation process would be promoted by the GOF mutation (R1308L) but slowed down by the LOF mutation (G1324S). These findings demonstrated a force-enhanced regulation mechanism for the VWF-induced platelet P-selectin translocation through the PI3K/Akt pathway and provided a novel insight into the mechano-chemical regulation mechanism for the key events, such as platelet activation and functional phenotype change in hemostasis and thrombosis.

Keywords: platelet, P-selectin, shear stress, PI3K/Akt pathway, VWF-A1 domain and its mutants

INTRODUCTION

Platelet activation is essential for thrombosis and hemostasis (Semple et al., 2011). P-selectin translocation is a key event that occurs in platelet activation and contributes to subsequent platelet aggregation and neutrophil recruitment (Ludwig et al., 2007; Korporaal et al., 2019; Tseng et al., 2019). Circulating platelets generally are at rest and coexist peacefully with endothelial cells under physiological conditions but can tether to, roll on, and adhere to injured vessel sites through the interaction of platelet glycoprotein (GP) Ibα to von Willebrand factor (VWF) which is secreted from the damaged vascular endothelial cells and ligated to the exposed subendothelial collagen (van der Meijden and Heemskerk, 2019). Once the recruited platelets are activated through transmembrane VWF-GPIbα signaling, P-selectin in platelet alpha particles can be expressed quickly on the platelet surface through membrane fusion (Furie et al., 2001; Gao et al., 2008; Li et al., 2010; Amelirad et al., 2019).

It is believed that soluble chemical agonists, such as thrombin and ADP as well as PAR1-AP, can induce platelet activation and P-selectin translocation through G protein-coupled receptors signaling in a dose-dependent manner in the absence of shear stress (Ivelin et al., 2019; St John et al., 2019; Schwarz et al., 2020), while prolonging the stimulus time will cause a decrease in platelet P-selectin surface density due to both the internalization and cleavage of P-selectin from the cell surface (Au and Josefsson, 2017). Besides the agonists, collagen can induce platelet P-selectin translocation through collagen-GPVI signaling (Ollivier et al., 2014), and shear stress does so (Lu and Malinauskas, 2011; Yin et al., 2011; Ding et al., 2015; Chen et al., 2016). The platelet P-selectin translocation would increase with applied shear stress and exposure time using a centrifugal flow-through Couette device (Chen et al., 2015). The P-selectin-positive platelet fraction can increase from 1.8 to 3.1% by applying a fluid load (shear rate of 1,000/s for 5 min) to whole blood with a cone-and-plate viscosimeter (Hu et al., 2003) but reaches 18.8% if shear stress of 70 dyn/cm^2 is applied to platelets for 10 min (Roka-Moiia et al., 2020). High shear stress of 150 dyn/cm^2 induced 12.8% P-selectin translocation after 5 min with a rotational viscometer and was enhanced with the increase of exposure time (Konstantopoulos et al., 1998; Merten et al., 2000). The response time of P-selectin translocation is not only agonist dependent (Whiss et al., 1998) but also force dependent. Fluid load (shear stress rate of 11,560/s) on whole blood makes the response time shorter than 1 s (Rahman and Hlady, 2019, 2021).

It is demonstrated that inhibiting VWF-GPIbα interaction can reduce effectively the force-induced platelet P-selectin translocation (Goto et al., 2000; Rahman and Hlady, 2021), while VWF-GPIbα signaling through PI3K/Akt participated in platelet integrin activation and high shear stress-induced platelet P-selectin translocation (Spater et al., 2018; Chen et al., 2019; Kral-Pointner et al., 2019). It is believed that catch–slip bond transition governs the interaction of VWF with GPIbα and retains but shifts the shear stress threshold in the cases of type 2B or 2M VWF mutations that result in bleeding disorders (Coburn et al., 2011). Pathological mutations on VWF might affect the binding of VWF to GPIbα. The gain of function (GOF) mutant R1308L has a higher binding affinity to GPIbα in comparison with wild-type (WT) VWF, and the loss-of-function (LOF) mutant G1324S does inversely (Baronciani et al., 2005; Morales et al., 2006; Auton et al., 2009; Federici et al., 2009). However, the regulation of both mechanical force and VWF mutation on platelet P-selectin translocation is not fully understood so far.

We herein studied the P-selectin translocation of platelets which were firmly adhered to a substrate coated with VWF-A1 or its two mutants (G1324S and R1308L) under various fluid shear stresses using parallel plate flow chamber (PPFC) and immunofluorescence staining. The present results showed that platelet P-selectin translocation was triggered, accelerated, and enhanced by shear stress but correlated with shear stress accumulation (SSA) instead of shear stress and mechanical stimulus time. Platelet P-selectin translocation was enhanced through GOF mutant R1308L but reduced by LOF mutant G1324S. The molecules PI3K and Akt were involved in the VWF-A1-induced P-selectin translocation. This work might provide a novel insight into the mechano-chemical regulation mechanism for the key early events in hemostasis and thrombosis.

MATERIALS AND METHODS

Reagents

Apyrase, phorbol 12-myristate 13-acetate (PMA), Akt1/2 kinase inhibitor, and wortmannin (PI3 kinase inhibitor) were gained from Sigma-Aldrich (Burlington, MO, United States). FITC-conjugated anti-P-selectin antibody was purchased from AbD Serotec (Kidlington, Oxford, United Kingdom). The rabbit anti-human P-selectin polyclonal antibody was from Sino Biological, Inc. (Beijing, China), and the Alexa Fluor 488-conjugated goat anti-rabbit IgG secondary antibody was obtained from Thermo Fisher Scientific^{TM} (Waltham, MA, United States). All the other reagents were of analytical grade or the best grade available.

Preparation of Washed Platelets

Washed platelets were prepared as reported elsewhere (Da et al., 2014). Briefly, blood was collected from healthy volunteers who had taken no medicine during the previous 2 weeks into vacuum blood collection tubes containing sodium citrate, according to the standard procedure. The blood was centrifuged at 200 × *g* for 10 min at room temperature. The platelet-rich plasma collected was supplemented with 5 U/ml apyrase to block platelet aggregation and centrifuged again at 1,000 × *g* for 10 min. The supernatant was removed, and the pellet was resuspended at a final concentration of 3×10^7/ml in phosphate-buffered saline (PBS) containing 5% platelet-poor plasma.

Expression and Purification of Recombinant VWF-A1 and Mutants

Recombinant VWF-A1 (amino acids Q1238–P1458) polypeptide was expressed in *Escherichia coli* as a fusion protein containing the His-tag in the N-terminus and purified as previously described (Cruz et al., 2000). Briefly, WTA1 protein was collected by centrifugation at 3,000 × *g* for 20 min at 4°C, resuspended in

50 mM phosphate buffer, pH 7.4, containing 500 mM NaCl, and sonicated. The clear lysate was applied to 5 ml HisTrap™ HP column (GE Healthcare, Marlborough, MA, United States). After being washed with 50 mM sodium phosphate, 500 mM NaCl, and 20 mM imidazole at pH 7.4, the bound protein was eluted with the same buffer containing 150 mM imidazole. Mutant (R1308L and G1324S) plasmids were constructed by site-directed mutagenesis with Quick-Change II XL Site-Directed Mutagenesis kit (Agilent, Santa Clara, CA, United States) using the WTA1 plasmid as a template. The recombinant mutants were prepared as described for the WTA1 protein. The purified proteins were verified by 12% sodium dodecyl sulfate polyacrylamide gel electrophoresis (SDS-PAGE) and Western blot (data shown in **Supplementary Figure 1**). To verify the function of the purified proteins, the proteins were incubated overnight at a concentration of 200 μg/ml on petri dishes and then blocked with 2% bovine serum albumin (BSA) at room temperature for 1 h after washing with PBS thrice. The washed platelets were perfused at a shear stress of 1 dyn/cm^2 for 5 min, and the number of adhering platelets at the last 1 min was recorded with an inverted microscope (Axio Observer A1, Zeiss, Oberkochen, Germany).

Flow Cytometry

To confirm the role of shear stress in platelet P-selectin translocation induced by VWF-A1, the washed platelets were incubated in five distinct solutions with (i) PBS which served as a blank control, (ii) 1 μM of PMA as a positive control, (iii) 200 μg/ml of WTA1, (iv) 200 μg/ml of the mutant R1308L, and (v) 200 μg/ml of the mutant G1324S for 10 min at room temperature and then centrifuged at 1,000 × *g* for 5 min to remove excessive agonists. The platelets were resuspended and fixed in 2% paraformaldehyde for 30 min. After washing with PBS, the fixed platelets were blocked with 2% BSA at room temperature for 1 h. The PBS, PMA, WTA1, R1308L, or G1324S-treated platelets were incubated with a FITC-conjugated anti-P-selectin antibody in dark condition for 1 h. After washing with PBS, the samples were analyzed using flow cytometry (BD Biosciences, Franklin Lakes, NJ, United States). For each condition, three replicative experiments were performed.

Immunostaining of Platelet P-Selectin in the Flow Assay

With the parallel-plate flow chamber (length × width × height = 20 mm × 2.5 mm × 0.254 mm) experimental system (**Supplementary Figure 2**), the platelets were loaded by shear stress. Purified VWF-A1 (WTA1, R1308L, and G1324S) were diluted with PBS to 200 μg/ml, respectively, and 20 μl of the solutions was added into petri dishes (Corning, NY, United States), which were held by a hollowed silicon gasket, marked in the cover slide center, and incubated overnight at 4°C. After washing with PBS containing 2% BSA thrice, the functionalized substrate was incubated with the same solution for 1 h at room temperature to block non-specific cell adhesion. Platelets (3 × 10^7/ml) were perfused into the flow chamber. The washed platelets were incubated in petri dishes coated with WTA1, R1308L, or G1324S for 10 min and adhered to the petri dishes. At the end of the incubation, the platelets were stimulated by perfusing PBS at various fluid shear stresses for a range of time (0, 1, 2, 4, and 8 min). Prior to incubation with a rabbit anti-human P-selectin polyclonal antibody at 5 μg/ml in PBS containing 2% BSA, the stimulated platelets were fixed in 2% paraformaldehyde for 30 min at room temperature and subjected to saturation with PBS containing 2% BSA. An Alexa Fluor 488-conjugated goat anti-rabbit IgG secondary antibody at 4 μg/ml was used as a secondary antibody. To explore the signal pathway involved in the platelet P-selectin translocation induced by VWF-A1 in flows, washed platelets were pretreated with 1 μM wortmannin (Wymann and Arcaro, 1994) or 10 μM Akt1/2 kinase inhibitor (Sandstrom et al., 2019) for 10 min or 1 h at 37°C, respectively, before the perfusion. Observation and acquisition of differential interference contrast and fluorescence microscopy images were made using a fluorescence microscope. To investigate the platelet P-selectin translocation induced by shear stress without VWF-A1, the platelets were allowed to incubate on an empty petri dish for 10 min, and shear stress of 0 and 10 dyn/cm^2 were applied to the platelets with a PPFC for 8 min, respectively. After fixing with 2% paraformaldehyde, the platelets were incubated with the rabbit anti-P-selectin antibody and goat anti-rabbit conjugated Alexa flour 488 secondary antibody, and the level of P-selectin translocation on the platelet surface was observed with a microscope. All images were processed with ImageJ software to derive the parameters.

Character Parameters for Scaling Platelet P-Selectin Translocation

To quantify P-selectin translocation on activated platelet, three parameters, such as F_P (the fraction of P-selectin-positive platelets to total immobilized platelets on substrates) and A_P (the mean of P-selectin coverage area per P-selectin-positive platelet) as well as FI_P (the mean normalized platelet P-selectin-related fluorescence intensity per P-selectin-positive platelet), were chosen herein. With the immunofluorescence experimental data, the characteristic parameters F_P, A_P, and FI_P were calculated by

$$\mathrm{F_P} = \frac{\mathrm{N_{positive}}}{\mathrm{N}},\ \mathrm{A_P} = \frac{\mathrm{A_1+A_2+\cdots+A_n}}{\mathrm{N_{positive}}} \text{ and}$$

$$\mathrm{FI_P} = \frac{\mathrm{FI_1+FI_2+\cdots+FI_n}}{\mathrm{N_{positive}}} \text{ with } \mathrm{FI_j} = \frac{\mathrm{FI^{(j)}-FI_B}}{\mathrm{FI_B}} \qquad (1)$$

A_P, FI_j, and $\mathrm{FI}^{(j)}$ were the P-selectin coverage area, the P-selectin-related fluorescence intensity, and its normalized one of the *j*-th immobile platelet, respectively. $N_{positive}$ and N represented the P-selectin-positive and total numbers of immobile platelets, respectively, and FI_B was the fluorescence intensity of the substrate background far away from each P-selectin-positive platelet. The fluorescent intensities on platelets were detected by Alexa Fluor 488-labeled antibody and used to estimate the platelet P-selectin translocation level.

Statistics

Data are expressed as means ± standard error of the mean (SEM) from at least three independent experiments. Statistical significance was assayed by one-way (or two-way) ANOVA for multiple comparisons with a Bonferroni *post hoc* test ($^{*}p < 0.05$, $^{**}p < 0.01$, $^{***}p < 0.001$, and NS means non-significant).

RESULTS

Force Is Necessary for VWF-A1-Induced Platelet P-Selectin Translocation

In studying the P-selectin translocation of platelets on VWF-coated substrates under flows, we first examined adhering platelets to substrates coated with or without 200 μg/ml VWF-A1 and/or its two mutants (R1308L and G1324S) at a fluid shear stress of 1 dyn/cm^2 ("Materials and Methods"). The platelet adhesion was specific for VWF-A1 because of the high adhesion levels for platelet on VWF-A1 (WTA1, R1308L, and G1324S) in comparison with the low non-specific adhesion of platelet on substrates coated with the blank group treated with 2% BSA (**Figure 1**). The adhesion level of platelets on WTA1 was lower than that on R1308L mutant but higher than that on G1324S mutant, demonstrating both R1308L mutation-induced enhancement and G1324S mutation-induced reduction of platelet adhesions (**Figure 1**) as shown in previous works (Baronciani et al., 2005; Morales et al., 2006).

To investigate the effect of external force on platelet P-selectin translocation, various fluid shear stresses were loaded to the firmly adhered platelets by perfusing PBS into the flow chamber (Materials and Methods). The rabbit anti-human P-selectin antibody was used to identify P-selectin-positive members of the immobilized platelets. We observed that P-selectin-positive platelets were rare for the platelets without mechanical preloads but became abundant for the platelets preloaded with fluid shear stresses of 10 dyn/cm^2 for 8 min (**Figures 2A,B**). Force led to increases of the mean P-selectin-positive platelet fractions from 10.5 to 41.9, 48.8, and 35.6% for WTA1, R1308L, and G1324S, respectively (**Figure 2B**). PMA could induce platelet P-selectin translocation in suspension (Whiss et al., 1998) but could not with the VWF-A1 (WTA1, R1308L, and G1324S) because of no mechanical stimulus on the suspended platelets (**Figures 2C,D**). Besides this, we found that fluid shear stress induced only a small amount of P-selectin translocation in the absence of VWF-A1 (**Figures 2A,B**) as demonstrated in previous studies (Hu et al., 2003; Zhang et al., 2003). These data indicated that fluid shear stress and VWF synergistically regulated platelet P-selectin translocation.

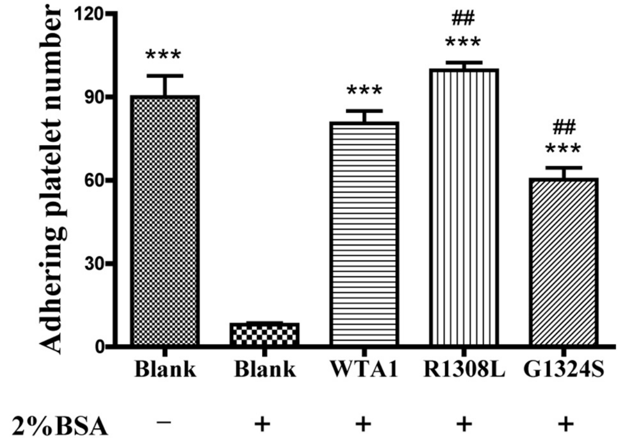

FIGURE 1 | Specificity of platelet binding to substrates with or without VWF-A1 and its two mutants (R1308L and G1324S). The firmly adhering platelets on substrates with various treatments were numbered after perfusing phosphate-buffered saline over the substrates in a parallel plate flow chamber under a fluid shear stress of 1 dyn/cm^2 for 5 min. The data represent the mean ± SEM from three independent experiments. Statistical significance was analyzed by one-way ANOVA for multiple comparisons with Bonferroni *post hoc* test; $^{***}p < 0.001$ compared with the blank group (treaded with 2% bovine serum albumin); $^{\#\#}p < 0.01$ compared with the WTA1 group.

VWF-Mediated P-Selectin Translocation Was PI3K and Akt Dependent for Platelet Under Flows

It was demonstrated that VWF-GPIbα signaling through PI3K and Akt was responsible for platelet integrin activation (Spater et al., 2018; Kral-Pointner et al., 2019). Thus, PI3K/Akt signaling might be involved in VWF-induced platelet P-selectin translocation because that P-selectin translocation was one of a series of platelet activation's landmark events, such as platelet morphology changes, integrin activation, particle release (P-selectin translocation, etc.), and so on. We herein examined VWF-induced P-selectin translocation for platelets without pretreated (as control) and pretreated with PI3K inhibitor (wortmannin) or Akt inhibitor (Akt1/2 kinase inhibitor) under the fluid shear stress of 10 dyn/cm^2 for 8 min ("Materials and Methods"). The data showed that there was no significant difference between the vehicle (DMSO) and controls (**Figure 3**) as it should be. The fraction of P-selectin-positive platelets decreased from 41.9 to 23.0 and 32.7% for treatments with wortmannin and Akt1/2 kinase inhibitors on substrates coated with WTA1, respectively (**Figure 3**), as did R1308L and G1324S. These results suggested VWF-GPIbα signaling through PI3K and Akt not only for platelet integrin activation but also for platelet P-selectin translocation (**Figure 3**). The reason might come from the fact that the P-selection translocation was a landmark event in platelet activation despite that there were some stimulators in platelet integrin activation and P-selectin translocation *via* different signal pathways (Kao et al., 2002; Li et al., 2010).

Fluid Shear Stress Triggered, Accelerated, and Enhanced the Kinetics-Dependent VWF-A1-Induced P-Selectin Translocation of Platelets

Pathological mutations would affect the binding of VWF to platelet GPIbα, leading to flow-enhanced or flow-reduced adhesion of circulating platelets (Baronciani et al., 2005; Morales et al., 2006). For example, GOF mutant R1308L would strengthen the binding affinity of VWF-A1 domain to platelet GPIbα, and LOF mutant G1324S did the opposite. Fluid shear stress was demonstrated to be necessary for VWF-induced platelet P-selectin translocation, as shown in **Figure 2**. However,

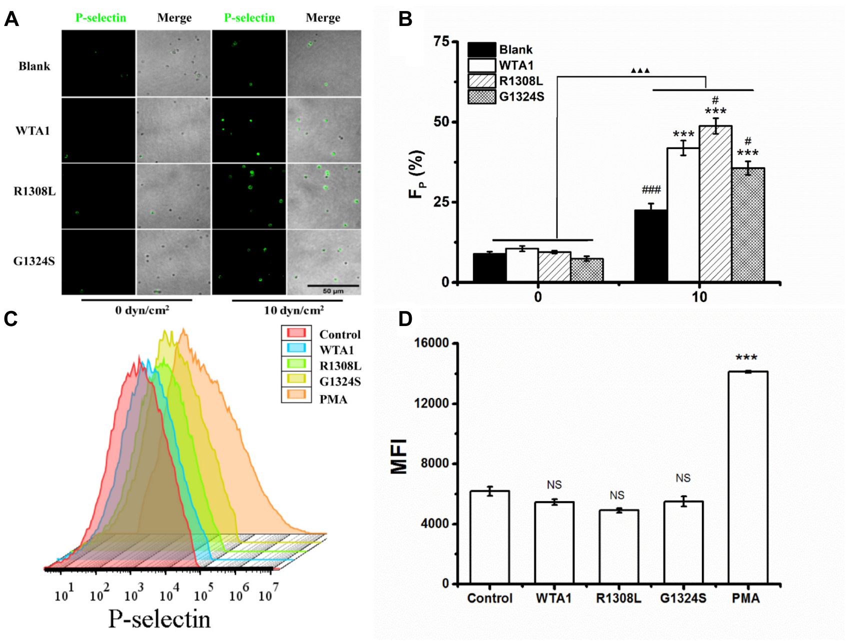

FIGURE 2 | P-selectin translocation of platelets adhered to either immobilized- and suspended-A1 domain of von Willebrand factor and its two mutants (R1308L and G1324S) with or without mechanical stimuli for 8 min. **(A)** P-selectin immunolocalization (green) and **(B)** P-selectin-positive fraction (F_P) of platelets on substrates coated with WTA1, R1308L, and G1324S without or with fluid shear stress stimulus of 10 dyn/cm^2 for a stimulus time of 8 min. Merged images of differential interference contrast and green fluorescence are shown with bar = 50 μm. The data represent the mean ± SEM from three independent experiments. Statistical significance was analyzed by two-way ANOVA for multiple comparisons with Bonferroni *post hoc* test; $^{***}p < 0.001$ compared with the blank group, $^{\#}p < 0.05$ and $^{\#\#\#}p < 0.001$ compared with WTA1 group, and $^{\Delta\Delta\Delta}p < 0.001$ compared with 0 dyn/cm^2 group. **(C)** Representative flow cytometry histograms of P-selectin translocation for platelets treated without (control) or with WTA1, R1308L, G1423S, and PMA. **(D)** Bar graph representing the mean fluorescence intensity of P-selectin-positive platelets (MFI) in various treatments from flow cytometry. All data are shown as mean ± SEM from three independent experiments and analyzed by one-way ANOVA for multiple comparisons. $^{***}p < 0.001$; NS, not significant compared with the control group.

mechano-chemical regulation on P-selectin translocation of platelets on VWF under flows remained unclear.

Through mechanical preloading treatments for platelets on the VWF-A1 (WTA1, R1308L, and G1324S)-coated substrates at fluid shear stresses of 0, 2.5, 5.0, and 10 dyn/cm^2 for stimulus times of 0, 1, 2, 4, and 8 min ("Materials and Methods"), we herein examined the effects of mechanical stimulus and mutation on VWF-A1-mediated P-selectin translocation on the immobilized platelets. Three parameters, such as the P-selectin-positive platelet fraction F_P and the mean of P-selectin coverage area per positive platelets A_P as well as the mean normalized P-selectin-related fluorescence intensity per positive platelets FI_P (formula 1 in "Materials and Methods"), were exploited to weigh the platelet P-selectin translocation. The results were shown in the plots of F_P, A_P, and FI_P against fluid shear stress τ_w with various mechanical stimulus time T of 0, 1, 2, 4, and 8 min for platelet on the immobilized VWF-A1 (WTA1, R1308L, and G1324S) (**Figure 4**). For platelets on each of the immobilized VWF-A1, P-selectin translocation in the absence of shear stress stimulus ($\tau_w = 0$) should be rare and weak due to the low P-selectin-positive fraction F_P and small P-selectin coverage area A_P (**Figures 4A–F**). Both F_P and A_P increased with fluid shear stress τ_w for each given stimulus time (0, 1, 2, 4, or 8 min), and increasing stimulus time T would cause an upswing of both $F_P \sim \tau_w$ and $A_P \sim \tau_w$ curves obviously, especially for $\tau_w < 5$ dyn/cm^2 (**Figures 4A–F**). It was suggested that fluid shear stress τ_w acted as an enhancer in platelet P-selectin translocation induced by VWF-A1, so did the mechanical stimulus time T. However, the $FI_P \sim \tau_w$ curve fluctuated slightly with increasing of fluid shear stress τ_w for each given stimulus time, which meant that the P-selectin-related fluorescence intensity FI_P remained almost constant at different mechanical conditions (**Figures 4G–I**), suggesting a fast but local VWF-mediated P-selectin translocation on A_P. These data suggested that mechanical stimulus served not only as a trigger but also as an accelerator or enhancer for VWF-induced translocation of platelet P-selectin, so did the mechanical stimulus time. LOF mutant (G1324S) reduced either F_P and A_P under diverse preloading, and GOF mutant (R1308L) did inversely, suggesting that VWF affinity to GPIbα regulated the force-dependent VWF-induced translocation of platelet P-selectin (**Supplementary Figure 3**).

VWF-Induced Platelet P-Selectin Translocation Under Flows Could Be Correlated With Shear Stress Accumulation

Similar effects of fluid shear stress τ_w and mechanical stimulus time T on the VWF-A1-induced platelet P-selectin translocation

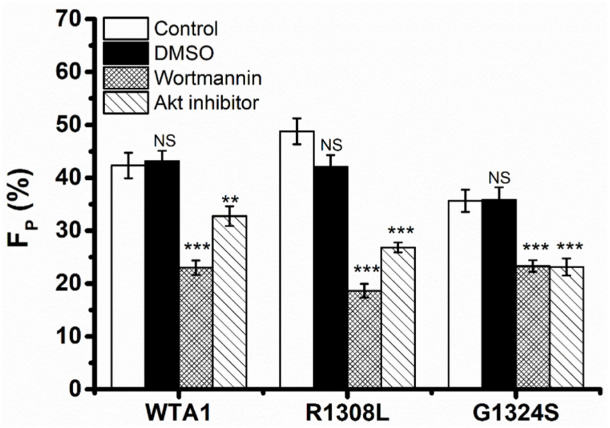

FIGURE 3 | Effects of inhibition to PI3K and Akt on von Willebrand factor (VWF)-induced P-selectin translocation in flows. Fractions of P-selectin-positive inhibitor-treated or untreated platelets on VWF-A1 and its two mutants (R1308L and G1324S). The dimethyl sulfoxide group was from vehicle control experiments, but in the control and inhibitor groups, the P-selectin-positive platelets were treated without (blank column) inhibitor and with either wortmannin or Akt1/2 kinase inhibitor. Data of F_P (fraction of P-selectin-positive platelets) were from the independent inhibition experiments thrice under a fluid shear stress of 10 dyn/cm^2 for a stimulus time of 8 min. All data are shown as the mean ± SEM and analyzed by one-way ANOVA for multiple comparisons. $^{**}p < 0.01$, $^{***}p < 0.001$; NS, not significant compared with the respective control groups.

were shown not only in $F_P \sim \tau_w$ and $A_P \sim \tau_w$ curves for each given T (**Figure 4**) but also in $F_P \sim$ T and $A_P \sim$ T curves for each given τ_w (**Supplementary Figure 4**). It indicated that τ_w and T might be similar in terms of efficacy but not independent in regulating the platelet P-selectin translocation despite that they were two independent determinants in the mechanical stimulus. These similar but synergistic effects of τ_w and T hinted that the shear stress accumulation, which denoted mechanical stimulus intensity and was the product of τ_w and T, might be a suitable biophysical parameter in scaling with the synergistic effects of τ_w and T on platelet P-selectin translocation (Sheriff et al., 2016). To examine this assumption, F_P, A_P, and FI_P were plotted against SSA for platelets on immobilized VWF-A1 (WTA1, R1308L, and G1324S) (**Figure 5**).

The plots of F_P, A_P, and FI_P against SSA (**Figure 5**) demonstrated that the VWF-A1-induced platelet P-selectin translocation could be correlated with SSA because all data for F_P, A_P, and FI_P at various fluid shear stresses and different stimulus times were clustered to the $F_P\sim$SSA, $A_P\sim$SSA, and $\mathrm{FI}_P\sim$SSA curves, respectively (**Figure 5** and **Supplementary Tables 1–3**). All of F_P in the same SSA values were very close and comparable (**Supplementary Table 1**), although the shear stresses and stimulation times were different. There was no coincidence that the fraction of P-selectin-positive platelets was similar at the same SSA because we could observe this phenomenon under all conditions with the same SSA value. F_P and A_P increased with SSA, while FI_P remained almost constant as SSA increased. The GOF mutation (R1308L) made both $F_P\sim$SSA and $A_P\sim$SSA curves upswing, and the LOF mutation (G1324S) did inversely, while these two different mutations had almost no effects on FI_P (**Figure 5C** and **Supplementary Table 3**). These results suggested a force-dependent VWF-induced platelet P-selection translocation process, in which the force-triggered P-selectin translocation occurred quickly but locally on the platelet surface with a small P-selectin coverage area A_P firstly and then extended gradually to the whole platelet surface with the increase of SSA. This process would be prompted by the GOF mutation (R1308L) but slowed down by the LOF mutation (G1324S). These results were consistent with previous work for SSA-prompted platelet activation using a modified prothrombinase assay (Sheriff et al., 2016).

DISCUSSION

As the first step for hemostasis, VWF recruits the circulating platelets to the vascular injured sites (Springer, 2014). The interaction of VWF to GPIbα initiates intracellular signal transduction to activate platelets and induce subsequent platelet P-selectin translocation in blood flows (Li et al., 2010; Amelirad et al., 2019). The P-selectin translocation could be induced also by both chemical agonists, such as thrombin, ADP, etc. (Ivelin et al., 2019; St John et al., 2019), and high shear stress (Ding et al., 2015; Chen et al., 2016) and contributed to platelet aggregation (Merten et al., 2000). The level of platelet P-selectin translocation is closely relevant with leukocyte inflammatory response, tumor cell hematogenous metastasis, hemostasis, thrombosis, and so on (Merten and Thiagarajan, 2004; Ludwig et al., 2007; Tseng et al., 2019; Schwarz et al., 2020), and VWF deficiency in quantity and quality can be caused by missense mutations and lead to bleeding and thrombotic von Willebrand diseases, such as microthrombosis found in patients with thrombotic thrombocytopenic purpura and bleeding found in patients with type 2B von Willebrand disease (Thiagarajan et al., 2013; Springer, 2014). Here, we studied VWF-A1-induced platelet P-selectin translocation under various shear stresses for different mechanical stimulus times using flow cytometry, parallel plate flow chamber, and immunofluorescence techniques. The present results demonstrated a mechano-chemical regulation mechanism on P-selectin translocation of platelets on substrates coated with VWF-A1 domain and its two mutants.

Previous studies demonstrated a force-dependent platelet P-selectin translocation through VWF-GPIbα signaling in flows (Rahman and Hlady, 2021), but for a low P-selectin translocation level of platelets in a high-shear-stress environment, it is said that high shear stress alone was likely to be insufficient in inducing platelet activation and aggregation (Zhang et al., 2003; Roka-Moiia et al., 2020). Our results also showed that the mechanical stimulus was necessary for VWF-A1 (including its two mutants)-induced platelet P-selectin translocation, but the level of platelet P-selectin translocation in the absence of VWF-A1 was significantly lower than that in the presence of VWF-A1 under all flow conditions (**Figures 2A,B**). The P-selectin translocation did not occur in either the suspended platelets (**Figure 2D**) or the immobilized platelets in the absence of shear

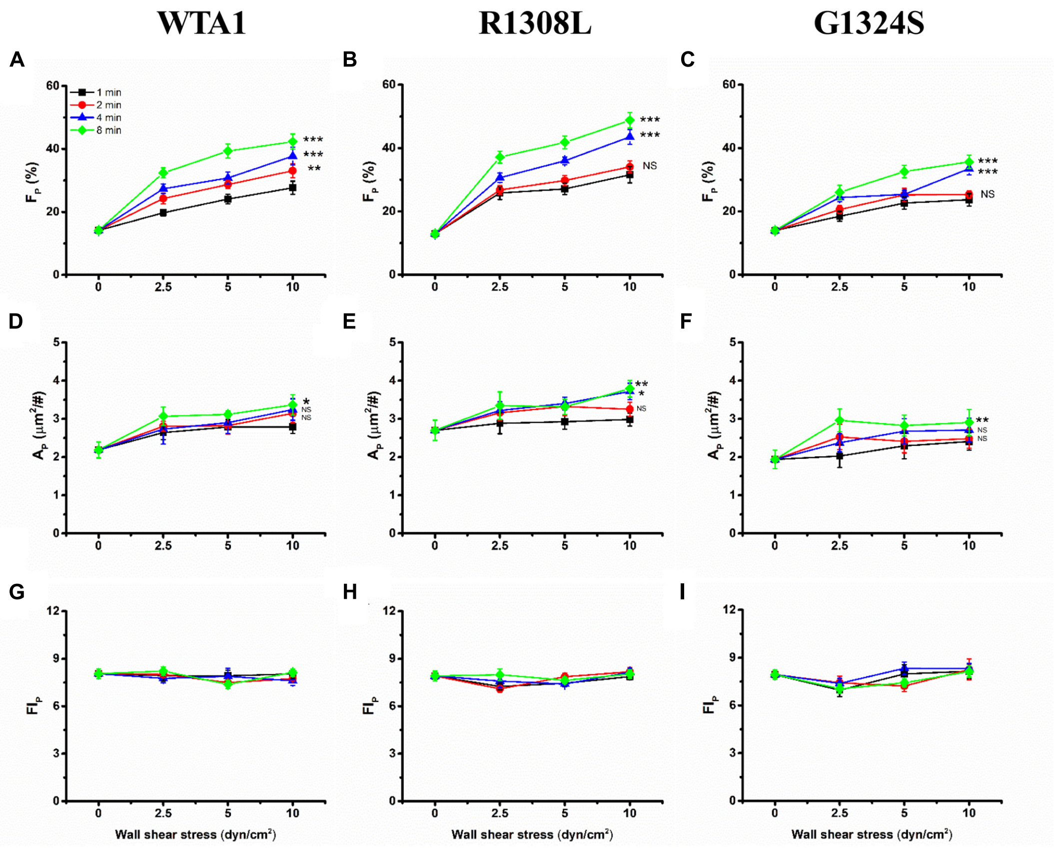

FIGURE 4 | Variations of F_P, A_P, and FI_P of the immobilized platelets *versus* fluid shear stress. All the platelets on substrates coated with WTA1, R1308L, or G1324S were preloaded with fluid shear stress τ_w for mechanical stimulus times of 1, 2, 4, and 8 min. The mean P-selectin-positive platelet fraction F_P was plotted against fluid shear stress τ_w for platelet on WTA1, R1308L, and G1324S **(A–C)**, respectively, and so did either the mean of P-selectin coverage area A_P in **(D–F)** or the normalized platelet P-selectin fluorescence intensity FI_P in **(G–I)**. All data are shown as the mean ± SEM from at least three independent experiments and analyzed by two-way ANOVA for multiple comparisons; $^*p < 0.05$, $^{**}p < 0.01$, $^{***}p < 0.001$; NS, not significant compared with the 1-min group.

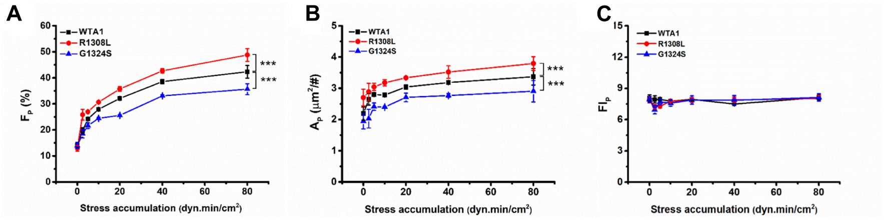

FIGURE 5 | Regulation of shear stress accumulation on von Willebrand factor (VWF)-induced P-selectin translocation. The platelets firmly adhered to substrates coated with WTA1, R1308L, and G1324S, respectively. **(A)** The mean P-selectin-positive platelet fraction F_P, **(B)** the mean of P-selectin coverage area A_P, and **(C)** the normalized P-selectin-related fluorescence intensity FI_P; all were well correlated with shear stress accumulation, whether VWF-A1 was mutated or not. All data are shown as mean ± SEM from at least three independent experiments and analyzed by two-way ANOVA for multiple comparisons; $^{***}p < 0.001$ compared with the WTA1 group.

stress (**Figure 2B**), suggesting that shear stress-mediated buildup of tension on VWF-A1/GPIbα complex might be required for platelet P-selectin translocation. The P-selectin-positive fraction and coverage area of platelets increased with either shear stress or stimulus time but could be correlated with shear stress accumulation instead of either fluid shear stress or mechanical stimulus time (**Supplementary Table 1; Figures 4, 5**). It is said that shear stress and stimulus time were not independent in inducing platelet P-selectin translocation and were coupled with each other by SSA, which coalesced out of the synergistic effects of shear stress and stimulus time on P-selectin translocation. So, serving as a crucial regulator, SSA promoted VWF-induced P-selectin translocation and activated the phenotype formation of platelets (**Figures 5A,B**). Platelet activation and P-selectin translocation shared with PI3K/Akt pathway in VWF-GPIbα signaling (**Figure 3**).

It was demonstrated that a mutation in the VWF-A1 domain might enhance or reduce platelet adhesion through changing VWF affinity to GPIbα, but less knowledge was relevant to the effects of VWF-A1 mutation on P-selectin translocation of the immobile platelets under shear stress. Similar to the previous work which found that the VWF cleaved by MMP-13 promoted the binding affinity to platelet and improved the platelet P-selectin translocation in comparison with intact VWF (Howes et al., 2020), our results showed that GOF mutant R1308L would cause an increment of about 10% in either P-selectin-positive platelet fraction or P-selectin coverage platelet area, while LOF mutant G1324S led to a reduction of 10% at least in either P-selectin-positive platelet fraction or P-selectin coverage platelet area in comparison with WTA1 for SSA larger than 5 dyn·min/cm^2 (**Figure 5**), suggesting the VWF affinity (to GPIbα)-dependent platelet P-selectin translocation. These findings indicated that GOF mutant R1308L would facilitate platelet aggregation, hemostasis, and thrombosis through enhancing not only platelet adhesion but also P-selectin translocation which were demonstrated to be dominant in platelet aggregation and thrombosis (Konstantopoulos et al., 1998; Merten et al., 2000), and LOF mutant G1324S did the opposite. These data further argued that R1308L was a GOF mutation instead of a LOF one, which was consistent with previous works for platelet adhesion (Baronciani et al., 2005). In contrast, one recent study classified R1308L to a LOF mutation based on the fact that the pause time of platelets on R1308L substrate under the shear rate of 1,500s^{-1} was less than that on WTA1 (Tischer et al., 2014). Perhaps the upregulated associated rate could counteract fully the effects of the upregulated dissociation rate on VWF affinity to GPIbα. This phenomenon also occurred in the GOF mutation R1450E. The ability of R1450E mutant to recruit platelets was significantly higher than that of WTA1 (Morales et al., 2006), but this mutation would make the mean stop time short (Coburn et al., 2011).

In conclusion, our data suggested that VWF-induced platelet P-selectin translocation would be triggered, accelerated, and enhanced by fluid shear stress but correlated with shear stress accumulation. This SSA-dependent P-selectin translocation of platelets would be enhanced by GOF mutant R1308L but reduced through LOF mutant G1324S. The present work provided a novel insight into the mechano-chemical regulation on adhesive molecule-mediated platelet P-selectin translocation and its relevant biological processes, such as tumor cell hematogenous metastasis, hemostasis, and inflammatory responses under flows.

DATA AVAILABILITY STATEMENT

The original contributions presented in the study are included in the article/**Supplementary Material**, further inquiries can be directed to the corresponding authors.

ETHICS STATEMENT

The studies involving human participants were reviewed and approved by the Guangzhou First People's Hospital. The patients/participants provided their written informed consent to participate in this study.

AUTHOR CONTRIBUTIONS

JW and YF designed this research. JFa supervised this study overall. XS, SL, PY, JFe, JL, MAC, and J-FD partly performed research and analyzed data. JFa, YF, and JW wrote this manuscript. All authors contributed to the article and approved the submitted version.

FUNDING

This work was supported by the National Natural Science Foundation of China (NSFC), grants 11672109 (to YF), 12072117, and 11432006 (to JW).

SUPPLEMENTARY MATERIAL

The Supplementary Material for this article can be found online at: https://www.frontiersin.org/articles/10.3389/fcell.2021.642108/full#supplementary-material

REFERENCES

Amelirad, A., Shamsasenjan, K., Akbarzadehlaleh, P., and Pashoutan Sarvar, D. (2019). Signaling pathways of receptors involved in platelet activation and shedding of these receptors in stored platelets. *Adv. Pharm. Bull.* 9, 38–47. doi: 10.15171/apb.2019.005

Au, A. E., and Josefsson, E. C. (2017). Regulation of platelet membrane protein shedding in health and disease. *Platelets* 28, 342–353. doi: 10.1080/09537104.2016.1203401

Auton, M., Sedlak, E., Marek, J., Wu, T., Zhu, C., and Cruz, M. A. (2009). Changes in thermodynamic stability of von Willebrand factor differentially affect the force-dependent binding to platelet GPIbalpha. *Biophys. J.* 97, 618–627. doi: 10.1016/j.bpj.2009.05.009

Baronciani, L., Federici, A. B., Beretta, M., Cozzi, G., Canciani, M. T., and Mannucci, P. M. (2005). Expression studies on a novel type 2B variant of the von Willebrand factor gene (R1308L) characterized by defective collagen binding. *J. Thromb. Haemost.* 3, 2689–2694. doi: 10.1111/j.1538-7836.2005.01638.x

Chen, Z., Li, T., Kareem, K., Tran, D., Griffith, B. P., and Wu, Z. J. (2019). The role of PI3K/Akt signaling pathway in non-physiological shear stress-induced platelet activation. *Artif. Organs* 43, 897–908. doi: 10.1111/aor.13465

Chen, Z., Mondal, N. K., Ding, J., Koenig, S. C., Slaughter, M. S., Griffith, B. P., et al. (2015). Activation and shedding of platelet glycoprotein IIb/IIIa under non-physiological shear stress. *Mol. Cell. Biochem.* 409, 93–101. doi: 10.1007/s11010-015-2515-y

Chen, Z., Mondal, N. K., Ding, J., Koenig, S. C., Slaughter, M. S., and Wu, Z. J. (2016). Paradoxical effect of nonphysiological shear stress on platelets and von Willebrand factor. *Artif. Organs* 40, 659–668. doi: 10.1111/aor.12606

Coburn, L. A., Damaraju, V. S., Dozic, S., Eskin, S. G., Cruz, M. A., and McIntire, L. V. (2011). GPIbalpha-vWF rolling under shear stress shows differences between type 2B and 2M von Willebrand disease. *Biophys. J.* 100, 304–312. doi: 10.1016/j.bpj.2010.11.084

Cruz, M. A., Diacovo, T. G., Emsley, J., Liddington, R., and Handin, R. I. (2000). Mapping the glycoprotein Ib-binding site in the von Willebrand factor A1 domain. *J. Biol. Chem.* 275, 19098–19105. doi: 10.1074/jbc.M002292200

Da, Q., Behymer, M., Correa, J. I., Vijayan, K. V., and Cruz, M. A. (2014). Platelet adhesion involves a novel interaction between vimentin and von Willebrand factor under high shear stress. *Blood* 123, 2715–2721. doi: 10.1182/blood-2013-10-530428

Ding, J., Chen, Z., Niu, S., Zhang, J., Mondal, N. K., Griffith, B. P., et al. (2015). Quantification of shear-induced platelet activation: high shear stresses for short exposure time. *Artif. Organs* 39, 576–583. doi: 10.1111/aor.12438

Federici, A. B., Mannucci, P. M., Castaman, G., Baronciani, L., Bucciarelli, P., Canciani, M. T., et al. (2009). Clinical and molecular predictors of thrombocytopenia and risk of bleeding in patients with von Willebrand disease type 2B: a cohort study of 67 patients. *Blood* 113, 526–534. doi: 10.1182/blood-2008-04-152280

Furie, B., Furie, B. C., and Flaumenhaft, R. (2001). A journey with platelet P-selectin: the molecular basis of granule secretion, signalling and cell adhesion. *Thromb. Haemost.* 86, 214–221. doi: 10.1055/s-0037-1616219

Gao, Z., Liu, F., Yu, Z., Bai, X., Yang, C., Zhuang, F., et al. (2008). Effects of von Willebrand factor concentration and platelet collision on shear-induced platelet activation. *Thromb. Haemost.* 100, 60–68. doi: 10.1160/TH07-03-0222

Goto, S., Ichikawa, N., Lee, M., Goto, M., Sakai, H., Kim, J. J., et al. (2000). Platelet surface P-selectin molecules increased after exposing platelet to a high shear flow. *Int. Angiol.* 19, 147–151. doi: 10.1053/ejvs.2000.1094

Howes, J. M., Knauper, V., Malcor, J. D., and Farndale, R. W. (2020). Cleavage by MMP-13 renders VWF unable to bind to collagen but increases its platelet reactivity. *J. Thromb. Haemost.* 18, 942–954. doi: 10.1111/jth.14729

Hu, H., Varon, D., Hjemdahl, P., Savion, N., Schulman, S., and Li, N. (2003). Platelet-leukocyte aggregation under shear stress: differential involvement of selectins and integrins. *Thromb. Haemost.* 90, 679–687. doi: 10.1160/TH03-05-0274

Ivelin, I. I., Apta, B. H. R., Bonna, A. M., and Harper, M. T. (2019). Platelet P-selectin triggers rapid surface exposure of tissue factor in monocytes. *Sci. Rep.* 9:13397. doi: 10.1038/s41598-019-49635-7

Kao, S., Turner, N. A., Moakey, J. L., and McIntire, L. V. (2002). A novel flow cytometric analysis for platelet activation on immobilized von Willebrand factor or fibrillar collagen. *J. Thromb. Haemost.* 1, 347–354. doi: 10.1046/j.1538-7836.2003.00051.x

Konstantopoulos, K., Neelamegham, S., Burns, A. R., Hentzen, E., Kansas, G. S., Snapp, K. R., et al. (1998). Venous levels of shear support neutrophil-platelet adhesion and neutrophil aggregation in blood via P-Selectin and β2-Integrin. *Circulation* 98, 873–882. doi: 10.1161/01.cir.98.9.873

Korporaal, S. J. A., Molenaar, T. J. M., Lutters, B. C. H., Meurs, I., Drost-Verhoef, S., Kuiper, J., et al. (2019). Peptide antagonists for P-selectin discriminate between sulfatide-dependent platelet aggregation and PSGL-1-mediated cell adhesion. *J. Clin. Med.* 8, 1266–1281. doi: 10.3390/jcm8081266

Kral-Pointner, J. B., Schrottmaier, W. C., Salzmann, M., Mussbacher, M., Schmidt, G. J., Moser, B., et al. (2019). Platelet PI3K modulates innate leukocyte extravasation during acid-induced acute lung inflammation. *Thromb. Haemost.* 119, 1642–1654. doi: 10.1055/s-0039-1693693

Li, Z., Delaney, M. K., O'Brien, K. A., and Du, X. (2010). Signaling during platelet adhesion and activation. *Arterioscler. Thromb. Vasc. Biol.* 30, 2341–2349. doi: 10.1161/ATVBAHA.110.207522

Lu, Q., and Malinauskas, R. A. (2011). Comparison of two platelet activation markers using flow cytometry after in vitro shear stress exposure of whole human blood. *Artif. Organs* 35, 137–144. doi: 10.1111/j.1525-1594.2010.01051.x

Ludwig, R. J., Schon, M. P., and Boehncke, W. H. (2007). P-selectin: a common therapeutic target for cardiovascular disorders, inflammation and tumour metastasis. *Expert Opin. Ther. Targets* 11, 1103–1117. doi: 10.1517/14728222.11.8.1103

Merten, M., Chow, T., Hellums, J. D., and Thiagarajan, P. (2000). A new role for P-Selectin in shear-induced platelet aggregation. *Circulation* 102, 2045–2050. doi: 10.1161/01.cir.102.17.2045

Merten, M., and Thiagarajan, P. (2004). P-selectin in arterial thrombosis. *Z. Kardiol.* 93, 855–863. doi: 10.1007/s00392-004-0146-5

Morales, L. D., Martin, C., and Cruz, M. A. (2006). The interaction of von Willebrand factor-A1 domain with collagen: mutation G1324S (type 2M von Willebrand disease) impairs the conformational change in A1 domain induced by collagen. *J. Thromb. Haemost.* 4, 417–425. doi: 10.1111/j.1538-7836.2006.01742.x

Ollivier, V., Syvannarath, V., Gros, A., Butt, A., Loyau, S., Jandrot-Perrus, M., et al. (2014). Collagen can selectively trigger a platelet secretory phenotype via glycoprotein VI. *PLoS One* 9:e104712. doi: 10.1371/journal.pone.0104712

Rahman, S. M., and Hlady, V. (2019). Downstream platelet adhesion and activation under highly elevated upstream shear forces. *Acta Biomater.* 91, 135–143. doi: 10.1016/j.actbio.2019.04.028

Rahman, S. M., and Hlady, V. (2021). Microfluidic assay of antiplatelet agents for inhibition of shear-induced platelet adhesion and activation. *Lab. Chip.* 21, 174–183. doi: 10.1039/d0lc00756k

Roka-Moiia, Y., Walk, R., Palomares, D. E., Ammann, K. R., Dimasi, A., Italiano, J. E., et al. (2020). Platelet activation via shear stress exposure induces a differing pattern of biomarkers of activation versus biochemical agonists. *Thromb. Haemost.* 120, 776–792. doi: 10.1055/s-0040-1709524

Sandstrom, J., Kratschmar, D. V., Broyer, A., Poirot, O., Marbet, P., Chantong, B., et al. (2019). In vitro models to study insulin and glucocorticoids modulation of trimethyltin (TMT)-induced neuroinflammation and neurodegeneration, and in vivo validation in db/db mice. *Arch. Toxicol.* 93, 1649–1664. doi: 10.1007/s00204-019-02455-0

Schwarz, S., Gockel, L. M., Naggi, A., Barash, U., Gobec, M., Bendas, G., et al. (2020). Glycosaminoglycans as tools to decipher the platelet tumor cell interaction: a focus on P-Selectin. *Molecules* 25:1039. doi: 10.3390/molecules25051039

Semple, J. W., Italiano, J. E. Jr., and Freedman, J. (2011). Platelets and the immune continuum. *Nat. Rev. Immunol.* 11, 264–274. doi: 10.1038/nri2956

Sheriff, J., Tran, P. L., Hutchinson, M., Decook, T., Slepian, M. J., Bluestein, D., et al. (2016). Repetitive hypershear activates and sensitizes platelets in a dose-dependent manner. *Artif. Organs* 40, 586–595. doi: 10.1111/aor.12602

Spater, T., Muller, I., Eichler, H., Menger, M. D., Laschke, M. W., and Ampofo, E. (2018). Dual inhibition of PI3K and mTOR by VS-5584 suppresses thrombus formation. *Platelets* 29, 277–287. doi: 10.1080/09537104.2017.1306040

Springer, T. A. (2014). von Willebrand factor, Jedi knight of the bloodstream. *Blood* 124, 1412–1425. doi: 10.1182/blood-2014-05-378638

St John, A. E., Newton, J. C., Martin, E. J., Mohammed, B. M., Contaifer, D. Jr., Saunders, J. L., et al. (2019). Platelets retain inducible alpha granule secretion by P-selectin expression but exhibit mechanical dysfunction during trauma-induced coagulopathy. *J. Thromb. Haemost.* 17, 771–781. doi: 10.1111/jth.14414

Thiagarajan, P., Dasgupta, S. K., and Thacker, S. (2013). A novel molecular mechanism in the interplay of platelet GPIb-VWF-Fibrin in thrombus formation. *Blood* 122:1065. doi: 10.1182/blood.v122.21.1065.1065

Tischer, A., Madde, P., Moon-Tasson, L., and Auton, M. (2014). Misfolding of vWF to pathologically disordered conformations impacts the severity of von Willebrand disease. *Biophys. J.* 107, 1185–1195. doi: 10.1016/j.bpj.2014.07.026

Tseng, C. N., Chang, Y. T., Yen, C. Y., Lengquist, M., Kronqvist, M., Eriksson, E. E., et al. (2019). Early inhibition of P-Selectin/P-Selectin glycoprotein ligand-1 reduces intimal hyperplasia in murine vein grafts through platelet adhesion. *Thromb. Haemost.* 119, 2014–2024. doi: 10.1055/s-0039-1697659

van der Meijden, P. E. J., and Heemskerk, J. W. M. (2019). Platelet biology and functions: new concepts and clinical perspectives. *Nat. Rev. Cardiol.* 16, 166–179. doi: 10.1038/s41569-018-0110-0

Whiss, P. A., Andersson, R. G., and Srinivas, U. (1998). Kinetics of platelet P-selectin mobilization: concurrent surface expression and release induced by thrombin or PMA, and inhibition by the NO donor SNAP. *Cell Adhes. Commun.* 6, 289–300. doi: 10.3109/15419069809010788

Wymann, M., and Arcaro, A. (1994). Platelet-derived growth factor-induced phosphatidylinositol 3-kinase activation mediates actin rearrangements in fibroblasts. *Biochem. J.* 298(Pt. 3), 517–520. doi: 10.1042/bj2980517

Yin, W., Shanmugavelayudam, S. K., and Rubenstein, D. A. (2011). The effect of physiologically relevant dynamic shear stress on platelet and endothelial cell activation. *Thromb. Res.* 127, 235–241. doi: 10.1016/j.thromres.2010.11.021

Zhang, J. N., Bergeron, A. L., Yu, Q., Sun, C., McBride, L., Bray, P. F., et al. (2003). Duration of exposure to high fluid shear stress is critical in shear-induced platelet activation-aggregation. *Thromb. Haemost.* 90, 672–678. doi: 10.1160/TH03-03-0145

Conflict of Interest: The authors declare that the research was conducted in the absence of any commercial or financial relationships that could be construed as a potential conflict of interest.

frontiers
in Cell and Developmental Biology

ORIGINAL RESEARCH
published: 28 June 2021
doi: 10.3389/fcell.2021.697539

Punicalagin Attenuates Disturbed Flow-Induced Vascular Dysfunction by Inhibiting Force-Specific Activation of Smad1/5

Gulinigaer Anwaier[1,2,3,4,5†], Guan Lian[1,2,3,4,5†], Gui-Zhi Ma[6,7†], Wan-Li Shen[1,2,3,4,5], Chih-I Lee[10], Pei-Ling Lee[10], Zhan-Ying Chang[6,7], Yun-Xia Wang[1,2,3,4,5], Xiao-Yu Tian[13], Xiao-Li Gao[6,7], Jeng-Jiann Chiu[8,9,10,11,12*] and Rong Qi[1,2,3,4,5*]*

[1] Department of Pharmacology, School of Basic Medical Sciences, Peking University Health Science Center, Beijing, China, [2] Key Laboratory of Molecular Cardiovascular Sciences, Ministry of Education, Peking University, Beijing, China, [3] State Key Laboratory of Natural and Biomimetic Drugs, Peking University, Beijing, China, [4] National Health Commission (NHC) Key Laboratory of Cardiovascular Molecular Biology and Regulatory Peptides, Peking University, Beijing, China, [5] Beijing Key Laboratory of Molecular Pharmaceutics and New Drug Delivery Systems, Peking University, Beijing, China, [6] College of Pharmacy, Xinjiang Medical University, Xinjiang, China, [7] Xinjiang Key Laboratory of Active Components and Drug Release Technology of Natural Drugs, Xinjiang, China, [8] School of Medical Laboratory Science and Biotechnology, College of Medical Science and Technology, Taipei Medical University, Taipei, Taiwan, [9] Taipei Heart Institute, Taipei Medical University, Taipei, Taiwan, [10] Institute of Cellular and System Medicine, National Health Research Institutes, Miaoli, Taiwan, [11] Institute of Biomedical Engineering, National Tsing Hua University, Hsinchu, Taiwan, [12] Institute of Polymer Science and Engineering, National Taiwan University, Taipei, Taiwan, [13] School of Biomedical Sciences, Chinese University of Hong Kong, Hong Kong, China

Edited by:
Claudia Tanja Mierke,
Leipzig University, Germany

Reviewed by:
Mabruka Alfaidi,
Louisiana State University Health Shreveport, United States
Donghui Liu,
South China University of Technology, China
Camelia Stancu,
Institute of Cellular Biology and Pathology (ICBP), Romania

***Correspondence:**
Xiao-Li Gao
xli_g@sina.com
Jeng-Jiann Chiu
jjchiu88@tmu.edu.tw;
jjchiu@nhri.org.tw
Rong Qi
ronaqi@bjmu.edu.cn

†These authors have contributed equally to this work and share first authorship

Specialty section:
This article was submitted to Cell Adhesion and Migration, a section of the journal Frontiers in Cell and Developmental Biology

***Received:** 19 April 2021*
***Accepted:** 07 June 2021*
***Published:** 28 June 2021*

Citation:
Anwaier G, Lian G, Ma G-Z, Shen W-L, Lee C-I, Lee P-L, Chang Z-Y, Wang Y-X, Tian X-Y, Gao X-L, Chiu J-J and Qi R (2021) Punicalagin Attenuates Disturbed Flow-Induced Vascular Dysfunction by Inhibiting Force-Specific Activation of Smad1/5. Front. Cell Dev. Biol. 9:697539. doi: 10.3389/fcell.2021.697539

Background: Pathophysiological vascular remodeling in response to disturbed flow with low and oscillatory shear stress (OSS) plays important roles in atherosclerosis progression. Pomegranate extraction (PE) was reported having anti-atherogenic effects. However, whether it can exert a beneficial effect against disturbed flow-induced pathophysiological vascular remodeling to inhibit atherosclerosis remains unclear. The present study aims at investigating the anti-atherogenic effects of pomegranate peel polyphenols (PPP) extraction and its purified compound punicalagin (PU), as well as their protective effects on disturbed flow-induced vascular dysfunction and their underlying molecular mechanisms.

Methods: The anti-atherogenic effects of PPP/PU were examined on low-density lipoprotein receptor knockout mice fed with a high fat diet. The vaso-protective effects of PPP/PU were examined in rat aortas using myograph assay. A combination of *in vivo* experiments on rats and *in vitro* flow system with human endothelial cells (ECs) was used to investigate the pharmacological actions of PPP/PU on EC dysfunction induced by disturbed flow. In addition, the effects of PPP/PU on vascular smooth muscle cell (VSMC) dysfunction were also examined.

Results: PU is the effective component in PPP against atherosclerosis. PPP/PU evoked endothelium-dependent relaxation in rat aortas. PPP/PU inhibited the activation of Smad1/5 in the EC layers at post-stenotic regions of rat aortas exposed to disturbed flow with OSS. PPP/PU suppressed OSS-induced expression of cell cycle regulatory and pro-inflammatory genes in ECs. Moreover, PPP/PU inhibited inflammation-induced VSMC dysfunction.

Conclusion: PPP/PU protect against OSS-induced vascular remodeling through inhibiting force-specific activation of Smad1/5 in ECs and this mechanism contributes to their anti-atherogenic effects.

Keywords: pomegranate, punicalagin, oscillatory shear stress, atherosclerosis, endothelial cell, Smads

INTRODUCTION

Atherosclerosis is a chronic inflammatory vascular disorder highly associated with endothelial cell (EC) dysfunction, vascular smooth muscle cell (VSMC) proliferation and migration, inflammatory monocyte infiltration, lipid deposition, and vascular wall remodeling (Gimbrone and Garcia-Cardena, 2016). The non-random distribution of atherosclerotic lesions is related to different patterns of blood flow and hemodynamic forces acting on the vascular wall. As an important signal transduction medium between blood flow and arterial wall, vascular ECs are constantly exposed to different flow patterns and shear stresses, including disturbed flow with low and oscillatory shear stress (OSS) and pulsatile flow with relatively high shear stress (PSS), leading to distinct impacts on the vascular wall (Zhou et al., 2014). Plaques preferentially occur at arterial branches and curvatures where the local flow is disturbed with OSS (Chiu et al., 2009). By contrast, arterial regions exposed to pulsatile flow with PSS are relatively lesion-free (Sorescu et al., 2003). Pulsatile flow with PSS generally is anti-inflammatory and anti-atherogenic, whereas disturbed flow with OSS promotes the formation and progression of atherosclerosis (Gimbrone and Garcia-Cardena, 2016). Our previous studies and others have shown that ECs are capable of perceiving OSS as a mechanical signal to induce force-specific activation of bone morphogenetic protein receptor (BMPR)-associated Smad1/5, leading to upregulation of cyclin A and downregulation of p21 and p27, thereby increasing EC cell cycle progression and proliferation (Sorescu et al., 2003; Chang et al., 2007; Zhou et al., 2012, 2013). OSS-activated Smad1/5 can further promote the activation of nuclear factor-κB (NF-κB) pathways and release of pro-inflammatory cytokines interleukin-1β (IL-1β) and tumor necrosis factor-α (TNF-α) to aggravate EC injury (Zhou et al., 2012, 2013). OSS-induced pro-inflammatory responses in ECs can elicit chemotaxis and adhesion of monocytes to the EC layers mediated by intercellular adhesion molecule-1 (ICAM-1), vascular cell adhesion molecule-1 (VCAM-1), and monocyte chemotactic protein-1 (MCP-1), which further promotes atherosclerosis progression (Chiu et al., 2004). On the other hand, the injured ECs produce pro-inflammatory cytokines such as TNF-α to promote phenotypic modulation, proliferation and migration of VSMCs to further aggravate atherosclerosis (Sorescu et al., 2003). Taken together, all of these sequential events suggest that force-specific activation of Smads may be a promising hemodynamic-based molecular target for intervention against disturbed flow-associated vascular disorders, such as atherosclerosis.

Pomegranate peel is rich in polyphenols with the main component of punicalagin. Pomegranate extraction (PE) was reported to exert anti-atherogenic effects *via* lowering circulating levels of low-density lipoprotein and formation of macrophage-derived foam cells (Al-Jarallah et al., 2013; Rosenblat et al., 2013; Atrahimovich et al., 2016, 2018). Prolonged PE supplementation inhibited OSS-related atherosclerosis by upregulating endothelial nitric oxide synthase (eNOS) expression and modulating oxidation-sensitive gene expression in ECs (de Nigris et al., 2007). However, whether the extraction of pomegranate peel polyphenols (PPP) and its purified compound punicalagin (PU) exert ameliorative effects on OSS-induced vascular dysfunction and hence protect against atherosclerosis remain unclear.

In the present study, we demonstrated for the first time that PU is the bioactive anti-atherogenic constituent of PPP. We further investigated the roles of PPP and PU in OSS-induced EC dysfunctions and inflammation-related VSMC pathophysiological responses *in vitro* and *in vivo*. Our results showed that PPP and PU exert protective effects on the arterial wall and atherosclerosis by attenuating disturbed flow/inflammation-induced vascular dysfunction, mainly through suppressing force-specific activation of Smad1/5 in ECs. Thus, our study provides new information to indicate that PPP and PU may have great potential to be developed as new therapeutic components for the treatment of atherosclerosis.

MATERIALS AND METHODS

Materials

PPP (containing 42.08% punicalagin) and PU (containing 90.6% punicalagin) (**Supplementary Table 1**) were provided by Prof. Xiao-Li Gao from Xinjiang Medical University, China. Extraction methods and HPLC analysis of PPP/PU were described in **Supplementary Data** (**Supplementary Figure 1**). Punicalagin reference substance (purity 98%) was purchased from Yuanye Biological Technology Co., Ltd., (Shanghai, China). Serum triglyceride (TG) and total cholesterol (TC) kits

---

Abbreviations: OSS, oscillatory shear stress; PE, pomegranate extraction; PU, purified punicalagin; PPP, pomegranate peel polyphenols extraction; EC, endothelial cell; VSMC, vascular smooth muscle cell; HFD, high fat diet; BMPR, bone morphogenetic protein receptor; ICAM-1, intercellular adhesion molecule-1; VCAM-1, vascular cell adhesion molecule-1; TNF-α, tumor necrosis factor-α; MCP, monocyte chemotactic protein; TC, total cholesterol; TG, total triglyceride; iNOS, inducible nitric oxide synthase; eNOS, endothelial nitric oxide synthase; L-NAME, L-N(G)-nitroarginine methyl ester; IL-6, interleukin-6; HPLC, high performance liquid chromatography.

were purchased from Biosino Bio-technology and Science Inc. (Nanjing, China). TNF-α was purchased from Peprotech (Rocky Hill, United States). Fetal bovine serum (FBS, Gibco), Dulbecco's Modified Eagle's Medium (DMEM) and medium 199 (M199, Gibco, Grand Island, NY, United States) were from GIBCO (Grand Island, United States). Rabbit anti-phospho-Smad1/5 (#AB3848-I), rabbit anti-von Willebrand Factor (#AB7356) were purchased from Millipore (Massachusetts, United States). Rabbit anti-Smad1/5 (#sc6031R) was from Santa Cruz Biotechnology (California, United States). Rabbit anti-Mac-2 (#ab217760), anti-VCAM-1 (#ab134047), anti-α-SMA (#ab14106), and mouse anti-α-SMA (#ab7817) were purchased from Abcam (Cambridge, United Kingdom). Rabbit anti-ICAM-1 (#4915), rabbit anti-phospho-Rb (#9308), mouse anti-Rb (#9309), mouse anti-Cyclin A (#4656) and mouse anti-Ki-67 (#9449) were purchased from Cell signaling (Massachusetts, United States). Rabbit anti-E-selectin (#GTX54691) was purchased from GeneTex (Irvine, CA). Mouse anti-GAPDH antibody was purchased from Santa Cruz (Dallas, United States). The HRP-conjugated secondary antibodies, affinity-purified mouse anti-rabbit IgG, and rabbit anti-mouse IgG were purchased from Sigma (St. Louis, MO, United States). All other chemical agents were purchased from Sigma Aldrich (St. Louis, MO, United States) unless otherwise noted.

Anti-atherogenic Studies of PPP/PU

Healthy 6-week-old male low-density lipoprotein receptor knockout (LDLR$^{-/-}$) mice (Jackson Laboratory, United States) were housed with free access to water and standard laboratory chow diet. Atherosclerosis was induced by feeding LDLR$^{-/-}$ mice with a high fat diet (HFD) containing 20% lard and 0.5% cholesterol for 12 weeks. LDLR$^{-/-}$ mice were randomly assigned to the treatment groups. Vehicle group mice were administrated with phosphate-buffered saline (PBS) by gavage. In drug treatment group, PPP or PU was dissolved in PBS and given daily to mice by gavage at different doses. After 12 weeks, all mice were euthanized with an overdose of sodium pentobarbital. The blood samples were taken from the mice after 12-h fasting and centrifuged (Eppendorf 5418R, Eppendorf Corporation, Hamburg, Germany) at 1,400 × *g* for 10 min at 4°C. And the plasma was taken for measure of plasma triglycerides (TG) and total cholesterol (TC) according to manufacturer's instructions. The aortas were isolated for *en face* immunostaining and aortic roots were used for Oil Red O and immunohistochemical staining. Briefly, mouse aortas were fixed with 4% paraformaldehyde for 2 h and dehydrated in 20% sucrose solution overnight and aortic span sections were stained by 0.5% Oil Red O for detecting lipid deposition in plaques. Positive areas of Oil Red O staining in the lesions were quantified using Image ProPlus 6.0 image analysis software. Mouse aortic roots were cut into serial frozen sections containing 300 cross-sections in 7 μm thickness, and ten cross-sections obtained from an interval of 30 sections were used for Oil Red O staining to analyze plaque areas. Atherosclerosis sections were blinded per individual to avoid the bias. Representative images of immunohistochemical staining of Mac-2 indicated the number of macrophages in atherosclerotic lesions.

Endothelium-Dependent Vaso-Protective Assay

Effects of PPP and PU on eNOS activity were detected by myograph. Briefly, Sprague Dawley male rats were euthanized by an overdose of carbon dioxide. The aorta was dissected and excised quickly and placed in ice-cold physiological saline solution (PSS) containing (in mmol/l) 119 NaCl, 4.7 KCl, 25 $NaHCO_3$, 1.17 KH_2PO_4, 1.17 $MgSO_4$, 1.6 CaCl, and 5.5 dextrose, gassed by 95% O_2–5% CO_2. The aorta was then cut into 3 mm vessel rings and the EC layer was stripped off in -endo group. The vessel rings were incubated with PPP or PU at different concentrations (from 1 to 75 μg/mL for PPP and 1–50 μg/mL for PU) in the presence and absence of nitric oxide synthase inhibitor L-N(G)-nitroarginine methyl ester (L-NAME, 100 μM). Vessel viability was detected by the stimulation of phenylephrine (PE) and acetylcholine. PE stimulation would constrict the integrated vessel ring and acetylcholine stimulation could relax the PE-constricted vessel. When the EC layer was removed or treated with L-NAME, acetylcholine could not make the constricted vessel ring relaxation.

Aortic Stenosis Studies in Rats

Aortic stenosis was induced in the rat by using a U-shaped titanium clip to constrict its abdominal aorta for 2 weeks as described (Miao et al., 2005; Zhou et al., 2012, 2013). Briefly, following anesthetization with isoflurane, the rat was laid supine and a lower midline abdomen incision was made. Thereafter, the part of the intestine was gently lifted out of abdomen and kept moist with saline throughout the surgical procedure. The aorta, left and right common iliac artery were exposed and the accompanying vein was carefully separated. The clip was held with a pair of forceps and placed around the isolated segment (approximate 1 cm from the arterial bifurcation) to partially constrict rat's abdominal aorta. The extent of clipping was controlled by placing a stopper of given size between the two arms of the forceps. Our previous study using ultrasonography indicated that placement of the U-clip resulted in a 65% constriction of the aorta diameter, which induced an accelerated forward laminar flow in the constricted region, followed by a pronounced oscillating flow with the existence of retrograde velocities downstream in the region of poststenotic dilatation (Zhou et al., 2012). The flow patterns and wall shear stress distributions in the constricted rat abdominal aorta were further characterized by computational fluid dynamic modeling using the Comsol Multiphysics software, which confirmed the existence of recirculation eddies with retrograde velocities downstream to the constricted sites (Zhou et al., 2012). PPP (750 mg/kg/day) or PU (500 mg/kg/day) was given daily by gavage 3 days before operation and the daily treatment lasted for additional 2 weeks. All rats were sacrificed by the end of treatment and aortas were perfusion-fixed with 4% paraformaldehyde at 120 mmHg. The fixed aortas were embedded in paraffin blocks for immunohistochemical studies.

Immunohistochemical Staining

Briefly, rats were euthanized with CO_2 and transcardially perfused with 150 mL of saline, followed by 500 mL of

10% (vol/vol) neutral-buffered zinc-formalin (Thermo Fisher Scientific). After perfusion, the aortas were harvested and postfixed in the fixative solution for 1 h, and then subjected to immunohistochemical staining. Tissues were washed in Tris-buffered saline (TBS) buffer, and the adventitia was carefully removed. The aorta was then longitudinally cut open with microdissecting scissors and pinned flatly on a black wax dissection pan. The luminal surface of the aorta was immediately blocked with 4% (vol/vol) FBS for 1 h, followed by incubation with the designed primary antibodies, including rabbit anti-phospho-Smad1/5 (1:100), rabbit anti-von Willebrand Factor (1:100) and mouse anti-α-SMA (1:100) at 4°C overnight. Dylight 594-conjugated anti-goat IgG (1:300; Jackson ImmunoResearch) and Alexa Fluor 488-conjugated goat anti-rabbit IgG (1:300; Invitrogen) were used as secondary antibodies. Samples were counterstained with 4′,6′-diamidino-2-phenylindole (DAPI) to show cell nuclei, rinsed three times in TBS, mounted with glycerol/PBS (1:1), and photographed with a Leica TCS SP5 confocal microscope.

Isolation and Culture of Primary ECs

ECs were isolated from fresh human umbilical cords with collagenase perfusion technique (Gimbrone, 1976). The cell pellets were resuspended in a culture medium consisting of medium 199 (M199, Gibco, Grand Island, NY, United States) supplemented with 20% fetal bovine serum (FBS, Gibco) and 1% penicillin/streptomycin (Gibco). ECs were grown in Petri dishes for 3 days and then seeded onto glass slides (75 by 38 mm, Corning, NY, United States) pre-coated with fibronectin (Sigma) to reach confluence. The culture medium was then replaced by the identical medium that contained only 2% FBS, and the cells were incubated for 24 h before use.

Oscillatory Flow Apparatus

The cultured ECs were subjected to shear stress in a parallel-plate flow chamber, as previously described (Zhou et al., 2012, 2013). The chamber containing the cell-seeded glass slide fastened with the gasket was connected to a perfusion loop system, kept in a constant-temperature controlled enclosure, and maintained at pH 7.4 by continuous gassing with a humidified mixture of 5% CO_2 in air. The fluid shear stress on the ECs can be estimated as $\tau = 6\mu Q/wh^2$, where τ is shear stress, Q is the flow rate, and μ is dynamic viscosity of the perfusate. The oscillatory flow is composed of a low level of mean flow with shear stress at 0.5 dynes/cm^2 supplied by a hydrostatic flow system and the superimposition of a sinusoidal oscillation using a piston pump with a frequency of 1 Hz and a peak-to-peak amplitude of 4 dynes/cm^2. In the *in vitro* experiments, ECs were pre-treated with PPP (50 μg/mL) or PU (50 μg/mL) for 30 min and then subjected to OSS (0.5 ± 4 dynes/cm^2) in a parallel-plate flow chamber for 4 or 24 h, or stimulated with BMP (100 ng/mL) for 30 min or TNF-α (100 U/mL) for 4 h in the presence of PPP or PU.

Immunofluorescence Assay (IFA)

ECs were seeded on coverslips in the culture plate wells and subjected to OSS. IFA was performed using antibodies against ki67 (Abcam), as described (Wang et al., 2016). The coverslips were mounted onto the slides using Fluoromount-G clear mounting medium containing DAPI (Southern Biotech, Birmingham, AL, United States). The fluorescence signals were observed *via* fluorescence microscopy (Nikon ECLIPSE Ti), and images were taken using NIS-Elements F software (Nikon).

Isolation and Culture of Primary VSMCs

Primary VSMCs were obtained from rat thoracic arteries, as described (Wang et al., 2015; Shen et al., 2019). Briefly, male SD rats weighing about 100 g were anesthetized and thoracic arteries were carefully excised, and the surrounding perivascular adipose tissues and connective tissues were trimmed off. The arteries were washed in 0.01 M PBS containing 100 g/mL streptomycin and 100 IU/mL penicillin. Arterial ectoderm was removed and sliced with an ophthalmic scissor, and the vascular endothelium was scratched gently using curved dissection forceps. Vascular tissues were washed and cut into small pieces. They were placed at the bottom of a 100 mm culture dish filled with 1 mL DMEM with 10% FBS, 100 g/mL streptomycin and 100 IU/mL penicillin and incubated at 37°C for 6 h until they all stick to the bottom of the dish. Thereafter, culture medium was replenished every 4 days. The cells between passages 4 and 7 were used.

VSMC Migration Assay

The wound healing assay was performed to test migratory capability of VSMCs. Briefly, VSMCs were seeded into 24-well tissue culture plates. The cells were incubated in DMEM supplemented with 0.5% FBS for 24 h to reach 70–80% confluence. The cell layer was scratched gently with a new 200 μL pipette tip across the center of the well. The cells were washed three times in 1 × PBS to remove the detached cells and incubated in DMEM supplemented with 0.5% FBS. The cells were treated with TNF-α (100 U/mL) in the absence and presence of PPP or PU for additional 24 h, and then washed twice in 1 × PBS and finally stained with 1% crystal violet in 2% ethanol for 30 min. Photos were taken for the stained monolayer on a microscope. Multiple views of each well were documented, and each experimental group was repeated 5 times.

Western Blot Analysis

The cells were lysed with a buffer containing 1% NP-40, 0.5% sodium deoxycholate, 0.1% SDS, and a protease inhibitor mixture (PMSF, aprotinin, and sodium orthovanadate). The total cell lysate (100 μg of protein) was separated by SDS-polyacrylamide gel electrophoresis (PAGE) (12% running, 4% stacking) and analyzed using the designated antibodies and detected by Western-Light chemilumi-nescent detection system (Applied Biosystems, Foster City, CA).

RNA Isolation and Quantitative Real-Time PCR (RT-PCR)

Total RNA was extracted using Trizol reagent (Invitrogen, United States) and the first-strand cDNA was generated using an RT kit (Invitrogen, United States). Quantitative real-time PCR was performed using primers shown in **Supplementary Table 2**.

Amplifications were performed using an Opticon-Continuous Fluorescence Detection System (MJ Research) with Eva Green fluorescence dye (Molecular Probes, Eugene, United States). All samples were quantitated by using the comparative CT method for relative quantitation of gene expression, normalized to GAPDH levels.

Statistical Analysis

All statistical analyses were performed using GraphPad Prism for Windows (Version 4, San Diego, CA, United States). Values were expressed as mean ± standard error of the mean (SEM). All data sets were tested for normal distribution. For normally distributed data, unpaired *t*-test, one-way ANOVA with Tukey post-test or paired *t*-test were used as most appropriate. All results were considered significantly as $p < 0.05$.

RESULTS

The Anti-atherogenic Effect of PPP

LDLR$^{-/-}$ mice in 6 weeks old were fed with a HFD and treated daily with PPP for 12 weeks (**Figure 1A**). The *En face* immunostaining revealed that treatment with PPP at 750 mg/kg reduced the areas of Oil Red O-stained plaques by 56% in mouse aortas, whereas PPP at 250 mg/kg and 500 mg/kg decreased the plaque areas by 23 and 37%, respectively. These data indicate that

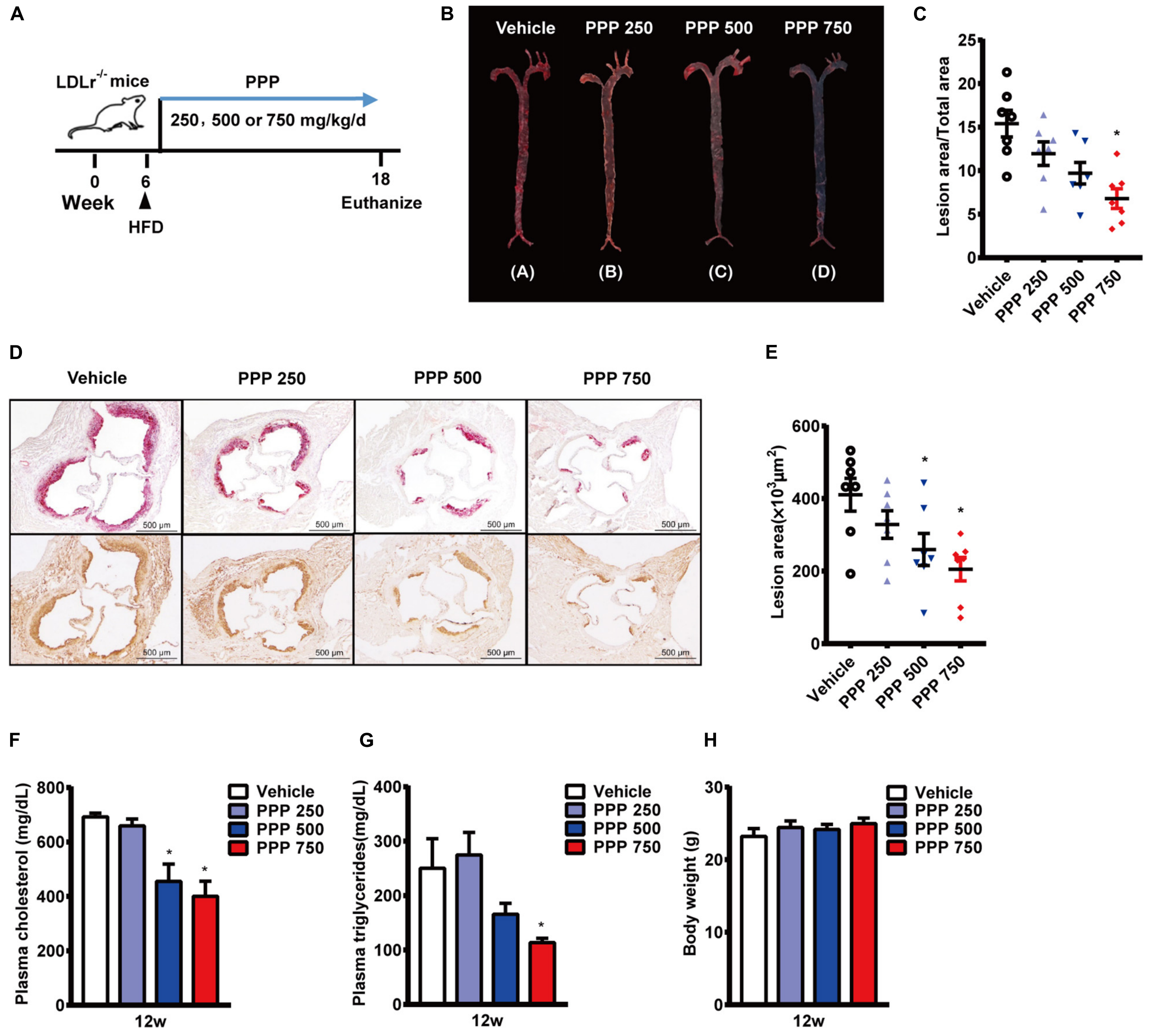

FIGURE 1 | Anti-atherogenic effects of PPP on LDLR$^{-/-}$ mice fed with HFD. **(A)** Schematic diagram of the experiments; **(B,C)** representative images of Oil Red O staining of mouse aortas **(B)** and quantitative results **(C)**; **(D,E)** representative images of Oil red O staining of mouse aortic outflow tract (upper) and immunostaining of Mac-2 (bottom); **(F,G)** plasma TC **(F)** and TG **(G)** levels after 12-week HFD feeding; **(H)** Body weights of the mice. PPP 250, PPP 500, and PPP 750 represent PPP at the doses of 250, 500, and 750 mg/kg/day, respectively, including $n = 6$ biological replicates. *$P < 0.05$ vs. Vehicle.

PPP exerts anti-atherogenic effects *in vivo* in a dose-dependent manner (**Figures 1B,C**).

The lesion area of the aortic root is an important parameter of aortic stenosis and correlates with the severity of atherosclerotic plaques. Thus, plaque areas were further measured in cross-sections of aortic roots. The Oil Red O-staining results showed that treatment with PPP at 750 mg/kg reduced the plaque area by 49% compared to the vehicle control, and plaque area in the aortic roots was also reduced in the other two PPP-treated groups, with 500 mg/kg being more effective than 250 mg/kg (**Figures 1D,E**). Immmunohistochemical staining of the aortic roots showed dramatic reduction in macrophage content stained by Mac-2 in the lesion areas from the PPP-treated LDLR$^{-/-}$ mice, indicating that PPP alleviated infiltration of inflammatory macrophages in the plaques (**Figure 1D**).

Disorder of plasma lipid metabolism has been deemed to play an important role in the progression of atherosclerosis. Treatment of LDLR$^{-/-}$ mice with 750 mg/kg or 500 mg/kg PPP significantly lowered plasma levels of TC and TG (**Figures 1F,G**). No difference was observed in body weight among all groups (**Figure 1**).

PU Is an Active Anti-atherogenic Compound in PPP

Since PU is the major bioactive compound in PPP, we investigated whether PU treatment produces the similar protective effects on atherosclerosis as PPP. PU was administered daily to LDLR$^{-/-}$ mice on HFD for 12 weeks (**Figure 2A**). The results showed that treatment with PU at 500 or

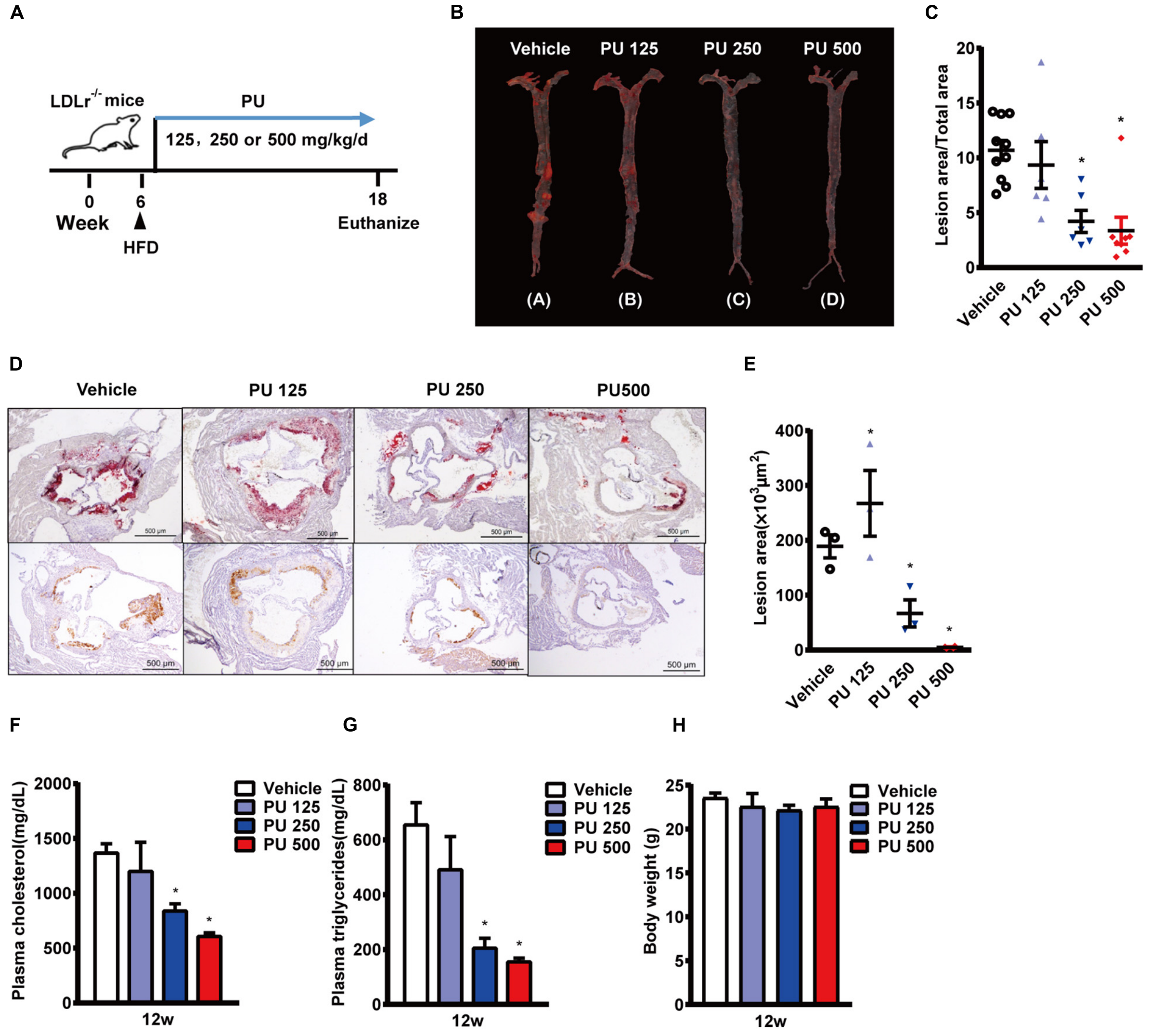

FIGURE 2 | Anti-atherogenic effects of PU on LDLR$^{-/-}$ mice fed with HFD. **(A)** Schematic diagram of the experiments; **(B,C)** representative images of Oil Red O staining of mouse aortas **(B)** and quantitative results **(C)**; **(D,E)** representative images of Oil red O staining of mouse aortic outflow tract (upper) and immunostaining of Mac-2 (bottom); **(F,G)**. plasma TC **(F)** and TG **(G)** levels after feeding HFD for 12 weeks; **(H)** Body weights of the mice. PU 125, PU 250, and PU 500 represent PU at the doses of 125, 250, and 500 mg/kg/day, respectively, including *n* = 5–10 biological replicates. $^{*}P < 0.05$ vs. Vehicle.

250 mg/kg reduced Oil Red O-stained atherosclerotic plaque areas in mouse aortas by 57 and 42%, respectively (**Figures 2B,C**). The Oil Red O staining of the plaque areas in aortic roots showed that PU treatment also decreased the lesion areas by 75 and 60%, respectively (**Figures 2D,E**). The number of infiltrated macrophages in aortic roots was reduced by PU (**Figure 2D**), and this effect was similar to that of PPP. In addition, PU treatment lowered plasma concentrations of TC and TG in HFD-fed LDLR$^{-/-}$ mice (**Figures 2F,G**) without affecting body weight (**Figure 2H**). These results indicate that PU is the major anti-atherogenic component in PPP.

Next, we examined whether PPP and PU could inhibit macrophages to uptake lipids and their transformation into foam cells. The Oil red O-staining results showed that both PPP and PU reduced ox-LDL uptake into macrophages and thus inhibited foam cell formation (**Supplementary Figure 2A**). Meanwhile, PPP and PU decreased the lipopolysaccharide (LPS, 1 μg/mL)-induced expression of pro-inflammatory cytokines or chemokines including IL-1β, IL-6, TNF-α, and MCP-1, and inducible nitric oxide synthase (iNOS) (**Supplementary Figures 2B–F**). The results showed that PPP and PU inhibited macrophage-directed foam cell formation and further blocked the inflammatory cascade of macrophages to retard atherosclerosis progression, which were in agreement with the results of previous reports (Kaplan et al., 2001; Rosenblat et al., 2013; Aharoni et al., 2015).

PPP and PU Exert Endothelium-Dependent Vaso-Protective Effects

Then we examined whether PPP and PU can exert atheroprotective effects beyond the above effects but through improving vascular function. It is known that ECs are exposed to regular laminar shear stress in the normal physiological condition, which stimulates the release of nitric oxide (NO) by the sustained activation of eNOS (Buga et al., 1991). However, eNOS activity is reduced at sites of perturbed shear stress with OSS (Wang et al., 2019). There was a study showing that pomegranate juice enhances the biological actions of NO (Ignarro et al., 2006). Therefore, we investigated the effects of PPP and PU on the vascular reactivity. Firstly, the aorta vessel rings were incubated with PPP or PU at the designated concentrations with or without eNOS inhibitor L-NAME. Myograph system was used to detect the relaxation on pre-constricted vessel rings with endothelium (control) or without endothelium (-endo). The results showed that PPP and PU had a relaxation effect on PE-induced vasoconstriction, and this effect was abolished when the aortas were treated with L-NAME or the endothelia on the aortas were stripped off, demonstrating that the vasodilation effects of PPP and PU are endothelium-dependent (**Figures 3A–D**). These results indicate that PPP and PU may exert atheroprotective effects through improvement of endothelial function.

PPP and PU Inhibit Activation of Smad1/5 in Vascular Endothelium Induced by Disturbed Flow *in vivo*

Our previous studies demonstrated that disturbed flow can induce force-specific activation of phospho-Smad1/5 in the post-stenotic sites, where the local flow is disturbed with OSS (Zhou et al., 2012). Thus, we examined whether PPP and PU could modulate this force-specific activation of Smad1/5 in post-stenotic sites *in vivo*. Rat abdominal aorta was subjected to a constriction by using a U-clip (**Figure 4A**), which can produce a disturbed flow region downstream to the constricted site, as described (Zhou et al., 2012, 2013). Either PPP or PU was administrated by gavage daily to the rats. Immunohistochemical examination of serial sections of the constricted aortas showed that the post-stenotic sites exhibited a high detection level of phospho-Smad1/5 in the luminal EC layer. By contrast, there was virtually no detectable staining of phospho-Smad1/5 in the upstream and middle point of constriction (**Figure 4B**). Treatment with PPP or PU dramatically decreased the elevation of phospho-Smad1/5 induced by disturbed flow at post-stenotic sites (**Figures 4C,D**). These results indicate that PPP and PU are effective in inhibiting force-specific activation of Smad1/5 in ECs induced by disturbed flow *in vivo*.

PPP and PU Inhibit OSS-Induced Smad1/5 Phosphorylation in ECs *in vitro*

We next further tested the effects of PPP or PU on Smad1/5 activation in ECs in response to disturbed flow with OSS. Application of OSS to ECs induced a sustained phosphorylation of Smad1/5 in ECs over the 24-h period. The phosphorylation of Smad1/5 in ECs was induced rapidly (4 h) by OSS and remained elevated after 24 h, as compared with static control ECs. This OSS-induced phosphorylation of Smad1/5 in ECs was normalized to the basal level after PPP or PU treatment (**Figures 5A,B**).

Previous studies showed that OSS-induced activation of Smad1/5 in ECs is specifically through the activation of BMPRs (Zhou et al., 2012, 2013). Thus, we treated ECs with BMP for 30 min to active BMPR and its downstream Smads as a control experiment to explore the effects of PPP and PU on the BMP-elicited signaling in ECs. The results showed that PPP and PU significantly suppressed BMP-induced phosphorylation of Smad1/5 in ECs (**Figure 5C**).

PPP and PU Inhibit OSS-Induced Pro-inflammatory Responses of ECs

EC inflammation is the early event in the pathogenesis of atherosclerosis, and OSS can activate EC pro-inflammatory responses by triggering the release of signaling molecules such as TNF-α to promote atherosclerosis progression (Zeiher et al., 1991; Sun et al., 2019). Thus, ECs were stimulated with OSS for 4 h or TNF-α for 4 h to stimulate the pro-inflammatory conditions of ECs and the effects of PPP or PU were examined. As expected, both OSS and TNF-α augmented the expressions of ICAM-1, VCAM-1 and E-selectin at both mRNA and protein

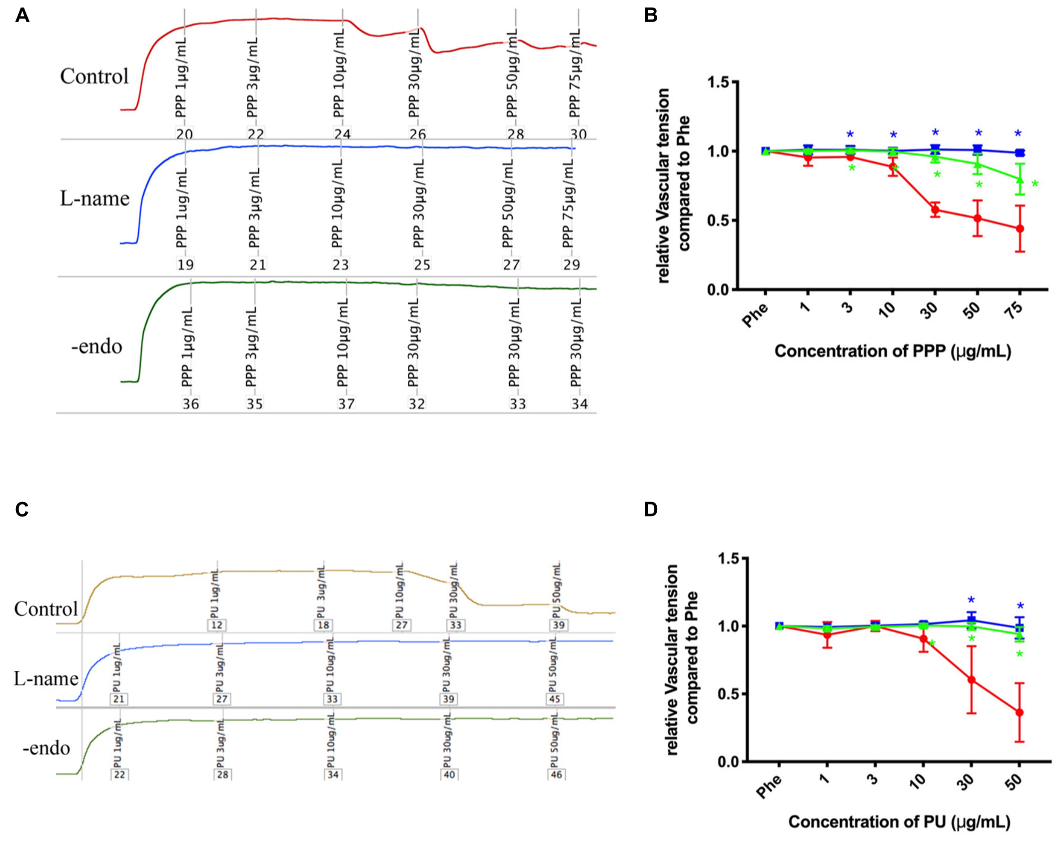

FIGURE 3 | Endothelium-dependent vaso-protective effects of PPP and PU. A-D. Endothelium-dependent vaso-protective effects of PPP **(A)** and PU **(C)** and the quantitative results [**(B,D)**, respectively], including $n = 4–6$ biological replicates. $^*P < 0.05$ vs. Control.

levels in ECs (**Supplementary Figure 3** and **Figure 6**). Pre-treatment with PPP or PU abolished either OSS or TNF-α–induced protein expression of these molecules (**Figures 6A,B**). Likewise, mRNA expression of these genes was also reversed by PPP or PU treatment (**Supplementary Figures 3A,B**). These results indicate that PPP and PU exert inhibitory effects on OSS-induced pro-inflammatory responses in ECs.

PPP and PU Inhibit OSS-Induced Proliferation of ECs

OSS-induced inflammation promotes proliferation of ECs. PPP or PU treatment significantly decreased protein expression of the pro-inflammatory molecules ICAM-1 and E-selectin in ECs after exposing to OSS for 24 h (**Figures 7A,B**). In addition, OSS-induced upregulation of cell cycle regulatory proteins in ECs, including Cyclin A and pRb, was all repressed by treating the ECs with either PPP or PU (**Figures 7A,B**). Results of immunofluorescence staining of Ki67, a marker of EC proliferation, showed that PPP or PU treatment significantly suppressed OSS-induced EC proliferation (**Figure 7C**). These data demonstrated that PPP and PU could inhibit force-specific activation of Smad1/5, which consequently attenuated pro-inflammatory responses and proliferation of ECs induced by disturbed flow with OSS.

PPP and PU Inhibit TNF-α-Induced VSMC Migration, Phenotypic Modulation, and Pro-inflammatory Responses

Injured ECs and activated monocytes in plaques can release various growth factors, such as platelet-derived growth factor (PDGF), to promote migration and phenotypic modulation of VSMCs (Schachter, 1997). Since migration, proliferation, and phenotypic modulation of VSMCs are the critical factors contributing to the progression of atherosclerosis (Gomez and Owens, 2012), we first examined the effects of PPP and PU on TNF-α-induced migration of VSMCs using the wound-healing assay. The results showed that PPP and PU inhibited TNF-α-induced migration of VSMCs (**Figure 8A**). To further explore the effects of PU on phenotypic modulation of VSMCs, the gene expression of the contractile VSMC marker, i.e., SMα-actin, was determined (**Figure 8B**). The results showed that SMα-actin expression was reduced by TNF-α and this effect was reversed by PU treatment. The synthetic phenotype of VSMCs can release pro-inflammatory IL-6, and c-fos was shown to promote VSMC proliferation (Sylvester et al., 1998). We found that PU inhibited TNF-α-induced expression of IL-6 and c-fos in VSMCs (**Figure 8C**). Taken together, these results indicate that PPP and PU can protect against TNF-α-induced proliferation, migration,

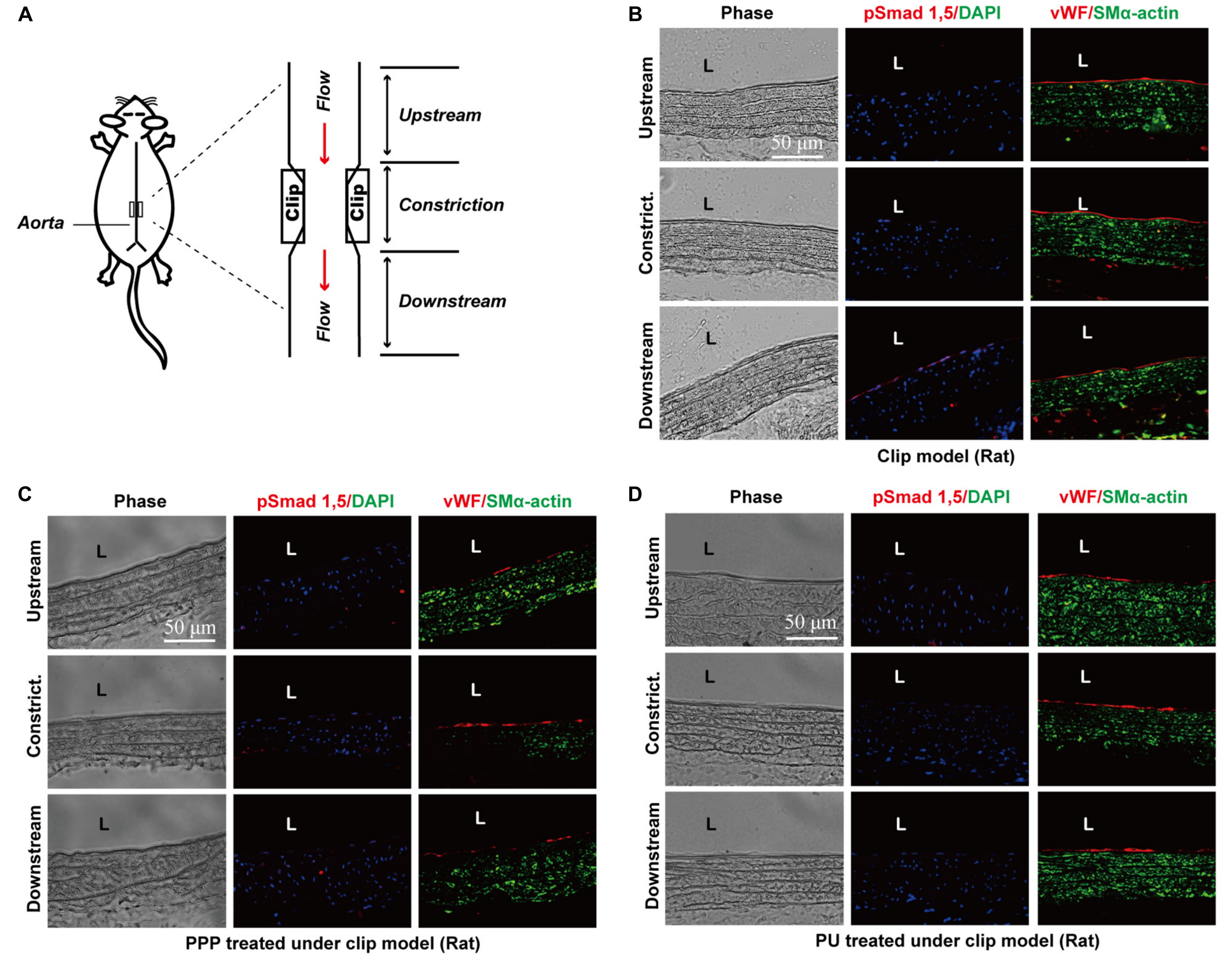

FIGURE 4 | PPP and PU inhibit force-specific activation of Smad1/5 in ECs induced by disturbed flow *in vivo*. A rat model with abdominal aortic stenosis was established by partially constricting rat abdominal aorta using a U-clip **(A)**. Protein expressions of phospho-Smad1/5/vWF/SMα-actin in the upstream, middle point, and downstream areas of the constricted sites were detected by immunofluorescence staining. **(B)** saline treatment group, **(C)** PPP treatment group, and **(D)** PU treatment group (five independent experiments performed).

inflammation, and phenotypic modulation in VSMCs. All of these responses participate in the progression of atherosclerosis.

DISCUSSION

Accumulating evidence show that polyphenols from pomegranate fruit, juice and PE are beneficial to human health (Al-Jarallah et al., 2013; Kalaycioglu and Erim, 2017). Extracts from natural plants may have potential to be developed as new drugs for prevention and treatment of cardiovascular diseases (AlMatar et al., 2018).

Previous studies have shown that PE exerts an anti-atherogenic effect (Aviram et al., 2000; Kaplan et al., 2001; Rosenblat et al., 2006; Estrada-Luna et al., 2019), and lipid-lowering effect may account for part of its anti-atherogenic properties (Hou et al., 2019). In the present study, we used a mouse model of atherosclerosis through feeding LDLR$^{-/-}$ mice with HFD for 12 weeks. The results showed that both PPP and PU can lower the lipids and reduce plaque formation. The effect of PU was greater than PPP, suggesting that PU is the effective anti-atherogenic agent in PPP. These results are consistent with the previous report showing that PE reduces plasma lipid levels in SR-B1/apoE double knockout mice (Al-Jarallah et al., 2013). In addition, other researchers reported that PE protects against atherosclerosis through inhibiting foam cell formation in the lesion areas (Aharoni et al., 2015; Bi et al., 2019). Our results provide the first line of evidence to show that treatment of macrophages with PPP or PU reduces ox-LDL uptake and inhibits LPS-induced pro-inflammatory responses, manifested by reduced mRNA expression of several pro-inflammatory factors, including IL-6, IL-1β, iNOS, MCP-1, and TNF-α.

Endothelial dysfunction is the initial step for the development of atherosclerosis. Disturbed flow with OSS is highly recognized to be the initial cause of EC dysfunction and pathogenesis of atherosclerosis (Buga et al., 1991; Lee et al., 2015). Under normal

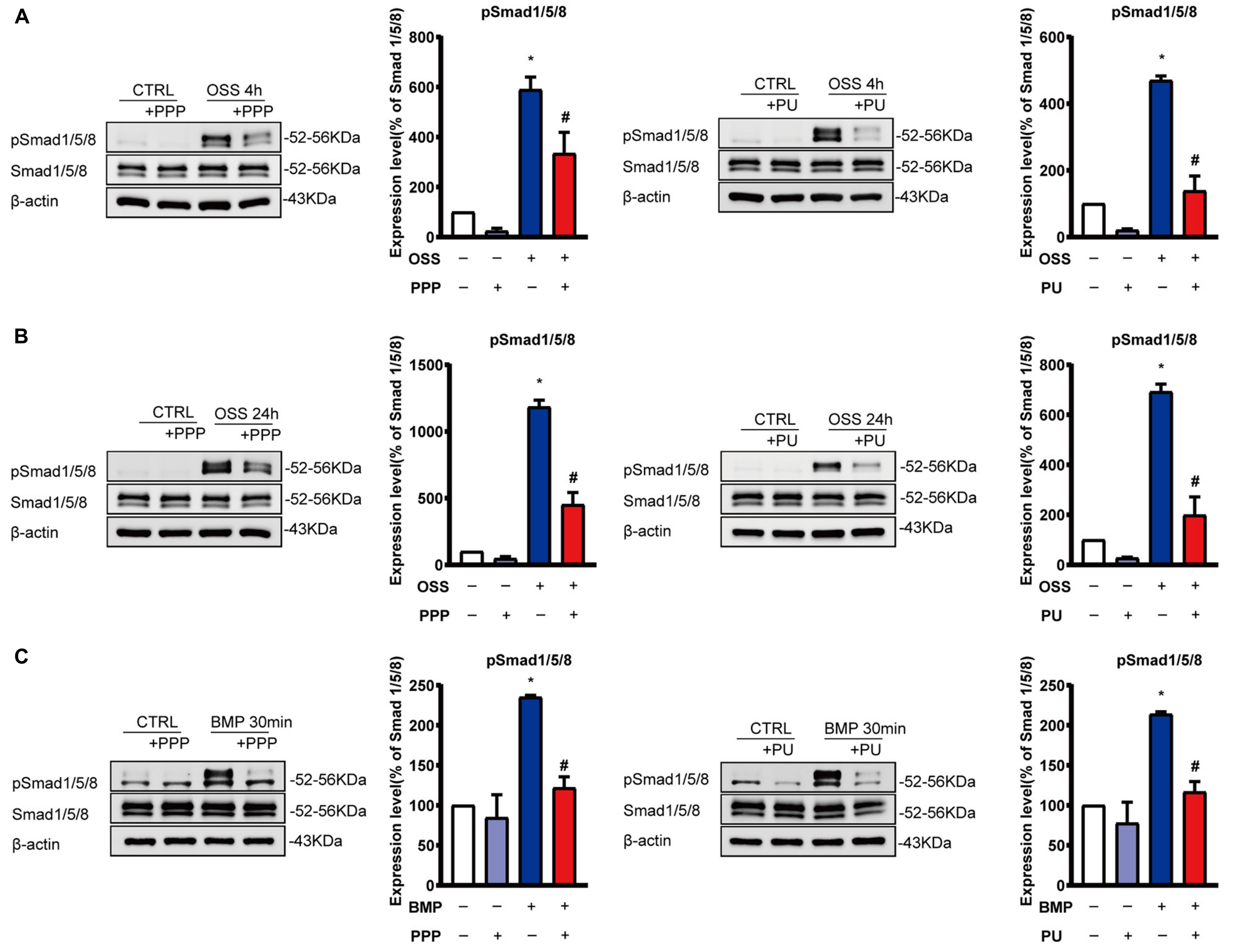

FIGURE 5 | PPP and PU inhibit Smad1/5 activation in ECs induced by OSS or BMP. **(A–C)** Western blot analysis of protein expression of the indicated molecules in ECs induced by OSS for 4 h **(A)** or 24 h **(B)** and BMP for 30 min **(C)**. Blot is a representative of five independent experiments. *$P < 0.05$ vs. Vehicle, $^{\#}P < 0.05$ vs. Model.

physiological condition, the hemodynamic forces stimulate NO release through expressing eNOS in ECs (Silacci et al., 2001), whereas eNOS activity is shown to be reduced at sites of perturbed shear stress (Go et al., 2014; Marchio et al., 2019). Previous studies showed that PE ameliorates perturbed shear stress-related atherosclerosis by regulating the expression of eNOS and oxidation-related genes in ECs (de Nigris et al., 2005; de Nigris et al., 2007). In addition, pomegranate juice was shown to enhance the biological actions of NO (Ignarro et al., 2006). Our results advanced the new notion to demonstrate that the vaso-protective effects of PPP and PU are endothelium-dependent. All these results suggest that the anti-atherogenic effects of PPP and PU may be attributable to their EC protective effects under disturbed flow with OSS.

Earlier studies suggest that laminar blood flow with PSS in the straight part of the arterial tree modulates cellular signaling and EC function, and is anti-atherogenic (Qin et al., 2007). By contrast, disturbed flow and its associated OSS in the branches and curvatures of the arterial tree promote EC dysfunction and thus aggravate atherosclerosis (Chiu and Chien, 2011). Our previous studies (Zhou et al., 2012, 2013) investigated the role of OSS in modulating EC mechanotransduction and hence the development of atherosclerosis, and demonstrated that EC layer expressed high levels of phosphorylation of BMPR-specific Smad 1/5 in the lesion areas exposed to disturbed flow with OSS. In this study we further generated an *in vivo* disturbed flow/OSS model in rats by using an U-shaped clip to constrict the rat abdominal aorta, and the results showed that high levels of phospho-Smad 1/5 were detected in the EC layer at post-stenotic regions of rat aortas, where disturbed flow with OSS occurred. PPP or PU administration significantly inhibited the OSS-induction of phospho-Smad 1/5 in the stenosed areas. *In vitro* studies on the ECs subjected to OSS also showed that PPP and PU attenuated OSS-induced Smad1/5 activation. In addition, PPP and PU could also reverse BMP-induced Smad1/5 activation. Our previous

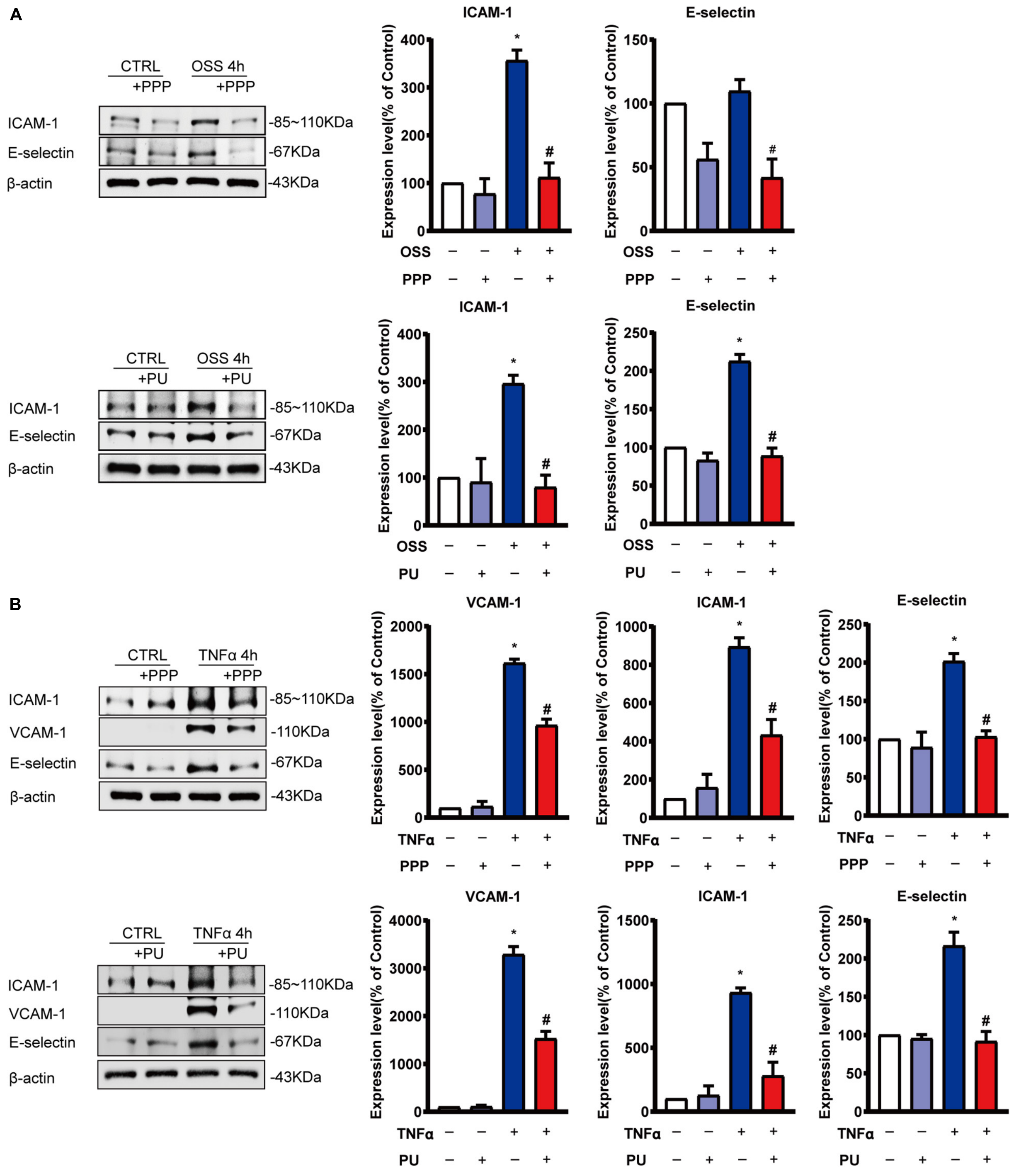

FIGURE 6 | PPP and PU inhibit pro-inflammatory responses of ECs induced by OSS or TNF-α. **(A,B)** Western blot analysis and quantitative results of the effects of PPP and PU on OSS—**(A)** or TNF-α **(B)**—induced pro-inflammatory responses of ECs. Blot is a representative of five independent experiments. *$P < 0.05$ vs. Vehicle, $^{\#}P < 0.05$ vs. Model.

studies have demonstrated that disturbed flow with OSS can induce Smad1/5 phosphorylation through the sustained induction of bone morphogenetic protein receptor (BMPR) type IB (BMPRIB)-αvβ3 integrin association in ECs (Zhou et al., 2012, 2013). This OSS-induced sustained association of BMPRIB-αvβ3 integrin was mediated by the intracytoplasmic kinase domain of BMPRII and subsequently activated the Shc/focal adhesion kinase (FAK)/extracellular signal-regulated kinase (ERK) cascade, leading to Smad1/5 activation. Thus, it is possible that PPP and PU may share common pathways

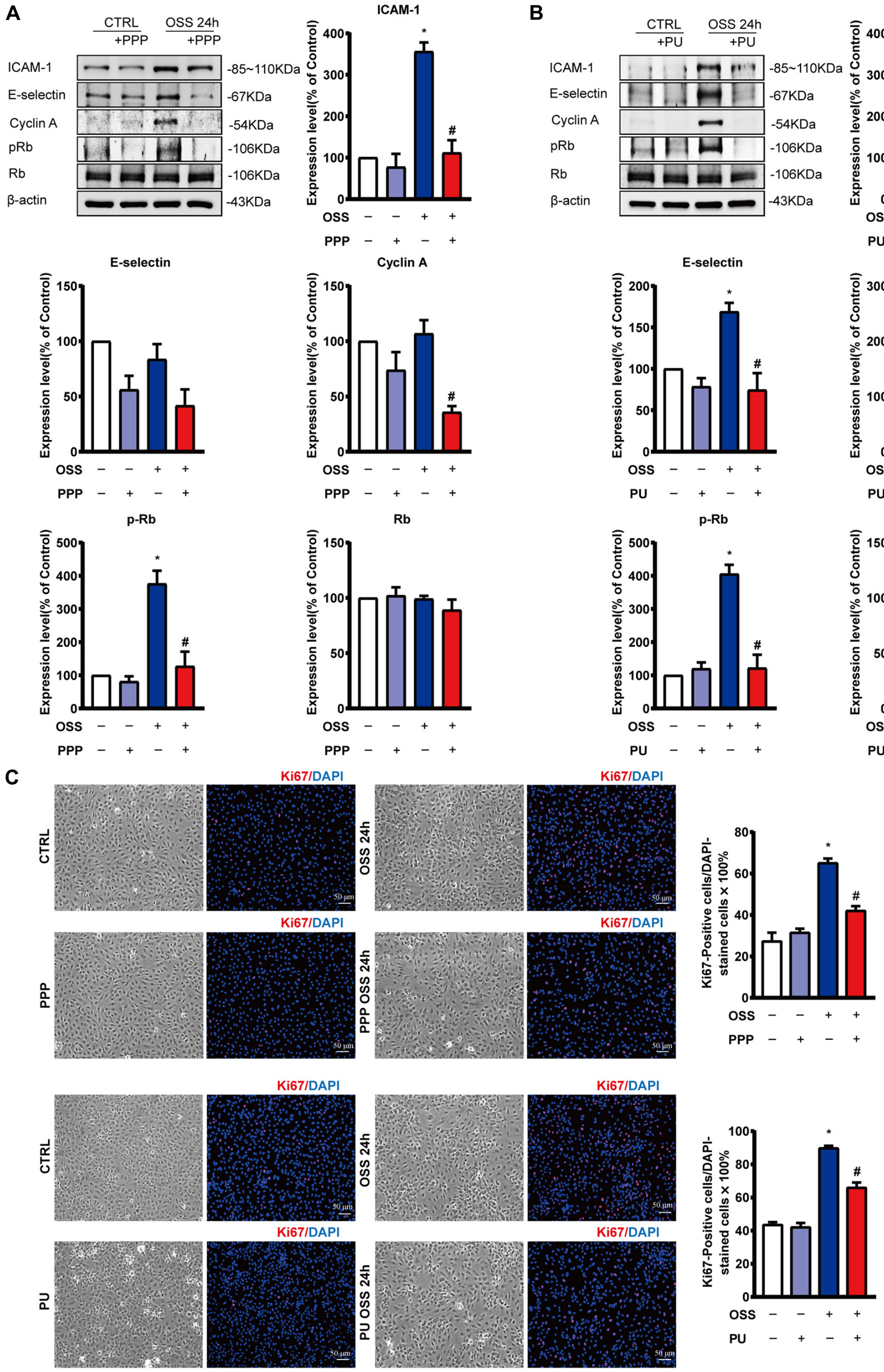

FIGURE 7 | PPP and PU inhibit pro-inflammatory responses and proliferation of ECs induced by OSS. **(A,B)** Western blot analysis and quantitative results of the effects of PPP **(A)** or PU **(B)** on the expression of pro-inflammatory molecules ICAM-1, E-selectin and cell cycle regulatory proteins Cyclin A and pRb/Rb in ECs. Blot is a representative of five independent experiments. Ki67 immunostaining indicates that PPP/PU. **(C)** Inhibits OSS-induced EC proliferation (five independent experiments performed). $^{*}P < 0.05$ vs. Vehicle, $^{\#}P < 0.05$ vs. Model.

to exert regulatory effects on Smad1/5 activation through the BMPRII/BMPRIB-αvβ3 integrin signaling cascade in ECs in response to disturbed flow or cytokines/growth factors. The detailed mechanisms by which PPP and PU exert protective effects on ECs remain an interesting issue that warrants further investigation.

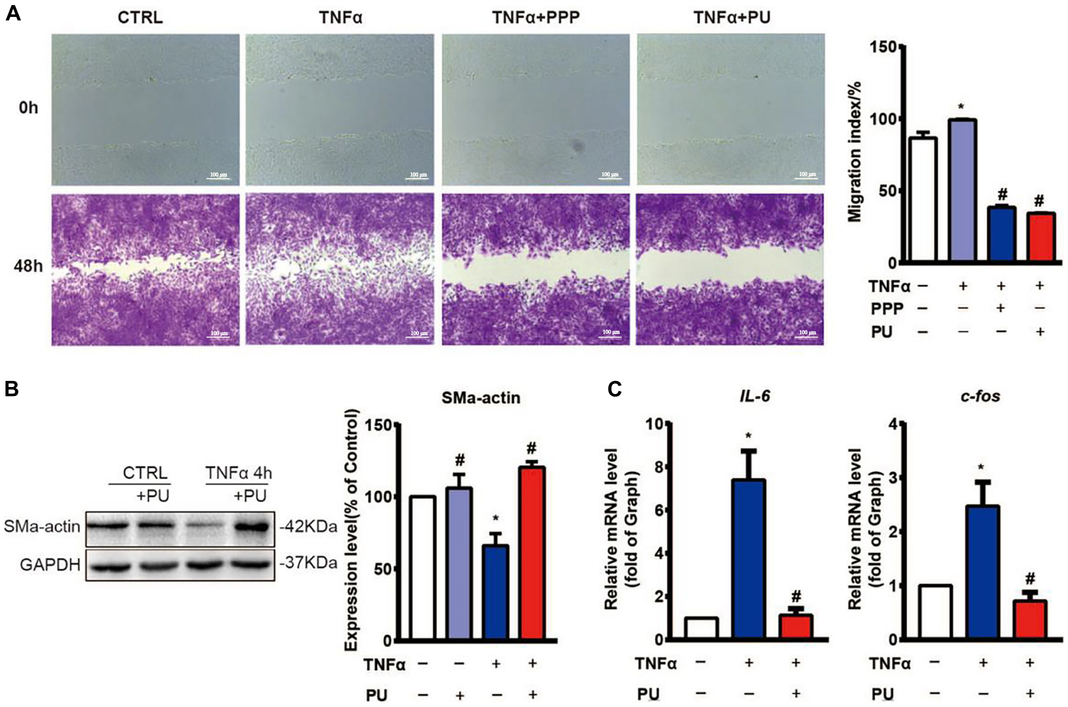

FIGURE 8 | PPP and PU inhibit migration, phenotypic modulation and inflammation in VSMCs induced by TNF-α. **(A)** The migration of VSMCs was detected by wound-healing assay (three independent experiments performed). **(B)** Western blot analysis and quantitative results of the effects of PU on α-SMA expression in VSMCs. Blot is a representative of four independent experiments. **(C)** Real time PCR results on the IL-6 and c-fos mRNA expressions. Experiments were repeated five times independently. $^{*}P < 0.05$, vs. Vehicle, $^{\#}P < 0.05$ vs. Model.

Previous studies indicated that OSS promotes inflammation and proliferation of vascular endothelium to aggravate EC dysfunction (Ajami et al., 2017; Sun et al., 2019). Application of OSS to ECs activated Smad 1/5 and led to up-regulation of cyclin A and down-regulation of p21 and p27 in ECs and hence EC proliferation (Zhou et al., 2012, 2013). Our results showed that PPP or PU treatment greatly retards cell cycle progression and proliferation of ECs. Besides, Gimbrone and Garcia-Cardena (2016) reported that OSS up-regulated the expression of adhesion molecules such as ICAM-1 and VCAM-1, which increased the recruitment of monocytes to endothelium, thus promoting vascular remodeling. Indeed, up-regulations of ICAM-1, VCAM-1, and E-selection in ECs after OSS exposure or TNF-α induction were also observed in the present study, and PPP or PU treatment inhibited the pro-inflammatory responses of ECs. We also found that the effect of PU on ICAM-1/VCAM-1 is more effective than PPP. This result is probably due to the reason that PU is a purified, effective compound of PPP, which is only a mixture. To sum up, our study advanced the new notion that treatment with PPP or PU can inhibit disturbed flow/OSS-induced activation of Smad1/5 and strongly suppressed the pro-inflammatory responses and proliferation of ECs induced by disturbed flow with OSS.

There is considerable evidence that laminar flow and associated shear stress significantly inhibit EC cell cycle progression and proliferation and enhance EC migration, and hence are atheroprotective. In contrast, disturbed flow with OSS can promote EC proliferation and inhibit EC migration, and hence is thought to be atherogenic (Chiu and Chien, 2011). Our previous studies also demonstrated that disturbed flow-induced activation of Smad1/5 can promote EC cell cycle progression and proliferation, which may contribute to the formation and progression of atherosclerosis (Zhou et al., 2012, 2013). In addition, there has been considerable evidence that disturbed flow with OSS or reduction in blood blow and shear stress can induce EC apoptosis and death (Chiu and Chien, 2011). Whether PPP/PU can modulate EC migration and exert protective effects on ECs to inhibit disturbed flow-induced EC apoptosis and death warrant further investigation.

In addition to ECs, VSMCs also play a vital role in maintaining vascular integrity and normal physiological function (Ross, 1975; Chistiakov et al., 2015; Lao et al., 2015). The aberrant interaction between ECs and VSMCs under pathological conditions promotes the occurrence and development of cardiovascular diseases, including atherosclerosis (Lao et al., 2015). It is widely accepted that VSMCs undergo phenotypic modulation during the progression of atherosclerosis, and the contractile phenotype of VSMCs converts to the synthetic phenotype, which triggers release of many pro-inflammatory factors, such as IL-6. Growth factors and inflammatory cytokines released from the injured ECs or other types of inflammatory cells in the plaques promote migration and pathological phenotypic modulation of VSMCs. Moreover, c-fos was shown to promote VSMC pathological proliferation (Hsieh et al., 1998; Sylvester et al., 1998;

Fang et al., 2004). OSS-induced EC injury may promote abnormal activation of VSMCs, thereby accelerating pathological remodeling of blood vessels and promoting atherosclerosis. Here we reported for the first time that PU may inhibit migration, proliferation and phenotypic modulation of VSMCs induced by TNF-α, suggesting that PU has protective effects on VSMCs in response to inflammation. In addition to the direct effects of PPP/PU on VSMCs, it is also possible that the protective effects of PPP/PU on VSMCs might come from the anti-inflammatory effects of PPP/PU on ECs which may reduce the release of cytokines, such as TNF-α.

In summary, the present study demonstrates for the first time that PPP and PU protect EC dysfunction by inhibiting OSS-induced proliferation and inflammation. These protective effects of PPP and PU may be attributable to their inhibition of force-specific activation of Smad1/5 in ECs. Furthermore, the present results show that PPP and PU can inhibit inflammation, migration and phenotypic modulation of VSMCs under pro-inflammatory stimulation. Our findings provide new insights into the mechanisms by which PPP and PU inhibit disturbed flow/inflammation-induced EC dysfunction and VSMC proliferation, migration, and phenotypic modulation, with the consequent inhibition in atherosclerosis.

DATA AVAILABILITY STATEMENT

The original contributions presented in the study are included in the article/**Supplementary Material**, further inquiries can be directed to the corresponding author/s.

ETHICS STATEMENT

The studies involving human participants were reviewed and approved by the experiments for the use of human umbilical cords were approved by the Hospital Human Subjects Review Committee (IRB Approval Nos. CGH-P101088 and CGH-CT9672) of Hsinchu Cathay General Hospital and were conducted under the guidelines established by the Ethics Review Board of National Health Research Institutes, Taiwan. Written informed consent was obtained from all individuals. The patients/participants provided their written informed consent to participate in this study. The animal study was reviewed and approved by This study was carried out in accordance with the principles of the Basel Declaration and Recommendations of Animal Care and Use Committee and PU IRB Laboratory Animal Welfare Committee in Peking University; the latter committee approved the protocol in this study (Approval No. LA2017193).

AUTHOR CONTRIBUTIONS

RQ and J-JC designed the study and revised the manuscript. X-LG and G-ZM prepared PPP extracts, purified PU, and analyzed the contents of PPP and PU by HPLC. Z-YC helped preparation and analysis of PPP and PU. GA and GL analyzed the data, prepared the figures, and wrote the manuscript. GL and W-LS performed *in vivo* studies. GA, C-IL, and P-LL performed *in vitro* experiments. Y-XW and X-YT performed endothelium-dependent vaso-protective assay. All authors read and approved the final manuscript.

FUNDING

This work was supported by the National Natural Science Foundation of China (Nos. U1803125, 81770268, and 81360054 to RQ), the National Key Research and Development Program of China (2019YFE0113500 to RQ), the Key Research and Development Projects of Xinjiang Uygur Autonomous Region (No. 2016B03044-1 to X-LG), and the Taiwan Ministry of Science and Technology grants MOST 109-2326-B-400-006 and MOST 109-2320-B-400-010-MY3 (to J-JC), TMU grant 108-AE1-B51 (to J-JC).

ACKNOWLEDGMENTS

We thank for Prof. Yu Huang from Chinese University of Hong Kong for his great research suggestion and his help in revising the manuscript.

SUPPLEMENTARY MATERIAL

The Supplementary Material for this article can be found online at: https://www.frontiersin.org/articles/10.3389/fcell.2021.697539/full#supplementary-material

REFERENCES

Aharoni, S., Lati, Y., Aviram, M., and Fuhrman, B. (2015). Pomegranate juice polyphenols induce a phenotypic switch in macrophage polarization favoring a M2 anti-inflammatory state. *BioFactors* 41, 44–51. doi: 10.1002/biof.1199

Ajami, N. E., Gupta, S., Maurya, M. R., Nguyen, P., Li, J. Y., Shyy, J. Y., et al. (2017). Systems biology analysis of longitudinal functional response of endothelial cells to shear stress. *Proc. Natl. Acad. Sci. U.S.A.* 114, 10990–10995. doi: 10.1073/pnas.1707517114

Al-Jarallah, A., Igdoura, F., Zhang, Y., Tenedero, C. B., White, E. J., MacDonald, M. E., et al. (2013). The effect of pomegranate extract on coronary artery atherosclerosis in SR-BI/APOE double knockout mice. *Atherosclerosis* 228, 80–89. doi: 10.1016/j.atherosclerosis.2013.02.025

AlMatar, M., Islam, M. R., Albarri, O., Var, I., and Koksal, F. (2018). Pomegranate as a possible treatment in reducing risk of developing wound healing, obesity, neurodegenerative disorders, and diabetes mellitus. *Mini Rev. Med. Chem.* 18, 507–526. doi: 10.2174/1389557517666170419114722

Atrahimovich, D., Khatib, S., Sela, S., Vaya, J., and Samson, A. O. (2016). Punicalagin induces serum low-density lipoprotein influx to macrophages. *Oxid. Med. Cell. Longev.* 2016:7124251.

Atrahimovich, D., Samson, A. O., Khattib, A., Vaya, J., and Khatib, S. (2018). Punicalagin decreases serum glucose levels and increases PON1 activity and

HDL anti-inflammatory values in Balb/c mice fed a high-fat diet. *Oxid. Med. Cell. Longev.* 2018:2673076.

Aviram, M., Dornfeld, L., Rosenblat, M., Volkova, N., Kaplan, M., Coleman, R., et al. (2000). Pomegranate juice consumption reduces oxidative stress, atherogenic modifications to LDL, and platelet aggregation: studies in humans and in atherosclerotic apolipoprotein E-deficient mice. *Am. J. Clin. Nutr.* 71, 1062–1076. doi: 10.1093/ajcn/71.5.1062

Bi, Y., Chen, J., Hu, F., Liu, J., Li, M., and Zhao, L. (2019). M2 macrophages as a potential target for antiatherosclerosis treatment. *Neural Plast.* 2019:6724903.

Buga, G. M., Gold, M. E., Fukuto, J. M., and Ignarro, L. J. (1991). Shear stress-induced release of nitric oxide from endothelial cells grown on beads. *Hypertension* 17, 187–193. doi: 10.1161/01.hyp.17.2.187

Chang, K., Weiss, D., Suo, J., Vega, J. D., Giddens, D., Taylor, W. R., et al. (2007). Bone morphogenic protein antagonists are coexpressed with bone morphogenic protein 4 in endothelial cells exposed to unstable flow in vitro in mouse aortas and in human coronary arteries: role of bone morphogenic protein antagonists in inflammation and atherosclerosis. *Circulation* 116, 1258–1266. doi: 10.1161/circulationaha.106.683227

Chistiakov, D. A., Orekhov, A. N., and Bobryshev, Y. V. (2015). Vascular smooth muscle cell in atherosclerosis. *Acta physiologica* 214, 33–50.

Chiu, J. J., and Chien, S. (2011). Effects of disturbed flow on vascular endothelium: pathophysiological basis and clinical perspectives. *Physiol. Rev.* 91, 327–387. doi: 10.1152/physrev.00047.2009

Chiu, J. J., Lee, P. L., Chen, C. N., Lee, C. I., Chang, S. F., Chen, L. J., et al. (2004). Shear stress increases ICAM-1 and decreases VCAM-1 and E-selectin expressions induced by tumor necrosis factor-[alpha] in endothelial cells. *Arterioscler. Thromb. Vasc. Biol.* 24, 73–79. doi: 10.1161/01.atv.0000106321.63667.24

Chiu, J. J., Usami, S., and Chien, S. (2009). Vascular endothelial responses to altered shear stress: pathologic implications for atherosclerosis. *Ann. Med.* 41, 19–28. doi: 10.1080/07853890802186921

de Nigris, F., Williams-Ignarro, S., Lerman, L. O., Crimi, E., Botti, C., Mansueto, G., et al. (2005). Beneficial effects of pomegranate juice on oxidation-sensitive genes and endothelial nitric oxide synthase activity at sites of perturbed shear stress. *Proc. Natl. Acad. Sci. U.S.A.* 102, 4896–4901. doi: 10.1073/pnas.0500998102

de Nigris, F., Williams-Ignarro, S., Sica, V., Lerman, L. O., D'Armiento, F. P., Byrns, R. E., et al. (2007). Effects of a pomegranate fruit extract rich in punicalagin on oxidation-sensitive genes and eNOS activity at sites of perturbed shear stress and atherogenesis. *Cardiovasc. Res.* 73, 414–423. doi: 10.1016/j.cardiores.2006.08.021

Estrada-Luna, D., Carreon-Torres, E., Bautista-Perez, R., Betanzos-Cabrera, G., Dorantes-Morales, A., Luna-Luna, M., et al. (2019). Microencapsulated pomegranate reverts High-Density Lipoprotein (HDL)-induced endothelial dysfunction and reduces postprandial triglyceridemia in women with acute coronary syndrome. *Nutrients* 11:1710. doi: 10.3390/nu11081710

Fang, L. H., Zhang, Y. H., Ma, J. J., Du, G. H., Ku, B. S., Yao, H. Y., et al. (2004). Inhibitory effects of tetrandrine on the serum- and platelet-derived growth factor-BB-induced proliferation of rat aortic smooth muscle cells through inhibition of cell cycle progression, DNA synthesis, ERK1/2 activation and c-fos expression. *Atherosclerosis* 174, 215–223. doi: 10.1016/j.atherosclerosis.2004.01.036

Gimbrone, M. A. Jr. (1976). Culture of vascular endothelium. *Prog. Hemost. Thromb.* 3, 1–28.

Gimbrone, M. A. Jr., and Garcia-Cardena, G. (2016). Endothelial cell dysfunction and the pathobiology of atherosclerosis. *Circ. Res.* 118, 620–636. doi: 10.1161/circresaha.115.306301

Go, Y. M., Son, D. J., Park, H., Orr, M., Hao, L., Takabe, W., et al. (2014). Disturbed flow enhances inflammatory signaling and atherogenesis by increasing thioredoxin-1 level in endothelial cell nuclei. *PLoS One* 9:e108346. doi: 10.1371/journal.pone.0108346

Gomez, D., and Owens, G. K. (2012). Smooth muscle cell phenotypic switching in atherosclerosis. *Cardiovasc. Res.* 95, 156–164. doi: 10.1093/cvr/cvs115

Hou, C., Zhang, W., Li, J., Du, L., Lv, O., Zhao, S., et al. (2019). Beneficial effects of pomegranate on lipid metabolism in metabolic disorders. *Mol. Nutr. Food Res.* 63:e1800773.

Hsieh, H. J., Cheng, C. C., Wu, S. T., Chiu, J. J., Wung, B. S., and Wang, D. L. (1998). Increase of reactive oxygen species (ROS) in endothelial cells by shear flow and involvement of ROS in shear-induced c-fos expression. *J. Cell. Physiol.* 175, 156–162. doi: 10.1002/(sici)1097-4652(199805)175:2<156::aid-jcp5>3.0.co;2-n

Ignarro, L. J., Byrns, R. E., Sumi, D., de Nigris, F., and Napoli, C. (2006). Pomegranate juice protects nitric oxide against oxidative destruction and enhances the biological actions of nitric oxide. *Nitric Oxide* 15, 93–102. doi: 10.1016/j.niox.2006.03.001

Kalaycioglu, Z., and Erim, F. B. (2017). Total phenolic contents, antioxidant activities, and bioactive ingredients of juices from pomegranate cultivars worldwide. *Food Chem.* 221, 496–507. doi: 10.1016/j.foodchem.2016.10.084

Kaplan, M., Hayek, T., Raz, A., Coleman, R., Dornfeld, L., Vaya, J., et al. (2001). Pomegranate juice supplementation to atherosclerotic mice reduces macrophage lipid peroxidation, cellular cholesterol accumulation and development of atherosclerosis. *J. Nutr.* 131, 2082–2089. doi: 10.1093/jn/131.8.2082

Lao, K. H., Zeng, L., and Xu, Q. (2015). Endothelial and smooth muscle cell transformation in atherosclerosis. *Curr. Opin. Lipidol.* 26, 449–456. doi: 10.1097/mol.0000000000000219

Lee, J., Packard, R. R., and Hsiai, T. K. (2015). Blood flow modulation of vascular dynamics. *Curr. Opin. Lipidol.* 26, 376–383. doi: 10.1097/mol.0000000000000218

Marchio, P., Guerra-Ojeda, S., Vila, J. M., Aldasoro, M., Victor, V. M., and Mauricio, M. D. (2019). Targeting early atherosclerosis: a focus on oxidative stress and inflammation. *Oxid. Med. Cell. Longev.* 2019:8563845.

Miao, H., Hu, Y. L., Shiu, Y. T., Yuan, S. L., Zhao, Y. H., Kaunas, R., et al. (2005). Effects of flow patterns on the localization and expression of VE-cadherin at vascular endothelial cell junctions: in vivo and in vitro investigations. *J. Vasc. Res.* 42, 77–89. doi: 10.1159/000083094

Qin, X., Tian, J., Zhang, P., Fan, Y., Chen, L., Guan, Y., et al. (2007). Laminar shear stress up-regulates the expression of stearoyl-CoA desaturase-1 in vascular endothelial cells. *Cardiovasc. Res.* 74, 506–514. doi: 10.1016/j.cardiores.2007.02.014

Rosenblat, M., Volkova, N., and Aviram, M. (2013). Pomegranate phytosterol (beta-sitosterol) and polyphenolic antioxidant (punicalagin) addition to statin, significantly protected against macrophage foam cells formation. *Atherosclerosis* 226, 110–117. doi: 10.1016/j.atherosclerosis.2012.10.054

Rosenblat, M., Volkova, N., Coleman, R., and Aviram, M. (2006). Pomegranate byproduct administration to apolipoprotein e-deficient mice attenuates atherosclerosis development as a result of decreased macrophage oxidative stress and reduced cellular uptake of oxidized low-density lipoprotein. *J. Agric. Food Chem.* 54, 1928–1935. doi: 10.1021/jf0528207

Ross, R. (1975). "Smooth muscle cell and atherosclerosis," in *Einundachtzigster Kongress. Verhandlungen der Deutschen Gesellschaft fur Innere Medizin*, 81, ed. B. Schlegel (Munich: J.F. Bergmann-Verlag), 843–847.

Schachter, M. (1997). Vascular smooth muscle cell migration, atherosclerosis, and calcium channel blockers. *Int. J. Cardiol.* 62(Suppl. 2), S85–S90.

Shen, W., Anwaier, G., Cao, Y., Lian, G., Chen, C., Liu, S., et al. (2019). Atheroprotective mechanisms of tilianin by inhibiting inflammation through down-regulating NF-kappaB pathway and foam cells formation. *Front. Physiol.* 10:825. doi: 10.3389/fphys.2019.00825

Silacci, P., Desgeorges, A., Mazzolai, L., Chambaz, C., and Hayoz, D. (2001). Flow pulsatility is a critical determinant of oxidative stress in endothelial cells. *Hypertension* 38, 1162–1166. doi: 10.1161/hy1101.095993

Sorescu, G. P., Sykes, M., Weiss, D., Platt, M. O., Saha, A., Hwang, J., et al. (2003). Bone morphogenic protein 4 produced in endothelial cells by oscillatory shear stress stimulates an inflammatory response. *J. Biol. Chem.* 278, 31128–31135. doi: 10.1074/jbc.m300703200

Sun, Z., Han, Y., Song, S., Chen, T., Han, Y., and Liu, Y. (2019). Activation of GPR81 by lactate inhibits oscillatory shear stress-induced endothelial inflammation by activating the expression of KLF2. *IUBMB Life* 71, 2010–2019. doi: 10.1002/iub.2151

Sylvester, A. M., Chen, D., Krasinski, K., and Andres, V. (1998). Role of c-fos and E2F in the induction of cyclin A transcription and vascular smooth muscle cell proliferation. *J. Clin. Invest.* 101, 940–948. doi: 10.1172/jci1630

Wang, Q., Liu, Z., Ren, J., Morgan, S., Assa, C., and Liu, B. (2015). Receptor-interacting protein kinase 3 contributes to abdominal aortic aneurysms via smooth muscle cell necrosis and inflammation. *Circ. Res.* 116, 600–611. doi: 10.1161/circresaha.116.304899

Wang, R., Zhang, Y., Xu, L., Lin, Y., Yang, X., Bai, L., et al. (2016). Protein inhibitor of activated STAT3 suppresses oxidized LDL-induced cell responses during atherosclerosis in apolipoprotein E-deficient mice. *Sci. Rep.* 6: 36790.

Wang, Z., Wang, F., Kong, X., Gao, X., Gu, Y., and Zhang, J. (2019). Oscillatory shear stress induces oxidative stress via TLR4 activation in endothelial cells. *Mediators Inflamm.* 2019:7162976.

Zeiher, A. M., Drexler, H., Wollschlager, H., and Just, H. (1991). Modulation of coronary vasomotor tone in humans. progressive endothelial dysfunction with different early stages of coronary atherosclerosis. *Circulation* 83, 391–401. doi: 10.1161/01.cir.83.2.391

Zhou, J., Lee, P. L., Lee, C. I., Wei, S. Y., Lim, S. H., Lin, T. E., et al. (2013). BMP receptor-integrin interaction mediates responses of vascular endothelial Smad1/5 and proliferation to disturbed flow. *J. Thromb. Haemost.* 11, 741–755. doi: 10.1111/jth.12159

Zhou, J., Lee, P. L., Tsai, C. S., Lee, C. I., Yang, T. L., Chuang, H. S., et al. (2012). Force-specific activation of Smad1/5 regulates vascular endothelial cell cycle progression in response to disturbed flow. *Proc. Natl. Acad. Sci. U.S.A.* 109, 7770–7775. doi: 10.1073/pnas.1205476109

Zhou, J., Li, Y. S., and Chien, S. (2014). Shear stress-initiated signaling and its regulation of endothelial function. *Arterioscler. Thromb. Vasc. Biol.* 34, 2191–2198. doi: 10.1161/atvbaha.114.303422

Conflict of Interest: The authors declare that the research was conducted in the absence of any commercial or financial relationships that could be construed as a potential conflict of interest.

Advantages of publishing in Frontiers

OPEN ACCESS
Articles are free to read
for greatest visibility
and readership

FAST PUBLICATION
Around 90 days
from submission
to decision

HIGH QUALITY PEER-REVIEW
Rigorous, collaborative,
and constructive
peer-review

TRANSPARENT PEER-REVIEW
Editors and reviewers
acknowledged by name
on published articles

Frontiers
Avenue du Tribunal-Fédéral 34
1005 Lausanne | Switzerland

Visit us: www.frontiersin.org
Contact us: frontiersin.org/about/contact

REPRODUCIBILITY OF RESEARCH
Support open data
and methods to enhance
research reproducibility

DIGITAL PUBLISHING
Articles designed
for optimal readership
across devices

FOLLOW US
@frontiersin

IMPACT METRICS
Advanced article metrics
track visibility across
digital media

EXTENSIVE PROMOTION
Marketing
and promotion
of impactful research

LOOP RESEARCH NETWORK
Our network
increases your
article's readership